

THEORETICAL STUDIES OF FREE AND SUPPORTED
NANOALLOY CLUSTERS

by

RAMLI ISMAIL

A thesis submitted to
The University of Birmingham
for the examination of
DOCTOR OF PHILOSOPHY

School of Chemistry
University of Birmingham
July 2012

UNIVERSITY OF
BIRMINGHAM

University of Birmingham Research Archive

e-theses repository

This unpublished thesis/dissertation is copyright of the author and/or third parties. The intellectual property rights of the author or third parties in respect of this work are as defined by The Copyright Designs and Patents Act 1988 or as modified by any successor legislation.

Any use made of information contained in this thesis/dissertation must be in accordance with that legislation and must be properly acknowledged. Further distribution or reproduction in any format is prohibited without the permission of the copyright holder.

Abstract

Nanoclusters offer unique physical and chemical behaviour, with the possibility of fine-tuning size and structures. Clusters of transition metals of group 10 (Ni, Pd, Pt), group 11 (Cu, Ag and Au), and crossover combinations (nanoalloys) between the two groups are of importance for their excellent physical, catalytic, optical, electronic and magnetic properties. Upon alloying, activity, selectivity and stability enhancement is possible and another dimension arises – chemical ordering (*i.e.*, mixed *vs.* segregated phases). Detailed theoretical studies can extend our understanding of these complicated systems, giving a better understanding of experimental observations and allowing prediction of chemical and physical properties. In this research, a good balance between accuracy and computational cost in describing electronic structure was sought via a combined Empirical Potential (EP) - Density Functional Theory (DFT) method. At the EP level, global optimisation searches were performed using the Birmingham Cluster Genetic Algorithm and Basin-Hopping Monte Carlo algorithm coupled with potentials derived from the semi-empirical Gupta potential. The sensitivity of the potentials was further studied for various potential parameterisations. The DFT calculations were performed with the NWChem and Quantum ESPRESSO codes. At the EP level, exploration of Pd-Au, Pd-Pt and Ni-Al clusters evidence the transition from polyicosahedra – decahedra – face-centered cubic (fcc), for small (≤ 100 atoms) clusters, but interrupted at 38- and 98-atoms, due to the magic size of the fcc truncated octahedron (TO) and Leary tetrahedron, respectively. Below 50 atoms, these motifs are energetically very competitive, which led to a detailed structural study for the 34- and 38-atom clusters, as a function of composition. A qualitatively good agreement between EP and DFT was found, with a prevalence towards core-shell Dh₃₄ and TO₃₈ structure for Pd-Au and Pd-Pt clusters. The performance of empirical calculations varies with composition and these were investigated by calculations on a TO motif at fixed compositions – (32,6) and (6,32). The DFT calculations showed that the **average** potential gave a good estimation of the heteronuclear interactions of Pd-Au and Pd-Pt systems. However, biased parameters exhibit better behaviour for Ni-Al, Pt-Au, Cu-Pd and Cu-Pt clusters. On an MgO support, Pd-Au clusters showed significant size and composition effects, based on 30- and 40-atom cluster models with variation in the bimetallic compositions (Pd-rich, Au-rich and medium composition). Consistent with the available experimental findings, Pd atoms preferentially bind to the oxygen sites at the interface and good cluster-substrate epitaxy was observed. The results gave fair confidence for application of the empirical potential for larger clusters, for which global exploration with the *ab initio* methods was not feasible.

Abbreviations and Acronyms

ANND	average nearest-neighbour distance
BCGA	Birmingham Cluster Genetic Algorithm
BHMC	Basin-Hopping Monte Carlo
DFT	Density Functional Theory
DZ	basis sets of double- ζ
EAM	Embedded-Atom Model
ECP	effective core potentials
EP-DF	Empirical Potential - Density Functional Theory approach
EP	Empirical Potential method
GA	genetic algorithm
GGA	generalised gradient approximation
GM	global minimum
LDA	local density approximation
LSDA	local spin density approximation
NP	nanoparticle
PBE	Perdew-Burke-Ernzerhof exchange-correlation functional
PDF	pair distribution functions
PES	potential energy surface
PEW	parallel excitable walkers
PW91	Perdew-Wang exchange-correlation functional
PWscf	plane-wave self-consistent field
PZ81	Perdew-Zunger local-density approximations
QE	Quantum ESPRESSO – ESPRESSO stands for opEn Source Package for Research in Electronic Structure, Simulation, and Optimisation
TZVP	basis sets of triple- ζ -plus-polarization
XC	exchange-correlation

Structural Motifs Abbreviations

detailed description in Chapter 4

Dh-Ih	mixed decahedral - icosahedral motifs
Dh-cp(DT)	mixed decahedral-close-packed motifs with a double tetrahedral core
Dh-cp(T)	mixed decahedral-close-packed motifs with a single tetrahedron core
Dh	decahedral motifs
Ih	icosahedral motifs
LT	Leary tetrahedron
Oh-Ih	mixed octahedra-icosahedra
TO	truncated octahedron
bcc	body-centered cubic motifs
cp(T)	close-packed with a tetrahedral core
cp	close-packed motifs
fcc-hcp	mixed face-centred cubic-hexagonal close-packed motifs
fcc	face-centred cubic motifs
hcp	hexagonal close-packed motifs
inc-Ih-Mackay	incomplete Mackay-polyicosahedral motifs
inc-Ih-anti-Mackay	incomplete anti-Mackay-polyicosahedral motifs
plh	polyicosahedral motifs
plh⁶	polyicosahedra with 6 interpenetrating Ih ₁₃ units
plh⁷	polyicosahedra with 7 interpenetrating Ih ₁₃ units
plh⁸	polyicosahedra with 8 interpenetrating Ih ₁₃ units
plh¹²	polyicosahedra with a 12 interpenetrating Ih ₁₃ units
plh(LS)	low-symmetry polyicosahedra motifs
plh(T)	polyicosahedra with a 10 atom tetrahedron core
plh-M(DT)	incomplete Mackay-icosahedron with a double tetrahedral component
plh-M-pc⁵	five-fold pancake Mackay-icosahedron
plh-M	Mackay-polyicosahedral motifs
plh-aM	anti-Mackay-polyicosahedral motifs
plh-db	polyicosahedra with a double Ih ₁₃ core

Teristimewa untuk Rose dan anak-anak yang tersayang.....

Siti Aisyah Farzana

Muhammad Afif Fahmi

bayi MMXIII

Acknowledgements

I would like to acknowledge my supervisor, **Professor Roy Johnston**, for the guidance and support throughout my Ph.D. program. I would like to thank my collaborators: **Prof. Riccardo Ferrando** (Università di Genova, Italy), **Dr. Ziyou Li** and **Dr. Yisong Han** (Nanoscale Physics Research Laboratory, Birmingham). I would also like to thank my second supervisor, **Dr. Graham Worth**.

Special thanks for funding /cpu-time from different sources: **Universiti Pendidikan Sultan Idris** (study leave /sponsorship), **Ministry of Higher Education, Malaysia** (sponsorship), **University of Birmingham, BlueBEAR** (Birmingham Environment for Academic Research), **COST** (European Cooperation in Science and Technology), **CINECA** supercomputing and **HPC-Europa2** Transnational Access project.

I would like to express my appreciation to past and present members of the Johnston research group for their help, encouragement and friendship: **Oliver, Paul West, Andy Logsdail, Andy Bennett, Alina, Josafat, Lewis, Mark, Paul Jennings, Chris, Ivaylo, Louis, Samara, Haydar, Sven** and **Joe Watkins**. I would also like to acknowledge friends in Molecular Processes and Theory (MPT) labs: **Jan, Heather, Laura, Adam, Duncan, Raja, Emma** and **Tom**.

To my wife, **Mrs. Rosmawati Razali**, thanks for your love and support. And last, but not least, thanks to all of those who give support and help during the completion of the program.

Contents

1	Introduction	1
1.1	Thesis Organisation	1
1.2	Nanoparticle Research	3
1.3	Cluster Chemistry	4
1.4	Mono-metallic Clusters	6
1.4.1	Gold	6
1.4.2	Palladium	7
1.4.3	Platinum	7
1.4.4	Nickel	9
1.4.5	Aluminium	10
1.5	Nanoalloy Clusters	10
1.6	Chemical Ordering in Nanoalloys	14
1.7	Transition Metal Nanoalloys	17
1.7.1	Group 10: Ni-Pd, Ni-Pt and Pd-Pt	20
1.7.2	Group 11: Cu-Ag, Cu-Au and Ag-Au	20
1.7.3	Group 10 – Group 11: (Ni, Pd, Pt)–(Ag, Au, Cu)	22
1.7.4	Group 10/11 – Other Transition Metals	23
1.8	Supported Clusters	25
1.8.1	Alumina, Al ₂ O ₃	26
1.8.2	Carbon (Graphite, Graphene, Carbon Nanotubes)	26
1.8.3	Silica, SiO ₂	27

Contents

1.8.4	Magnesia, MgO	27
2	Theoretical Background and Methods	29
2.1	Electronic Structure Theory	29
2.1.1	First Principles Methods	31
2.1.2	Empirical Methods	32
2.2	Density Functional Approach	32
2.2.1	The Schrödinger Equation	32
2.2.2	Variational Principle	34
2.2.3	Hohenberg-Kohn Theorem	34
2.2.4	Levy-Constrained Search Proof	35
2.2.5	Thomas-Fermi (TF) Model	36
2.2.6	Kohn-Sham Equation	36
2.3	Density Functional Theory (DFT)	38
2.4	Genetic Algorithm (GA)	41
2.4.1	Birmingham Cluster Genetic Algorithm (BCGA)	42
2.5	Basin-Hopping Monte Carlo (BHMC) Algorithm	46
2.6	Gupta Semi-empirical Potential	48
2.6.1	Heteronuclear Interactions	50
2.6.2	Parameterisations of the Gupta Potential	52
2.7	Combined Empirical Potential – Density Functional Method	54
2.7.1	Empirical Global Searches	55
2.7.2	DFT Local Optimisations	56
2.8	Energetic Analysis	59
2.9	Bonding Profile Analyses	60
2.10	Chemical Ordering	62
2.11	Symmetry Analysis	62

3	Small Pd-Au and Pd-Pt Clusters	65
3.1	Introduction	65
3.2	Computational Details	68
3.3	Results and Discussion	68
3.3.1	(Pd-Au) _N , N ≤ 100	68
3.3.2	(Pd-Pt) _N , N ≤ 100	77
3.3.3	98-atom Pd-Pt Clusters	81
3.4	Chapter Conclusions	83
 4	 Structure Database of Pd-Au, Pd-Pt and Ni-Al Clusters	 86
4.1	Introduction	86
4.2	Computational Details	88
4.2.1	Compositional Mixing Degree, σ_N	89
4.3	Structural Motifs of 34- and 38-atom Clusters	90
4.3.1	Decahedral Packing	90
4.3.2	Close-packing	94
4.3.3	Anti-Mackay-icosahedral Packing	95
4.3.4	Mackay-icosahedral Packing	101
4.3.5	Mixed Packing	101
4.4	Global Minima Variations	104
4.4.1	(Pd-Au) ₃₄	104
4.4.2	(Pd-Pt) ₃₄	105
4.4.3	(Ni-Al) ₃₄	109
4.4.4	(Pd-Au) ₃₈	110
4.4.5	(Pd-Pt) ₃₈	110
4.4.6	(Ni-Al) ₃₈	114
4.5	Chemical Ordering	115
4.5.1	Pd-Au	116

Contents

4.5.2	Pd-Pt	117
4.5.3	Ni-Al	118
4.5.4	General Observation of Ordering Profiles Based on the σ_N	123
4.6	Energetic Profiles	126
4.6.1	Pd-Au	126
4.6.2	Pd-Pt	129
4.6.3	Ni-Al	132
4.7	Chapter Conclusions	132
5	34- and 38-atom Pd-Au clusters by a Combined EP-DF Method	137
5.1	Introduction	137
5.2	Computational Details	139
5.3	Results and Discussion	140
5.3.1	Structural Motifs of 34-atom Clusters	140
5.3.2	Structural Motifs of 38-atom Clusters	141
5.3.3	Bonding Analyses of the Global Minima	141
5.3.4	Statistics of the BCGA Searches	143
5.3.5	BCGA-BHMC Searches	144
5.3.6	Structural Effects at the EP and DFT Levels	145
5.3.7	Chemical Ordering Effects	150
5.4	Chapter Conclusions	153
6	34- and 38-atom Pd-Pt Clusters by a Combined EP-DF Method	154
6.1	Introduction	154
6.2	Computational Details	156
6.3	Results and Discussion	157
6.3.1	34-atom Pd-Pt Clusters	157
6.3.2	38-atom Pd-Pt Clusters	160

Contents

6.3.3	Chemical Ordering Effects	163
6.4	Chapter Conclusions	165
7	Benchmarking the Gupta Empirical Potentials	167
7.1	Introduction	167
7.2	Computational Details	168
7.3	Pd-Au	170
7.3.1	The Average , DFT-fit and Exp-fit <i>vs</i> the Weighted (Parameter Sets I–III) Potentials	170
7.3.2	The DFT Calculations of Pd ₃₂ Au ₆ and Pd ₆ Au ₃₂	174
7.4	Pd-Pt	177
7.4.1	The Average and DFT-fit <i>vs</i> the Weighted (Parameter Sets I–III) Potentials	177
7.4.2	The DFT Calculations of Pd ₆ Pt ₃₂ and Pd ₃₂ Pt ₆	179
7.5	Ni-Al	181
7.5.1	The Exp-fit <i>vs</i> the Weighted (Parameter Sets I–III) Potentials	181
7.5.2	The DFT Calculations of Ni ₃₂ Al ₆ and Ni ₆ Al ₃₂	182
7.6	Pt-Au, Cu-Pd, Cu-Au and Cu-Pt	186
7.6.1	Pt-Au	186
7.6.2	Cu-Pd	188
7.6.3	Cu-Au	188
7.6.4	Cu-Pt	192
7.7	Chapter Conclusions	192
8	Pd-Au Clusters Supported on MgO(100)	195
8.1	Introduction	195
8.2	Computational Details	198
8.2.1	Empirical Potential Global Optimisation	198

Contents

8.2.2	Metal-Oxide Interactions	200
8.2.3	Potential Parameterisations	201
8.2.4	Density Functional Theory Calculations	201
8.3	Optimisation of the Calculations	202
8.3.1	Structural Variations of Pd ₁₉ Au ₁₉ : Effect of the Monte Carlo Elemental Move	202
8.3.2	Structural Variations of Pd ₁₉ Au ₁₉ : Effect of the Choice of Em- pirical Potential	203
8.3.3	Optimisation of the DFT Calculations (Code, Functionals, Con- vergence)	204
8.3.4	Parameterisation of the “New” Potential	207
8.4	Results and Discussion	211
8.5	Chapter Conclusions	219
9	Concluding Remarks and Future Work	221
A	Gupta Potential Parameters	A-1
A.1	Gupta potential parameterisations of Pd-Au	A-2
A.2	Gupta potential parameterisations of Pd-Pt	A-3
A.3	Gupta potential parameterisations of Ni-Al	A-4
B	Publications	B-1
	<i>Phys. Chem. Chem. Phys.</i> 2010, 12 , 8607-8619	B-2
	<i>Nanoscale</i> 2013, 5 , 646-652	B-16
	<i>J. Phys. Chem. C</i> 2013, 117 , 293-301	B-24

List of Figures

1.1	High symmetry cluster structures: (a) 38-atom truncated octahedron, (b) 55-atom Mackay icosahedron and (c) 75-atom Marks' decahedron.	5
1.2	High resolution electron microscopy (HREM) images of Pd particles with (a) fcc, (b) decahedra and (c) icosahedra structures from different orientations.	8
1.3	Cross section of the four main types of chemical ordering patterns – core-shell, subcluster segregated, mixed and multishell.	14
2.1	Flow chart of the BCGA program.	43
2.2	Schematic representation of GA crossover.	45
2.3	Schematic diagram of the one-dimensional PES, in which the original energy is mapped onto the \tilde{E}	47
2.4	A generic pair distribution function for a metal cluster.	61
3.1	Mackay and anti-Mackay growth in polyicosahedra.	66
3.2	Plots of binding energy and second difference in energy of $(\text{Pd-Au})_{N/2}$, $N \leq 100$ global minima found for the average , DFT-fit and exp-fit potentials.	69
3.3	Plots of mixing degree and ANND of $(\text{Pd-Au})_{N/2}$, $N \leq 100$ global minima found for the average , DFT-fit and exp-fit potentials.	76
3.4	Global minima of $(\text{Pd-Pt})_{N/2}$, $N \leq 100$ clusters obtained by calculation with the average and DFT-fit potentials.	79

List of Figures

3.5	Plots of binding energy, second difference in energy, mixing degree and ANND of (Pd-Pt) _{N/2} , $N \leq 100$ global minima found for the average and DFT-fit potentials.	80
3.6	Structural motifs of global minima found for 98-atom Pd-Pt clusters.	82
3.7	Excess energies of 98-atom Pd-Pt global minima for the average and DFT-fit potentials.	83
3.8	Plots of mixing degree, σ and ANND of 98-atom Pd-Pt global minima found for the average and DFT-fit potentials.	84
4.1	Variation of polyicosahedra and the closely-related motifs.	96
4.2	Variants of pIh ¹² motifs.	98
4.3	Comparison between atomic growth in (a) Dh-cp(T), (b) LT ₉₈ and (c) cp ₉₈	103
4.4	Atomic growth in (a) pIh-M(DT) and (b) Dh-cp(DT).	104
4.5	Structural map of 34-atom global minima found for (a) Pd-Au, (b) Pd-Pt and (c) Ni-Al.	108
4.6	Structural map of 38-atom global minima found for (a) Pd-Au, (b) Pd-Pt and (c) Ni-Al.	113
4.7	Chemical ordering patterns of small clusters of 34 and 38 atoms.	115
4.8	Chemical ordering analyses based on ordering maps (qualitative) and compositional mixing degrees, σ_N , curves (quantitative) of (a) 34- and (b) 38-atom Pd-Au global minima for the parameter sets I , II and III	120
4.9	Chemical ordering analyses based on ordering maps (qualitative) and compositional mixing degrees, σ_N , curves (quantitative) of (a) 34- and (b) 38-atom Pd-Pt global minima for the parameter sets I , II and III	122
4.10	Chemical ordering analyses based on ordering maps (qualitative) and compositional mixing degrees, σ_N , curves (quantitative) of (a) 34- and (b) 38-atom Ni-Al global minima for the parameter sets I , II and III	125

List of Figures

4.11	Combined compositional mixing degrees of PdAu-34, PdAu-38, PdPt-34, PdPt-38, NiAl-34 and NiAl-38 clusters.	126
4.12	Excess energy variation of (a) 34- and (b) 38-atom Pd-Au clusters calculated with the parameter sets I , II and III	127
4.13	Excess energy variation of (a) 34- and (b) 38-atom Pd-Pt clusters calculated with the parameter sets I , II and III	130
4.14	Excess energy variation of (a) 34- and (b) 38-atom Ni-Al clusters calculated with the parameter sets I , II and III	133
5.1	Structural motifs of global minima found for PdAu-34 clusters.	141
5.2	Structural motifs of global minima found for PdAu-38 clusters.	142
5.3	ANND variation of 34- and 38- atom PdAu global minima for the parameter set III ($w_a = 0.5, 0.7-0.9$), DFT-fit and exp-fit potentials. . .	143
5.4	Progression of the BCGA-BHMC approach.	145
5.5	Excess energies of 34-atom clusters at the (a) EP and (b) DFT levels. .	146
5.6	Excess energies of 38-atom clusters at the, (a) EP and (b) DFT levels. .	148
5.7	Magic compositions of 38-atom Pd-Au clusters.	149
5.8	Excess energies at (a) the EP and (b) the DFT levels of TO_{38} clusters from the average , DFT-fit and exp-fit potentials, with the DFT (c) bond length and (d) compositional mixing, σ_N	151
6.1	Structural motifs found in the EP searches of 34-atom Pd-Pt clusters. .	158
6.2	Excess energies of 34-atom Pd-Pt clusters from the average and DFT-fit potentials at the (a) EP and (b) DFT levels.	159
6.3	Dh variants of global minima observed for PdPt-34 clusters.	160
6.4	Excess energies of 38-atom Pd-Pt clusters from the average and DFT-fit potentials at the (a) EP and (b) DFT levels.	162
6.5	Dh variants of global minima observed for PdPt-38 clusters.	163

List of Figures

6.6	Excess energies, compositional mixing degrees, σ_N and bond lengths (Pd-Pd, Pt-Pt and Pd-Pt, in Å) of TO and pIh-M-pc ⁵ motifs from the average and DFT-fit potentials.	164
7.1	TO motif with the three different high symmetry arrangements and their reverse compositions.	169
7.2	Structural motifs and excess energy variation of (a) 34- and (b) 38-atom Pd-Au global minima found for the DFT-fit , exp-fit and parameter set III ($w_a = 0.5, 0.7-0.9$) potentials.	171
7.3	Configurational changes in PdAu-38: (a) $N_{Au} = 12$ to 13, (b) $N_{Au} = 24$ to 25, (c) $N_{Au} = 32$ to 33 and (d) structural change ($N_{Au} = 31$ to 32).	173
7.4	Stability ordering of the three TO homotops of (32,6) and (6,32) Pd-Au clusters for the EP calculations with the weighted potential of the parameter sets I , II and III	176
7.5	Structural motifs and excess energy variation of (a) 34- and (b) 38-atom Pd-Pt global minima found for the average , DFT-fit and parameter set I ($w = 0.4-0.6$) potentials.	178
7.6	Stability ordering of the three TO homotops of (32,6) and (6,32) Pd-Pt clusters for the EP calculations with the weighted potential of the parameter sets I , II and III	180
7.7	Structural motifs and excess energy variation of (a) 34- and (b) 38-atom Ni-Al global minima found for the exp-fit and parameter set III ($w_a = 0.5, 0.8-0.9$) potentials.	183
7.8	Stability ordering of the three TO homotops of (32,6) and (6,32) Ni-Al clusters for the EP calculations with the weighted potential of the parameter sets I , II and III	185

List of Figures

7.9	Stability ordering of the three TO homotops of (32,6) and (6,32) (a) Pt-Au, (b) Cu-Pd, (c) Cu-Au and (d) Cu-Pt clusters for the EP calculations with the weighted potential of parameter sets I , II and III	191
8.1	Energetic profiles of various structural motifs for 38-atom Pd-Au calculated with the average , DFT-fit and exp-fit potentials.	203
8.2	Effect of different GGA on the DFT calculations of (6,32) and (32,6) Pd-Au clusters.	204
8.3	Effect of parameter choice on the convergence times and the total energies of the DFT calculations.	206
8.4	Comparison of the DFT excess energies of (6,32) and (32,6) Pd-Au clusters of the three studied homotops for several empirical potentials.	208
8.5	Parameterisation of the Gupta potential.	209
8.6	Structural motifs of 30- and 40-atom Pd-Au clusters: decahedral, icosahedra, crystalline and close-packed.	211
8.7	Relative energies of decahedra with different orientations and interfaces.	213
8.8	Global minima of 30-atom Pd-Au clusters for compositions (22,8), (15,15) and (8,22).	214
8.9	Global minima of 40-atom Pd-Au clusters for compositions (30,10), (20,20) and (10,30).	215
8.10	Structural motifs crossover of 30-atom Pd-Au clusters.	217
8.11	Structural motifs crossover of 40-atom Pd-Au clusters.	218

List of Tables

1.1	Cohesive energies, atomic radii, average surface energies and Pauling electronegativities of the studied elements.	16
1.2	Bulk chemical ordering of the studied bimetallic systems.	18
1.3	Various chemical orderings of bimetallic clusters.	19
2.1	Timeline of historical landmarks in DFT development.	39
2.2	Elemental Gupta potential parameters.	49
2.3	The average and fitted parameters of the Gupta potential for Pd-Au, Pd-Pt and Ni-Al.	51
2.4	Computational details of the DFT calculations with the NWChem code.	57
2.5	Classification of clusters based on point group symmetry.	64
3.1	Global minima of $(\text{Pd-Au})_{N/2}$, $N \leq 100$ clusters obtained by calculations with the average , the DFT-fit and the exp-fit potentials.	70
3.2	Cluster energies, structural motifs and point group symmetries of $(\text{Pd-Au})_{N/2}$, $N \leq 100$ global minima found for the average potential.	72
3.3	Cluster energies, structural motifs and point group symmetries of $(\text{Pd-Au})_{N/2}$, $N \leq 100$ global minima found for the DFT-fit potential.	73
3.4	Cluster energies, structural motifs and point group symmetries of $(\text{Pd-Au})_{N/2}$, $N \leq 100$ global minima found for the exp-fit potential.	74
3.5	Cluster energies, structural motifs and point group symmetries of $(\text{Pd-Pt})_{N/2}$, $N \leq 100$ GM using the average and DFT-fit potentials.	78

List of Tables

4.1	Effects of the parameter sets I , II and III on the Pd-Au, Pd-Pt and Ni-Al system.	89
4.2	Detailed views of global minima motifs of 34- and 38-atom clusters for Pd-Au, Pd-Pt and Ni-Al nanoalloys.	91
4.3	Excess energy series of (a) 34-atom and (b) 38-atom Pd-Au global minima for the parameter sets I , II and III	128
4.4	Excess energy series of (a) 34-atom and (b) 38-atom Pd-Pt global minima for the parameter sets I , II and III	131
4.5	Excess energy series of (a) 34-atom and (b) 38-atom Ni-Al global minima for the parameter sets I , II and III	134
5.1	Frequencies of motifs found in the GA searches.	143
6.1	Cohesive energies (in eV) of the Pd-Pd, Pt-Pt and Pd-Pt dimers.	165
7.1	The A and ξ parameters of the average and fitted potentials.	174
7.2	Excess energies of the three TO homotops of (32,6) and (6,32) Pd-Au clusters at the DFT and EP levels.	176
7.3	Excess energies of the three TO homotops of (32,6) and (6,32) Pd-Pt clusters at the DFT and EP levels.	180
7.4	Excess energies of the three TO homotops of (32,6) and (6,32) Ni-Al clusters at the DFT and EP levels.	185
7.5	Summary of the weighting representation for Pt-Au and Cu-based systems in the parameter sets I , II and III	187
7.6	Ratio of the Gupta potential parameters for the extended studies.	187
7.7	Excess energies (in eV) of the three TO homotops for Pt-Au, Cu-Pd, Cu-Au and Cu-Pt clusters from the DFT and EP (the average and weighted potentials) calculations for compositions (32,6) and (6,32).	189

List of Tables

8.1	Gupta potential parameters for elemental Pd and Au; and bimetallic Pd-Au.	199
8.2	Average magnitude of difference between the EP (with the weighted potential) and DFT calculations.	210
8.3	Relative energies of core-shell and inverse core-shell for (15,15) and (20,20) Pd-Au clusters.	216
8.4	Relative energies of (15,15) and (20,20) Pd-Au clusters at the DFT and EP levels.	219

Chapter 1

Introduction

This chapter starts with organisation of the thesis (Section 1.1), followed by a literature review of the related subject matter, beginning with a general overview of the nanoparticle research (1.2) that has a focus on areas of cluster chemistry (1.3). It will then be followed by mono-metallic clusters (1.4), consisting of a discussion of gold (Au) (Subsection 1.4.1), palladium (Pd), (1.4.2), platinum (Pt) (1.4.3), nickel (Ni) (1.4.4) and aluminium (Al) (1.4.5). Overall, the major theme of the thesis is the theoretical calculations of nanoalloy clusters (1.5), with emphasis on structural and chemical ordering (1.6), especially for transition metal nanoalloys (1.7) of group 10 (1.7.1), 11 (1.7.2) and crossover between the two groups (1.7.3). Combination of these metals with other transition metals such as Co, Fe, Ru (1.7.4) will also be reviewed. Finally, clusters supported (1.8) on alumina (1.8.1), carbon (1.8.2), silica (1.8.3) and magnesia (1.8.4) will also be mentioned.

1.1 Thesis Organisation

Background and principles of the electronic structure calculations (*ab initio* – especially the **Density Functional Theory (DFT)** and **Empirical Potential (EP)** levels) will be presented in **Chapter 2**, along with the research methodology. Results of the theoretical calculations will be described in **Chapters 3–8** and finally the conclusions of the studies will be given in **Chapter 9**. For every results chapter, a brief introduction

of the topic will be outlined, followed by the details of the computational studies, discussion of the results and conclusions.

The global optimisation searches (using the **Birmingham Cluster Genetic Algorithm (BCGA)**) with the potentials derived from the semi-empirical Gupta parameters (the **average**, **DFT-fit** and **exp-fit** potentials) in describing homo and heteronuclear interactions will be presented as a function of size and composition. Variation in the size (clusters with ≤ 100 atoms) will be explained in **Chapter 3**, for Pd-Au and Pd-Pt clusters of composition 1:1 (50%/50%). Variation in the composition will be discussed in **Chapter 4**, based on a fixed 34- and 38-atom Pd-Au, Pd-Pt and Ni-Al clusters. The areas of focus are structure (geometry and symmetry), energetics/stabilities and ordering (mixed/segregated). The effect of a three way parameterisation of the Gupta potential - namely sets **I**, **II**, **III**, will also be described.

The structural motifs from the EP searches of 34- and 38-atom clusters serves as a library for initial configurations of the DFT optimisations – *i.e.*, the combined **Empirical Potential - Density Functional Theory (EP-DF)** method. Investigation on Pd-Au (**Chapter 5**) and Pd-Pt (**Chapter 6**) clusters of all compositions will be outlined, comprising the BCGA and the **Basin-Hopping Monte Carlo (BHMC)**) for the EP searches and the **NWChem** code with the **Perdew-Wang (PW91)** functional for the DFT calculations. The discussion will include the stabilities of the **global minimum (GM)** and other competitive minima for both levels of theory, size and composition effects, chemical ordering, bonding analyses and structural motif crossover.

As a validation procedure, the EP calculations were compared against the DFT, on a fixed truncated octahedron (TO) structure in **Chapter 7**. Results from two fixed compositions – (6,32) and (32,6) will be presented, to include possible composition effects. In addition to the Perdew-Burke-Ernzerhof (PBE), results with the other functional – **PBE** will also be included. Observation on Pt-Au and Cu-based systems

– Cu-Pd, Cu-Pt and Cu-Au will also be provided, alongside the three main systems of Pd-Au, Pd-Pt and Ni-Al.

Finally, the effect of MgO support on the structures and chemical ordering of Pd-Au clusters will be discussed in detail in **Chapter 8**. The chapter will focus on 30- and 40-atom clusters with a variation in the bimetallic compositions (Pd-rich, Au-rich and medium composition). A different code for the DFT – **Quantum ESPRESSO (QE)** was used, combined with the PBE functional. Results from this code will be compared against calculations with the other code – NWChem. Moreover, comparison against the other available functionals will be presented for the accuracy checks.

1.2 Nanoparticle Research

Nanomaterials (such as nanoparticles (NPs)) and nanotechnology have emerged in recent years as a new field at the interface between several science and technology disciplines [1]. NPs have novel physical and chemical properties, due to quantum and electronic effects and large surface area relative to bulk materials [2–4]. By definition, NPs are classified by a size range of 1-100 nm, which is intermediate between atomic/molecular and bulk material [5]. However, the transition of certain physical properties is non-linear and varies depending on size, shape and composition [6, 7].

Interplay between the structures of NPs and their properties are of interest, as the former can be tuned by using templating/seeding agents and/or controlled experimental conditions. Several different structural changes of NPs have been reported: cubic/spherical [8, 9], cubic/closed-packed [10–14], prism/spherical [15], disc/spherical [16] and wire/tube [17–20]. Transformation of shapes leads to modification in the ratio of facets (corners, edges, kinks, steps), which are significant for their reactivity, especially in catalysis [21, 22].

Smaller NPs have a higher catalytic activity due to the higher proportion of surface atoms [23–27]. There is much evidence for how evolution in size and/or struc-

ture change the optical, electronic, magnetic, chemical and other physical properties (*e.g.*, crystallinity, melting point, thermodynamics) of NPs [1, 3, 4]. Studies of NPs with well-defined size and structure are critical for the understanding of their structure-activity interplay and can suggest possible modification for a better performance.

The rapid increase in NP-related publications is due to their unique properties. There is a great promise for their utilisation in photochemistry, nanoelectronics, optics, catalysis, sensors, biological labelling, photonics, optoelectronics, information storage and magnetic device applications [1, 3, 28–30]. In catalysis, different charge and electrical properties [31] make it possible for certain NPs to be involved in reactions which may not occur for the bulk, for example, reactions involving cross-coupling, electron transfer, hydrogenation and oxidation [23].

It is interesting to mention that rare colour characteristics of NPs have been exploited since the middle ages, particularly in stained glass windows of cathedrals (Europe), colouring vases and other ornaments (China). But it is only recently that scientists could explain the vibrant colour as being due to the collective oscillation of the electrons at the interface, called the surface plasmon. The distinct optical properties of NPs are of interest, for their use in consumer products such as home pregnancy test devices, digital imaging and display systems [2, 3, 23].

1.3 Cluster Chemistry

Nanoclusters are classified as assemblies of ~ 10 to 10^6 atoms or molecules within a nanometre size range [32]. The component could be neutral or ionic and either single or more species, stabilised in certain (physical or chemical) media. Examples of some different types of clusters are fullerenes, metal clusters, molecular clusters and ionic clusters [32–34].

The most remarkable feature of clusters is the size-dependent evolution of structure [5, 32, 35, 36]. It is fascinating that such evolution is non-monotonic, making it very

appealing to study [37]. Furthermore, electronic energy levels of clusters are quantised, giving rise to atomic-like character [38, 39]. These phenomena have been connected to the enhancement in the optical and electrical properties of some clusters [40, 41].

Nanometre-size clusters can present both crystalline (*e.g.*, face-centred cubic (fcc), octahedra or TO) and noncrystalline (*e.g.*, icosahedra, decahedra, polytetrahedra and polyicosahedra) structures. The noncrystalline shapes normally exist at small sizes, with icosahedra and Marks truncated decahedra dominating for noble and transition metals [42]. For large clusters, these structures are not favourable due to the strain arising from their noncrystalline packing, which is proportional to the cluster volume [34]. This strain, however, can be released by locating a smaller atom in the core of the nanoalloy [43].

Clusters of transition metals group 11 (Cu, Ag, Au) have completely filled d orbitals, leaving a single s electron in the valence shell [37]. It leads to similar shell effects [44–48] as observed experimentally for clusters of the alkali elements (Li, Na, K, Rb, Cs) [49–51]. Shell closing has also been reported for bimetallic nanoalloys of the coinage metals (*e.g.*, Cu-Ag [52, 53]). On the contrary, shell closing behaviour for clusters of transition metals with unfilled d -shells is accounted for geometric shell of concentric polyhedra [42]. Examples of magic size clusters commonly found for the transition metals are shown in Figure 1.1 [54].

The spherical jellium model [55] can be used to describe shell closing behaviour. In

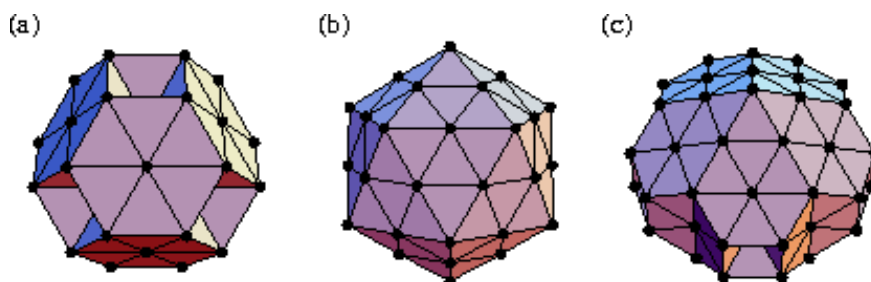


Figure 1.1: High symmetry cluster structures: (a) 38-atom truncated octahedron, (b) 55-atom Mackay icosahedron and (c) 75-atom Marks' decahedron [54].

this model, core electrons and the nuclei are modelled as positive ions and the delocalised valence electrons are treated as the interacting component. Cluster orbitals are described by a principal quantum number, $n = 1, 2, \dots$ and orbital angular momentum, $l = 0(\text{S}), 1(\text{P}), \dots$, (capital letters are used for cluster orbitals to avoid confusion with electronic orbitals) in which the maximum number of electrons for each shell is $2(2l + 1)$. Similarly to inert gas atoms, fully filled shells (shell closing) are relatively stable and give rise to magic sizes that correspond to $n = 2, 8, 18, 20, 34, 40, 58, \dots$ electrons, which are explained by a shell filling sequence of $(1\text{S})^2(1\text{P})^6(1\text{D})^{10}(2\text{S})^2(1\text{F})^{14}(2\text{P})^6(1\text{G})^{18}\dots$ [56]. Shell closing effects have been identified as the main reason for the occurrence of even-odd effects in the mass spectral abundance, ionisation potential and other properties of clusters [57, 58].

1.4 Mono-metallic Clusters

1.4.1 Gold

Gold has received considerable attention in the clusters study. In the size range of less than 250 atoms (~ 2 nm), there is variation from “molecular” to decahedral and bulk-like fcc. The fcc structures are normally stabilised by truncations, *e.g.*, TO motif [59].

Preparation of clusters *via* a chemical reaction route is likely to produce co-structures (decahedral (Dh), TO, icosahedron and amorphous) as has been the case for gold reduction at the oil-water interface with the presence of a surface passivating agent. The Marks and Ino-decahedra, however, are favoured for particles of a few nanometres diameter, with Marks decahedra prevailing at sizes ~ 15 Å. Meanwhile, the existence of small fcc clusters are at the expense of truncation of the octahedron edges [60].

The complexity in the structural characterisation of clusters can be aided by a combined experimental-theoretical approach. For example, Cleveland *et al.* [61] utilised atomistic modelling in describing stable truncated-decahedral motif of gold clusters

from the X-ray powder diffraction analyses. Of the 1 – 2 nm size range clusters, they have been able to single-out Marks decahedra of 75, 101 and 146-atoms.

1.4.2 Palladium

Palladium has fcc symmetry in the bulk phase but, depending on the diameter, its clusters can be stabilised as icosahedral, decahedral or fcc motifs [62]. For small sizes, the stability of Pd clusters decreases from linear, to planar and further to three-dimensional clusters [63]. Moreover, icosahedral structures are preferred for $N = 55$ and 147 [64]. Large clusters are likely to adopt bulk-like fcc structures, with the exception for $N = 147$, 231 and 309, where magic clusters of icosahedra ($N = 147$), octahedra ($N = 231$) and cuboctahedra ($N = 309$) prevail [65].

Experimentally, several motifs appeared to be separated by a very small energy gap and a co-existence of structures has been reported. For example, colloidal methods by José-Yacamán *et al.* [66] give fcc cuboctahedra, icosahedra and truncated decahedra in the range of 1-5 nm, as shown in Figure 1.2 [66]. Stabilisation of the decahedra and cuboctahedral particles is enhanced because the extent of truncation makes them close to spherical in structure. Icosahedra, which are only expected for very small clusters (due to high strain), are also present due to kinetic trapping effects.

1.4.3 Platinum

Studies of small Pt clusters have found low-energy planar isomers for the trimer, tetramer and pentamer [67]. Theoretical simulations mainly found Pt behaviour being close to Au, with the preference for very small icosahedral clusters before fcc prevails [68].

In the intermediate size range, Pt clusters composed of 13, 38 and 55 atoms are of interest due to significantly different ground state structures [69]. Of these sizes, the EP calculations exhibit icosahedral minima [68], however, the DFT predicts the shrinking of (100) faces of close-packed structures (which are optimised at $N = 38$)

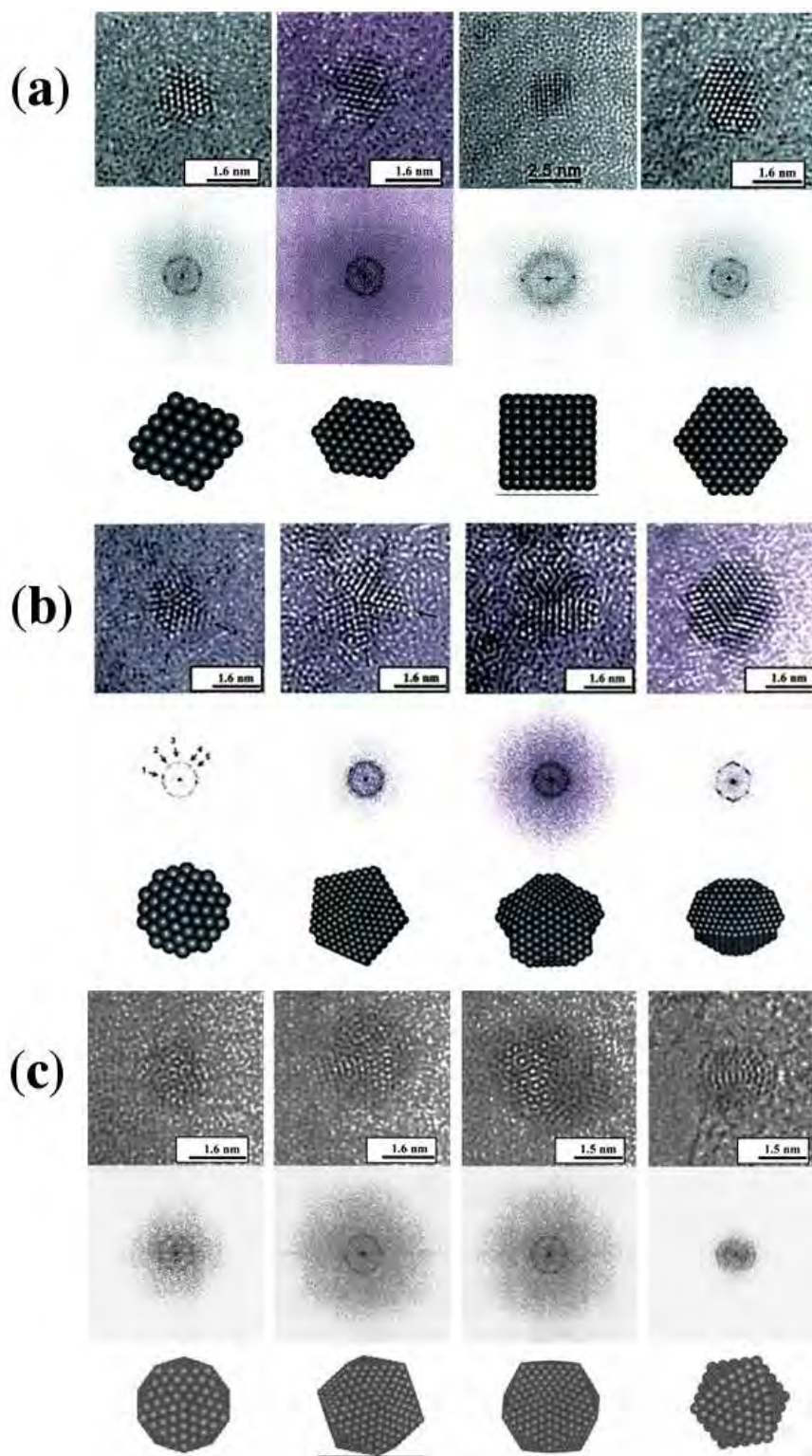


Figure 1.2: High resolution electron microscopy (HREM) images of 1-5 nm Pd particles with (a) fcc, (b) decahedra and (c) icosahedra structures from different orientations. The corresponding fast Fourier transform (FFT) is included in each case [66].

giving considerable stability of D_{4h} and O_h configurations for Pt_{13} and Pt_{55} clusters, respectively [69]. This unique property is the evidence of intermediate finite-size effects in small clusters [70].

1.4.4 Nickel

Icosahedral clusters that were first observed for small rare-gas clusters [71] are also adopted by Ni, with a very strong increase in the abundance of photoionisation peaks at $N = 55, 147, 309$ and 561 [72]. Chemical probe experiments indicate that these icosahedral clusters are derivatives of the 13-atom icosahedron units [73]. The stability of Ni_{13} and Ni_{19} icosahedral clusters is further proved by chemical probe experiments with nitrogen [73–75] and CO [76].

The great stability of Ni_{13} is confirmed by DFT calculations [77] but computational limitations require empirical calculations for larger sizes. The Embedded-Atom Model (EAM), which correctly predicted the bulk nickel structure [78], is one of the earliest to be applied to clusters. It shows a preference for icosahedral packing in small clusters of up to a hundred atoms, with magic stabilisation of 13- and 19-atom clusters [79–81].

Structural diversity is possible, with variation in size as has been seen in the fcc-icosahedron transition from Ni_{38} to Ni_{39} clusters [82]. Even for magic icosahedra of 13 and 19, the DFT calculations show a strong competition between icosahedra, Dh and fcc structures [83]. Similar results have also been reported using a semi-empirical tight-binding method [84, 85] for larger clusters ($N \leq 55$). Doye and Wales [54] postulate that the ground-state may adopt structures far from the usual packing (icosahedral, decahedral, close packed). Moreover, the DFT study by Wetzel and DePristo [86] suggests the structures that differ from rare gas clusters. An EAM study for a broader range of sizes exhibits the prevalence of small icosahedral clusters before the transformation to Marks decahedra (intermediate sizes $N > 2,300$) and fcc (very large sizes, $N > 11,700$) [87].

1.4.5 Aluminium

Studies of aluminium clusters are of importance as they represent a simple metal system and are of interest for microelectronics or nanocatalysis [88]. For neutral clusters, photoionisation spectroscopy by Schriver *et al.* [89] confirms the electronic shell effects in Al clusters, with exceptionally strong peaks at $N = 14, 17, 23$ and 29 . Further electronic shell closings are reported for $N = 36, 46$ and 66 , as the prominent maxima in the melting temperatures [90].

Clusters of only a few atoms are predicted to be stable in a planar shape ($N \leq 5$) [91] and increasing size stabilises compact icosahedral motifs, with the magic size at $N = 13$. This is supported by many *ab initio* (mostly based on the DFT) calculations [92–104], as well as empirical models [104–106], although differences in functional, pseudopotential and/or basis set in the DFT calculations [107–110] suggested the decahedron as the more stable structure.

The DFT studies also indicate stable icosahedral clusters of around $N = 55$ [92] and icosahedra-based onion-like Al_{77} [111]. However, many local minima on the potential energy surface (PES) are observed, give rise to the structural variation. Hexagonal [112], bulk-like fcc [92, 93, 113], decahedral and disordered structure [88] clusters are observed as competitive candidates for small to medium sizes ($N \leq 80$), due to interplay between structural and electronic effects. Small fcc clusters were eventually observed by Breaux *et al.* [114] based on the calorimetry measurements of the multi-collision induced dissociation experiment.

1.5 Nanoalloy Clusters

There are remarkable uses of noble metals in various technologically important areas for their excellent catalytic, electronic and magnetic properties [115–121]. Enhancement of properties is possible when two or more of these metals are combined [116, 122, 123]. The use of nanoalloys has been reported since the 19th century, when Michael Faraday

studied optically active Au-Ag nanoparticles [124] but without a clear understanding of the underlying physics and chemistry [125]. Advancement in methods and characterisation made it possible for modern research to utilise the diversities in nanoalloy compositions [34, 116, 122] and chemical ordering: intermetallic, random, non-random or phase segregation [126–136], in addition to size, atomic order and structure.

Theoretically, the combination of two or more non-alike atoms increases the complexity of the PES landscape due to the increased number of possible isomers especially “homotops” (permutation of unlike atoms – *i.e.*, similar in composition and geometry but differing in atomic arrangement in configurational space) [33, 137–139]. However, there is also an economic driving force for nanoalloy research as low cost (Ni, Cu and Co) metal can be combined with an expensive noble-metal such as palladium, platinum and ruthenium without reduction in the activity [140]. Careful selection of method and alloy combination have proved to give enhancement over mono-metallic clusters [23, 32, 122, 141].

Much emphasis on structure-activity relationships is made in experimental and theoretical research, with the aim of fabricating new materials with well-defined and controllable properties. Synergistic effects are dependent on many factors, *e.g.*, size and structure [142–145] and, for catalysis, in addition to activity, improvement in selectivity and stability (resistance to poisoning) [146] is achievable with nanoalloys. Intermetallic interactions produce different neighbouring atoms [147] and new activated sites (*e.g.*, point defects, interfaces, edges) [148–150]. Furthermore, electronic, geometric, ligand and ensemble effects [151–154] affect the *d*-band centre position which is crucial for catalytic activity [155].

The electronic and/or geometric effects and their interplay with structure-activity relationships of nanoalloys are very interesting due to the possibility to fine-tune catalysts which need optimum strength (neither too strong nor too weak) of adsorbate-metal interaction [156]. Electronically, this is possible *via* electron transfer by a flow of charge

[157] or modifications of the d -band [158–161]. The latter is supported by X-Ray Photoelectron Spectroscopy (XPS) and X-ray Absorption Near Edge Structure (XANES) experiments coupled with theoretical calculations but some researchers [162, 163] disagree, stating that the improvement arises from dilution of the metal surface. Likewise, geometric effects also contribute to catalysis, as changes in size and/or geometry of the cluster lead to alteration of electron bandwidth and core electrons, as well as the exposed planes and the surface topology [156, 164, 165]. Large clusters contain mainly high coordination sites (facets, planes) but reduction in size introduces more activated sites (kinks, edges, corners) [164, 166, 167], which are demonstrated to provide a more active catalyst [168–171]. Moreover, in nanoalloys, more than one type of metal may occupy active sites, which is required in some reactions [156].

Meanwhile, magnetic properties can be induced in non-magnetic metals ($4d$ metals: Rh, Pd, Ag or $5d$ metals: Pt, Au) or even insulators in nanoalloys containing magnetic $3d$ metals (Cr, Fe, Co and Ni) [37, 116]. Co-Rh is a candidate for application in high-density magnetic recording [172]. Moreover, enhanced improvement by nanoalloys have also benefited biomedical applications, for example in bioconjugation, cellular labels, bioassays and DNA/protein markers [173, 174].

Cluster production (including mono-metallics) can be classified into two domains: chemical – involving metal reduction followed by particle stabilisation and physical – usually involving vapour deposition. Cost-wise, chemical methods such as chemical reduction (co-reduction, successive reduction, reduction of co-complexes), thermal decomposition, ion implantation, electrochemical synthesis (electrodeposition at liquid-liquid interfaces), radiolysis, sonochemical synthesis or biosynthesis (biomimetic synthesis, *in-vivo* biogeneration) are more effective but agglomeration is always a major issue [2, 23]. This, however, is solved by the introduction of stabilisers in the reactions, such as ligands [175], polymers [176] or tetraalkylammonium salts [177]. Meanwhile, physical methods such as molecular beams are obviously more expensive but “free”

clusters (in an interaction-free environment) can be studied. Other physical means include laser vaporisation, pulsed arc cluster ion source, ion sputtering/scattering and magnetron sputtering.

Variation in the parameters of experiment gives variation in the structural-properties of clusters. For instance, large icosahedral clusters (up to 11 nm in diameter) of Ag are observed by the inert-gas aggregation technique [52, 178] but at high temperature and pressure transform into mainly fcc clusters [179]. Likewise, the introduction of nitrogen to the argon sputtering produced single-crystalline, instead of multiply twinned particles of Fe-Pt clusters [180]. For Au clusters, the same method gives icosahedra as the most frequent morphology, followed by decahedra [181]. Interestingly, subsequent landing on the carbon surface gave stabilisation of fcc clusters, identified by High-Resolution Transmission Electron Microscopy (HRTEM) and supported by theoretical calculations [182]. Size-wise, varying the flow rates of inert gas (Ar and/or He) corresponded to increasing particle size, as have been reported for Pd clusters with decahedral shape [183]. For Ag-Au clusters, size-tuning in the laser vaporisation method have been carried out with the cooling scheme [184, 185].

The information about particle size, structure and chemical ordering of clusters can be gathered *via* electron microscopy (Scanning Electron Microscopy (SEM), field-emission SEM (FESEM), Transmission Electron Microscopy (TEM), High-Resolution TEM (HRTEM), Scanning Transmission Electron Microscopy (STEM), STEM-Electronic Energy Loss Spectroscopy (STEM-EELS)) and scanning probe microscopy (Scanning Tunnelling Microscopy (STM), Atomic Force Microscopy (AFM)) techniques. For example, the High-Angle Annular Dark-Field Imaging (HAADF)-STEM exploits the difference in atomic number of metals and chemical ordering (mixed, segregated or intermediate) can be determined by the “Z-contrast” [186, 187]. Also, X-ray spectroscopy (X-ray Absorption Spectroscopy (XAS), Extended X-ray Absorption Fine Structure (EXAFS), Near-edge X-ray Absorption Fine Structure (NEXAFS), X-ray

Absorption Near-Edge Structure (XANES), X-ray Photoelectron Spectroscopy (XPS), Auger Electron Spectroscopy (AES), Energy-Disperse X-ray Microanalysis (EDX / EDS) give more detailed information on the atomic arrangement and surface composition. Other spectroscopic techniques are Ultraviolet-Visible (UV-vis), Fourier-transform Infrared (FT-IR), Photoelectron, Surface-Enhanced Raman, Mössbauer, Nuclear Magnetic Resonance (NMR), Electrochemical NMR (EC-NMR), while specific magnetic (SQUID magnetometry) and electrochemistry (Cyclic-voltammetry (CV), *in situ* (XAS, SEM and STM)) are also available. (*For a detailed review of synthetic methods and characterisation techniques, see Refs. [4, 29, 116]*)

1.6 Chemical Ordering in Nanoalloys

The design of physically and/or chemically unique nanoalloy materials is further enhanced by the possibility to fine tune the chemical ordering (mixing pattern). Chemical ordering is dependent upon structure, size and composition, among others [188]. Generally, combination of bimetallic A and B can lead to four main possible types of chemical ordering patterns [116, 188]: core-shell, subcluster segregated, mixed and multiple shell, as outlined in Figure 1.3.

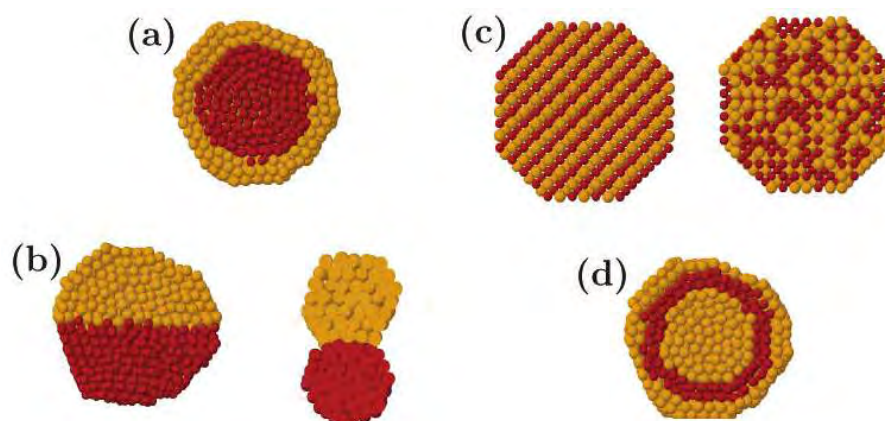


Figure 1.3: Cross section of the four main types of chemical ordering patterns; (a) core-shell, (b) subcluster segregated, (c) mixed and (d) multishell [116].

In Figure 1.3(a), A and B phases are segregated in which element A (red colour) resides in the core and is surrounded by a shell of B (yellow colour), though this core-shell arrangement may give some inter-mixing between the shells. Subcluster segregated nanoalloys (or “Janus” nanoparticles) are shown in Figure 1.3(b) for which two patterns can be classified, mixed A-B interface (left) and limited A-B interface (right). A-B nanoalloys can mix (Figure 1.3(c)) in two ways, ordered (left) or random (*i.e.*, a solid solution, right). Lastly, it is also possible for layered or onion-like alternating A-B-A or B-A-B shells in a multishell nanoalloy as in Figure 1.3(d). This arrangement has been observed for Pd-Au [189], Au-Ag [190], Pd-Pt [191] and trimetallic Au-Pt-Ag [192] nanoparticles and theoretically predicted for Au-Cu [193], Co-Rh [172] and Pd-Pt [194] nanoalloys. Moreover, simulations of Cu-Ag, Ni-Ag and Pd-Ag clusters found this ordering as a metastable state [195]. Alternating layers of dielectric and metal (*e.g.*, Au-SiO₂ [196, 197] and CdSe-ZnMnS [198]) also known as “nanomatyushkas” are also based on this type of ordering and yield interesting plasmonic responses. In the chemical ordering classification, it should be noted, however, that imperfect patterns are likely to be observed, giving some intermediate arrangements.

The adopted chemical arrangement of an A-B nanoalloy may be influenced by a complex competition between many factors. Relative strengths of homo- and heteronuclear bonds, relative atomic sizes, surface energies, charge transfer, electronic/magnetic effects and external (environmental) effects [116, 188] are the main contributors. With the help of Table 1.1, these six main effects can be briefly explained as follows:

- (i) Relative strengths of A-A, B-B and A-B bonds which correlate to the cohesive energy of the bulk metals and alloy. Mixing is favoured if the interatomic interaction of A-B is the strongest. Otherwise, segregation is preferred with a core of elements of the stronger homonuclear bonds.
- (ii) Relative atomic sizes between A and B. For a core-shell cluster, especially of icosahedral geometry, there is preference of the smaller atoms for core positions

Table 1.1: Cohesive energies, ε_{coh} , atomic radii, average surface energies, E_{surf} and Pauling electronegativities of the studied elements.

Properties	Ni	Pd	Pt	Cu	Ag	Au	Al
ε_{coh} (eV) [199]	-4.44	-3.89	-5.84	-3.49	-2.95	-3.81	-3.39
Atomic radii, r (Å) [199, 200]	1.245	1.375	1.385	1.28	1.445	1.44	1.43
E_{surf} (meVÅ ⁻²) [201–203]	149	131	159	113.9	78.0	96.8	71-75
Electronegativity [204]	1.9	2.2	2.2	1.9	1.9	2.4	1.6

to reduce the strain. This stabilisation mechanism is predicted for Au-Cu and Ag-Cu systems [205]. For the studied metals in this thesis, the classes discussed are small (atomic radii, r_{Ni} : 1.245 Å, r_{Cu} : 1.28 Å), medium (r_{Pd} : 1.375 Å, r_{Pt} : 1.385 Å) and large (r_{Ag} : 1.445 Å, r_{Au} : 1.44 Å), where the effect will be more apparent for a larger size mismatch between A and B.

- (iii) Minimisation of the surface energy by locating elements with the lower surface energy on the surface (segregation ordering). From Table 1.1, elements with high surface energies (Ni: 149, Pd: 131, Pt: 159 meVÅ⁻²), will have greater preferences for core sites, compared with those of low surface energy (Cu: 113.9, Ag: 78.0, Au: 96.8, Al: 71 – 75 meVÅ⁻²).
- (iv) Charge transfer. Significant difference in the electronegativities between A and B metals can lead to electron transfer and induce A-B mixing.
- (v) Electronic and/or magnetic effects. There is very strong interplay of these effects and other properties; at certain sizes and/or compositions, core-shell segregation or ordering is favoured due to the stabilisation by the electronic shell structure (as in the jellium model), *e.g.*, the stabilisation of core-shell polyicosahedra-based clusters for Ag-Cu [206].
- (vi) External effects. Chemical ordering is determined by the preparation method and experimental conditions. The use of supports, ligands and templates may promote certain elements to the surface if the interaction is very strong. A detailed discussion of the support effects will be presented in Chapter 8.

Surface studies are very important especially in catalytic chemical reactions, where the outer-layer or shell is the most active region [207]. For a bimetallic system, instead of inter-mixing, it is more likely to have surface segregation (including core-shell), enriched in one component [208–210]. Interestingly, the equilibrium of surface compositions are very dependent on the nature of surrounding media (phase, reagents, support) and their physical parameters (temperature, pressure, concentration, pH) [154, 210–214]. Therefore, discussion of surface segregation is as important as other cluster parameters (size, structure, among others).

Core-shell ordering receives considerable attention in nanoalloy cluster research [4]. It provides an extra dimension for tailoring chemical and physical properties by varying core to shell ratio [215], shell thickness [216] or core and/or surface dispersions [2, 217]. Not only spherical shape core-shell particles have been studied but (for example) core-shell rods (Au/Pt) [218], prisms (Ag/Au) [219], flowers (Au/Pd) [220], cubes (Au/Ag) [221], octahedra (Au/Pt) [222], hexagons (Ag/Au) [223] and dumbbells (Au/Ag) [224] show very interesting results.

The obvious benefit of the core-shell segregation is from an economic point of view in which optimum use of the precious metal (*e.g.*, Pd and Pt) [225] is attained by spreading it thinly on a shell, coated on a relatively inexpensive but less catalytically active metal (*e.g.*, Co, Ni, Cu). However, much interest has shifted towards the potential for synergistic improvement of catalysts [4, 116, 126, 226, 227].

1.7 Transition Metal Nanoalloys

Although chemical ordering in bulk alloys is often distinct from that in nanoalloy clusters, their mixing profiles are powerful tools in structure and ordering predictions. This is due to the fact that in addition to composition and temperature, bulk phases (mixed or segregated) are dependent on many factors: charge transfer, atomic lattice, bulk strain, cohesive energy, mixing energy and surface energy. Table 1.2 shows the bulk

phases of alloys (segregated/immiscible, disordered/solid solutions or ordered, mixed phases) combining transition metals of group 10 (Ni, Pd, Pt), group 11 (Cu, Ag, Au) and crossover combinations between the two groups. Ordered phases (commonly at low temperature), are observed at stoichiometric bulk compositions of Au-Cu (L1₂-Cu₃Au, L1₂-CuAu₃, L1₀-CuAu), Pd-Pt (L1₂-PdPt), Ni-Pt (L1₂-Ni₃Pt, L1₂-NiPt₃, L1₀-NiPt), Cu-Pd (B2-CuPd, L1₂-Cu₃Pd, tetragonal-Cu₄Pd) and Pt-Cu (L1₂-PtCu₃, L1₁-Pt-Cu) [228].

Taking into account all metals from the periodic table, there are more than 3,000 possible combinations of binary alloy [116]. Table 1.3 summarises the variety of patterns in which cluster phases can be segregated (core-shell or reversed core-shell) or mixed (ordered or disordered), prepared *via* chemical or physical means and/or with the external (*e.g.*, ligand, seed, support). Also included are results from theoretical calculations at the EP and DFT levels.

Comparison of cohesive energies (ϵ_{coh}), atomic radii (r_{M}), average surface energies (E_{surf}) and Pauling electronegativities as shown in Table 1.1 give simple prediction of the chemical ordering tendency. For nanoalloys of group 10, these favour Ni_{core}Pd_{shell} ($\epsilon_{\text{coh, Ni}} > \epsilon_{\text{coh, Pd}}$, $r_{\text{Ni}} < r_{\text{Pd}}$, $E_{\text{surf, Ni}} > E_{\text{surf, Pd}}$), Pt_{core}Pd_{shell} ($\epsilon_{\text{coh, Pt}} > \epsilon_{\text{coh, Pd}}$, $E_{\text{surf, Pt}} > E_{\text{surf, Pd}}$) and Pt_{core}Ni_{shell} ($\epsilon_{\text{coh, Pt}} > \epsilon_{\text{coh, Ni}}$, $E_{\text{surf, Pt}} > E_{\text{surf, Ni}}$). In a similar fashion,

Table 1.2: Bulk chemical ordering of the studied bimetallic systems (Review by [116] based on Refs.[228–234]), with segregated/immiscible (*i*), disordered/solid solutions (*s*) or ordered (*o*) mix phases. Some ordering only observed at either high (*ht*) or low (*lt*) temperatures.

	Cu	Ag	Au	Ni	Pd	Pt
Cu	-					
Ag	<i>s</i>	-				
Au	<i>o</i>	<i>s</i>	-			
Ni	<i>s</i>	<i>i</i>	<i>s</i>	-		
Pd	<i>s</i> ^{ht} , <i>o</i> ^{lt}	<i>s</i>	<i>s</i>	<i>s</i> ^{ht} , <i>o</i> ^{lt}	-	
Pt	<i>s</i> ^{ht} , <i>o</i> ^{lt}	<i>i</i>	<i>s</i> ^{ht} , <i>i</i> ^{lt}	<i>s</i> ^{ht} , <i>o</i> ^{lt}	<i>o</i>	-

Table 1.3: Various chemical orderings of bimetallic clusters prepared *via* chemical (chem.) or physical (phys.) means or with external (ext.) (*i.e.*, ligand, seed, support) effects, along with the theoretical (EP and DFT) predictions.

A	B	A _{core} B _{shell}	B _{core} A _{shell}	ordered mix.	disordered mix.
group 10					
Ni	Pd	chem. [225, 235, 236], DFT [237]	chem. [238], ext. [239]		chem. [240]
Ni	Pt	EP [241]	ext. [242–244]	DFT [245]	chem. [246]
Pd	Pt	chem. [247, 248]	chem. [144, 249–251], ext. [252], DFT [253–256], EP [171, 194, 257, 258]		phys. [259, 260], chem. [261, 262]
group 11					
Cu	Ag	phys. [263, 264], chem. [265], EP [43, 148, 203, 266–269], DFT [43, 269, 270]	chem. [271–273]		EP [274]
Cu	Au	EP [275–278]	chem. [279], EP [275, 276, 280]	phys. [281, 282], DFT [245], EP [283]	phys. [282, 284, 285], chem. [286–288] EP [275]
Ag	Au	phys. [186, 187, 289], chem. [290–292], ext. [293–297], DFT [255, 298–300]	chem. [271, 297, 301–304], ext. [293, 297, 305], EP [278, 306],	ext. [307]	phys. [184, 185, 289, 308], chem. [303, 309, 310], ext. [293, 305, 311, 312], DFT [313, 314]
Gr. 10 - Gr. 11					
Ni	Cu	DFT [315], EP [316]			
Ni	Ag	phys. [125, 308, 317], EP [43, 203]			chem. [240]
Ni	Au	phys. [318], chem. [319], ext. [320], EP [125]	chem. [321], ext. [320]		ext. [322], EP [135, 274]
Cu	Pd	chem. [279, 323], EP [316]	phys. [279], ext. [168, 324, 325]	chem. [326, 327], ext. [328], EP [316, 329, 330]	chem. [160, 327, 331]
Cu	Pt	chem. [332]	chem. [332]	chem. [326]	chem. [332], ext. [333]
Pd	Ag	ext. [334, 335]	chem. [336], ext. [337]		chem. [338, 339], ext. [340, 341]
Pd	Au	ext. [342–344], DFT [255, 345]	chem. [155, 346–349], ext. [350, 351], DFT [352]	ext. [353]	chem. [354], ext. [355]
Pt	Ag	DFT [255]	chem. [291]		ext. [340], EP [274]
Pt	Au	phys. [356], chem. [192, 271], DFT [357, 358]	chem. [192, 271, 291, 359]		chem. [338], ext. [145, 360, 361], EP [274],

nanoalloys of group 11 show prevalence of $\text{Cu}_{\text{core}}\text{Ag}_{\text{shell}}$ ($\varepsilon_{\text{coh, Cu}} > \varepsilon_{\text{coh, Ag}}$, $r_{\text{Cu}} < r_{\text{Ag}}$, $E_{\text{surf, Cu}} > E_{\text{surf, Ag}}$), $\text{Cu}_{\text{core}}\text{Au}_{\text{shell}}$ ($r_{\text{Cu}} < r_{\text{Au}}$, $E_{\text{surf, Cu}} > E_{\text{surf, Au}}$) and $\text{Au}_{\text{core}}\text{Ag}_{\text{shell}}$ ($E_{\text{surf, Au}} > E_{\text{surf, Ag}}$, $\varepsilon_{\text{coh, Au}} > \varepsilon_{\text{coh, Ag}}$) [116]. Moreover, nanoalloys formed by a combination of group 10 (Ni, Pd, Pt) and group 11 (Cu, Ag, Au) metals favour cores of the former (significantly larger ε_{coh}) and shells of the latter (larger in size and relatively small E_{surf}).

1.7.1 Group 10: Ni-Pd, Ni-Pt and Pd-Pt

Ni-Pd clusters are more efficient catalysts compared with their mono-metallic counterparts for Sonogashira coupling [225], nitro-substituted aromatic hydrogenation [362] and Hiyama cross-coupling [363] reactions, although there are no improvements of activity shown in the CO oxidation [235] and butadiene hydrogenation [364]. However, in these experiments, $\text{Ni}_{\text{core}}\text{Pd}_{\text{shell}}$ is formed, agrees with theoretical results [241], which is very interesting from an economic point of view.

Meanwhile, there is a potential for Ni-Pt alloy incorporation in polymer electrolyte fuel cells, based on the observed kinetic enhancement in the low-temperature oxygen reduction experiments [365]. Structurally, small Ni-Pt clusters have been predicted to adopt icosahedral shapes and as the number of atoms increases fcc-based cubooctahedra prevailed [366, 367]. However, the use of ligands such as CO has been shown to stabilise small fcc clusters [242–244].

The Pd-Pt system is one of the main nanoalloys studied in this thesis; hence, more detailed discussion will be presented in Chapters 3, 4, 6 and 7.

1.7.2 Group 11: Cu-Ag, Cu-Au and Ag-Au

Polyicosahedra are found as the most stable motif at the DFT level for 34-, 38-, 40- and 45-atom Cu-Ag clusters [43, 203, 206, 270, 368]. There are large HOMO-LUMO gaps (~ 0.8 eV), indicating electronic shell closure, in agreement with the magic jellium sizes for which peaks at $N = 8, 20, 34, 40$ and 58 are observed from the mass spectra

[369]. The stability of small polyicosahedra clusters is enhanced by the size mismatch, which is also evident in the stabilisation of 2D planar structures [369].

A similar series of jellium magic numbers are reported for Cu-Au clusters from laser vaporisation experiments [370]. On the other hand, several motifs co-exist for clusters prepared *via* chemical methods [286, 371, 372], due to a small energy gap [373]. However, specific shapes can be stabilised by thermodynamic equilibrium (*e.g.*, using an electron beam [374]) or external (*e.g.*, capping agent [288]) effects.

Calculations of 34- and 38-atom Cu-Au clusters give consistent conclusions, in which depending on composition, polyicosahedral, decahedral and fcc structures appeared as GM [203, 375, 376]. Greater resemblance of Cu-Au structures toward those of Cu clusters are however predicted by the many-body Gupta-type potential [188, 373, 377–379]. Size mismatch causes stabilisation of ordered stoichiometric [275, 276] and disordered [253] small icosahedral clusters. Large (up to 561 atoms) clusters also exhibit this effect [280] but bulk-like fcc is likely to prevail with the formation of “spherical” clusters [281, 283].

The optical properties of Ag-Au are one of the most interesting features of nanoalloys, which are essential for example in anti-counterfeiting measures [295]. More importantly, these properties have been shown to be tuneable by varying the composition, shape and chemical ordering of clusters [289, 295, 299, 380, 381]. This fine-tuning ability also made it possible to use them in the DNA detection [173, 382]. Moreover, Ag-Au clusters proved to be selective catalysts for alkene epoxidation [383, 384]. Theoretical researches by the Johnston group have shown that there is competition between several motifs [385], due to composition [386], ordering [306, 387] and charge transfer [388] effects.

Studies of 34- and 38-atom Ag-Au clusters [306, 329] showed a strong dependence of size and/or composition on the structural motifs. Fcc, Dh and polyicosahedral (pIh) motifs are competitive, with fcc-TO preferred at $N = 38$ due to magic size. Changes

in composition give a prevalence of icosahedra clusters, which are predicted for magic sizes 55, 147, 309 and 561. For the non-magic sizes, crossover of several motifs is expected [385]. Recently, EP-DF calculations have shown that small Ag-Au clusters are also strongly influenced by the dipole moment [389].

1.7.3 Group 10 – Group 11: (Ni, Pd, Pt)–(Ag, Au, Cu)

Nanoalloys formed between transition metals from group 10 (Ni, Pd, Pt) and group 11 (Cu, Ag, Au) show significantly different activation towards catalysis, in which group 10 is known as active while group 11 is less active/inactive [390]. Promising results are reported for a wide range of catalytic applications; thermolysis of ammonium perchlorate (Ni-Cu [391]), steam reforming of *n*-butane (Ni-Au [322]), NO reduction (Cu-Pt [332]), oxidation and hydrogenation of CO and unsaturated hydrocarbons (Cu-Pd [325, 392, 393], Pt-Au [394, 395]). Catalytic enhancement of Pt-based nanoalloys for the oxidation of methanol [396] and formic acid [397–399] proved to be significant towards the development of fuel cells.

Combined EP-DF searches of Cu-Pd [329], Pd-Ag [329], Ag-Pt [255] and Pt-Au [358, 400] clusters found several competitive morphologies (fcc, decahedral, icosahedral), that are dependent on size and composition. At certain sizes, magic character gives significant stabilisation of specific motifs, *e.g.*, fcc-TO ($N = 38$) and Leary Tetrahedron (LT) ($N = 98$). Large size mismatch (*e.g.*, in Ag-Ni) is predicted to stabilise polyicosahedral clusters, *via* minimisation of the internal strain [203]. On the other hand, systems with a small size mismatch (*e.g.*, Ag-Pd) have less tendency to adopt polyicosahedral structures [205]. There are consistent predictions between the two levels of theory (*i.e.*, EP and DFT) but due to charge transfer/directionality effects, some discrepancies have been observed for Ag-Pt and Ag-Au [255].

The combination between Pd and Au is one of the most interesting binary systems of these groups, especially for their immense potential as a catalyst. A detailed discussion of this system will be presented in Chapters 3, 4, 5, 7 and 8.

1.7.4 Group 10/11 (Ni, Pd, Pt, Ag, Au, Cu) – Other Transition Metals

Co-based Clusters

In proton exchange membrane fuel cells (PEMFCs) development, cost of the metallic elements is one of the concerns. Use of the expensive platinum, however, can be reduced by using Co-Pt nanoalloys [401]. Promising enhancement of performance is predicted based on the study of oxygen reduction [365, 402]. Although there is an issue of Co dissolution, recent studies show that Co-Pt can be stabilised by using alkaline media [403]. Moreover, Co-based nanoalloys are also effective in catalytic growth of carbon nanotubes (Co-Ni [404, 405]) and hydrogenation of aromatics (Co-Ni [406]). It is possible that magnetic properties of Co are reduced due to alloying with other transition metals [407–412] but better stability is achieved [413]. In terms of the ordering, there is a good agreement between experimental and theoretical research for a prevalence of a core-shell with Co core in nanoalloy clusters with Pd [414–416], Pt [411–413, 417], Ag [270, 418–421], Au [418] or Cu [409, 411, 422], due to greater cohesive energy [199], greater surface energy [201–203] and smaller atomic size [199, 200] of Co. For Co-Ag, the stabilisation of this ordering is further enhanced by the quantum effects in which magnetic moments are modified for buried Co [116]. Variation of the preparation methods, however, gives a reversed core-shell ordering (*i.e.*, Co shell) [417]. Depending on size, the evolution in cluster shape (fcc structure [241, 417, 423] or icosahedral [409, 411, 422]) and other physical properties (*e.g.*, optical [125]) are also observed.

Fe-based Clusters

Similar to Co, Fe-(Pt [424, 425], Au [410, 426]) nanoalloys are also of interest due to their magnetic properties and are good candidates for ultrahigh-density magnetic recording media [116]. Noble metal coating solves the stability problems of Fe towards oxidation [427]. The core-shell clusters are observed when Fe combines with Ni [428],

Pt [70] or Au [426], with the tendency of Fe to occupy core sites. CO ligands, however, reverse this ordering [429, 430] *via* electron transfer [116]. Due to size mismatch in Fe-Au, large icosahedra are stabilised [427]. This is in contrast to Pt-Fe, for which the theoretical predictions show a preference for fcc packing over icosahedral, even for small clusters [70]. In the nanoparticle growth process, both are stabilised by kinetic trapping [431]. Also, structure [424, 425] and site preference [432, 433] are significantly influenced by temperature and cluster composition.

Ru-based Clusters

Combination of Ru and many transition metals (Pd, Pt, Cu and Ag) shows greater activity, selectivity and resistance to sulphur poisoning in hydrogenation reactions [434–436]. However, their potential in fuel cell applications [23, 437] have received more interest, in which an improvement in the oxidation of methanol [438–440] and CO [441, 442] is observed. Ru also promotes a better tolerance against catalyst poisoning, which is suggested based on the bifunctional mechanism (provision of adjacent oxophilic sites to facilitate oxidative removal of poisoning intermediates) and modification of electronic structure to reduce the strength of the Pt-CO bond [443–445].

In the bulk, Ru-Pt alloys adopt hexagonal close-packed (hcp) packing but for small clusters, fcc are adopted [446], with $\text{Ru}_{\text{core}}\text{Pt}_{\text{shell}}$ ordering. Reversed core-shell, however, can be prepared, for example by an electro-deposition method [447], or the inclusion of a support [448]. Interaction between cluster and support also plays an important role in Cu-Ru, for which mixing ordering is stabilised, even though it is immiscible in the bulk [434, 449].

Mo-, Re-, Rh-, Sn- and Zn-based Clusters

Synergistic effects in catalysis are observed in the following bimetallic systems: Rh-Pt (hydrogenation of crotonic acid [450], reduction of NO [451]), Au-Re (DNA-probe [452]), Mo-Pt (oxidation of H_2/CO mixtures [441, 453]), Cu-Sn (Ullmann etherification

[454]), Zn-Ni (detection of uric acid (UA) [455]) and Cu-Zn (Ullmann etherification [454]). Moreover, enhanced magnetisation (Ni-Rh [456]) and surface plasmon (Cu-Zn [457]) properties of these clusters are also of interest. In the Cu-Zn case, pseudo-spherical clusters with a more faceted shape are produced, with a variation in the ordering – dependent on the method and type of surfactant [457, 458].

1.8 Supported Clusters

Although many theoretical calculations have focussed on the free clusters, it is difficult to get interaction-free clusters [459]. As an alternative, many supports have been included, either reactive or non-reactive. This adds extra complexity when determining the geometric structures and stabilities of the clusters. However, the inclusion of a support is very interesting from a catalysis point of view, as distinct behaviour from a variation of support is expected.

Depending on the metal systems being studied, a support can be chosen based on reaction needs. For example, in the gold catalysed oxidation of CO, enhanced reactivity is achieved with Al₂O₃ support, due to the presence of Au-O back-bonding. However, a similar observation is not detected for Au/SiO₂ and Au/TiO₂ catalytic systems, in which gold structures remain unchanged [460].

Metal-support interactions have a targeted and very specific function in catalytic reactions. In the conversion of methanol to CO₂, the Pt nanocluster performance order is Pt/MgO \geq Pt/TiO₂ \gg Pt/Al₂O₃. Combustion in NH₃ atmosphere still favours the MgO support. Analysis of the X-ray Absorption Spectroscopy reveals the metallic state of Pt but a strong interaction with the TiO₂ and Al₂O₃ resulted in a weaker catalytic behaviour. In contrast, there is no evidence for interaction between Pt and MgO [461].

One might argue that the improvement of catalysis might be due to support participation. However, this is not always true as inactive γ -Al₂O₃ are reported to increase

the action of Pt catalysts in the hydrolysis of NH_3BH_3 . In this reaction, hydrogen release rates are in the order $\text{Pt}/\gamma\text{-Al}_2\text{O}_3 > \text{Pt}/\text{C} > \text{Pt}/\text{SiO}_2$, with a strong influence of particle size [462].

1.8.1 Alumina, Al_2O_3

Both $\alpha\text{-Al}_2\text{O}_3$ and $\gamma\text{-Al}_2\text{O}_3$ have been reported as supports for cluster nanoparticles. The $\alpha\text{-Al}_2\text{O}_3$ supports are shown to stabilise elongated prisms, icosahedra and cubes of Pd, pre-formed by the capping agent. These structures show variation of (111)/(100) facet ratios, in which the (111) site is more efficient for selective butadiene hydrogenation [463]. Generally, Pd-Pd bonds are stronger than Pd-alumina interactions, resulting in a bad wetting regime for large Pd particles and Pd clusters adopt 3D structures on alumina, starting from very small sizes [464].

One of the challenges in very small cluster research is to prevent particles from agglomeration, which is successful in the presence of $\gamma\text{-Al}_2\text{O}_3$, as reported for Pt, Rh [465] and Ir [466] clusters. Highly dispersed bimetallic Pd-Cu [467, 468] and Re-Pt [469] have also been reported, being confirmed from Extended X-Ray Absorption Fine Structure (EXAFS) analysis.

1.8.2 Carbon (Graphite, Graphene, Carbon Nanotubes)

The use of a support might alter chemical ordering profiles of bimetallic systems. One reason for this is due to different interactions of the metal component to the substrate. For instance, weaker binding of Cu and Au to the graphite surface leads to segregation of Cu-Ni and Pt-Au clusters. However, Cu and Au (in Cu-Ni and Pt-Au, respectively) tend to diffuse towards the core upon heating, forming island-like layers instead of a mixed phase [470]. Similarly, core-shell to mixed phase transformations are predicted for Pd-Cu, Pd-Rh and Pd-Pt nanoclusters [471]. Island formation is associated with the high mobility of adatoms and single clusters on graphite surfaces [472].

Graphene and single wall carbon nanotubes (SWNTs) have also attracted wide at-

tention as a support, especially for their strong bonds to the metal. Upon interaction with the graphene surface, the shapes of 13-atom icosahedral Pt clusters are significantly deformed. Pt-Pt bonds are elongated from 2.76 (in the free Pt₁₃ cluster) to 2.85 Å. Greater stability of this small cluster is attained by replacing graphene with SWNTs [473].

1.8.3 Silica, SiO₂

Careful consideration of the type of support is needed when dealing with heterogeneous catalytic reactions. For example, silica supports have been reported as a non-reactive phase in the oxidation of CO, catalysed by Pt or Pt-Fe, otherwise, CO adsorption would be hindered [474]. Moreover, silica supports show the ability to increase the degree of Ni-Ag nanoparticle dispersion, which is linked to an improvement in catalytic hydrogenation reactions [475].

1.8.4 Magnesia, MgO

In the gas phase, there is considerable stability of planar shapes for small clusters ($N \leq 15$) for Au and Pd. On the MgO support, however, compact structures are competitive, in which the cluster-support adhesion is maximised [476, 477]. Furthermore, strong cube-on-cube epitaxy of metal-support stabilises the fcc structure of these metals at a very small sizes (below 30 atoms) [478], while in large clusters, truncation, stacking faults and dislocations dominate [479, 480].

Studies of bimetallic clusters have shown epitaxial growth, such as the Pd-Cu [481] and Pd-Pt [386] systems. The complex competition between mono-metallic, bimetallic and metal-oxide interactions can, however, change the chemical order of clusters. Without support, Co-Ag appears as stable mixed phase clusters [482] but a relatively stronger Co-O bonding (compared with Ag-O) leads to Co segregation to the interface and significantly reduces the magnetic properties of Co-Ag [483].

Very small clusters (< 5 atoms) of Pd, Ag and Au on the MgO substrate are very

interesting, as they are more mobile than a single atom, in agreement with molecular beam epitaxy data. A variety of mechanisms such as rotation, walking, rolling and sliding are involved [484, 485]. The occurrence of local defects stabilises these clusters, either by oxygen vacancy (F_s -centre) [486] or the removal of an MgO dimer (double vacancy, DV). The DV however, causes structural modification of MgO and the energy decreases by ~ 2.90 eV [487]. Based on the spherical jellium model, Ag_8 is a magic cluster and upon interaction with the DV site retains this feature. However, alloys of eight-atom Ag-based clusters give different magic character in the order of Au-Ag > Cu-Ag > Pd-Ag, with Pd-Ag actually losing magic character, confirmed by the HOMO-LUMO gap [488]. Furthermore, DV sites give rise to fascinating new planar structures and cage motifs [476].

Chapter 2

Theoretical Background and Methods

This chapter will discuss the theoretical background of the electronic structure calculations (Section 2.1), both at the *ab initio* (2.1.1) (especially the DFT) and EP (2.1.2) levels. Furthermore, the predecessor to the DFT (2.2) and DFT development (2.3) will be presented, followed by details of the theoretical (2.4 – genetic algorithm, 2.5 – Basin-Hopping Monte Carlo, 2.6 – Gupta potentials, 2.7 – combined EP-DF) calculations, along with the chosen parameters. Post-calculation analyses (2.8 – energetic, 2.9 – bonding, 2.10 – ordering and 2.11 – point group symmetry) will also be described.

2.1 Electronic Structure Theory

Mathematical and theoretical principles have been applied to solve many chemical problems and the introduction of computers sped-up the process along with giving better prospects of studying more complicated systems. The behaviour of individual molecules can be described, for which a better understanding of experimental observations can be achieved. Theoretical methods are alternatives for impractical experiments, measurements or characterisations. Moreover, having a good theoretical understanding of certain reactions before they are ever studied in the laboratory is far cheaper than a trial-and-error approach [32, 33, 37, 371, 489]. The heats of formation, energies (bond, reaction, activation), structures (thermodynamics, kinetics and mechanisms),

mechanisms (transition states, pathways, charges) and molecular spectra (IR, Raman spectra, UV/Visible, NMR spectra) [490] are candidates for theoretical calculations and are commonly combined with the electron [491] and X-ray [492] diffraction patterns, photoelectron spectra [493] or cluster mobility data [494] for structural determinations.

Electronic structure can be described by either *ab initio* Molecular Orbital (MO) or semi-empirical atomistic potentials with the aim to find a GM [188, 495]. The GM is the most preferred structure to be found experimentally [496] but other structures (metastable) are frequently observed due to kinetic effects [497], in agreement with the theoretical searches which give many competitive structural motifs [54, 498–504]. As a result, calculations are computationally heavy and a good balance between accuracy and calculation time is becoming the main objective.

Some high level *ab initio* theory methods (*e.g.*, DFT) have been shown to give accurate predictions for catalyst improvements (activity, selectivity and stability) [505] and complex systems (*e.g.*, enzymes, biological compounds) [506, 507]. However, high accuracy in the *ab initio* methods generally comes at a high computational cost and is only feasible for small systems (tens of atoms). For medium-sized systems (hundreds of atoms), less rigorous calculations are more reasonable and can be done by using the empirical or semi-empirical methods. Here, instead of solely quantum physics (as in the *ab initio*), experimental parameters and extensive approximations (*e.g.*, by considering only valence electrons) are incorporated. On the other hand, Molecular Mechanics (MM) is more suitable for very large (thousands of atoms) and non-symmetric chemical systems, such as enzymes, proteins and polymers. This modelling technique, however, only studies motions of the nuclei and does not involve the explicit treatment of electrons. Less computational effort is needed, although it is system-dependent, limited (often involving commercial software) and not suitable for systems or processes which involve bond breaking mechanisms.

2.1.1 First Principles Methods

Ab initio (Latin term meaning “from the beginning”) or first principles methods are the electronic structure methods that are based upon the principles of quantum mechanics. They take into account the laws of quantum mechanics, atomic properties (masses, electron charges, atomic nuclei), electronic properties (structure, spin states) and the values of fundamental physical constants, without any approximations or experimental-based data. The methods give accurate and consistent estimations of a variety of molecular systems – for diverse properties, ground states, excited states and reactions. A system can be studied quantitatively either by short single-point energy calculation or by letting the system geometrically relax to a more stable configuration.

In quantum theory, the distribution of electrons in an atom can only be described probabilistically as a complex-valued function – the wave function. This mathematical function satisfies the Schrödinger equation. However, due to the nature of electrons, a solution for the equation is very complex and there is a need of knowledge and experience, so that the calculations are feasible and reliable. With more electrons involved in a system, the complexity of the solution grows rapidly. In “Molecular Orbital” methods, a set of mathematical functions (called the “basis set”) is used and depending on the required accuracy of calculation, there are options in choosing the basis sets. A better approximation can be obtained using a large basis set but at the expense of more computer resources.

There are two major sub-classes of *Ab initio* methods, where the first are methods that treat the wave function directly, with the simplest being a solution for just a single-particle. Reasonable accuracy can be achieved with the Hartree-Fock (HF) method [508–510] but for better approximation of the electronic structure, more expensive Configuration Interaction (CI) method can be used [511]. The second class of methods involved a solution of a wave function indirectly, using objects related to the wave function, such as the electronic density (*e.g.*, DFT) [512].

2.1.2 Empirical Methods

Empirical methods are an alternative to computationally-demanding *ab initio* methods. The methods, however, show inaccuracy when encountering hydrogen-bonding, chemical transitions or nitrated compounds [513, 514] and are system-dependent, in which the results are doubtful for general situations. Satisfactory accuracy levels may be obtained, for example with a validation against the *ab initio* results.

Semi-empirical techniques are useful in preliminary theoretical studies when the complexity of a system is unknown. Since it is still, at present, relatively too expensive for *ab initio* methods to be applied to large systems, the development of empirical atomistic potentials continues to be relevant [188].

In the study of nanoalloys, “homotop” issues give an additional reason to implement semi-empirical methods. Among highly efficient unbiased optimisation methods that have been developed for clusters are the genetic algorithm (GA) [515–517], the basin hopping (BH) method and its variants [495, 518, 519]. The inter-atomic potential is described by several models (*e.g.*, Gupta, Sutton Chen, Morse, EAM) [188] and for clusters of transition metals (metallic and bimetallic), Gupta-based potentials have shown to give convincing results [43, 203, 277, 280]. The main problem with these optimisations is the need for an extensive sampling of the PES. A common solution is a combined empirical-*ab initio* approach, in which unbiased searches are carried out at empirical level before some of the candidate structures (global and local minima) are chosen for the optimisation at the *ab initio* level [116].

2.2 Density Functional Approach

2.2.1 The Schrödinger Equation

The N interacting electrons of the many-body problem are defined by the Schrödinger equation,

$$\left(-\frac{\hbar^2}{2m_e} \sum_{i=1}^N \nabla_i^2 + \frac{1}{2} \sum_{i,j=1, j \neq i}^N \frac{e^2}{|r_i - r_j|} + \sum_{i=1}^N v_{ext}(r_i) \right) \psi(x_1, \dots, x_N) = E\psi(x_1, \dots, x_N) \quad (2.1)$$

where E is the total energy, ψ is the wave function, $v_{ext}(r_i)$ is the external potential and $x_i = (r_i, \sigma_i)$ represents a set of both position and spin values for the i -th electron. Other terms are electron mass, m_e , electron charge, e , reduced Planck constant, \hbar and Laplacian, ∇_i^2 . In the operator form, the equation becomes,

$$\left(\hat{T} + \hat{V}_{ee} + \hat{V}_{ext} \right) \psi(x_1, \dots, x_N) = E\psi(x_1, \dots, x_N) \quad (2.2)$$

where the kinetic energy operator, \hat{T} , the electron-electron interaction \hat{V}_{ee} and the external potential, \hat{V}_{ext} are,

$$\hat{T} = -\frac{\hbar^2}{2m_e} \sum_{i=1}^N \nabla_i^2 \quad (2.3)$$

$$\hat{V}_{ee} = \frac{1}{2} \sum_{i,j=1, j \neq i}^N \frac{e^2}{|r_i - r_j|} \quad (2.4)$$

$$\hat{V}_{ext} = \sum_{i=1}^N v_{ext}(r_i) \quad (2.5)$$

The Coulombic attraction is normally used as the external potential for solid-state physics and chemistry,

$$v_{ext}(r) = -\sum_{j=1}^N \frac{Z_j e^2}{|r - R_j|} \quad (2.6)$$

where for nuclei j , R_j are the locations and Z_j are the charges. The positions of the nuclei can be treated as static due to the considerable difference in mass between the nucleus and the electron (Born-Oppenheimer approximation [520]). Hence, only the

electronic part needs to be solved in the Schrödinger equation and the total density of electrons is defined as,

$$\rho(r) = N \sum_{\sigma_1, \dots, \sigma_N} \int dr_2, \dots, dr_N |\psi(x_1, \dots, x_N)|^2 \quad (2.7)$$

2.2.2 Variational Principle

Many theoretical calculations rely on the variational principle in finding the solution for the ground-state structure,

$$E_0 = \min_{\psi} \langle \psi | \hat{H} | \psi \rangle / \langle \psi | \psi \rangle \quad (2.8)$$

The algorithm searches for the total energy minimum from a trial wave function to get the true ground-state wave function, ψ [521]. HF and CI theory are based on this minimisation.

2.2.3 Hohenberg-Kohn Theorem

In principle, the ground-state electronic structure can be solved starting from the external potential of Eq. 2.1, to give the wave function and subsequently other related properties. Solution of the many-body wave function, however, is not easy and theoretically, the functionals of the electronic density, $F[\rho(r)]$ can be used as an alternative.

$$F[\rho(r_{trial})] \geq E_0 \quad (2.9)$$

Assuming that the ground-state is non-degenerate, one-to-one connection between this functional and the potential is proven by “*reductio ab absurdum*” [522].

2.2.4 Levy-Constrained Search Proof

In 1979, further proof that density uniquely characterises a system was presented by Levy [523]. By rewriting the variational principle, Eq. 2.8, the total energy now becomes,

$$E[\rho(r)] = \min_n \left[F[\rho(r)] + \int d^3r v_{ext}(r) \rho(r) \right] \quad (2.10)$$

where the functionals of the electronic density, $F[\rho(r)]$ are from the minimisation over all many-body wave functions,

$$F[\rho(r)] = \min_{\psi \rightarrow n} \langle \psi | \hat{T} + \hat{V}_{ee} | \psi \rangle \quad (2.11)$$

$F[\rho(r)]$ is universal and independent of the external potential. Using the variational principle, the ground state density satisfies the stationary principle,

$$\delta \{ F[\rho(r)] + \int d^3r v_{ext}(r) \rho(r) - \mu \int d^3r \rho(r) \} = 0 \quad (2.12)$$

and establishes a relationship between the external potential and the electron density,

$$v_{ext}(r) = \mu - \frac{\delta F[\rho(r)]}{\delta \rho(r)} \quad (2.13)$$

Splitting $F[\rho(r)]$ into kinetic, $T[\rho(r)]$ and interaction, $V_{ee}[\rho(r)]$, parts, the total energy is expressed as a functional of the density,

$$E[\rho(r)] = T[\rho(r)] + V_{ee}[\rho(r)] + \int d^3r v_{ext}(r) \rho(r) \quad (2.14)$$

By assuming $F[\rho(r)]$ is approximated accurately, there will be equivalence between Eq. 2.14 and the Schrödinger equation (Eq. 2.1) but here involving three components with only one variable, the electronic density.

2.2.5 Thomas-Fermi (TF) Model

The Thomas-Fermi (TF) model is a simple approach, writing the total energy as a functional of the electronic density [524, 525],

$$E[\rho(r)] = T_{TF}[\rho(r)] + U_H[\rho(r)] + \int d^3r v_{ext}(r) \rho(r) \quad (2.15)$$

with

$$T_{TF}[\rho(r)] = \frac{3}{10}(2\pi^2)^{\frac{2}{3}} \int d^3r \rho^{\frac{5}{3}}(r) \quad (2.16)$$

is from the kinetic energy of a uniform non-interacting electron gas and,

$$U_H[\rho(r)] = \frac{1}{2} \int d^3r \int d^3r' \frac{\rho(r) \rho(r')}{|r - r'|} \quad (2.17)$$

is the classical Hartree term. The approximation of this theory remains inaccurate mainly due to the way kinetic energy is represented. It, however, still made a major contribution towards the development of modern DFT.

2.2.6 Kohn-Sham Equation

The realisation of DFT implementation only happened in 1965 when Kohn-Sham (KS) [526] developed the fictitious non-interacting system with the same (exact) density as the real system. A Slater determinant of single-particle orbitals, ϕ_s is used,

$$T_s[\rho(r)] = \min_{\phi_s \rightarrow n} \langle \phi_s | \hat{T} | \phi_s \rangle \quad (2.18)$$

and the functional, $F[\rho(r)]$, is the sum of this non-interacting kinetic part, the classical Hartree contribution and the exchange-correlation term, $E_{XC}[\rho(r)]$ (or separated parts, $E_X[\rho(r)]$ and $E_C[\rho(r)]$). The total energy now becomes,

$$E[\rho(r)] = T_s[\rho(r)] + U_H[\rho(r)] + E_{XC}[\rho(r)] + \int d^3r v_{ext}(r) \rho(r) \quad (2.19)$$

and the Euler-Lagrange variation with constrained electron number gives the KS equation,

$$v_{KS}(r) = \mu - \frac{\delta T_s[\rho(r)]}{\delta \rho(r)} \quad (2.20)$$

which is equivalent to,

$$\left(-\frac{1}{2}\nabla^2 + v_{KS}([\rho(r)]; r) \right) \phi_i(r) = \epsilon_i \phi_i(r) \quad (2.21)$$

and the KS orbitals are,

$$v_{KS}(r) = v_{ext}(r) + v_H(r) + v_{XC}(r) \quad (2.22)$$

with

$$v_H(r) = \frac{\delta U_H[\rho(r)]}{\delta \rho(r)} \quad (2.23)$$

$$v_{XC}(r) = \frac{\delta E_{XC}[\rho(r)]}{\delta \rho(r)} \quad (2.24)$$

and electronic density,

$$\rho(r) = \sum_i \theta(\mu - \epsilon_i) |\phi_i(r)|^2 \quad (2.25)$$

Starting with the initial guess *via* a self-consistent scheme, the solution of the KS equation (2.21) can be achieved. This equation solves the complex many-electron problem, *e.g.*, total energy calculations. For the occupied KS orbitals,

$$E[\rho(r)] = \sum_{occ} \epsilon_{KS} + U_H[\rho(r)] + E_{XC}[\rho(r)] - \int d^3r v_H(r) \rho(r) - \int d^3r v_{XC}(r) \rho(r) \quad (2.26)$$

The exchange-correlation functional, E_{XC} , however, must be approximated, either by local or semi-local representations [527, 528]. The local density approximation (LDA) is the simplest one but over-emphasis on the metallic character made it only suitable for a homogeneous electron gas [529]. Meanwhile, generalised gradient approximation (GGA) includes both density and the gradient of the density. Improvement in exchange-correlation functionals has been found for hybrid functionals, *e.g.*, by Becke [530] and Ernzerhof [531] to solve many issues with molecular calculations, including bond lengths and vibration frequencies.

2.3 Density Functional Theory (DFT)

DFT, the density-based description of matters is a new approach to quantum mechanics. Compared to the wave function, electron density is more manageable and practical, for which larger systems can be considered. Table 2.1 shows the significant landmark towards the development of the modern DFT. The DFT and HF scaled at N^3 or even N (N is the calculation effort over the number of electrons), as compared with N^5 for approximate CI methods (full CI would be as high as $exp(N)$). [511].

Generally, DFT methods can be applied to many systems of different type of bonding (metallic, covalent and ionic). Classical troublesome systems of super-conductivity [556], magnetic properties of alloys [557, 558], quantum fluid dynamics [559], molecular dynamics [560] and nuclear physics [561, 562] are now being well-handled by DFT. However commonly used DFT functionals fail to deal adequately with dispersion forces, even when they are corrected by the gradient of the electron density [563].

There are a large number of benchmarks which can be used for DFT validation, either against experiments [typically cohesive energy (ΔE_{coh}) or atomisation energy;

Table 2.1: Timeline of historical landmarks in DFT development.

1926	Quantum state physics description by Schrödinger [532].
1927	Introduction of the density-based Thomas and Fermi model [524, 525].
1928	Dirac adds an exchange energy functional term to the Thomas-Fermi model [533]. Hartree proposed a method for a solution of problems in atomic structure, which became an approximation to the self-consistent field Hartree-Fock method [508, 534, 535].
1930	Work of Hartree perfected by Slater [536] and Fock [537].
1933	Pioneering electronic structure calculation of sodium by Wigner and Seitz [538, 539].
1935	First gradient density functional by von Weizsäcker [540].
1937	Augmented plane wave method (APW) is developed by Slater [541].
1951	Important simplification of Hartree-Fock theory by Slater with the use of $X\alpha$ approximation [542].
1959	Introduction of the pseudopotential method [543].
1964	Hohenberg and Kohn justified Slater's work [522] and suggested the contribution of the Kohn-Sham non-interacting particles, which can be approximated by LDA, a known approximation from uniform gas exchange-correlation energy [526, 539, 544, 545].
1972	Spin-polarised DFT [546].
1975	Linear augmented plane waves (LAPW) and linear muffin-tin orbitals (LMTO) methods are introduced [547].
1979	Constrained minimisation approach by Levy proves the existence of a universal functional in the DFT [523, 548].
1984	Formal foundation of the time-dependent DFT by Runge and Gross [549, 550].
1985	Implementation of DFT in Car-Parrinello molecular dynamics [551].
1988	DFT successfully used for chemical problems with the Becke [552] and Lee-Yang-Parr (LYP) [553] functionals. GGA is adopted to improve the LDA description of the binding energy of molecules [552, 553].
1989	Significant use of <i>ab initio</i> programs by non-theorists with the implementation of the DFT in the Pople's electronic structure code, Gaussian [554].
1998	Nobel Prize in Chemistry for Walter Kohn “for his development of the density-functional theory” and John A. Pople “for his development of computational methods in quantum chemistry” [555].

equilibrium volume (V_0); elastic properties such as bulk modulus (B_0) and elastic constants (C_{ij}); and thermal quantities such as melting temperature (T_m) and thermal expansion coefficient, ($\alpha_{V,rt}$)] or against high-level wave-function based calculations, although there are no conclusive results when comparing LDAs, GGAs and hybrid functionals.

LDA functionals are the simplest but are effective for many applications, in particular, for solid-state physics [564], where accurate phase transitions in solids [565] and liquid metals [566, 567] are predicted and lattice constants within 1% precision are successfully achieved [568].

Development of more accurate functionals allowed for more complex calculations, *e.g.*, involving reactions, complex molecules or sterically hindered sites. For example, GGA (*e.g.*, PW91 [569–571], Becke-Lee-Yang-Parr functional (BLYP) [553] and PBE [572]) gives comparable results to CI for which strong bonds, bond angles, dihedral angles, binding energies and vibrational frequencies can be calculated within errors of only a few percent of experimental measurements [573]. The introduction of the electron density gradient in GGA improves the exchange-correlation (XC) energy approximation, *e.g.*, giving better lattice constants. Although the advancement is significant for systems such as atoms and molecules, PBE for example, shows inaccuracy in predicting surface jellium energies [574].

A better approach, using hybrid functionals (*e.g.*, B3LYP), in which nonlocal Fock exchange is mixed in with local or semi-local DFT exchange, is one of the alternatives. Better agreement with experiments is reported [575] for the B3LYP hybrid functional, which is commonly used in organic chemistry.

However, for metallic systems, the performance for main group metals is quite distinct from that for transition metals. Studied by Paier *et al.* [576] indicate the failure (worse compared to, for example PBE) of B3LYP in describing the localised-delocalised electron transition in transition metals of Rh, Pd, Cu and Ag. In contrast, agreement

between PBE's predecessor, PW91 [577] and experiments [578] has been found for the properties of bond length, binding energy, vibration frequency of the dimers of Cu, Ag and Au. The PW91 functional also shows better accuracy in predicting the bulk moduli (of Cu, Ag, Ta and W) [579] and cohesive energies (of 3d transition metals) [580]. Most striking is the work by Schultz *et al.* [581, 582], where a database for transition metal dimers of Zr, V, Cr, Mo, Ni, Cu and Ag was built based on various different density functionals (local spin density approximations (LSDAs); GGAs: BP86, SLYP, BLYP, PW91, PBE, PBELYP, mPWPW, mPWLYP; hybrid GGAs: B3PW91, B3LYP, B1LYP, PBE0, MPW1K, B3LYP*, HSE; meta-GGAs: BB95, TPSS; hybrid meta-GGAs: B1B95, TPSSh). Analyses of atomisation energies, bond energies, atomic ionisation energies, bond lengths found the accuracy is in the order of GGAs > meta-GGAs >> hybrid GGAs \geq hybrid meta-GGAs > LSDAs.

Electronic structure codes such as Gaussian [554], Abinit [583], Octopus [584], NWChem [585] and QE [586] gain very much interest, along with the improvement in the accuracy of functionals. Meanwhile, the advancement in pseudopotential theory significantly reduces the gap between *ab initio* and empirical methods, which benefits the study of large systems (*e.g.*, biology and mineralogy [587–591]).

2.4 Genetic Algorithm (GA)

Solution of many applied mathematics and theoretical science problems is not feasible by exhaustive searches. The emergence of many minima on the PES raises the calculation complexity, as the studied size (*i.e.*, number of atoms) is increased. Hence, several search algorithms have been introduced to resolve the global optimisation problem (*i.e.*, geometry optimisation).

GA is a popular choice among evolutionary algorithms, compared with other techniques (evolution strategies, differential evolution, genetic programming, evolutionary programming, gene expression programming, neuro-evolution, learning classifier sys-

tems). It is inspired by a natural evolution, such as mating (or “crossover”), mutation and natural selection in exploring the solution [188]. The GA has been reported as the better choice in cluster studies compared with the “traditional” stochastic methods (Monte Carlo (MC) and Molecular Dynamics (MD) Simulated Annealing), for example in the calculations of a Morse model [116].

The GA cluster optimisations can be traced back to the 1990’s, when Xiao and Williams [592] published their findings for molecular clusters (benzene, naphthalene and anthracene) followed by Hartke [496] (small clusters of silicon, water and mercury). Zeiri [593] then introduced a procedure so that clusters are represented by real-valued cartesian coordinates, as opposed to a binary gene code. The most significant stage of the development was contributed by Deaven and Ho [594] in 1995, which implements the gradient-driven local minimisation of the cluster energy. This step simplifies the cluster PES, which is divided into basins of local minima. There has been a dramatic increase in GA applications in many fields, such as biochemistry (proteins, biomolecules, pharmacophores, drugs), solid state physics (clusters, crystals, structure prediction) and structural characterisations (diffraction data, NMR spectra) [188].

2.4.1 Birmingham Cluster Genetic Algorithm (BCGA)

BCGA is the in-house GA that has been developed for clusters and nanoparticles studies. It is tested for many systems, ranging from model Morse clusters [595] to fullerenes [188], ionic clusters [596], water clusters [597], metal clusters [105] and bimetallic “nanoalloy” clusters [257, 258, 378, 598, 599] (*the latest review of “nanoalloy” clusters with the BCGA can be found in Refs. [116, 600]*).

A flow chart representing the BCGA is shown in Figure 2.1 [188]. The various operators and features of the BCGA are described below.

Initial population: Randomly generated individuals (variables), known as genes form the starting set. Sometimes it may be beneficial to use any available prior knowledge

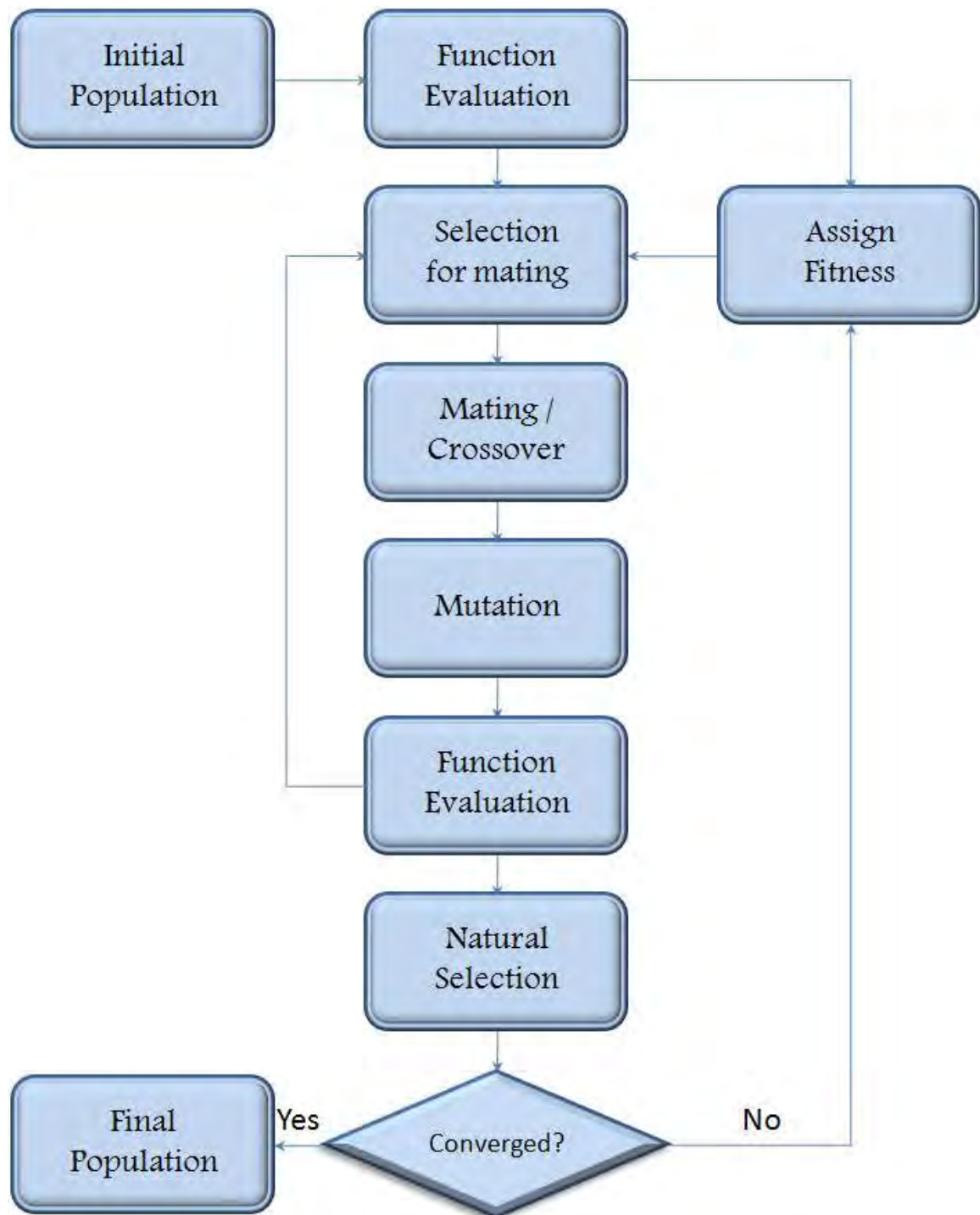


Figure 2.1: Flow chart of the BCGA program.

or chemical intuition in generating these variables.

For a cluster of N atoms, this initial population are coordinates which are chosen randomly and are then relaxed using the quasi-Newton L-BFGS (limited memory Broyden-Fletcher-Goldfarb-Shanno) [601] local minimisation algorithm.

Fitness: The trial solution is assign the fitness, which is the degree of quality. Better structures have higher fitness and are more likely to be selected for the new generation.

For minimisations of the cluster potential energy, V_{clus} (where V is a negative quantity), the highest fitness individual is the lowest energy cluster, $V = V_{min}$, while the lowest fitness individual is the highest energy cluster, $V = V_{max}$. For each generated cluster in the BCGA, $\rho \rightarrow 0$ for bad quality structures and $\rho \rightarrow 1$ for good quality structures. The choice of fitness function controls how rapidly fitness falls off with increasing cluster energy. The most common fitness functions that have been used are:

- (i) *Exponential:* $f_i = \exp(-\alpha\rho_i)$, where α is typically set to 3.
- (ii) *Linear:* $f_i = 1 - 0.7\rho_i$
- (iii) *Hyperbolic tangent:* $f_i = \frac{1}{2}[1 - \tanh(2\rho_i - 1)]$

Selection of parents for crossover: In the BCGA, clusters with high fitness values (*i.e.*, low energy), are more likely to be selected for crossover and in the next generation one or more clusters will adopt structural properties from this individual. Methods of selection that are utilised in the BCGA: roulette wheel selection, in which a parent is randomly chosen and the selection for crossover is based on the fitness; and tournament selection, in which a population of strings is formed – a “tournament” pool and parents are selected from the two fittest.

Mating / Crossover: The generation of new offspring, partially from each parent of part with a good fitness. In the BCGA, this is performed using the Deaven and Ho cut and splice operator [594] as shown in Figure 2.2. The produced offspring is then locally minimised with the L-BFGS routine [601].

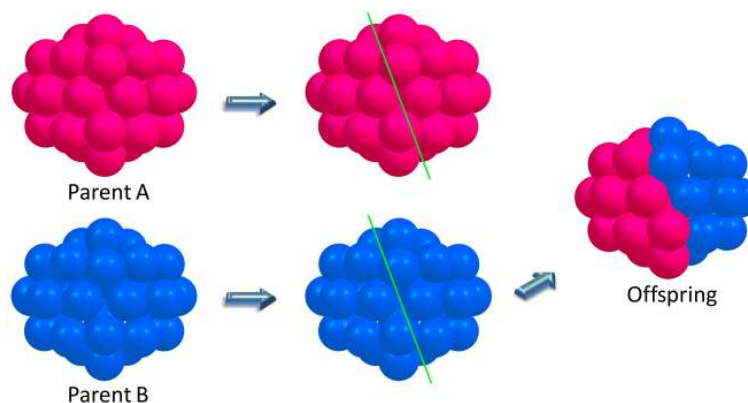


Figure 2.2: Schematic representation of GA crossover.

Mutation: This operator enhances variation in the population, as the crossover operation can lead to the problem of stagnation of the population. The new values can be generated from random (static) or just a small change from existing values (dynamic).

BCGA adopts a number of mutation schemes, depending on the type of cluster being studied:

- (i) Atom displacement - a change of atomic coordinates from random values.
- (ii) Twisting - rotation by a random angle.
- (iii) Cluster replacement - the whole cluster is replaced with a new random coordinate.
- (iv) Atom permutation - existing structure is kept but a pair of atoms is exchanged, which is practical for hetero-elemental (*e.g.*, bimetallic) clusters.

Again, the L-BFGS routine [601] is used for the minimisation of the product from mutation procedure.

“Natural” selection: Generally, individuals which are more “fit” have better potential for survival, as in the well-known phrase “survival of the fittest” in the Darwinian evolution principle.

Convergence: Each step in the GA is repeated until convergence criteria are met – constant energy after several generations.

2.5 Basin-Hopping Monte Carlo (BHMC) Algorithm

The BHMC is another popular type of optimisation algorithm to determine global minimum structures. It is based on the Monte Carlo minimisation or “basin-hopping” algorithm by Li and Scheraga [602], who studied the multiple-minima problem of brain pentapeptide [Met⁵]enkephalin. The PES is simplified (*i.e.*, fewer minima) by transforming the energy, resulting in a smoother landscape, so these methods are known as “hypersurface deformation” methods [603]. The Metropolis Monte Carlo (MC) walk is easier on this surface with only the temperature as a variable [116].

The energies of global and local minima are unchanged [604], but other points are transformed by:

$$\tilde{E}(\mathbf{X}) = \min\{E(\mathbf{X})\} \quad (2.27)$$

where \tilde{E} is the transformed energy, \mathbf{X} is the $3N$ -dimensional vector of nuclear coordinates and, the stochastic minimisation is performed starting from \mathbf{X} . These steps will eventually map any given configuration space onto that of the nearest local minimum and, the PES is converted into a set of interpenetrating staircases with steps representing basins of attraction, as shown in Figure 2.3 [518].

The new PES would then have no transition state regions, giving an acceleration of the dynamics of the minimisation: no more barrier to overcome for transition to a lower energy minimum and inter-basin hopping is possible from and to any point on the PES. There will be a significant reduction in the simulation time for this inter-basin move, in contrast to the original PES in which many attempts fail due to the high potential energy [54]. Furthermore, the success of this method for a multiple-funnel surface (*e.g.*, LJ₃₈) is associated to the broadening of the thermodynamic transitions [605].

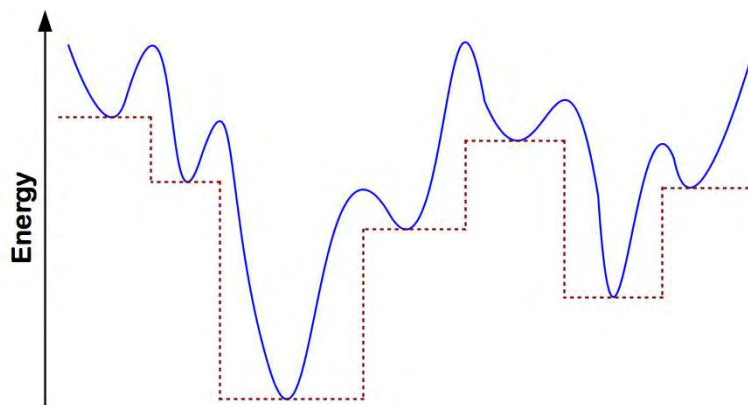


Figure 2.3: Schematic diagram of the one-dimensional PES, in which the original energy (solid line) is mapped onto the \tilde{E} [518].

The concept of PES transformation generally is also applied in the genetic algorithms described by Deaven *et al.* [515] and Niese and Mayne [606], although the approach for the PES exploration is different [518]. Many studies involving bio-molecules [607–609] exhibit significant benefit from these methods. Moreover, calculations on water, metal and silicon clusters give explanation for the experimental data [605]. For the metallic clusters, accurate predictions for the global minimum structure were achieved using the Lennard-Jones [518], Morse [610, 611] and Sutton-Chen potentials [54].

In this work, BHMC [518] algorithm search is performed within the parallel excitable walkers (PEW) framework [612]. PES is modified by connecting each configuration to the closest minimum. Metropolis Monte Carlo walks are then carried out on this simplified PES [613].

The Monte Carlo [518, 612] calculations let us choose the type of elementary move on the system: *bonds*, *ball*, *shell*, *shake*, *higher energy atoms*, *exchange* or *Brownian* either single or combined moves [614]. These moves are designed as follows:

Bonds: displacement of weakly bonded atoms that have only a few neighbours (bonded atoms < 5).

Ball: single atom displacement to a random position within the spherical cluster volume. For a better percentage of accepted true moves, simulation at higher temperature

is appropriate.

Shell: atomic rearrangement on the surface of the cluster within a fixed thickness of shell (1.5 Å)

Single: random displacement of single atom within the spherical cluster volume controlled by the lattice parameter of the defined potential.

Shake: combination of multiple *single* moves for every atom in the cluster. This move allows exploration for a wider range of structural variation (including high energy isomers), requires a high set temperature.

High energy atoms: displacement of an atom for which the energy exceeds the threshold value.

Exchange: Random swapping of two heterogeneous atoms. The structural motifs will be limited but are the best for predicting clusters “homotops”.

Brownian (dynamics): similar to the *shake* move but the movement is physical in which a very short (~ 5 femtoseconds) Langevin dynamics is applied. For a better acceptance of move percentage, simulation at a very high temperature (2,000-3,000 K) is required. This move is more efficient than the *shake* move for clusters of $N > 200$.

The basic criterion for a move to be accepted in the BH algorithm is the reduction in energy. Alternatively, a move is considered based on the probability as given by the Boltzmann factor $e^{-\Delta E/k_B T}$, where ΔE is the difference of energies for two consecutive steps at the temperature T . Ground state configuration will be dominant provided that the temperature is low enough but this will resist the hopping between local minima wells (restricted structural variations) [615] and necessitating simulation at a higher T .

2.6 Gupta Semi-empirical Potential

The Gupta potential is a semi-empirical potential derived within the tight-binding second-moment approximation and is used to model inter-atomic interactions of metallic systems [377, 616]. The cluster energy is defined as the overall attractive and re-

pulsive energy components from each atom:

$$V_{clus} = \sum_i^N \{V^r(i) - V^m(i)\} \quad (2.28)$$

where the Born-Mayer pair repulsive term $V^r(i)$ is expressed as:

$$V^r(i) = \sum_{j \neq i}^N A(\alpha, \beta) \exp \left\{ -p(\alpha, \beta) \left(\frac{r_{ij}}{r_0(\alpha, \beta)} - 1 \right) \right\} \quad (2.29)$$

and the many-body attractive term $V^m(i)$ is expressed as:

$$V^m(i) = \sqrt{\sum_{j \neq i}^N \xi^2(\alpha, \beta) \exp \left\{ -2q(\alpha, \beta) \left(\frac{r_{ij}}{r_0(\alpha, \beta)} - 1 \right) \right\}} \quad (2.30)$$

In Eqs. 2.29 and 2.30, α and β represent the atomic species of atoms i and j , respectively. A , ξ , p and q are the potential parameters that are usually fitted to experimental properties of bulk metals and alloys (*e.g.*, cohesive energy, lattice parameters, elastic constants, among others). The nearest neighbour distance, r_0 , is often taken as the average of the pure bulk distances but can also be taken from some specific ordered bulk alloy, while r_{ij} is the atomic distance.

This potential function can be applied to describe homonuclear and heteronuclear interactions. For pure metals involved in this thesis, the parameter values are used based on published data by Cleri and Rosato [377] and are listed in Table 2.2.

Table 2.2: Elemental Gupta potential parameters [377].

parameters	Ni	Pd	Pt	Cu	Au	Al
A	0.038	0.175	0.298	0.086	0.206	0.122
ξ	1.070	1.718	2.695	1.224	1.790	1.316
p	16.999	10.867	10.612	10.960	10.229	8.612
q	1.189	3.742	4.004	2.278	4.036	2.516
r_0	2.491	2.749	2.775	2.556	2.884	2.864

2.6.1 Heteronuclear Interactions

A study of Pd-Pt clusters by Massen *et al.* [257] concludes that parameters obtained by averaging the parameters of elemental Pd and Pt (from Table 2.2 [377]) give a good qualitative fit to previous experimental and theoretical studies [259, 260, 617]. This scheme is commonly adopted for the other systems as well and in this thesis will be referred to as the “**average**” potential. In addition to this, other schemes (the so-called fitted potentials – “**DFT-fit**” and “**exp-fit**”) were also investigated as presented in Table 2.3.

Pd-Au

Based on the work by Pittaway *et al.* [345], there are two ways (in addition to the “**average**” potential) to define Pd-Au heteronuclear interactions, the first one being the parameters that were fitted to the first-principles DFT calculations, hereafter referred to as the “**DFT-fit**” potential. The properties involved are the cohesive energy, in which the curve from the DFT calculations of the pure systems is rescaled to fit the experimental data (cohesive energy, lattice parameter and stickiness). The obtained rescaling factors have been used for another rescaling but this time to the cohesive energy curves of the ordered alloys of type L1₀ (PdAu) and L1₂ (Pd₃Au₁ and Pd₁Au₃) and finally fitted to the heteronuclear Pd-Au parameters.

The other, the “**exp-fit**” potential is the scheme in which the Pd-Pd, Pd-Au and Au-Au parameters are simultaneously fitted to the dissolution energy data calculated from the enthalpy curves of the Pd-Au phase-diagram [234]. In the fitting procedure, considerations of possible relaxations around the impurity have been made due to a small size mismatch of Pd and Au. Moreover, these two show a strong tendency to mix (solid solutions in the bulk) and a possible AuCu₃-like L1₂ ordered phase (near Pd₄₀Au₆₀ composition).

Only a pair (repulsive) energy scaling parameter (A) and many-body (attractive)

Table 2.3: The **average** and fitted parameters of the Gupta potential for Pd-Au, Pd-Pt and Ni-Al.

(a) Pd-Au						
parameter	average			DFT-fit		
	Pd-Pd	Au-Au	Pd-Au	Pd-Pd	Au-Au	Pd-Au
A	0.1746	0.2060	0.1900	0.1653	0.2091	0.1843
ξ	1.7180	1.7900	1.7500	1.6805	1.8097	1.7867
p	10.8670	10.2290	10.5400	10.8535	10.2437	10.5420
q	3.7420	4.0360	3.8900	3.7516	4.0445	3.8826
r_0	2.7485	2.8840	2.8160	2.7485	2.8840	2.8160

parameter	exp-fit		
	Pd-Pd	Au-Au	Pd-Au
A	0.1715	0.2096	0.2764
ξ	1.7019	1.8153	2.0820
p	11.0000	10.1390	10.5690
q	3.7940	4.0330	3.9130
r_0	2.7485	2.8840	2.8160

(b) Pd-Pt						
parameter	average			DFT-fit		
	Pd-Pd	Pt-Pt	Pd-Pt	Pd-Pd	Pt-Pt	Pd-Pt
A	0.1746	0.2975	0.2300	0.1639	0.2814	0.2172
ξ	1.7180	2.6950	2.2000	1.6764	2.6466	2.1256
p	10.8670	10.6120	10.7400	10.8577	10.6369	10.7349
q	3.7420	4.0040	3.8700	3.7177	3.9994	3.8802
r_0	2.7485	2.7747	2.7600	2.7485	2.7747	2.7600

(c) Ni-Al						
parameter	average			exp-fit		
	Ni-Ni	Al-Al	Ni-Al	Ni-Ni	Al-Al	Ni-Al
A	0.0376	0.1221	0.0799	0.0376	0.1221	0.0563
ξ	1.0700	1.3160	1.1930	1.0700	1.3160	1.2349
p	16.9990	8.6120	12.8050	16.9990	8.6120	14.9970
q	1.1890	2.5160	1.8525	1.1890	2.5160	1.2823
r_0	2.4911	2.8637	2.6774	2.4911	2.8637	2.5222

energy scaling parameter (ξ) are fitted, while the pair and many-body range exponents (p and q) and the nearest neighbour distance, r_0 are kept at average. Maximising the A value results in a preference for layer-like segregation, while maximising the ξ value favours ordered heteronuclear mixing [256].

Pd-Pt

Compared to Pd-Au, studies of Pd-Pt clusters have mainly focussed on the **average** potential as qualitative agreement against the DFT has been met [259, 260, 617]. It is, however, interesting to see how the potential derived from a scheme adopted for Pd-Au – the “**DFT-fit**”, effects the Pd-Pt clusters prediction. Also, the aim is to observe the sensitivity of the Gupta potential to the structure and geometry of clusters [618].

Ni-Al

Unlike the empirical study of Pd-Au, Pd-Pt and many other bimetallic nanoalloy clusters (*see reviews in* Refs. [116] and [600]), calculations of Ni-Al [599, 619] have been carried out using the “**exp-fit**” potential of Cleri and Rosato [377] instead of the **average** potential. Along with Cu-Au, these potentials have been derived by fitting the potential to the experimental data of the cohesive energy and the mixing enthalphy for bulk A_3B -type alloys of $L1_2$ configuration (basic fcc cube with Ni resides on each of the central faces, leaving Al on each corners).

2.6.2 Parameterisations of the Gupta Potential

Following earlier work of Paz-Borbón *et al.* [256], in investigating the effect of the variation in the Gupta parameters on the structure and chemical ordering of 34-atom Pd-Pt clusters, it was decided to expand the procedures to the other systems – Pd-Au and Ni-Al. In addition to the 34-atom, the searches were also carried out on 38-atom clusters (as have been reported in [620]). In [256], however, only one parameterisation has been examined and here is defined as weighting set **I**. The studies were then ex-

tended to the weighting sets **II** and **III**, where the effect of A and ξ parameters of the Gupta potential were focussed on.

The heteronuclear A-B Gupta potential parameters, P were derived as the weighted average of the corresponding pure metal A-A and B-B parameters,

$$P_{A-B} = wP_{A-A} + (1 - w)P_{B-B} \quad (2.31)$$

Weighting parameters were investigated in the range of $0 \leq w \leq 1$, in steps $\Delta = 0.1$.

Parameter Set I

Eq. 2.31 was applied to all parameters, A , ξ , p , q and r_0 – a symmetrical weighting of all parameters, since all of the parameters vary in the same sense, *i.e.*, from the value of B-B (for $w = 0$) to the value of A-A (for $w = 1$).

In the parameter sets **II** and **III**, instead of weighting all the parameters, only A (pair repulsion) and ξ (many-body) were varied, with p , q and r_0 parameters being fixed at their arithmetic mean values ($w = 0.5$).

Parameter Set II

As for parameter set **I**, A and ξ parameters were varied in the same sense (“symmetric”), with the weighting factor being denoted as w_s :

$$\begin{aligned} A_{A-B} &= w_s A_{A-A} + (1 - w_s) A_{B-B} \\ \xi_{A-B} &= w_s \xi_{A-A} + (1 - w_s) \xi_{B-B} \end{aligned} \quad (2.32)$$

Results of the parameter sets **I** and **II** were being compared, to give information about the importance of the energy scaling parameters (A and ξ), over the range exponents (p and q).

Parameter Set III

In contrast to the parameter set **II**, A and ξ parameters were varied in the opposite sense (“anti-symmetric” - *i.e.*, as A varies between the limits of the values for A-A and B-B, ξ varies in the opposite direction), with the weighting factor being denoted as w_a ,

$$\begin{aligned} A_{A-B} &= w_a A_{A-A} + (1 - w_a) A_{B-B} \\ \xi_{A-B} &= (1 - w_a) \xi_{A-A} + w_a \xi_{B-B} \end{aligned} \tag{2.33}$$

The reason for investigating parameter set **III** was that it allows regions of A-B parameter space to be explored: (i) low A and high ξ values, corresponding to strong A-B bonding; (ii) high A and low ξ , corresponding to weak A-B bonding. Parameter values of the sets **I**, **II** and **III** are listed in Appendix A. It should be noted that the “average” (arithmetic mean) potential corresponds to $w = 0.5$ (set **I**), $w_s = 0.5$ (**II**) and $w_a = 0.5$ (**III**).

2.7 Combined Empirical Potential – Density Functional Theory Method (EP-DF)

Due to computational cost, theoretical investigations in this thesis were mainly performed using the combined Empirical Potential - Density Functional Theory (EP-DF) approach. The global optimisation technique was carried out first at the EP level, to build a database of structural motifs. Global searches were performed with the BCGA and BHMC algorithms, by employing Gupta and Gupta-derivates potentials. Previous work of the combined EP-DF approach [254–256, 269, 376, 400, 620] has given a strong indication of the need to consider low-lying isomers. Selected minima were then locally optimised at the DFT level, using the Northwest Computational Chemistry (NWChem) [621] and Quantum ESPRESSO (QE) (ESPRESSO stands for opEn Source Package for Research in Electronic Structure, Simulation and Optimization) [586] packages.

The NWChem package was designed for maximum efficiency for massively parallel computing and, contains both a gaussian module and an independent pseudopotential plane wave module. Meanwhile, the QE package is a plane wave pseudopotential code for solid-state calculations which is freely available and, has been tested for classical dynamics, geometry optimisation and transition state searches.

2.7.1 Empirical Global Searches

BCGA

The BCGA parameters used in this work were: population size = 40 clusters, crossover rate = 80% (*i.e.*, 32 offspring were produced per generation), crossover type = one-point weighted cut-and-splice (the cut position was calculated based on the fitness values of the parents), selection = roulette wheel; mutation rate = 0.1, mutation type = mutate_move, number of generations = 400. The GA was terminated when the population was found to have converged for 10 consecutive generations. 100 GA runs were normally performed for each calculation, although for calculations that require higher accuracy and involving many atoms (complex PES), extended searches of at least 500 global optimisation runs were performed.

BHMC

The BCGA was coupled with the modified version of BHMC (only involving the *exchange* move) as the strategy to improve configurational searches of clusters. BHMC allowed a more detailed homotop search at a fixed composition and/or structural motif. This was done by performing 3000 Monte Carlo optimisation steps, with a thermal energy $k_B T$ of 0.02 eV (low value allowed a deeper exploration of a certain local structural funnel on the PES) [614, 622].

The different approaches were completed for the cluster-support interaction studies (*more details in* Chapter 8). While the *exchange* move is the best in locating the GM, stand-alone BHMC needed other elementary moves – *shake* and *dynamics*, for a

wider variation in structures and energies. For each cluster size (and composition), 10-15 searches of 200,000 elementary moves were performed at several temperatures (0-3,500 K) [614].

2.7.2 DFT Local Optimisations

NWChem Code

DFT parallel calculations with the NWChem package [585] were mainly carried out with the PW91 XC functional [569–571]. In Chapter 7, for which calculations were focussing on fixed compositions (32,6) and (6,32) for Pd-Au, Pd-Pt and Ni-Al clusters, comparisons were made against PBE gradient-corrected exchange-correlation functionals [572]. The PW91 and PBE are more suitable for large metallic systems, compared with hybrid functionals (such as B3LYP) which tend to underestimate atomisation energies of *d*-metals [69, 576].

DFT geometry optimisations were carried out using spherical Gaussian-type-orbital basis sets of double- ζ (DZ) quality [623, 624] combined with the scalar relativistic effective core potentials (ECP) [625]. Higher quality basis sets (triple- ζ -plus-polarization, TZVP) were then used for a subsequent single point calculations [623, 624], as it is recommended for transition metals [581]. In order to reduce the computational effort, charge density (CD) fitting basis sets were used for the evaluation of Coulombic contributions [626]. Table 2.4 shows detail of DZ, TZVP, ECP and CD for involved elements in this thesis. All calculations were performed spin unrestricted, using a Gaussian smearing technique with a smearing parameter of 0.14 eV for the fractional occupation of the one-electron energy levels [69].

Quantum ESPRESSO (QE) Code

The QE [586] plane-wave self-consistent field (PWscf) DFT code was chosen for the study of the support effect on bimetallic clusters (Pd-Au/MgO), due to their efficiency over the NWChem [585] code (which was mostly used for the DFT calculations by

Table 2.4: Computational details of the DFT calculations with the NWChem code.

Pd	DZ	$(7s6p5d)/[5s3p2d]$
	TZVP	$(7s6p5d1f)/[5s3p3d1f]$
	ECP	28 e ⁻
	CD	$(8s7p6d5f4g)/[8s6p6d3f2g]$
Au	DZ	$(7s6p5d)/[6s3p2d]$
	TZVP	$(7s6p5d1f)/[6s3p3d1f]$
	ECP	60 e ⁻
	CD	$(9s4p4d3f4g)/[8s4p3d3f2g]$
Pt	DZ	$(7s6p5d)/[6s3p2d]$
	TZVP	$(7s6p5d1f)/[6s3p3d1f]$
	ECP	60 e ⁻
	CD	$(9s4p3d3f4g)/[9s4p3d3f2g]$
Cu	DZ	$(7s6p6d)/[5s3p3d]$
	TZVP	$(8s7p6d1f)/[6s3p3d1f]$
	ECP	10 e ⁻
	CD	$(11s9p7d6f4g)/[9s7p5d3f2g]$
Ni	DZ	$(14s9p5d)/[5s3p2d]$
	TZVP	$(17s11p6d1f)/[6s4p3d1f]$
	CD	$(11s9p7d6f4g)/[9s7p5d3f2g]$
Al	DZ	$(10s7p1d)/[4s3p1d]$
	TZVP	$(14s9p2d1f)/[5s5p2d1f]$
	CD	$(10s7p7d3f)/[8s5p5d2f]$

the Johnston research group [43, 255, 269, 270, 306, 345, 352, 374, 376, 620, 627]). Calculations were mainly performed with the PBE [572] XC functional and ultrasoft pseudopotentials, although test calculations were also carried out with the other functionals: Perdew-Zunger (PZ81) LDA [628] and potentials which treated the semi-core states d as valence (PBE_d and PZ81_d) [586]. (For note, omission of PW91 [569–571] functional is due to its unavailability for Pd in QE). For validation purposes, a comparison of results from different codes (QE and NWChem) and functionals (PBE, PZ81, PBE_d and PZ81_d) will be presented in Chapter 8.

The initial calculations on very small clusters (up to ten atoms) [629] indicated that there were several parameters of the QE code to be optimised by convergence tests, in order to get a good balance between computing cost (CPU time) and accuracy. These

are as follows [586]:

Kinetic energy cut-off: high values of the cut-off for the wave function expansion leads to high accuracy calculations. Similar to previous work on pure Au clusters on MgO [485, 630], the cut-off parameters for all DFT calculations were 40 Ry for kinetic energy and 160 Ry for the density. Calculations on fixed cluster but with variation of the energy cut-offs show that energy differences between calculations vary by less than 0.002 eV.

Cell size: lattice parameters (in Bohr) can be defined by Cartesian coordinates or using standard cells: cubic, hexagonal, trigonal, tetragonal, orthorhombic, monoclinic or triclinic. Enough space in the periodic boundary is needed for wave expansion but additional of empty region requires longer calculation runs.

Smearing: in order to soften the metallic occupations (and hence improve convergence), the smearing approach is introduced in which the local density of states is convoluted [631]. The default of the smearing type is ordinary Gaussian spreading but other types are also available: Methfessel-Paxton first-order spreading, Marzari-Vanderbilt cold smearing or Fermi-Dirac function.

Degauss: when ordinary Gaussian spreading is used, there is a need to optimise the degauss parameter, which is the value of the Gaussian broadening (Ry) for Brillouin-zone integration in metals. Easier convergence is achieved with an increased degauss parameter but at the cost of some accuracy loss.

Convergence threshold: the pre-defined value of the total energy difference between two consecutive self-consistent-field (scf) steps was the criterion to satisfy for the conclusion of scf steps. A very low threshold gives the better accuracy but then more CPU time is required.

Mixing- β : determines the proportion of the past values to be retained for the next iterations in the scf cycle. The default mixing mode is the plain (Broyden) and other options are the simple TF screening (homogeneous systems) or local-density-dependent

TF screening (surfaces, *etc.*).

After several test runs (*for details, refer* Chapter 8), the following parameters were selected: *Kinetic energy cut-off* = 40 Ry (544 eV), *cell size* = 30 Bohr (15.9 Å) (tetragonal Bravais-lattice), *degauss* = 0.004 (ordinary Gaussian spreading), *convergence threshold* = 1.00×10^{-6} - 1.00×10^{-8} and low *mixing- β* (≤ 0.5).

2.8 Energetic Analysis

In this research, cluster stability was explored by several quantities. At the Gupta level, the **average binding energy** of an N -atom cluster is defined as:

$$\Delta_b^{\text{Gupta}} = \frac{-V_{clus}}{N} \quad (2.34)$$

where V_{clus} is the potential energy total for cluster. Larger values indicate clusters with better stability (more favourable atomic arrangements). Another analysis to give information in regards to the stability of clusters is the **second difference in binding energy**, $\Delta_2 E_b(N)$. For bimetallic systems, this is defined as:

$$\Delta_2 E_b(A_m B_n) = E_b(A_{m+1} B_{n+1}) + E_b(A_{m-1} B_{n-1}) - 2E_b(A_m B_n) \quad (2.35)$$

The quantity demonstrates relative stability of a cluster $A_m B_n$, with respect to its neighbours.

When studying a fixed-size bimetallic cluster of A-B, the **excess (or mixing) energy** as a function of composition, Δ_N^{Gupta} , is a useful quantity. For binary nanoalloys with fixed size ($N = 34$ or 38) but different compositions, it is defined as:

$$\Delta_N^{\text{Gupta}} = E_N^{\text{Gupta}}(A_M B_{N-M}) - M \frac{E_N^{\text{Gupta}}(A_N)}{N} - (N - M) \frac{E_N^{\text{Gupta}}(B_N)}{N} \quad (2.36)$$

where $E_N^{\text{Gupta}}(A_M B_{N-M})$ is the total energy of a bimetallic cluster and $E_N^{\text{Gupta}}(A_N)$ and $E_N^{\text{Gupta}}(B_N)$ are the total energies for clusters of A and B metals. The excess energy is an unbiased quantity, defined as zero for the pure clusters and negative for a mixed cluster.

At the DFT level, the **average binding energy** was calculated from the total and single atom energy as follows:

$$\Delta_b^{\text{DFT}} = -\frac{1}{N} \left(E_{\text{total}}^{\text{DFT}}(A_M B_{N-M}) - M \{E_{\text{atom}}^{\text{DFT}}(\text{A})\} - (N - M) \{E_{\text{atom}}^{\text{DFT}}(\text{B})\} \right) \quad (2.37)$$

where N is the total atom in $A_M B_{N-M}$ binary clusters. Meanwhile, the **excess energy**, Δ_N^{DFT} was calculated in similar way as at the EP level, using Eq. 2.36.

2.9 Bonding Profile Analyses

For a complete structural analysis, the radial distribution functions (RDF), were taken into account and, are defined as follows:

$$g_r(r) = \frac{1}{m} \sum_{k=1}^n \delta(kdr - r_i) \quad (2.38)$$

where m is a normalisation factor; k is the number of increments in length (dr) in the distance r measured from the centre of mass (c.m.) of the cluster and r_i is the distance from the i^{th} -atom to the c.m.

For quantitative purposes, the **pair distribution functions (PDF)**, $g_p(r)$, were calculated as follows:

$$g_p(r) = \frac{V}{N^2} \left\langle \sum_i^N \sum_{j \neq i}^N \delta[r - r_{ij}] \right\rangle \quad (2.39)$$

where N is the total number of atoms, V is the volume, r_{ij} denotes the distance between atoms i and j and the brackets represent a time average. The $g_p(r)$ function gives the

probability of finding an atom of any type at a distance r and it allows characterisation of the lattice structure during the generation of the nanoalloy [632]. The calculated PDF generally shows the pattern in Figure 2.4 for metals such as Cu [633], Pd [634], Pt and Au [632].

From the $g_p(r)$, the **average nearest-neighbour distance (ANND)** can be defined as:

$$ANND = \frac{\int_0^{r_c} r g(r) 4\pi r^2 dr}{\int_0^{r_c} g(r) 4\pi r^2 dr} \quad (2.40)$$

where the cut-off r_c was chosen to be half way between the average nearest- and next (2nd)-nearest-neighbour distances in the cluster [633]. This term can be simplified as the sum of the nearest neighbour atomic distances divided by the number of bonds in a cluster [635].

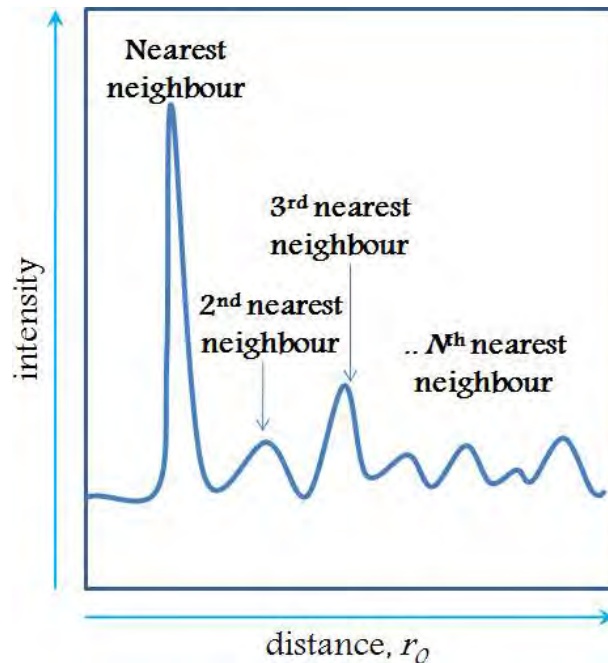


Figure 2.4: A generic pair distribution function for a metal cluster [632–634].

2.10 Chemical Ordering

For A-B alloy systems, the mixing degree, σ is defined as;

$$\sigma = \frac{N_{A-A} + N_{B-B} - N_{A-B}}{N_{A-A} + N_{B-B} + N_{A-B}} \quad (2.41)$$

where N_{A-B} is the number of nearest-neighbour A–B bonds, while N_{A-A} and N_{B-B} denote the numbers of homonuclear bonds in the binary cluster. The σ value is positive for phase separation (segregation), close to zero for disordered mixing and negative for mixing (also for layer-like structures) [636].

In Chapter 4, a new formulation for chemical ordering parameter will be proposed. The new approach gives clearer values, as σ is only significant for clusters of medium compositions.

2.11 Symmetry Analysis

Symmetry plays very significant role in life and, in science the ancient Greeks applied this concept to understand pitch and harmony. Later on, Kepler used a mathematical description to explain the elliptical geometry of planetary orbits [637].

The word symmetry comes from the Greek “symmetria”, meaning “the same measure” [638] and, is defined as “(*Beauty resulting from*) *right proportion between the parts of the body or any whole, balance, congruity, harmony, keeping*” in the Concise Oxford Dictionary [639]. The beauty concept [640, 641] of symmetry is understandable as generally high symmetry (or high similarity) is related to high stability, although it means losing a degree of diversity.

Many symmetries are observed as nature’s way of preserving harmony and stability. The periodicity of the DNA structure [642], the symmetrical spiral tubes of α -helices of myoglobin [643] and the high symmetry (2- and 3-fold symmetry) of zinc insulin hexamer [644] are a few examples of symmetry adoption in biomolecules.

In cluster studies, the very well-known cage-like fullerene molecules are stabilised due to the symmetry principle [645]. Moreover, the high-symmetry (T_d) tetrahedral clusters of 20-atom gold clusters show very large energy gap and electron affinity by the photoelectron spectroscopy experiments [646]. The stability of this motif was previously predicted by DFT calculations for Na_{20} [647]. However, there are cases in which the most stable cluster has low symmetry, for example due to the Jahn-Teller effect. This is understood to exist in very small clusters of Al, Sn and As, based on *ab initio* studies [103]. Interestingly, these calculations show that the low-symmetry ground state structure is derived from the high symmetry configuration.

Symmetry has a direct relationship with many other properties, for example energetics in which symmetrical structures (*e.g.*, protein [644], crystal [648]) generally have the lowest energy. Higher symmetry is also correlated with a higher degree of similarity (indistinguishability) and entropy. Sometimes, symmetry is misinterpreted as an “order”; more “order”, less entropy – based on thermodynamic entropy (second law of thermodynamics) [649]. Correlation between symmetry and entropy has broad relevance, for example in statistical mechanics; higher symmetry – higher stability and higher symmetry – lower entropy relations [648, 650]. In 1952, Schrödinger [651] indicated that negative entropy corresponds to asymmetry, broken symmetry or less symmetry [652, 653]. Symmetry can also be explained based on the equilibrium concept, in which the system is at the highest state of indistinguishability (a symmetry, the highest similarity) at equilibrium or a fully relaxed system, which has of course the maximum entropy. Leaving this state means reduction of both the total entropy and the symmetry [648, 654, 655].

To correlate symmetry and entropy, the Curie-Rosen symmetry principle [656] controversially rejected statements by Gibbs [657], Prigogine’s entropy theory [649] and von Neumann [658] (high similarity, low entropy). Based on their observations [648], alternative correlation is suggested – the higher similarity, the higher entropy and the

higher stability [659–661]. However, these principles have in common the idea that high symmetry basically corresponds to high stability.

For theoretical research, symmetry greatly simplifies many calculation problems, for example, the existence of crystal lattices in solids. In a 2D analog of NaCl, the lattice is invariant under inversion $(x, y) \rightarrow (-x, -y)$, reflections about the x $(x, y) \rightarrow (x, -y)$ and y $(x, y) \rightarrow (-x, y)$ axes, etc. Degeneracy of points saves computational expense by a factor of 8, for example in band structure calculations. In 3D systems, greater reduction in calculation effort is possible from 8 operations of group theory: identity, inversions, reflections (about x -axis, y -axis and $x = y$), rotations, inversion-reflections and inversion-rotations [199]. In this research, clusters are classified based on point group symmetries as follows:

Table 2.5: Classification of clusters based on point group symmetry.

Symbol	Meaning
C_j	$(j=1,2,3,4,6)$ j -fold rotation axis
S_j	j -fold rotation-inversion axis
D_j	j 2-fold rotation axes \perp to a j -fold principle rotation axis
T	4 three-and 3 two-fold rotation axes, as in a tetrahedron
O	4 three-and 3 four-fold rotation axes, as in a octahedron a centre of inversion
C_s	a mirror plane

Chapter 3

Small Pd-Au and Pd-Pt Clusters

This chapter will discuss the theoretical study of small Pd-Au (Subsection 3.3.1) and Pd-Pt (3.3.2) bimetallic clusters ($N \leq 100$) at the empirical level, using the Gupta-based potentials. Results for clusters of 1:1 compositions will be presented. The study focused on the structural (geometry and point group symmetry), energetics/stabilities (binding energy, second difference in binding energy) and ordering (mixed/segregated). A brief discussion of a fixed-size 98-atom Pd-Pt clusters will also be included (3.3.3).

3.1 Introduction

Studies of many transition metal clusters agree that the progression of structural motifs is small icosahedral (Ih or polyicosahedral (pIh)), intermediate-size Dh and large fcc. The preference for icosahedral structures is driven by surface energy minimisation, whilst larger clusters gain significant stability by reducing bulk energy with the fcc structure [68]. The structural transition sizes are system-dependent and a good degree of agreement between theoretical and experimental results has been reported [662–664].

Transition metal clusters with $N < 100$ are predicted to appear primarily as pIh-based motifs, over the Dh or fcc [54]. For Lennard-Jones clusters, magic character is observed at sizes 13, 19, 31, 38, 55 and 75 atoms [665, 666], which are derived from a 13-atom icosahedron built of twenty strained tetrahedra [610]. Two growth modes of the icosahedral overlayers (as shown in Figure 3.1) are possible, resulting in two types

of motif - “Mackay” (pIh-M) [667] and “anti-Mackay” (pIh-aM or simply pIh) [668]. Fcc-like growth yields Mackay as in Figure 3.1(b), with non-polytetrahedral structures and geometric close-shells at $N = 55, 147$ and 309 [669]. Furthermore, mass spectra of rare-gases clusters (Ar, Kr, Xe) have shown stability at $N = 39, 43, 46$ and 49 [670].

More familiar overlayers are hcp-like (Figure 3.1(a)) growth of anti-Mackay clusters, which retain polytetrahedral character. These motifs are best described by $N = 19$ (dimer), 23 (equilateral triangle), 26 (tetrahedron), 29 (trigonal bipyramid), 34 (pentagonal bipyramid) and 45 (icosahedron), all with strong stability peaks [610] in agreement with noble gas experiments: xenon [71] and argon [670].

Very small (<10 atoms) clusters are trickier as electronic and geometrical structures are more dependent on the types of atoms [671]. The DFT and *ab initio* calculations have found planar Cu ($N \leq 6$) [672], Au ($3 \leq N \leq 6$) [422, 673–675], Ag ($N \leq 12$) [676, 677] and Pt ($3 \leq N \leq 6$) [678] clusters. Furthermore, at certain sizes, clusters show remarkable stabilisation corresponding to geometric shell closure, such as $N = 38$ (TO [611, 679]), 55 (icosahedron [71]) and 98 (Leary tetrahedron (LT) [519]).

Meanwhile, medium-size Dh clusters are based on a fivefold-symmetric eight-atom pentagonal bipyramid (with one atom in the centre) or a 13-atom elongated pentagonal bipyramid. Subsequent layers are grown on (100) facets by capping atoms and concluded by re-entrant (111) faces [54, 680]. Truncation of vertices produces a stable, quasi-spherical shape of the Marks-Dh [681, 682], with a distinct stability of 75-, 101-

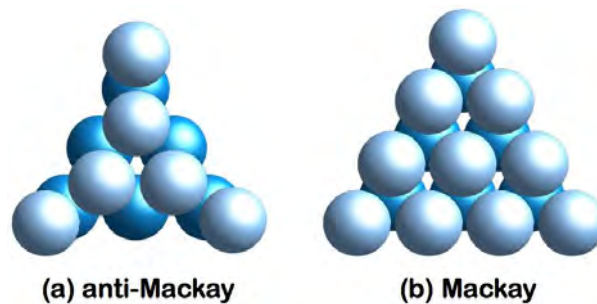


Figure 3.1: Mackay and anti-Mackay growth in polyicosahedra [610].

and 146-atom clusters [54, 61, 611].

Gold nanoparticles prepared by chemical means are reported to have a high proportion of Marks-Dh structures [61, 683, 684] but have recently been observed to co-exist with Ino's and other truncated Dh [681]. The Dh have also been reported as a stable gas phase motif for gold clusters on amorphous carbon substrates, predicted to be of size approximately 309-atoms [685].

Moving to larger sizes, clusters start to approach the behaviour of the bulk with preference for close-packed geometries. For Morse clusters, the stability order is: hcp ($N = 26$), TO (38), tetrahedral (59) and twinned TO (50 and 79) [54]. Of these shapes, the TO shows remarkable stabilisation due to surface-energy minimisation by the spherical-like structure [68].

DFT calculations with the inclusion of relativistic effects predict the dominance of larger TO (over ~ 1.5 nm or > 100 atoms) for gold clusters [686], agreeing with experimental observations [492, 687, 688]. Also, many other calculations and experiments have shown the prevalence of this arrangement, ranging from metallic to Lennard-Jones clusters [68, 689, 690]. For Pt-clusters, fcc-like nanoparticles have been resolved *via* electron microscopy techniques [120, 684]. Different systems are likely to adopt close-packed-based motifs beginning at different sizes; Au (> 600 atoms) $<$ Pt and Pd (6000–7000) $<$ Cu (30 000) [68]. Interestingly, the preference of Cu forces Fe (body-centered cubic (bcc)-phase in bulk) to adopt an fcc arrangement in the gas phase (Fe_{core}Cu_{shell} nanoparticles with a sufficiently thick (~ 20 monolayers) Cu shell) [691].

There is, however, a very thin line separating cluster motif regimes. Depending on the preparation method, system, experimental conditions and other parameters, contrasting results are probable and several published results [66, 181, 692, 693] have highlighted the co-existence of several structures. Furthermore, addition of a second element (*i.e.*, bimetallic alloys) gives more determinant for their structures, arising from variation in relative atomic radius, cohesive energy, surface energy and electronegativity

[116].

3.2 Computational Details

The BCGA program was used to find the GM for Pd-Au and Pd-Pt clusters. Calculations were performed for sizes ≤ 100 atoms, taking into account only 1:1 compositions but for 98-atom Pd-Pt clusters, the explorations were performed for all compositions. 100 GA runs were performed for each composition, although for large clusters (≥ 50 atoms) extended (500) GA runs were performed as it is more difficult to find the GM due to the high number of homotops.

Inter-atomic interactions in a cluster were described by potentials derived from the Gupta parameters [377, 616]. For Pd-Au, three-types of potentials were studied: the **average**, **DFT-fit** and **exp-fit** [345], while for Pd-Pt, the **average** potential was compared with the new **DFT-fit** potential.

For each GM, examination of the motif/structure, symmetry and ordering were undertaken. Furthermore, numerical analysis for energetic profiles was achieved from the average binding energy (E_b^{Gupta}), excess energy as a function of size, Δ_N^{Gupta} and second difference in energy, $\Delta_2 E_b^{\text{Gupta}}$. Post-calculation of the ANND gave bonding characters for the cluster, while the mixing degree was calculated with σ values (see Chapter 2).

3.3 Results and Discussion

3.3.1 (Pd-Au) $_N$, $N \leq 100$

The GM structures found in this work are shown in Table 3.1. Generally, small clusters up to $N = 24$ have similar shapes to pure clusters [32, 34]: tetrahedral (Th) ($N = 4$), octahedral (Oh) ($6 - 8$) and structures based on 13-atom icosahedral, Ih_{13} ($N \geq 10$). For $N \geq 24$, the **average** and **DFT-fit** potentials exhibit a competition of fcc/Dh/TO/Mackay-polyicosahedral (pIh-M) structures ($N = 26-50$), followed by a

dominant region of pIh-M ($N = 52-62$) and Dh ($N \geq 64$). On the other hand, the **exp-fit** potential adopts significantly different GM with a wider icosahedral region (up to $N = 32$) and pIh-M ($N = 34-68$), before Dh prevalence for $N \geq 70$.

Energetic analyses of Pd-Au clusters is shown in Figure 3.2. In Figure 3.2(a), the GM binding energies of the **DFT-fit** and **exp-fit** potentials are larger than for the **average** potential, indicates greater overall bonding of clusters. While the cohesive energy and size [199] differences between Pd and Au are small, the stability of these clusters is enhanced by the heteronuclear Pd-Au bonds. Further stabilisation is shown by the **exp-fit** potential and it is driven by the shorter bonds in the cluster, with more distortion for a compact but low-symmetry shape.

Figure 3.2(b) shows a plot of the second difference in binding energy, $\Delta_2 E_b^{\text{Gupta}}$, with intense peaks indicate strong stability of a particular size (compared with the next size clusters, *i.e.*, two atoms smaller and two atoms larger). For all potentials, there are strong peaks (*labelled in figure*) at $N = 16, 22, 28, 38$ (except for the **exp-fit**), 48, 54 and 90 (for Pd₈Au₈, Pd₁₁Au₁₁, ...). These fluctuations are correlated to structures and/or symmetries of the GM found – shown in Table 3.2, 3.3 and 3.4 (for

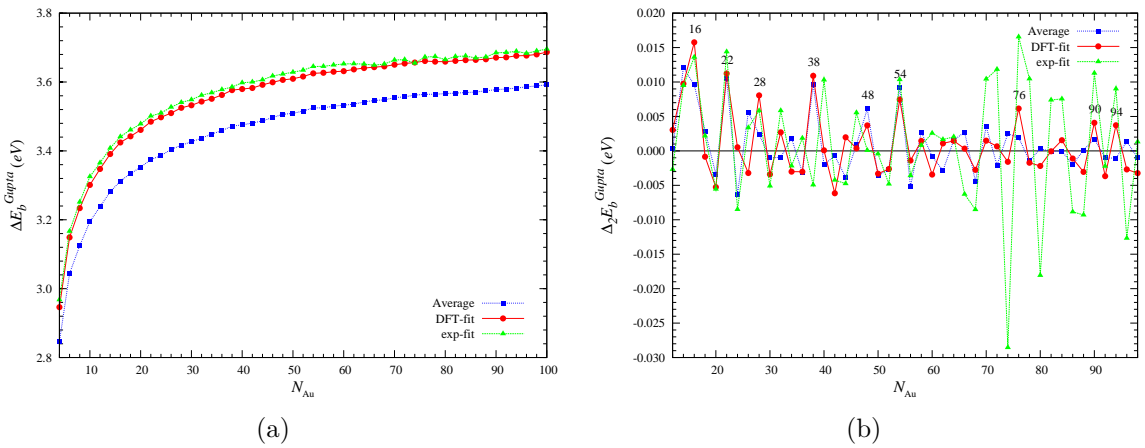
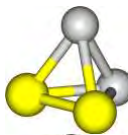
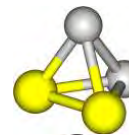
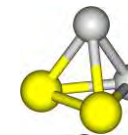
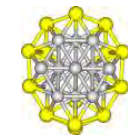
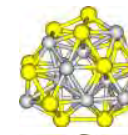
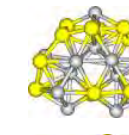
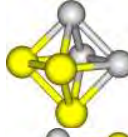
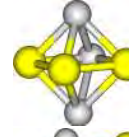
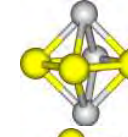
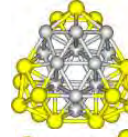
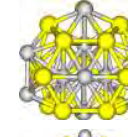
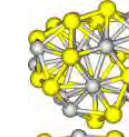






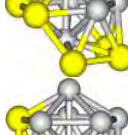
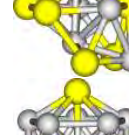
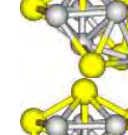
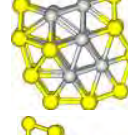
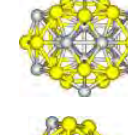
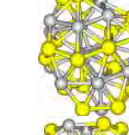
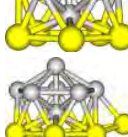
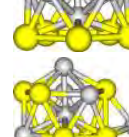
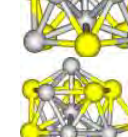
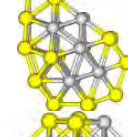
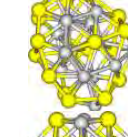
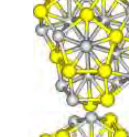
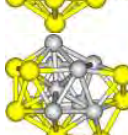
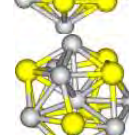
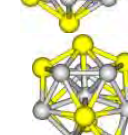
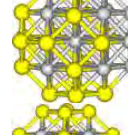
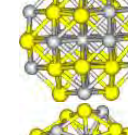
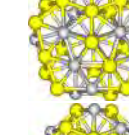
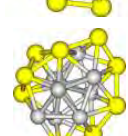
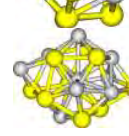
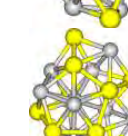
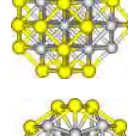
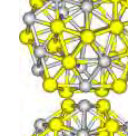
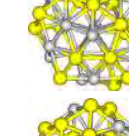

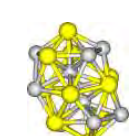
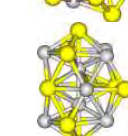
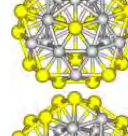
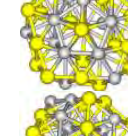
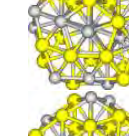
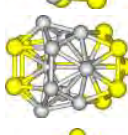
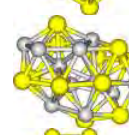
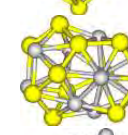
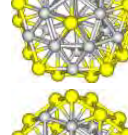
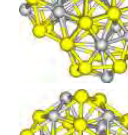
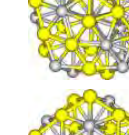
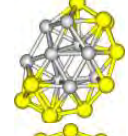
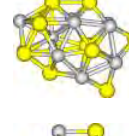
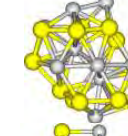
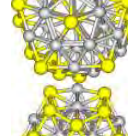
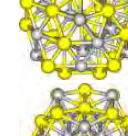
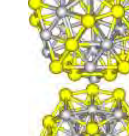
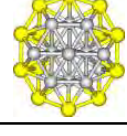
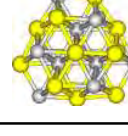
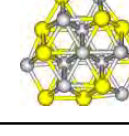
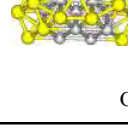
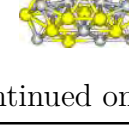
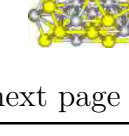

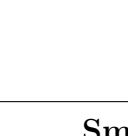



Figure 3.2: Plots of (a) binding energy (E_b^{Gupta}) and (b) second difference in energy ($\Delta_2 E_b^{\text{Gupta}}$) of $(\text{Pd-Au})_{N/2}$, $N \leq 100$ global minima found for the **average**, **DFT-fit** and **exp-fit** potentials.

Table 3.1: Global minima of $(\text{Pd-Au})_{N/2}$, $N \leq 100$ clusters obtained by calculations with the **average**, the **DFT-fit** and the **exp-fit** potentials. (*Pd and Au atoms are denoted by grey and yellow colours, respectively, here and in subsequent figures.*)

N	ave	DFT-fit	exp-fit	N	ave	DFT-fit	exp-fit
4				28			
6				30			
8				32			
10				34			
12				36			
14				38			
16				40			
18				42			
20				44			
22				46			
24				48			
26							

continued on next page ...

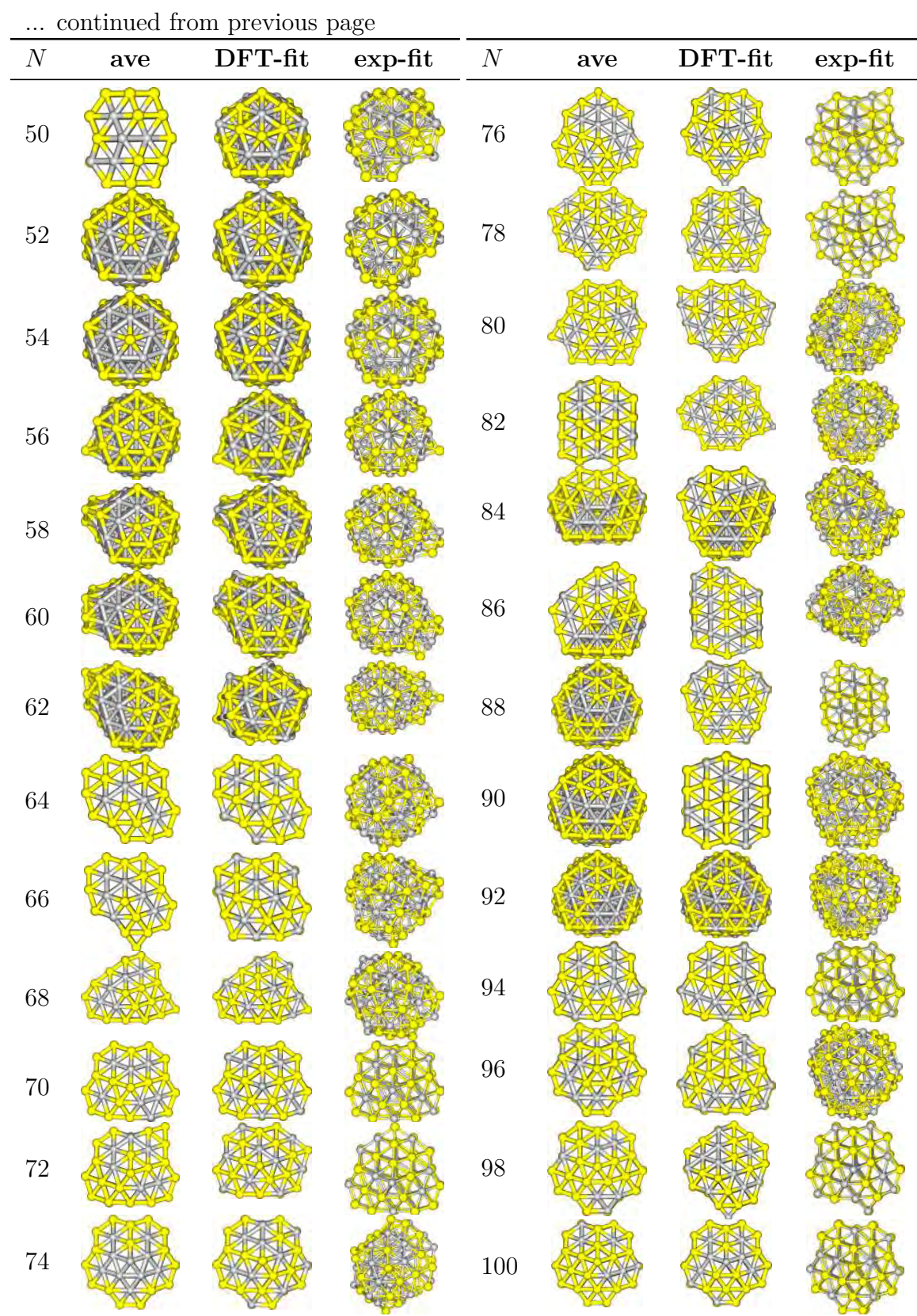


Table 3.2: Cluster energies, structural motifs and point group symmetries of $(\text{Pd-Au})_{N/2}$, $N \leq 100$ global minima found for the **average** potential.

Composition	V_{clust} (eV)	Motif	Symmetry	Composition	V_{clust} (eV)	Motif	Symmetry
Pd ₁ Au ₁	-4.51746	dimer	C_∞	Pd ₂₆ Au ₂₆	-182.814	pIh-M	C_1
Pd ₂ Au ₂	-11.3834	Th	C_{2v}	Pd ₂₇ Au ₂₇	-190.345	pIh-M	C_s
Pd ₃ Au ₃	-18.2640	Oh	C_{3v}	Pd ₂₈ Au ₂₈	-197.395	pIh-M	C_1
Pd ₄ Au ₄	-24.9984	Oh	C_2	Pd ₂₉ Au ₂₉	-204.745	pIh-M	C_1
Pd ₅ Au ₅	-31.9459	Ih	C_s	Pd ₃₀ Au ₃₀	-211.953	pIh-M	C_1
Pd ₆ Au ₆	-38.8571	Ih	C_s	Pd ₃₁ Au ₃₁	-219.219	pIh-M	C_1
Pd ₇ Au ₇	-45.9385	Ih	C_s	Pd ₃₂ Au ₃₂	-226.681	Dh	C_1
Pd ₈ Au ₈	-52.9995	Ih	C_1	Pd ₃₃ Au ₃₃	-234.065	Dh	C_1
Pd ₉ Au ₉	-60.0126	Ih	C_1	Pd ₃₄ Au ₃₄	-241.281	Dh	C_1
Pd ₁₀ Au ₁₀	-67.0545	Ih	C_1	Pd ₃₅ Au ₃₅	-248.812	Dh	C_1
Pd ₁₁ Au ₁₁	-74.2458	Ih	C_s	Pd ₃₆ Au ₃₆	-256.115	Dh	C_1
Pd ₁₂ Au ₁₂	-81.2728	Ih	C_1	Pd ₃₇ Au ₃₇	-263.582	Dh	C_1
Pd ₁₃ Au ₁₃	-88.5106	fcc	C_1	Pd ₃₈ Au ₃₈	-270.879	Dh	C_1
Pd ₁₄ Au ₁₄	-95.6624	fcc	C_s	Pd ₃₉ Au ₃₉	-278.033	Dh	C_1
Pd ₁₅ Au ₁₅	-102.791	Ih	C_s	Pd ₄₀ Au ₄₀	-285.305	Dh	C_1
Pd ₁₆ Au ₁₆	-109.991	Dh	C_1	Pd ₄₁ Au ₄₁	-292.557	fcc-hep	C_1
Pd ₁₇ Au ₁₇	-117.273	Dh	C_s	Pd ₄₂ Au ₄₂	-299.822	fcc	C_1
Pd ₁₈ Au ₁₈	-124.522	Dh	C_1	Pd ₄₃ Au ₄₃	-307.097	fcc	C_1
Pd ₁₉ Au ₁₉	-131.937	TO	C_s	Pd ₄₄ Au ₄₄	-314.553	pIh-M	C_1
Pd ₂₀ Au ₂₀	-139.019	TO	C_s	Pd ₄₅ Au ₄₅	-322.011	pIh-M	C_1
Pd ₂₁ Au ₂₁	-146.197	pIh-M	C_s	Pd ₄₆ Au ₄₆	-329.324	pIh-M	C_1
Pd ₂₂ Au ₂₂	-153.430	pIh-M	C_1	Pd ₄₇ Au ₄₇	-336.739	Dh	C_1
Pd ₂₃ Au ₂₃	-160.863	pIh-M	C_1	Pd ₄₈ Au ₄₈	-344.267	Dh	C_1
Pd ₂₄ Au ₂₄	-168.293	fcc	C_1	Pd ₄₉ Au ₄₉	-351.677	Dh	C_1
Pd ₂₅ Au ₂₅	-175.454	TO	C_1	Pd ₅₀ Au ₅₀	-359.197	Dh	C_1

Table 3.3: Cluster energies, structural motifs and point group symmetries of $(\text{Pd-Au})_{N/2}$, $N \leq 100$ global minima found for the **DFT-fit** potential.

Composition	V_{clust} (eV)	Motif	Symmetry	Composition	V_{clust} (eV)	Motif	Symmetry
Pd ₁ Au ₁	-4.74075	dimer	C_∞	Pd ₂₆ Au ₂₆	-188.028	pIh-M	C_1
Pd ₂ Au ₂	-11.7847	Th	C_{2v}	Pd ₂₇ Au ₂₇	-195.753	pIh-M	C_2
Pd ₃ Au ₃	-18.8930	Oh	C_{2v}	Pd ₂₈ Au ₂₈	-203.098	pIh-M	C_1
Pd ₄ Au ₄	-25.8700	Oh	C_2	Pd ₂₉ Au ₂₉	-210.531	pIh-M	C_1
Pd ₅ Au ₅	-33.0114	Ih	C_s	Pd ₃₀ Au ₃₀	-217.889	pIh-M	C_1
Pd ₆ Au ₆	-40.1703	Ih	C_5	Pd ₃₁ Au ₃₁	-225.467	pIh-M	C_1
Pd ₇ Au ₇	-47.4721	Ih	C_s	Pd ₃₂ Au ₃₂	-232.996	Dh	C_1
Pd ₈ Au ₈	-54.7912	Ih	C_1	Pd ₃₃ Au ₃₃	-240.444	Dh	C_1
Pd ₉ Au ₉	-61.9609	Ih	C_1	Pd ₃₄ Au ₃₄	-247.881	Dh	C_1
Pd ₁₀ Au ₁₀	-69.2190	Ih	C_2	Pd ₃₅ Au ₃₅	-255.519	Dh	C_1
Pd ₁₁ Au ₁₁	-76.6674	Ih	C_1	Pd ₃₆ Au ₃₆	-263.069	Dh	C_1
Pd ₁₂ Au ₁₂	-83.9422	Ih	C_1	Pd ₃₇ Au ₃₇	-270.585	Dh	C_1
Pd ₁₃ Au ₁₃	-91.2541	Dh	C_3	Pd ₃₈ Au ₃₈	-278.233	Dh	C_1
Pd ₁₄ Au ₁₄	-98.7046	Ih	C_1	Pd ₃₉ Au ₃₉	-285.419	Dh	C_1
Pd ₁₅ Au ₁₅	-105.975	Ih	C_s	Pd ₄₀ Au ₄₀	-292.735	Dh	C_1
Pd ₁₆ Au ₁₆	-113.384	Ih	C_1	Pd ₄₁ Au ₄₁	-300.231	Dh	C_1
Pd ₁₇ Au ₁₇	-120.744	Ih	C_s	Pd ₄₂ Au ₄₂	-307.741	fcc	C_1
Pd ₁₈ Au ₁₈	-128.244	Dh	C_1	Pd ₄₃ Au ₄₃	-315.127	fcc-hcp	C_1
Pd ₁₉ Au ₁₉	-135.904	TO	C_3	Pd ₄₄ Au ₄₄	-322.613	Dh	C_1
Pd ₂₀ Au ₂₀	-143.185	Dh	C_1	Pd ₄₅ Au ₄₅	-330.381	fcc-hcp	C_1
Pd ₂₁ Au ₂₁	-150.474	pIh-M	C_1	Pd ₄₆ Au ₄₆	-337.793	pIh-M	C_1
Pd ₂₂ Au ₂₂	-158.047	pIh-M	C_1	Pd ₄₇ Au ₄₇	-345.553	Dh	C_1
Pd ₂₃ Au ₂₃	-165.566	pIh-M	C_s	Pd ₄₈ Au ₄₈	-352.973	Dh	C_1
Pd ₂₄ Au ₂₄	-173.096	fcc	C_1	Pd ₄₉ Au ₄₉	-360.661	Dh	C_1
Pd ₂₅ Au ₂₅	-180.469	pIh-M	C_1	Pd ₅₀ Au ₅₀	-368.684	Dh	C_1

Table 3.4: Cluster energies, structural motifs and point group symmetries of $(\text{Pd-Au})_{N/2}$, $N \leq 100$ global minima found for the **exp-fit** potential. (*dist.* = *distorted motif*)

Composition	V_{clust} (eV)	Motif	Symmetry	Composition	V_{clust} (eV)	Motif	Symmetry
Pd ₁ Au ₁	-4.79233	dimer	C_∞	Pd ₂₆ Au ₂₆	-188.988	pIh-M	C_1
Pd ₂ Au ₂	-11.8711	Th	C_{2v}	Pd ₂₇ Au ₂₇	-196.835	pIh-M	C_2
Pd ₃ Au ₃	-19.0004	Oh	C_{2v}	Pd ₂₈ Au ₂₈	-204.145	pIh-M	C_1
Pd ₄ Au ₄	-26.0123	Oh	C_2	Pd ₂₉ Au ₂₉	-211.665	pIh-M	C_1
Pd ₅ Au ₅	-33.2528	Ih	C_s	Pd ₃₀ Au ₃₀	-219.153	pIh-M	C_1
Pd ₆ Au ₆	-40.3839	Ih	C_s	Pd ₃₁ Au ₃₁	-226.494	pIh-M	C_1
Pd ₇ Au ₇	-47.7126	Ih	C_1	Pd ₃₂ Au ₃₂	-233.732	pIh-M	C_1
Pd ₈ Au ₈	-55.0601	Ih	C_s	Pd ₃₃ Au ₃₃	-240.831	pIh-M	C_1
Pd ₉ Au ₉	-62.2956	Ih	C_1	Pd ₃₄ Au ₃₄	-248.345	pIh-M	C_1
Pd ₁₀ Au ₁₀	-69.5662	Ih	C_s	Pd ₃₅ Au ₃₅	-256.468	Dh	C_1
Pd ₁₁ Au ₁₁	-77.0285	Ih	C_1	Pd ₃₆ Au ₃₆	-263.887	Dh	C_1
Pd ₁₂ Au ₁₂	-84.2377	Ih	C_1	Pd ₃₇ Au ₃₇	-270.435	pIh-M(dist.)	C_1
Pd ₁₃ Au ₁₃	-91.7021	fcc	C_{3v}	Pd ₃₈ Au ₃₈	-279.111	Dh	C_1
Pd ₁₄ Au ₁₄	-99.1405	Ih	C_2	Pd ₃₉ Au ₃₉	-286.567	Dh	C_1
Pd ₁₅ Au ₁₅	-106.459	Ih	C_1	Pd ₄₀ Au ₄₀	-293.193	pIh-M(dist.)	C_1
Pd ₁₆ Au ₁₆	-113.972	Ih	D_{2d}	Pd ₄₁ Au ₄₁	-301.264	pIh-M	C_1
Pd ₁₇ Au ₁₇	-121.338	pIh-M	C_1	Pd ₄₂ Au ₄₂	-308.75	pIh-M	C_1
Pd ₁₈ Au ₁₈	-128.811	pIh-M	C_1	Pd ₄₃ Au ₄₃	-315.594	pIh-M(dist.)	C_1
Pd ₁₉ Au ₁₉	-136.251	pIh-M	C_1	Pd ₄₄ Au ₄₄	-323.193	fcc-hcp	C_1
Pd ₂₀ Au ₂₀	-143.918	pIh-M	C_1	Pd ₄₅ Au ₄₅	-331.641	pIh-M	C_1
Pd ₂₁ Au ₂₁	-151.202	pIh-M	C_1	Pd ₄₆ Au ₄₆	-339.099	pIh-M	C_1
Pd ₂₂ Au ₂₂	-158.681	pIh-M	C_1	Pd ₄₇ Au ₄₇	-346.77	Dh	C_1
Pd ₂₃ Au ₂₃	-166.404	pIh-M	C_1	Pd ₄₈ Au ₄₈	-353.588	pIh-M(dist.)	C_1
Pd ₂₄ Au ₂₄	-173.905	fcc	C_1	Pd ₄₉ Au ₄₉	-361.626	Dh	C_1
Pd ₂₅ Au ₂₅	-181.424	pIh-M	C_1	Pd ₅₀ Au ₅₀	-369.559	Dh	C_1

the **average**, **DFT-fit** and **exp-fit** potentials, respectively).

Generally, variation in bonding and nearest neighbour contacts between different motifs is represented by a distinct peaks in $\Delta_2 E_b^{\text{Gupta}}$ [32, 42, 518]. This is observed at $N = 28$, corresponding to the Dh to icosahedral (Ih) (**DFT-fit**) and fcc to Ih (**exp-fit**) transitions. The **average** potential peak at neighbour size ($N = 26$), however, is not due to motif transition but a variation in the symmetry of the cluster (C_1 to C_s). Peaks caused by transition between motifs are identified at $N = 48$ (pIh-M to fcc), 94 (pIh-M to Dh, only with **DFT-fit** and **exp-fit**) and 98 (Dh to mixed face-centred cubic-hexagonal close-packed (fcc-hcp) to pIh-M).

It is apparent that there is considerable stability of clusters at $N = 38$ (TO [611, 679]) and 54 (variant of 55-atom pIh-M [71]). Strong $\Delta_2 E_b$ of the 38-atom cluster is associated with the Dh₃₆-TO₃₈ structural transition. However, there is no observed peak at this size for the **exp-fit** potential, as pIh-M is predicted instead of TO. Similarly, the strong peak at $N = 54$ is due to the transition from a less stable structure (incomplete pIh-M) to the magic pIh-M₅₅, with size 54 having one atom missing in the innermost site. The stability is also enhanced by the higher symmetry than the neighbouring sizes (C_2/C_s compared with C_1).

Other peaks of the $\Delta_2 E_b$ plot that may be the results of the symmetry enhancement are: $N = 16$ (C_s to C_1) and 22 (C_2/C_s to C_1). This effect, however, disappears for $N \geq 50$ clusters, as structures of low symmetries (C_1) are adopted, arising from the complexity of the structure (size, shell, ordering). This is also the reason why the peaks become less intense moving to larger sizes.

Turning now to the mixing degree of the clusters as shown in Figure 3.3(a), it can be seen that the **DFT-fit** and **exp-fit** potentials have close σ values but are a distance from the **average** potential. This observation is consistent with the energetic profiles in Figure 3.2. Figure 3.3(b), however, shows that in terms of the ANND profile, the **exp-fit** potential gives more fluctuations, especially in the range of $N \geq 26$. This

results from a strong variation in bond lengths.

The higher (positive) values of σ for the **average** potential indicate less phase mixing in the clusters, as compared with those of the **DFT-fit** and **exp-fit** potentials (negative values) [636]. Detailed analyses of the structure reveals a surface segregated core-shell configuration, with Au atoms occupying low-coordinate surface sites for all of the GM of the **average** potential. Meanwhile, the **DFT-fit** and **exp-fit** potentials also prefer a core-shell but with surface mixing. However, from $N = 22$, one of the Au atoms resides in the off-centred core for the **DFT-fit** potential. GM of the **exp-fit** potential adopt core-shell (with a mixed surface) ordering up to $N = 60$. From $N \geq 62/64$ (for **DFT-fit/exp-fit**, respectively), clusters start to adopt onion-like ordering, in a similar fashion to those found experimentally [189] – Au-Pd-Au, with a single Au atom in the centre-core but from $N \geq 78/80$, multiple Au atoms are observed. This arrangement has also been reported for the other bimetallic systems, experimentally (Au-Ag [190], Pd-Pt [191]) and theoretically (Au-Cu [193], Co-Rh [172], Pd-Pt [194], Cu-Ag, Ni-Ag and Pd-Ag [195]).

The mixing degree basically determines the symmetry level of clusters, as seen in Tables 3.2, 3.3 and 3.4. The easiest example is Pd_3Au_3 with an octahedral (Oh)

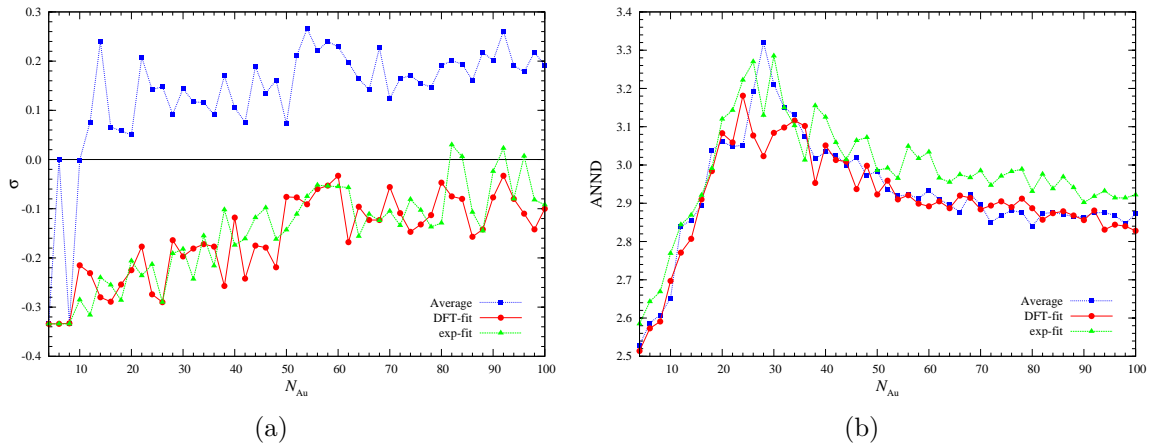


Figure 3.3: Plots of (a) mixing degree (σ) and (b) ANND of $(\text{Pd-Au})_{N/2}$, $N \leq 100$ global minima found for the **average**, **DFT-fit** and **exp-fit** potentials.

motif, in which C_3n symmetry (**average**) is reduced to C_2n (**DFT-fit** and **exp-fit**) to maximise the heteronuclear bonds. The C_3n symmetry results from having all three Au and three Pd atoms on the same triangular facets (maximising homonuclear bonds), while the C_2n symmetry has three of four atoms in the square plane from the same elements. This effect is more profound in the larger cluster, for which high symmetry structures are found as GM of the **DFT-fit**: $N = 12$ (Ih, C_5), 20 (Ih, C_2), 26 (Dh, C_3) and 38 (TO, C_3) and **exp-fit** potentials: $N = 26$ (fcc, C_3v), 28 (Ih, C_2) and 32 (Ih, D_2d). On the other hand, the effect does not occur for the **average** potential, as the adopted surface segregation surface restricts the structure from having an even distribution of the two atom types.

3.3.2 (Pd-Pt) $_N$, $N \leq 100$

The energetics and structural properties of the GM of (Pd-Pt) $_{N/2}$, $N \leq 100$ using the **average** and **DFT-fit** potentials are summarised in Table 3.5 and the structures are shown in Figure 3.4. For all the sizes studied here, GM of the **DFT-fit** are energetically less stable than those of the **average** potential (*i.e.*, higher V_{clust} values). In terms of structural motifs, there are only minor differences between the two potentials. Small clusters up to $N = 10$ mainly are from pIh-based motifs. Moving to the larger sizes, transition of pIh ($N = 12-24$) to pIh-M (20–24) to Dh (28–36) to fcc/fcc-hcp (38–54) to close-packed with a tetrahedral core (cp(T)) (46–62) to Dh (64–80) to LT (82–100) is observed.

The stability of clusters increases with increasing sizes, as shown by more positive binding energy in Figure 3.5(a)). The plateau is reached when clusters have bulk-like properties. The **average** potential has slightly higher values than those of the **DFT-fit**, despite the fact that most of the GM observed for both potentials are the same (structures and ordering). The difference can be attributed to a significant difference in strength between Pd-Pd and Pt-Pt bonds (the cohesive energies of the pure Pd and Pt clusters are 3.89 and 5.84 eV, respectively [116]) and the **average** potential seems

Table 3.5: Cluster energies, structural motifs and point group symmetries of (Pd-Pt) $_{N/2}$, $N \leq 100$ GM using the **average** and **DFT-fit** potentials.

N	average			DFT-fit		
	V_{clust} (eV)	Structure	Symmetry	V_{clust} (eV)	Structure	Symmetry
2	-5.65111	dimer	C_∞	-5.54904	dimer	C_∞
4	-14.6002	Th	T_d	-14.4167	Th	T_d
6	-23.6266	Oh	C_{2v}	-23.3443	Oh	C_{2v}
8	-32.7173	Oh	C_{2v}	-32.3702	Oh	C_{2v}
10	-41.8096	Ih	C_s	-41.3994	Ih	C_s
12	-50.9032	Ih	C_{5v}	-50.3549	Ih	C_1
14	-69.1298	Ih	C_{3v}	-59.4147	Ih	C_s
16	-69.1300	Ih	C_s	-68.4492	Ih	C_s
18	-78.3811	Ih	C_s	-77.5943	Ih	C_{4v}
20	-87.6304	pIh-M	C_s	-86.7313	pIh-M	C_s
22	-96.8239	pIh-M	C_s	-95.8595	pIh-M	C_s
24	-106.016	pIh-M	C_s	-105.016	pIh-M	C_s
26	-115.235	Ih	C_{2v}	-114.142	pIh	C_1
28	-124.513	Dh	C_1	-123.314	Dh-cp(DT)	C_1
30	-133.874	Dh	C_1	-132.588	pIh	C_s
32	-143.246	Dh	C_1	-141.884	Dh	C_1
34	-152.560	Dh	C_1	-151.178	Dh	C_1
36	-161.900	Dh	C_1	-160.454	Dh	C_1
38	-171.610	fcc(TO)	C_{2v}	-170.020	fcc(TO)	C_{2v}
40	-180.834	fcc-hcp	C_{2h}	-179.267	fcc-hcp	C_{2h}
42	-190.152	fcc-hcp	C_1	-188.467	fcc-hcp	C_1
44	-199.412	fcc-hcp	C_1	-197.735	fcc-hcp	C_1
46	-208.978	fcc-hcp	C_1	-207.174	fcc-hcp	C_s
48	-218.392	LT	C_1	-216.577	LT	C_1
50	-228.215	fcc-hcp	C_1	-226.268	fcc-hcp	C_1
52	-237.483	fcc-hcp	C_1	-235.537	fcc	C_{2v}
54	-246.746	fcc	C_1	-244.678	fcc-hcp	C_1
56	-256.211	cp(T)	C_1	-254.040	cp(T)	C_1
58	-266.036	LT	C_{2v}	-263.770	LT	C_s
60	-275.480	cp(T)	C_1	-273.133	cp(T)	C_1
62	-284.802	cp(T)	C_1	-282.420	cp(T)	C_1
64	-294.521	Dh	C_1	-291.835	Dh	C_1
66	-303.873	Dh	C_1	-301.188	Dh	C_1
68	-313.267	fcc-hcp	C_1	-310.653	Dh	C_1
70	-323.025	Dh	C_s	-320.184	Dh	C_1
72	-332.416	Dh	C_1	-329.593	Dh	C_1
74	-342.140	Dh	C_1	-339.434	Dh	C_1
76	-351.695	Dh	C_1	-348.667	Dh	C_1
78	-360.829	Dh	C_1	-357.684	Dh	C_1
80	-370.070	Dh	C_1	-367.469	fcc-hcp	C_1
82	-379.602	cp(T)	C_1	-376.659	fcc-hcp	C_1
84	-389.009	LT	C_1	-386.088	LT	C_1
86	-398.624	LT	C_1	-395.326	LT	C_1
88	-408.318	cp(T)	C_1	-405.047	pIh-M	C_1
90	-417.796	LT	C_1	-414.762	cp(T)	C_1
92	-427.255	LT	C_1	-423.832	LT	C_1
94	-437.125	LT	C_s	-433.213	LT	C_1
96	-446.597	LT	C_1	-443.300	Dh	C_1
98	-456.392	LT	C_1	-453.333	LT	C_1
100	-466.022	Dh	C_1	-462.309	Dh	C_1

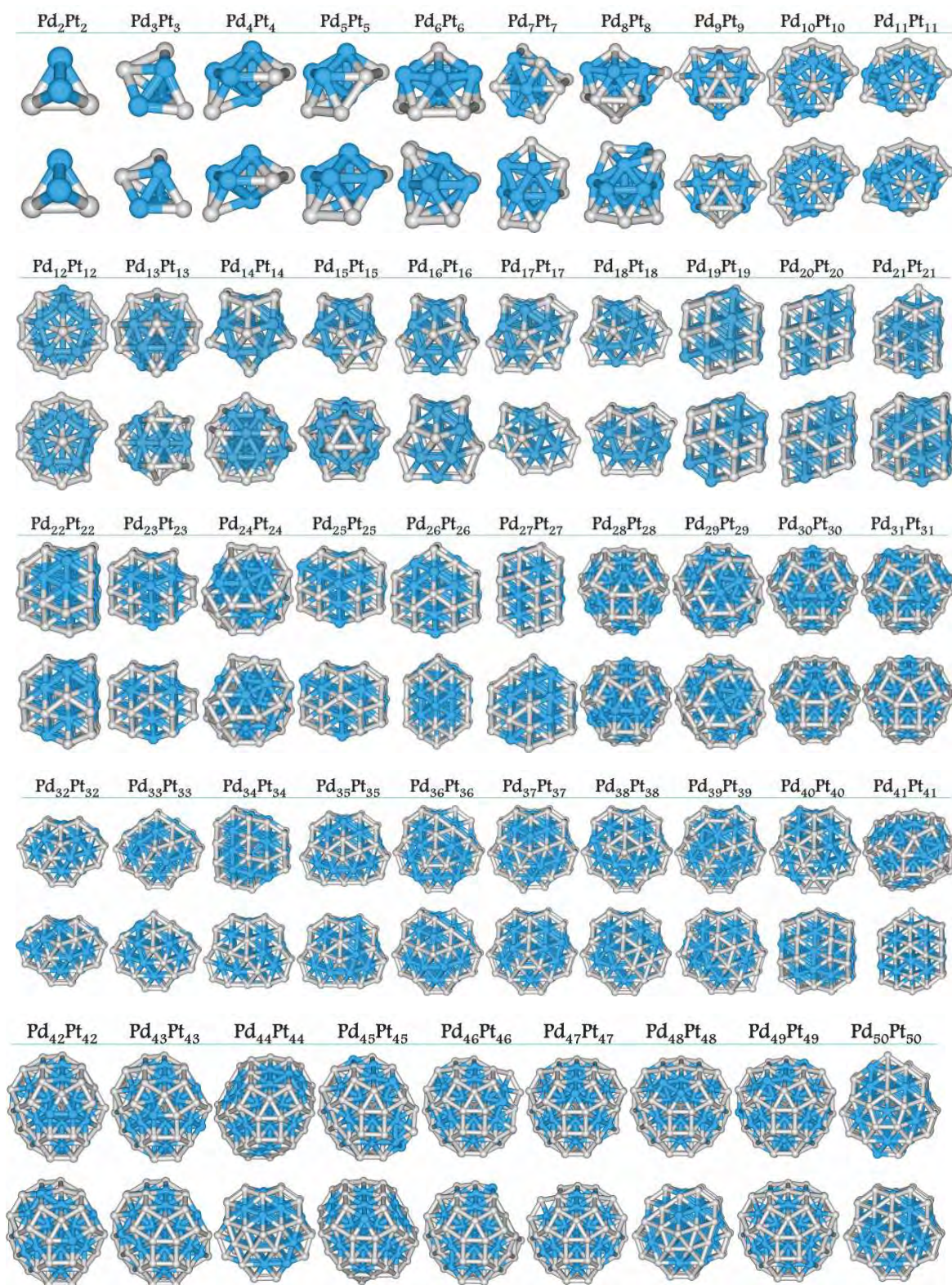


Figure 3.4: Global minima of $(\text{Pd-Pt})_{N/2}$, $N \leq 100$ clusters obtained by calculation with the **average** (first rows) and **DFT-fit** (second rows) potentials. (*Pd* and *Pt* atoms are denoted by grey and blue colours, respectively, here and in subsequent figures.)

to have more Pt character.

Meanwhile, Figure 3.5(b) shows more fluctuations in the plot of second difference in binding energy of the **average** potential compared with the **DFT-fit**. The peaks indicate stable sizes compared with their neighbours; hence, sudden changes in structure give peaks at $N = 18-20$ (p1h to p1h-M transition), 38 (Dh to TO), 46 (fcc to LT), 50 (LT to fcc-hcp), 58 – 60 (cp(T) to LT to cp(T)), 64 (cp(T) to Dh), 66 (Dh to fcc-hcp), 70 (fcc-hcp to Dh) and 98 (LT to Dh) for the **average** potential. (The dip before each peak shows that the neighbour is a less stable structure and vice versa.) Meanwhile, peaks for the **DFT-fit** potential are of lower intensity but no peaks at N

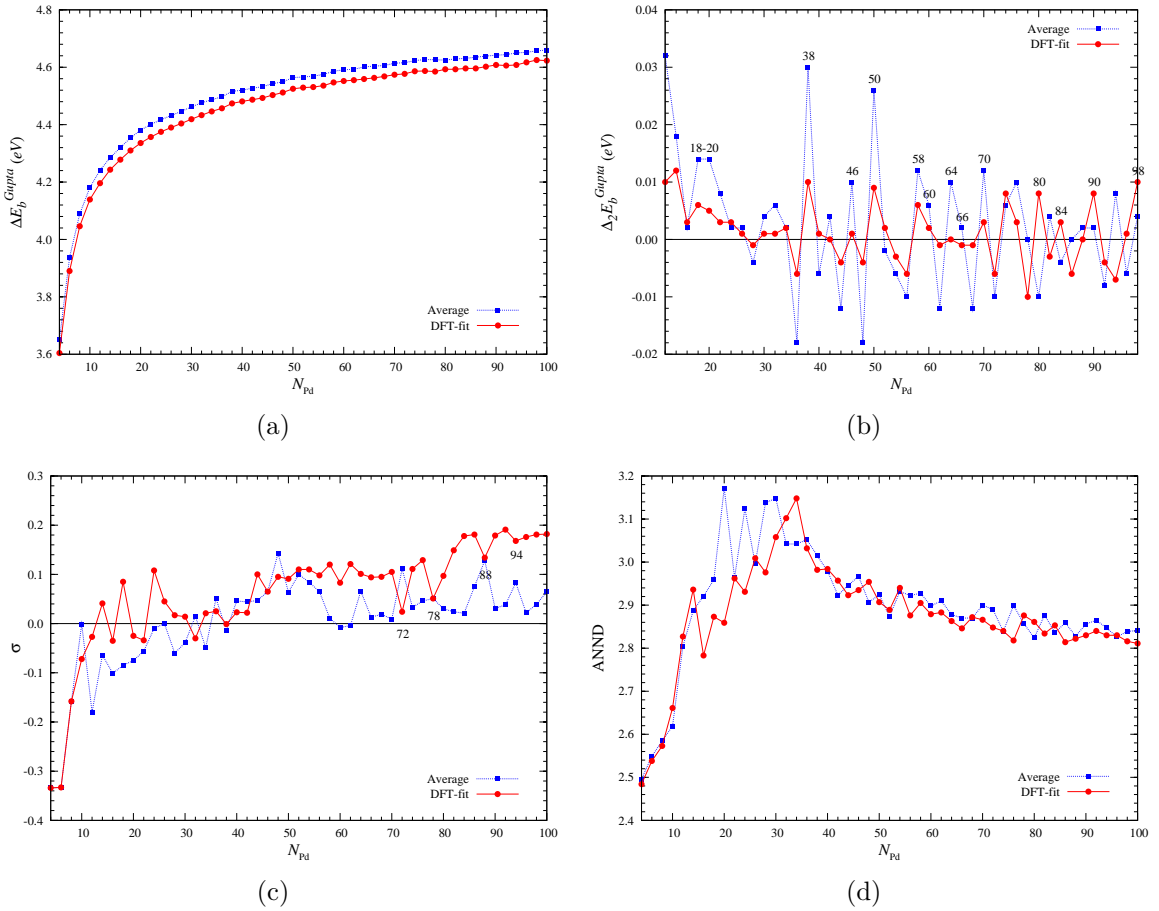


Figure 3.5: Plots of (a) binding energy (E_b^{Gupta}), (b) second difference in energy ($\Delta_2 E_b^{\text{Gupta}}$), (c) mixing degree (σ) and (d) ANND of $(\text{Pd-Pt})_{N/2}$, $N \leq 100$ global minima found for the **average** and **DFT-fit** potentials.

= 64, 66 are observed. Moreover, additional peaks are visible at 80 (Dh/fcc-hcp), 84 (fcc-hcp/LT) and 90 (LT/pIh-M/cp(T)). The $N = 38$ peak being the most intense for both potentials, due to magic clusters of TO [611, 679], while magic LT [519] is also apparent for the **DFT-fit** potential at $N = 98$.

Mixing degree (σ) analyses of the GM are shown in Figure 3.5(c). Overall, the **average** potential shows more mixing (on the surface) than the **DFT-fit** potential, as can be seen by lower σ values especially in the size regions $N \leq 30$ and $N \geq 54$. With limited number of layers, clusters of this size regime have core-shell ordering but for $N \geq 54$, onion-like ordering: Pd(centre atom)-Pt(inner layer)-Pd(outer layer) is adopted (**average** potential). The GM of the **DFT-fit** potential mostly favour a core-shell ordering, except for the minor dips at $N = 72, 78-82, 88$ and 94 (*labelled on figure*), which correspond to onion-like ordering.

Only little can be extracted from the ANND profiles in Figure 3.5(d) but they provide information on bond character in clusters. Large clusters exhibit bulk-like properties; hence, the ANND shows a plateau from the mid-size region. For small clusters ($N \leq 50$), there are fluctuations of high-low peaks linked to a significant variation of the bond character. This is one of the interesting features for small clusters which depend on many factors – size, structure, symmetry, among others.

3.3.3 98-atom Pd-Pt Clusters

Studies by Paz-Borbón *et al.* [694] on fixed 98-atom Pd-Pt nanoalloys have shown, using the **average** potential, that LT is relatively stable LT compared with other motifs. The present work expands the searches with inclusion of the new **DFT-fit** potential. Five main structural motifs are identified, as shown in Figure 3.6. Only single variants of cp(T), fcc and fcc-hcp are found, while two LT variants are classified as GM, with a minor orientation difference on the outer layer. The Dh describes more the packing group (rather than cluster motif) and eventually as many as 23 variants are observed.

The LT are adopted as GM in the medium composition, $N_{\text{Pd}} = 45-67$ and $N_{\text{Pd}} =$

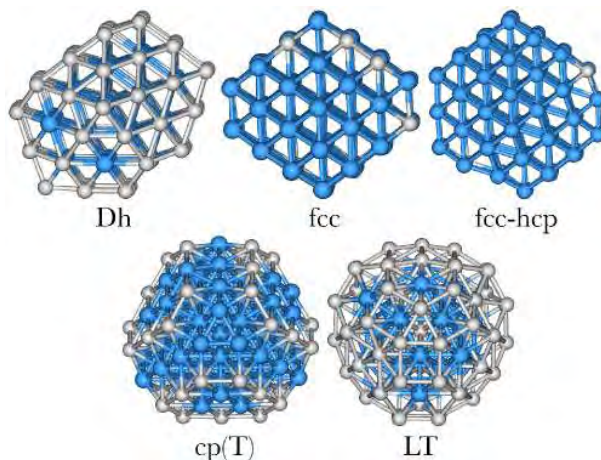


Figure 3.6: Structural motifs of global minima found for 98-atom Pd-Pt clusters.

39-64, for the **average** and **DFT-fit** potentials, respectively as shown in Figure 3.7. Energetically, this motif is the most stable compared with the other motifs for both potentials. The Dh meanwhile, is favoured over a wider composition range, spanning both Pd- and Pt-rich regions. Statistically, 70/75 Dh and 23/23 LT (for the **average**/**DFT-fit** potential, respectively) GM (different compositions) are found in the calculations. The Dh dominance can be attributed to the preferences of this motif for pure Pd₉₈ (and also Pt₉₈ for the **DFT-fit** potential). For the **average** potential, fcc is favoured for Pt₉₈ and consistently four fcc and one fcc-hcp GM are found (while no fcc/fcc-hcp structures are found for the **DFT-fit** potential). Apart from that, one cp(T) motif is found for both potentials at a significantly different composition ($N_{\text{Pd}} = 70$ and 33, for the **average** and **DFT-fit** potentials, respectively).

Bonding profiles of the 98-atom Pd-Pt clusters, as shown in Figures 3.8(a) and 3.8(b), are consistent with the earlier findings in clusters of 1:1 composition. More mixing is favoured by the **average** potential based on the lower values of σ . However, the ANND profiles (Figure 3.8(b)) show smooth transitions in the Pd- and Pt-rich regions for both potentials, since the ANND of these regions are mainly made up of homonuclear bonds. In the medium region, both potentials show elevated ANND, indicating different bond lengths of the cluster. Comparing the ANND profiles and

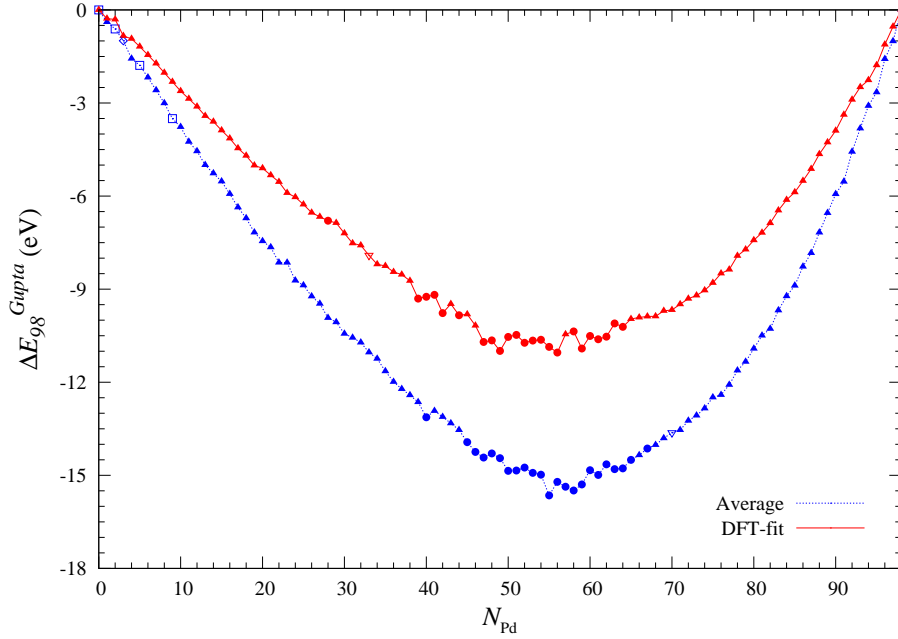


Figure 3.7: Excess energies of 98-atom Pd-Pt global minima for the **average** and **DFT-fit** potentials. Each symbol denotes different motifs: LT (filled circle), Dh (filled triangle), cp(T) (open inverse-triangle), fcc (open square) and fcc-hcp (open diamond).

the motif stability in Figure 3.7, this elevated region in ANND belongs to the LT GM, which generally have longer bonds compared with the Dh (Pd- and Pt-rich regions). It appears that the values of ANNDs for the **average** potential are higher for the entire compositions. As has been mentioned for the 1:1 composition clusters, this seems to imply that the **average** potential adopts more Pt character than Pd.

3.4 Chapter Conclusions

Calculations for clusters with $N \leq 100$ atoms provide evidence of the prevalence of very small polyicosahedral motif. The plh–Dh transition is observed in the mid-size of cluster with 1:1 compositions, both for Pd-Au and Pd-Pt. For Pd-Pt, this occurs at a smaller size ($N = 28$) compared with Pd-Au ($N = 64$). Further increase in the number of atoms eventually transforms the cluster to the bulk-like close-packed structure, which for Pd-Pt is observed at $N \geq 82$. It is interesting that in the range of $N \leq 50$, there is strong competition between several structural motifs (fcc, Dh, TO,

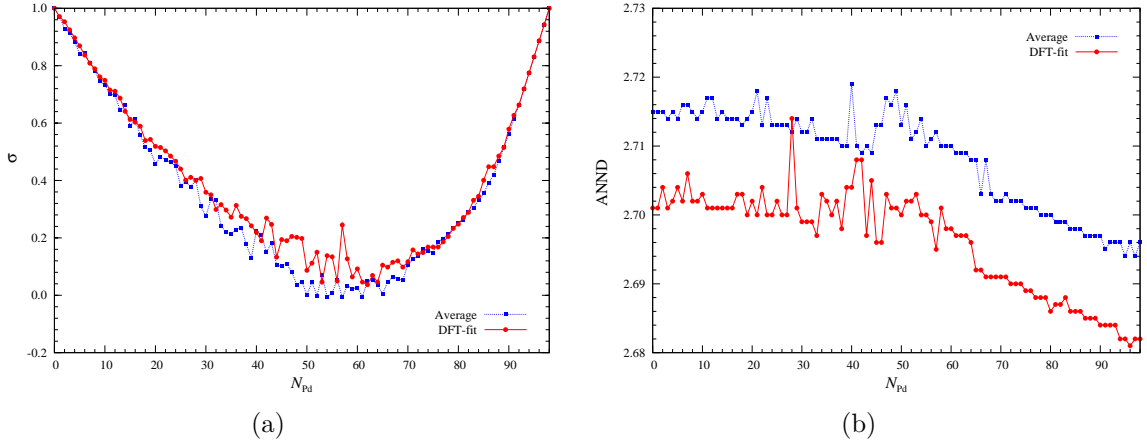


Figure 3.8: Plots of (a) mixing degree, σ and (b) ANND of 98-atom Pd-Pt global minima found for the **average** and **DFT-fit** potentials.

pIh-M), which is the reason for undertaking a more detailed study of 34 and 38-atom clusters in this thesis.

Analysis of the binding energy of Pd-Au shows that $E_{b,\text{exp-fit}} \geq E_{b,\text{DFT-fit}} \gg E_{b,\text{average}}$. The higher binding energies for the **DFT-fit** and **exp-fit** potentials are due to more heteronuclear Pd-Au interactions (*i.e.*, more mixing in the surface of a core-shell clusters). The slightly better stabilisation for the **exp-fit** (compared with **DFT-fit**) potential arises from distortion of the structures. On the other hand, the GM from calculations with the **average** potential show a preference for the surface-segregated core-shell clusters.

In contrast to the Pd-Au system, calculations of Pd-Pt clusters with the the **DFT-fit** potential produce GM which are energetically very close to the **average** potential, with the **average** showing greater mixing due to a preference for more Pd-Pt bonds, which is confirmed by the mixing degree, σ values.

Analysis of second difference in energy, $\Delta_2 E_b^{\text{Gupta}}$ raises two of many issues in determining cluster stability. First, the structural motif where a large jump is observed for the transition between motifs, with the most obvious findings for the magic TO_{38} , LT_{98} and motif derived from pIh- M_{55} . Secondly, geometric shell closing gives rise to

significant fluctuations in $\Delta_2 E_b^{\text{Gupta}}$, corresponding to point group symmetry transitions (high symmetry *vs.* low symmetry). Notably for Pd-Au clusters, the **DFT-fit** and **exp-fit** potentials adopt a better mixing on the surface and this allows structures with a high symmetry.

Results for 98-atom Pd-Pt clusters confirm the behaviour of the **average** and **DFT-fit** potentials – greater mixing is preferred for the **average** potential, including onion-like ordering. At this size, pure clusters already adopt bulk-like close-packed motifs but variation in the composition resulting in Dh as the most widely found GM. The second most frequent is the magic LT, which is a close-packed motif, along with three other found structures: cp(T), fcc and fcc-hcp, testifying to the prevalence of bulk character.

Chapter 4

Structure, Energetic and Chemical Ordering of 34- and 38-atom Palladium-Gold, Palladium-Platinum and Nickel-Aluminium Nanoalloy Clusters

This chapter will discuss theoretical searches at the EP level for three systems: Pd-Au, Pd-Pt and Ni-Al. In the computational details section (4.2), the newly proposed compositional mixing degree, σ_N , (4.2.1) is presented. For results and discussion, the focus is on general motifs (Section 4.3), GM motifs (4.4), chemical ordering (4.5) and energetic profiles (4.6).

4.1 Introduction

Nanoparticles of pure metals or alloys based on Pd, Au or Pt exhibit interesting optical, electronic, chemical and magnetic properties [3] and are of importance for the applications in microelectronics, chemical sensing, information storage, photochemistry, nanoelectronics and optics [28, 695–699]. The resistance to oxidation makes them beneficial in catalytic reactions. Moreover, combination of these metals can be utilised to obtain better activity and selectivity of catalysts due to unique heteronuclear interactions and

the interplay with other physical properties [3].

Compared with the other alloys, nickel-based alloys are typically of more importance in advanced material technologies, such as structural components in gas turbines for power generation and in aircraft [700], diesel engine turbocharger rotors, high-temperature die and moulds, hydro-turbines and cutting tools [701]. In the Ni-Al alloy family, Ni₃Al is commonly used for its high resistance to oxidation, corrosion and thermal fatigue [702, 703]. In the nano-size range, reactive Ni-Al is an important material for nano-heaters [704].

All elemental bulk solids of palladium, gold, platinum, nickel and aluminium exhibit fcc packing [59, 62, 228] and the phase diagrams of their bimetallic mixtures can be classified as slightly mixed (Pd-Au), disordered (Pd-Pt) and ordered mixed (Ni-Al). The Pd-Au phase diagram shows that ordered phases can only be achieved with Pd concentrations of 25%, 50% and 75% [705]. Pd-Pt, meanwhile, displays random mixing solid solutions for all compositions [706] and, for Ni-Al, ordered inter-metallic compounds are formed at various compositions: NiAl, NiAl₃, Ni₃Al, Ni₅Al₃, Ni₃Al₄ and Ni₂Al₃ [704, 707]. X-Ray Diffraction (XRD) analysis and electron probe microanalysis (EPMA) results reveal the cubic AuCu₃-type (Ni₃Al), cubic CsCl-B2 type (NiAl), hexagonal Ni₂Al₃-type and orthorhombic NiAl₃-type structures [708, 709]. However, the bulk phase diagram is not the sole determinant when discussing nanoscale particles, as phase stabilities will differ significantly especially for small nanoparticles with relatively large surface areas [459].

The reason for concentrating here on 34- and 38-atom clusters is that previous works on several nanoalloy systems [254–256, 345] have shown that 34-atom clusters typically exhibit a wide range of structural motifs as a function of composition. On the other hand, TO structures typically dominate 38-atom clusters and have been found as the GM for many (*e.g.*, Ni, Cu, Ag, Au, Cu-Au and Ni-Al) clusters for the Gupta many-body potential [378, 599, 710], as well as the other many-body and pair potentials

[54, 85, 86, 595, 610]. This preference is of interest for testing how different chemical orderings are stabilised by different heteroatomic interaction strengths.

In this chapter, three different systems will be discussed in which the mixing of the bulk alloy is varied. Upon comparison of these systems, the findings will: (i) improve the large structural database that has been built from several bimetallic systems, focussing on the size 34 and 38 atoms, (ii) give a better picture of the system-specific, size and compositional effects on structural motifs, chemical ordering and energetic profiles of the clusters.

4.2 Computational Details

Global optimisation at the empirical level for the Pd-Au, Pd-Pt and Ni-Al clusters were carried out with the BCGA program. 100 GA runs were performed in finding the GM of 34- and 38-atom clusters, for all compositions. Based on the Gupta potential in Table 2.2, the following differences between the studied systems can be identified: (i) Pd-Au - slightly differ in atomic sizes but all Gupta potential parameters are very close. (ii) Pd-Pt - atomic sizes are very close but A and ξ parameters are very different. (iii) Ni-Al - have a significant differences in atomic size and parameters of p and q .

For each binary system, three modifications of the potential, as in Subsection 2.6.2 were studied: parameter set **I** in which all parameters (A , ξ , p , q and r_0) in the Gupta potential [377, 616] were weighted in a symmetrical fashion; parameter set **II** (symmetric weighting of only the pair and many-body energy scaling parameters A and ξ); parameter set **III** (anti-symmetric weighting of A and ξ). For consistency for all the three systems, rules in Table 4.1 were applied and different notations – w , w_s and w_a are used, indicating the weighting in parameter sets **I**, **II** and **III**, respectively. The GM were classified by their motif and ordering, while energetically they were analysed by the excess energy as a function of size, Δ_N^{Gupta} (see Chapter 2).

Table 4.1: Effects of the parameter sets **I**, **II** and **III** on the Pd-Au, Pd-Pt and Ni-Al system.

Parameter set	weighting	
	w (set I), w_s (set II) and w_a (set III)	
	$w, w_s, w_a = 0.0$	\longrightarrow $w, w_s, w_a = 1.0$
I ($P=A, \xi, p, q$)	$P_{\text{Pd-Au}} = P_{\text{Au-Au}}$	$P_{\text{Pd-Au}} = P_{\text{Pd-Pd}}$
	$P_{\text{Pd-Pt}} = P_{\text{Pd-Pd}}$	$P_{\text{Pd-Pt}} = P_{\text{Pt-Pt}}$
	$P_{\text{Ni-Al}} = P_{\text{Al-Al}}$	$P_{\text{Ni-Al}} = P_{\text{Ni-Ni}}$
II ($P=A, \xi$)	$P_{\text{Pd-Au}} = P_{\text{Au-Au}}$	$P_{\text{Pd-Au}} = P_{\text{Pd-Pd}}$
	$P_{\text{Pd-Pt}} = P_{\text{Pd-Pd}}$	$P_{\text{Pd-Pt}} = P_{\text{Pt-Pt}}$
	$P_{\text{Ni-Al}} = P_{\text{Al-Al}}$	$P_{\text{Ni-Al}} = P_{\text{Ni-Ni}}$
III	$A_{\text{Pd-Au}} = A_{\text{Au-Au}} (0.206)$	$A_{\text{Pd-Au}} = A_{\text{Pd-Pd}} (0.175)$
	$\xi_{\text{Pd-Au}} = \xi_{\text{Pd-Pd}} (1.718)$	$\xi_{\text{Pd-Au}} = \xi_{\text{Au-Au}} (1.790)$
	$A_{\text{Pd-Pt}} = A_{\text{Pt-Pt}} (0.298)$	$A_{\text{Pd-Pt}} = A_{\text{Pd-Pd}} (0.175)$
	$\xi_{\text{Pd-Pt}} = \xi_{\text{Pd-Pd}} (1.718)$	$\xi_{\text{Pd-Pt}} = \xi_{\text{Pt-Pt}} (2.695)$
	$A_{\text{Ni-Al}} = A_{\text{Al-Al}} (0.122)$	$A_{\text{Ni-Al}} = A_{\text{Ni-Ni}} (0.038)$
	$\xi_{\text{Ni-Al}} = \xi_{\text{Ni-Ni}} (1.070)$	$\xi_{\text{Ni-Al}} = \xi_{\text{Al-Al}} (1.316)$

4.2.1 Compositional Mixing Degree, σ_N

Previously, the mixing degree, σ has been used (*described in Section 2.10*) to define mixing or segregation level in the nanoalloy clusters. However, this value is only significant for medium composition clusters. At compositions biased towards the first/second elements, there is overlap of values. In this work, a better way of working with this problem was found by using the compositional mixing degree, σ_N . Similar to the old σ , the analysis takes into account the total number of bond, by emphasising the mixed bonds. However, the new formulation also considers the composition effect. The compositional mixing degree, σ_N defined as follows:

$$\sigma_N = -\frac{\% \text{ mixed (heteronuclear) bonds}}{\text{compositions}} = -\frac{N_{\text{AB}} \times 100\%}{N_{\text{AA}} + N_{\text{BB}} + N_{\text{AB}}} \times \frac{1}{n_{\text{A}} \times n_{\text{B}}} \quad (4.1)$$

where N_{AA} , N_{BB} and N_{AB} are the total bonds of A-A, B-B and A-B, respectively, while n_{A} and n_{B} are the number of each A and B atoms in the cluster.

4.3 Structural Motifs of 34- and 38-atom Clusters

A variety of structural motifs are competitive (found as a GM) at sizes 34 and 38 atoms and detailed views of these are shown in Table 4.2. Certain motifs are found only for specific systems (Pd-Au, Pd-Pt, Ni-Al) or sizes (34 or 38 atoms) and will be mentioned. The motifs are classified into decahedral, close-packed, polyicosahedra (anti-Mackay and Mackay) and mixed packing.

4.3.1 Decahedral Packing


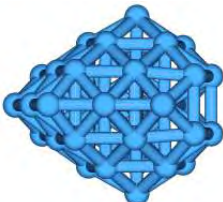
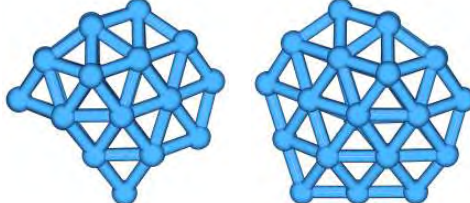

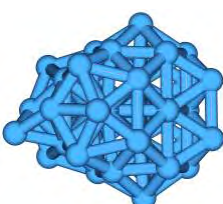
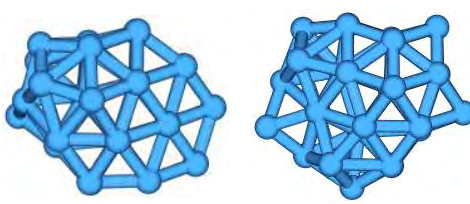

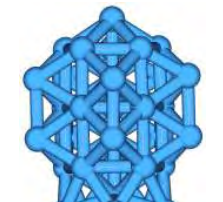
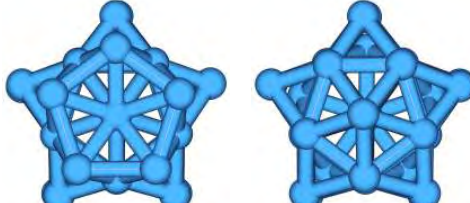

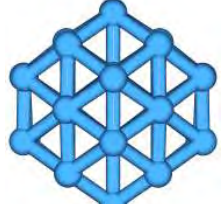
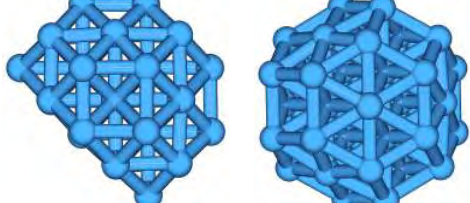

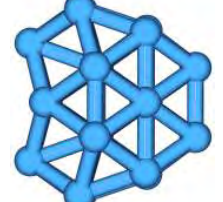
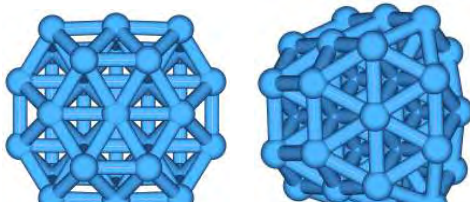
The decahedral (Dh) motifs

This motif is an incomplete polyhedron based on the 75-atom Marks decahedron [610, 711], which is very stable and found to be the GM for the Lennard-Jones cluster [611]. The Dh structures have regularly been characterised in supported metal clusters [682] and also the motif for 75- [683] and 146-atom [492] gold clusters *via* the alkylthiolate passivation method. Found for all studied systems and sizes, it is a structure of a seven-atom pentagonal bi-pyramid core, with an additional six-atom umbrella capping on top and bottom, giving a D_{5h} -symmetry 19-atom central unit. Additional atoms grow by capping on exposed (100) faces and a shell is completed with (111) arrangements around the pentagonal bi-pyramidal core.

The mixed decahedral - icosahedral (Dh-Ih) motifs


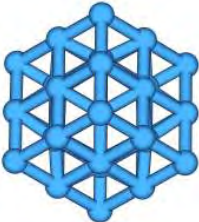
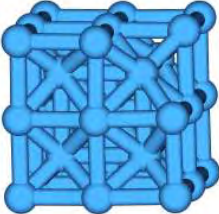
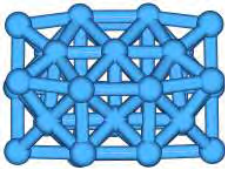

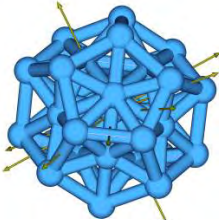
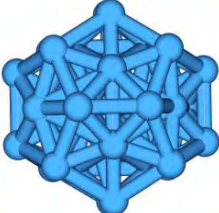
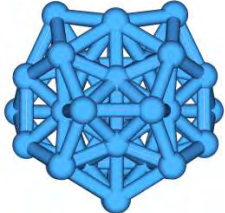


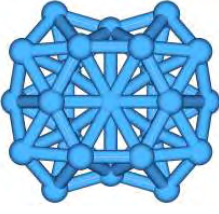
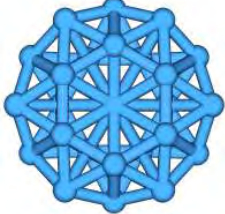
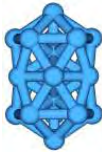
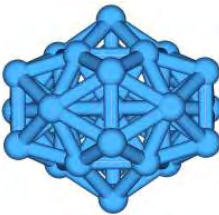
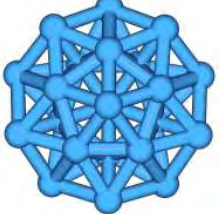
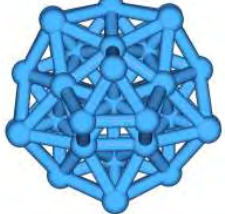

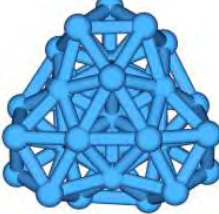
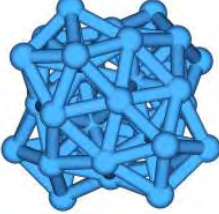
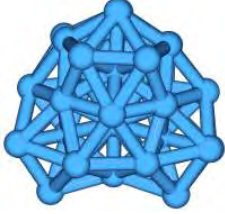

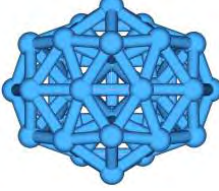
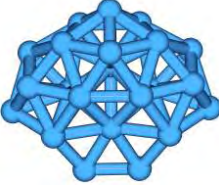
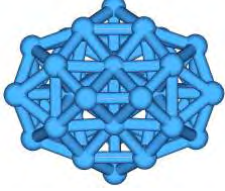
Previously, it was reported that incomplete Dh structures dominate as the GM for 34-atom Pd-Au clusters [620] and exhibit a large composition range of stability for 34-atom Pd-Pt, especially of the Pd- and Pt-rich compositions [256]. However, detailed investigation of both systems shows that these actually can be classified into two main classes, one is the Dh as mentioned above and the other is the Dh-Ih. Only medium compositions (around 17,17) of Pd-Au and Pd-Pt adopt a pure Dh geometry, while Pd-rich, Au-rich and Pt-rich regimes show prevalence of the Dh-Ih, which is also the GM for pure clusters of Pd₃₄, Au₃₄ and Pt₃₄. The Dh-Ih can be classified as mixed-packing

Table 4.2: Detailed views of global minima motifs of 34- and 38-atom clusters for Pd-Au, Pd-Pt and Ni-Al nanoalloys.

Motif [system] [max. symm.]	Core	Views	
Dh [all] [$C_s(34)$, $C_{2v}(38)$]			
		34	38
Dh-Ih [all] [$C_2(34)$, $C_s(38)$]			
		34	38
<i>Dh-Ih*</i> (star-shaped) [34-atom] [C_{5v}]			
fcc (TO) [all] [$C_{4v}(34)$, $T_h(38)$]			
		34 (incomplete TO)	38
fcc-hcp [34-atom] [C_{2v}]			

Continued on next page

Table 4.2 – continued from previous page

Motif [system] [max. symm.]	Core	Views		
bcc [all] [$C_{3v}(34)$, $C_{2v}(38)$]				
			34	38
inc-pIh¹² [all] [$D_{5d}(34)$, $C_{5v}(38)$]				
		33 (D_{5d})	34	38
pIh⁶ [all] [$D_{2h}(34)$, $D_{6h}(38)$]				
			inc-pIh ⁶ (34)	38
pIh⁷ (capped and incomplete) [Ni-Al only] [$D_{5h}(34)$, $C_s(38)$]				
			34	38
pIh⁸ [(Ni-Al) ₃₈ only] [T_d]				
pIh-db [34-atom only] [C_{2v}]				

Continued on next page

Table 4.2 – continued from previous page

Motif [system] [max. symm.]	Core	Views		
pIh-M-pc⁵ [38-atom only] [C_{5v}]				
pIh-M(DT) [all] [$C_s(34), C_1(38)$]		 $C_{2v} (26)$	 34	 38
Oh-Ih [38-atom only] [D_{4h}]				
pIh(T) [Ni-Al only] [$T(34), D_{2h}(38)$]			 $T (34)$	 38
Dh-cp(T) [(Pd-Pt) ₃₄ only] [T_d]				
Dh-cp(DT) [34-atom only] [C_s]				

but is included here due to a significantly larger fraction of decahedral compared with icosahedral packing.

The Dh and Dh-Ih have large similarities in the growth of atoms around the core but the core itself can easily be distinguished. In contrast to a perfect capping of six-atoms on both top and bottom of a seven-atoms pentagonal bi-pyramid (in the Dh), there is the distortion at the bottom to accommodate a vertically fused pentagonal bi-pyramid, as the basis of partial Ih packing. The mixing of Dh and Ih results in the loss of D_{5h} symmetry of the Dh core.

Also included in this class is where the structure of the Ih configuration which is adopted partially by overlayer atoms, instead of the 7/19-atom core. Introduction of the Ih, however, alters the 19 core-atom Dh, producing a non-symmetric (100) facet that is larger than the others to accommodate the difference in arrangement.

For 34-atom Pd-Pt clusters, highly symmetric (C_{5v}) star-shape Dh-Ih motifs are also observed. The core of this variant is similar to those of the Dh but partial Ih arrangement is overgrown on the bottom of the Dh axial, keeping the high symmetry.

4.3.2 Close-packing

The truncated octahedron (TO)

38-atoms is a magic size for fcc-based TO and all pure clusters in this work (Pd, Au, Pt, Ni and Al) adopt TO_{38} as the GM. The 38-atom TO has O_h symmetry, with eight (111) hexagonal and six (100) square faces. It has widely been reported how stable the TO of this size is [54, 206, 255] and experimental results show the prevalence of this motif for mono-metallic [178] and bimetallic [483] nanoparticles.

The mixed face-centred cubic-hexagonal close-packed (fcc-hcp) motifs

For a cluster of 34-atoms, the close-packed structures are either of the incomplete TO or the structure in which the incomplete part is re-arranged into hcp packing, resulting in a fcc-hcp motif. The fcc growth corresponds to removal of one square plane from

the 38-atom TO; hence, the symmetry is only reduced from O_h to C_{4v} . On the other hand, the fcc-hcp motif is a pseudo-crystalline fcc-like structure with a hcp stacking fault, further reducing the symmetry to C_{2v} . In addition to a square face removal, there is a distortion of the 10 outer atoms in a hcp arrangement. These fcc and fcc-hcp motifs may look fairly similar but the stacking fault becomes more obvious for larger clusters, for example with 98-atoms [694], for which both motifs are competitive for Pd-Pt clusters.

The body-centered cubic (bcc) motifs

Previous published results [620] have identified other close-packed motifs for Pd-Au clusters: the bcc, which is observed for the extreme weighting of the Gupta potentials. This motif is preferred for a cluster of a high mixed (heteronuclear) bonds, *i.e.*, ordered mixing arrangement. Hence, it is easier to find the motif in the Pd-Pt or Ni-Al systems than in the Pd-Au nanoalloys. However, the bcc structure is less likely to be found than the fcc, which is the bulk phase for all involved elements.

4.3.3 Anti-Mackay-icosahedral Packing

Normally, the pIh structures have an Ih_{13} unit as the main component but the subsequent layer could be either anti-Mackay (hcp) or Mackay (fcc) [611] (*see* Section 3.1 *for more details*). The hcp overlayer growth preserves poly-tetrahedral character, resulting in an icosahedron of interpenetrating icosahedra, while the fcc growth peaks at sizes 55, 147, 309 and 561 [387] – the magic Mackay icosahedron. Many pIh structures are found but only highly ordered structures, especially motifs with a high symmetry are classified. Figure 4.1 shows a 2D representation of all pIh classified in this thesis, with comparison with the other closely related motifs. All pIh motifs are of the anti-Mackay type, unless otherwise stated.

The specific pIh family prevails when there are geometric and electronic shell-closure effects [206]. In the sizes studied, however, no pure clusters favour pIh families but the

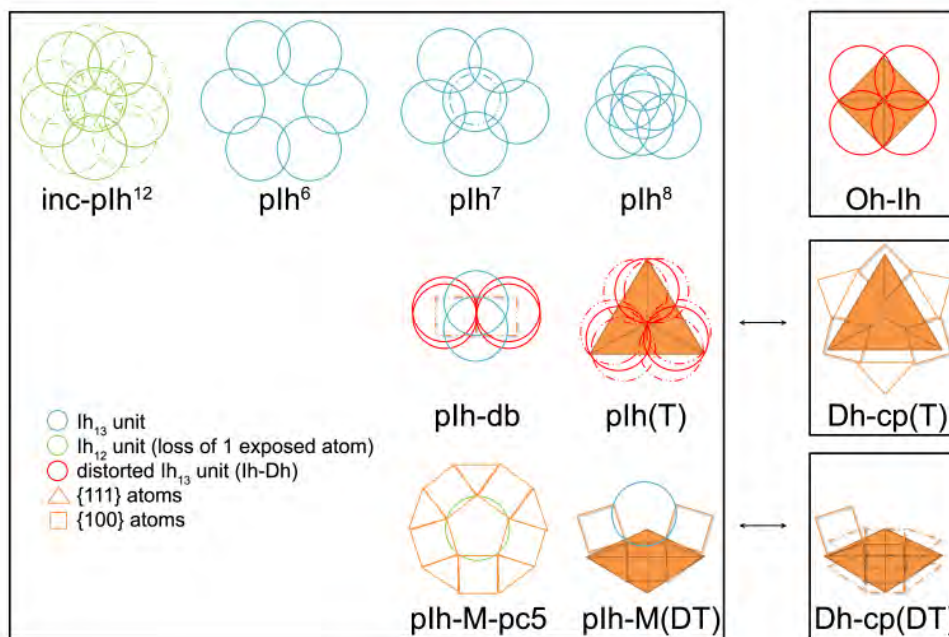


Figure 4.1: Variation of polyicosahedra and the closely-related motifs. Dashed lines represent the other side of the clusters

binary clusters have been shown to stabilise these motifs, for several reasons: difference in atomic radii (size mismatch) [712], metallic bond-order correlation [713] and the tendency to lower the surface energy (formation of core shell) [205] (*see* Table 1.2).

The Ih_{13} has internal bonds which are 5% shorter compared with those of the surface, resulting in a large internal strain and not favourable for pure transition metal clusters. However, the strain can be relaxed by locating an atom of the smaller binary element in the core, *i.e.*, core-shell ordering, which also maximises the heteronuclear bonds. This behaviour has been observed in all of the studied systems – Pd-Au, Pd-Pt and Ni-Al [257, 378, 599], as well as the other nanoalloy particles – Ag-Cu, Ag-Co, Ag-Pd, Ag-Ni, Au-Ni, Au-Co and Au-Cu [43].

Among the studied systems, the size mismatch is apparent in the Ni-Al system, which is comparable with Ag-Ni, Au-Cu, Ag-Cu and Ag-Au alloys [43]. Hence, it is reasonable for the pIh variant with very large strain (pIh^7 and pIh^8 [205, 206] – *will be discussed later in this section*) are observed as GM for Ni-Al clusters only.

Earlier studies of 38-atom clusters led to the classification of several pIhs [255, 269, 376, 620] but for 34-atom clusters [256, 620], the motifs are either incomplete, capped or mixed and the variation of structures is large.

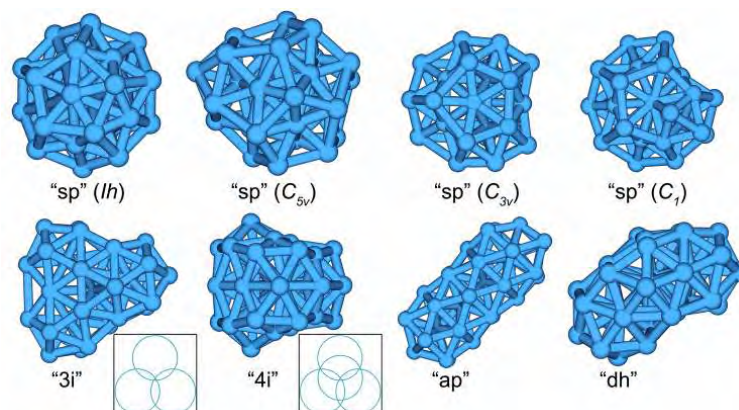
The incomplete polyicosahedra with a 12 interpenetrating Ih_{13} units (pIh¹²) and the mixed-pIh

This pIh motif is a fragment of the 45-atom anti-Mackay pIh cluster, with I_h symmetry [43, 54, 255, 611, 668]. Removal of 12 vertex atoms (33 atoms) maintains I_h symmetry but subsequent addition of atoms (to form 34- and 38-atom cluster) on the outer shell reduces the symmetry to D_{2h} and C_{5v} , respectively.

This motif is observed for Pd-Pt and Ni-Al clusters of both sizes but is more frequently for Pd-Pt, where the onion-like segregation with a single Pd in the centre, followed by Pt (inner) and Pd (outer) layers, is adopted. This ordering has been predicted for 147- (Pd-Pt-Pd-Pt) and 309-atom (Pd-Pt-Pd-Pt-Pd) clusters [714], due to the preference of Pt to stay in the subsurface layer, coupled with the general tendency for Pd to lie on the surface (to lower the surface energy, as $E_{Pd} \approx 125 - 131$ vs. $E_{Pt} \approx 155 - 159$ meVÅ⁻²) [201, 202, 715]. Moreover, results from a laser vaporisation source show that free Pd-Pt clusters are influenced by the mono-atomic bond strength, thus Pd atoms are less bound than Pt atoms in a mixed cluster, resulting in segregation, with Pd atoms lying on the surface [716].

The pseudo-spherical shape (I_h symmetry) is preserved when the removal of outer atoms from the complete 45-atom pIh¹² is even on all sides. However, many observed structures do not show this tendency and there is instead clear character of anti-Mackay pIh, as in Figure 4.2. These clusters are classified as mixed-pIh. Meanwhile, the uneven removal still produces a spherical pIh (denoted pIh “sp” hereafter) but with lower symmetries; from high (C_{5v} and C_{3v}) to low (C_1), depending on which site is involved.

Other structures with a distinct character of anti-Mackay pIh are mainly of low sym-

Figure 4.2: Variants of pIh^{12} motifs.

metry motifs, due to the binary nature of the clusters (atomic positions) and distortion of the bonds. Previously, many of these were reported as low-symmetry polyicosahedra ($\text{pIh}(\text{LS})$) but, as more systems are included, systematic classification, especially those found more frequently is needed.

The pIh with three interpenetrating Ih_{13} units (pIh “3i”) structure is mainly found as a GM of Pd-Pt clusters for $N_{\text{Pd}} = 31$ (34-atom cluster) and $N_{\text{Pd}} = 35$ (38-atom cluster), in which three Pt atoms reside in the centre of each Ih_{13} unit. Next, the pIh with four interpenetrating Ih_{13} units (pIh “4i”) motif, which is comparable with the 38-atom pIh^8 (*will be discussed later in this section*) clusters but differs in the position of the Ih_{13} units (twisted and distorted). It is observed only for 34-atom clusters (Pd-Au and Pd-Pt systems). Meanwhile, the mixed pIh “dh” structure is mainly a distorted anti-Mackay pIh but has a Dh character in the exposed outer layer. This motif is found for 34-atom clusters (Pd-Au and Pd-Pt systems). The last variant is the hexagonal anti-prism (pIh “ap”), which is based on repeating units of six-sided anti-prisms, with Ih_{13} units on the edge of the cluster. This structure is a minor GM of Pd-Pt and Ni-Al clusters.

In addition to these four, there are many other GM (especially of the Pd-Pt system) which only have a minor degree of anti-Mackay pIh character. They are difficult

to recognise, having low symmetry, primarily distorted/mixed clusters and, are collectively described as fused-icosahedra pIh “fs”. Great variation of pIh structures for Pd-Pt clusters is possibly due to a good match in size ($r(\text{Pd}) = 1.38$, $r(\text{Pt}) = 1.39$ [199]) or electronic shell-closure effects [205, 206] in which atoms are easily exchanged.

The polyicosahedra with 6 interpenetrating Ih_{13} units (pIh^6)

This motif has a pancake structure where a hexagonal bi-pyramidal core is exposed on two-sides (top and bottom) and could be represented as a 2D system of fused Ih_{13} units. Hence, the internal strain only comes from one direction and is minimal compared with the other pIh variants. This factor leads the stabilisation of pIh^6 for most systems, even when size mismatch is not significant: Au-Cu [203, 206, 270], Ag-Au [205, 255, 306], Ag-Cu [43, 203, 206, 270], Ag-Ni [43, 203, 270], Ag-Pt [255] and Ag-Pd [205, 270]. However, more pIh^6 GM are found for the system with a small heteroatomic size mismatch, *e.g.*, Pd-Pt [203, 255].

This motif is one of the magic core-shell pIh for 38 atoms. At this size, clusters display D_{6h} symmetry with a core surrounded by six interpenetrating Ih_{13} units. The prevalence of this motif is most obvious at and around composition (6,32), which fits well with the ideal core-shell configuration.

While 38-atom motifs exhibit high symmetry bimetallic clusters, removal of four atoms reduces the symmetry. The core, however, is identical, consisting of an inner ring of six atoms of the smaller elements. The highest symmetry found for 34-atom clusters is D_{2h} for Pd-Au and Pt-Pt, in which the motif loses two side atoms on opposing Ih_{13} units. For Ni-Al, a different structure is adopted – four adjacent atoms are removed from a perfect D_{6h} 38-atom motif and the highest symmetry found is only C_s . The inner-ring core has four unexposed sites, occupied by Ni while two exposed sites are filled by Al, resulting in the stabilisation of this motif at around composition (4,30) for Ni-Al, compared with (6,28) for Pd-Au and (28,6) for Pd-Pt.

The polyicosahedra with 7 interpenetrating Ih₁₃ units (pIh⁷) (Ni-Al clusters only)

This is a high symmetry motif (D_{5h} for 34-atom clusters) of Ni-Al clusters (for both 34 and 38 atoms) but is not observed as a GM at any weighting/composition for Pd-Au or Pd-Pt clusters. This motif can be defined as the interpenetration of seven Ih₁₃ units, formed around a seven-atom decahedral core. It exhibits a wide stability range of compositions for NiAl-34, comparable with the dominance of the Dh-Ih for PdAu-34. NiAl-38 clusters also adopt this motif but the addition of four extra capping atoms reduces the symmetry of the clusters.

The polyicosahedra with 8 interpenetrating Ih₁₃ units (pIh⁸) (38-atom Ni-Al clusters only)

This motif has a very high ideal symmetry (T_d) and has previously been found for 38-atom Ag-Ni and Ag-Cu nanoclusters [43]. The motif is best described for the composition (8,30), which consists of eight smaller (Ni) core atoms and 30 larger (Al) exposed atoms. The eight core atoms are arranged in a tetra-capped-tetrahedral fashion and four icosahedra are fused-sharing the central T_d unit (*see* Figure 4.1).

The polyicosahedra with a double Ih₁₃ core (pIh-db) (34-atom clusters only)

This motif was not discussed in the earlier publication [620] as it was grouped together with the other pIh motifs. However, for PdAu-34 clusters, this is the most common pIh structure found. It is not highly symmetrical (maximum at C_{2v}) but the motif is well-defined with exposed double icosahedral units. Pd is significantly smaller than Au and the preference for the Pd-core is seen in the pIh-db motif, in which two Pd atoms occupy the central position of each of the two Ih₁₃ interpenetrating units.

This motif is rarely found as the GM of the PdPt-34 and appears mostly for compositions $N = 2-4$. However, it is significant for NiAl-34, as it is highly competitive with the pIh-M(DT) (*discussed later*) for Al-rich clusters, due to a large size mismatch.

4.3.4 Mackay-icosahedral Packing

The five-fold pancake Mackay-icosahedron (pIh-M-pc⁵) (38-atom clusters only)

This motif is derived from the 55-atom Mackay icosahedron [54, 255, 611, 667], where set of atoms around the lower part of the cluster is eliminated, resulting in C_{5v} symmetry. In this motif, the single Ih of the cluster core only consists of 12 atoms (loses one exposed atom) and is surrounded by five square (100) faces. The upper part of the cluster retains the coordination of the 55-atom Mackay-icosahedron – a 16-atom umbrella cap with decahedral arrangement. Another variant is also found, where the top atom of the umbrella vertex is re-located to the opposite side of the cluster to complete the Ih₁₃ core unit. This variant, however, is a minority of Ni-Al (not observed for Pd-Au and Pd-Pt) and has been found as a less stable variant of 38-atom Pd-Pt, Ag-Au, Ag-Pt [255], both at the EP and DFT levels.

The incomplete Mackay-icosahedron with a double tetrahedral component (pIh-M(DT))

Similarly to the pIh-M-pc⁵, this motif is also based on the 55-atom Mackay-icosahedron. Atoms are removed in such a way that one Ih₁₃ unit is exposed on one side and one joined distorted double tetrahedron of 14 atoms (with exposed dual tetragonal face) appears on the opposite site. It is a low symmetry structure (C_s and C_1 for 34- and 38-atom, respectively) but of significance as it is the ground-state structure for 34-atom pure Al clusters. For this reason, this motif is adopted as a GM by many Al-rich Ni-Al clusters. It is also found for Pd-Au and Pd-Pt clusters but is less competitive compared with the other motifs.

4.3.5 Mixed Packing

The mixed octahedra-icosahedra (Oh-Ih) (38-atom cluster only)

This motif consists of four interpenetrating distorted Ih₁₃ units as the outer layer, with an internal octahedral core, similar to the TO structure. The surface atoms grow in an

icosahedral arrangement, for which only two square faces are created (in contrast to six of the TO) with no hexagonal faces. This motif has previously been found for 38-atom homonuclear clusters of Ag, Ni and Al but did not receive much attention because it exists only as a low-lying (non-GM) isomer [105, 710]. However, the GA searches, using the system comparison approach, combined with the DFT calculations [255], confirm Oh-Ih as the most stable structure of Pd-Pt and Ag-Pt clusters for composition (24,14). For the other compositions and systems, it shows close competition against the TO.

The polyicosahedra with a 10 atom tetrahedron core (pIh(T)) (Ni-Al clusters only)

Similarly to the pIh⁸, this motif is only adopted by systems with a large size mismatch (*i.e.*, Ni-Al). However, compared with the pIh⁸, pIh(T) is found as a GM for both sizes (34- and 38-atom). This motif is built from a 10-atom tetrahedral core, with each of the four vertices as the centres of three interpenetrating Ih₁₃ units (*see* Figure 4.1).

This motif is observed as a GM for pure Ni₃₄ and is prevalent for Ni-rich 34-atom clusters. 38-atom clusters also adopt this motif, in which four additional atoms reside in the outer shell. To accommodate these extra atoms, there is a distortion of the tetrahedral core giving only D_{2h} as the highest symmetry (compared with T symmetry for 34-atom clusters).

The mixed decahedral-close-packed motifs with a single tetrahedron core (Dh-cp(T)) (34-atom Pd-Pt clusters only)

This motif has a similar core of the pIh(T) – the tetrahedra of 10 atoms but, for this motif, the subsequent layer is a mixture of (111) and (100) orientations. This motif has previously been mentioned [205, 254, 717] as a highly symmetrical GM structure for Pd₂₄Pt₁₀ (T_d symmetry), where the cluster adopts Pt_{core}Pd_{shell} ordering. It is interesting to note that, in addition to the pIh(T) and Dh-cp(T), the LT [519, 694, 718] and the cp(T) motifs (competitive structures for 98-atom clusters, *see* Subsection 3.3.3) also have a similar close-packed T_d core (20-atom T_d core for the 98-atom LT), as shown

in Figure 4.3. On top of fcc (111) faces of the tetrahedron core for the Dh-cp(T) and LT, there are layers of hcp (111) stacking and the shell is completed with (100) atoms on the edge, with additional (100) and (111) layers for the LT (Figure 4.3(b)). Meanwhile, the cp(T) motif (Figure 4.3(c)) has a larger fcc (111) core (52 atoms), which is a truncated tetrahedron and an additional shell is formed by adding only the fcc (111) atoms.

The mixed decahedral-close-packed motifs with a double tetrahedral core (Dh-cp(DT))(34-atom clusters only)

This motif is comparable with the pIh-M(DT) and the building blocks are compared in Figure 4.4. The significant difference between these motifs is that there is no single Ih₁₃ unit present in the Dh-cp(DT). For both motifs, a 14-atom double tetrahedron is the core but in Dh-cp(DT) it is a perfect (distorted in pIh-M(DT)) close-packed arrangement. Further atoms adopt hcp (111) stacking on the (111) faces of the six tetrahedral faces, producing (111)-(100)-(111) alternates with a local incomplete decahedral arrangement. Even coverage of all tetragonal faces gives D_{3d} symmetry for the 32-atom unit but the addition of another two atoms in 34-atom clusters reduces

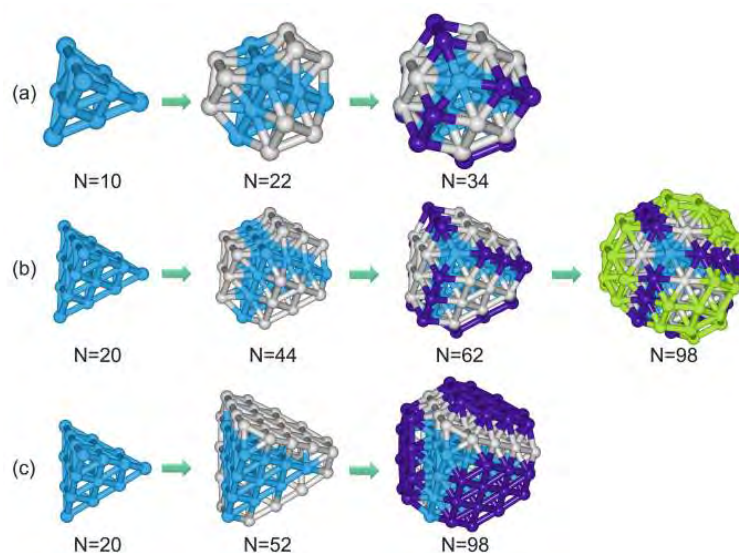


Figure 4.3: Comparison between atomic growth in (a) Dh-cp(T), (b) LT₉₈ and (c) cp₉₈: close-packed tetrahedral (*blue*), hcp (111) stacking (*grey*), (100) stacking (*purple*) and outer layer of (100) and (111) mixture (*green*).

symmetry to only C_s .

The Dh-cp(DT) has been described in detail [254–256] as a motif with a distinct stability for 34-atom clusters of Pd-Pt. For the composition (20,14), the internal double tetrahedral core is occupied exclusively by Pt atoms – a very stable configuration arises from a combination of the bulk preferences of Pt (close-packed) and favourable Dh motif of Pd for this size regime [254]. These interconversion phenomena have been reported experimentally [275] and are consistent with theoretical predictions [34, 497] but disappear for larger clusters where crystalline arrangements are favoured [259, 260]. Meanwhile, 38-atom Pd-Pt clusters do not prefer this motif, due to the additional strain caused by introducing two extra Pd dimers on the edges [254] and destabilised by 2 eV at the DFT level over the magic cluster of TO_{38} .

4.4 Global Minima Variations

4.4.1 $(\text{Pd-Au})_{34}$

As reported previously [620], Dh is the dominant motif for PdAu-34 (for all parameter sets). However, the Dh-Ih motif, which was included in the Dh classification, is actually the structure adopted by pure Pd_{34} and Au_{34} clusters, as shown in Figure 4.5(a).

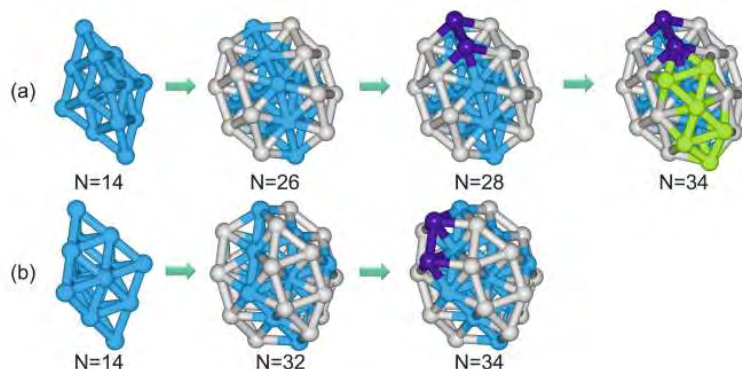


Figure 4.4: Comparison between atomic growth in (a) pIh-M(DT) and (b) Dh-cp(DT): internal double tetrahedral core (*blue*), hcp (100) stacking (*grey*), (100) edges (*purple*) and icosahedral stacking (*green*).

Accordingly, Pd- and Au-rich compositions favour this motif, while Dh is observed for medium compositions.

For parameter sets **I** and **II**, high weighting corresponds to a bias in the parameter towards the slightly stronger (Pd-Pd) bonding and gives more variation to structural motifs (*i.e.*, fcc, pIh-M(DT), pIh-db and mixed-pIh). The pIh-M(DT) motif, which was also previously included in the Dh grouping (Dh arrangement of the outer layer) is apparently the GM at $N_{\text{Au}} = 27-30$ for high weightings (w , w_s and $w_a > 0.8$) of all three parameter sets.

Meanwhile, the parameter set **III** represents a competition between weaker and stronger bonds because of the anti-symmetric movement of the parameters related to bonding attraction (A) and repulsion (ξ). As a result, the other structure, pIh⁶ ($N_{\text{Au}} = 28-30$ of $w_a = 0.9-1.0$), is also found as GM structure.

It should be noted that in the previous publication [620], pIh motifs have been treated as a single group, omitting any variation of the motifs. This is a reasonable classification for parameter sets **I** and **II**, as the pIh motif is rarely observed. However, for parameter set **III**, the motif is found in a wider region. The pIh-db motif, which is observed at $N_{\text{Au}} = 32$ for all three parameter sets, also prevails in the mid-region of composition ($w_a > 0.6$). The other class, mixed-pIh, can be seen at both extremes of weighting – pIh “4i” and pIh “4d” ($w_a \rightarrow 1.0$) and pIh “dh” ($w_a \rightarrow 0.0$) (“4d” is the variant of “4i” but with significant distortion).

4.4.2 (Pd-Pt)₃₄

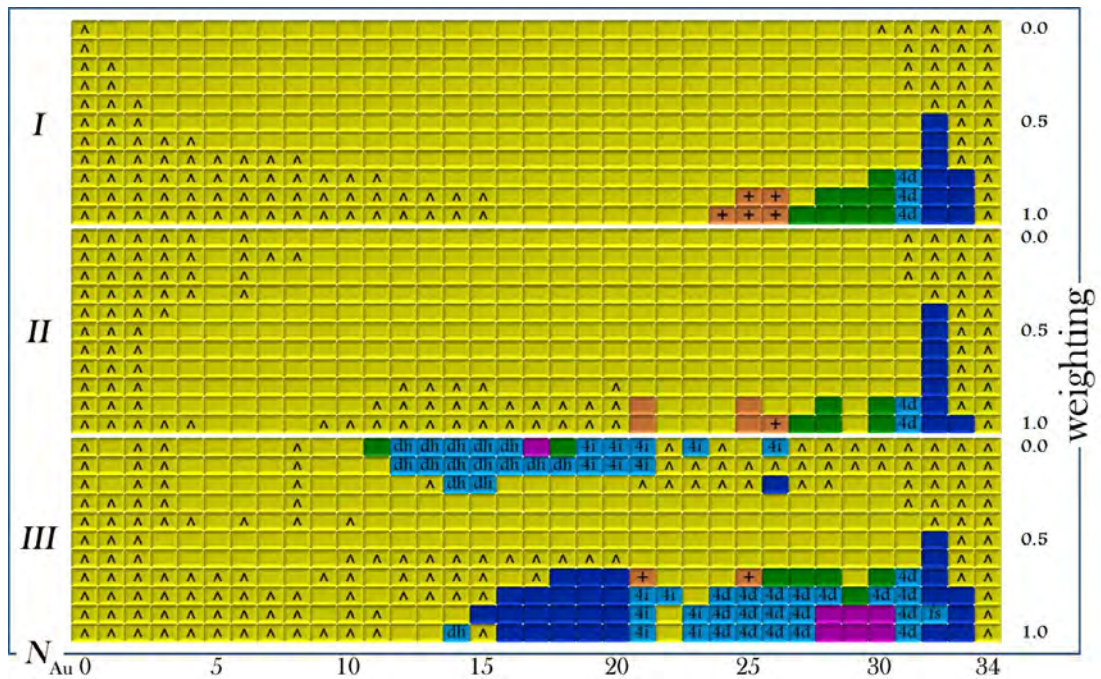
For parameter sets **I** and **II**, the Dh-Ih appears as GM for low N_{Pd} , while the Dh motif is only stabilised at medium compositions, as shown in Figure 4.5(b). On the other hand, Pd-rich compositions show a competition between Dh (including Dh-Ih) and Dh-cp(DT), pIh⁶ and mixed-pIh. The Dh-cp(DT), which have been reported in the previous mentioned work by Paz-Borbon *et al.* [254] as the lowest energy structure at the DFT level, appear as a GM for w , $w_s = 0.4-0.5$ ($N_{\text{Pd}} = 18-25$).

The pIh⁶ is preferred for $w, w_s > 0.5$ at $N_{\text{Pd}} = 25-30$, for which at least four Pt atoms are needed in the ring core, and maintains D_{2h} symmetry. This is the evidence of the higher tendency for Pt to occupy the core site. Moreover, the other pIh-type motif, pIh-db, is the minority ($N_{\text{Pd}} = 26-27 - w, w_s = 0.8, 1.0$ and $N_{\text{Pd}} = 10 - w, w_s = 0.0-0.2$). Meanwhile, the prevalence of pIh-based structures for Pd-Pt is further enhanced by a wide GM of pIh-M(DT) ($N_{\text{Pd}} = 7-12, 16-17, 28, 30, w, w_s = 0.2-0.7$). The stabilisation of this low-symmetry motif is due to the close-packed arrangement of Pt atoms – single four-atom tetrahedra ($N_{\text{Pd}} = 30$) and six-atom capped double-tetrahedra ($N_{\text{Pd}} = 28$), which is preferred for small Pt clusters [34, 254, 275, 497].

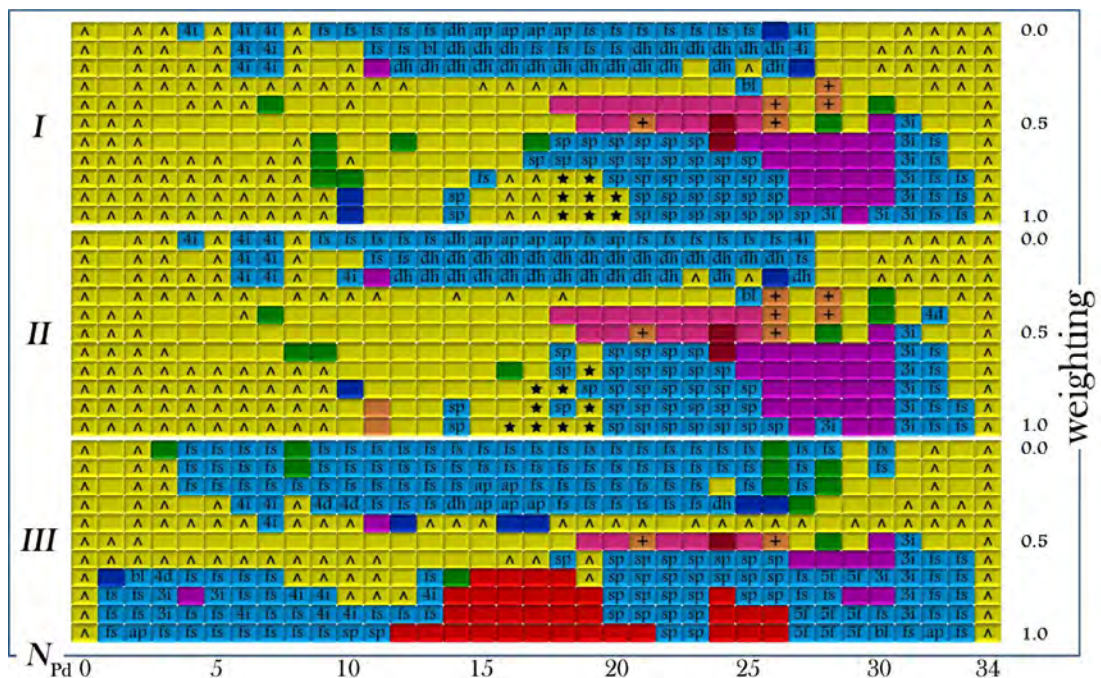
Other motifs are stabilised at specific compositions: Dh-cp(T) ($N_{\text{Pd}} = 24, w, w_s = 0.4-0.5$) and fcc-hcp ($N_{\text{Pd}} = 26, 28, w, w_s = 0.5-0.7$). This is also true for the pIh-M(DT) motif ($N_{\text{Pd}} = 28, 30$). At $N_{\text{Pd}} = 24$, the Dh-cp(T) prevails, possibly due to high symmetry ($C_{3v} - T_d$ if all the atoms are the same), similarly to fcc-hcp motifs (C_{2v} symmetry) at $N_{\text{Pd}} = 26, 28$, in which all six Pt atoms reside in the core ($N_{\text{Pd}} = 28$) and additional two Pt atoms are located in the centroid of (111) facets ($N_{\text{Pd}} = 26$).

With the extreme parameterisation, mixed-pIh is observed to dominate for the medium (pIh “dh” and pIh “fs” – $w, w_s \rightarrow 1.0$) and Pd-rich (pIh “sp” – $w, w_s \rightarrow 0.0$) compositions. The other variant, pIh “3i”, is favourable at $w, w_s = 0.0-0.5$ (also with parameter set **III**), where three Pt atoms occupy the centre of each of the interpenetrating Ih but is not stable for other compositions, indicating composition-specific stabilisation.

Parameter sets **I** and **II** of Pd-Pt give more structural variation compared with Pd-Au, for both low and high weightings. The Gupta potential of Pd-Pt shows differences of less than 10% in the p, q and r_0 parameters (see Table 2.2). As a result, the GM pattern for parameter sets **I** and **II** have only small dissimilarities, suggesting that p and q parameters are insignificant (for this system) for the overall structures and energies of clusters. Hence, it is valid to focus on the A and ξ parameters for the



(a)



(b)

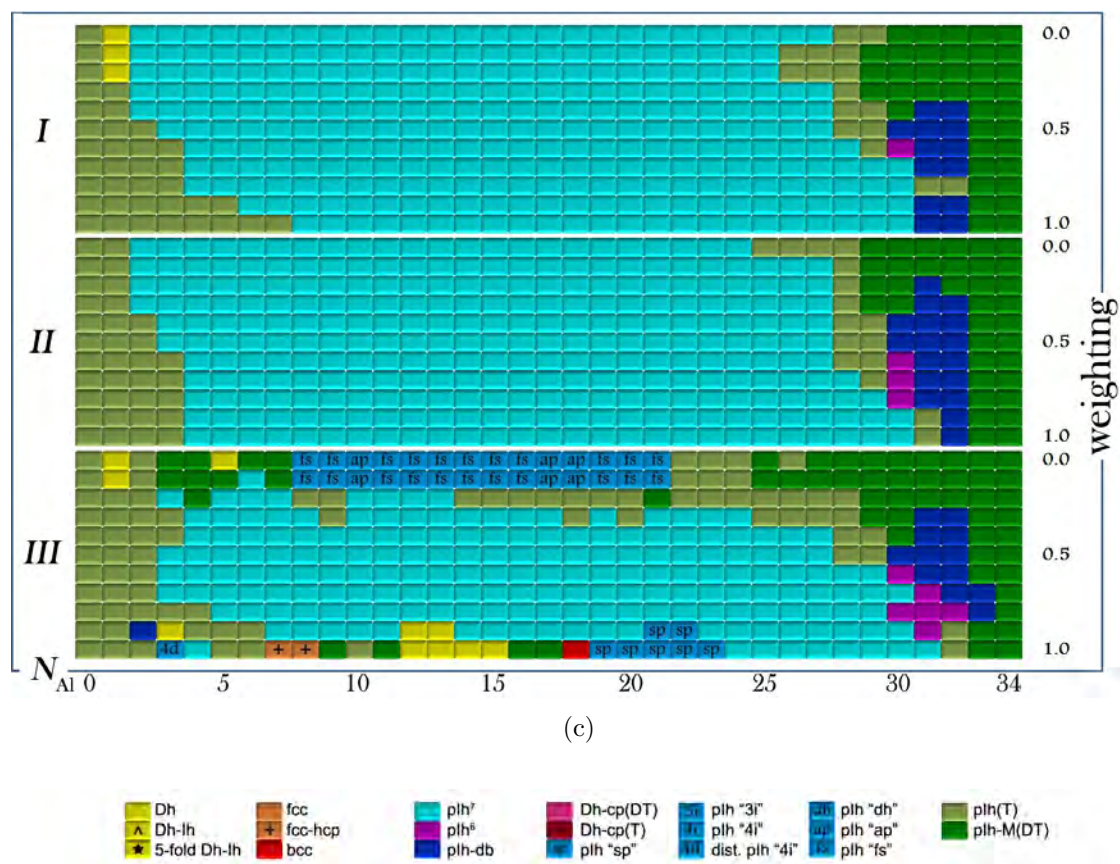


Figure 4.5: Structural map of 34-atom global minima found for (a) Pd-Au, (b) Pd-Pt and (c) Ni-Al.

parameter set **III**, for which the differences between Pd and Pt are 70% (A) and 56% (ξ).

A distinct structural map is observed for the parameter set **III**, in which a wide range of mixed-pIh prevails. Detailed analysis of pIh structures gives the following pattern: for $w_a > 0.5$, the pIh “fs” is adopted, while for $w_a < 0.5$, GM domination is composition-dependent: pIh “fs” (Pt-rich) and pIh “sp” (Pd-rich). Three other variants, pIh “ap”, pIh “4i” and pIh “3i”, are also found but very limited. The significant difference in structural maps for this parameter set may arise from contrasting values for the homonuclear parameters of the Gupta potential between Pd and Pt.

4.4.3 (Ni-Al)₃₄

This is the only system and size in this chapter for which the pure cluster adopted different types of structure: pIh(T) and pIh-M(DT) for Ni₃₄ and Al₃₄, respectively (Pd₃₄, Au₃₄ and Pt₃₄ adopted Dh-Ih, while all pure cluster of 38-atom adopted TO), corresponding to the prevalence of pIh(T) in the Ni-rich and pIh-M(DT) in the Al-rich regions.

Between structural maps of parameter sets **I** and **II** in Figure 4.5(c), the clear difference is the Dh GM at $N_{Al} = 1$ for parameter set **I** ($w = 0.0-0.2$), which is not seen for the parameter set **II**. Other areas are closely matched, especially a wide area ($N_{Al} = 3-31$, all w , w_s) of pIh⁷ GM (incomplete and capped), which is not found for the GM of Pd-Au and Pd-Pt.

The differences in the p and q parameters between the Ni and Al homonuclear potentials (*see* Table 2.2) are very large but yield only minor variation for parameter sets **I** and **II** – pIh⁶ ($N_{Al} = 30$, $w = 0.6$, $w_s = 0.6-0.8$, ring-type ordering) and pIh-db ($N_{Al} = 30-32$, w , $w_s = 0.2-1.0$, Ni-centred Ih₁₃ units). It is believed that this variation is not influenced by the parameterisation effect but rather by the composition effect, in which a smaller Ni is located in the centre of Ih units. Similar effects are predicted to afford prevalence of pIh(T) ($N_{Al} = 25-32$, all w and w_s), in addition of GM at Ni-rich

region. For these compositions, clusters are stabilised by filling Ni in six sites of a 10-atom tetrahedron core (minus the four exposed atoms).

The pIh⁷ dominance is repeated for parameter set **III**; hence, the difference of structural preference of pure clusters does not induce a GM variation of 34-atom Ni-Al clusters, although at extreme weightings, some structural variation can be seen: pIh “fs” ($N_{\text{Al}} = 8-21$) at low ($w_a = 0.0-0.2$) and fcc-hcp / Dh / bcc / pIh “sp” ($N_{\text{Al}} = 7-23$) at high ($w_a = 0.9-1.0$) weightings. Further evidence of the composition effects is seen, in which pIh⁶, pIh-db, pIh(T) and pIh-M(DT) motifs are found mostly for compositions similar to those of the parameter sets **I** and **II**.

4.4.4 (Pd-Au)₃₈

The structural motifs of 38-atom Pd-Au clusters in Figure 4.6(a) are much simpler than their 34-atom counterparts, in which the TO motif dominates. The only other motif found for the parameter sets **I** and **II** is pIh-M-pc⁵, at $N_{\text{Au}} = 28-33$, for w , $w_s = 0.6-1.0$. On the other hand, at $w_a = 1.0$ for the parameter set **III**, the pIh⁶ ($N_{\text{Au}} = 32$) and Oh-Ih ($N_{\text{Au}} = 22-23$) motifs are also observed. Meanwhile, extreme (low and high) weightings of this parameter set exhibit the low symmetry pIh “fs” with ill-defined structures but only a minority as compared with the Dh and Dh-Ih, especially at $w_a \rightarrow 0.0$ region. The Dh preference is seen at the Pd-rich compositions and the Dh-Ih at the medium compositions.

4.4.5 (Pd-Pt)₃₈

38-atom Pd-Pt gives results consistent with the 34-atom clusters, in which a large overlap between parameter sets **I** and **II** (Figure 4.6(b)) is observed but, at $w_s = 1.0$, the parameter set **II** exhibits a bcc configuration ($N_{\text{Pd}} = 18-20$). As the most stable motif for pure Pd₃₈ and Pt₃₈, TO is adopted for Pd and Pt-rich compositions, as well as for the mid-composition region (w , $w_s = 0.3-0.7$). In addition to the structure of pure clusters, wide prevalence (compositions and weightings) of fcc-based TO can be

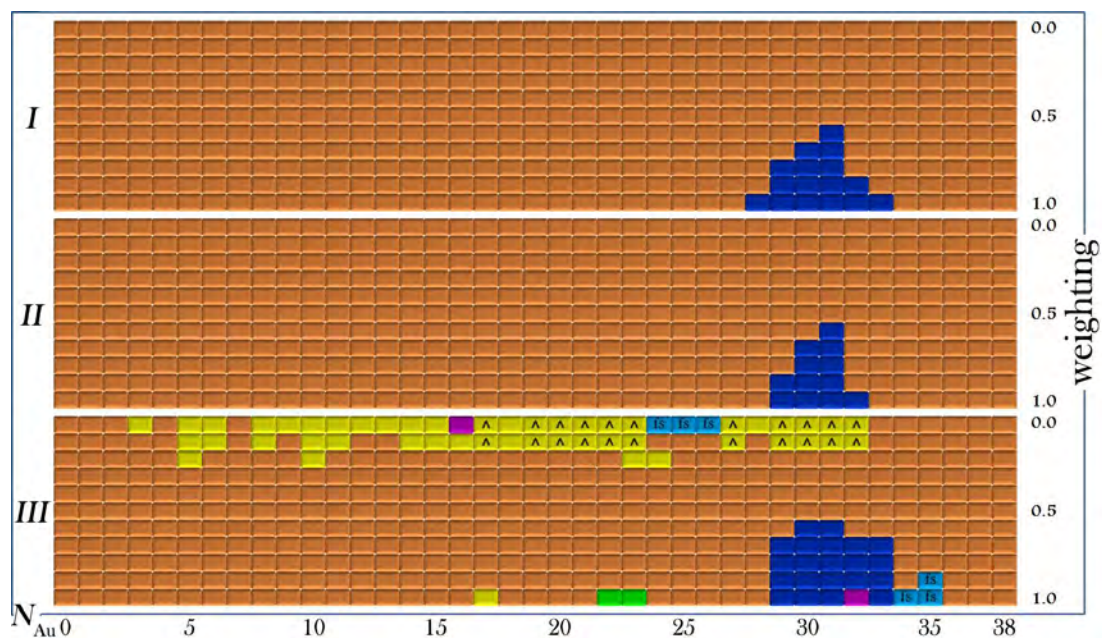
correlated to the small size mismatch [205, 254] and the fact that $N = 38$ is the magic number for TO [719]. Moreover, the tendency of Pd-Pt bimetallic clusters to adopt fcc structures has also been supported by several experimental studies [259, 260].

At the low weighting ($w, w_s = 0.0-0.2$), Dh is found for almost the entire composition region, except for $N_{\text{Pd}} = 1-2$ (TO). In the mid-composition region, there is a competition from several mixed-pIh variants (non-dominant of pIh “3i”, pIh “fs” and pIh “ap”). The mixed-pIh is also found at high weightings ($w, w_s = 0.8-1.0$), from a variant of pIh “sp” ($N_{\text{Pd}} = 18-26$) and pIh “fs” ($N_{\text{Pd}} = 33-36$).

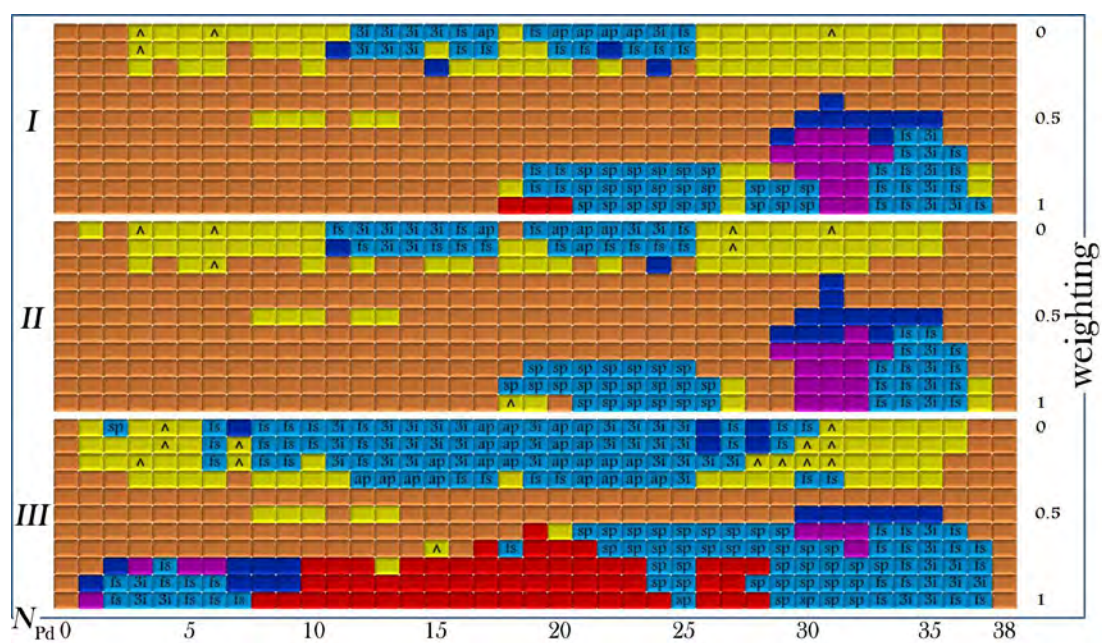
High symmetry structures of pIh⁶ and pIh-M-pc⁵ are only observed in isolated regions: pIh⁶ at $N_{\text{Pd}} = 29-33$ ($w, w_s = 0.6-1.0$) and pIh-M-pc⁵ at $N_{\text{Pd}} = 29-35$ (**average** potential, $w = w_s = w_a = 0.5$). These two motifs are stabilised by a core-shell ordering, in which Pt occupies a six-atom hexagonal ring and a seven-atom decahedral core of the pIh⁶ and pIh-M-pc⁵, respectively.

More pIh variation is seen for Pd-Pt compared with Pd-Au clusters. However, for both systems, the widest pIh variants region are observed for high weightings ($w, w_s \rightarrow 1.0$) of the parameter sets **I** and **II**. These weightings are actually biased towards Pd and can be associated with the greater tendency of Pd to adopt pIh structures, as has been observed for clusters of small to medium sizes [257, 720].

Moving to the parameter set **III**, the regions of stability for the pIh “sp” ($w_a \rightarrow 1.0$) and other mixed-pIh (pIh “fs”, pIh “3i”, pIh “ap”) ($w_a \rightarrow 0.0$) are broadened. The bcc motif, which can also be seen for the parameter set **I**, spans a larger area in the structural map ($N_{\text{Pd}} = 8-28, w_a = 0.6-1.0$). However, this parameter set would be insignificant, as the DFT study [256, 622] shows that the **average** potential (or slightly biased parameter sets **I** and **II**) gives a qualitatively good estimate for the Pd-Pt. In addition, the parameter set **III** gives too large an excess energy and is not likely to produce better results (compared with the higher level calculations) than those of the parameter sets **I** and **II**.



(a)



(b)

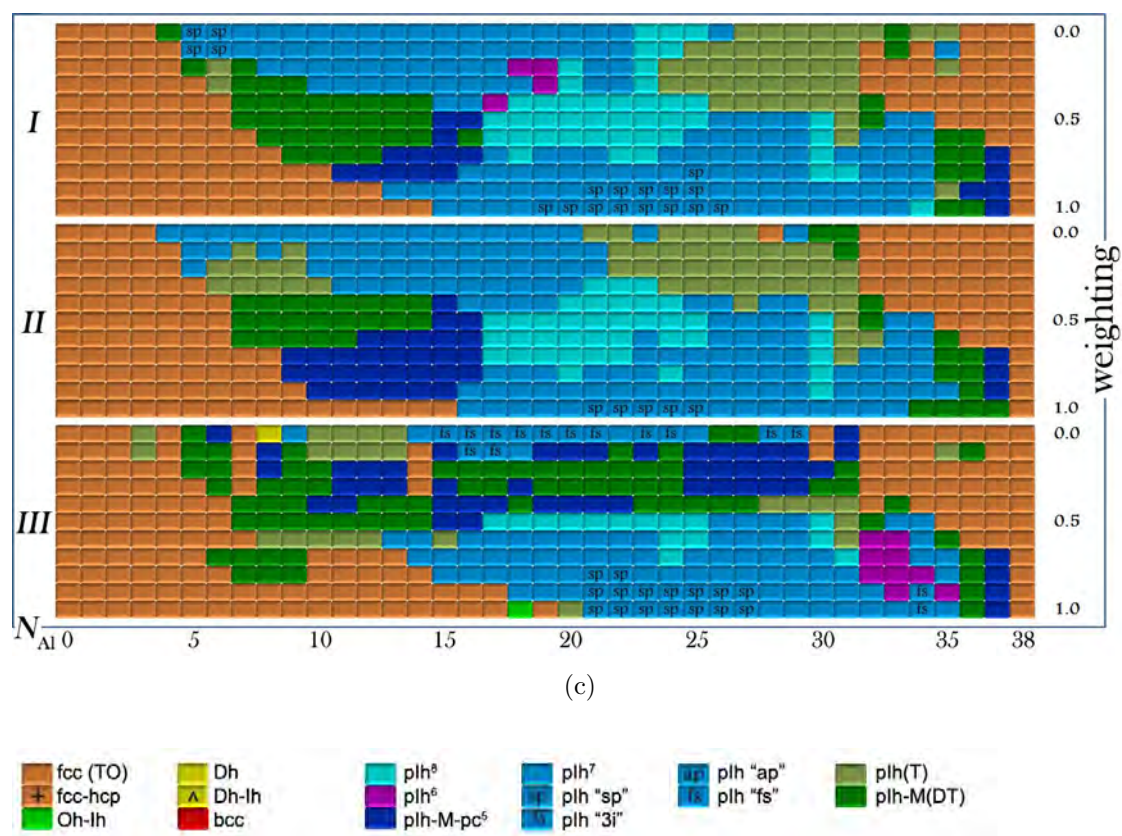


Figure 4.6: Structural map of 38-atom global minima found for (a) Pd-Au, (b) Pd-Pt and (c) Ni-Al.

4.4.6 (Ni-Al)₃₈

Figure 4.6(c) shows that the pure Ni₃₈ and Al₃₈ clusters adopt the same motif (TO) but the combination of these elements show more variation, compared with their 34-atom counterparts. There are large areas of similarity between structural maps of the parameter sets **I** and **II**, in which the pIh⁷ motif dominates at the medium composition range. This motif is not found as GM of the same size cluster for Pd-Au and Pd-Pt, enhancing the assertion of this motif's stabilisation due to a large size mismatch, similar to those of Cu-Ag, Ag-Ni and Au-Cu systems [203].

In the mid-composition region of the parameter sets **I** and **II**, there is occurrence of the regional tendency for several motifs: pIh-M(DT) ($N_{\text{Al}} = 7-14$, w , $w_s = 0.4-0.6$), pIh-M-pc⁵ ($N_{\text{Al}} = 9-16$, w , $w_s = 0.6-0.9$), pIh⁸ ($N_{\text{Al}} = 17-25$, w , $w_s = 0.0-0.8$) and pIh(T) ($N_{\text{Al}} = 21-31$, w , $w_s = 0.0-0.4$). However, the parameter set **II** shows a broader GM region of pIh-M-pc⁵ at the expense of pIh-M(DT) and pIh⁸ disappears (as compared with the parameter set **I**) at low weightings ($w_s = 0.0-0.2$). An additional GM region of the pIh(T) ($N_{\text{Al}} = 6-10$, $w_s = 0.1-0.3$) is also visible.

Anti-symmetric weighting of the parameter set **III** does not entirely change the pattern but there is a more scattered distribution of the pIh-M(DT) ($N_{\text{Al}} = 6-31$, $w_a = 0.1-0.4$) and pIh-M-pc⁵ ($N_{\text{Al}} = 5-31$, $w_a = 0.0-0.5$) GM and less prominence of the pIh⁸ and pIh(T) motifs. The TO dominance for both Ni- and Al-rich compositions is repeated and, similarly, the pIh⁷ motif is widely found for the medium compositions ($w_a > 0.5$). The disruption of pIh⁷ dominance can only be seen at extreme weightings, for which pIh “sp” ($w_a \rightarrow 1.0$) and pIh “fs” ($w_a \rightarrow 0.0$) are observed. Meanwhile, the pIh⁶ motif, which is observed at a non-specific composition for the parameter set **I**, is shifted to around its magic composition ($N_{\text{Al}} = 32-35$) for $w_a = 0.6-0.9$.

4.5 Chemical Ordering

Parameterisation of the Gupta potentials led to a variation of the chemical ordering as shown in Figure 4.7, classified as: (i) segregated (spherical cap, core-shell – complete and incomplete), (ii) mixed (random, onion-like) and (iii) intermediate of segregated and mixed (ball-and-cup).

An incomplete core-shell is adopted for A-B (Pd-Au, Pt-Pd and Ni-Al) clusters, when a limited number of B atoms are on the surface. Three types of configuration are observed: **incomplete core-shell type-A** (“**i-CS(A)**”), where B atoms occupy the low-coordinate surface sites (*e.g.*, edge and corner sites), **incomplete core-shell type-B** (“**i-CS(B)**”), having a uniform partial monolayer coverage of B atoms on the surface and **incomplete core-shell type-C** (“**i-CS(C)**”), where the surface is intermixed of A and B. The “**i-CS(A)**” configuration has also been adopted by AgCu-34 clusters, in which Ag atoms occupy the low coordination surface sites [203].

The ball-and-cup configuration has several exposed A atoms and a preponderance of surface B atoms on one side, making a “core” of A atoms off-centre and, corresponds to an intermediate between core-shell and spherical cap orderings. This configuration has been reported for PdPt-34 by Paz-Borbon *et al.* [256] and is similar to the “Janus-like”

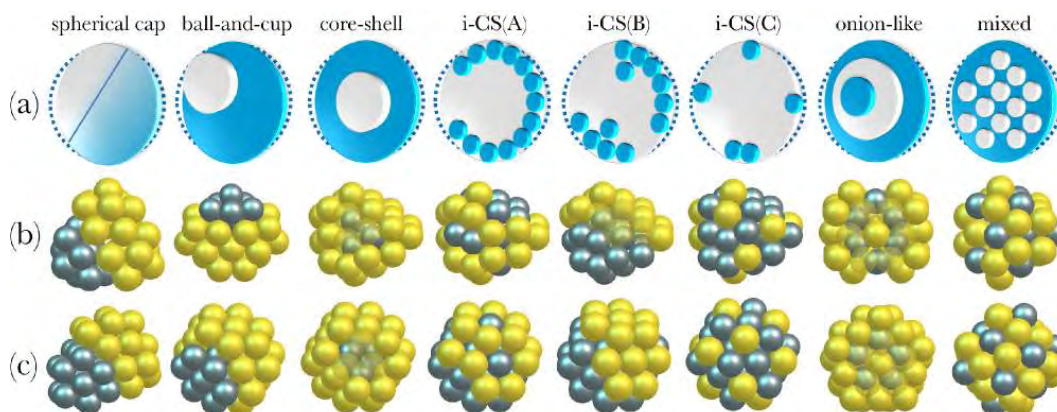


Figure 4.7: Chemical ordering patterns of small clusters – (a) general and examples from the study of sizes, (b) 34 and (c) 38 atoms.

particle phase-segregation that has recently been observed for Ag-Au clusters by inert gas aggregation experiments [721]. For the small sizes (34 and 38-atom) studied here, it is possible to carry out exhaustive searches for the ordering observations. It is, however, intended to develop better ways of performing this analysis (*e.g.*, compositional mixing degree, σ_N).

The examples of 34- and 38-atom clusters shown in Figure 4.7 are mainly based on the most common motif for each size, *i.e.*, Dh₃₄ and TO₃₈, to give a better picture of the ordering differences. However, some of the orderings are only stabilised by a certain motif; for example, the spherical cap is mostly observed for the Dh and pIh motifs but not for TO, whilst mixing is normally found for the pIh or the other distorted motifs. Meanwhile, the **i-CS(C)** ordering evolves into the **i-CS(A)** whenever enough shell atoms are available (Au for Pd-Au, Pd for Pd-Pt or Al for Ni-Al) before a complete core-shell is attained. Thus, the chemical ordering is sometimes dependent on the structure, though this is not true for all weightings. The difference between some orderings is very small (only by a few atoms), so at the ideal parameterisation (around average) competition between several configurations is expected.

4.5.1 Pd-Au

Detailed discussion of the chemical ordering profiles of Pd-Au has been reported previously [620] but here there will be a discussion on the new compositional mixing degree, σ_N analysis, as shown in Figure 4.8. As discussed above, the parameter sets **I** and **II** give closely-matched structural maps for Pd-Au, both at sizes 34 and 38. This pattern is extended to their ordering but with significant difference for the **i-CS(C)** of the Pd-rich compositions, which is observed at low weightings ($w \rightarrow 0.0$) for the parameter set **I** but at high weightings ($w_s \rightarrow 1.0$) for the parameter set **II**. Interestingly, this behaviour is matched by the σ_N data, which give higher (less negative, ~ -0.10) values for the parameter sets **I** compared with the parameter sets **II** (~ -0.15). Furthermore, from low to high weightings, the parameter set **III** exhibits a gradual decrease of

the σ_N values, consistent with the ordering transition: spherical cap/ball-and-cup ($w_a = 0.0-0.2$) > **i-CS(B)** ($w_a = 0.2-0.4$) > **i-CS(A)/i-CS(C)** ($w_a = 0.2-1.0$) > mixed (random/onion-like) ($w_a = 0.8-1.0$).

In comparing the new σ_N with the old σ , there is the clearer representation for the cluster ordering. While the σ description (positive for phase segregation and negative for ordered mixing [636]) is only meaningful for the mid-range compositions, the σ_N can be applied regardless of the composition. Hence, the compositional effects that gives an ordering transition for a particular parameter set can be clearly seen.

4.5.2 Pd-Pt

Theoretical investigations [171, 257, 258] have found very good agreement with the experimental results [257, 722] with regards to the $\text{Pt}_{\text{core}}\text{Pd}_{\text{shell}}$ ordering preference. Based on Table 1.1, no atomic size and charge transfer effects are expected to be involved but there is a considerably larger cohesive energy of Pt (favouring Pt-core) and lower surface energy of Pd (favouring Pd-shell).

Figure 4.9 shows that each of the weightings has an almost isolated σ_N line (*i.e.*, no crossover between weighting), for all three parameter sets, which seems to indicate a distinct chemical ordering between weightings. Compared to Pd-Au, there are lower values of σ_N (*i.e.*, more mixing) for the high weighting parameters and higher values of the σ_N for the low weighting parameters. This is consistent with the ordering maps, in which the larger effects of parameterisation is seen for Pd-Pt, as compared with Pd-Au.

For the parameter sets **I** and **II**, the ordering progression is: spherical cap/ball-and-cup ($w, w_s = 0.0-0.2$) > **i-CS(B)** ($w, w_s = 0.2-0.3$) > **i-CS(A)/i-CS(C)** ($w, w_s = 0.4-0.6$) > mixed (random/onion-like) ($w, w_s = 0.6-1.0$). A similar progression is also visible for the parameter set **III** but with the expansion of the spherical cap (low weightings) and random mixed (high weightings) phases.

Examination of the mixed clusters of the Pd-rich region for $w, w_s = 0.6-1.0$ provides evidence of a strong tendency for Pt atoms to form a ring-core (due to limited number

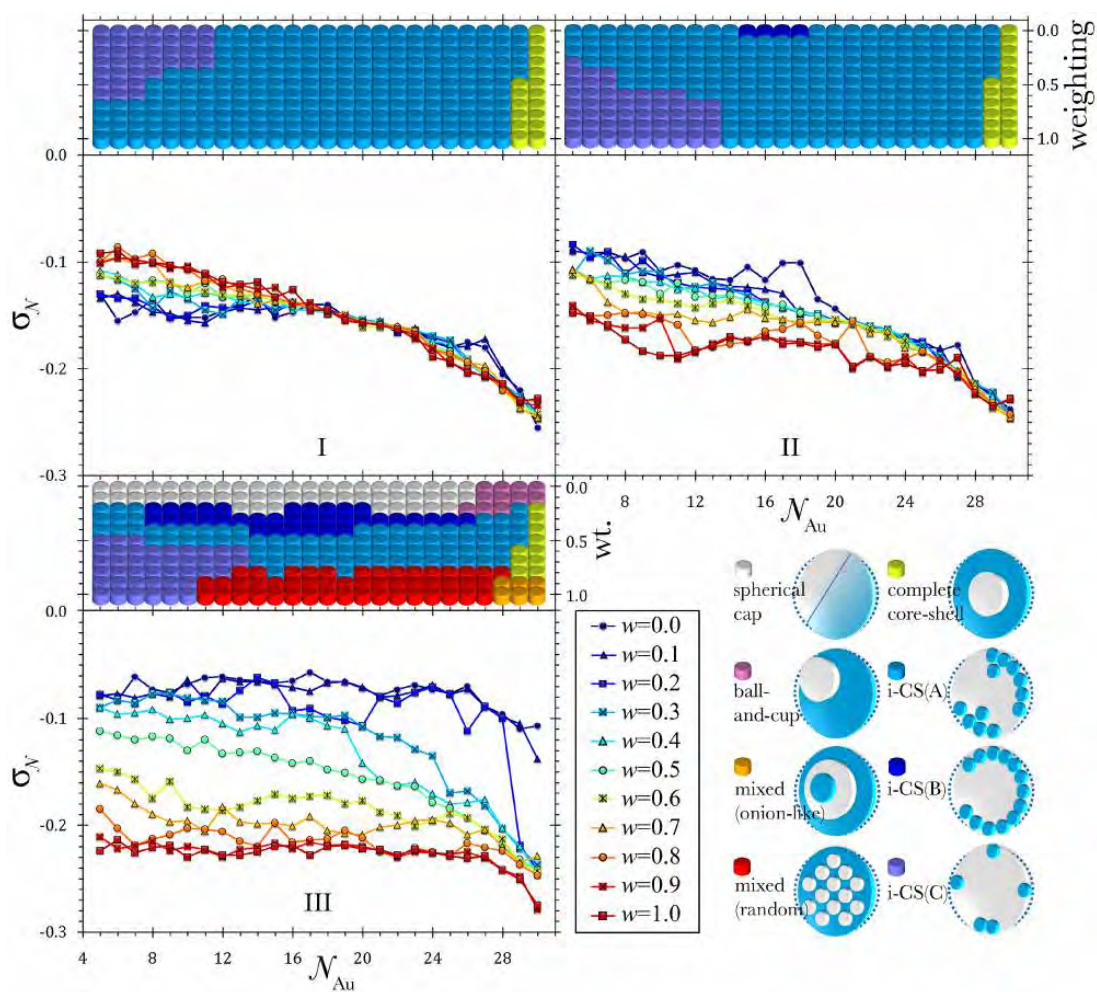
of Pt) for both sizes: 34 ($N_{\text{Pd}} = 25\text{-}29$) and 38 ($N_{\text{Pd}} = 29\text{-}33$). This character is accounted for a very low σ_N , as Pd-Pt bonds are maximised.

For the high weighting parameters ($w, w_s, w_a \geq 0.6$), there is a significant regime of the onion-like Pd-Pt-Pd ordering, potentially due to the competition between Pd/Pt site preference and the size effects, which tends to overcome the $\text{Pt}_{\text{core}}\text{Pd}_{\text{shell}}$ tendency [257]. On the other hand, the extreme high weighting ($w, w_s, w_a \rightarrow 1.0$) parameters are found to shift a mixed-ordering from disordered to ordered, as indicated by very low σ_N and clusters are distorted towards bcc structures.

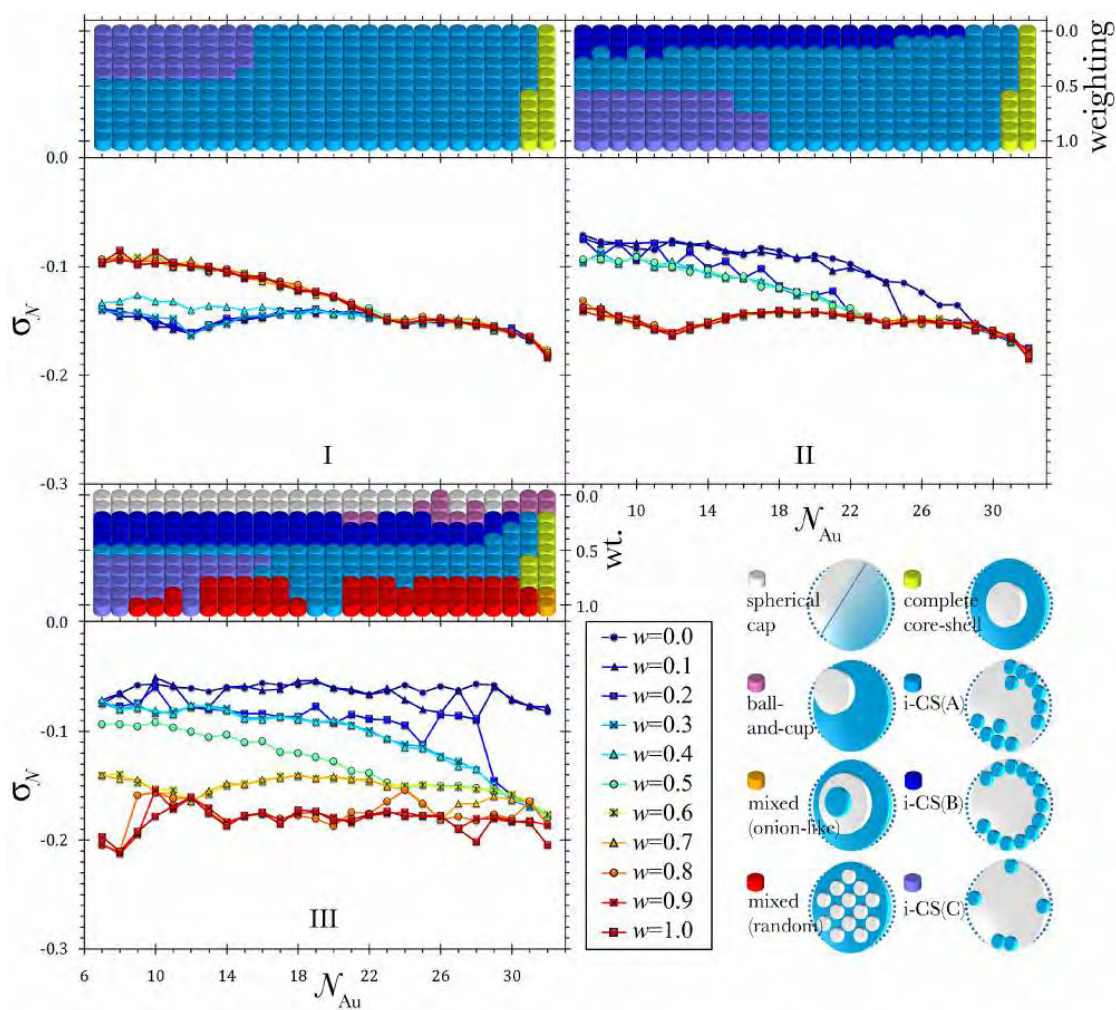
Even though 34- and 38-atom Pd-Pt clusters show essentially the same chemical ordering maps, it can be noted that a wider region of the onion-like ordering is found for 34- ($w, w_s = 0.6\text{-}1.0$) compared with 38-atom clusters ($w, w_s = 0.8\text{-}1.0$) for the parameter sets **I** and **II**. This is influenced by the adopted motifs, as the p1h ($N = 34$) favours the onion-like segregation pattern more than that of the fcc-TO ($N = 38$), which is consistent with results for the larger (*e.g.*, 147- and 309-atom [723]) clusters. Also for size 34, the lower σ_N values (~ -0.3) are seen for high weightings ($w, w_s, w_a \rightarrow 1.0$), consistent with the previously discussed structural map, in which more bcc are observed. This motif has a perfect atomic configuration to support the ordered mixing with alternating binary atoms. On the other hand, less variation of the structure for size 38 (in which TO is the magic cluster) is reflected in the less negative σ_N values (minimum ~ -0.2) and provides evidence for less mixing in clusters of this size.

4.5.3 Ni-Al

The ordering profiles for 34- and 38-atom Ni-Al clusters (Figure 4.10) are fairly simple for the parameter sets **I** and **II**, in which only a core-shell (incomplete types **i-CS(A)** and **i-CS(B)** and complete) ordering is observed, similar to Pd-Au. The progression of **i-CS(C)** – **i-CS(A)** – complete core-shell only gives a small range variation in the σ_N , resulting in crossover between weightings. For both parameter sets, a better mixing is identified for 34- compared with 38-atom clusters, based on results of the low weighting

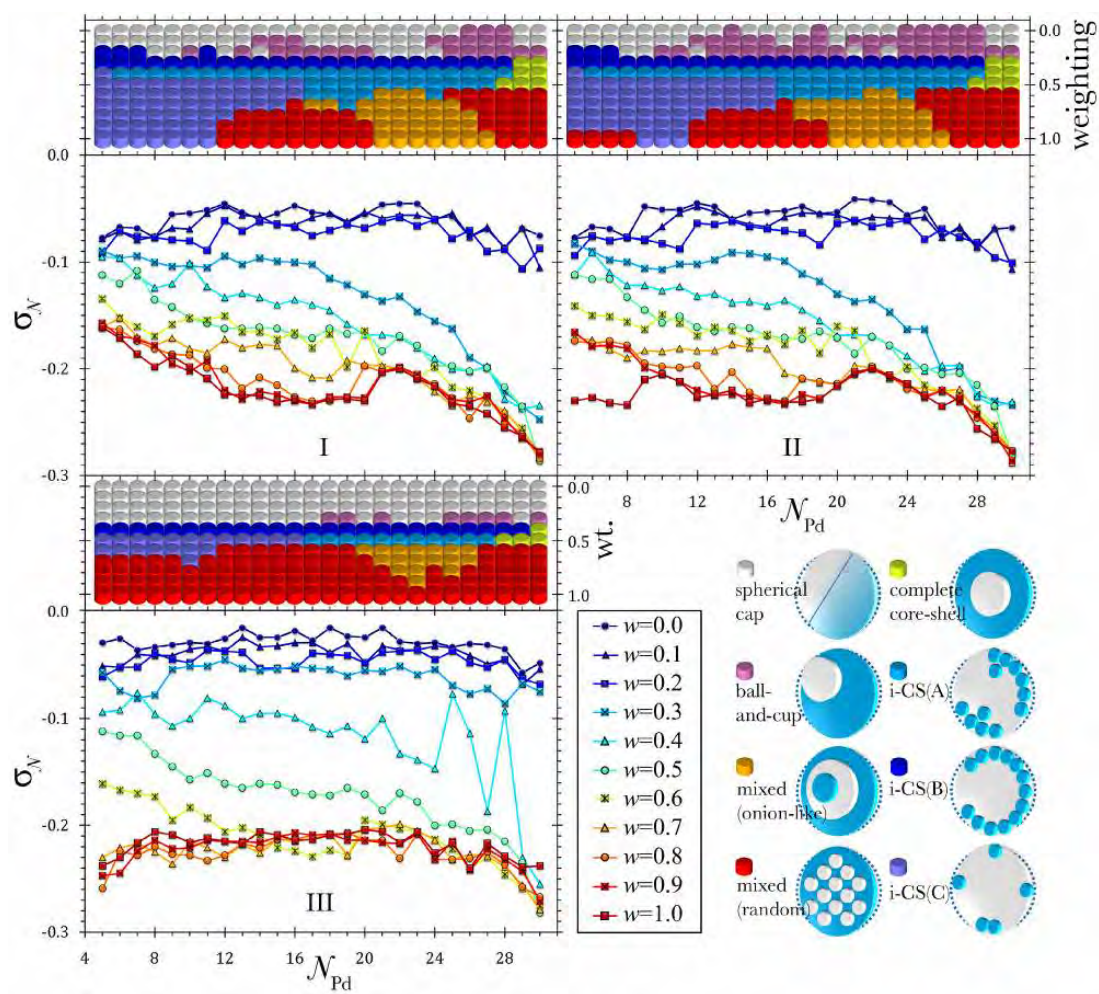


(a)

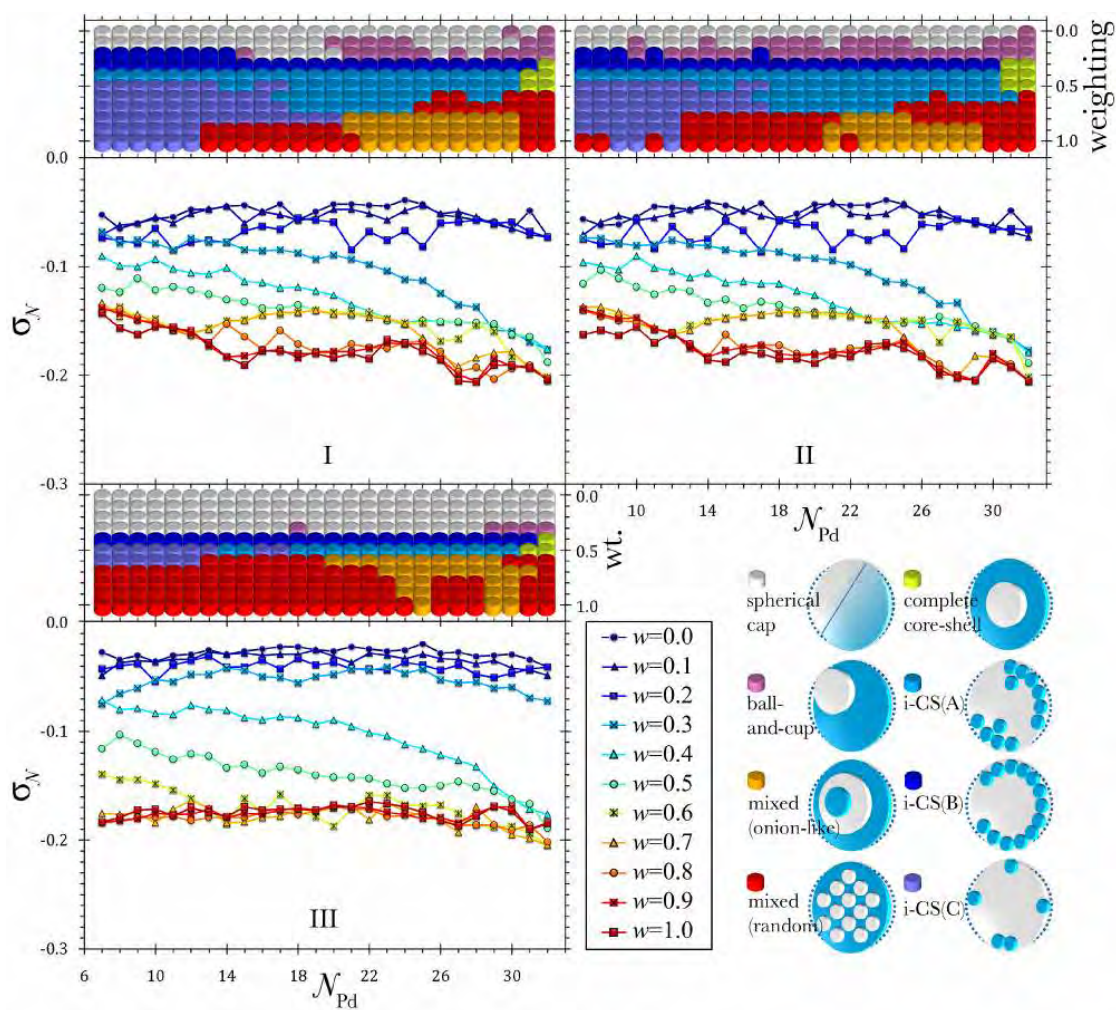


(b)

Figure 4.8: Chemical ordering analyses based on ordering maps (qualitative) and compositional mixing degrees, σ_N , curves (quantitative) of (a) 34- and (b) 38-atom Pd-Au global minima for the parameter sets **I**, **II** and **III**.



(a)



(b)

Figure 4.9: Chemical ordering analyses based on ordering maps (qualitative) and compositional mixing degrees, σ_N , curves (quantitative) of (a) 34- and (b) 38-atom Pd-Pt global minima for the parameter sets **I**, **II** and **III**.

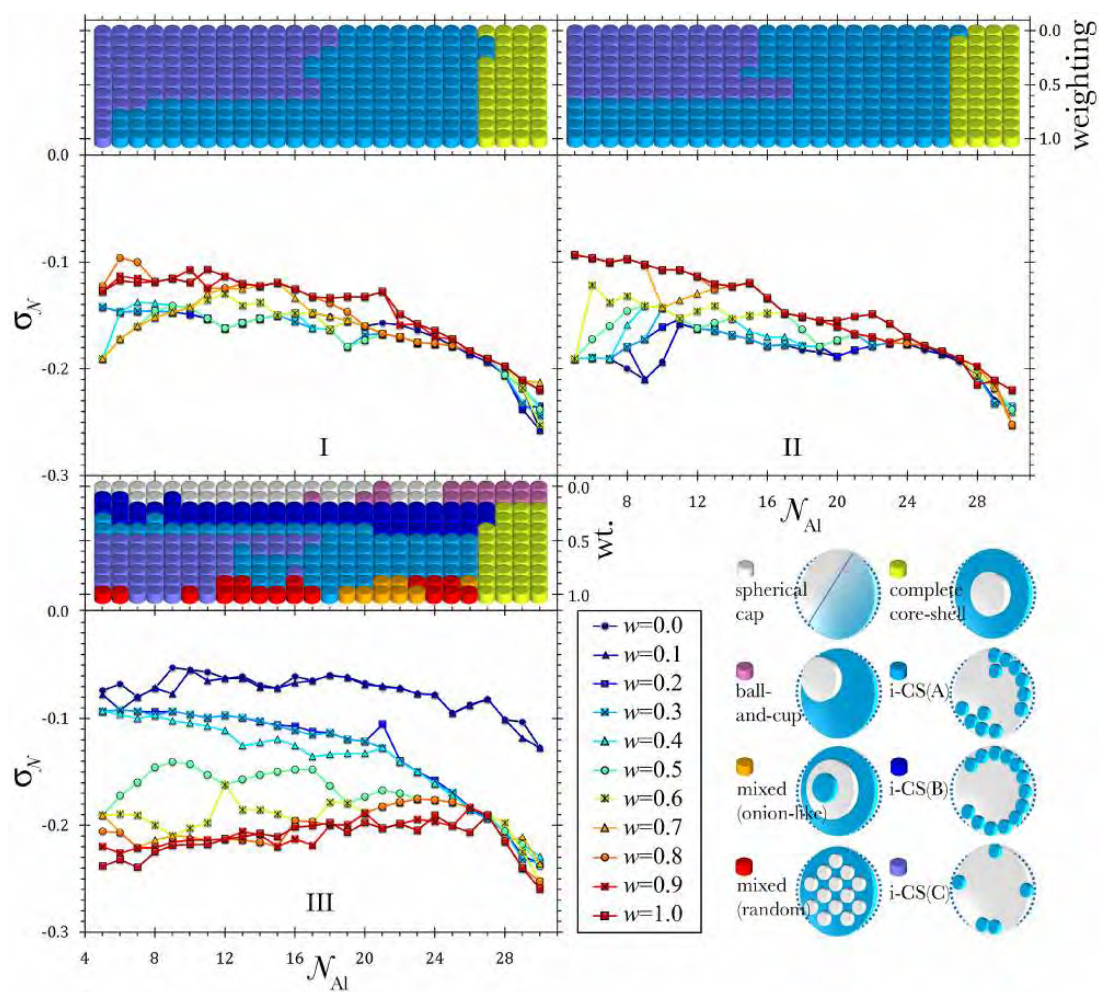
parameters for the Ni-rich compositions.

For the parameter set **III**, the σ_N values are consistent with the progression of spherical cap/ball-and-cup ($w_a = 0.0-0.1$) > **i-CS(B)** ($w_a = 0.1-0.4$) > **i-CS(A)**/**i-CS(C)** ($w_a = 0.1-1.0$) > mixed (random/onion-like) ($w_s = 0.8-1.0$). Interestingly, a wider range of the σ_N values for size 34 is found compared with size 38. This is in contrast to the earlier discussed structural map, in which size 34 displays less variation of the structural motifs. It seems therefore, that there is less correlation between the σ_N values (*i.e.*, chemical ordering / mixing degree) and the structural motifs. However, some orderings are clearly preferred by a specific motif (*e.g.*, onion-like chemical ordering in the p1h and ordered mixing in the bcc structures).

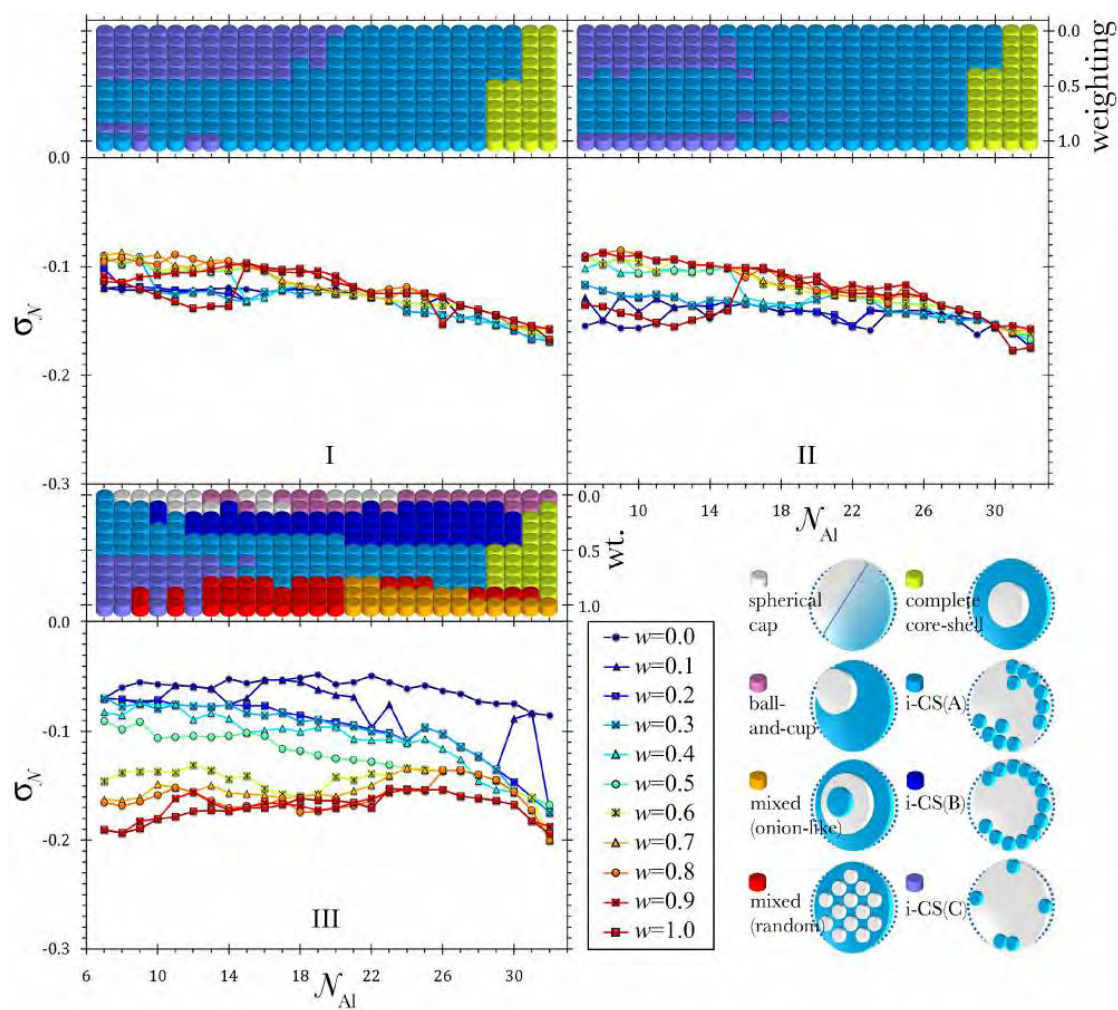
4.5.4 General Observation of Ordering Profiles Based on the σ_N

The ordering profiles for 34- and 38-atom bimetallic nanoalloys of Pd-Au, Pd-Pt and Ni-Al give a confirmation for the accuracy and consistency of the newly defined compositional mixing degree, σ_N , analysis. The compositional effects (*i.e.*, A-rich, B-rich and medium-composition for A-B clusters) which is the limitation of the old mixing degree, σ , analysis is resolved. This is crucial for future use of this analysis in predicting a chemical ordering of the cluster.

Figure 4.11 shows a summary of combined σ_N values of the eight-types of ordering mentioned above. The differences are not very large and, generally, the σ_N values are as follows: spherical cap (-0.02 to -0.08) > ball-and-cup (-0.04 to -0.17) > **i-CS(B)** (-0.05 to -0.20) >> **i-CS(C)** (-0.07 to -0.23) \geq **i-CS(A)** (-0.09 to -0.23) >> core-shell (-0.14 to -0.29) \geq onion-like (-0.13 to -0.28) \simeq random mixing (-0.13 to -0.28).



(a)



(b)

Figure 4.10: Chemical ordering analyses based on ordering maps (qualitative) and compositional mixing degrees, σ_N , curves (quantitative) of (a) 34- and (b) 38-atom Ni-Al global minima for the parameter sets **I**, **II** and **III**.

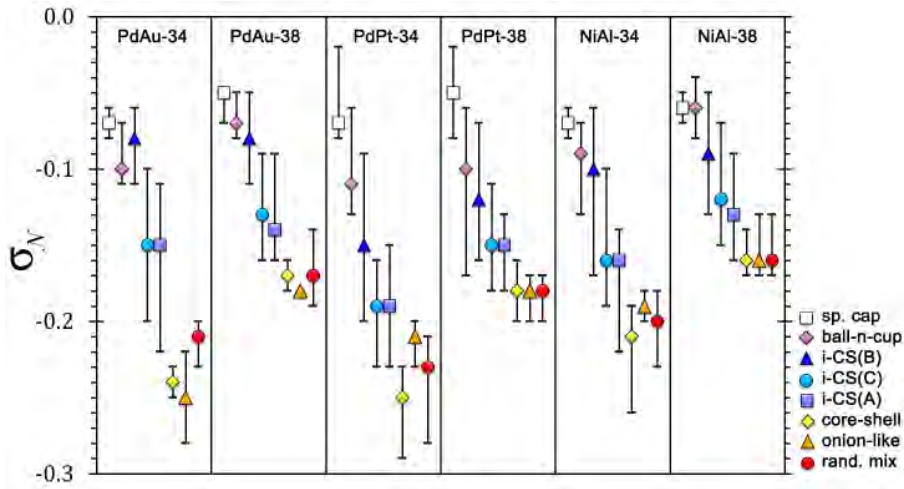


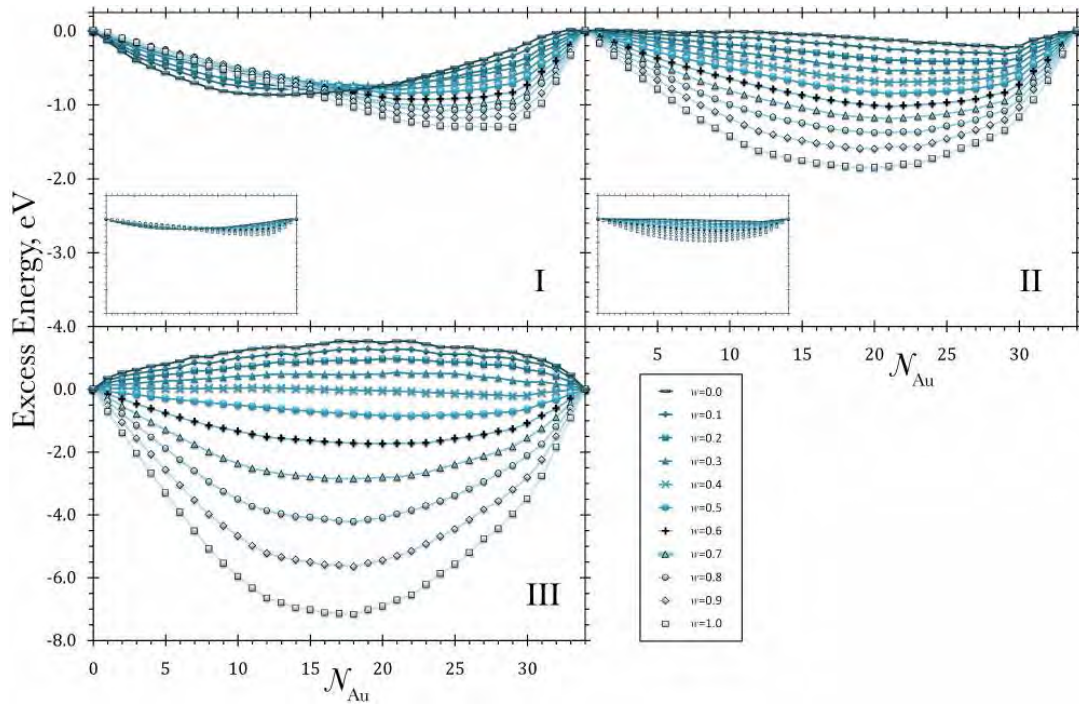
Figure 4.11: Combined compositional mixing degrees, σ_N , of PdAu-34, PdAu-38, PdPt-34, PdPt-38, NiAl-34 and NiAl-38 clusters.

4.6 Energetic Profiles

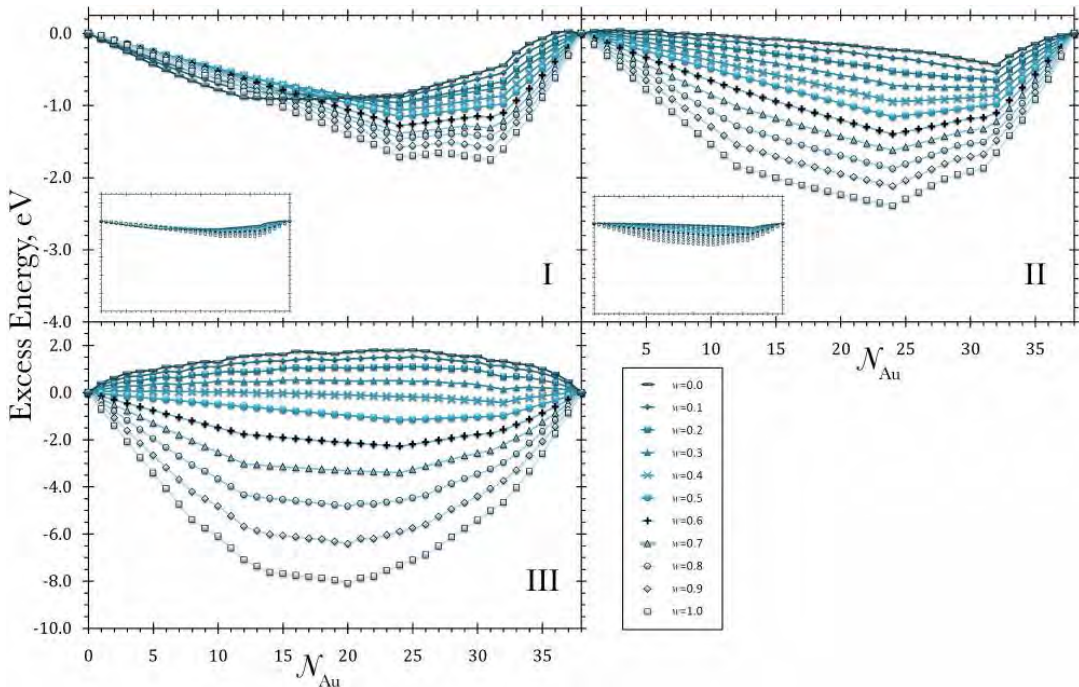
4.6.1 Pd-Au

The patterns of excess energies for Pd-Au are shown in Figure 4.12, where for the parameter sets **I** and **II**, small gaps between weightings are evident, especially when they are plotted on the same scale as the parameter set **III** (inset figures). The energy crossover of the parameter set **I** for both sizes can be attributed to these small gaps but arises from a slight variation in chemical ordering rather than structural motifs (as GM are mostly Dh and TO, for 34- and 38-atom clusters, respectively).

Energy values for the most stable compositions are given in Table 4.3. The energy gap between weightings (*i.e.*, highest minus lowest) in the parameter set **I** (0.439 and 0.847 eV, for 34- and 38-atom, respectively) are lower than those of the parameter set **II** (1.629 and 1.951 eV). On the other hand, the parameter set **III** exhibits a considerably larger range – 8.709 and 9.907 eV. Furthermore, Table 4.3 also shows that there is a variation for the most stable composition, in which for the parameter set **I**, it is shifted down to $N_{\text{Au}} = 13$ (PdAu-34) and $N_{\text{Au}} = 16$ (PdAu-38). Both sizes provide evidence for the slightly Au-rich preference for Pd-Au clusters – $N_{\text{Au}} \sim 21$ (PdAu-34) and N_{Au}



(a)



(b)

Figure 4.12: Excess energy variation of (a) 34- and (b) 38-atom Pd-Au clusters calculated with the parameter sets **I**, **II** and **III**. The inset figures show energetic profiles at the same scale as the parameter set **III**.

Table 4.3: Excess energy series of (a) 34-atom and (b) 38-atom Pd-Au global minima for the parameter sets **I**, **II** and **III**.

Weighting, w, w_s, w_a	Excess energy, eV (composition, N_{Au})		
	I	II	III
(a) 34-atom Pd-Au			
0.0	-0.863 (13)	-0.226 (29)	1.544 (17)
0.1	-0.791 (15)	-0.311 (29)	1.293 (19)
0.2	-0.777 (17)	-0.414 (27)	0.974 (20)
0.3	-0.739 (21)	-0.540 (23)	0.535 (21)
0.4	-0.796 (21)	-0.696 (21)	-0.209 (29)
0.5	-0.848 (21)	-0.848 (21)	-0.848 (21)
0.6	-0.924 (22)	-1.022 (21)	-1.732 (19)
0.7	-1.009 (24)	-1.187 (21)	-2.846 (18)
0.8	-1.075 (24)	-1.379 (20)	-4.217 (18)
0.9	-1.176 (26)	-1.596 (20)	-5.648 (18)
1.0	-1.303 (29)	-1.855 (19)	-7.165 (18)
(b) 38-atom Pd-Au			
0.0	-0.908 (16)	-0.441 (32)	1.807 (25)
0.1	-0.889 (24)	-0.536 (32)	1.526 (25)
0.2	-0.961 (24)	-0.645 (32)	1.102 (25)
0.3	-0.968 (24)	-0.748 (32)	0.542 (16)
0.4	-1.067 (24)	-0.947 (24)	-0.414 (32)
0.5	-1.158 (24)	-1.158 (24)	-1.158 (24)
0.6	-1.278 (24)	-1.397 (24)	-2.273 (24)
0.7	-1.383 (24)	-1.622 (24)	-3.394 (24)
0.8	-1.460 (24)	-1.878 (24)	-4.823 (20)
0.9	-1.591 (31)	-2.120 (24)	-6.415 (20)
1.0	-1.755 (31)	-2.392 (24)	-8.101 (20)

~ 25 (PdAu-38).

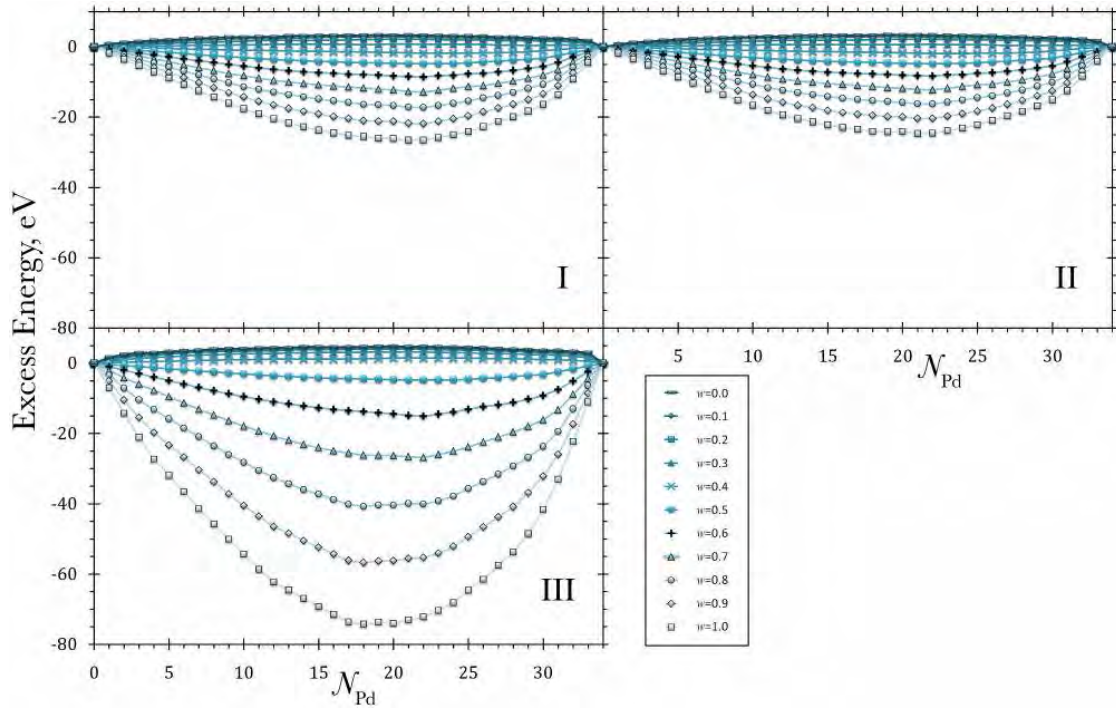
4.6.2 Pd-Pt

Parameterisation of the Gupta potential for Pd-Pt does not lead to crossover of the energy profiles for either 34- or 38-atom clusters. For all compositions, energy is decreased moving from low to high weightings, as shown in Figure 4.13. The parameter set **II** produces equivalent energy profiles to that of the parameter set **I**, consistent with the closely-matched structural motifs and ordering profiles.

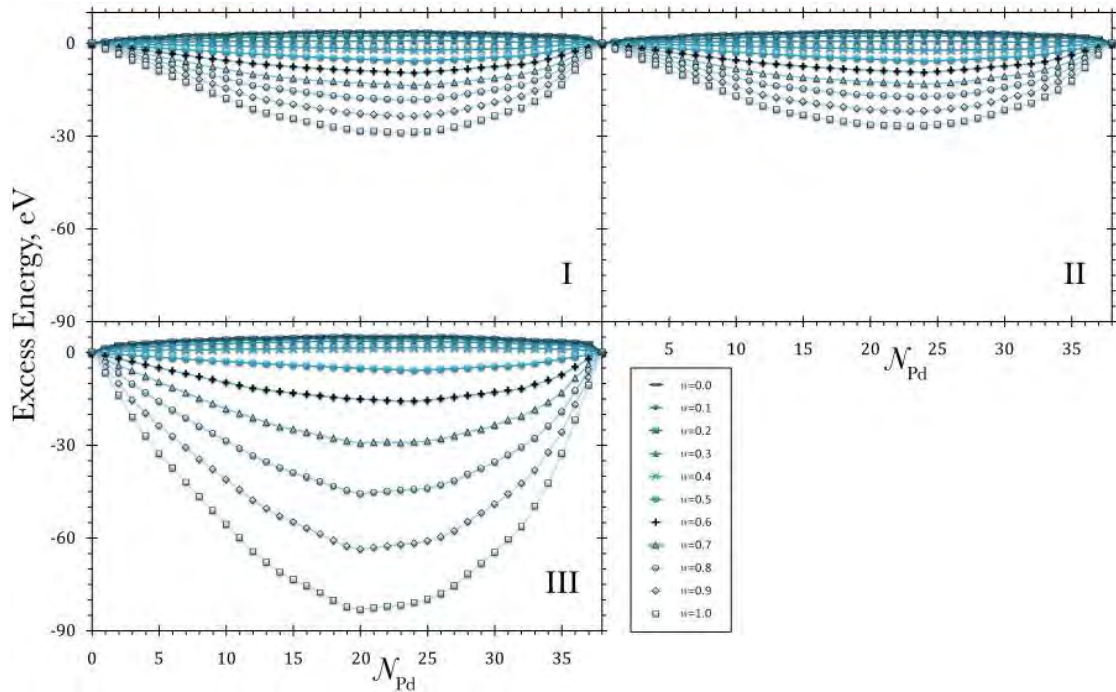
It is noticed from the low weighting ($w, w_s = 0.0-0.3$) parameters that clusters have positive value of the excess energy for all compositions, consistent with the observation of a heavily segregated ordering. These are energetically unfavourable because the interaction between phases is reduced and the bimetallic bonding is minimised.

Excess energy ranges for the parameter sets **I** and **II** are ~ 30 eV, whilst the parameter set **III** resulted in 79 and 88 eV minima gaps for 34- and 38-atom clusters, respectively, as shown in Table 4.4. A broad range of excess energies for the parameter set **III** is expected based on significant differences in the A and ξ values between Pd and Pt, which also accords with earlier observations on the chemical ordering, in which clusters are evolved towards highly ordered mixing for $w_a \rightarrow 1.0$. While energy curves of the parameter set **III** are deepened, the overall pattern is similar to those of the other sets.

The most stable composition is observed at a slightly biased Pd-rich composition, $N_{\text{Pd}} = 21 \pm 3$ (size 34) and $N_{\text{Pd}} = 23 \pm 4$ (size 38). For 38-atom clusters, the lowest energy is frequently found at Pd₂₄Pt₁₄ composition, where TO motif with Pt atoms occupying 14 sites with the highest coordination – six in the interior and eight on the surface (each occupying the centre of a (111) facets). This is a high-symmetry (O_h) configuration, for which Pd-Pt interactions are maximised and results in a very low energy, as has previously been reported [205].



(a)



(b)

Figure 4.13: Excess energy variation of (a) 34- and (b) 38-atom Pd-Pt clusters calculated with the parameter sets **I**, **II** and **III**.

Table 4.4: Excess energy series of (a) 34-atom and (b) 38-atom Pd-Pt global minima for the parameter sets **I**, **II** and **III**.

Weighting, w, w_s, w_a	Excess energy, eV (composition, N_{Pd})		
	I	II	III
(a) 34-atom Pd-Pt			
0.0	3.416 (19)	3.495 (19)	4.877 (20)
0.1	2.859 (19)	2.916 (19)	4.555 (19)
0.2	2.161 (19)	2.159 (19)	4.083 (19)
0.3	0.816 (21)	0.716 (21)	3.253 (19)
0.4	-1.833 (24)	-1.926 (24)	1.500 (21)
0.5	-4.793 (21)	-4.783 (21)	-4.783 (21)
0.6	-8.580 (22)	-8.317 (22)	-15.079 (22)
0.7	-12.838 (22)	-12.237 (22)	-26.823 (22)
0.8	-17.262 (22)	-16.260 (22)	-40.764 (18)
0.9	-21.844 (22)	-20.417 (21)	-56.759 (18)
1.0	-26.576 (22)	-24.690 (21)	-74.245 (18)
(b) 38-atom Pd-Pt			
0.0	3.919 (23)	4.008 (23)	5.511 (19)
0.1	3.408 (23)	3.461 (23)	5.248 (19)
0.2	2.563 (24)	2.583 (24)	4.681 (19)
0.3	0.750 (20)	0.694 (20)	3.787 (23)
0.4	-2.137 (24)	-2.248 (24)	1.632 (27)
0.5	-5.761 (24)	-5.750 (24)	-5.750 (24)
0.6	-9.575 (24)	-9.413 (24)	-15.689 (23)
0.7	-13.576 (24)	-13.187 (24)	-29.290 (20)
0.8	-18.287 (23)	-17.261 (23)	-45.676 (20)
0.9	-23.528 (23)	-21.982 (23)	-63.615 (20)
1.0	-28.968 (23)	-26.829 (23)	-83.223 (20)

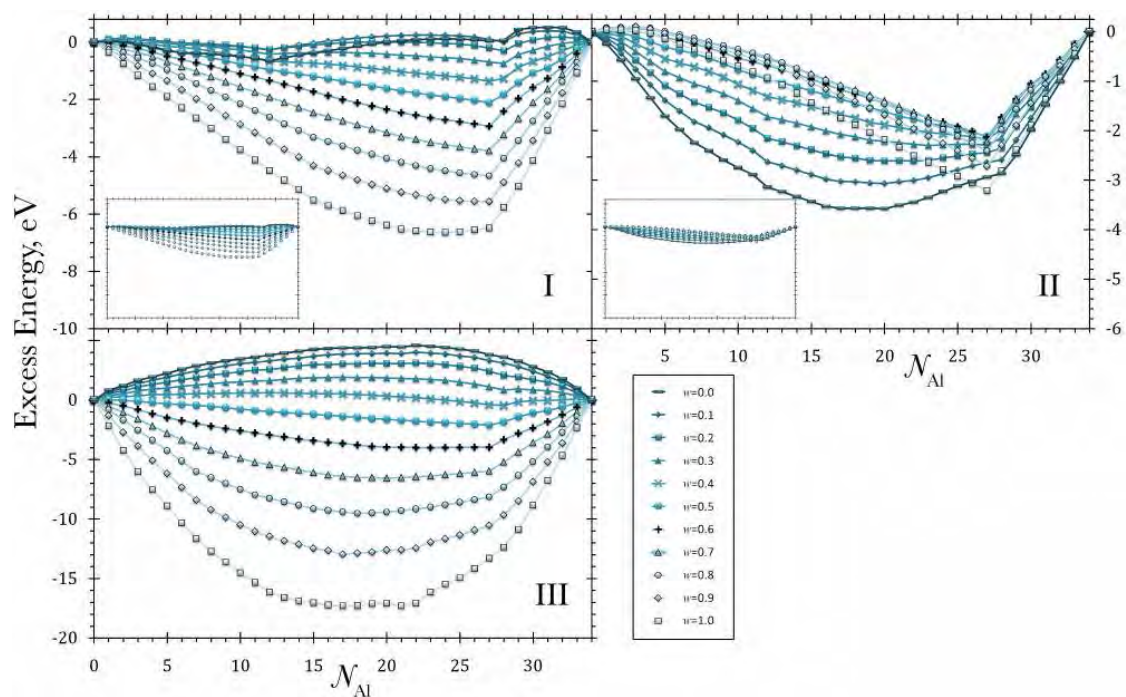
4.6.3 Ni-Al

Energetic profiles of Ni-Al clusters exhibit a clear crossover between weightings, shown in Figure 4.14. This behaviour, however, is more apparent for the parameter set **II**, compared with Pd-Au, which is observed for the parameter set **I**. For high weightings ($w, w_s \rightarrow 1.0$) of the parameter sets **I** and **II**, the minima are located at the Al-rich compositions. However, variation is seen for the lower weightings ($w, w_s \rightarrow 0.0$), in which minima dips are observed from medium to Ni-rich compositions, especially for the parameter set **II**. It is interesting to note that, at $w_s = 0.0$ (parameter set **II**), the most stable composition has a lower energy than those of high weighting parameters. This inversion can be attributed to the large differences of the p and q parameters of the Gupta potential (*see* Table 2.2) between Ni and Al. The excess energies data in Table 4.5 give more explanation of the crossover, for which the energy separation in the parameter set **II** is much closer than those in the parameter set **I**.

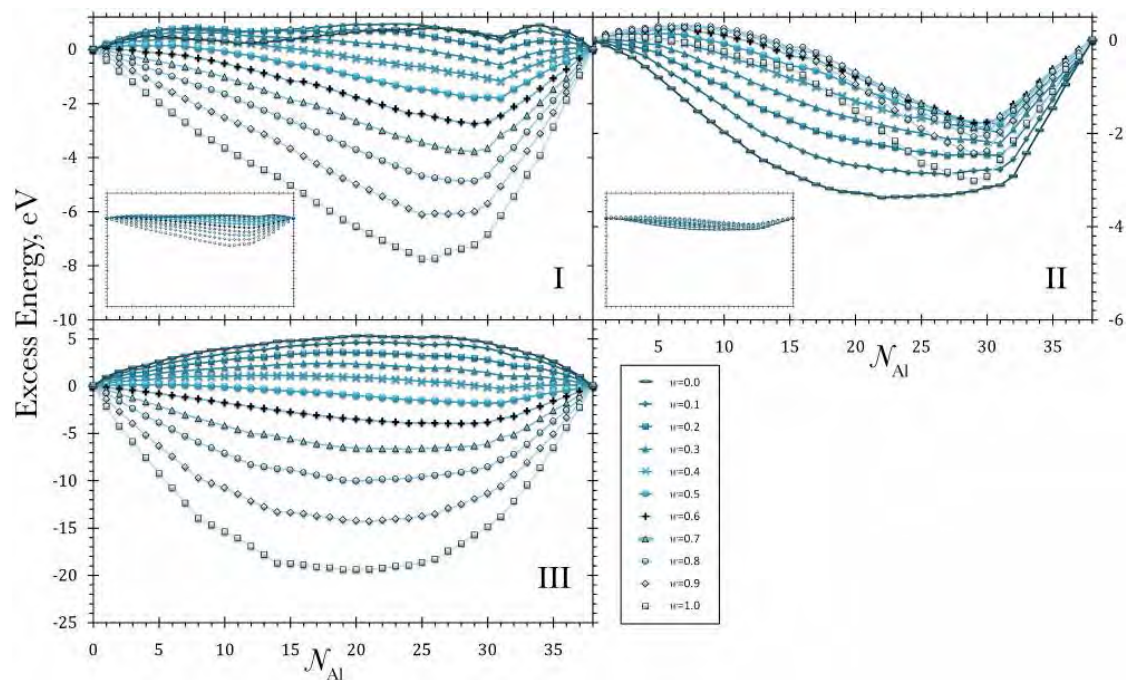
There is a better correlation of the energy-ordering than the energy-motif (it is however necessary to mention that between competitive motifs there is very close difference of the atomic arrangement/packing). For example, the **i-CS(C)** ordering is preferred over **i-CS(B)** for the low weightings of the parameter set **II** (*refer to* Figure 4.10) and this is translated into a lower excess energy due to more heteronuclear bonds.

4.7 Chapter Conclusions

This chapter is not aimed at determining the best parameters for the Gupta potentials but, rather, to build a library of structural motifs, including information on energetics and orderings. Based on the three studied parameterisations, it is found that variations in bimetallic parameters of the Gupta potential lead to a range of structural motifs. Moreover, some motifs are only found for specific size and system: pIh-db (34-atom), Dh-cp(T) (PdPt-34), Dh-cp(DT) (34-atom), pIh⁸ (NiAl-38), Oh-Ih (38-atom)



(a)



(b)

Figure 4.14: Excess energy variation of (a) 34- and (b) 38-atom Ni-Al clusters calculated with the parameter sets **I**, **II** and **III**. The inset figures show energetic profiles at the same scale as the parameter set **III**.

Table 4.5: Excess energy series of (a) 34-atom and (b) 38-atom Ni-Al global minima for the parameter sets **I**, **II** and **III**.

Weighting, w, w_s, w_a	Excess energy, eV (composition, N_{Al})		
	I	II	III
(a) 34-atom Ni-Al			
0.0	-0.650 (12)	-3.577 (20)	4.586 (22)
0.1	-0.270 (12)	-3.069 (20)	4.022 (22)
0.2	-0.304 (28)	-2.616 (22)	3.111 (22)
0.3	-0.752 (28)	-2.299 (23)	1.919 (17)
0.4	-1.357 (27)	-2.174 (27)	-0.450 (28)
0.5	-2.113 (27)	-2.113 (27)	-2.113 (27)
0.6	-2.937 (27)	-2.130 (27)	-4.012 (23)
0.7	-3.795 (27)	-2.228 (27)	-6.569 (20)
0.8	-4.670 (27)	-2.413 (27)	-9.528 (18)
0.9	-5.566 (27)	-2.722 (27)	-12.974 (17)
1.0	-6.646 (24)	-3.213 (27)	-17.305 (17)
(b) 38-atom Ni-Al			
0.0	0.907 (34)	-3.373 (22)	5.296 (20)
0.1	0.947 (23)	-2.874 (27)	4.618 (22)
0.2	-0.058 (31)	-2.472 (27)	3.590 (19)
0.3	-0.583 (31)	-2.214 (31)	2.402 (18)
0.4	-1.171 (31)	-1.985 (31)	-0.279 (31)
0.5	-1.799 (31)	-1.799 (31)	-1.799 (31)
0.6	-2.748 (29)	-1.772 (29)	-3.952 (28)
0.7	-3.780 (29)	-1.866 (29)	-6.650 (24)
0.8	-4.860 (28)	-2.068 (29)	-10.014 (20)
0.9	-6.109 (25)	-2.425 (29)	-14.308 (21)
1.0	-7.748 (25)	-3.015 (29)	-19.410 (20)

and pIh-M-pc⁵ (38-atom). Due to considerable differences in atomic size and electronic structure, the structural maps of Ni-Al clusters distinct from those of Pd-Au and Pd-Pt, with a rise of the pIh(T) and pIh⁷ motifs, which are only observed for Ni-Al.

Selection of two sizes (34 and 38 atoms) allows the investigation on size effects. Although they differ only by four atoms, distinct results are observed, in which a larger variation of the GM structures for 34-atom clusters is found (Dh and several pIh are competitive). Meanwhile, 38-atoms is the magic size of the TO cluster and shows a dominance over a wide composition range for Pd-Au and Pd-Pt. The 38-atom Ni-Al clusters, however, do not show a similar structural preference but have a complex interchange of (mainly) several pIh variants. Compared to Pd-Au and Pd-Pt, the size difference in Ni-Al is very notable; hence, the core-shell pIh stabilisation (smaller Ni core and large Al shell) wins over the magic character.

The mixing in clusters is affected by interplay between several factors (size, cohesive energy, E_{coh} , surface energy, E_{surf} , electronegativity, among others). For Pd-Au, a preference of the core-shell ordering is observed, even for very biased (high and low) weighting of the parameter sets **I–III**. This is possibly due to a very low surface energy of Au ($E_{surf, Au} < E_{surf, Pd}$) and clusters are stabilised when Au atoms are segregated on the surface. Meanwhile, Pd-Pt exhibits more mixing that can be associated to their relative bonding – Pd-Pd bonds are significantly weaker ($E_{coh, Pt} < E_{coh, Pd}$), thus being avoided. Similar to Pd-Au, Ni-Al clusters also show a preference for core-shell ordering but this is mainly due to the size effects.

It is interesting that, in varying the composition of the fixed (34 and 38 atoms) clusters, some motifs arise at a limited range (*i.e.*, composition specific). These composition effects are seen for both sizes of all studied systems. Of the 34-atom clusters, Dh-cp(DT) and Dh-cp(T) are found at around composition (24,10) for Pd-Pt, where 10 Pt atoms occupy the core sites. Similarly, the most stable pIh-db motif is identified for composition (2,34) for all three systems, where the smaller atoms (Pd for Pd-Au

and Ni for Ni-Al) are located in the icosahedral core. This composition-dependent core-shell stabilisation is also notable for 38-atom clusters, for which pIh-M-pc⁵ and pIh⁶ are mainly found around composition (32,6). Furthermore, incomplete pIh⁶ is observed as a GM specifically for composition (30,4) of 34-atom clusters. Clusters of a biased-composition tend to be influenced by a major component preference, as seen by the adoption of Dh-Ih (Pd₃₄, Pt₃₄, Au₃₄), pIh(T) (Ni₃₄) and pIh-M(DT) (Al₃₄) for Pd-rich, Pt-rich, Au-rich, Ni-rich and Al-rich clusters.

While the core-shell ordering is observed for the **average** parameters ($w = 0.5$) for all studied systems, segregated and mixed (onion-like, ordered and disordered) clusters are found at low and high weightings for the parameterised potential, respectively. Consistently, a higher excess energy is shown for the low weightings (segregated phases) and decreased moving to the high weightings (*i.e.*, towards the mixed phase). The ball-and-cup ordering, which is intermediate between the segregated and mixed, is also found between the **average** and low weightings. Variation in the chemical ordering is correlated with the new compositional mixing degree, σ_N , analysis. Moreover, it is able to show a small variation in the incomplete core-shell (surface mixed *vs.* surface segregated) ordering, independent of the composition of the clusters.

Chapter 5

34- and 38-atom Pd-Au Clusters by a Combined Empirical Potential – Density Functional Theory Method

This chapter will discuss the investigation of Pd-Au clusters at the EP and DFT levels. Firstly, structures of the cluster as a function of composition for 34- (Subsection 5.3.1) and 38-atom (5.3.2) clusters at the EP level will be discussed, aided by the bonding analyses (5.3.3). An improved method for global searches at the EP level will then be presented in Subsection 5.3.5. Secondly, calculations at the DFT level will be described, with focus on the structural (5.3.6) and the chemical ordering effects (5.3.7).

5.1 Introduction

Bimetallic Pd-Au nanoalloys are of great interest to theoretical and experimental researchers because of their interesting properties that are not found for the respective pure metals, for example, distinct electronic structures due to differences in the atomic electron configuration and electronegativity [116]. In catalysis, Pd-Au is a green alternative to the toxic chromates [724] or permanganates [725] for primary alcohol oxidations [726]. Recent studies also suggest that a Pd-Au nanoalloy is the solution for the deactivation problem in the Pd-catalysed formic acid fuel cell [727–730].

Improvements in activity, selectivity and stability over mono-metallic Au and/or Pd nanoparticles have been reported widely, especially for the selective oxidation of

primary alcohols [731], CO [732], formic acid [733, 734] and glycerol [735, 736]. Significant improvements have also been observed in the hydrogenation of acetylene [737], [142], cinnamaldehyde, styrene [738] and 3-hexyn-1-ol [739]. Other reactions benefiting from synergetic bimetallic interaction are selective hydrodechlorination [740], synthesis of hydrogen peroxide at a low-temperature [249, 741], direct synthesis of hydrogen peroxide [741, 742] and synthesis of vinyl acetate [128, 743].

It is possible that the catalysis improvement is due to the summation of individual metal contributions but in the direct synthesis of hydrogen peroxide, mono-metallic gold is completely inactive [744]. Also, in the oxidation of crotyl alcohol, there are insignificant contributions from individual Au and Pd [745], proving that the catalytic enhancement is due to synergistic Pd-Au interactions. The mechanism is still unclear, although several possible explanations are suggested based on chemical, structural, morphological and electronic properties. It is believed that there are changes of occupancy for the valence orbitals [746–748], leading to the modification of geometry [155], adsorption sites [743], lattice [749] and adsorbate-metal interaction [143]. Moreover, enhancement of stability is proposed due to the ability of Au to prevent Pd aggregation [736, 750] and kinetic studies show how these particles change the reaction order [751] by avoiding the precursor dissociation [752, 753], inhibiting by-product formation [128] and assisting the rate-limiting step [754].

Effects of the structure have been extensively studied in connection with the other physical (electronic, optical, among others) properties [755–758]. However, there is a serious challenge in controlling compositional homogeneity and size, therefore more of a focus on model catalysts with a well-defined structure [759]. For clusters, it is very likely to have a co-existence of several structures due to close separation of energies [123, 760]. Furthermore, with bimetallic clusters, the alloying degree also gives a variation to the chemical ordering (mixed/alloys, partial-mixed, core-shell or segregated) and subsequently their properties.

5.2 Computational Details

The work involved two step computational calculations combining EP-DF methods. At the EP level calculations, the BCGA program [188] was used in searching competitive (GM and the other low-lying) structures for 34- and 38-atom Pd-Au clusters. The EP searches were carried out for the selected mid-range ($N_{\text{Au}} = 15 - 30$) compositions for 34-atom and all compositions for 38-atom clusters (but only $N_{\text{Au}} = 14 - 24$ for studies on the chemical ordering effects in Subsection 5.3.7), for which 500 GA runs were performed. Searches of the distribution of several structural arrangements (including low-lying energy minima) are improved with the addition of another searching strategy - the BHMC [518] calculations, in which 2,500 atomic exchange Monte Carlo steps were performed.

The interatomic interactions for the EP calculations were described by the “**average**” potential, although for chemical ordering study, the “**DFT-fit**” (parameters were fitted to the results of the first-principles DFT calculations [345]) and the “**exp-fit**” (those fitted to the experimental properties of the bulk Pd, Au and Pd-Au alloys [234]) were also used for comparisons.

Due to computational cost, the combined EP-DF approach was chosen as an alternative to a global exploration at the DFT level. The EP method was applied in preparing a database of the structural motifs, which were then used as the initial configurations for the DFT local optimisations.

The NWChem package [621] was employed with the PW91 XC functional [571] for the DFT calculations and 18- and 17-effective valence electrons, for Pd and Au, respectively, were treated in a geometry optimisation using double- ζ (DZ) basis sets followed by triple- ζ -plus-polarisation (TZVP) single point calculations.

For both EP and DFT calculations, energetic profiles were investigated by calculating the excess energy as a function of composition, Δ_N^{Gupta} and Δ_N^{DFT} . Moreover, the composition and ordering effects on the structure of clusters were described by several

analyses: bond length, ANND and compositional mixing degree, σ_N .

Details of BCGA, BHMC, DFT and energetic analyses are elaborated in Chapter 2.

5.3 Results and Discussion

5.3.1 Structural Motifs of 34-atom Clusters

The EP calculations using the **average**, **exp-fit** and **DFT-fit** potentials show that incomplete Dh structures dominate as the GM for 34-atom Pd-Au clusters, which corroborate those results obtained previously [345]. In addition to the Dh motif, pIh [43] and close-packed are also found as stable structures. The classification of ten GM motifs are shown in Figure 5.1: decahedral (“Dh1”, “Dh2”), mixed decahedral - icosahedral (“Dh-Ih”), mixed face-centred cubic-hexagonal close-packed (“fcc-hcp1”, “fcc-hcp2”), incomplete Mackay-icosahedron with a double tetrahedral component (“pIh-M(DT)1”, “pIh-M(DT)2”), polyicosahedra with a double Ih₁₃ core (“pIh-db”) and two distorted pIh (“dist1”, “dist2”). (*A more detailed description of the names is given in Chapter 4.*) The two variants of Dh, fcc-hcp and pIh-M(DT) are the two most abundant variants, while distorted pIh is varied from one another and the two selected are based on their energetic stabilities.

“Decahedra” generally refers to the packing type, not the geometry, so many variations are possible. In the selected region ($N_{\text{Au}} = 15 - 30$) of 34-atom clusters, however, Dh1 and Dh2 make up $\geq 50\%$ from a total of 500 structures of the EP search for each composition. They differ in the arrangement of the 19-atom cluster core and also the subsequent layers for which Dh2 (diameter 9.4 Å) is more compact than Dh1 (10.4 Å). Meanwhile, Dh-Ih is a mixed motif (with a minor icosahedral character) and is the GM for both pure Pd₃₄ and Au₃₄. Between the two variants, fcc-hcp1 has more hcp character than fcc-hcp2, while pIh-M(DT)2 is more expanded than pIh-M(DT)1. For a monometallic cluster, pIh-M(DT)1 has a significantly higher symmetry (C_s compared with C_1) variant.

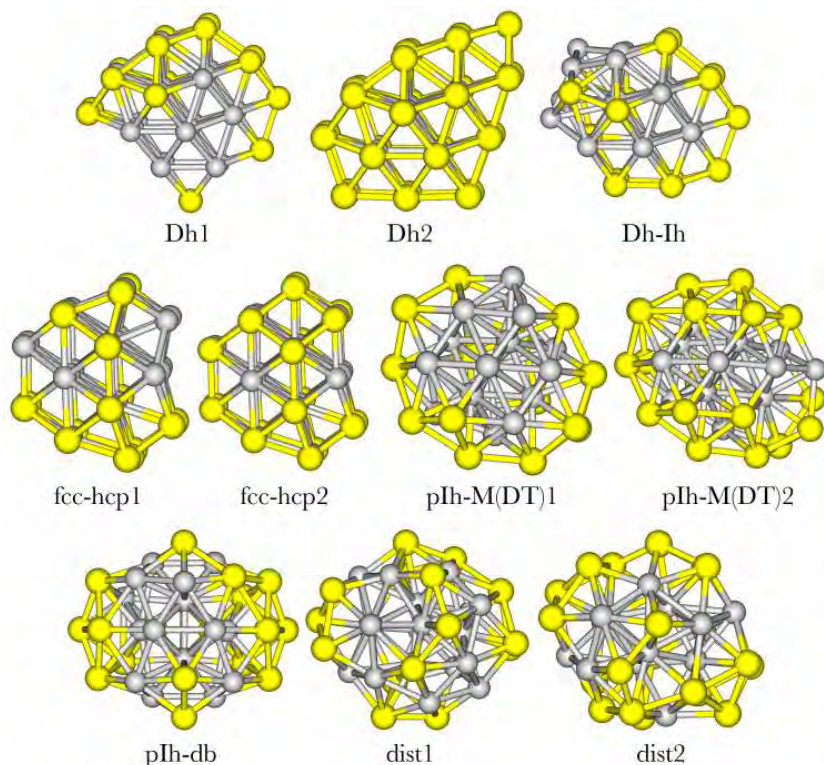


Figure 5.1: Structural motifs of global minima found for PdAu-34 clusters. (*Pd and Au atoms are denoted by yellow and grey colours, respectively, here and in subsequent figures.*)

5.3.2 Structural Motifs of 38-atom Clusters

38-atom Pd-Au clusters do not exhibit a rich diversity of structures (compared with 34-atom clusters), as the EP searches very often found a TO motif [255, 345], which is a fragment of fcc packing – as in the bulk phases of pure palladium and gold [59, 62]. In addition to the TO, mixed Oh-Ih [255], pIh-M-pc⁵, Dh, Dh-Ih and D_{6h} symmetry pIh⁶ [43] structures were found, as shown in Figure 5.2.

5.3.3 Bonding Analyses of the Global Minima

Based on the bulk fcc lattice, the nearest-neighbour distances are 2.749 Å and 2.884 Å, while the second-nearest neighbour distances are 3.848 Å and 4.037 Å, for Pd and Au, respectively. These values are a guide and, by examining each of the PDF plots, it was decided to select the values of 3.3 Å (Pd-Pd), 3.5 Å (Au-Au) and 3.4 Å (Pd-Au), as

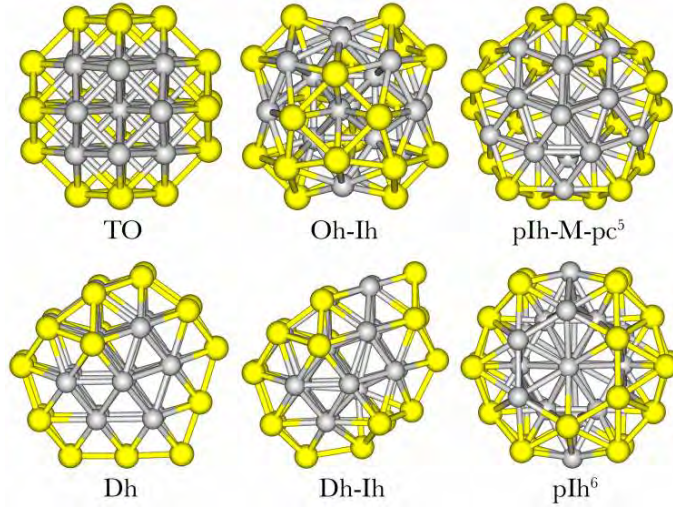


Figure 5.2: Structural motifs of global minima found for PdAu-38 clusters.

the cut-off for defining each respective type of bond. This is consistent with the bulk data ($r_{\text{Pd-Pd}} < r_{\text{Pd-Au}} < r_{\text{Au-Au}}$) and the bulk distances mentioned above. The PDFs of 34-atom clusters are more complex than those of the 38-atoms, due to the greater variation of structural families.

The calculated ANNDs from the GM of the pure Pd clusters are 2.68 Å(34-atoms) and 2.69 Å(38-atoms), while pure Au clusters display larger values – 2.79 Å(34- and 38-atoms). For Pd-Au bimetallic clusters, there is a steady increase in ANND with increasing Au content, as shown in Figure 5.3, due to the larger atomic radius of Au, in accordance with Vegard’s law.

Due to a relatively small difference in the Gupta potential parameters between Pd and Au [377], it is expected that the ANND for bimetallic clusters combining the two would result in a straightforward pattern. This is observed for 38-atom clusters, especially with the **average** potential but there is a slight deviation of the curve for the **DFT-fit** and **exp-fit** potentials, due to a variation in the structural motif [345]. PdAu-34 however, shows more fluctuations, for which the heterogeneous pIh structures are observed, compared with the continual TO structures for PdAu-38. The ANNDs for the **DFT-fit** and **exp-fit** potentials exhibit a high degree of Pd-Au mixing, compared

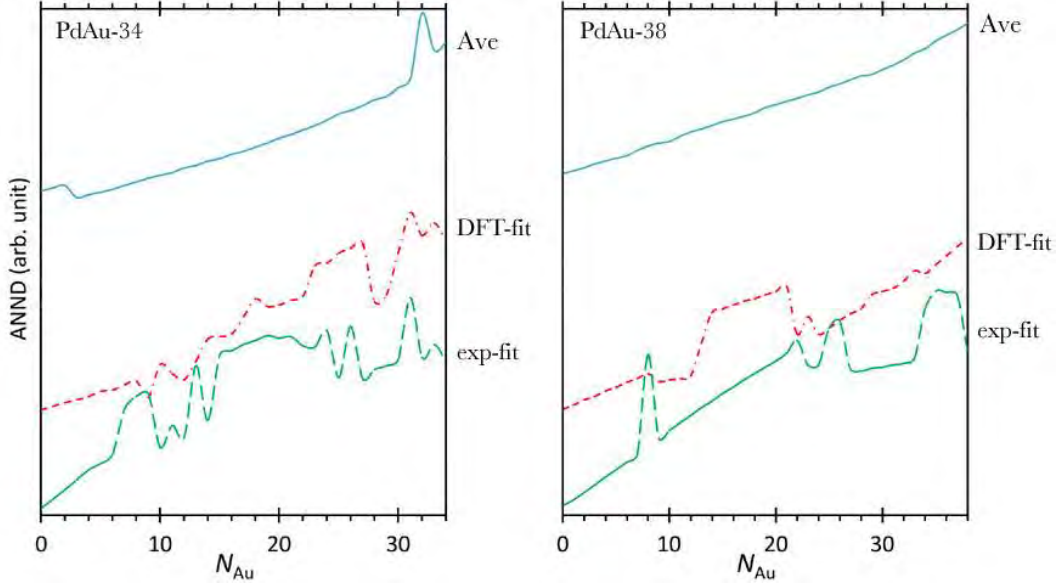


Figure 5.3: ANND variation of 34- and 38- atom PdAu global minima for the parameter set **III** ($w_a = 0.5, 0.7-0.9$), **DFT-fit** and **exp-fit** potentials.

with the **average** potential.

5.3.4 Statistics of the BCGA Searches

34-atom (or 38-atom) clusters are a computationally reasonable size for the BCGA searches, for which high percentages (more than a-third) of the total runs comprise the GM structure (compared with, for example, only $\approx 1\%$ in the study of 98-atom clusters). For 34-atom Pd-Au, the frequency of finding a motif in 500 GA runs (with the **average** potential) is illustrated in Table 5.1, showing only the dominant motifs. A larger number only shows that the motif (and the homotops) is easily found but does not necessarily mean it is the most stable (lowest in energy) structure.

Table 5.1: Frequencies of motifs found in the GA searches.

Motif/ N_{Au}	15	16	17	18	19	20	21	22	23	24	25	26	27	28	29
Dh1	57	56	55	60	55	52	50	46	42	38	33	23	18	7	0
Dh2	6	6	7	6	8	10	10	13	20	18	20	27	53	91	99
fcc-hcp1	0	0	0	1	2	3	6	11	18	29	32	30	17	0	0

The Dh1 variant is found as the GM for all compositions, with the only exception for composition (5,29), of which Dh2 prevails (*all motifs are shown in* Figure 5.1). The data show a strong correlation between the most stable motif and the frequency, in which at least 42% of the GA runs find Dh1 for $N_{\text{Au}} = 15\text{-}23$. There is a strong distribution between Dh1 (18-38%) / Dh2 (18-53%) / fcc-hcp1 (17-32%) for the $N_{\text{Au}} = 24\text{-}27$ region, while Dh2 strongly dominates for $N_{\text{Au}} = 28\text{-}29$.

For composition (5,29), the complete core-shell configuration is attained for Dh2 and might be the reason for this motif's prevalence over Dh1 (no Dh1 is found for this composition). The composition (6,28) also shows the same behaviour, in which one Pd atom is located at the highest coordinate site of the surface. Dh1 however, is eventually found as the GM for this composition (but with only 7% frequency). These statistics may not seem very significant but the DFT results (*discussed later in this chapter*) give some evidence for their correlation.

5.3.5 BCGA-BHMC Searches

Exhaustive examination of 500 GA runs give several structural motifs as shown in Figure 5.4(a), with a clear prevalence of Dh1. A total of 10 motifs (including low-lying isomers) are found but not for all compositions. For example, pIh-db is found at one composition only and pIh-M(DT)2 is found for a few compositions. This presents an incomplete series of the motif as a function of composition. To resolve this, a combined BCGA-BHMC (500 MC steps) is performed to give curves as shown in Figure 5.4(b), in which the missing motif is now connected. However the curves are rough and, by performing more runs (2,500 MC steps), smoother curves are obtained (Figure 5.4(c)). The deeper exploration of the PES is observed with a lower choice of k_bT , as shown in Figure 5.4(d) (*only an example of the Dh1 calculation is shown*).

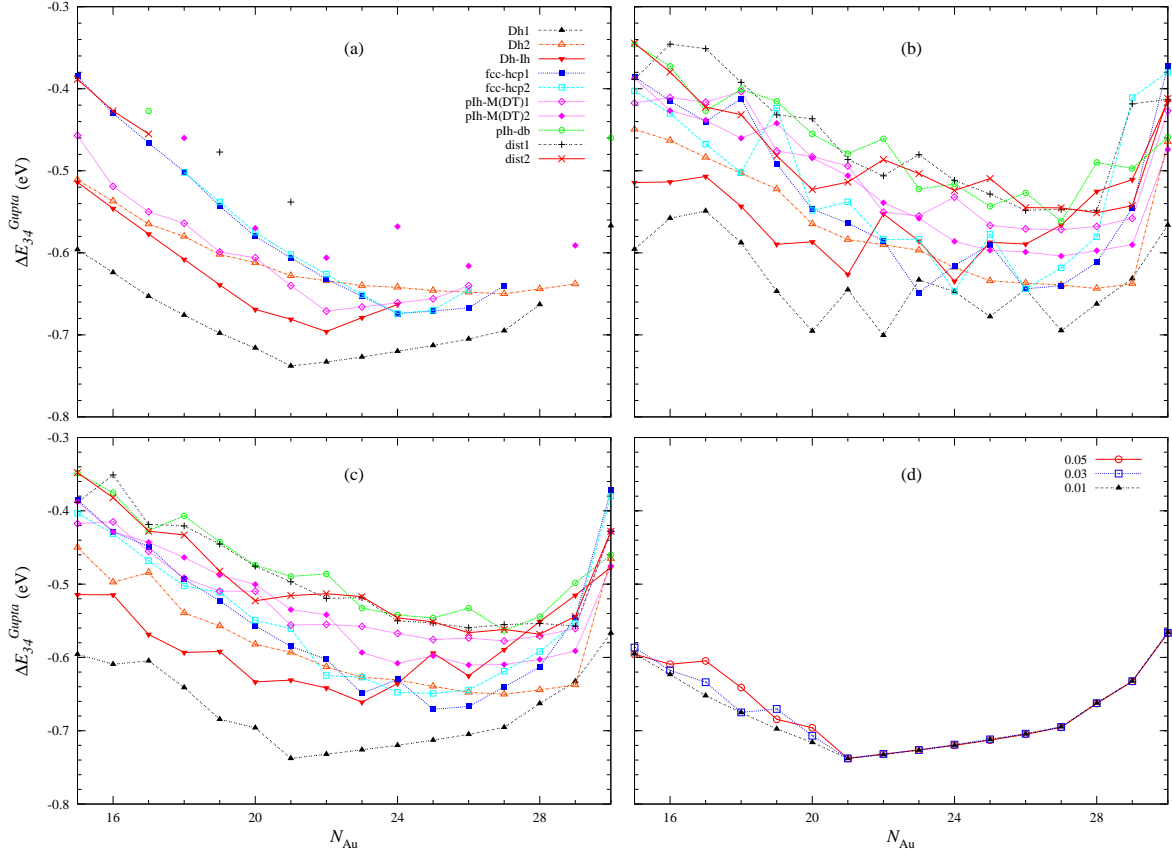


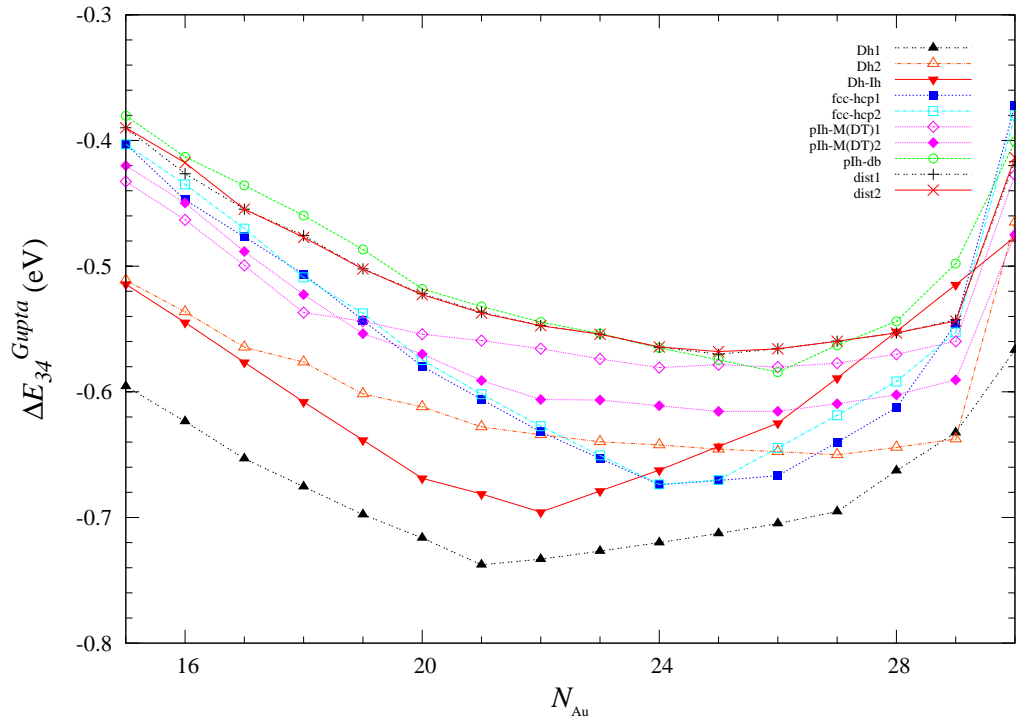
Figure 5.4: Progression of BCGA-BHMC approach: (a) motifs from 500 GA runs, (b) BCGA followed by 500 MC steps, (c) BCGA followed by 2,500 MC steps and (d) effects of different $k_b T$.

5.3.6 Structural Effects at the EP and DFT Levels

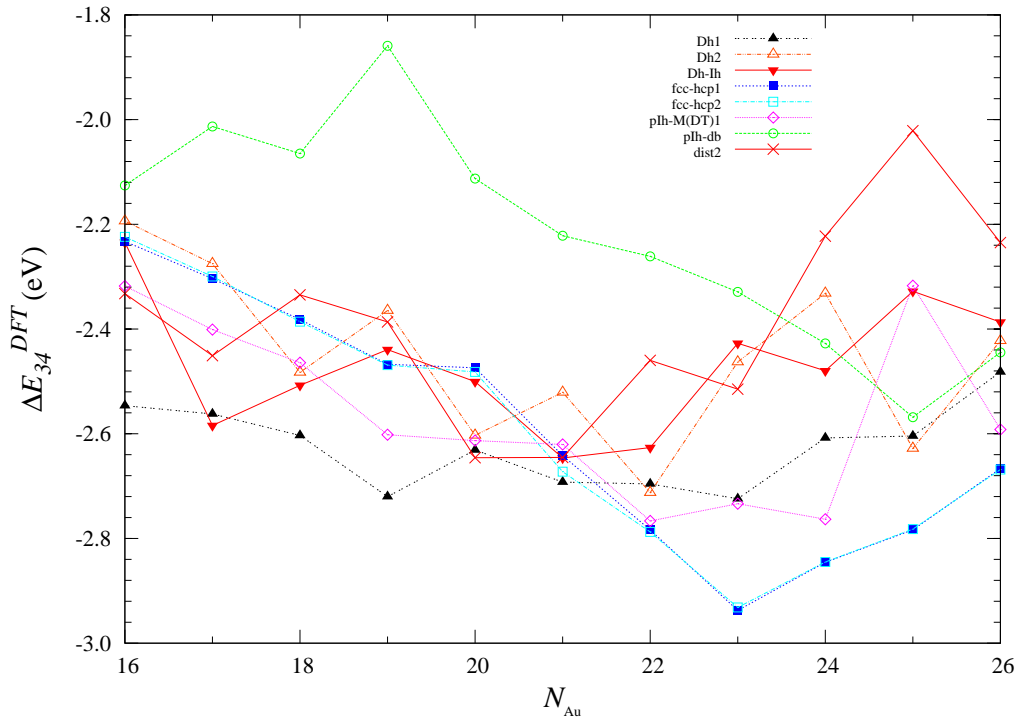
34-atom Clusters

The energetic profiles for the 10 defined motifs at the EP level are shown in Figure 5.5(a) and a subsequent re-optimisation at the DFT level gives the results in Figure 5.5(b). At the EP level (Figure 5.5(a)), there is a clear gap between Dh (the GM structure) and the other motifs. Even so, the separations between all 10 studied motifs are only ~ 0.2 eV, indicating that these motifs are energetically competitive.

At the DFT level (Figure 5.5(b)), a particularly disordered pattern of preference is observed. (As a strategy to reduce the computational effort for the calculations at the DFT level, only one variant was considered for the dist and plh-M(DT) motif – the



(a)



(b)

Figure 5.5: Excess energies of 34-atom clusters at the (a) EP and (b) DFT levels.

most energetic motifs.) Dh1 is singled-out for $N_{\text{Au}} = 16-21$ but is destabilised for $N_{\text{Au}} = 22-26$, for which fcc-hcp structures prevail. The difference between Dh1 and Dh2 are reflected in the energetic profiles for both EP and DFT levels. On the contrary, fcc-hcp1 and fcc-hcp2 are very close in structure (only a minor difference in the hcp *vs.* fcc character; hence, the arrangement of atoms is very close) as are the stabilities for both levels of theory.

In addition to the above mentioned motifs, calculations were also performed for a bcc cluster for the composition (17,17) that is produced when the heteronuclear interaction is extremely parameterised (*see* Chapter 4). It is, however, destabilised by > 1 eV compared with the Dh1 motif.

Overall, there is reasonably good consistency between the EP and DFT predictions for $N_{\text{Au}} = 16-21$. However, for the slightly biased Au-rich ($N_{\text{Au}} = 22-27$) clusters, close-packed fcc-hcp structures are more favourable but are not predicted by the EP calculations. However, this motif is statistically more favourable than Dh (*as shown in* Table 5.1).

38-atom Clusters

The stability of the motifs for 38-atom clusters at the EP level is shown in Figure 5.6(a). There is a clear preference for TO over the whole composition range and significant destabilisation of pIh⁶. Four other motifs compete with TO but, depending on the compositions, the order of preferences varies.

Complex competition is observed for the Au-rich region, in which there are very close energy gaps between Dh, Oh-Ih and Dh-Ih, whilst pIh-M-pc⁵ is slightly destabilised with increasing Au content. In the Pd-rich region, the order is: Dh \approx pIh-M-pc⁵ $<$ Oh-Ih \approx Dh-Ih, while the medium compositions display a greater gap of stability: pIh-M-pc⁵ $<$ Dh $<$ Oh-Ih $<$ Dh-Ih.

For composition (6,32), only 0.002 eV separates pIh-M-pc⁵ from TO, enhanced by the high symmetry (C_{5v}), complete core-shell comprising six-core Pd atoms of

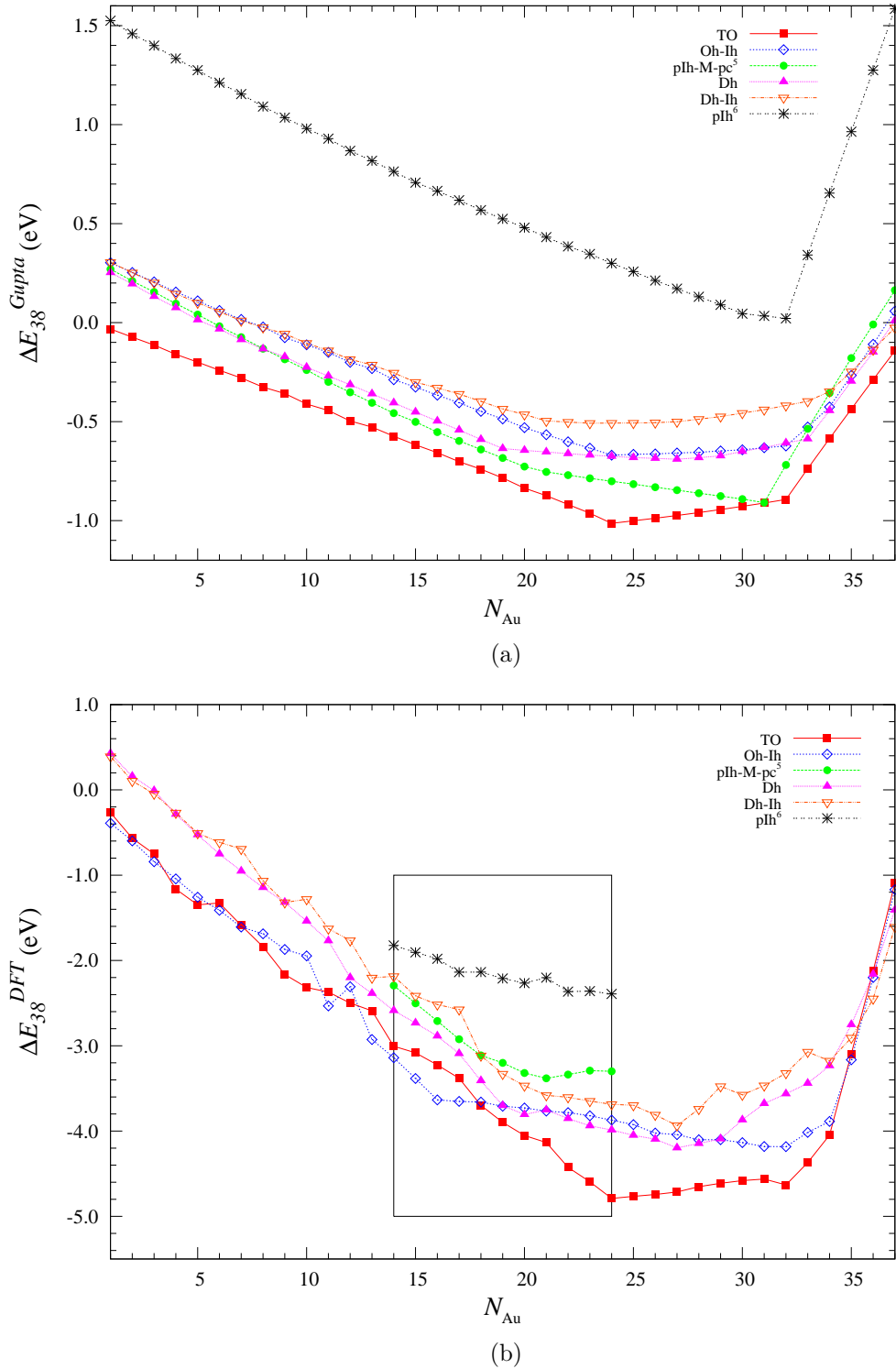


Figure 5.6: Excess energies of 38-atom clusters at the (a) EP and (b) DFT levels. (*box in the bottom figure*) In the initial DFT calculations, plh-M-pc^5 and plh^6 were also considered.

pIh-M-pc⁵. This can be considered to be the magic composition for the motif and also appears to be the magic composition for O_h (TO) and D_{6h} symmetry (pIh⁶), both of which adopt core-shell ordering. Related to this, maximum stabilisation of TO is observed for composition (14,24) (also with O_h symmetry), having Pd atoms at each site of the hexagonal centroid, giving the maximum number of Pd-Au bonds and minimum number of Pd-Pd bonds. All of these high symmetry stabilisations (*i.e.*, geometric shell closings) are shown in Figure 5.7 and can be seen to give rise to a clear dip in the excess energy in Figure 5.6(a). Stabilisation due to geometric shell closings, however, is weaker than the effect of atomic arrangements (*i.e.*, structural motif). Here, clusters are seen to adopt the TO motif (and disfavour pIh⁶) for all compositions.

The previous EP-DF calculations on 38-atom Pd-Au clusters by Paz-Borbón *et al.* [345] only concentrated on composition $N_{\text{Au}} = 19-25$ and observed a preference for TO with close competition from Oh-Ih. The expanded calculations (in this work) over the whole composition range and taking into account six different motifs, are shown in Figure 5.6(b). The initial calculations (*box in the figure*) for composition $N_{\text{Au}} = 14-24$ give consistent findings (DFT *vs.* EP) that pIh⁶ is the least competitive motif. The pIh-M-pc⁵ motif is also disfavoured and these two motifs were omitted from the further DFT study (*reducing computational cost*) for other compositions.

TO clearly dominates for $N_{\text{Au}} \geq 18$ but there is a close competition between TO and

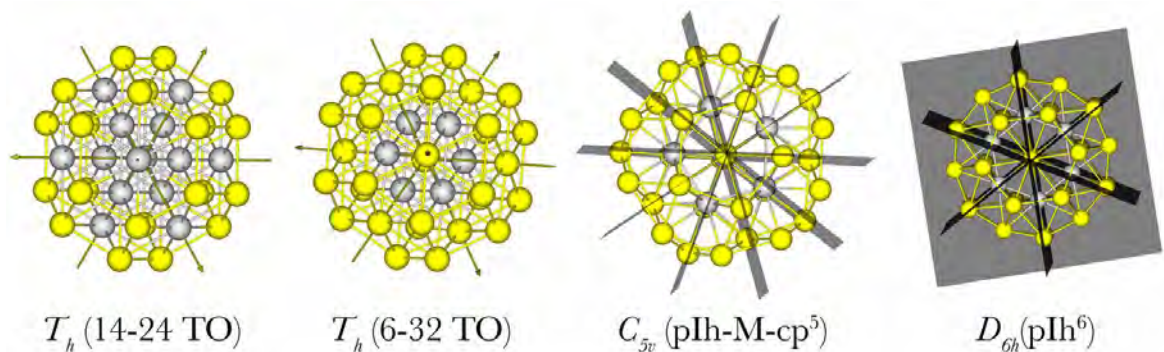


Figure 5.7: Magic compositions of 38-atom Pd-Au clusters.

Oh-Ih motif for the Pd-rich ($N_{\text{Au}} \leq 18$) compositions, with Oh-Ih prevailing in the $N_{\text{Au}} = 13-17$ region. Dh and Dh-Ih are constantly less preferred for the entire composition range, except for the crossover at $N_{\text{Au}} = 36-37$. Both dips at (14,24) and (6,32) of the TO curve are still visible (similar to the EP results), which show qualitative agreement on the shell-closing and magic composition effects.

5.3.7 Chemical Ordering Effects

There are a number of experimental results [123, 171, 761, 762] and theoretical calculations [123, 171, 255, 345, 763] that indicate a prevalence of the $\text{Pd}_{\text{core}}\text{Au}_{\text{shell}}$ ordering and are consistent with the lower heat of formation, compared with the inverse $\text{Au}_{\text{core}}\text{Pd}_{\text{shell}}$ and other configurations [123]. The $\text{Pd}_{\text{core}}\text{Au}_{\text{shell}}$ ordering is also favoured by the lower surface energy of Au ($E_{\text{surf, Au}} = 96.8$ vs. $E_{\text{surf, Pd}} = 131$ meV/Å² [201, 202]) – forming a shell of Au lowers the overall cluster surface energy, the higher cohesive energy of Pd ($E_{\text{coh, Au}} = 3.81$ vs. $E_{\text{coh, Pd}} = 3.89$ eV/atom [203]) – maximising the number of stronger (Pd-Pd) bonds, by locating Pd in the core – and the smaller atomic radius of Pd ($r_{\text{Pd}} = 1.375$ vs. $r_{\text{Au}} = 1.440$ Å [203]) – a Pd-core minimises bulk elastic strain.

The combination of the structural and ordering effects on the cluster make it difficult to distinguish each effect individually. For 34-atom clusters, Dh (and Dh-Ih) structures dominate but a large number of variants means that both effects always co-exist. In contrast, the dominant magic TO for 38-atom clusters is a single variant. The TO prevails for the **average**, **DFT-fit** and **exp-fit** potentials at $N_{\text{Au}} = 14-24$ and this composition region is selected for the study on the chemical ordering effects for a fixed motif (TO) as shown in Figure 5.8.

At the EP level (Figure 5.8(a)), there is a straightforward correlation between the chemical ordering and the cluster energy. A greater mixing for the **DFT-fit** and **exp-fit** potentials (as been discussed in Chapter 3) translates to a lower energy. However, the DFT calculations show several crossovers of the energy curves (Figure 5.8(b)), indicating a complex ordering effect in the clusters. To understand this behaviour,

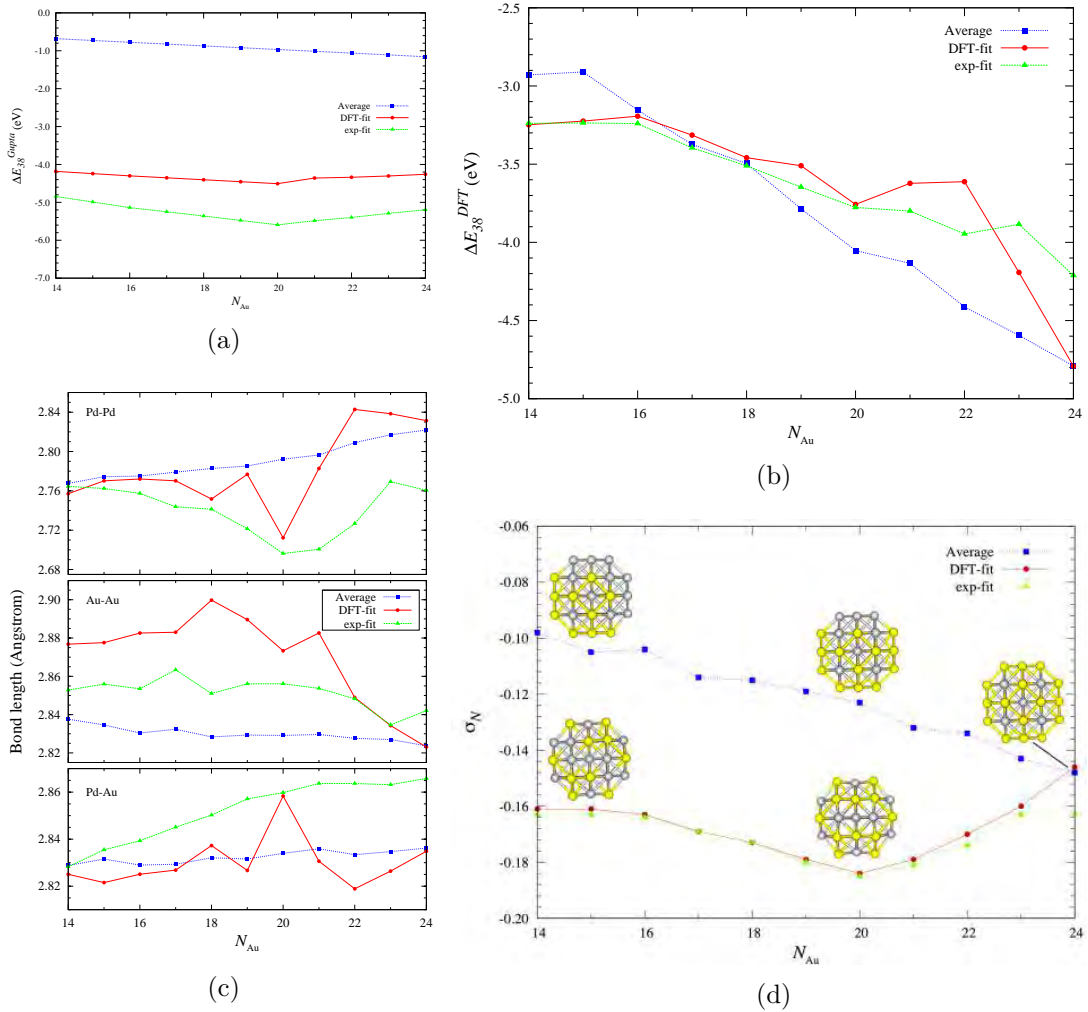


Figure 5.8: Excess energies at (a) the EP and (b) the DFT levels of TO_{38} clusters from the **average**, **DFT-fit** and **exp-fit** potentials. For the DFT calculations, post-analyses of (c) bond length and (d) compositional mixing, σ_N were performed.

analyses of bonding (Figure 5.8(c)) and mixing (Figure 5.8(d)) profiles follows.

All Pd-Pd, Au-Au and Pd-Au bonding of GM for the **average** potential progress smoothly with composition (Figure 5.8(c)), consistent with the smooth progression in the DFT excess energy. Except for Pd-Pd bonds, the **exp-fit** potential also shows a smooth transition in bonding (and also the excess energy). In contrast, there are clear dip and peak at $N_{\text{Au}} = 20$ and 22 observed for the **DFT-fit** potential. Interestingly, the $\text{Pd}_{18}\text{Au}_{20}$ cluster is stabilised (low energy) with the opposite effect to that of $\text{Pd}_{16}\text{Au}_{22}$.

At $N_{\text{Au}} = 20$, a maximum number of heteronuclear Pd-Au bonds is achieved when all (111) centroid sites are occupied by Au atoms and the cluster is slightly distorted. For TO, there are more (111) sites compared with (100) and a high number of heteronuclear interactions reflects the lowest σ_N for this composition, as shown in Figure 5.8(d). Meanwhile, Pd-Pd bonds are only present in the core, resulting in a dip in the Pd-Pd curve. On the other hand, TO clusters of $N_{\text{Au}} = 22$ have a core consisting of two Au atoms, due to the tendency for a mixed ordering for the **DFT-fit** potential. This ordering prevents TO from distorting but core occupation by Au atoms is unfavourable, as shown by the peak of DFT excess energy (Figure 5.8(b)) for the **DFT-fit** potential.

The **average** potential generally leads to the incomplete core-shell configuration, having Au atoms occupying the low-coordinate surface sites (centroids of the (111) hexagonal facets). The **DFT-fit** and **exp-fit** potentials also lead to the incomplete core-shell configurations but display a higher degree of surface mixing (consistent with the other analyses). These differences can be seen in Figure 5.8(d), for which the more mixed clusters (of the **DFT-fit** and **exp-fit** potentials) have the lower σ_N . For $N_{\text{Au}} = 24$, there is the similar preference for the **average** and **DFT-fit** potentials (O_h symmetry) results in overlap of the curves.

5.4 Chapter Conclusions

In the EP searches, Dh, Dh-Ih, fcc-hcp, pIh-M(DT), pIh-db and distorted pIh are found as the minima (global and local) of 34-atom clusters. Less variation of the structure is seen in 38-atom clusters in which the magic cluster of TO dominates. Other motifs identified are the Oh-Ih, pIh-M-pc⁵, Dh, Dh-Ih and pIh⁶.

Between different structural motifs, the energy gaps are very close (at the EP level) and this is manifested in a complex crossover at the DFT level. Some qualitative agreement between the EP and DFT predictions is seen, in which Dh ($N_{\text{Au}} = 16-21$) and TO ($N_{\text{Au}} \leq 18$) prevail as the most stable motifs for 34- and 38-atom clusters, respectively. Moreover, for 38-atom clusters, the pIh⁶ motif is disfavoured for both levels of calculation. There is, however, a disagreement between the EP and DFT results for the Au-rich region of both sizes. For 34-atoms, the DFT calculations show a preference of the fcc-hcp motif (pIh at the EP level), while 38-atom pIh-M-pc⁵, which is competitive at the EP level, is disfavoured.

In terms of chemical ordering, the surface mixing (predicted by the **DFT-fit** and **exp-fit** potentials) is favoured for clusters with a limited Au ($N_{\text{Au}} < 16$), while in the Au-rich region, Au atoms are likely to avoid the higher-coordination surface sites (as adopted for the **average** potential). In the medium region ($N_{\text{Au}} = 16-18$), there are only small energy gaps between the ordering adopted by the **average** and fitted potentials, showing a strong composition effect on the cluster's chemical ordering, as is the case for the structural motif preferences.

Due to the ordering variation predicted by the different potentials at the EP level, their accuracy against the DFT calculations also varies, depending on which composition is being considered. In addition to the composition effects, this study shows that Pd-Au nanoalloy clusters are also influenced by many other factors: size (34, 38), motifs (atomic arrangements), symmetry (shell closing effects) and chemical ordering (core-shell/mixed).

Chapter 6

34- and 38-atom Pd-Pt Clusters by a Combined Empirical Potential – Density Functional Theory Method

This chapter will discuss combined EP-DF calculations on 34-atom (Subsection 6.3.1) and 38-atom (6.3.2) Pd-Pt for all cluster compositions. The focus of the discussion is stabilities and structural of the GM and effects of the chemical ordering (6.3.3).

6.1 Introduction

Most research of Pd-Pt catalysts is centred on two main areas of fuels: diesel and fuel cells. In diesel fuel, the main problem is the undesirable aromatic hydrocarbons [764] which reduce the fuel quality [765]. Furthermore, aromatic hydrocarbons are environmentally undesirable due to their carcinogenic nature [766] and emitted particulate matter [767, 768] in exhaust gases. For all of these reasons, there is an urgency to reduce the amount of aromatic hydrocarbons by using Pt as a hydrogenation catalyst. However, due to economic factors, cheaper alternatives such as Pd are proposed [146].

Diesel fuel is also often contaminated by sulphur, which is known to poison Pt catalysts, even at the low concentrations [767]. Several methods have been suggested, where alloying Pd and Pt reported to increase sulphur tolerance in the catalytic reduction of aromatics in the diesel feed [769]. Moreover, promising results have been published for test reactions of several different aromatics: orthoxylene [770], diben-

zothiophene [771], naphthalene [772, 773], tetralin [146, 774, 775] and toluene [776]. Strong Pd-Pt interaction [773], due to the electronic effects [769, 777, 778], may explain the sulphur-resistance, for which electron-deficient platinum sites are needed [779] or structural transformations [780].

The study of Pd-Pt nanoparticles is also a hot topic in another popular research area, fuel cells. Polymer electrolyte membrane fuel cell (PEMFC) [781, 782], direct methanol fuel cell (DMFC) and direct formic acid fuel cell (DFAFC) [783, 784] are of interest due to their potential in portable devices (cell phones, compact computers, automobiles). There is a possible decrease in activity [785] compared with pure Pt [786], although more resistance to poisonous species such as CO intermediates [787] and nitrogen-based chemicals [788] is reported.

In catalysis, enhancement of the activity is possibly due to a simple additivity of individual components [259, 260, 789]. However, it is agreed that catalyst performance is dependent on many factors, especially the method of preparation and the type of chemical reactions [156]. There is also a possible effect from the support [790–792] but a considerable synergistic effect of alloying is observed in Pd-Pt catalytic reactions of selective hydrogenation (1,3-cyclooctadiene, methyl acrylate [144, 247], styrene [793], toluene [764] and allyl alcohol [794]), direct synthesis of hydrogen peroxide [795], sulfidation [216], hydrodesulfurization of thio compounds [796] and *n*-decane hydroconversion [797]. The most striking evidence comes from the chemical probe experiment, using the CCl_2F_2 compound [798]. The other important catalytic properties, selectivity [799] and stability at high temperatures [800, 801], are also highlighted.

The degree of bimetallic alloying [802] directly affects the geometry/structure [144, 250, 803] and size [804] of Pd-Pt nanoparticles. Bimetallic composition can be a discrete parameter [261] and, depending on the studied reaction, even composition between Pd and Pt [805], Pt-rich [779, 806, 807] or Pd-rich [765, 808, 809] clusters might be needed for optimum impact on catalysis. For certain compositions, further catalytic activation

can arise due to core-shell chemical ordering [810], where $\text{Pt}_{\text{core}}\text{Pd}_{\text{shell}}$ configurations are favourable and, the catalysts have been characterised by Transmission Electron Microscopy (TEM) [249, 811] and other spectroscopic techniques such as Low-Energy Ion Scattering (LEIS) [812], Extended X-ray Absorption Fine Structure (EXAFS) [250], Energy-Dispersive X-ray (EDX) [716], X-ray Absorption (XAS) [617] and X-Ray Photoelectron (XPS) [252, 813] spectroscopies. The preference for a surface Pd atom in the core-shell clusters is confirmed by theoretical studies of the Johnston research group [254, 255, 257, 258, 814] and many others [140, 205] (*also review in* [116]).

Pd-Pt interactions in a cluster are affected by electronic [815, 816], geometric [817], kinetic [818–820], thermodynamic [821], size [822, 823], active sites [796], particle dispersion [801, 824] and lattice reconstruction [722, 821, 825, 826], to name a few. In the theoretical research, however, more focus has been channelled into a study of the active sites, in which the cluster varies in composition and structure. This in turn, gives a promising prospect of structure-activity tuning, towards the development of better materials in many different applications.

6.2 Computational Details

Similarly to Pd-Au (Chapter 5), theoretical investigations for 34- and 38-atom Pd-Pt clusters were carried out by a combined EP-DF method. At the EP level calculations, 500 BCGA runs were performed for all compositions. The potentials based on the Gupta many-body potential: **average** and **DFT-fit** were used to describe the interatomic interactions.

At the DFT level, the GM structures (from the EP searches) were locally optimised with the NWChem package [621] and the PW91 XC functional [571]. Geometry optimisations were performed using the double- ζ (DZ) basis sets followed by the triple- ζ -plus-polarisation (TZVP) single point calculations.

Energetic stabilities were determined by the excess energy as a function of compo-

sition, Δ_N^{Gupta} and Δ_N^{DFT} (see Chapter 2). The effects of composition on the structures and the ordering were described by the compositional mixing degree, σ_N .

6.3 Results and Discussion

6.3.1 34-atom Pd-Pt Clusters

There are nine GM motifs that are found for 34-atom Pd-Pt clusters, as shown in Figure 6.1: decahedral (“Dh”), mixed decahedral - icosahedral (“Dh-Ih”), fcc-based incomplete truncated octahedron (“TO”), mixed decahedral-close-packed motifs with a double tetrahedral core (“Dh-cp(DT)”), mixed decahedral-close-packed motifs with a single tetrahedron core (“Dh-cp(T)”), anti-Mackay-polyicosahedral (“pIh-aM”), incomplete Mackay-icosahedron with a double tetrahedral component (“pIhM(DT)”), incomplete polyicosahedra with 6 interpenetrating Ih₁₃ units (“pIh⁶”) and low-symmetry polyicosahedra (“pIh(LS)”).

A comparison of the structure and energetics between GM from calculations with the **average** and **DFT-fit** potentials is shown in Figure 6.2. Structurally, GM progression along the composition is almost identical, with only minor difference at $N_{\text{Pd}} = 21$, for which an anti-Mackay-polyicosahedral (pIh-aM) is found for the **DFT-fit** potential, compared with an incomplete TO for the **average**. The preference for Dh-cp(DT), as the signature of 34-atom Pd-Pt clusters [254] for the $N_{\text{Pd}} = 19$ -25 region, are repeated for both potentials. On the other hand, there is a clear preference for Dh in the Pt-rich region ($N_{\text{Pd}} \leq 18$), while for the Pd-rich region ($N_{\text{Pd}} \geq 26$), there is a complex progression involving TO, Dh, pIh-M(DT), pIh⁶, Dh-Ih and pIh(LS) structures.

Although there is a variation in the structural motif, the excess energy curve at the EP level (Figure 6.2(a)) is smooth, indicating very close energy gaps. For both potentials, the most stable cluster is observed for the composition (13,21) but with different motifs: TO (**average**) and pIh-aM (**DFT-fit**).

Excess energies at the DFT level are plotted in Figure 6.2(b). There is a quali-

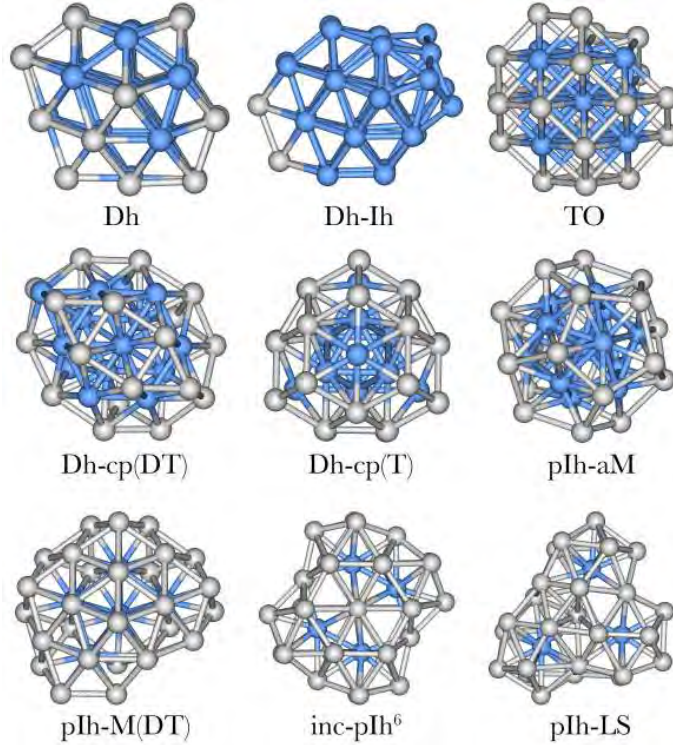


Figure 6.1: Structural motifs found in the EP searches of 34-atom Pd-Pt clusters. (*Pd* and *Pt* atoms are denoted by grey and blue colours, respectively, here and in subsequent figures.)

tative agreement between the EP and DFT results for the preferences of Dh (in the Pt-rich) and Dh-cp(DT) (for $N_{\text{Pd}} = 19-25$). The prevalence of the Dh-cp(DT) motif in the medium to Pd-rich compositions of 34-atom Pd-Pt clusters is consistent with the previous study [254]. For the Pd-rich composition region, many structural motifs are competitive at the EP level but the DFT calculations suggest pIh⁶, pIh-aM and Dh-cp(T) structures are strongly disfavoured over Dh, TO ($N_{\text{Pd}} = 21,26$) and pIh-M(DT) ($N_{\text{Pd}} = 28$).

The energy gap between the **average** and **DFT-fit** potentials is very small (at the EP level) and, upon DFT re-optimisation, it becomes smaller. However, there is a significant gap in the $N_{\text{Pd}} = 9-18$ region. The structures from the **average** potential are energetically more stable than those of the **DFT-fit** for $N_{\text{Pd}} = 9-13, 18$ but a reverse order is observed for $N_{\text{Pd}} = 14-17$. It is very interesting that all GM

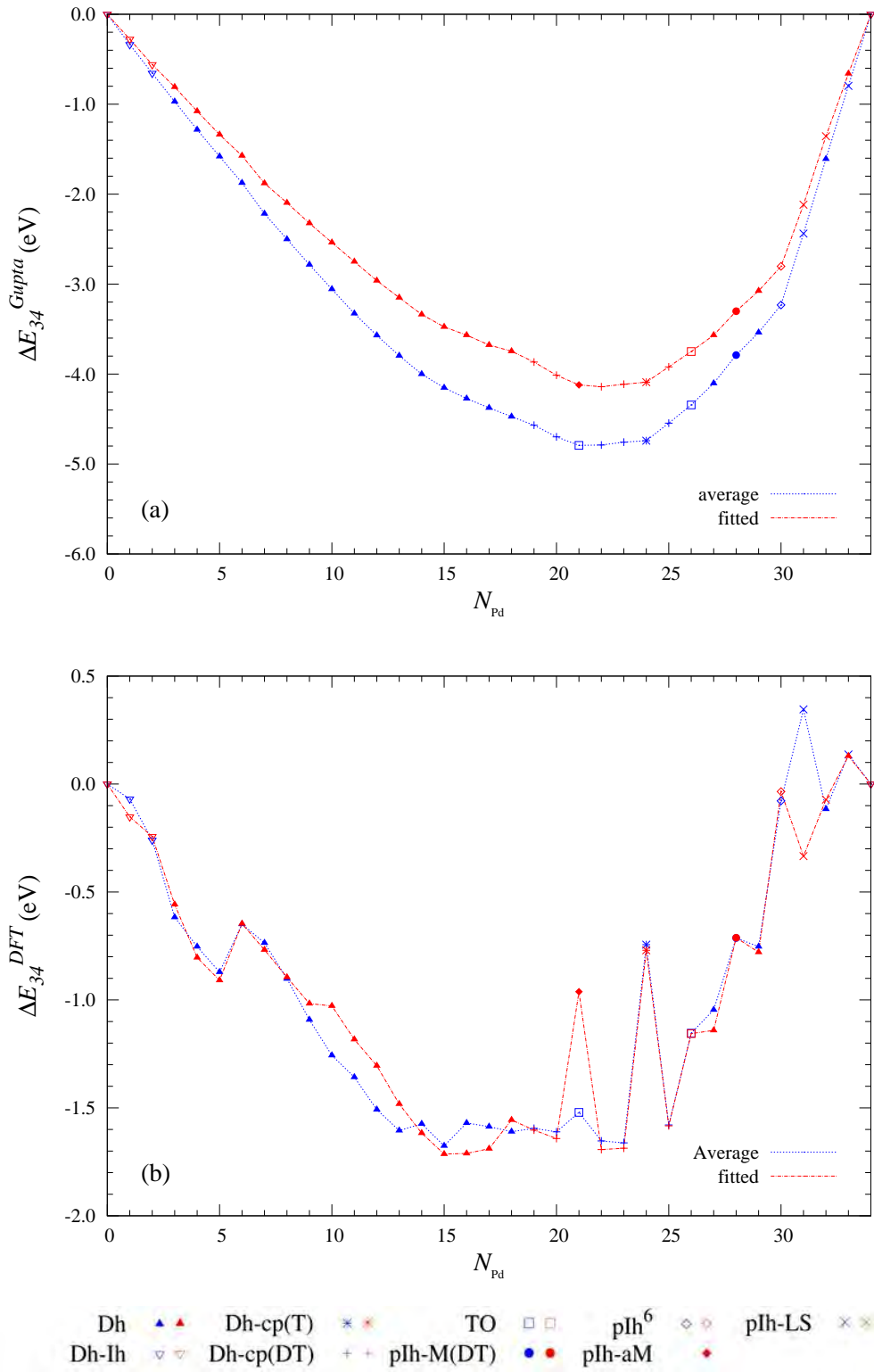


Figure 6.2: Excess energies of 34-atom Pd-Pt clusters from the **average** and **DFT-fit** potentials at the (a) EP and (b) DFT levels.

found for this composition region are of the Dh motif but a detailed examination of the structures (Figure 6.3) explains the occurrence of the crossover. The DFT data show the destabilisation of **Dh2** compared with **Dh1** and **Dh3**. For the $N_{\text{Pd}} = 9-16$ composition range, DFT prefers **Dh1** over **Dh2**, which is predicted partially by the **average** ($N_{\text{Pd}} = 9-13$) and **DFT-fit** ($N_{\text{Pd}} = 14-16$) potentials, resulting in the energy crossover between potentials at $N_{\text{Pd}} = 13-14$. Meanwhile, another crossover at $N_{\text{Pd}} = 17-18$ is caused by the prevalence of the other variant, **Dh3**, which is predicted by the **DFT-fit** (at $N_{\text{Pd}} = 17$) and **average** (at $N_{\text{Pd}} = 18$) potentials, respectively.

Another variant, **Dh4**, is observed for both potentials for $N_{\text{Pd}} = 0-5$. This variant has fewer (100) facets for overgrown layers, as two of the internal atoms are left exposed (*marked with purple colour in Figure 6.3*). An overgrown atom on a (100) site is less coordinated than that on (111) and this seems to be a preferred site for Pd, as all are occupied one-by-one until all five are filled. The subsequent addition of another Pd ($N_{\text{Pd}} = 6$), eventually destabilises this motif at the DFT level – an indication of the Pd preference for the lowest coordinated sites on the surface of Pd-Pt clusters.

6.3.2 38-atom Pd-Pt Clusters

Less variation of the GM structural motif is observed for 38-atom clusters, for which only Dh ($N_{\text{Pd}} = 5-14$), pIh-M-pc⁵ ($N_{\text{Pd}} = 5-30$) and the dominant TO (Pt-rich, medium and Pd-rich compositions) prevail. The comparison of structures and energies of GM for the **average** and **DFT-fit** potentials are shown in Figure 6.4, in which mostly

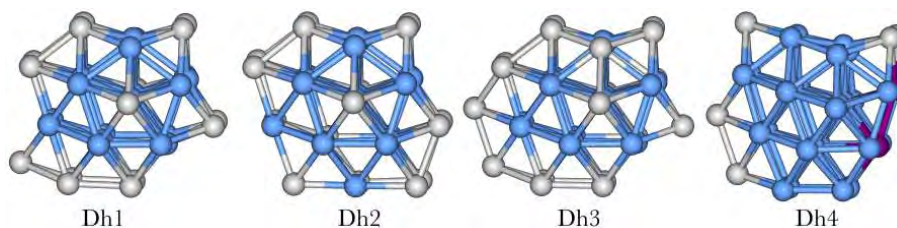


Figure 6.3: Dh variants of global minima observed for PdPt-34 clusters.

the same motifs are adopted, with the exception for $N_{\text{Pd}} = 5-8$; Dh prevails for the **DFT-fit** potential, instead of TO (the **average**).

The most stable composition (*i.e.*, minimum energy) is (14,24), for both potentials, for which the TO motif with the O_h symmetry is adopted. The remarkable stabilisation is shown by steep dips in the excess energy curves for both EP (Figure 6.4(a)) and DFT (Figure 6.4(b)) levels and this can be classified as a magic composition for the bimetallic TO. Similar stabilisation is also observed for Pd-Au (*see* Chapter 5). The other magic composition for TO, (6,32), which shows a distinct stability for Pd-Au (*see* Figure 5.7), could not be identified, as the GM is a non-TO structure. Small dips of the EP curves at composition (6,32), however, are due to the magic composition of the other motif: pIh-M-pc⁵ with the C_{5v} symmetry.

Apart from the sharp peaks at the composition (14,24), the excess energy curves for the EP in Figure 6.4(a) are very smooth as a function of cluster composition. It is possible to relate this to the fact that only three motifs are observed as GM but there is no significant disruption, even when structural transitions occur: TO to Dh (Pt-rich), Dh to TO (medium), TO to pIh-M-pc⁵ (Pd-rich) and pIh-M-pc⁵ to TO (Pd-rich). This observation is not unexpected, however, as the energy gap between different structural motifs in the small clusters are normally very close.

In addition to the qualitative agreement for the most stable cluster at the composition (14,24), the DFT curves in Figure 6.4(b) agree on the strong preference of TO over a very wide composition region. However, pIh-M-pc⁵ and Dh are disfavoured in the Pd-rich ($N_{\text{Pd}} = 11-12$) region, while in the Pt-rich region, Dh is relatively competitive against TO.

There should be no argument about the stability/instability of TO and pIh-M-pc⁵, as these motifs are found as the single variant. Dh however, is different, where several variants of GM are found, as illustrated in Figure 6.5. At the EP level, all of these variants are almost degenerate but, the DFT calculations reveal that **Dh4** is less pre-

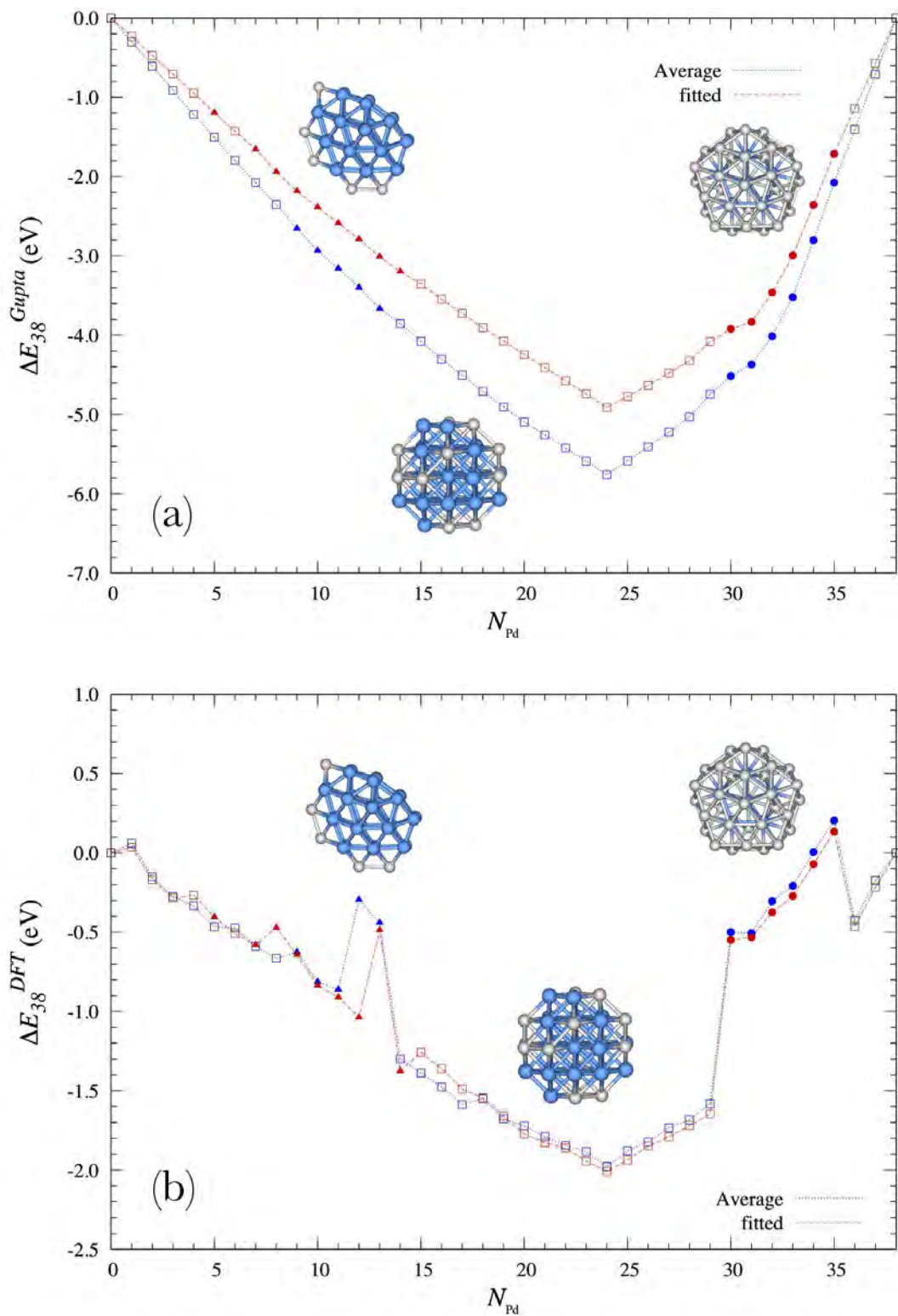


Figure 6.4: Excess energies of 38-atom Pd-Pt clusters from the **average** and **DFT-fit** potentials at the (a) EP and (b) DFT levels. Each symbol denotes different motifs: Dh (triangle), TO (square) and pIh-M-pc⁵ (circle).

ferred than **Dh1**, **Dh2** and **Dh3** variants. The **Dh4** structure that is found as the GM for $N_{\text{Pd}} = 12-13$, lacks the edges atom (on top of the (100) sites) compared with the other Dh variants. These edge locations are the least coordinated sites and are shown to be the preferred sites for Pd, as also observed for 34-atom clusters.

6.3.3 Chemical Ordering Effects

38-atoms is the ideal size to investigate the chemical ordering effects in Pd-Pt clusters, as there is less variation of GM. However, to concentrate fully on this effect, it is best to have a fixed motif. For this purpose, the Dh motif is omitted, as it comprises several variants. Analyses on the single variant TO (Pt-rich and medium compositions) and pIh-M-pc⁵ are shown in Figure 6.6, comparing excess energies, compositional mixing degrees, σ_N and bonding profiles (bond lengths) for the **average** and **DFT-fit** potentials.

For $N_{\text{Pd}} = 15-17$, the difference between the two potentials is notable for the excess energy. It also can be seen that there is a consistent and significant gap in σ_N . The lower σ_N (for the **average** potential) represents more mixing in the cluster and has a greater stability at the DFT level. The surface mixing enhancement is also present for the composition $N_{\text{Pd}} = 4$ ($\text{TO}_{\text{average}} < \text{TO}_{\text{DFT-fit}}$). It is important to note that all TO adopt core-shell chemical ordering, hence the higher/lower σ_N values are only due to the surface mixing/segregation.

For the $N_{\text{Pd}} = 20-28$ region, the fluctuations in σ_N do not reflect the excess energy,

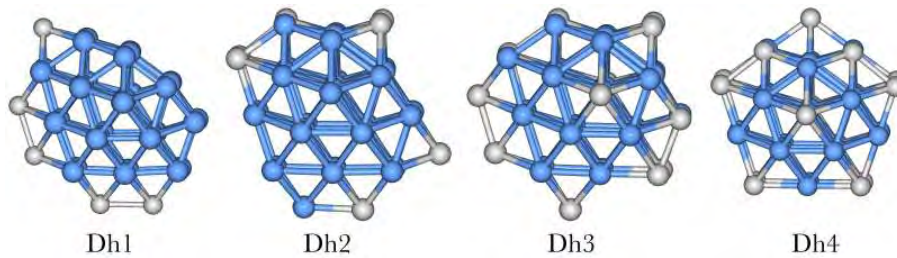


Figure 6.5: Dh variants of global minima observed for PdPt-38 clusters.

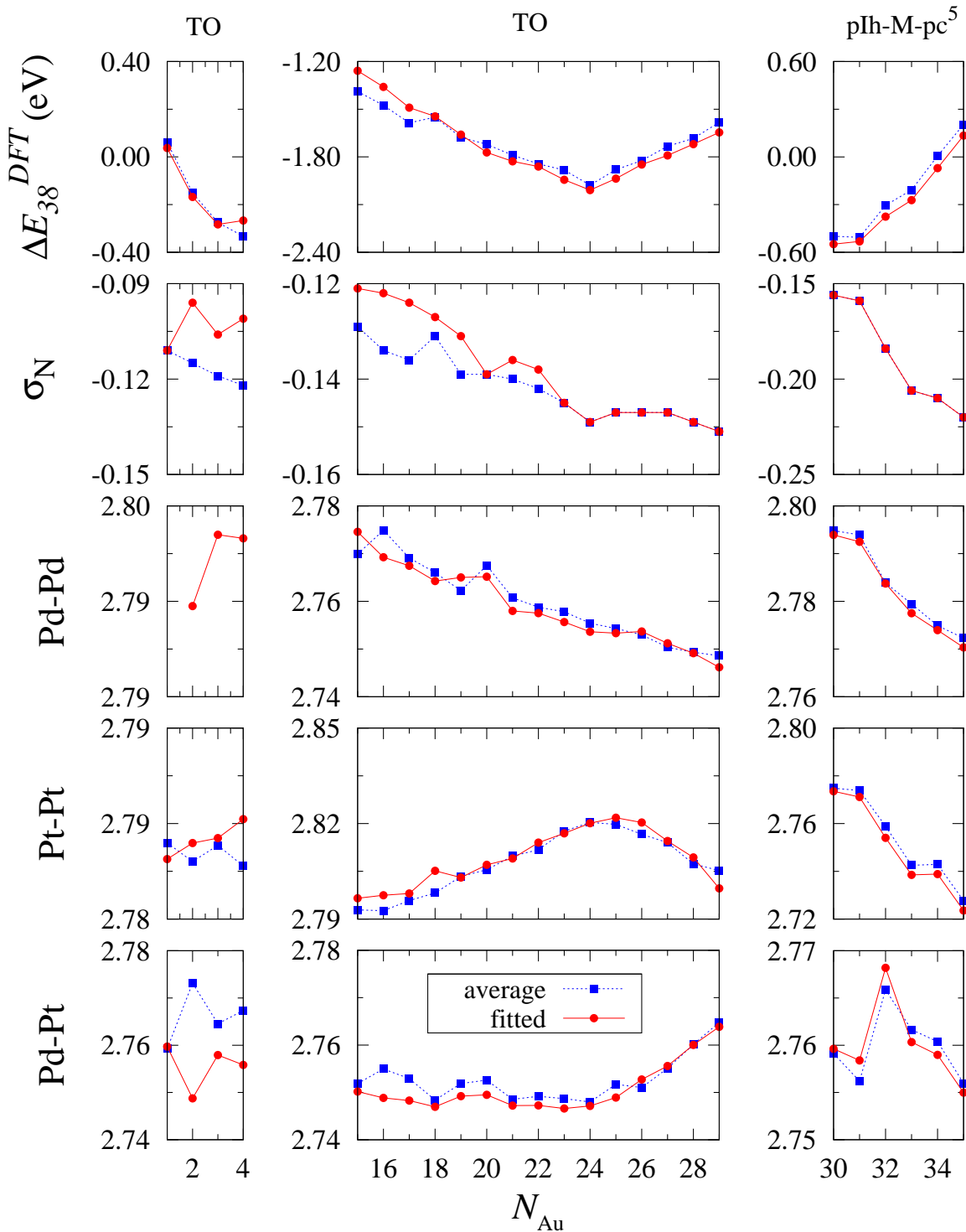


Figure 6.6: Excess energies, compositional mixing degrees, σ_N and bond lengths (Pd-Pd, Pt-Pt and Pd-Pt, in Å) of TO and pIh-M-pc⁵ motifs from the **average** and **DFT-fit** potentials.

as the TO configurations from the **DFT-fit** potential are consistently lower in energy than those of the **average**. The gap, however, is small and can be linked to the bonding in clusters – shorter heteronuclear Pd-Pt bonds. Meanwhile, the pIh-M-pc⁵ motifs show the similar ordering for both potentials, as evidenced by the overlapped σ_N . Small gap of excess energy, however, could be associated to the shorter (*i.e.*, stronger) Pt-Pt bonds for the **DFT-fit** potential.

As the **average** potential generally prefers more mixed ordering (*as also been seen previously in* Chapter 3), the observed variations give a strong indication for a dependency of the chemical ordering on the motif and the composition of a cluster. Compared with Pd-Au, the stabilisation of Pd-Pt cluster is mostly contributed by maximising Pt-Pt bonds (Pt-Pt > Pd-Pt > Pd-Pd), which can be seen from the cohesive energies of the dimer in Table 6.1.

6.4 Chapter Conclusions

There are many factors which determine the stability of clusters, especially for small sizes. Distinct results are seen between 34- and 38-atom clusters, with more variation in the structures for 34-atom clusters. Meanwhile, TO is dominant for 38-atom clusters due to its magic size. For both sizes, the GM motif is strongly influenced by the cluster composition. However, there are very small energy gaps between several different structural motifs. While core-shell ordering is generally preferred, composition effects lead to a variation in the surface ordering, *i.e.*, high surface-mixed (Pt-rich clusters) *vs.* surface-segregated (Pd-rich clusters).

Table 6.1: Cohesive energies (in eV) of the Pd-Pd, Pt-Pt and Pd-Pt dimers.

dimer	DF	EP: average	EP: fitted
Pd-Pd	1.54	4.23	4.28
Pt-Pt	3.29	7.07	7.06
Pd-Pt	2.43	5.65	5.55

The remarkable stability of the TO for the composition (14,24) is associated with the shell closing effect, in which the cluster is stabilised by very high point group symmetry (O_h). For the p1h-M-pc⁵ motif, similar effects are seen for the composition (6,32) (C_{5v} symmetry).

At the EP level, only a small difference is seen between calculations with the **average** and **DFT-fit** potentials and they are in a qualitatively good agreement with the DFT predictions. However, some discrepancies are observed: several Dh variants are almost energetically degenerate at the EP level but, at the DFT level, the structure with Pd on the edges (lower coordination sites) is more favourable.

Chapter 7

Benchmarking the Gupta Empirical Potentials for Bimetallic Clusters against Density Functional Calculations

This chapter provides reliability check of the Gupta EP for Pd-Au (7.3), Pd-Pt (7.4) and Ni-Al (7.5) based on the study of TO clusters at fixed compositions (32,6) and (6,32). The discussion will mainly focus on the variation between different EPs (the **average**, fitted and weighted – parameter sets **I–III**) and the performance of these potentials against the DFT predictions. Brief discussion will also be presented for the other bimetallic nanoalloys: Pt-Au (7.6.1), Cu-Pd (7.6.2), Cu-Au (7.6.3) and Cu-Pt (7.6.4).

7.1 Introduction

The main challenge in studies of the nanoalloy cluster is the complexity of the PES, where there are considerably more minima compared with the pure clusters due to the existence of homotops. Finding the GM is a formidable task, even for clusters containing only a few atoms. Accurate prediction can be achieved *via* the DFT method but this requires very large computational effort. Commonly, only a few selected structures are explored at the DFT level, leaving the question of whether the “real”

GM is included [116].

A more feasible strategy in finding the GM is global optimisation using EP models. The method, however, does not take into account specific electronic effects such as Jahn-Teller distortions, which are important in predicting the behaviour of a small cluster. Moreover, results sometimes vary between different empirical methods, quantitatively and qualitatively [827]. However, by using the EP, there is a significant saving of cost and time. Acceptable and meaningful predictions can be achieved, for example, through verification against experimental results or calculation at a higher level theory (*e.g.*, CI) [828].

In order to study a complete conformation space of the PES and/or involving large systems, computational resources become an issue and a combined EP-DF method is one of the alternatives. The EP calculations are used to build a structural bank of possible structures, containing several different structural families, which can be the starting point for the first principles calculations. It is also possible to re-parameterise the potentials, based on the DFT calculations, to bridge the gap of accuracy between methods [116].

7.2 Computational Details

The EP and DFT calculations were carried out on 38-atom clusters of the two opposite compositions, (6,32) (B-rich) and (32,6) (A-rich), to include any possible compositional effects. Instead of exploring a variation in the structural motif, verification checks were carried out on TO of the three high symmetry homotops with different chemical ordering, as shown in Figure 7.1. These selections have been used by West *et al.* [352], to give variation of O_h symmetry core-shell (“*core*”), C_{3v} symmetry surface segregation (“*hex*”) and D_{3d} symmetry surface-mixing (“ D_{3d} ”). These high symmetry configurations are feasible for the DFT calculations, for which the computing cost is significantly reduced.

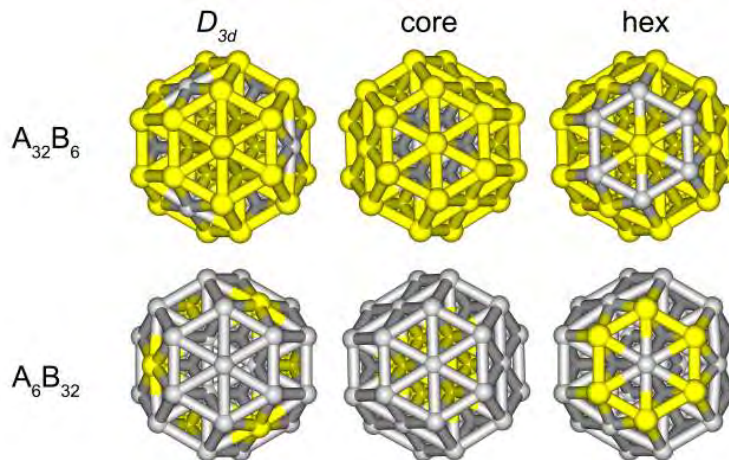


Figure 7.1: TO motif with the three different high symmetry arrangements and their reverse compositions.

Three main systems studied in this thesis: Pd-Au, Pd-Pt, Ni-Al (*see* Chapter 3–6), were further explored with this scheme. In addition, calculations were extended to some other bimetallics formed from transition metals of groups 10 and 11: Pt-Au, Cu-Pd, Cu-Au and Cu-Pt. Pt-Au was chosen to complete the binary series involving Pd, Pt and Au metals, whilst several studies have been reported involving Cu-based (combined with each of Pd, Pt and Au) systems (*see reviews in* Refs. [116] and [600]). Some physical properties of the elements involved are listed in Table 1.1, while the cluster motifs were previously described in Chapter 4.

Combined EP-DF calculations were carried out for all systems. At the EP level, each homotop was optimised and the excess energy, $\Delta E_N^{\text{Gupta}}$, was calculated using the **average** and the weighted Gupta potentials – parameter sets **I–III**. For Pd-Au, Pd-Pt and Ni-Al binary systems, comparisons were also made against fitted potentials – the **DFT-fit** and/or **exp-fit**. At the DFT level, geometry optimisation and energy (ΔE_N^{DFT}) calculation were performed with the NWChem package [621] with the two XC functionals: PW91 [571] and PBE [572]. For each of the DFT runs, geometry optimisations were performed using double- ζ (DZ) basis sets followed by triple- ζ -plus-

polarisation (TZVP) single point calculations.

For the Pd-Au (Section 7.3), Pd-Pt (7.4) and Ni-Al (7.5) sections, the discussion will begin with the mapping (structural and energies) of potential sets **I–III** against the **average** and fitted potentials. These were done by performing 500 extended BCGA runs for 34- and 38-atom clusters, for all compositions (*see* Chapter 2).

7.3 Pd-Au

7.3.1 The Average, DFT-fit and Exp-fit *vs* the Weighted (Parameter Sets I–III) Potentials

34-atom Clusters

Based on the work in Chapter 4, the parameter sets **I** and **II** give excess energies and GM structures that are comparable with those of the **average** potential. On the other hand, more variation (structural and energies) is seen for the parameter set **III** and, for the high weighting, the **DFT-fit** and **exp-fit** potentials are reproduced. Hence, only the parameter set **III** is considered for this section. Structures and energetics of the GM for 34-atom clusters, calculated with the parameter set **III** (for $w_a = 0.5$ and 0.7-0.9) and the fitted potentials (**DFT-fit** and **exp-fit**) are shown in Figure 7.2(a). GM structures for the **DFT-fit** potential are similar to those for the parameter set **III** with $w_a = 0.8$ and 0.9, in which Dh (including Dh-Ih) dominate in the Pd-rich region, while competition of several plh motifs (plh-db, plh-M(DT), plh⁶, distorted plh) is observed in the Au-rich region. GM structures of the **exp-fit** potential, however, do not match any of the weightings (w_a) of the set **III**.

Energetically, the **DFT-fit** curve lies between those of the parameter set **III** for $w_a = 0.7$ and 0.8. For the **exp-fit** potential, the plot overlaps with that for $w_a = 0.8$, especially for the mid-range compositions. The excess energy curves indicate the preference of more mixing for the **DFT-fit** and **exp-fit** potentials, as compared with the **average**. This highly exothermic mixing is similar to the energy curves obtained

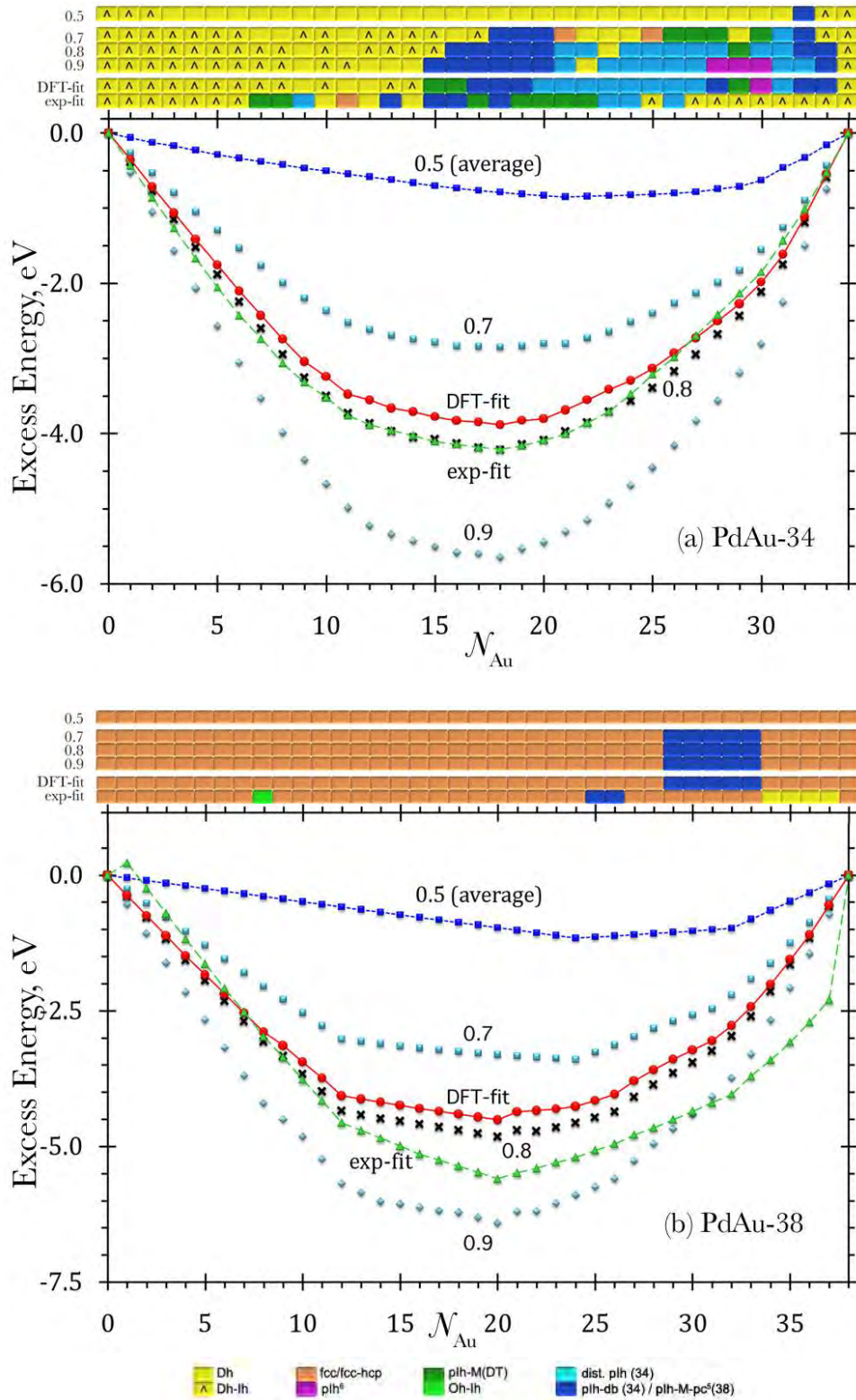


Figure 7.2: Structural motifs (*square maps*) and excess energy variation (*curves*) of (a) 34- and (b) 38-atom Pd-Au global minima found for the **DFT-fit** and **exp-fit** potentials compared with the parameter set **III** ($w_a = 0.5, 0.7-0.9$) potential.

for 34-atom Pd-Pt clusters, with the parameters weighted toward the strongest (Pt-Pt) homonuclear interactions [256, 345].

38-atom Clusters

Less variation is observed for 38-atom (as compared with 34-atom) clusters, for which only TO, pIh-M-pc⁵, Dh and Oh-Ih are observed as GM, as shown in Figure 7.2(b). Consistent with the 34-atom results, the structural motifs are similar for the **DFT-fit** and set **III** ($w_a = 0.7-0.9$) parameters: TO for all compositions except $N_{\text{Au}} = 29-33$ (pIh-M-pc⁵). Meanwhile, the **exp-fit** potential gives a distinct variation; along with the dominant TO, other structures from the **exp-fit** potential calculations are Dh [(4,34) to (1,37)], pIh-M-pc⁵ [(13,25) and (12,26)] and Oh-Ih [(30,8)]. As reported earlier [345], the structures derived from both fitted potentials tend to maximise the number of Pd-Au bonds; hence, they tend to form incomplete icosahedra or pIh.

Energetically, the **DFT-fit** potential plot for 38-atom Pd-Au clusters is consistent with that for 34 atoms; it is located between weights $w_a = 0.7$ and 0.8 for the parameter set **III**. On the other hand, the excess energy plot for the **exp-fit** dips down below $w_a = 0.8$ and at some points (for very rich Au compositions) the GM of this potential are more stable than the extreme parameters of set **III** ($w_a = 0.9$). The composition (18,20) shows the lowest excess energy for the **DFT-fit** and **exp-fit** potentials, for which the GM is TO but a distorted structure towards Oh-Ih, similar to the parameter set **III** ($w_a = 0.8$ and 0.9). It should be noted that the mixed Oh-Ih motif is only found for composition (30,8) for the **exp-fit** potential, while the TO distorted towards Oh-Ih structure is found for the medium compositions.

Several straight line regions ($w = 0.7-0.8$) are evident from the plotted excess energies that are not found for the 34-atom clusters. The first straight line region is from the pure-Pd composition (38,0) to composition (26,12), after which more gradual changes of excess energy correspond to the formation of new Au-Au bonds on the surface of the cluster, as shown in Figure 7.3(a). The next straight line region commences at compo-

sition (14,24) (Figure 7.3(b)), after which point Au atoms start to occupy the centroids of the (111) facets on the cluster surfaces. The transition from 12 to 13 Au atoms and from 24 to 25 Au atoms specifically shows how Au prefers (100) sites, leaving Pd on (111) facets, consistent with findings of the DFT calculations [829]. This behaviour, which is also observed for Au_{55} , Au_{98} , Au_{79} and Au_{92} , is promoted because of the stronger Pd-Au bonds compared with either Au-Au or Pd-Pd bonds [830]. Subsequent transitions with large jumps of energy for compositions (6,32) to (5,33) correspond to Au atoms starting to occupy the inner cluster core, as shown in Figure 7.3(c). For $w_a = 0.7-0.9$ and the **DFT-fit** potential, an almost identical transition occurs as a result of the structure changing from a pIh with seven interior Pd atoms into a TO with six interior Pd atoms (Figure 7.3(d)).

Comparing results of the parameter set **III** and the fitted (**DFT-fit** and **exp-fit**) potentials generates some interesting conclusions that can be associated with the Gupta potential parameters (Table 2.3 and Appendix A). The pure (Au-Au and Pd-Pd) parameters only differ slightly for the p , q and r_0 parameters but more significantly for the A and ξ parameters, as shown in Table 7.1 (*also discussed in Chapter 4*).

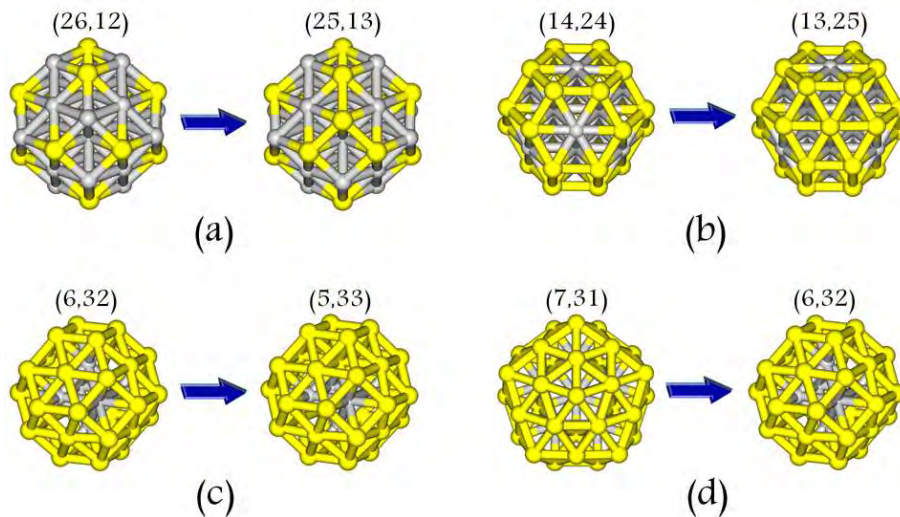


Figure 7.3: Configurational changes in PdAu-38: (a) $N_{\text{Au}} = 12$ to 13, (b) $N_{\text{Au}} = 24$ to 25, (c) $N_{\text{Au}} = 32$ to 33 and (d) structural change from $N_{\text{Au}} = 31$ to 32.

Table 7.1: The A and ξ parameters of the **average** and fitted potentials.

param.	DFT-fit	exp-fit	parameter set III			
			$w_a = 0.5$ (ave.)	$w_a = 0.7$	$w_a = 0.8$	$w_a = 0.9$
A	0.1843	0.2764	0.19	0.1840	0.1809	0.1778
ξ	1.7867	2.0820	1.75	1.7684	1.7756	1.7828

Parameter set **III** with $w_a > 0.5$ gives a stronger Pd-Au bonding, as shown by the lower excess energies for both cluster sizes. This weighting scheme results in less Pd-Au repulsion ($A_{\text{PdAu}} \rightarrow A_{\text{Pd}}$) and more Pd-Au attraction ($\xi_{\text{PdAu}} \rightarrow \xi_{\text{Au}}$) in the clusters. This is because $A_{\text{Pd}}(0.1746) < A_{\text{Au}}(0.2061)$ and $\xi_{\text{Pd}}(1.7180) < \xi_{\text{Au}}(1.7900)$; so that as $w_a \rightarrow 1.0$, the A parameter (repulsion) is reduced and the ξ parameter (attraction) increases. The **DFT-fit** potential has more comparable results to those of the parameter set **III** and can be linked to $A_{\text{DFT-fit}}(0.1843) \approx A_{w_a=0.7}(0.1841)$ and $\xi_{\text{DFT-fit}}(1.7867) \approx \xi_{w_a=0.9}(1.7828)$.

These correlations are consistent with the overall results for 34- and 38-atom PdAu clusters, that show the **DFT-fit** potential giving similar results for the energies and structures to those for $w_a = 0.8$. The **exp-fit** potential also gives similar excess energies to the results for $w_a = 0.8$, though the shape of the curve is a little different – but the structures and homotops are often quite different to the results of those of the parameter set **III**. This is not surprising, since, as noted previously [345], the **exp-fit** potential is qualitatively very different. In particular it should be noted that for the **exp-fit** potential: $A_{\text{Pd-Au}} > A_{\text{Pd-Pd}}$ and $A_{\text{Au-Au}}$; $\xi_{\text{Pd-Au}} > \xi_{\text{Pd-Pd}}$ and $\xi_{\text{Au-Au}}$.

7.3.2 The DFT Calculations of $\text{Pd}_{32}\text{Au}_6$ and $\text{Pd}_6\text{Au}_{32}$

Results of the DFT calculations for the compositions (32,6) and (6,32) of Pd-Au clusters are shown in Table 7.2 in comparison with the EP (the **average**, **DFT-fit** and **exp-fit**). The stability order between the *core*, *hex* and D_{3d} homotops is then compared with that given by the calculations with parameter sets **I–III** of the weighted potentials

(Figure 7.4). Generally, the DFT calculations using the PW91 and PBE functionals are consistent, especially where the energy gap between homotops is concerned. While composition (6,32) exhibits a similar order of homotop stability ($core < D_{3d} \ll hex$) for all parameters (**average**, **DFT-fit** and **exp-fit**), only the **average** potential agrees with the DFT calculations ($hex < D_{3d} \ll core$) for composition (32,6).

Results for composition (32,6) indicate that Pd-Au clusters with the surface-segregated core-shell (hex) configuration are favoured. The surface-mixed D_{3d} homotop, which is preferred by the **DFT-fit** and **exp-fit** potentials, is disfavoured by 1.2 eV (PW91 and PBE). Clusters avoid having a core of Au atoms as this leads to energetically very unstable chemical ordering. In addition, data for composition (6,32) demonstrates the strongest stability of the $core$ homotop, providing further evidence for the preference of $Pd_{core}Au_{shell}$.

At the EP level (Figure 7.4), the parameter sets **I** and **II** give the same order of homotop stability as that predicted by the DFT, except for $w_s = 1.0$ (set **II**). Furthermore, the excess energy is very close to that of the **average** ($w, w_s, w_a = 0.5$) potential. These circumstances could be associated with the small gap between the Gupta potential parameters for Pd and Au, with ratios of 1.18 (A), 1.04 (ξ), 0.94 (p) and 1.08 (q). Hence, weighting all parameters (set **I**) or just A and ξ (set **II**) in a symmetrical fashion does not have a significant effect on the bimetallic interactions. Moreover, the data in Chapter 4 show that these parameter sets adopt the same chemical ordering as seen for the **average** potential.

Meanwhile, the anti-symmetric weighting of A and ξ in the parameter set **III** exhibits a large deviation of the excess energy and changes in the order of homotop stability (high w_a for composition (32,6) and low w_a for composition (6,32)). The deviation in homotop order means the weighting is unacceptable for reproducing the DFT predictions. Only $w_a = 0.4-0.6$ give the same homotop rank as the DFT for both compositions (32,6) and (6,32). In addition, $\Delta E_{hex-D_{3d}}$ of the DFT calculations is

Table 7.2: Excess energies (in eV) of the three TO homotops of (32,6) and (6,32) Pd-Au clusters at the DFT and EP (the **average**, **DFT-fit** and **exp-fit** potentials) levels. (* Denotes potentials for which the homotop ordering is not consistent with the DFT calculations.)

homotops	DFT		EP		
	PW91	PBE	average	DFT-fit	exp-fit
Pd ₃₂ Au ₆					
<i>hex</i>	-0.729	-1.373	-0.294	-1.443*	-1.562*
<i>D_{3d}</i>	0.500	-0.131	0.161	-2.186*	-2.101*
<i>core</i>	3.202	2.528	1.350	-0.728*	-0.120*
Pd ₆ Au ₃₂					
<i>core</i>	-1.047	-4.622	-0.976	-2.660	-2.575
<i>D_{3d}</i>	0.347	-3.241	-0.051	-2.015	-2.238
<i>hex</i>	2.245	-1.282	0.337	-0.836	-0.989

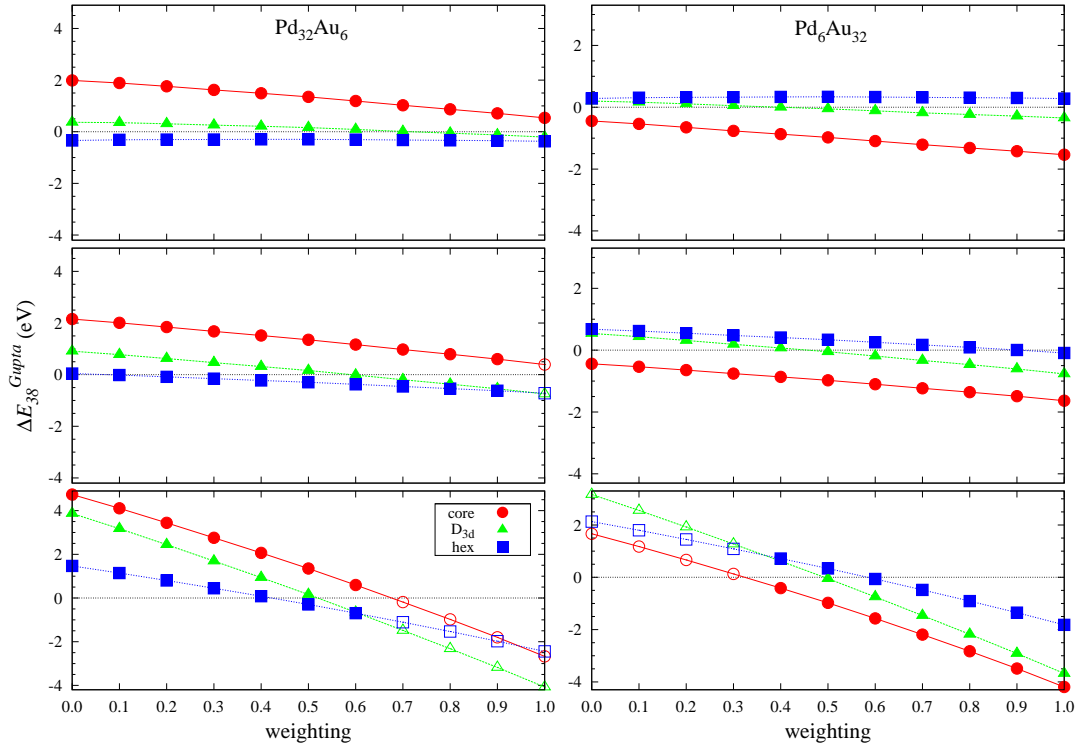


Figure 7.4: Stability ordering of the three TO homotops of (32,6) and (6,32) Pd-Au clusters for the EP calculations with the weighted potential of the parameter sets **I** (*top*), **II** (*middle*) and **III** (*bottom*). Consistent ordering compared with the DFT calculations is denoted with the filled point symbols.

more than double that of $\Delta E_{D_{3d}\text{-core}}$, which is replicated with the **average** potential. It is worth mentioning that the **DFT-fit** and **exp-fit** potentials are revealed earlier (Subsection 7.3.1) to be similar to those for $w_a = 0.8$, which disagrees with the DFT predictions for composition (32,6).

7.4 Pd-Pt

7.4.1 The Average and DFT-fit *vs* the Weighted (Parameter Sets I–III) Potentials

Comparison between excess energies and structural motifs of 34- and 38-atom GM for the **average** ($w = 0.5$) and **DFT-fit** potentials are shown in Figure 7.5. The figure also shows results of the calculation for the parameter set **I** ($w = 0.4$ and 0.6). As the **DFT-fit** potential is very close to the **average** (for structures and energetics), it is best to compare only with those of the set **I** weightings, as the set **III** give excessive deviations. As the differences of the p and q parameters of the Gupta potential between Pd and Pt is insignificant ($p_{\text{Pt}}/p_{\text{Pd}} = 0.98$ and $q_{\text{Pt}}/q_{\text{Pd}} = 1.07$), the parameter set **II** potentials are not very different from those of the parameter set **I** (*see* Chapter 4).

In contrast to Pd-Au, the difference in the Gupta potential parameters between Pd-Pd and Pt-Pt are large for A and ξ ($A_{\text{Pt}}/A_{\text{Pd}} = 1.7$ and $\xi_{\text{Pt}}/\xi_{\text{Pd}} = 1.6$). Hence, there is a clear variation in GM (energetics and structures), moving from $w = 0.4$ to 0.6 . For both sizes, the **DFT-fit** potential results are closely matched to that of the **average**. Excess energies and structural data, however, exhibit that the **DFT-fit** set is slightly biased towards $w = 0.4$ (*i.e.*, towards Pd-Pd). Chemical ordering analysis for both sizes revealed the prevalence of core-shell segregation but Pd and Pt atoms are mixed on the surface. The **DFT-fit** potential shows a slightly lower degree of surface mixing (*i.e.*, a lower percentage of Pd-Pt bonds) compared with the **average**.

The **average** and **DFT-fit** potentials predicted Dh as the preferred motif for the Pt-rich compositions of 34-atom clusters as shown in Figure 7.5(a). Some competition from

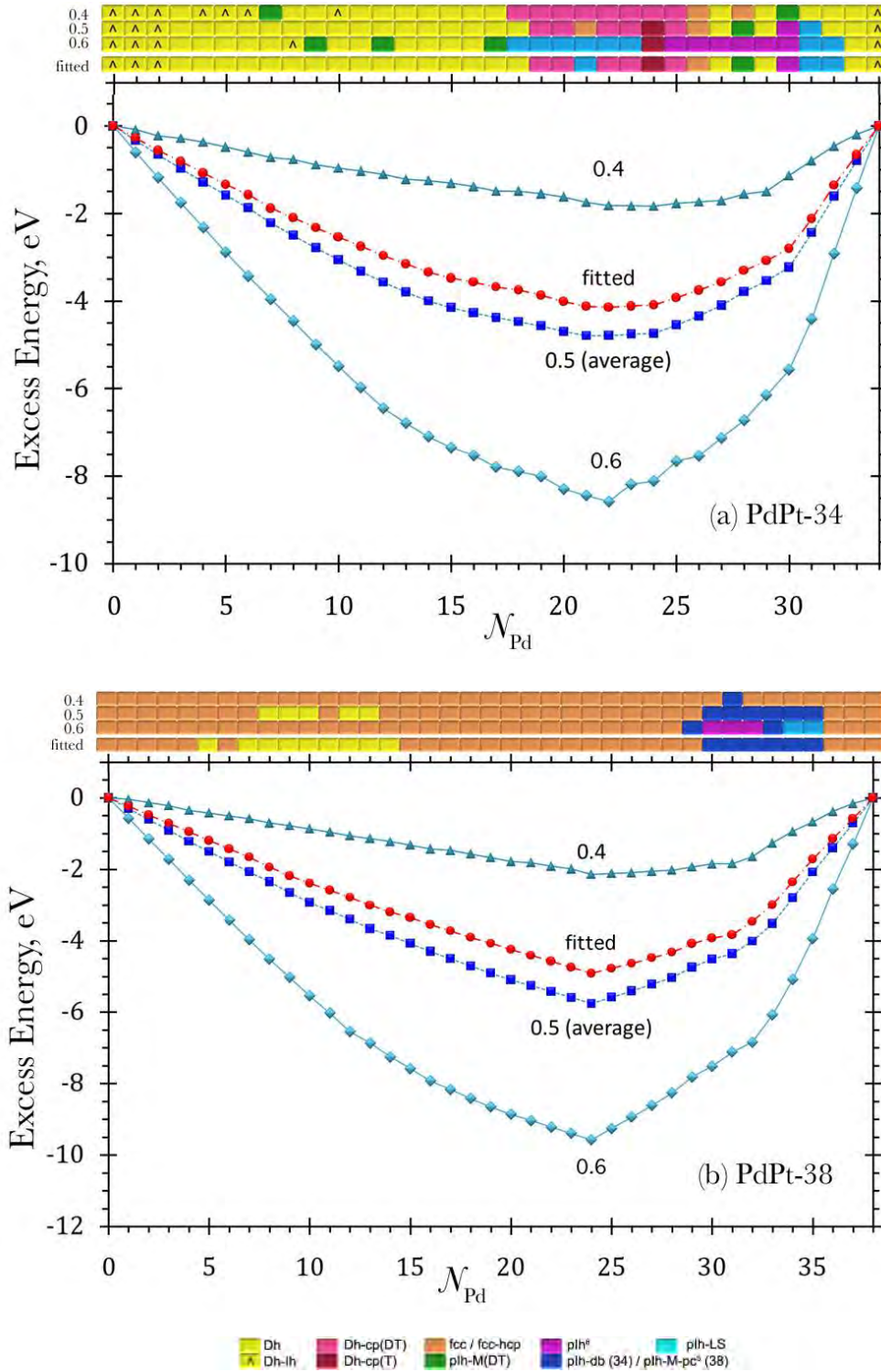


Figure 7.5: Structural motifs (*square maps*) and excess energy variation (*curves*) of (a) 34- and (b) 38-atom Pd-Pt global minima found for the **average** and **DFT-fit** potentials and compared with the parameter set **I** ($w = 0.4-0.6$) potential.

the other motifs is seen for the Pd-rich compositions but the Dh-cp(DT) is prevalent for $N_{\text{Pd}} = 18-25$. For 38-atom clusters in Figure 7.5(b), TO dominates for the whole composition, with some interruption from Dh ($N_{\text{Pd}} = 7-14$) and pIh-M-pc⁵ ($N_{\text{Pd}} = 29-35$). The results for 34- and 38-atom clusters further reinforce the small difference between the potentials, as also seen for the clusters of 1:1 compositions (size 1-100 atoms) and 98-atoms (Chapter 3).

7.4.2 The DFT Calculations of Pd₆Pt₃₂ and Pd₃₂Pt₆

Results of the DFT calculations on 38-atom Pd-Pt clusters, focussing on the TO homotops of the compositions (6,32) and (32,6) are presented in Table 7.3, along with the EP predictions (the **average** and **DFT-fit** potentials). It can be seen that calculations with the PW91 and PBE functionals give consistent values. At the EP level, the **average** and **DFT-fit** give the same order of homotop stability to those of the DFT, for both compositions. These results, show that the **average** and **DFT-fit** potentials are fairly acceptable in reproducing the DFT predictions.

For composition (6,32), the order is $hex \leq D_{3d} < core$, with very close separation between surface segregation (hex) and surface mixing (D_{3d}). It can thus be seen that calculations with the **average** potential are slightly closer to that of the DFT, as compared with the **DFT-fit** potential. On the other hand, putting all six Pd atoms in the core sites (of the composition (6,32)) gives positive excess energies, signifying relatively unstable clusters and indicating Pt preference for core sites of TO. The further proof of this is the observation for the composition (32,6), in which $core$ is the most stable homotop (*i.e.*, Pt_{core}Pd_{shell}) and the order is $core < D_{3d} \ll hex$.

The comparison of the homotop order between the DFT and the parameter sets **I-III** calculations are shown in Figure 7.6. As mentioned in Chapter 4, parameter set **I** \simeq parameter set **II**, for energetics and structures. After taking into consideration both compositions (6,32) and (32,6), the DFT predictions are reproduced for w , $w_s = 0.4-0.7$ of the parameter sets **I-III** and only for $w_a = 0.5-0.6$ of the parameter set **III**

Table 7.3: Excess energies (in eV) of the three TO homotops of (32,6) and (6,32) Pd-Pt clusters at the DFT and EP (the **average** and **DFT-fit** potentials) levels.

homotops	DFT		EP	
	PW91	PBE	average	DFT-fit
Pd ₆ Pt ₃₂				
<i>hex</i>	-0.785	-0.529	-1.629	-1.333
<i>D_{3d}</i>	-0.739	-0.422	0.090	0.644
<i>core</i>	0.003	0.345	1.195	1.693
Pd ₃₂ Pt ₆				
<i>core</i>	-1.457	-1.434	-3.870	-3.331
<i>D_{3d}</i>	-1.137	-1.109	-2.400	-1.667
<i>hex</i>	-0.140	-0.036	0.131	0.493

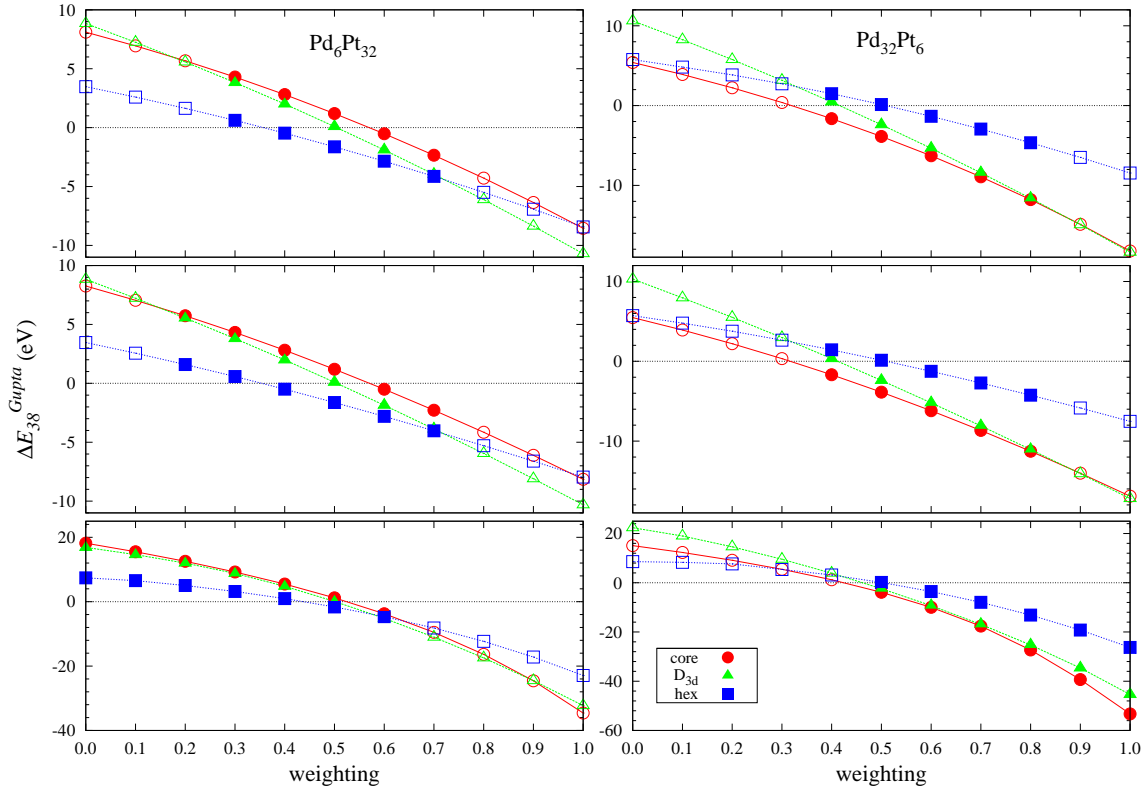


Figure 7.6: Stability ordering of the three TO homotops of (32,6) and (6,32) Pd-Pt clusters for the EP calculations with the weighted potential of the parameter sets **I** (*top*), **II** (*middle*) and **III** (*bottom*). Consistent ordering compared with the DFT calculations is denoted with the filled point symbols.

(with $w = w_s = w_a = 0.5$ giving the **average** potential).

For the composition (6,32), DFT predicts that $hex \leq D_{3d}$ and this resemblance can only be seen for $w, w_s = 0.6-0.7$ (of the parameter sets **I** and **II**). Meanwhile, the positive excess energy (*i.e.*, unstable) for the *core* homotop is only seen for $w, w_s \leq 0.6$. The instability of this homotop is not found for $w_a = 0.6$ of the parameter set **III**. Meanwhile, for the composition (32,6), the energy gap of $D_{3d}-hex$ is three times greater than that of the *core*- D_{3d} , which is the case for $w, w_s \geq 0.6$. Combining all of this information, $w, w_s = 0.5-0.6$ of the parameter sets **I** and **II** is the most accurate, indicating that the **average** potential is possibly the best in representing Pd-Pt homonuclear interaction. Biasing towards $w, w_s = 0.6$ could give better results but possibly on a quantitatively smaller-scale and the opposite is observed for the **DFT-fit** potential (slightly biased towards $w, w_s = 0.4$).

7.5 Ni-Al

7.5.1 The Exp-fit *vs* the Weighted (Parameter Sets I–III) Potentials

Unlike Pd-Au and Pd-Pt, for which the **average** potential has been used in most of the EP studies of the Johnston research group (*see reviews in* Refs. [116] and [600]), studies of Ni-Al clusters [599, 619] have been carried out using the **exp-fit** potential of Cleri and Rosato [377]. Along with Cu-Au, the potential is derived by fitting the potential to the experimental data (cohesive energy and mixing enthalpy) of the bulk A_3B -type alloys with the $L1_2$ configuration (basic fcc cube with Ni residing on each of the faces, leaving Al at each corner).

Compared with the parameter sets **I–III**, the **exp-fit** potential is more comparable to the high weighting end of the set **III**, as shown in Figure 7.7. For 34-atom clusters (Figure 7.7(a)), the excess energies curve is in between $w_a = 0.8-0.9$ but overlaps with $w_a = 0.9$ for the Al-rich compositions. The GM variation is consistent with this

pattern but is closer to $w_a = 0.8$, for which no Dh and pIh structures are found. This trend is repeated for 38-atom clusters (Figure 7.7(b)) but the GM variation is closer to $w_a = 0.9$, for which no pIh-M(DT) is adopted for the Ni-rich compositions.

For $w_a = 0.5$ (*i.e.*, **average** potential), GM variation of 34-atom Ni-Al clusters is not very different compared with those of the other weightings and the **exp-fit** potential, although several significant deviations are observed for 38-atom clusters: wide pIh-M(DT) (Ni-rich) and pIh⁷ (medium compositions) prevalence and disfavouring of pIh⁶ and pIh-db (Al-rich). Furthermore, this set gives relatively very high excess energies.

Interestingly, the weighting region ($w_a = 0.8$ - 0.9) that is close to the **exp-fit** potential is the area (of the structural map) of progression from core-shell to mixed ordering (*see* Chapter 4), although there is slight variation of the results between 34- (core-shell _{$w_a=0.8$} \rightarrow mixed _{$w_a=0.9$}) and 38-atom (core-shell _{$w_a=0.7$} \rightarrow mixed _{$w_a=0.8$}). Consistently, a variation is also seen for the **exp-fit** potential: $\text{GM}_{34(\text{exp-fit})} \simeq \text{GM}_{34(w_a=0.8)}$ and $\text{GM}_{38(\text{exp-fit})} \simeq \text{GM}_{38(w_a=0.9)}$. 34-atom clusters adopt the core-shell configurations for all compositions (progressing from **i-CS(C)** (Ni-rich) to **i-CS(A)** (medium) to the complete core-shell (Al-rich)), while the mixing ordering is observed for several 38-atom clusters, especially for the Ni-rich compositions.

7.5.2 The DFT Calculations of Ni₃₂Al₆ and Ni₆Al₃₂

Results of the DFT calculations for the three studied homotops are shown in Table 7.4, in comparison with the EP (the **average** and **exp-fit** potentials) predictions. The stability order at the DFT level is then set as a benchmark for the weighted (the parameter sets **I**–**III**) potentials in Figure 7.8. It should be noted that the **average** potential has not used in the previous [599, 619] Gupta-based study of Ni-Al clusters but is included here for comparison, as the other systems (*e.g.*, Pd-Au, Pd-Pt [116]) show that the scheme (averaging pure potential) is reasonable in describing heteronuclear interactions in the cluster.

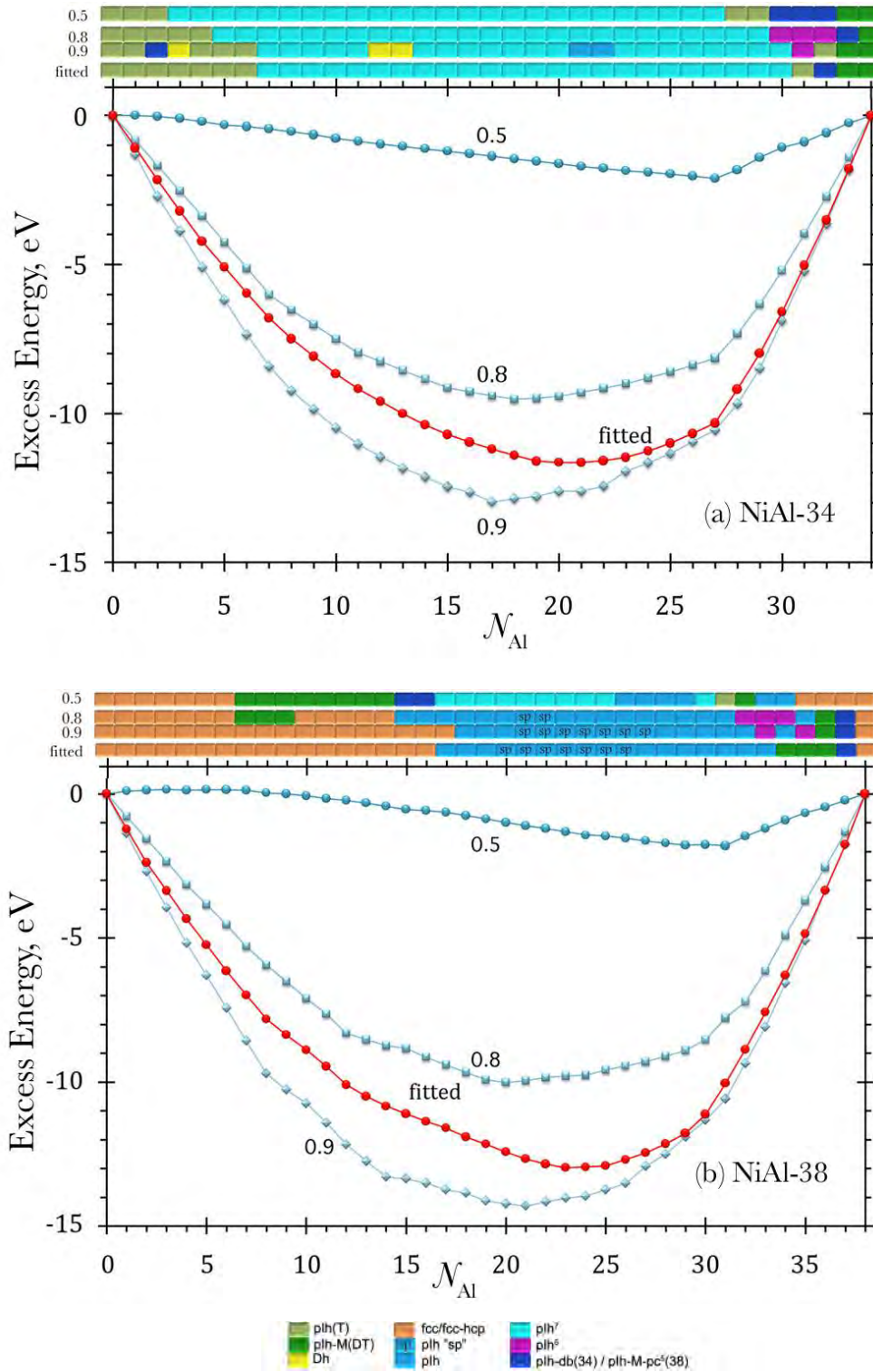


Figure 7.7: Structural motifs (*square maps*) and excess energy variation (*curves*) of (a) 34- and (b) 38-atom Ni-Al global minima found for the **exp-fit** potential and in compared with the parameter set **III** ($w_a = 0.5, 0.8-0.9$) potential.

Overall, the excess energies of all homotops are very low compared with those of Pd-Au and Pd-Pt, due to very strong preference for mixed phases in Ni-Al nanoalloys [704, 707–709]. The DFT calculations with the PW91 and PBE functionals are consistent for both compositions (32,6) and (6,32). For composition (32,6), the order is $D_{3d} < hex \leq core$, which is not predicted by the **average** potential. There is a distinct stability of the D_{3d} homotop, signifying a preference for forming mixed bonds (*i.e.*, Ni-Al compared with Ni-Ni and Al-Al). Furthermore, having smaller Ni (*hex*) or larger Al (*core*) atoms in the core does not cause much difference in the cluster stability (*i.e.*, close DFT excess energy between *hex* and *core*).

Turning now to the composition (6,32), the order is $core < D_{3d} \ll hex$ and the stability of the *core* homotop is linked to a significant size-mismatch, for which the strain is released by putting the smaller Ni in the cluster core. However, the D_{3d} homotop is separated by only ~ 1 eV (compared with over 3 eV for the D_{3d} –*hex* gap), showing a close competition between the mixed and core-shell chemical ordering. This is not the case for the composition (32,6), in which mixing is clearly preferred (D_{3d} is 4.7 and 4.8 eV more stable than *hex* and *core*, respectively).

A comparison between the homotop order at the DFT level and the parameter sets **I–III** in Figure 7.8 suggests that the composition (32,6) is crucial for Ni-Al. The DFT predictions are reproduced only for $w = 1.0$ (set **I**) and $w_a = 0.7$ – 0.9 (set **III**) while none are reproduced for the set **II**. On the other hand, the DFT prediction for composition (6,32) is seen for all weighted potentials, except for $w_a = 0.0$ – 0.3 (set **III**).

For composition (6,32), the DFT calculations show a very close gap between *hex* and *core* (~ 0.175 eV). Taking this into context, parameter sets **I** ($w = 1.0$) and **III** ($w_a = 0.7$) can be eliminated, leaving only $w_a = 0.8$ – 0.9 of the parameter set **III**. Coincidentally, this is the range where the results (structural and energies) matched those of the **exp-fit** potential (based on the observation of size 34 and 38-atom clusters, *see* Subsection 7.5.1).

Table 7.4: Excess energies (in eV) of the three TO homotops of (32,6) and (6,32) Ni-Al clusters at the DFT and EP (the **average** and **exp-fit** potentials) levels. (* Denotes potentials for which the homotop ordering is not consistent with the DFT calculations.)

homotops	DFT		EP	
	PW91	PBE	average	exp-fit
$\text{Ni}_{32}\text{Al}_6$				
D_{3d}	-10.592	-10.433	2.514*	-6.144
hex	-5.937	-5.817	0.145*	-4.392
$core$	-5.762	-5.793	5.322*	-3.890
$\text{Ni}_6\text{Al}_{32}$				
$core$	-10.888	-10.729	-1.362	-7.806
D_{3d}	-9.840	-9.768	0.487	-5.759
hex	-6.289	-6.245	1.701	-2.664

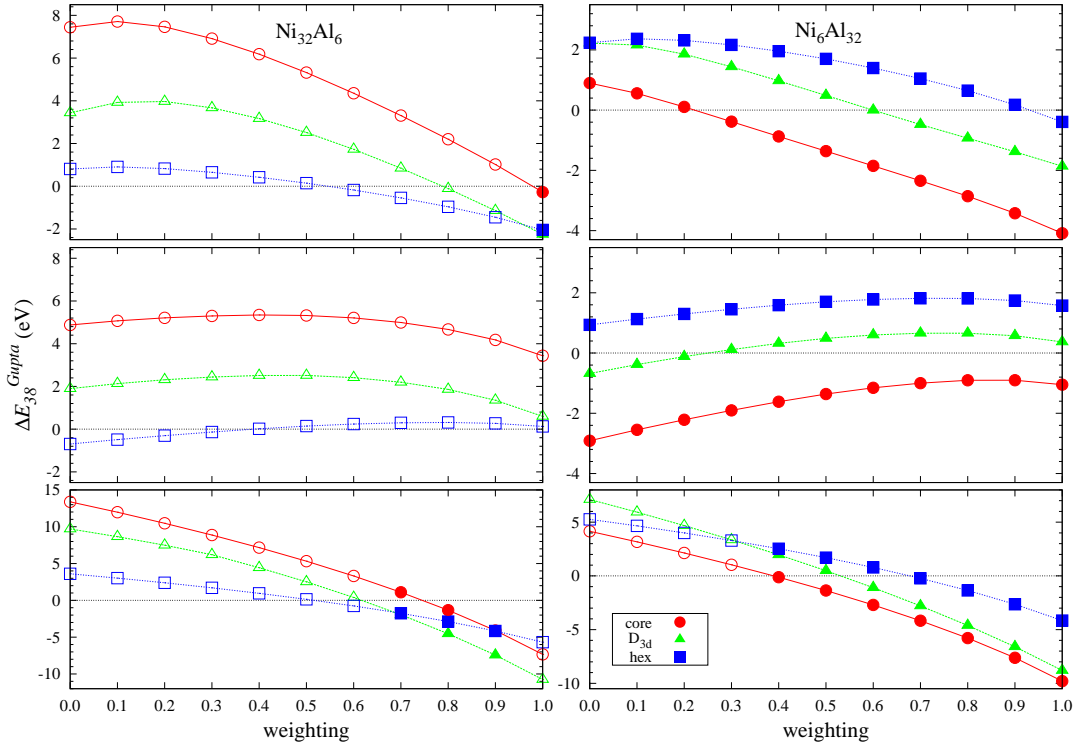


Figure 7.8: Stability ordering of the three TO homotops of (32,6) and (6,32) Ni-Al clusters for the EP calculations with the weighted potential of the parameter sets **I** (*top*), **II** (*middle*) and **III** (*bottom*). Consistent ordering compared with the DFT calculations is denoted with the filled point symbols.

7.6 Pt-Au, Cu-Pd, Cu-Au and Cu-Pt

The simple EP-DF method focussing on the compositions (32,6) and (6,32) is shown to give some insight into the heteronuclear interactions in binary nanoalloy clusters of Pd-Au, Pd-Pt and Ni-Al. Therefore, it was decided to extend the investigation to the other systems – Pt-Au, Cu-Pd, Cu-Au and Cu-Pt. Table 7.5 illustrates how the weighting of the parameter sets **I–III** is accomplished in each system.

Meanwhile, Table 7.6 provides the ratios of the A , ξ , p and q parameters for the homonuclear interaction of the Gupta potential in these extended systems. (Small differences between parameters are represented by values $\rightarrow 1.0$, where a value of '1' indicates that a perfect matching is attained.) For all studied binary systems, the p ratios are very close (*i.e.*, no effect in parameterisation). Pt-Au is a similar case to Pd-Pt, as the difference in q (as well as p) is small, so the A and ξ parameters contribute most to the weighting parameters. Cu-based potentials are more complicated, as the q component cannot be neglected. However, it remains to be seen how much this will affect the potential. For Cu-Pd and Cu-Au, there is similar resemblance to Pd-Au clusters.

A summary of the DFT and EP results for the TO homotops of how of compositions (32,6) and (6,32) is presented in Table 7.7, while detailed results for each weighting are shown in Figure 7.9(a-d), highlighting the weighting for which the DFT results are reproduced. The magnitudes of excess energy vary between calculations with the PW91 and PBE functionals (Table 7.7), although the homotop orders are consistent.

7.6.1 Pt-Au

For composition (32,6), the stability order is $D_{3d} < hex \ll core$ with $\Delta E_{D_{3d}-hex}^{PW91} = 0.4 / \Delta E_{D_{3d}-hex}^{PBE} = 0.3$ and $\Delta E_{hex-core}^{PW91} = 5.3 / \Delta E_{hex-core}^{PBE} = 5.4$, which is not reproduced by the **average** potential but is observed for high weightings of the parameter sets **I–III**. Concerning a very strong destabilisation of *core* homotop ($\Delta E_{hex-core} > 10$

Table 7.5: Summary of the weighting representation for Pt-Au and Cu-based systems in the parameter sets **I**, **II** and **III**.

Parameter set	weighting	
	w (set I), w_s (set II) and w_a (set III)	
	$w, w_s, w_a = 0.0$	\longrightarrow $w, w_s, w_a = 1.0$
I ($P=A, \xi, p, q$)	$P_{\text{Pt-Au}} = P_{\text{Au-Au}}$	$P_{\text{Pt-Au}} = P_{\text{Pt-Pt}}$
	$P_{\text{Cu-Pd}} = P_{\text{Cu-Cu}}$	$P_{\text{Cu-Pd}} = P_{\text{Pd-Pd}}$
	$P_{\text{Cu-Au}} = P_{\text{Cu-Cu}}$	$P_{\text{Cu-Pd}} = P_{\text{Au-Au}}$
	$P_{\text{Cu-Pt}} = P_{\text{Cu-Cu}}$	$P_{\text{Cu-Pd}} = P_{\text{Pt-Pt}}$
II ($P=A, \xi$)	$P_{\text{Pt-Au}} = P_{\text{Au-Au}}$	$P_{\text{Pt-Au}} = P_{\text{Pt-Pt}}$
	$P_{\text{Cu-Pd}} = P_{\text{Cu-Cu}}$	$P_{\text{Cu-Pd}} = P_{\text{Pd-Pd}}$
	$P_{\text{Cu-Au}} = P_{\text{Cu-Cu}}$	$P_{\text{Cu-Pd}} = P_{\text{Au-Au}}$
	$P_{\text{Cu-Pt}} = P_{\text{Cu-Cu}}$	$P_{\text{Cu-Pd}} = P_{\text{Pt-Pt}}$
III	$A_{\text{Pt-Au}} = A_{\text{Pt-Pt}}$	$A_{\text{Pt-Au}} = A_{\text{Au-Au}}$
	$\xi_{\text{Pt-Au}} = \xi_{\text{Au-Au}}$	$\xi_{\text{Pt-Au}} = \xi_{\text{Pt-Pt}}$
	$A_{\text{Cu-Pd}} = A_{\text{Pd-Pd}}$	$A_{\text{Cu-Pd}} = A_{\text{Cu-Cu}}$
	$\xi_{\text{Cu-Pd}} = \xi_{\text{Cu-Cu}}$	$\xi_{\text{Cu-Pd}} = \xi_{\text{Pd-Pd}}$
	$A_{\text{Cu-Au}} = A_{\text{Au-Au}}$	$A_{\text{Cu-Au}} = A_{\text{Cu-Cu}}$
	$\xi_{\text{Cu-Au}} = \xi_{\text{Cu-Cu}}$	$\xi_{\text{Cu-Au}} = \xi_{\text{Au-Au}}$
	$A_{\text{Cu-Pt}} = A_{\text{Pt-Pt}}$	$A_{\text{Cu-Pt}} = A_{\text{Cu-Cu}}$
	$\xi_{\text{Cu-Pt}} = \xi_{\text{Cu-Cu}}$	$\xi_{\text{Cu-Pt}} = \xi_{\text{Pt-Pt}}$

Table 7.6: Ratio of the Gupta potential parameters for the extended studies (for each binary system, A is the first element and B is the second element).

parameter	Pt-Au	Cu-Pd	Cu-Au	Cu-Pt
A_B/A_A	0.69	2.04	2.41	3.48
ξ_B/ξ_A	0.66	1.40	1.46	2.20
p_B/p_A	0.96	0.99	0.93	0.97
q_B/q_A	1.01	1.64	1.77	1.76

$\Delta E_{D_{3d}-hex}$), the closest to give this is $w, w_s = 0.8$ of the parameter sets **I** and **II**. Meanwhile, the DFT calculations for the $core \ll D_{3d} < hex$ ($\Delta E_{core-D_{3d}}^{PW91/PBE} = 2.6$ and $\Delta E_{D_{3d}-hex}^{PW91} = 0.6$ / $\Delta E_{D_{3d}-hex}^{PBE} = 0.7$) are reproduced qualitatively by wider parameter weights for composition (6,32). Hence, the composition (32,6) becomes a determinant, for which the heteronuclear interaction between Pt-Au should be biased ($w, w_s = 0.8$) towards Pt-Pt.

7.6.2 Cu-Pd

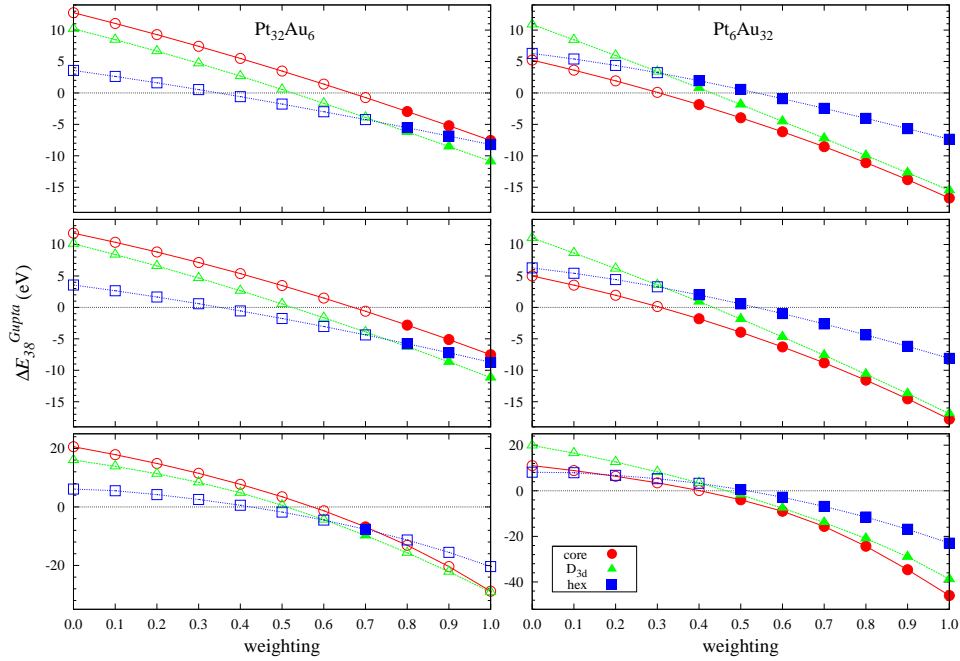
The **average** potential does not reproduce the DFT homotop order of Cu-Pd for both compositions. For composition (32,6), high weightings of the parameter sets **I–III** gives a similar homotop rank to that calculated by the DFT: $D_{3d} < core < hex$. The gaps between homotops are: $\Delta E_{D_{3d}-core}^{PW91/PBE} = 1.2$ and $\Delta E_{core-hex}^{PW91/PBE} = 0.8$, leaving only $w, w_s = 0.9/1.0$ (sets **I** and **II**) and $w_a = 0.6$ (set **III**). Meanwhile, composition (6,32) shows that $core$ and D_{3d} homotops are very competitive and the overall order is $core \leq D_{3d} < hex$ ($\Delta E_{core-D_{3d}}^{PW91} = 0.02$ / $\Delta E_{core-D_{3d}}^{PBE} = 0.03$ and $\Delta E_{D_{3d}-hex}^{PW91/PBE} = 0.3$). Similarly to the composition (32,6), this stability order is reproduced for high weightings of the parameter sets **I–III** (except for $w = 0.9-1.0$ of set **I**). It is apparent from the observation of composition (32,6) that surface mixing between Cu and Pd (D_{3d}) is preferred. For the other composition, (6,32), $core$ prevails but, D_{3d} is separated by only a very small gap.

7.6.3 Cu-Au

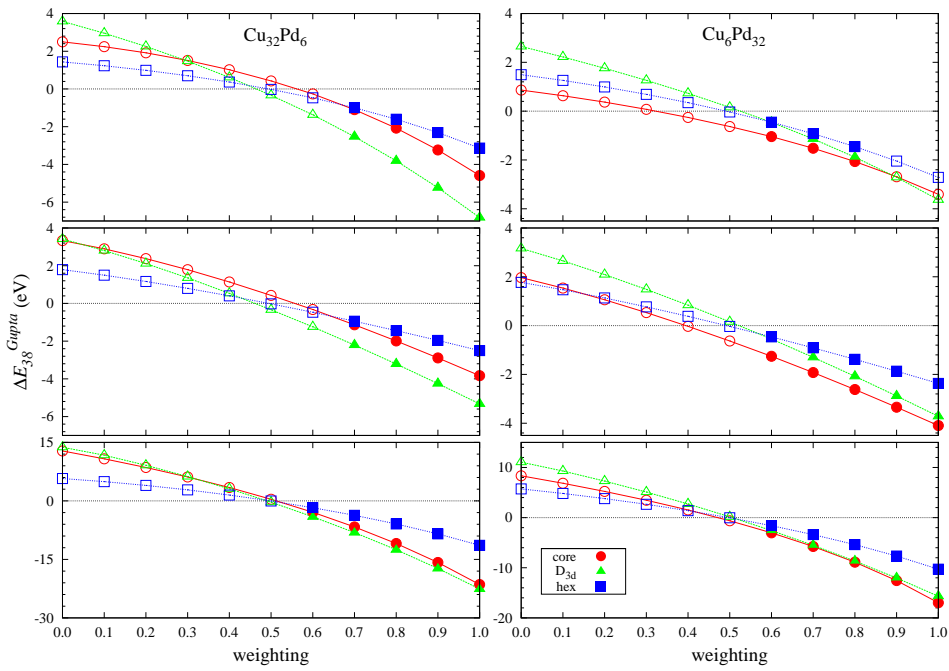
Of the Cu-based series studied in this work, Cu-Au is the only binary for which the **average** potential agrees with the DFT predictions on the stability of the three homotops (*i.e.*, reproduced the DFT predictions) for both compositions of the TO clusters. In addition, a qualitative agreement is also observed for lower weightings for the parameter sets **I–II** (*i.e.*, biased towards Cu, $w = 0.2-0.5$ of set **I** and $w_s = 0.3-0.6$ of set **II**). On the other hand, the plots for the parameter set **III** show that the homotop

Table 7.7: Excess energies (in eV) of the three TO homotops for Pt-Au, Cu-Pd, Cu-Au and Cu-Pt clusters from the DFT and EP (the **average** and weighted potential) calculations for compositions (32,6) and (6,32). For the parameter sets **I–III** of the weighted potentials, only weightings that reproduced the homotop stability rank in the DFT predictions is shown. (* Denotes potential where the homotop order is not consistent with the DFT calculations.)

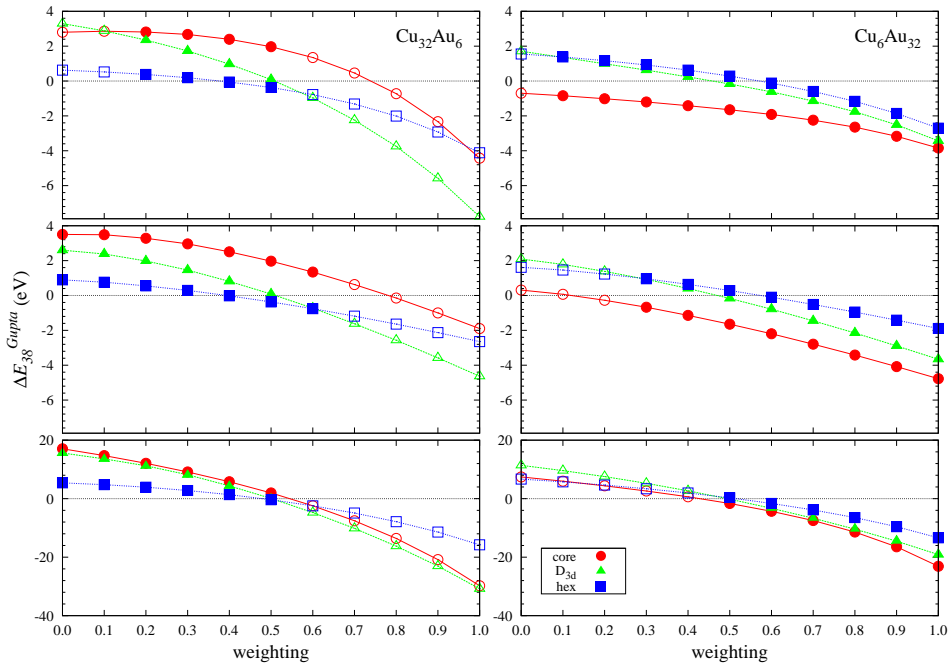
homotops	DF		EP	
	PW91	PBE	average	parameter sets I–III
			Pt ₃₂ Au ₆	
<i>D</i> _{3d}	-0.354	-0.653	0.549*	0.8-1.0 (I), 0.8-1.0 (II) and 0.7 (III)
<i>hex</i>	0.056	-0.346	-1.769*	
<i>core</i>	5.405	5.076	3.483*	
			Pt ₆ Au ₃₂	
<i>core</i>	-0.166	-3.730	-3.946	0.4-1.0 (I), 0.4-1.0 (II) and 0.5-1.0 (III)
<i>D</i> _{3d}	2.415	-1.115	-1.841	
<i>hex</i>	3.053	-0.408	0.559	
			Cu ₃₂ Pd ₆	
<i>D</i> _{3d}	-3.940	-3.882	-0.336*	0.7-1.0 (I), 0.7-1.0 (II) and 0.6-1.0 (III)
<i>core</i>	-2.731	-2.700	0.427*	
<i>hex</i>	-1.894	-1.878	-0.023*	
			Cu ₆ Pd ₃₂	
<i>core</i>	-1.902	-1.887	-0.631*	0.6-0.8 (I), 0.6-1.0 (II) and 0.6-1.0 (III)
<i>D</i> _{3d}	-1.875	-1.850	0.156*	
<i>hex</i>	-1.590	-1.538	-0.033*	
			Cu ₃₂ Au ₆	
<i>hex</i>	-1.237	-1.921	-0.370	0.2-0.5 (I), 0.0-0.6 (II) and 0.0-0.5 (III)
<i>D</i> _{3d}	-0.890	-1.556	0.083	
<i>core</i>	3.528	2.796	1.970	
			Cu ₆ Au ₃₂	
<i>core</i>	0.974	-2.672	-1.647	0.1-1.0 (I), 0.3-1.0 (II) and 0.5-1.0 (III)
<i>D</i> _{3d}	1.908	-1.727	-0.169	
<i>hex</i>	2.957	-0.599	0.284	
			Cu ₃₂ Pt ₆	
<i>D</i> _{3d}	-5.653	-5.557	-4.271*	0.7-1.0 (I), 0.8-1.0 (II) and 0.7 (III)
<i>core</i>	-3.451	-3.446	-5.846*	
<i>hex</i>	-2.787	-2.698	-0.858*	
			Cu ₆ Pt ₃₂	
<i>D</i> _{3d}	-3.526	-3.260	-1.039*	0.9-1.0 (I), 0.8-1.0 (II) and 0.6-0.7 (III)
<i>core</i>	-3.159	-2.855	-1.497*	
<i>hex</i>	-1.924	-1.636	-2.389*	



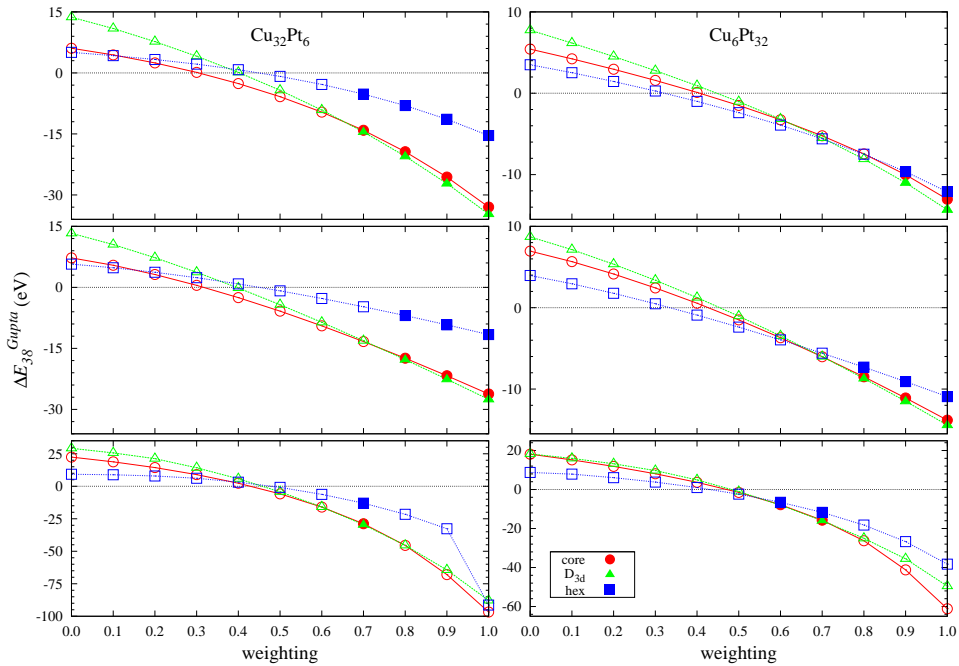
(a) Pt-Au



(b) Cu-Pd



(c) Cu-Au



(d) Cu-Pt

Figure 7.9: Stability ordering of the three TO homotops of (32,6) and (6,32) (a) Pt-Au, (b) Cu-Pd, (c) Cu-Au and (d) Cu-Pt clusters for the EP calculations with the weighted potential of parameter sets **I** (*top*), **II** (*middle*) and **III** (*bottom*). Consistent ordering compared with the DFT calculations is denoted with the filled point symbols.

rank is only reproduced for $w_a = 0.5$ (*i.e.*, the **average** potential).

For composition (32,6), *hex* is preferred but by only 0.3/0.4 eV (with the PW91 / PBE, respectively) over D_{3d} . It is, however, very clear that the larger Au ($r_{\text{Au}} = 1.44$ *vs.* $r_{\text{Cu}} = 1.28$ Å) is unlikely to reside in the core sites ($\Delta E_{D_{3d}\text{-core}}^{\text{PW91/PBE}} = 4.4$). Meanwhile, $\Delta E_{D_{3d}\text{-core}} \approx 10 \times \Delta E_{\text{hex-}D_{3d}}$, which is reproduced when the weighting $\rightarrow 0.5$ (*i.e.*, the **average** potential). On the other hand, the homotop order for the composition (6,32) is *core* < D_{3d} < *hex*, where equivalent gaps between homotops ($\Delta E_{\text{core-}D_{3d}}^{\text{PW91/PBE}} = 0.9$ and $\Delta E_{D_{3d}\text{-hex}}^{\text{PW91}} = 1.0$ / $\Delta E_{D_{3d}\text{-hex}}^{\text{PBE}} = 1.1$) are observed and this behaviour is reproduced for weighting $\rightarrow 1.0$. Hence, no concrete conclusion can be made for the parameter weight to give the most accurate predictions.

7.6.4 Cu-Pt

Cu-Pt is another system where the **average** potential is unfavourable in defining the bimetallic interactions, similar to Cu-Pd. Combination of observations for the compositions (32,6) and (6,32) shows the need for biased parameters towards Pt-Pt ($w = 0.9$ -1.0, $w_s = 0.8$ -1.0 and $w_a = 0.7$, for sets **I**–**III**, respectively). For both compositions, the mixed ordering (D_{3d}) prevails, with $D_{3d} \ll \text{core} < \text{hex}$ for the composition (32,6) and $D_{3d} < \text{core} \ll \text{hex}$ for the composition (6,32).

7.7 Chapter Conclusions

Parameterisation of the Gupta potential (parameter set **III** ($w_a = 0.7$ -0.9)) is seen to reproduce the **DFT-fit** potential for Pd-Au clusters but the **exp-fit** parameters show quite different results for structures and homotops. The surface mixing (of the core-shell clusters) predicted by these potentials is, however, disfavoured at the DFT level for cluster compositions (32,6) and (6,32). The closest agreement to the DFT calculations is given by the **average** potential.

For Pd-Pt clusters, the **average** is also the potential that gives the most accurate

predictions against the DFT calculations, as compared with the **DFT-fit** or weighted (parameter sets **I–III**) potentials. Clusters are predicted to adopt a slightly more surface-mixed core-shell ordering, although there is a strong competition from the surface-segregated ordering. Meanwhile, having the potential towards w , $w_s = 0.6$ (*i.e.*, slightly biased to to the Pt-Pt) gives only a slightly improvement to the calculation results.

Mixed ordering is preferred for Ni-Al. This ordering is clearly preferred for the composition (32,6) and is competitive for the composition (6,32), although the latter composition shows a slight prevalence of the core-shell. These predictions are closely matched for $w_a = 0.8-0.9$ of the parameter set **III**, which is the region where the **exp-fit** is located.

Biased parameterisation (towards the stronger Pt-Pt, $w_s = 0.8$ of parameter set **III**) emulates the DFT prediction for $\text{Pt}_{\text{core}}\text{Au}_{\text{shell}}$ clusters, with a close competition between surface-mixed and surface-segregated. For Cu-Pd and Cu-Pt clusters, mixed ordering is adopted at the DFT level, which can be reproduced at the EP level by highly weighted (towards the stronger bonds Pd-Pd and Pt-Pt, respectively) potentials. On the other hand, a prevalence of the core-shell configuration for Cu-Au clusters is best represented by the **average** potential.

This work shows the ability to benchmark the existing (**average** and fitted) potentials against the parameters sets **I–III** for several bimetallic systems. The EP-DF method gives acceptable estimation of the potential accuracy and indicates that simple parameterisation reproduces the DFT predictions. However, unlike polyicosahedral motifs, the stabilisation due to atomic size effects in TO is not very obvious. Furthermore, with only two-layers available, it is not possible for the cluster to adopt intermediate core-shell/mixed (*i.e.*, onion-like) configurations, as has been shown in larger sizes of Pd-Pt clusters.

The observations in this chapter only focussed on the three homotops (*core*, *hex* and

D_{3d}) of a fixed TO, excluding many other effects, *e.g.*, size, structure and composition (as only two compositions are considered). Hence, it seems to be a good procedure for the EP calculations to involve several parameters, with a simplified combination of methods, in the hope of achieving accurate predictions and a better coverage of all possible solutions.

Chapter 8

Pd-Au Clusters Supported on MgO(100)

This chapter will discuss 30- and 40-atom Pd-Au clusters supported on MgO(100) by a combined EP-DF approach. In Section 8.2, details of the EP (Subsection 8.2.1), metal-oxide interactions (8.2.2), potential parameterisations (8.2.3) and the DFT calculations (8.2.4) will be described, as a slightly different method was applied from that used for the free clusters (in the previous chapters). In the results and discussion (Section 8.4), the focus will be on the variations and the crossovers of structures for the three different studied compositions (Pd-rich, medium and Au-rich). Optimisation at the DFT (8.3.3) and EP (8.3.4) levels will also be discussed, in addition to the EPs checks (8.3.1 - 8.3.2).

8.1 Introduction

Nanoclusters of the transition metals have been shown to adopt a variety of structures (*e.g.*, fcc, icosahedra and decahedra), due to their energetic competition [66, 358, 371, 620, 630, 831]. This means that cluster structures and properties can be tailored for different applications. Recently, supported clusters have attracted many researchers as the combination of metal-metal and metal-substrate [630, 832] interactions give more ways of optimising the catalysts. The use of amorphous carbon, for example, produces a wide range of differently shaped gold and palladium particles but selection of magnesium oxide (MgO) stabilises fcc-based motifs [480, 833, 834].

In addition to being a support, an oxide substrate is widely believed to act as an active medium in catalytic chemical reactions. Different supports have been reported to show optimum catalytic performance for Pd-Au, especially in the selective oxidation of styrene (Al_2O_3 [835]), toluene (carbon [836]), glycerol [735] and benzyl alcohol [731] (TiO_2). In the direct synthesis of hydrogen peroxide, equivalent results between carbon and SiO_2 supports have been observed [837].

Much modelling of bimetallic clusters [345, 620, 622], however, focuses on free particles, due to computational limitations. However, the inclusion of the support would be of great importance in gaining a more accurate representation of the real heterogeneous catalytic system. For this reason, nanocluster interactions with the surfaces of several types of support have been reported: Al_2O_3 , Carbon, MgO, SiO_2 , Fe_2O_3 , TiO_2 and CeO_2 [460, 461, 838]. Metal oxides such as MgO particularly are interesting for their strong electrostatic interactions [839]. Furthermore, MgO surfaces with minimum structural defects are relatively easy to prepare [840] and act as a perfect background image for the electron microscopy [833]. Computationally, it is possible for the MgO to be modelled as a flexible slab [841, 842].

As regards the the MgO surface, single atom calculations have shown a preference for adhesion of metal on oxygen sites (over surface Mg and hollow sites) for Pd [832, 843, 844] and Au [477, 487, 845]. This preference is supported by findings from grazing incidence X-Ray diffraction [846] and electron microscopy [847]. This behaviour is associated with the “metal-on-top” stabilisation [487], van der Waals interactions [848] and also charge transfers [849]. In contrast, few studies [850, 851] have suggested otherwise – a preference for the Mg site.

On interaction with the MgO support, compact structures of Pd clusters are favoured, starting at very small sizes [852, 853], as the best configuration to reduce the surface energy [854, 855]. Au, however, shows a more complex combination of metal-substrate interactions with additional effects of stickiness, directionality and electronic

shell closure [487, 856, 857]. Interestingly, both metals show very good epitaxy of Au(100) [833, 858] or Pd(100) [846, 859] on MgO(100) that can be linked with small lattice mismatch (4.08 Å(Au), 3.89 Å(Pd) and 4.20 Å(MgO) [860]). A small lattice expansion (<3% for Au [833, 841] and Pd [854, 859, 861, 862]) has been observed and by the size of 400 atoms, relaxation occurs [854, 859] *via* misfit transfer from the interfacial area into the clusters [480] and structural transformation [478].

Even at room temperature, good cube-on-cube epitaxy between Pd cluster and MgO substrate has been reported [859], indicating a strong metal-support interaction. As a result, different magic numbers arise compared to the free particles [853]. The DFT approach has reproduced this behaviour [484, 852, 863] and, in combination with the EP global optimisation [485, 717, 864], small to large clusters can be studied. Understanding epitaxial phenomena would be beneficial as it is suggested to enhance catalytic activity through a spillover mechanism [865] in CO oxidation [866–870], NO dissociation [871] and the CO+NO reaction [872, 873]. Other proposed explanations for the enhancement by the MgO support are: strain effects [874], better dispersion [724], introduction of new active sites [875, 876] and electronic effects [834].

An extensive database of energetics, structures and segregation has been developed [345, 620, 622] for small Pd-Au clusters (<100 atoms) as free particles. Combined with the previous findings for pure Au and Pd clusters on the MgO(100) surface [484, 485, 630, 831, 864, 877–879], the aim is to extend the study on the behaviour of Pd-Au nanoalloy clusters when supported on MgO(100), by observing the structural and chemical ordering of 30- and 40-atom clusters. Compositional variation is also taken into account by selecting three compositions that represent Pd-rich, medium and Au-rich clusters.

8.2 Computational Details

Study of the interaction between Pd-Au nanoalloy clusters and the MgO substrate involved two steps combining computational methods [485, 717, 864]: global optimisation using the EP and DFT calculations. At the EP level, the Gupta potential was used to model inter-atomic interactions within the cluster [377, 616]. On the other hand, metal-oxide interactions were used from parameters that have been fitted to the *ab initio* calculations [478, 880].

The effect of the Monte Carlo elemental move on small free clusters was investigated for composition (19,19) of 38-atom Pd-Au. This size was selected as it is well understood, based on many previous studies [43, 203, 205, 255, 269, 270, 306, 345, 352, 374, 376, 620, 627, 881]. The effects of different EPs (**average**, **DFT-fit** and **exp-fit**) were also investigated using clusters of this composition.

For optimisation of the DFT and parameterisation of the EP, the calculations were carried out on 38-atom clusters of the compositions (6,32) and (32,6), as described in Chapter 7 (*see* Figure 7.1). The stability rank of “*core*”, “*hex*” and “*D_{3d}*” homotops was used as an indicator for qualitative checks.

8.2.1 Empirical Potential Global Optimisation

At the EP level, calculations were performed with the BHMC [518] algorithm. For each cluster size (and composition), 10-15 *unseeded* searches of 200,000 elementary moves each were performed, where the searches were started from random positions in a cubic box just on top of the MgO slab. In addition, *seeded* searches were also performed, in which the simulation was started with pre-defined coordinates, mostly from the previous calculations either from the same system, other bimetallics or pure clusters [613]. Moreover, the Monte Carlo steps were performed at several temperatures (0-3,500 K).

One of the most crucial aspects in the global optimisation exploration is obtaining

an accurate empirical or semi-empirical potential. If experimental data are available, then it is possible to fit the potential but new materials (for example bimetallic clusters) preclude these and, as an alternative, the fitting of the potential is carried out to the data from higher level calculations (*e.g.*, DFT). For this reason, a considerable amount of modification of the Gupta potential has been undertaken and three alternative sets of heteronuclear Pd-Au parameters have been considered in previous studies: the “**average**”, “**DFT-fit**” and “**exp-fit**” potentials [345, 620, 622] (*see* Table 2.3(a)). For this chapter, these three potentials were used and compared with another potential, namely the “**new**” potential: the potential that has been derived by further fitting of the existing potential [68, 205, 255, 377]. The differences between potentials is shown in Table 8.1.

For the **new** potential, the weaknesses of the previous potentials have been taken into account, including metal *stickiness*, fcc-hcp energy gap and surface energy. (1) *Stickiness* is the tendency of clusters to maintain the non-crystalline structures upon

Table 8.1: Gupta potential parameters for elemental Pd and Au; and bimetallic Pd-Au.

parameters	average	DFT-fit	exp-fit	new
Pd parameters				
A (eV)	0.1746	0.1653	0.1715	0.0501
ξ (eV)	1.7180	1.6805	1.7019	1.1924
p	10.8670	10.8535	11.0000	17.0000
q	3.7420	3.7516	3.7940	2.0900
Au parameters				
A (eV)	0.2061	0.2091	0.2096	0.1289
ξ (eV)	1.7900	1.8097	1.8153	1.5223
p	10.2290	10.2437	10.1390	12.5000
q	4.0360	4.0445	4.0330	3.5500
Pd-Au parameters				
A (eV)	0.1900	0.1843	0.2764	0.0895
ξ (eV)	1.7500	1.7867	2.0820	1.3574
p	10.540 0	10.5420	10.5690	16.5500
q	3.8900	3.8826	3.9130	2.2360

internal strain and is seen experimentally. For the EP to be consistent with this, parameters have been fitted to the experimental bulk modulus, cohesive energy and lattice spacing. (2) Gupta-based potentials [68, 205, 255, 345, 377, 620] tend to predict hcp stability only for very large sizes. This is because the binding energy for hcp is lower than fcc and has been corrected in this potential. (3) Surface energy would be important for the binary clusters (compared with the pure) and the inclusion of this effect has been achieved by taking the data from the experimental data or DFT (when the former is not available). Corrections of factors (2) and (3) require simultaneous modifications of the p (increase) and q (decrease) parameters. By doing this, the range of the repulsion is shortened, with the opposite effect on the range of the attraction (up to the third-neighbour distance). However, this new fitting requires binary systems that have tendency to mix with small lattice mismatch [881].

8.2.2 Metal-Oxide Interactions

Metal-oxide interactions are described in detail in Ref. [613]. The parameters have been fitted to first-principles calculations, taking into account the weak metal-oxide from nonreactive interfaces [882]. The metal-oxide features include: no inter-diffusion, small charge transfer (due to the polarisation effects and the van der Waals interactions) and a very small contribution of covalent bonds. However, they do not include the “metal-on-top” effect [487] but, as an alternative, the parameters are fitted to the ideal systems and DFT calculations. Also, due to the relatively small (of the order of few hundredths of eV) contribution to the total energy, van der Waals interactions are not included.

Interactions between metal atoms and the substrate are described by the contribution in the x , y and z directions. The z -coordinate models the interactions with Morse-like character while the x - and y -coordinates, which are parallel to the (110) directions, are represented by a periodic cosine function. The total energy is a sum from each of the metal-substrate interactions, which is given by the functional in Eq. 8.1

[478].

$$\begin{aligned}
 E_i^{mo}(x_i, y_i, z_i, Z_i) &= a_1(x_i, y_i, Z_i) \left\{ e^{-2a_2(x_i, y_i, Z_i)} - 2e^{-a_2(x_i, y_i, Z_i)[z_i - a_3(x_i, y_i, Z_i)]} \right\}, \\
 a_j(x_i, y_i, Z_i) &= b_{j1}(x_i, y_i) + b_{j2}(x_i, y_i)e^{-Z_i/b_{j3}(x_i, y_i)} \\
 b_{jk}(x_i, y_i) &= c_{jk1} + c_{jk2} \{ \cos(\chi x_i) + \cos(\chi y_i) \} \\
 &\quad + c_{jk3} \{ \cos(\chi(x_i + y_i)) + \cos(\chi(x_i - y_i)) \}
 \end{aligned} \tag{8.1}$$

where i = each metal atom, Z_i = nearest neighbours (within 125% of the bulk distance) and $\chi = 2\pi/a$ (where a is the oxygen-oxygen distance). A total of 27 c_{jkl} parameters for each metal is listed on the internet [883], taken from Pd/MgO [478] and Au/MgO [613] works. For the small clusters ($N \leq 30$), the potential gives fairly good results in comparison with the DFT calculations [484, 485].

8.2.3 Potential Parameterisations

Parameterisation of the Gupta potential (Chapter 2) has been carried out for the **new** potential. Weighting parameters have been investigated in the range $0 \leq w \leq 1$, in steps $\Delta w = 0.1$. A single parameterisation (A , ξ , p or q) is investigated by employing Equation 2.31 (parameter set **I**), while combined parameterisations were applied using Equation 2.32 (parameter set **II**: $A+\xi$ or $p+q$) or Equation 2.33 (parameter set **III**: $A-\xi$ or $p-q$). The latter provides varied parameters in the opposite sense (“anti-symmetric”), allowing regions of Pd-Au parameter space to be explored which have: (i) low A and high ξ values (or p and q), corresponding to strong Pd-Au bonding and (ii) high A and low ξ (or p and q), corresponding to weak Pd-Au bonding.

8.2.4 Density Functional Theory Calculations

After generating a database from the EP searches, the lowest-energy and several higher energy (*i.e.*, low-lying) local minimum clusters for each size and composition were then re-optimised by the DFT calculations using the QE [586] PWscf DFT code, with the PBE XC functional [572] and the ultrasoft pseudopotentials.

The MgO(100) substrate was modelled by a two-layer slab of 36 Mg and 36 O atoms (6×6 cell) in each layer, fixed in the lattice positions of the MgO rock-salt bulk structure (with an experimental MgO distance of 2.104 Å). The lattice spacing in the perpendicular (100) direction is about 13 Å [485]. Different slab sizes have been used [630] to allow sufficient distance between periodic images but, in this work, the 6×6 cell is necessary for the particular studied sizes. The MgO substrate was fixed at the experimental distances of Mg and O atoms, as it has been shown [630] that a non-rigid substrate plays a qualitatively very minor role in the PBE calculations. However, selected clusters were also studied by allowing the substrate to relax together with the clusters, with differences in energy of less than 0.1 eV, and no changes of ordering were observed (although there was an increase in the time taken to reach convergence).

8.3 Optimisation of the Calculations

8.3.1 Structural Variations of Pd₁₉Au₁₉: Effect of the Monte Carlo Elemental Move

The TO motif is the most stable isomer at the DFT level for 38-atom clusters [255, 345, 622] and, during the BHMC searches, the *shake* or *dynamics* move is the best Monte Carlo elementary move for finding this motif. Runs with these moves give a minimum that deviates only 0.03 and 0.10 eV (for *shake* and *dynamics*, respectively at 0 K) relative to the GM, indicating exploration near to the ground state. These deviations are increased with increasing temperature (0.09 and 0.16 eV at 2,000 K), for which other close-competitive motifs (Dh and incomplete Mackay-polyicosahedral (inc-Ih-Mackay)) start to be found. However, only one or two non-TO motifs are found at a certain temperature, suggesting that these elemental moves do not provide a variation of structure. For the same reason, *bonds*, *ball*, *shell* or *high energy atoms* elemental moves are also insignificant. This leaves the *exchange* move, which is identified to provide a wider energy variation, *i.e.*, variation in structural motifs. The searches with the *exchange*

move also give unfavourable fcc-hcp structures (in addition to the other competitive structures: TO, Dh and inc-Ih-Mackay), which is not found with the other elementary moves.

8.3.2 Structural Variations of Pd₁₉Au₁₉: Effect of the Choice of Empirical Potential

Different EPs are likely to give variation in the structural motif and ordering preferences; however, their accuracy can be benchmarked, for example against the DFT calculations. Figure 8.1 shows how the selected motifs of 38-atom Pd-Au clusters from the EP (the **average**, **DFT-fit** and **exp-fit** potentials) runs fare at the DFT level. High accuracy is said to be achieved when the total energy at the EP level matches with the DFT calculations. The observation, however, reveals that none of these potentials is clear-cut to be the best, explaining why previous works [345, 620] do not focus on a single potential. This is a known issue with semi-empirical calculations and closing the gap between the semi-empirical and first principle methods is always a challenge.

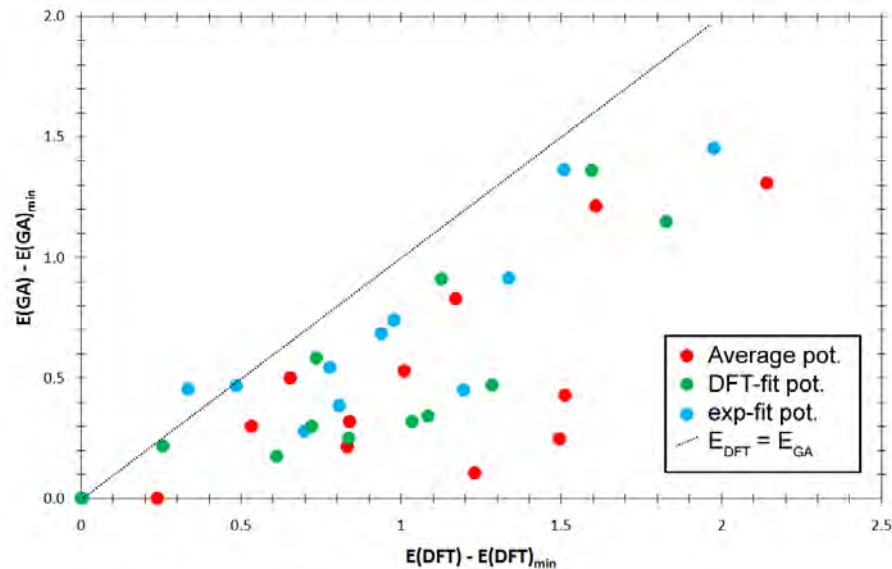


Figure 8.1: Energetic profiles of various structural motifs for 38-atom Pd-Au calculated with the **average**, **DFT-fit** and **exp-fit** potentials.

8.3.3 Optimisation of the DFT Calculations (Code, Functionals, Convergence)

Comparison of the discrepancy of outcomes between the QE and NWChem codes is meaningful for validation. Our earlier works with the NWChem code mostly used the PW91 exchange and correlation functionals [569–571] but this functional is not available for the Pd in QE. Hence, the PBE functional (which are available for both DFT codes) is selected for a comparison between two codes, as shown in Figure 8.2. Also shown in the figure are calculations with the other functionals (which are available for both Pd and Au): PBE, PZ81 LDA [628], PBEd and PZ81d [586].

All calculations lead to similar homotop rank (based on energy) for both compositions. For the composition (6,32), there is high agreement of the gap of $hex > D_{3d} > core$. The different codes (plane wave QE *vs.* orbital based NWChem), however, exhibit a slight variation for the composition (32,6) results ($core > D_{3d} > hex$); nevertheless, the energy ordering is consistent.

In addition to the qualitative agreement, there are only small variations (*i.e.*, quan-

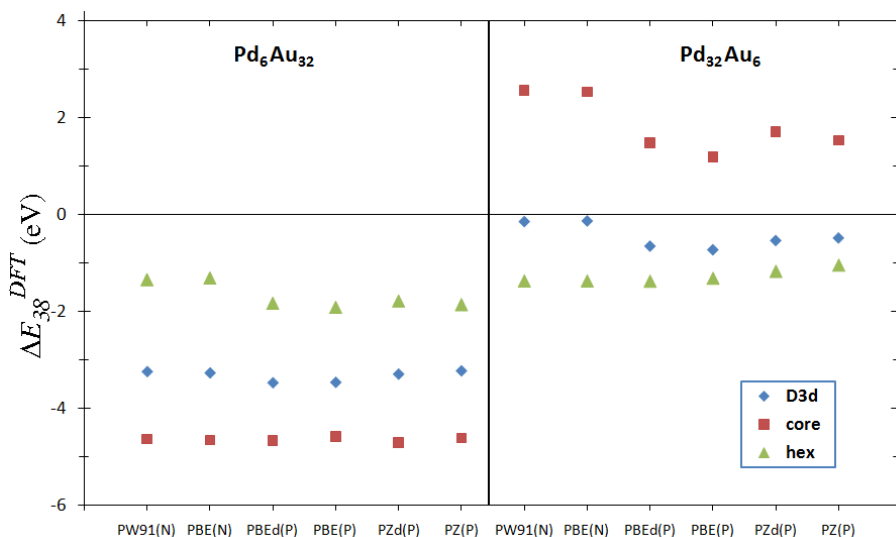


Figure 8.2: Effect of different GGA on the DFT calculations of (6,32) and (32,6) Pd-Au clusters (in the bracket, N=NWChem and P=Plane wave QE).

titative agreement) between all possible combinations of functionals for the QE calculations. It can therefore be assumed that there are acceptable effects of the differences in the code and functional being used, hence, comparison with the previous calculations [255, 345] is reasonably valid.

Results for the CPU time optimisation (for QE) on compositions (32,6) and (6,32) are shown in Figure 8.3. The first y -axis (bar graph) shows CPU time (for a completed calculation) as a measurement for the degree of convergence and the second y -axis (line graph) shows total energy, reflecting accuracy of the calculations. This calculation is based on 16 processors on the BlueBEAR computer at the University of Birmingham, UK [884]. Generally, the calculation is said to be accurate when the error for the energy differences <5 meV/atom or $< 1\%$ [586].

Careful consideration is needed for the *kinetic energy cut-off* and *cell size* selection, as these parameters not only affect the convergence but also the accuracy of the calculation. The *kinetic energy cut-off* parameter of 40 Ry (544 eV) is the lowest on the plateau, reflecting the minimum of acceptable cut-offs before the energy rises dramatically (lower cut-off, non-accurate), while equilibrium lattice constant for the *cell size* parameter is seen at 30 Bohr (15.9 Å) for the tetragonal Bravais-lattice. Meanwhile, the *degauss* parameter does not severely affect the accuracy as it is normally set at a very low value and, up to *degauss* = 0.004 (ordinary Gaussian spreading), the level of tolerance, is acceptable. On the other hand, *convergence threshold* and *mixing- β* parameters only affect the convergence of calculation. For *convergence threshold*, a parameter between 1.00×10^{-6} and 1.00×10^{-8} is best for the optimum CPU time. Meanwhile, *mixing- β* parameter (upon enforcing the plain (Broyden) mixing mode) seems insignificant for the free 38-atom clusters of a fixed motif (TO). However, these optimisation runs only take into account the high symmetry homotops which do not indicate how crucial this factor in a more complicated system (*i.e.*, system dependence), especially when the support is in action and the cluster has a low symmetry structure

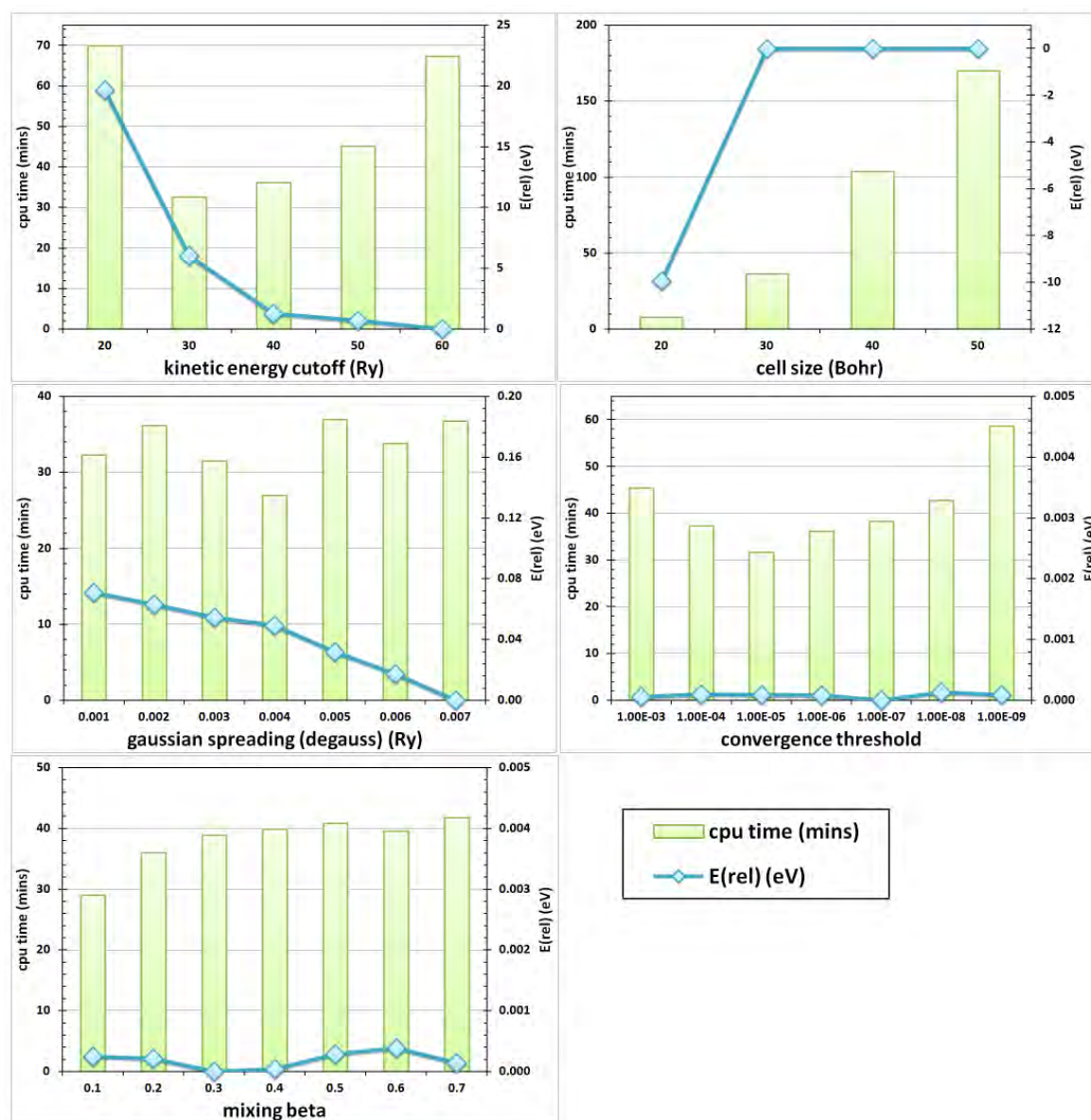


Figure 8.3: Effect of parameter choice on the convergence times and the total energies of the DFT calculations.

for which very low *mixing- β* is to be applied.

For the checks on supported clusters, the model of 20-atom Pd₁₀Au₁₀ on MgO is used. The EP calculations show that the cluster with the fcc motif is the GM. Hence, this motif with (100)PdAu-(100)MgO interface is then re-optimised with QE, using the PBE and PZ81 (available for involved all elements: Pd, Au, Mg, O) functionals to see the effects of different functionals. The results show that calculation with the PZ81 functional gives lower total energy (-0.146 eV/atom) than that of the PBE. Nevertheless, structural observations suggest there is consistency in both calculations.

8.3.4 Parameterisation of the “New” Potential

A **new** potential (see Section 8.2) is then included, in the hope for better EP exploration. Figure 8.4 shows a comparison between three previous potentials used for Pd-Au cluster calculations [345, 620] and the **new** potential which is derived in two ways: arithmetic (a) and geometric (b) means for the Pd-Au heteronuclear interactions (bimetallic potential). In terms of homotop order, all potentials show agreement with the DFT predictions for the composition (6,32); *hex* > *D*_{3d} > *core*. However, for the composition (32,6), only the **average** and **new**(a) potentials reproduce the DFT results (*core* > *D*_{3d} > *hex*). The other potentials predict the *D*_{3d} motif as the most stable configuration. Looking at the energy levels, these two potentials give a close result but the magnitude is rather far from those given by the DFT calculations. However, as far as the homotop rank is concerned, these potentials are in very good agreement with the DFT calculations.

Based on the DFT calculations, the **new**(a) potential proves to be the most consistent in both tested regimes, hence it is parameterised based on the method described in Chapter 2. The results of these parameter sets are compared with the DFT predictions, as shown in Figure 8.5. Figure 8.5(a) shows parameterisation of the *A* and ξ parameters and Figure 8.5(b) of the *p* and *q* parameters. There are four ways of parameterising: (i) *first row* represents only *A* (or *p*), (ii) *second row* – only ξ (or *q*),

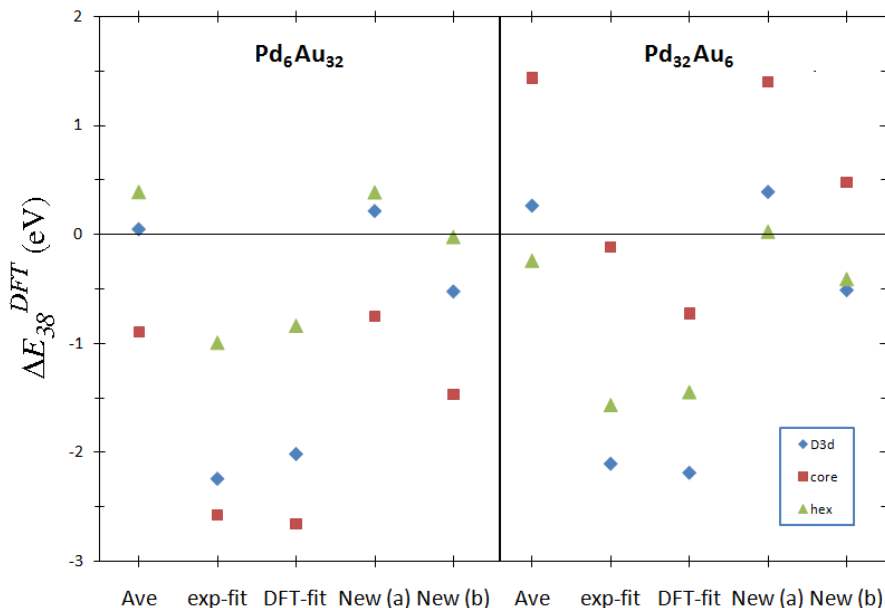


Figure 8.4: Comparison of the DFT excess energies of (6,32) and (32,6) Pd-Au clusters of the three studied homotops for several empirical potentials.

(iii) *third row* – combine A and ξ (p and q), which will be referred as $A+\xi$ or $(p+q)$ and
 (iv) *fourth row* – reverse combine A and ξ (p and q), which will be referred as $A-\xi$ or $(p-q)$. (i) to (iii) were weighted by using the Eq. 2.32 and (iv) is weighted by Eq. 2.33. Meanwhile, Figure 8.5(c) is also a result from a parameterisation with Eq. 2.32 but it involved all the parameters (A , ξ , p and q). In all styles, the non-parameterised value is kept at the average, in which $w = 0.5$ is basically the **new(a)** potential. To simplify the effects of the parameterisation, Table 8.2 shows the average of the gap between each parameter set and the DFT results. Only matching homotop ranks (EP *vs.* DFT: $core > D_{3d} > hex$ for $Au_{32}Pd_6$ and $hex > D_{3d} > core$ for Au_6Pd_{32}) are shown, with lower numbers indicating a better correlation.

Previous work [620] shows that for Pd-Au clusters, the A and ξ parameters are the main contributors to affect structure and energy. Hence, parameterisation of these components significantly affects the total energy but at the expense of crossover between the three studied motifs. This could be seen for all parameter sets involving A

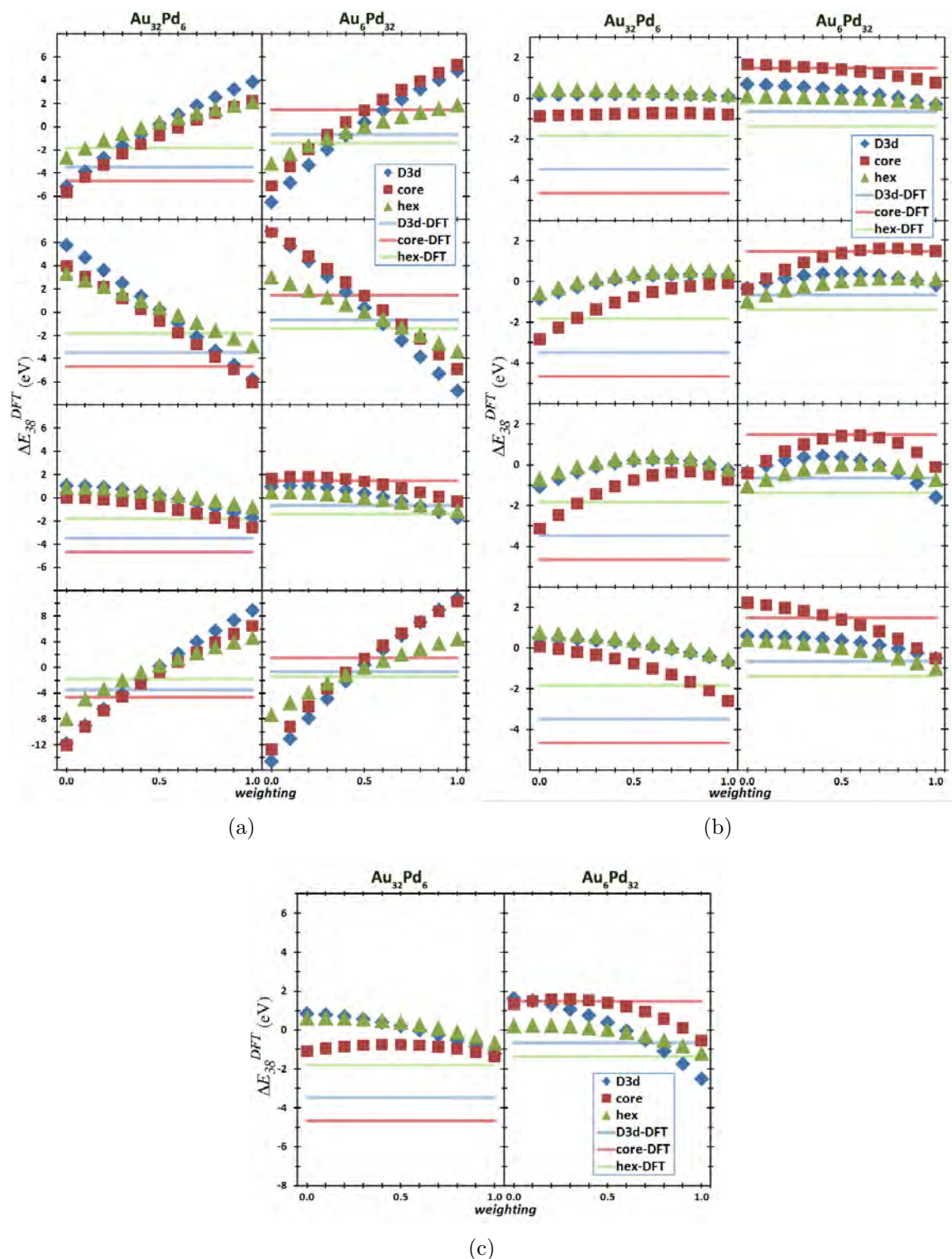


Figure 8.5: Parameterisation of the Gupta potential, with the effect of changing (solid lines are the DFT calculations): (a) parameters A and/or ξ , (b) parameters p and/or q ; (c) all the parameters (A , ξ , p and q).

Table 8.2: Average magnitude of difference between the EP (with the weighted potential) and DFT calculations. (Whenever the EP and DFT is unmatched, no value will be shown.)

w	0.0	0.1	0.2	0.3	0.4	0.5	0.6	0.7	0.8	0.9	1.0
A	-	-	-	-	-	2.1	-	-	-	-	-
ξ	-	-	-	-	-	2.1	-	-	-	-	-
$A+\xi$	-	-	-	-	-	2.1	1.9	1.7	-	-	-
$A - \xi$	-	-	-	-	-	2.1	-	-	-	-	-
p	2.1	2.1	2.1	2.1	2.1	2.1	2.0	2.0	2.0	2.0	1.9
q	-	1.6	1.8	1.9	2.0	2.1	2.1	2.2	2.2	-	-
$p+q$	-	1.5	1.7	1.9	2.0	2.1	2.1	2.1	-	-	-
$p - q$	2.5	2.5	2.4	2.3	2.2	2.1	2.0	1.9	1.8	1.6	-
all ($A+\xi+p+q$)	-	-	-	-	-	2.1	-	-	-	-	-

and/or ξ in Figures 8.5(a) and 8.5(c) and, based on Table 8.2, it is clear that only the mid-weights (close to average or just $w = 0.5$) produce matching order to those predicted by the DFT. Based on the parameters of the **new** potential (Table 8.1), the ratio between homonuclear Pd and Au for the A parameter is more than two-fold (2.574), while the ratio for the ξ is 1.277. These large differences indicate that, even with the change of just $\Delta w = 0.1$, addition/reduction is imposed to the attractive/repulsive intermetallic Pd-Au bonding.

The p and q parameters (Fig. 8.5(b)), however, only serve as determinants of the range of the repulsive and attractive interactions, respectively [377], so varying these parameters only affects the energy and the homotop rank is retained. Weighting the p and/or q parameters mostly (except extreme weighting $w \rightarrow 0.0/1.0$) gives results that agree with those of the DFT for both cluster compositions. Also from Table 8.2, the best parameterisation is identified for $w(p+q) = 0.1$, which gives the most accurate total energy (in addition of reproducing the DFT predictions of homotop rank). This weighted potential is then used in the EP global optimisation searches for 30- and 40-atom Pd-Au clusters on MgO(100).

8.4 Results and Discussion

From the EP searches, several low energy structures are selected. Compared with free clusters, supported Pd-Au clusters on MgO exhibit structures with more distortion to enable greater contact area with the substrate. These motifs are classified into four general categories: Dh, Ih, crystalline and close-packed (cp), as shown in Figure 8.6.

Only a single Dh variant (shown in the *first row* of Figure 8.6) is considered, as the others are not energetically competitive. For the icosahedral motif (*second row*), there are five variants that are in close-competition with the GM in the EP searches: incomplete anti-Mackay-polyicosahedral (inc-Ih-anti-Mackay), inc-Ih-Mackay, low symmetry polyicosahedral (anti-prism) and capped pIh⁶ [43]. Of the inc-Ih-Mackay motif, two isomers are found (difference in the cluster-substrate interfaces), one with the regular Ih arrangement in contact with MgO and the other with more atoms at the in-

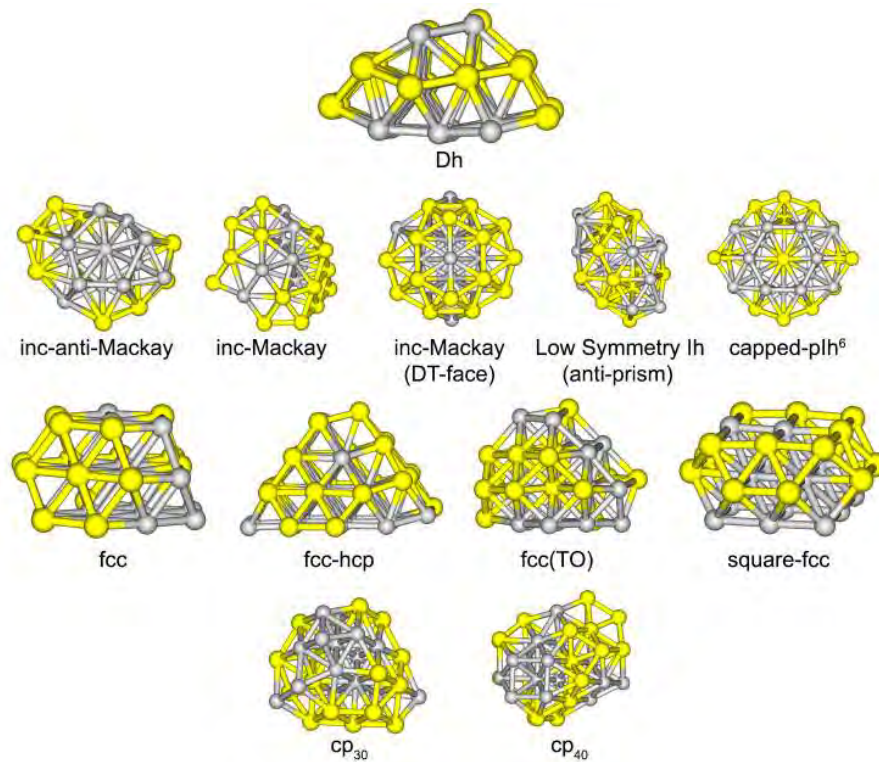


Figure 8.6: Structural motifs of 30- and 40-atom Pd-Au clusters: decahedral, icosahedra (*second-row*), crystalline (*third-row*) and close-packed (*fourth-row*).

terface - the double-tetrahedral face (DT-face). All icosahedral-based motifs are found for both sizes (30- and 40-atom clusters), except for the capped-pIh⁶ which is not found for 30-atom clusters.

Meanwhile, four fcc-based crystalline structures (*third row*) are observed at the EP level: fcc, fcc-hcp, fcc-TO and square-fcc. The first variant (fcc) is a cluster with uneven shape, square-fcc with overhanging atoms on each side of the square-shape cluster, fcc-TO is the motif derived from the 38-atom TO and fcc-hcp is hexagonal close-packed motif with an fcc stacking-fault. Although visibly they are fairly similar, the energetic profiles of all these structures are distinct.

The last group of motifs is cp (*fourth row*), which is the truncated tetrahedron based on a 20-atom tetrahedral core (30 atoms clusters, cp₃₀) and a motif with an additional fcc-hcp layer under cp₃₀ motif (40-atom clusters, cp₄₀). These two arrangements resemble the mixed decahedral-close-packed motifs commonly found for 34-atom bimetallic clusters [205, 254, 717], of which the tetrahedral (T) core (Dh-cp(T) or double-tetrahedral (DT) core (Dh-cp(DT))) is built of 10 atoms. Further atoms are growing in the (111) arrangement on the tetrahedron face, while on the vertex, the (100) configuration would complete the outer shell. It is interesting to note that in addition to Dh-cp(T), the Leary Tetrahedron (LT) [519, 694, 718] and a cp(T) motifs are competitive for clusters of 98 atoms.

In total, 11 and nine motifs (for 30- and 40-atom clusters, respectively) were chosen from the EP searches, after discarding very unfavourable (very high energy) motifs. This is basically the database (first part of the combined EP-DF method) that acts as the initial configuration for the DFT re-minimisation (second part).

Most of the selected motifs (GM and low-lying isomers) were of the clusters with uneven shapes. Upon rotation, different faces are in contact with the MgO surface. The EP searches, however, agree with the DFT, that Pd-Au clusters are the most stable when there are the most Pd atoms (of the flat surface) in contact with the substrate

(oxygen sites), as shown in Figure 8.7. In this example, all three clusters basically have the same structural arrangement (Dh) but they have different cluster-substrate interfaces. As a free cluster, the three are approximately of the same energy (only a slight variation caused by the structural distortions) but, on MgO, the greater the numbers of atoms in contact with the MgO substrate, the more stable the supported cluster. It is also seen, that, in comparison with free clusters, interaction with the MgO substrate is likely to flatten the Pd-Au clusters. However, there is a limit to the flattening process because homo- and heteroatomic metal-metal interactions retain the overall three-dimensional shape of the clusters.

The putative GM structures (at the DFT level) for the three different compositions of 30-atom [(8,22), (15,15) and (22,8)] and 40-atom [(8,22), (15,15) and (22,8)] Pd-Au clusters on a MgO(100) slab are shown in Figures 8.8 and 8.9, respectively. 30-atom clusters show strong competition between structural motifs, in which putative GM evolve from inc-Ih-Mackay [composition (8,22)], to Dh [(15,15)] and fcc-TO [(22,8)]. For clusters of the bigger sizes (40-atom), the GM start to adopt motifs which are close to the bulk (fcc), as can be seen for the compositions (30,10) (fcc-hcp) and (20,20) (fcc). The other composition, (10,30) however, adopts inc-Ih-Mackay with complete core-shell ordering (with Au at the MgO interface), consistent with the DFT calculations for the free clusters [255, 345, 620, 622]. These structural observations show that, although there are cluster-substrate effects, the structure tuning is still possible by varying the composition, as is the case for free Pd-Au clusters [345, 620, 622].

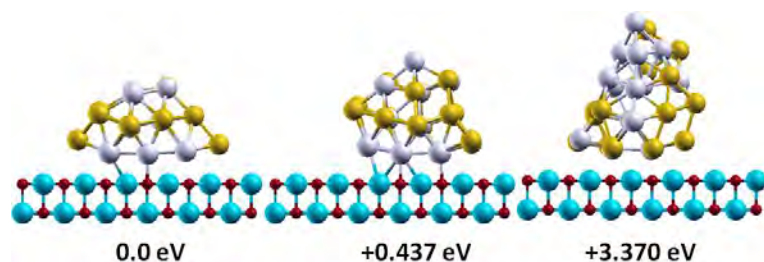


Figure 8.7: Relative energies of decahedra with different orientations and interfaces.

However, the tunability is likely to vanish for bigger clusters, based on the observation of cluster progression from 30- to 40-atoms when bulk-like fcc starts to prevail.

The second rows (*top view*) of both Figures 8.8 and 8.9 exhibit core-shell chemical ordering characteristics with Pd occupying core positions, leaving Au on the cluster surface. It seems that the ordering is similar to those of the free clusters [620], however, the third rows (*bottom view*) and fourth rows (*first layer*) of the figures give evidence for the difference. The Au preference on the surface is only applicable for the exposed sites, while the cluster-substrate interfacial sites favour Pd-O over Au-O. This observation can be correlated with the stronger bonds of oxide to the transition metals of Ni-group

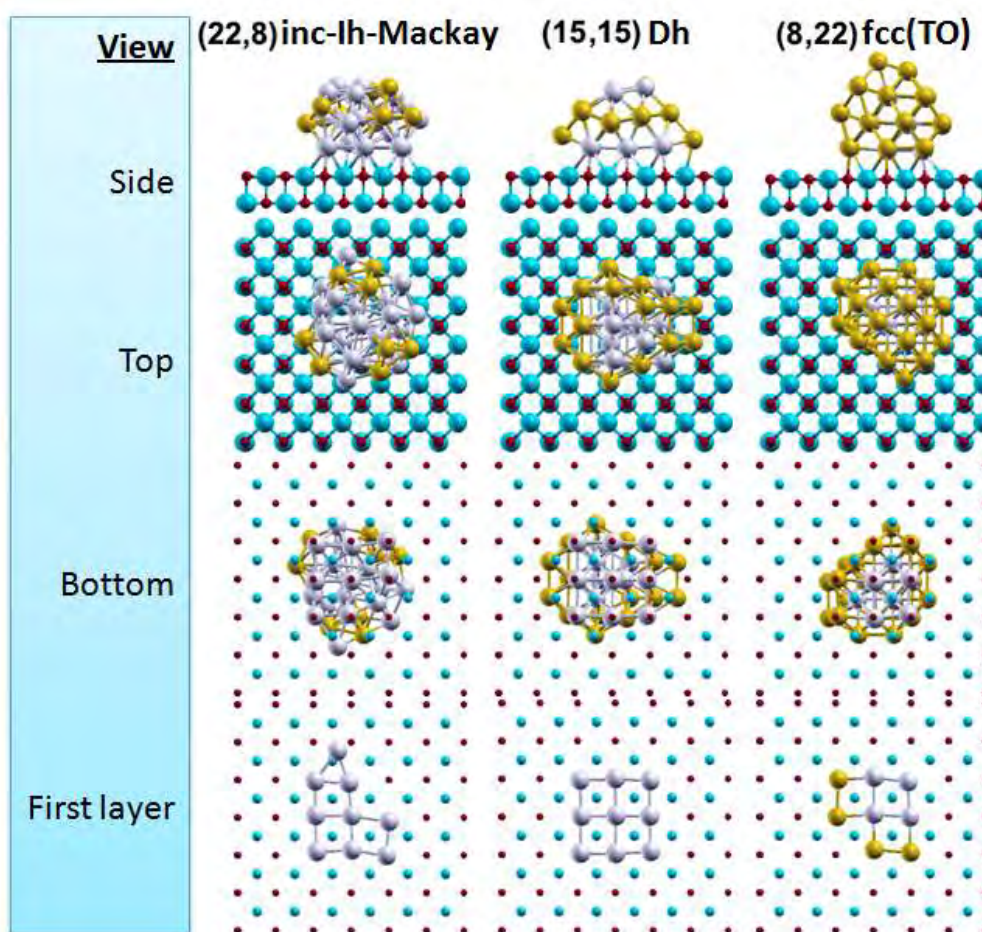


Figure 8.8: Global minima of 30-atom Pd-Au clusters for compositions (22,8), (15,15) and (8,22).

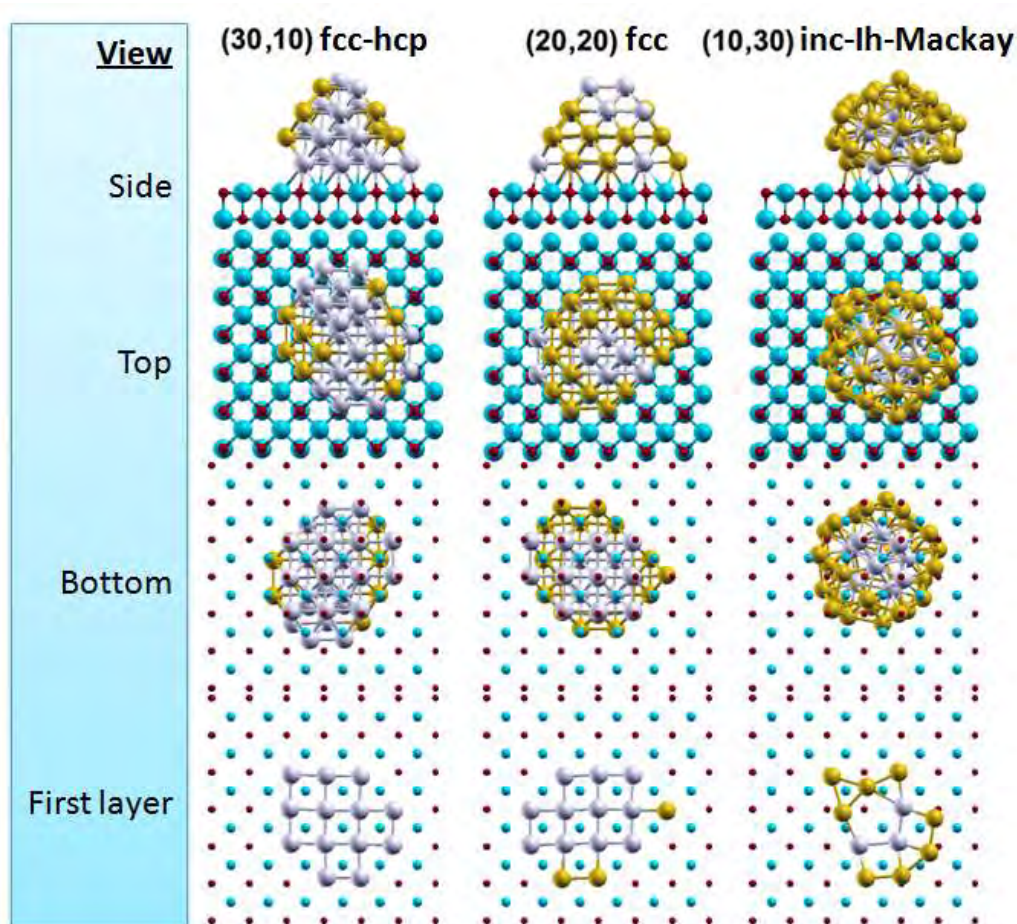


Figure 8.9: Global minima of 40-atom Pd-Au clusters for compositions (30,10), (20,20) and (10,30).

(Ni, Pd, Pt) (approx. 1 eV) as compared with those of the Cu-group (Cu, Ag, Au) (approx. 0.3 eV) metals. Ni-group metals have the ability to form *s-d* hybrid orbitals due to small *s-d* separation (0.51 eV for Pd, compared with 1.7 eV for Au). These hybrid orbitals can then interact with the *p* orbitals of oxygen to produce stronger covalent bonds *via* charge transfer. On the other hand, the *d* shell is filled for Cu-group elements and interaction can only be formed by polarisation and/or dispersion effects [845]. For Au-rich compositions, however, Au occupies the interface (outer shell) to avoid the core position, which would increase the strain and cause instability of the cluster [201–203]. The other significant observation is the preference of O site over Mg for the interactions from MgO to the cluster. This tendency is also reported

theoretically and experimentally for Cu, Ag, Ni and Fe [854].

The fourth rows (*first layer*) for each figure show only direct interactions of cluster-substrate (*i.e.*, the bottom layer of cluster and the top layer of MgO slab) and indicate the occurrence of epitaxial phenomena. There is, however, a clear trend of a decrease in epitaxy, moving from Pd-rich, to medium and Au-rich compositions, consistent with the addition of Au on the cluster-substrate interface. A good cube-on-cube epitaxy of Pd is driven by the strong preference for Pd to sit on top of the surface oxygen over other sites (Mg or hollow) [832, 842, 852] and their ability to transfer the strain to the edges [846]. In contrast, Au has complicated character [487, 857] that leads to the stabilisation of planar [422, 477, 673–675] and cage structures [630, 864, 885]. Hence, increasing the content of Au is thought to dilute the cube-on-cube epitaxy of Pd. In addition to this compositional effect, the progression from composition (8,22) to (10,30) (30- to 40-atom, respectively) gives evidence of the disappearance of the epitaxy character as the size is increased.

The EP and DFT calculations clearly agree on a preference for the Pd_{core}Au_{shell} ordering. It is also significant to note that all other selected (low lying) isomers adopt the same ordering. Table 8.3 provides the numerical evidence for this preference over the reverse ordering - Pd_{shell}Au_{core} (*i.e.*, swapping atoms Pd \rightarrow Au and *vice versa*). The reverse ordering is highly disfavoured (4-5 eV higher in energy) and further enhances the preference of Pd over Au on the MgO surface.

Figure 8.10 shows a complex crossover between the structural motifs of 30-atom

Table 8.3: Relative energies of core-shell and inverse core-shell for (15,15) and (20,20) Pd-Au clusters. (* after DFT local optimisation.)

Cluster	ΔE (Pd _{core} Au _{shell}) (eV)	ΔE (Pd _{shell} Au _{core}) (eV)
(15,15)	0.00	+4.375*
		+6.329
(20,20)	0.00	+5.091*
		+6.329

clusters that can be associated with the small energy gaps [66]. The inc-Ih-Mackay motif, which is the most stable structure for the composition (22,8), is unfavourable for the compositions (15,15) (+0.645 eV) and (8,22) (+0.241 eV). The Dh motif (putative GM for the composition (15,15)) is only disfavoured by +0.100 and +0.047 eV for compositions (22,8) and (8,22), respectively. The other putative GM – fcc-TO (compositions (8,22)) are disfavoured by +0.572 and +1.047 eV for compositions (15,15) and (22,8), respectively. The other studied motifs (fcc-hcp, anti-prism and cp) are energetically less stable for these three compositions, while DT, square-fcc, DT-face, fcc and inc-Ih-anti-Mackay motifs are very competitive but do not prevail as the GM for any compositions.

Structural crossovers for 40-atom Pd-Au clusters in Figure 8.11 are less complex than that of the 30-atom clusters. The anti-prism, cp, pIh⁶ and inc-Ih-anti-Mackay are

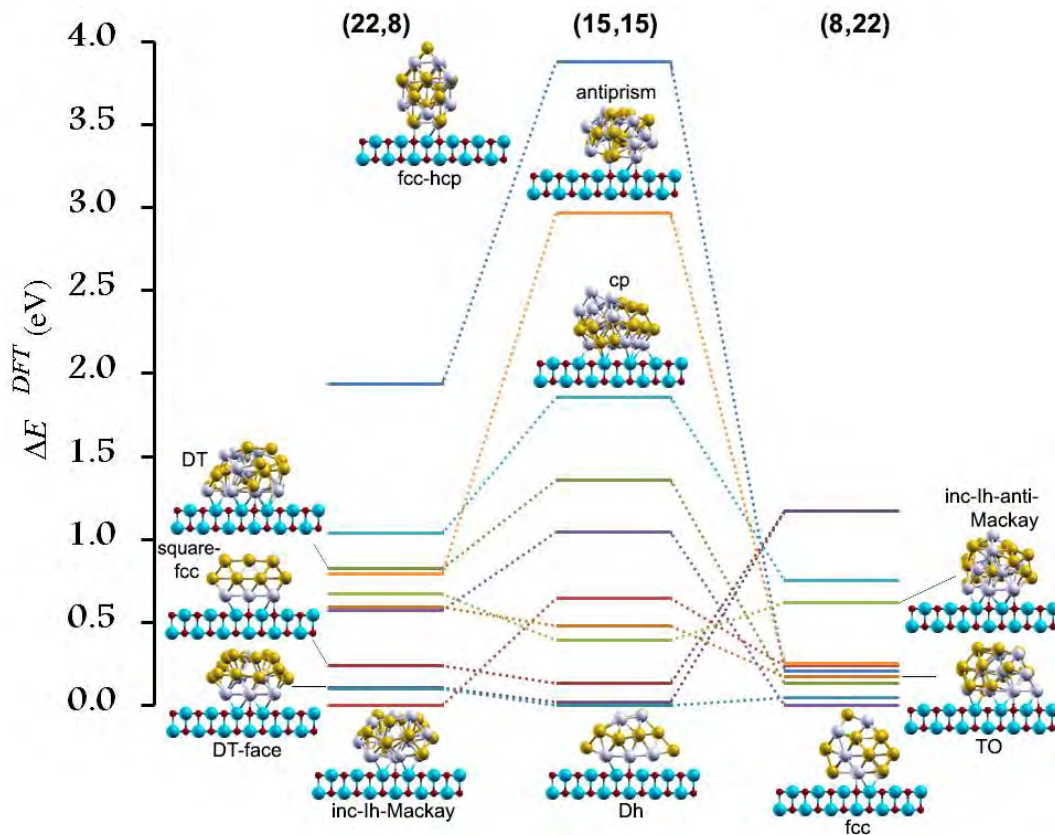


Figure 8.10: Structural motifs crossover of 30-atom Pd-Au clusters.

identified as high energy isomers while Dh and DT-face are the competitive non-GM structures. For this size, bulk-like (fcc) clusters are evidenced for the compositions (20,10) (fcc-hcp) and (20,20) (fcc). For the composition (30,10), these motifs do not emerge as the putative GM but they are relatively very competitive, with gaps of +0.522 and +0.330 eV (for fcc and fcc-hcp, respectively) compared with the putative GM. The putative GM for this composition is inc-Ih-Mackay, however, it is disfavoured for the other compositions (+1.628 and +0.642 eV for compositions (30,10) and (20,20), respectively).

The combination of findings for 30- and 40-atom Pd-Au clusters on MgO provides some support that there are small energy gaps between motifs which indicates the possibility of co-existence of several motifs, in agreement with the experimental observations (for example by Liu *et al.* [123]). Moreover, very small energy barriers seem

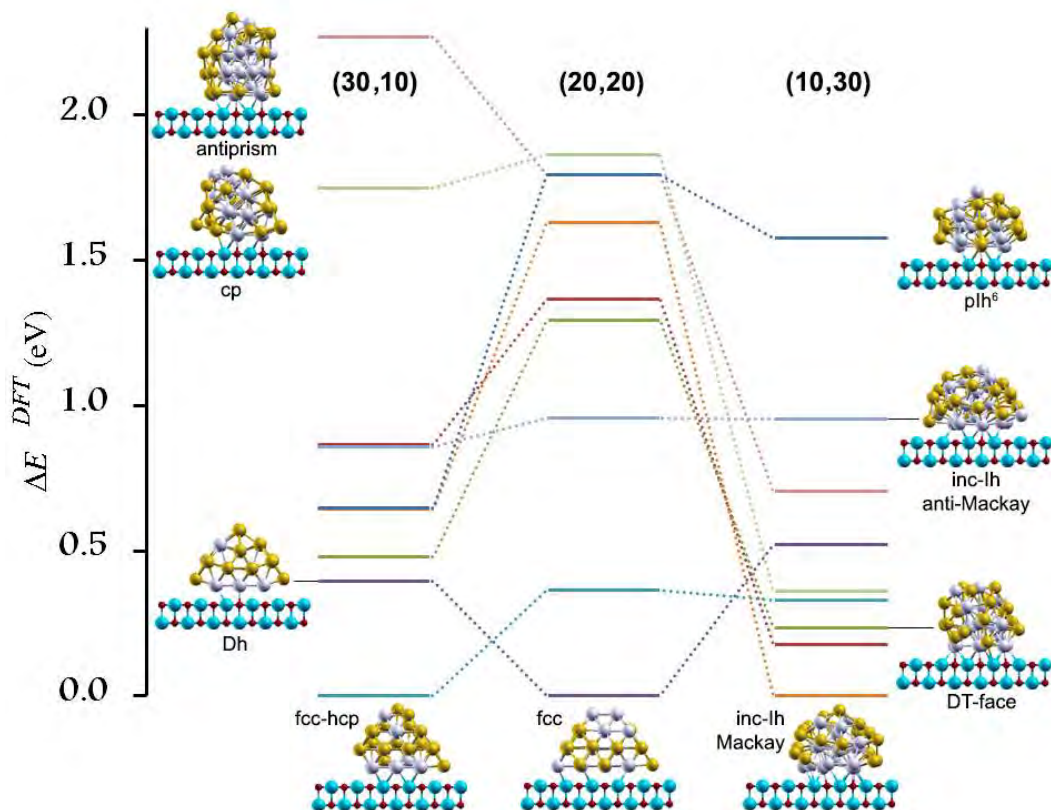


Figure 8.11: Structural motifs crossover of 40-atom Pd-Au clusters.

to suggest that structural rearrangements of the clusters is possible upon interaction with the substrates. It is also interesting to point out that the variation of structure is significantly affected by composition of the clusters. Hence, uncontrolled/changes of the composition in the preparation of clusters is also predicted to lead to structural co-existence.

Finally, it is significant to see how the potential used in this work corroborates the DFT calculations, as shown in Table 8.4. Both the putative GM at the DFT level for 30-(Dh) and 40-atom (fcc-hcp) clusters are apparently not predicted as the best isomers according to the EP calculations; however, they are very competitive and actually the best (energetically) of the non-GM structure. The improvement in accuracy at the EP level with the use of the **new** potential in this work suggests that model potentials are of crucial importance for studying larger nanoparticles containing several hundred or thousand atoms, which are not accessible to the DFT calculations but are of great interest with respect to the experiments [123].

8.5 Chapter Conclusions

The DFT calculations show that Pd-Au nanoalloys on an MgO support exhibit a preference for the core-shell ordering, similar to those of the the gas phase clusters. Due to stronger metal-oxide interactions, Pd is preferred over Au to reside on the cluster-substrate interfacial area. A very good epitaxy of Pd-MgO is shown for Pd-rich clusters but the swapping of Pd to Au atoms reduced these features. The epitaxy also

Table 8.4: Relative energies of (15,15) and (20,20) Pd-Au clusters at the DFT and EP levels.

Motif	ΔE_{DFT} (eV)	ΔE_{EP} (eV)
Dh (30)	0.00	0.14
square-fcc (30)	0.13	0.00
fcc-hcp (40)	0.00	0.03
fcc (40)	0.39	0.00

reduced upon increasing the cluster size.

The energy gaps between structures are small and there is complex crossover for clusters in the 30-40 atoms region. The co-existence of several structural motifs is highly possible, which corroborates many experimental observations. Analysis of the cluster structure also suggests that there is a structural transformation of the clusters, due to cluster-surface interactions.

This study shows that, similarly to the free clusters, small Pd-Au/MgO is still dependent on the composition. However, the effects are significantly reduced on increasing size. The findings also indicate that 40-atom clusters already started to adopt fcc-based bulk-like motifs.

This work gives good confidence in the **new** potential, which has been proved as accurate in predicting the behaviour of pure Pd and Au clusters on MgO substrates. For the bimetallic Pd-Au, the parameterisation method is seen as adequate in reproducing the DFT predictions. With this in mind, this potential could be employed in studying bigger clusters on the MgO substrate, in the hope that the complex mechanism of the interaction between clusters-support can be better understood.

Chapter 9

Concluding Remarks and Future Work

Study of $(\text{Pd-Au})_N$ and $(\text{Pd-Pt})_N$ clusters with $N \leq 100$ gives results consistent with experimental observations, in which small clusters adopt polyicosahedral structures and increasing size leads to the prevalence of Dh in the mid-size region, before bulk-like fcc structures prevail at larger sizes. In the $N \leq 50$ region, there is a strong competition between several structural motifs (fcc, Dh and pIh), which inspired further investigation (sizes 34 and 38).

While atomic arrangements were mostly examined by visual methods, the results are confirmed numerically by the binding energy, E_b^{Gupta} (for stability) and σ (for chemical ordering) analyses. Magic character, which is a very interesting feature in cluster studies, is manifested in relatively distinct stabilities that are consistent with the second difference in energy, $\Delta_2 E_b^{\text{Gupta}}$. For both Pd-Au and Pd-Pt clusters of the $N \leq 100$ region, magic sizes are observed at $N = 38, 55$ and 98 , signifying a fcc-like TO, Mackay icosahedron and LT, respectively.

A more focussed theoretical investigation of 34- and 38-atom clusters was carried out using the combined EP-DF method. Exploration of the parameter space at the EP level *via* parameterisations of the Gupta potential (A, ξ, p or q) in symmetrical and anti-symmetrical fashion give a very large variation in motifs and ordering. A structural database of Pd-Au, Pd-Pt and Ni-Al clusters provides evidence that there is a strong dependence on cluster size, composition and parameter weighting towards

the structural motifs.

34-atom clusters show a larger variation in the structures of GM compared with the 38-atom clusters, in which the magic size TO is dominant. For 38-atom Ni-Al, however, core-shell pIh is more favourable due to the significant difference of size between heteroatomic atoms. Magic character is also valid for specific compositions (*i.e.*, magic compositions), *e.g.*, compositions (24,10) for mixed decahedral-close-packed motifs with a double tetrahedral core (Dh-cp(DT)) and (32,6) for five-fold pancake Mackay icosahedra (pIh-M-pc⁵) and polyicosahedra with six interpenetrating Ih₁₃ units (pIh⁶).

Variation in the chemical ordering is also seen: segregated (spherical cup, core-shell, incomplete core-shell), mixed (onion-like, ordered and disordered) and segregated-mixed intermediate (ball-and-cup). The newly proposed compositional mixing degree, σ_N , is able to show these variations, regardless of the cluster composition. The lower surface energy of Au leads to a more favourable Pd_{core}Au_{shell} configuration, while stronger (cohesive energy) Pd-Pt bonds result in more mixing in the Pd-Pt clusters. These observations are consistent with the DFT predictions of 34- and 38-atom clusters.

The EP-DF studies show very small energy gaps between several motifs of 34- and 38-atom Pd-Au and Pd-Pt clusters. The DFT calculations generally show overall preference for Dh₃₄ and TO₃₈, which is mainly reproduced at the EP level. Furthermore, the EP calculations successfully predict a better preference for the novel Dh-cp(DT) structure in the medium composition region of 34-atom Pd-Pt clusters. By focussing on specific compositions, there are some disagreements between EP and DFT predictions, *e.g.*, the EP fails to predict a more stable fcc-hcp structure of Au-rich PdAu-34 clusters. As several motifs are energetically competitive at the EP level, many motifs prevail as the GM (over a generally stable Dh₃₄ and TO₃₈) as a function of composition but some of them are totally disfavoured at the DFT level.

The discrepancy in the EP predictions are mostly associated with the type of potential being used. The **average** potential – *i.e.*, parameters obtained by averaging the

parameters of elemental semi-empirical Gupta potentials, is reasonably good in giving results consistent with the DFT calculations. However, there are still some gaps to be closed and fitting the potential against experimental or DFT calculations (*i.e.*, **fitted** potential) is one of the options. The **fitted** potential is not always better than the **average**, as the DFT shows the motifs and ordering of putative GM vary strongly with size (*e.g.*, magic size) and composition (*e.g.*, shell closing effect).

The effect of composition on the clusters was studied by taking cluster compositions of (32,6) and (6,32) of a fixed TO motif. The DFT results show that the **average** potential is slightly more sensitive to variations in chemical ordering, due to the composition effect, for the Pd-Au, Pd-Pt and Cu-Au clusters. The equal contribution by each element in heteronuclear interactions (*i.e.*, **average** potential), however, is unable to reproduce the DFT predictions for the Ni-Al, Pt-Au, Cu-Pd and Cu-Pt clusters. For these systems, better results are achieved using parameterised potentials biased towards a relatively more stronger bonding, *i.e.*, Al (Ni-Al), Pt (Pt-Au, Cu-Pt) and Pd (Cu-Pd), although this observation may not be valid for other sizes and motifs.

On interaction with the MgO substrates, some features of the gas phase clusters of Pd-Au are retained – core-shell chemical ordering (with Pd enrichment at the cluster-substrate interface due to stronger Pd-O bonds) and structural crossover on varying the composition. However, based on the EP-DF calculations, the inclusion of the MgO support is observed to reverse the stability order of several motifs. Moreover, very good epitaxy of Pd-MgO leads to structural modification of Pd-rich clusters. By studying different sizes (30 and 40), some features are observed to reduce for increasing size – composition effects and epitaxy.

Overall, good agreement is achieved between the EP and DFT calculations for the studied systems. A similar approach was also applied to Rh-Pd clusters but this is not included in the thesis. Likewise, the effects of other parameters (*i.e.*, p and q) of the Gupta potential were also studied, in addition to the A and ξ parameterisation (in this

thesis). Studies of pure Au and Pd cluster and larger Pd-Au clusters on MgO have also been initiated.

Bibliography

- [1] A. Zabet-Khosousi and A.-A. Dhirani, *Chem. Rev.*, 2008, **108**, 4072.
- [2] M.-C. Daniel and D. Astruc, *Chem. Rev.*, 2004, **104**, 293.
- [3] S. K. Ghosh and T. Pal, *Chem. Rev.*, 2007, **107**, 4797.
- [4] R. Ghosh Chaudhuri and S. Paria, *Chem. Rev.*, 2012, **112**, 2373.
- [5] A. P. Alivisatos, *Science*, 1996, **271**, 933.
- [6] M. A. Kastner, *Phys. Today*, 1993, **46**, 24.
- [7] M. Haruta, *CATTECH*, 2002, **6**, 102.
- [8] Q. Song and Z. J. Zhang, *J. Am. Chem. Soc.*, 2004, **126**, 6164.
- [9] G. Salazar-Alvarez, J. Qin, V. Šepelaák, I. Bergmann, M. Vasilakaki, K. N. Trohidou, J. D. Ardisson, W. A. A. Macedo, M. Mikhaylova, M. Muhammed, M. D. Baró and J. Nogués, *J. Am. Chem. Soc.*, 2008, **130**, 13234.
- [10] E. Schmidt, A. Vargas, T. Mallat and A. Baiker, *J. Am. Chem. Soc.*, 2009, **131**, 12358.
- [11] Z. Wang, T. Ahmad and M. El-Sayed, *Surf. Sci.*, 1997, **380**, 302.
- [12] L. Wu, J. C. Yu, L. Zhang, X. Wang and S. Li, *J. Solid State Chem.*, 2004, **177**, 3666.
- [13] J. Ahmed, S. Sharma, K. V. Ramanujachary, S. E. Lofland and A. K. Ganguli, *J. Colloid Interface Sci.*, 2009, **336**, 814.
- [14] S. A. El-Safty, *J. Colloid Interface Sci.*, 2008, **319**, 477.
- [15] M. Jitianu and D. V. Goia, *J. Colloid Interface Sci.*, 2007, **309**, 78.
- [16] X. Qu, L. Omar, T. B. H. Le, L. Tetley, K. Bolton, K. W. Chooi, W. Wang and I. F. Uchegbu, *Langmuir*, 2008, **24**, 9997.
- [17] Z. Liu, D. Elbert, C.-L. Chien and P. C. Searson, *Nano Lett.*, 2008, **8**, 2166.
- [18] X. Peng, L. Manna, W. Yang, J. Wickham, E. Scher, A. Kadavanich and A. Alivisatos, *Nature*, 2000, **404**, 59–61.
- [19] R. Xiao, S. I. Cho, R. Liu and S. B. Lee, *J. Am. Chem. Soc.*, 2007, **129**, 4483.
- [20] G. Cao and D. Liu, *Adv. Colloid Interface Sci.*, 2008, **136**, 45.
- [21] N. Lopez and J. K. Nørskov, *J. Am. Chem. Soc.*, 2002, **124**, 11262.
- [22] R. Narayanan and M. A. El-Sayed, *J. Phys. Chem. B*, 2004, **108**, 5726.
- [23] C. Burda, X. Chen, R. Narayanan and M. A. El-Sayed, *Chem. Rev.*, 2005, **105**, 1025.
- [24] T. S. Ahmadi, Z. L. Wang, T. C. Green, A. Henglein and M. A. El-Sayed, *Science*, 1996, **272**, 1924.
- [25] A. Wolf and F. Schüth, *Appl. Catal., A*, 2002, **226**, 1.

Bibliography

- [26] M. Brust and C. J. Kiely, *Colloids Surf., A*, 2002, **202**, 175.
- [27] C. R. Henry, *Appl. Surf. Sci.*, 2000, **164**, 252.
- [28] A. Roucoux, J. Schulz and H. Patin, *Chem. Rev.*, 2002, **102**, 3757.
- [29] B. M. Muñoz-Flores, B. I. Kharisov, V. M. Jiménez-Pérez, P. Elizondo Martínez and S. T. López, *Ind. Eng. Chem. Res.*, 2011, **50**, 7705.
- [30] R. W. Murray, *Chem. Rev.*, 2008, **108**, 2688.
- [31] A. Henglein, *Chem. Rev.*, 1989, **89**, 1861.
- [32] R. L. Johnston, *Atomic and Molecular Clusters*, Taylor and Francis, London, 2002.
- [33] J. Jellinek, *Theory of Atomic and Molecular Clusters: with a Glimpse at Experiments*, Springer, Berlin, 1999.
- [34] F. Baletto and R. Ferrando, *Rev. Mod. Phys.*, 2005, **77**, 371.
- [35] J. Jortner, *Z. Phys. D: At., Mol. Clusters*, 1992, **24**, 247.
- [36] R. L. Johnston, *Philos. Trans. R. Soc. London, Ser. A*, 1998, **356**, 211.
- [37] J. A. Alonso, *Chem. Rev.*, 2000, **100**, 637.
- [38] W. P. Halperin, *Rev. Mod. Phys.*, 1986, **58**, 533.
- [39] D. C. Ralph, C. T. Black and M. Tinkham, *Phys. Rev. Lett.*, 1995, **74**, 3241.
- [40] J. R. Heath, *Science*, 1995, **270**, 1315.
- [41] G. Papavassiliou, *Prog. Solid State Chem.*, 1979, **12**, 185.
- [42] T. P. Martin, *Phys. Rep.*, 1996, **273**, 199.
- [43] G. Rossi, A. Rapallo, C. Mottet, A. Fortunelli, F. Baletto and R. Ferrando, *Phys. Rev. Lett.*, 2004, **93**, 105503.
- [44] I. Katakuse, T. Ichihara, Y. Fujita, T. Matsuo, T. Sakurai and H. Matsuda, *Int. J. Mass Spectrom. Ion Processes*, 1985, **67**, 229.
- [45] I. Katakuse, T. Ichihara, Y. Fujita, T. Matsuo, T. Sakurai and H. Matsuda, *Int. J. Mass Spectrom. Ion Processes*, 1986, **74**, 33.
- [46] W. A. de Heer, *Rev. Mod. Phys.*, 1993, **65**, 611.
- [47] G. Gantefor, M. Gausa, K.-H. Meiwes-Broer and H. O. Lutz, *J. Chem. Soc., Faraday Trans.*, 1990, **86**, 2483.
- [48] D. G. Leopold, J. Ho and W. C. Lineberger, *J. Chem. Phys.*, 1987, **86**, 1715.
- [49] A. Lattes, I. Rico, A. de Savignac and A.-Z. Samii, *Tetrahedron*, 1987, **43**, 1725.
- [50] F. Chen, G.-Q. Xu and T. Hor, *Mater. Lett.*, 2003, **57**, 3282.
- [51] A. Taleb, C. Petit and M. P. Pileni, *J. Phys. Chem. B*, 1998, **102**, 2214.
- [52] Y. Yamada and A. W. Castleman, *J. Chem. Phys.*, 1992, **97**, 4543.
- [53] B. J. Winter, E. K. Parks and S. J. Riley, *J. Chem. Phys.*, 1991, **94**, 8618.
- [54] J. P. K. Doye and D. J. Wales, *New J. Chem.*, 1998, **22**, 733.
- [55] N. D. Lang and W. Kohn, *Phys. Rev. B*, 1973, **8**, 6010.
- [56] W. D. Knight, K. Clemenger, W. A. de Heer, W. A. Saunders, M. Y. Chou and M. L. Cohen, *Phys. Rev. Lett.*, 1984, **52**, 2141.
- [57] W. Ekardt and Z. Penzar, *Phys. Rev. B*, 1988, **38**, 4273.
- [58] Z. Penzar and W. Ekardt, *Z. Phys. D: At., Mol. Clusters*, 1990, **17**, 69.
- [59] D. M. P. Mingos, *J. Chem. Soc., Dalton Trans.*, 1996, **5**, 561.

Bibliography

- [60] J. Ascencio, C. Gutiérrez-Wing, M. Espinosa, M. Marín, S. Tehuacanero, C. Zorrilla and M. José-Yacamán, *Surf. Sci.*, 1998, **396**, 349.
- [61] C. L. Cleveland, U. Landman, T. G. Schaaff, M. N. Shafigullin, P. W. Stephens and R. L. Whetten, *Phys. Rev. Lett.*, 1997, **79**, 1873.
- [62] D. Schebarchov and S. C. Hendy, *Phys. Rev. B*, 2006, **73**, 121402.
- [63] W. Zhang, Q. Ge and L. Wang, *J. Chem. Phys.*, 2003, **118**, 5793.
- [64] V. Kumar and Y. Kawazoe, *Phys. Rev. B*, 2002, **66**, 144413.
- [65] P. Nava, M. Sierka and R. Ahlrichs, *Phys. Chem. Chem. Phys.*, 2003, **5**, 3372.
- [66] M. José-Yacamán, M. Marín-Almazo and J. Ascencio, *J. Mol. Catal. A: Chem.*, 2001, **173**, 61.
- [67] H. Grönbeck and W. Andreoni, *Chem. Phys.*, 2000, **262**, 1.
- [68] F. Baletto, R. Ferrando, A. Fortunelli, F. Montalenti and C. Mottet, *J. Chem. Phys.*, 2002, **116**, 3856.
- [69] E. Aprà and A. Fortunelli, *J. Phys. Chem. A*, 2003, **107**, 2934.
- [70] A. Fortunelli and A. M. Velasco, *THEOCHEM*, 1999, **487**, 251.
- [71] O. Echt, K. Sattler and E. Recknagel, *Phys. Rev. Lett.*, 1981, **47**, 1121.
- [72] M. Pellarin, B. Baguenard, J. Vialle, J. Lermé, M. Broyer, J. Miller and A. Perez, *Chem. Phys. Lett.*, 1994, **217**, 349.
- [73] E. K. Parks, L. Zhu, J. Ho and S. J. Riley, *J. Chem. Phys.*, 1995, **102**, 7377.
- [74] E. K. Parks, B. J. Winter, T. D. Klots and S. J. Riley, *J. Chem. Phys.*, 1992, **96**, 8267.
- [75] E. K. Parks, L. Zhu, J. Ho and S. J. Riley, *J. Chem. Phys.*, 1994, **100**, 7206.
- [76] S. Vajda, S. Wolf, T. Leisner, U. Busolt, L. H. Wöste and D. J. Wales, *J. Chem. Phys.*, 1997, **107**, 3492.
- [77] F. A. Reuse, S. N. Khanna and S. Bernel, *Phys. Rev. B*, 1995, **52**, R11650.
- [78] S. M. Foiles, M. I. Baskes and M. S. Daw, *Phys. Rev. B*, 1986, **33**, 7983.
- [79] J. García-Rodeja, C. Rey, L. J. Gallego and J. A. Alonso, *Phys. Rev. B*, 1994, **49**, 8495.
- [80] C. Rey, L. J. Gallego, J. García-Rodeja, J. A. Alonso and M. P. Iñiguez, *Phys. Rev. B*, 1993, **48**, 8253.
- [81] J. M. Montejano-Carrizales, M. P. Iñiguez, J. A. Alonso and M. J. López, *Phys. Rev. B*, 1996, **54**, 5961.
- [82] E. K. Parks, G. C. Nieman, K. P. Kerns and S. J. Riley, *J. Chem. Phys.*, 1998, **108**, 3731.
- [83] M. S. Stave and A. E. DePristo, *J. Chem. Phys.*, 1992, **97**, 3386.
- [84] N. N. Lathiotakis, A. N. Andriotis, M. Menon and J. Connolly, *Europhys. Lett.*, 1995, **29**, 135.
- [85] N. N. Lathiotakis, A. N. Andriotis, M. Menon and J. Connolly, *J. Chem. Phys.*, 1996, **104**, 992.
- [86] T. L. Wetzel and A. E. DePristo, *J. Chem. Phys.*, 1996, **105**, 572.
- [87] C. L. Cleveland and U. Landman, *J. Chem. Phys.*, 1991, **94**, 7376.
- [88] A. Aguado and J. M. López, *J. Chem. Phys.*, 2009, **130**, 064704.
- [89] K. E. Schriver, J. L. Persson, E. C. Honea and R. L. Whetten, *Phys. Rev. Lett.*,

Bibliography

- 1990, **64**, 2539.
- [90] A. K. Starace, C. M. Neal, B. Cao, M. F. Jarrold, A. Aguado and J. M. López, *J. Chem. Phys.*, 2009, **131**, 044307.
- [91] R. O. Jones, *J. Chem. Phys.*, 1993, **99**, 1194.
- [92] R. Ahlrichs and S. D. Elliott, *Phys. Chem. Chem. Phys.*, 1999, **1**, 13.
- [93] H.-P. Cheng, R. S. Berry and R. L. Whetten, *Phys. Rev. B*, 1991, **43**, 10647.
- [94] U. Röthlisberger, W. Andreoni and P. Giannozzi, *J. Chem. Phys.*, 1992, **96**, 1248.
- [95] V. Kumar, *Phys. Rev. B*, 1998, **57**, 8827.
- [96] J. Akola, H. Häkkinen and M. Manninen, *Phys. Rev. B*, 1998, **58**, 3601.
- [97] F. Duque and A. Mañanes, *Eur. Phys. J. D*, 1999, **9**, 223.
- [98] B. K. Rao, S. N. Khanna and P. Jena, *Phys. Rev. B*, 2000, **62**, 4666.
- [99] V. Kumar, S. Bhattacharjee and Y. Kawazoe, *Phys. Rev. B*, 2000, **61**, 8541.
- [100] J. Akola and M. Manninen, *Phys. Rev. B*, 2001, **63**, 193410.
- [101] S. N. Khanna, B. K. Rao and P. Jena, *Phys. Rev. B*, 2002, **65**, 125105.
- [102] A. Mañanes, F. Duque, F. Méndez, M. J. López and J. A. Alonso, *J. Chem. Phys.*, 2003, **119**, 5128.
- [103] R. Pushpa, S. Narasimhan and U. Waghmare, *J. Chem. Phys.*, 2004, **121**, 5211.
- [104] F.-C. Chuang, C. Z. Wang and K. H. Ho, *Phys. Rev. B*, 2006, **73**, 125431.
- [105] L. D. Lloyd, R. L. Johnston, C. Roberts and T. V. Mortimer-Jones, *ChemPhysChem*, 2002, **3**, 408.
- [106] J. P. K. Doye, *J. Chem. Phys.*, 2003, **119**, 1136.
- [107] B. K. Rao and P. Jena, *J. Chem. Phys.*, 1999, **111**, 1890.
- [108] R. R. Zope and T. Baruah, *Phys. Rev. A*, 2001, **64**, 053202.
- [109] M. D. Deshpande, D. G. Kanhere, I. Vasiliev and R. M. Martin, *Phys. Rev. B*, 2003, **68**, 035428.
- [110] Y. Sun, M. Zhang and R. Fournier, *Phys. Rev. B*, 2008, **77**, 075435.
- [111] X. G. Gong, D. Y. Sun and X.-Q. Wang, *Phys. Rev. B*, 2000, **62**, 15413.
- [112] N. Drebov and R. Ahlrichs, *J. Chem. Phys.*, 2010, **132**, 164703.
- [113] A. Aguado and J. M. López, *J. Phys. Chem. B*, 2006, **110**, 14020.
- [114] G. A. Breaux, C. M. Neal, B. Cao and M. F. Jarrold, *Phys. Rev. Lett.*, 2005, **94**, 173401.
- [115] X. Teng, Q. Wang, P. Liu, W. Han, A. I. Frenkel, Wen, N. Marinkovic, J. C. Hanson and J. A. Rodriguez, *J. Am. Chem. Soc.*, 2008, **130**, 1093.
- [116] R. Ferrando, J. Jellinek and R. L. Johnston, *Chem. Rev.*, 2008, **108**, 845.
- [117] A. Henglein, *J. Phys. Chem.*, 1993, **97**, 5457.
- [118] S. C. Davis and K. J. Klabunde, *Chem. Rev.*, 1982, **82**, 153.
- [119] L. N. Lewis, *Chem. Rev.*, 1993, **93**, 2693.
- [120] G. Schmid, *Chem. Rev.*, 1992, **92**, 1709.
- [121] G. Schön and U. Simon, *Colloid. Polym. Sci.*, 1995, **273**, 101.
- [122] H. Y. Oderji and H. Ding, *Chem. Phys.*, 2011, **388**, 23.
- [123] H. B. Liu, U. Pal, A. Medina, C. Maldonado and J. A. Ascencio, *Phys. Rev. B*, 2005, **71**, 075403.

Bibliography

- [124] M. Faraday, *Philos. Trans. R. Soc. London*, 1857, **147**, 145.
- [125] M. Gaudry, E. Cottancin, M. Pellarin, J. Lermé, L. Arnaud, J. R. Huntzinger, J. L. Vialle, M. Broyer, J. L. Rousset, M. Treilleux and P. Mélinon, *Phys. Rev. B*, 2003, **67**, 155409.
- [126] R. W. J. Scott, O. M. Wilson, S.-K. Oh, E. A. Kenik and R. M. Crooks, *J. Am. Chem. Soc.*, 2004, **126**, 15583.
- [127] J. A. Rodriguez and D. W. Goodman, *Science*, 1992, **257**, 897.
- [128] M. Chen, D. Kumar, C.-W. Yi and D. W. Goodman, *Science*, 2005, **310**, 291.
- [129] J. Knudsen, A. U. Nilekar, R. T. Vang, J. Schnadt, E. L. Kunkes, J. A. Dumesic, M. Mavrikakis and F. Besenbacher, *J. Am. Chem. Soc.*, 2007, **129**, 6485.
- [130] S. Maksimuk, S. Yang, Z. Peng and H. Yang, *J. Am. Chem. Soc.*, 2007, **129**, 8684.
- [131] H. Ye and R. M. Crooks, *J. Am. Chem. Soc.*, 2007, **129**, 3627.
- [132] X. Teng and H. Yang, *J. Am. Chem. Soc.*, 2003, **125**, 14559.
- [133] E. Casado-Rivera, D. J. Volpe, L. Alden, C. Lind, C. Downie, T. Vázquez-Alvarez, A. C. D. Angelo, F. J. DiSalvo and H. D. Abruña, *J. Am. Chem. Soc.*, 2004, **126**, 4043.
- [134] C. J. Zhong and M. M. Maye, *Adv. Mater.*, 2001, **13**, 1507.
- [135] A. V. Ruban, H. L. Skriver and J. K. Nørskov, *Phys. Rev. B*, 1999, **59**, 15990.
- [136] G. Bozzolo, J. Ferrante, R. D. Noebe, B. Good, F. S. Honey and P. Abel, *Comput. Mater. Sci.*, 1999, **15**, 169.
- [137] J. Jellinek and E. Krissinel, *Chem. Phys. Lett.*, 1996, **258**, 283.
- [138] E. Krissinel and J. Jellinek, *Chem. Phys. Lett.*, 1997, **272**, 301.
- [139] E. B. Krissinel and J. Jellinek, *Int. J. Quantum Chem.*, 1997, **62**, 185.
- [140] A. Radillo-Díaz, Y. Coronado, L. A. Pérez and I. L. Garzón, *Eur. Phys. J. D*, 2009, **52**, 127.
- [141] J. P. Wilcoxon and B. L. Abrams, *Chem. Soc. Rev.*, 2006, **35**, 1162.
- [142] N. Toshima, M. Harada, Y. Yamazaki and K. Asakura, *J. Phys. Chem.*, 1992, **96**, 9927.
- [143] A. F. Lee, C. J. Baddeley, C. Hardacre, R. M. Ormerod, R. M. Lambert, G. Schmid and H. West, *J. Phys. Chem.*, 1995, **99**, 6096.
- [144] N. Toshima, M. Harada, T. Yonezawa, K. Kushihashi and K. Asakura, *J. Phys. Chem.*, 1991, **95**, 7448.
- [145] R. Esparza, J. Ascencio, G. Rosas, J. Sanchez Ramirez, U. Pal and R. Perez, *J. Nanosci. Nanotechnol.*, 2005, **5**, 641.
- [146] J. Rousset, F. C. S. Aires, F. Bornette, M. Cattenot, M. Pellarin, L. Stievano and A. Renouprez, *Appl. Surf. Sci.*, 2000, **164**, 163.
- [147] G. Schmid, A. Lehnert, J.-O. Malm and J.-O. Bovin, *Angew. Chem. Int. Ed. (English)*, 1991, **30**, 874.
- [148] F. Lequien, J. Creuze, F. Berthier and B. Legrand, *J. Chem. Phys.*, 2006, **125**, 094707.
- [149] G. Trégliã, B. Legrand, F. Ducastelle, A. Saúl, C. Gallis, I. Meunier, C. Mottet and A. Senhaji, *Comput. Mater. Sci.*, 1999, **15**, 196.
- [150] J. Creuze, F. Berthier, R. Tétot and B. Legrand, *Surf. Sci.*, 2001, **491**, 1.

Bibliography

- [151] J. Sinfelt, *J. Catal.*, 1973, **29**, 308.
- [152] A. Ruban, B. Hammer, P. Stoltze, H. Skriver and J. Nørskov, *J. Mol. Catal. A: Chem.*, 1997, **115**, 421.
- [153] P. Liu and J. K. Nørskov, *Phys. Chem. Chem. Phys.*, 2001, **3**, 3814.
- [154] S. M. Oxford, P. L. Lee, P. J. Chupas, K. W. Chapman, M. C. Kung and H. H. Kung, *J. Phys. Chem. C*, 2010, **114**, 17085.
- [155] M. G. Montes de Oca, D. Plana, V. Celorrio, M. J. Lazaro and D. J. Fermín, *J. Phys. Chem. C*, 2012, **116**, 692.
- [156] B. Coq and F. Figueras, *J. Mol. Catal. A: Chem.*, 2001, **173**, 117.
- [157] J. C. Fuggle, F. U. Hillebrecht, R. Zeller, Z. Zolnierok, P. A. Bennett and C. Freiburg, *Phys. Rev. B*, 1983, **27**, 2145.
- [158] R. Budhani, A. Banerjee, T. Goel and K. Chopra, *J. Non-Cryst. Solids*, 1983, **55**, 93.
- [159] J. A. Rodriguez and M. Kuhn, *J. Phys. Chem.*, 1996, **100**, 381.
- [160] M. Fernández-García, J. A. Anderson and G. L. Haller, *J. Phys. Chem.*, 1996, **100**, 16247.
- [161] M. Fernández-García, J. Conesa, A. Clotet, J. Ricart, N. López and F. Illas, *J. Phys. Chem. B*, 1998, **102**, 141–147.
- [162] F. Skoda, M. P. Astier, G. M. Pajonk and M. Primet, *Catal. Lett.*, 1994, **29**, 159.
- [163] A. Venezia, L. Liotta, G. Deganello, Z. Schay and L. Guzzi, *J. Catal.*, 1999, **182**, 449.
- [164] B. Coq, A. Goursot, T. Tazi, F. Figueras and D. R. Salahub, *J. Am. Chem. Soc.*, 1991, **113**, 1485.
- [165] C. Balseiro and J. Morán-López, *Surf. Sci.*, 1985, **156**, Part 1, 404.
- [166] R. V. Hardeveld and F. Hartog, *Surf. Sci.*, 1969, **15**, 189.
- [167] L. V. Nosova, A. V. Kalinkin, E. A. Paukshtis, E. P. Talsi and Y. A. Ryndin, *React. Kinet. Catal. Lett.*, 1994, **53**, 139.
- [168] A. Renouprez, K. Lebas, G. Bergeret, J. Rousset and P. Delichère, in *11th International Congress On Catalysis - 40th Anniversary Proceedings of the 11th ICC*, ed. E. I. Joe W. Hightower, W. Nicholas Delgass and A. T. Bell, Elsevier, 1996, vol. 101, p. 1105.
- [169] Y. Debauge, M. Abon, J. Bertolini, J. Massardier and A. Rochefort, *Appl. Surf. Sci.*, 1995, **90**, 15.
- [170] G. D. Angel, B. Coq and F. Figueras, *J. Catal.*, 1985, **95**, 167.
- [171] J. L. Rousset, J. C. Bertolini and P. Miegge, *Phys. Rev. B*, 1996, **53**, 4947.
- [172] M. C. Fromen, J. Morillo, M. J. Casanove and P. Lecante, *Europhys. Lett.*, 2006, **73**, 885.
- [173] N. L. Rosi and C. A. Mirkin, *Chem. Rev.*, 2005, **105**, 1547.
- [174] P. Alivisatos, *Nat. Biotechnol.*, 2004, **22**, 47–52.
- [175] M. Vargaftik, V. Zagorodnikov, I. Stolarov, I. Moiseev, D. Kochubey, V. L. Kholobov, A. Chuvilin and K. Zamaraev, *J. Mol. Catal.*, 1989, **53**, 315.
- [176] J. S. Bradley, J. M. Millar and E. W. Hill, *J. Am. Chem. Soc.*, 1991, **113**, 4016.
- [177] J. Kiwi and M. Graetzel, *J. Am. Chem. Soc.*, 1979, **101**, 7214.
- [178] D. Reinhard, B. D. Hall, P. Berthoud, S. Valkealahti and R. Monot, *Phys. Rev.*

Bibliography

- Lett.*, 1997, **79**, 1459.
- [179] B. D. Hall, M. Flüeli, R. Monot and J.-P. Borel, *Phys. Rev. B*, 1991, **43**, 3906.
- [180] O. Dmitrieva, M. Acet, G. Dumpich, J. Kästner, C. Antoniak, M. Farle and K. Fauth, *J. Phys. D: Appl. Phys.*, 2006, **39**, 4741.
- [181] K. Koga and K. Sugawara, *Surf. Sci.*, 2003, **529**, 23.
- [182] A. N. Patil, D. Y. Paithankar, N. Otsuka and R. P. Andres, *Z. Phys. D: At., Mol. Clusters*, 1993, **26**, 135.
- [183] K. Stevens, B. Ingham, M. Toney, S. Brown and A. Lassesson, *Curr. Appl Phys.*, 2008, **8**, 443.
- [184] E. Cottancin, J. Lermé, M. Gaudry, M. Pellarin, J.-L. Vialle, M. Broyer, B. Prével, M. Treilleux and P. Mélinon, *Phys. Rev. B*, 2000, **62**, 5179.
- [185] M. Gaudry, J. Lermé, E. Cottancin, M. Pellarin, J. L. Vialle, M. Broyer, B. Prével, M. Treilleux and P. Mélinon, *Phys. Rev. B*, 2001, **64**, 085407.
- [186] Z. Y. Li, J. Yuan, Y. Chen, R. E. Palmer and J. P. Wilcoxon, *Appl. Phys. Lett.*, 2005, **87**, 243103.
- [187] Z. Li, J. Yuan, Y. Chen, R. Palmer and J. Wilcoxon, *Adv. Mater.*, 2005, **17**, 2885.
- [188] R. L. Johnston, *Dalton Trans.*, 2003, **22**, 4193.
- [189] D. Ferrer, A. Torres-Castro, X. Gao, S. Sep^olveda-Guzmán, U. Ortiz-Méndez and M. José-Yacamán, *Nano Lett.*, 2007, **7**, 1701.
- [190] G. C. Papavassiliou, *J. Phys. F: Met. Phys.*, 1976, **6**, L103.
- [191] H. Zhang, M. Jin, J. Wang, M. J. Kim, D. Yang and Y. Xia, *J. Am. Chem. Soc.*, 2011, **133**, 10422.
- [192] A. Henglein, *J. Phys. Chem. B*, 2000, **104**, 2201.
- [193] D. Cheng, S. Huang and W. Wang, *Eur. Phys. J. D*, 2006, **39**, 41.
- [194] D. Cheng, S. Huang and W. Wang, *Chem. Phys.*, 2006, **330**, 423.
- [195] F. Baletto, C. Mottet and R. Ferrando, *Phys. Rev. Lett.*, 2003, **90**, 135504.
- [196] R. Bardhan, S. Mukherjee, N. A. Mirin, S. D. Levit, P. Nordlander and N. J. Halas, *J. Phys. Chem. C*, 2010, **114**, 7378.
- [197] C. Radloff and N. J. Halas, *Nano Lett.*, 2004, **4**, 1323.
- [198] S. Wang, B. R. Jarrett, S. M. Kauzlarich and A. Y. Louie, *J. Am. Chem. Soc.*, 2007, **129**, 3848.
- [199] C. Kittel, *Introduction to Solid State Physics*, Wiley, Chichester, New York, 1986.
- [200] N. N. Greenwood and A. Earnshaw, *Chemistry of the Elements (2nd ed.)*, Butterworth-Heinemann, Oxford, 1997.
- [201] A. R. Miedema, *Z. Metallkd.*, 1978, **69**, 287.
- [202] W. Tyson and W. Miller, *Surf. Sci.*, 1977, **62**, 267.
- [203] A. Rapallo, G. Rossi, R. Ferrando, A. Fortunelli, B. C. Curley, L. D. Lloyd, G. M. Tarbuck and R. L. Johnston, *J. Chem. Phys.*, 2005, **122**, 194308.
- [204] R. Lide, *CRC Handbook of Chemistry and Physics*, CRC Press, Boca Raton, Florida, 2003.
- [205] G. Rossi, R. Ferrando, A. Rapallo, A. Fortunelli, B. C. Curley, L. D. Lloyd and R. L. Johnston, *J. Chem. Phys.*, 2005, **122**, 194309.
- [206] G. Barcaro, A. Fortunelli, G. Rossi, F. Nita and R. Ferrando, *J. Phys. Chem. B*,

Bibliography

- 2006, **110**, 23197.
- [207] Z. Duan and G. Wang, *J. Phys.: Condens. Matter*, 2011, **23**, 475301.
- [208] R. V. Santen and W. Sachtler, *J. Catal.*, 1974, **33**, 202.
- [209] M. Kelley, *J. Catal.*, 1979, **57**, 113.
- [210] W. M. H. Sachtler, *Cat. Rev.*, 1976, **14**, 193.
- [211] R. Bouwman and W. Sachtler, *J. Catal.*, 1970, **19**, 127.
- [212] W. van Dijk, J. Groenewegen and V. Ponec, *J. Catal.*, 1976, **45**, 277.
- [213] F. Kuijers and V. Ponec, *Surf. Sci.*, 1977, **68**, 294.
- [214] H. de Jongste and V. Ponec, *J. Catal.*, 1980, **64**, 228.
- [215] S. Oldenburg, R. Averitt, S. Westcott and N. Halas, *Chem. Phys. Lett.*, 1998, **288**, 243.
- [216] F. Bernardi, M. C. M. Alves, A. Traverse, D. O. Silva, C. W. Scheeren, J. Dupont and J. Morais, *J. Phys. Chem. C*, 2009, **113**, 3909.
- [217] F. Caruso, *Adv. Mater.*, 2001, **13**, 11.
- [218] L. Feng, X. Wu, L. Ren, Y. Xiang, W. He, K. Zhang, W. Zhou and S. Xie, *Chem. Eur. J.*, 2008, **14**, 9764.
- [219] D. Aherne, M. Gara, J. M. Kelly and Y. K. Gun'ko, *Adv. Funct. Mater.*, 2010, **20**, 1329.
- [220] X. Chen, H. Pan, H. Liu and M. Du, *Electrochim. Acta*, 2010, **56**, 636.
- [221] Y. Wu, P. Jiang, M. Jiang, T.-W. Wang, C.-F. Guo, S.-S. Xie and Z.-L. Wang, *Nanotechnology*, 2009, **20**, 305602.
- [222] M. Min, C. Kim and H. Lee, *J. Mol. Catal. A: Chem.*, 2010, **333**, 6.
- [223] Y. Z. Fu, X. D. Xiang, J. H. Liao and J. M. Wang, *J. Dispersion Sci. Technol.*, 2008, **29**, 1291.
- [224] C.-C. Huang, Z. Yang and H.-T. Chang, *Langmuir*, 2004, **20**, 6089.
- [225] S. U. Son, Y. Jang, J. Park, H. B. Na, H. M. Park, H. J. Yun, J. Lee and T. Hyeon, *J. Am. Chem. Soc.*, 2004, **126**, 5026.
- [226] G. Schmid, A. Lehnert, J.-O. Malm and J.-O. Bovin, *Angew. Chem. Int. Ed. (English)*, 1991, **30**, 874.
- [227] G. Schmid, H. West, J.-O. Malm, J.-O. Bovin and C. Grenthe, *Chem. Eur. J.*, 1996, **2**, 1099.
- [228] W. Pearson, *The Crystal Chemistry and Physics of Metals and Alloys*, Wiley-Interscience, Chichester, New York, 1972.
- [229] T. B. Massalki, H. Okamoto and P. R. Subramanian, *Binary Alloy Phase Diagrams, 2nd ed.*, ASM International, Metals Park, OH, 1990.
- [230] L. V. Pourovskii, A. V. Ruban, I. A. Abrikosov, Y. K. Vekilov and B. Johansson, *Phys. Rev. B*, 2001, **64**, 035421.
- [231] Y. Gauthier, Y. Joly, R. Baudoing and J. Rundgren, *Phys. Rev. B*, 1985, **31**, 6216.
- [232] J. Vrijen and S. Radelaar, *Phys. Rev. B*, 1978, **17**, 409.
- [233] O. Proux, J. Regnard, I. Manzini, C. Revenant, B. Rodmacq and J. Mimault, *EPJ Appl. Phys.*, 2000, **9**, 115–124.
- [234] R. Hultgren, P. D. Desai, D. T. Hawkins, M. Gleiser and K. K. Kelley, *Selected Values of the Thermodynamic Properties of Binary Alloys*, American Society for

Bibliography

- Metals, Metals Park, Ohio, 1973.
- [235] S. Sao-Joao, S. Giorgio, J. M. Penisson, C. Chapon, S. Bourgeois and C. Henry, *J. Phys. Chem. B*, 2005, **109**, 342.
- [236] T. Manago, Y. Otani, H. Miyajima and E. Akiba, *J. Appl. Phys.*, 1996, **79**, 5126.
- [237] J. Guevara, A. Llois, F. Aguilera-Granja and J. Montejano-Carrizales, *Physica B*, 2004, **354**, 300.
- [238] T. Teranishi and M. Miyake, *Chem. Mater.*, 1999, **11**, 3414.
- [239] C. Femoni, M. C. Iapalucci, G. Longoni, P. H. Svensson and J. Wolowska, *Angew. Chem. Int. Ed.*, 2000, **39**, 1635.
- [240] Z. Zhang, T. M. Nenoff, K. Leung, S. R. Ferreira, J. Y. Huang, D. T. Berry, P. P. Provencio and R. Stumpf, *J. Phys. Chem. C*, 2010, **114**, 14309.
- [241] G. Wang, M. A. V. Hove, P. N. Ross and M. I. Baskes, *J. Chem. Phys.*, 2005, **122**, 024706.
- [242] F. Demartin, F. Fabrizi de Biani, C. Femoni, M. C. Iapalucci, G. Longoni, P. Macchi and P. Zanello, *J. Cluster Sci.*, 2001, **12**, 61.
- [243] C. Femoni, M. Carmela Iapalucci, G. Longoni and P. H. Svensson, *Chem. Commun.*, 2001, 1776.
- [244] A. Ceriott, F. Demartin, G. Longoni, M. Manassero, M. Marchionna, G. Piva and M. Sansoni, *Angew. Chem. Int. Ed.*, 1985, **24**, 697.
- [245] L. G. Wang and A. Zunger, *Phys. Rev. B*, 2003, **67**, 092103.
- [246] Y. Benguedouar, N. Keghouche and J. Belloni, *Mater. Sci. Eng., B*, 2012, **177**, 27.
- [247] N. Toshima, Y. Shiraishi, A. Shiotsuki, D. Ikenaga and Y. Wang, *Eur. Phys. J. D*, 2001, **16**, 209.
- [248] Y. Wang and N. Toshima, *J. Phys. Chem. B*, 1997, **101**, 5301.
- [249] N. Toshima, T. Yonezawa and K. Kushihashi, *J. Chem. Soc., Faraday Trans.*, 1993, **89**, 2537.
- [250] U. Kolb, S. A. Quaiser, M. Winter and M. T. Reetz, *Chem. Mater.*, 1996, **8**, 1889.
- [251] N. V. Long, M. Ohtaki, T. D. Hien, J. Randy and M. Nogami, *Electrochim. Acta*, 2011, **56**, 9133.
- [252] L. Fiermans, R. D. Gryse, G. D. Doncker, P. A. Jacobs and J. A. Martens, *J. Catal.*, 2000, **193**, 108.
- [253] E. Fernández, L. Balbás, L. Pérez, K. Michaelian and I. Garzón, *Int. J. Mod. Phys. B*, 2005, **19**, 2339–2344.
- [254] L. O. Paz-Borbón, R. L. Johnston, G. Barcaro and A. Fortunelli, *J. Phys. Chem. C*, 2007, **111**, 2936.
- [255] L. O. Paz-Borbón, R. L. Johnston, G. Barcaro and A. Fortunelli, *J. Chem. Phys.*, 2008, **128**, 134517.
- [256] L. O. Paz-Borbón, A. Gupta and R. L. Johnston, *J. Mater. Chem.*, 2008, **18**, 4154.
- [257] C. Massen, T. V. Mortimer-Jones and R. L. Johnston, *J. Chem. Soc., Dalton Trans.*, 2002, **23**, 4375.
- [258] L. D. Lloyd, R. L. Johnston, S. Salhi and N. T. Wilson, *J. Mater. Chem.*, 2004,

Bibliography

- 14**, 1691.
- [259] J. L. Rousset, L. Stievano, F. J. C. S. Aires, C. Geantet, A. J. Renouprez and M. Pellarin, *J. Catal.*, 2001, **202**, 163.
- [260] A. Renouprez, J. L. Rousset, A. M. Cadrot, Y. Soldo and L. Stievano, *J. Alloys Compd.*, 2001, **328**, 50.
- [261] Y. Y. Tong, T. Yonezawa, N. Toshima and J. J. van der Klink, *J. Phys. Chem.*, 1996, **100**, 730.
- [262] Y.-J. Deng, N. Tian, Z.-Y. Zhou, R. Huang, Z.-L. Liu, J. Xiao and S.-G. Sun, *Chem. Sci.*, 2012, **3**, 1157.
- [263] M. Cazayous, C. Langlois, T. Oikawa, C. Ricolleau and A. Sacuto, *Phys. Rev. B*, 2006, **73**, 113402.
- [264] C. Langlois, T. Oikawa, P. Bayle-Guillemaud and C. Ricolleau, *J. Nanopart. Res.*, 2008, **10**, 997.
- [265] M. Grouchko, A. Kamyshny and S. Magdassi, *J. Mater. Chem.*, 2009, **19**, 3057.
- [266] F. Lequien, J. Creuze, F. Berthier, I. Braems and B. Legrand, *Phys. Rev. B*, 2008, **78**, 075414.
- [267] M. Molayem, V. G. Grigoryan and M. Springborg, *J. Phys. Chem. C*, 2011, **115**, 22148.
- [268] V. Moreno, J. Creuze, F. Berthier, C. Mottet, G. Trégliá and B. Legrand, *Surf. Sci.*, 2006, **600**, 5011.
- [269] S. Núñez and R. L. Johnston, *J. Phys. Chem. C*, 2010, **114**, 13255.
- [270] R. Ferrando, A. Fortunelli and G. Rossi, *Phys. Rev. B*, 2005, **72**, 085449.
- [271] J. Belloni, M. Mostafavi, H. Remita, J.-L. Marignier and M.-O. Delcourt, *New J. Chem.*, 1998, **22**, 1239.
- [272] M. Tsuji, S. Hikino, R. Tanabe and D. Yamaguchi, *Chem. Lett.*, 2010, **39**, 334–336.
- [273] A. Henglein and R. Tausch-Treml, *J. Colloid Interface Sci.*, 1981, **80**, 84.
- [274] S. Xiong, W. Qi, B. Huang and M. Wang, *ChemPhysChem*, 2011, **12**, 1317.
- [275] J. L. Rodríguez-López, J. M. Montejano-Carrizales, U. Pal, J. F. Sánchez-Ramírez, H. E. Troiani, D. García, M. Miki-Yoshida and M. José-Yacamán, *Phys. Rev. Lett.*, 2004, **92**, 196102.
- [276] J. Rodríguez-López, J. Montejano-Carrizales and M. José-Yacamán, *Appl. Surf. Sci.*, 2003, **219**, 56.
- [277] R. A. Lordeiro, F. F. Guimarães, J. C. Belchior and R. L. Johnston, *Int. J. Quantum Chem.*, 2003, **95**, 112.
- [278] M. Zhang and R. Fournier, *THEOCHEM*, 2006, **762**, 49.
- [279] G. Mattei, C. Maurizio, P. Mazzoldi, F. D'Acapito, G. Battaglin, E. Cattaruzza, C. de Julián Fernández and C. Sada, *Phys. Rev. B*, 2005, **71**, 195418.
- [280] N. T. Wilson and R. L. Johnston, *J. Mater. Chem.*, 2002, **12**, 2913.
- [281] B. Pauwels, G. Van Tendeloo, E. Zhurkin, M. Hou, G. Verschoren, L. Theil Kuhn, W. Bouwen and P. Lievens, *Phys. Rev. B*, 2001, **63**, 165406.
- [282] H. Yasuda and H. Mori, *Z. Phys. D: At., Mol. Clusters*, 1996, **37**, 181.
- [283] G. J. Ackland and V. Vitek, *Phys. Rev. B*, 1990, **41**, 10324.
- [284] H. Mori, M. Komatsu, K. Takeda and H. Fujita, *Philos. Mag. Lett.*, 1991, **63**,

Bibliography

- 173.
- [285] H. Yasuda and H. Mori, *Z. Phys. D: At., Mol. Clusters*, 1994, **31**, 131.
- [286] U. Pal, J. Sanchez Ramirez, H. Liu, A. Medina and J. Ascencio, *Appl. Phys. A*, 2004, **79**, 79.
- [287] S. Pal and G. De, *J. Mater. Chem.*, 2007, **17**, 493.
- [288] D. Tran, I. Jones, J. Preece, R. Johnston and C. van den Brom, *J. Nanopart. Res.*, 2011, **13**, 4229.
- [289] J. H. Hodak, A. Henglein, M. Giersig and G. V. Hartland, *J. Phys. Chem. B*, 2000, **104**, 11708.
- [290] J. Zhu, Y. Wang, L. Huang and Y. Lu, *Phys. Lett. A*, 2004, **323**, 455.
- [291] L. M. Liz-Marzan and A. P. Philipse, *J. Phys. Chem.*, 1995, **99**, 15120.
- [292] H. Chen, R. Liu, L.-Y. Jang, J.-F. Lee and S. Hu, *Chem. Phys. Lett.*, 2006, **421**, 118.
- [293] Y. Feng, J. He, H. Wang, Y. Y. Tay, H. Sun, L. Zhu and H. Chen, *J. Am. Chem. Soc.*, 2012, **134**, 2004.
- [294] C. de Cointet, M. Mostafavi, J. Khatouri and J. Belloni, *J. Phys. Chem. B*, 1997, **101**, 3512.
- [295] J. P. Wilcoxon and P. P. Provencio, *J. Am. Chem. Soc.*, 2004, **126**, 6402.
- [296] R. Sanedrin, D. Georganopoulou, S. Park and C. Mirkin, *Adv. Mater.*, 2005, **17**, 1027.
- [297] I. Srnová-Šloufová, B. Vlcková, Z. Bastl and T. L. Hasslett, *Langmuir*, 2004, **20**, 3407.
- [298] S. Bruzzone, G. Arrighini and C. Guidotti, *Mater. Sci. Eng., C*, 2003, **23**, 965.
- [299] F. Y. Chen and R. L. Johnston, *Appl. Phys. Lett.*, 2007, **90**, 153123.
- [300] G. F. Zhao and Z. Zeng, *J. Chem. Phys.*, 2006, **125**, 014303.
- [301] S. W. Han, Y. Kim and K. Kim, *J. Colloid Interface Sci.*, 1998, **208**, 272.
- [302] S. Xing, Y. Feng, Y. Y. Tay, T. Chen, J. Xu, M. Pan, J. He, H. H. Hng, Q. Yan and H. Chen, *J. Am. Chem. Soc.*, 2010, **132**, 9537.
- [303] M. Treguer, C. de Cointet, H. Remita, J. Khatouri, M. Mostafavi, J. Amblard, J. Belloni and R. de Keyser, *J. Phys. Chem. B*, 1998, **102**, 4310.
- [304] T. Shibata, B. A. Bunker, Z. Zhang, D. Meisel, C. F. Vardeman and J. D. Gezelter, *J. Am. Chem. Soc.*, 2002, **124**, 11989.
- [305] W. Benten, N. Nilius, N. Ernst and H.-J. Freund, *Phys. Rev. B*, 2005, **72**, 045403.
- [306] B. C. Curley, G. Rossi, R. Ferrando and R. L. Johnston, *Eur. Phys. J. D*, 2007, **43**, 53.
- [307] C. J. Kiely, J. Fink, J. G. Zheng, M. Brust, D. Bethell and D. J. Schiffrin, *Adv. Mater.*, 2000, **12**, 640.
- [308] M. Gaudry, J. Lermé, E. Cottancin, M. Pellarin, B. Prével, M. Treilleux, P. Mélinon, J.-L. Rousset and M. Broyer, *Eur. Phys. J. D*, 2001, **16**, 201.
- [309] S. Link, Z. L. Wang and M. A. El-Sayed, *J. Phys. Chem. B*, 1999, **103**, 3529.
- [310] Q. Zhang, J. Y. Lee, J. Yang, C. Boothroyd and J. Zhang, *Nanotechnology*, 2007, **18**, 245605.
- [311] N. Lidgi-Guigui, P. Mulheran and R. E. Palmer, *Appl. Phys. Lett.*, 2008, **93**, 123107.

Bibliography

- [312] A. Santra, F. Yang and D. Goodman, *Surf. Sci.*, 2004, **548**, 324.
- [313] V. Bonačić-Koutecký, J. Burda, R. Mitrić, M. Ge, G. Zampella and P. Fantucci, *J. Chem. Phys.*, 2002, **117**, 3120.
- [314] R. Mitrić, C. Bürgel, J. Burda, V. Bonačić-Koutecký and P. Fantucci, *Eur. Phys. J. D*, 2003, **24**, 41.
- [315] J. Ricardo-Chávez and G. Pastor, *Comput. Mater. Sci.*, 2006, **35**, 311.
- [316] J. M. Montejano-Carrizales, M. P. Iñiguez and J. A. Alonso, *Phys. Rev. B*, 1994, **49**, 16649.
- [317] H. Portales, L. Saviot, E. Duval, M. Gaudry, E. Cottancin, M. Pellarin, J. Lermé and M. Broyer, *Phys. Rev. B*, 2002, **65**, 165422.
- [318] J. L. Rousset, F. J. Cadete Santos Aires, B. R. Sekhar, P. Mélinon, B. Prevel and M. Pellarin, *J. Phys. Chem. B*, 2000, **104**, 5430.
- [319] D. Boerma, G. Dorenbos, G. Wheatley and T. Buck, *Surf. Sci.*, 1994, **307D309**, Part B, 674.
- [320] H. She, Y. Chen, X. Chen, K. Zhang, Z. Wang and D.-L. Peng, *J. Mater. Chem.*, 2012, **22**, 2757.
- [321] M. Tsuji, D. Yamaguchi, M. Matsunaga and K. Ikeda, *Cryst. Growth Des.*, 2011, **11**, 1995.
- [322] A. M. Molenbroek, J. K. Nørskov and B. S. Clausen, *J. Phys. Chem. B*, 2001, **105**, 5450.
- [323] J. S. Bradley, G. H. Via, L. Bonneviot and E. W. Hill, *Chem. Mater.*, 1996, **8**, 1895.
- [324] M. Jin, H. Zhang, J. Wang, X. Zhong, N. Lu, Z. Li, Z. Xie, M. J. Kim and Y. Xia, *ACS Nano*, 2012, **6**, 2566.
- [325] A. M. Molenbroek, S. Haukka and B. S. Clausen, *J. Phys. Chem. B*, 1998, **102**, 10680.
- [326] N. Toshima and Y. Wang, *Langmuir*, 1994, **10**, 4574.
- [327] F. Gimenez, C. Chapon and C. R. Henry, *New J. Chem.*, 1998, **22**, 1289.
- [328] S. Giorgio, C. Chapon and C. R. Henry, *Langmuir*, 1997, **13**, 2279.
- [329] C. Mottet, G. Tréglia and B. Legrand, *Phys. Rev. B*, 2002, **66**, 045413.
- [330] L. Rubinovich, M. I. Haftel, N. Bernstein and M. Polak, *Phys. Rev. B*, 2006, **74**, 035405.
- [331] L. Zhu, K. Liang, B. Zhang, J. Bradley and A. DePristo, *J. Catal.*, 1997, **167**, 412.
- [332] S. Zhou, B. Varughese, B. Eichhorn, G. Jackson and K. McIlwrath, *Angew. Chem. Int. Ed.*, 2005, **44**, 4539.
- [333] J. Kugai, T. Moriya, S. Seino, T. Nakagawa, Y. Ohkubo, H. Nitani, H. Daimon and T. Yamamoto, *Int. J. Hydrogen Energy*, 2012, **37**, 4787.
- [334] X. Liu and X. Liu, *Angew. Chem. Int. Ed.*, 2012, **51**, 3311.
- [335] J. Zeng, C. Zhu, J. Tao, M. Jin, H. Zhang, Z.-Y. Li, Y. Zhu and Y. Xia, *Angew. Chem. Int. Ed.*, 2012, **51**, 2354.
- [336] P. Mulvaney, *Langmuir*, 1996, **12**, 788.
- [337] C.-L. Lu, K. S. Prasad, H.-L. Wu, J. A. Ho and M. H. Huang, *J. Am. Chem. Soc.*, 2010, **132**, 14546.

Bibliography

- [338] S. Remita, M. Mostafavi and M. Delcourt, *Radiat. Phys. Chem.*, 1996, **47**, 275.
- [339] C. M. Doudna, M. F. Bertino and A. T. Tokuhira, *Langmuir*, 2002, **18**, 2434.
- [340] K. Patel, S. Kapoor, D. Dave and T. Mukherjee, *J. Chem. Sci.*, 2005, **117**, 311.
- [341] N. Khan, A. Uhl, S. Shaikhutdinov and H.-J. Freund, *Surf. Sci.*, 2006, **600**, 1849.
- [342] B. Lim, H. Kobayashi, T. Yu, J. Wang, M. J. Kim, Z.-Y. Li, M. Rycenga and Y. Xia, *J. Am. Chem. Soc.*, 2010, **132**, 2506.
- [343] L. Zhang, W. Niu, Z. Li and G. Xu, *Chem. Commun.*, 2011, **47**, 10353.
- [344] J. H. Shim, J. Kim, C. Lee and Y. Lee, *Chem. Mater.*, 2011, **23**, 4694.
- [345] F. Pittaway, L. O. Paz-Borbón, R. L. Johnston, H. Arslan, R. Ferrando, C. Motet, G. Barcaro and A. Fortunelli, *J. Phys. Chem. C*, 2009, **113**, 9141.
- [346] P.-P. Fang, A. Jutand, Z.-Q. Tian and C. Amatore, *Angew. Chem. Int. Ed.*, 2011, **50**, 12184.
- [347] C.-W. Yang, K. Chanda, P.-H. Lin, Y.-N. Wang, C.-W. Liao and M. H. Huang, *J. Am. Chem. Soc.*, 2011, **133**, 19993.
- [348] Y. Yu, Q. Zhang, B. Liu and J. Y. Lee, *J. Am. Chem. Soc.*, 2010, **132**, 18258.
- [349] A. J. Logsdail, N. J. Cookson, S. L. Horswell, Z. W. Wang, Z. Y. Li and R. L. Johnston, *J. Phys. Chem. C*, 2010, **114**, 21247.
- [350] W. Annan, P. Qing and L. Yadong, *Chem. Mater.*, 2011, **23**, 3217.
- [351] H. Chen, Y. Li, F. Zhang, G. Zhang and X. Fan, *J. Mater. Chem.*, 2011, **21**, 17658.
- [352] P. S. West, R. L. Johnston, G. Barcaro and A. Fortunelli, *J. Phys. Chem. C*, 2010, **114**, 19678.
- [353] Y. Ding, F. Fan, Z. Tian and Z. L. Wang, *J. Am. Chem. Soc.*, 2010, **132**, 12480.
- [354] J. Chai, F. Li, Y. Hu, Q. Zhang, D. Han and L. Niu, *J. Mater. Chem.*, 2011, **21**, 17922.
- [355] C. J. DeSantis, A. C. Sue, M. M. Bower and S. E. Skrabalak, *ACS Nano*, 2012, **6**, 2617.
- [356] J. H. Hodak, A. Henglein and G. V. Hartland, *J. Chem. Phys.*, 2001, **114**, 2760.
- [357] Q. Ge, C. Song and L. Wang, *Comput. Mater. Sci.*, 2006, **35**, 247.
- [358] D. T. Tran and R. L. Johnston, *Proc. R. Soc. A*, 2011, **467**, 2004.
- [359] L. Cao, L. Tong, P. Diao, T. Zhu and Z. Liu, *Chem. Mater.*, 2004, **16**, 3239.
- [360] M. J. Hostetler, C.-J. Zhong, B. K. H. Yen, J. Andereg, S. M. Gross, N. D. Evans, M. Porter and R. W. Murray, *J. Am. Chem. Soc.*, 1998, **120**, 9396.
- [361] R. P. Doherty, J.-M. Krafft, C. Méthivier, S. Casale, H. Remita, C. Louis and C. Thomas, *J. Catal.*, 2012, **287**, 102.
- [362] R. Raja, V. B. Golovko, J. M. Thomas, A. Berenguer-Murcia, W. Zhou, S. Xie and B. F. G. Johnson, *Chem. Commun.*, 2005, 2026.
- [363] L. Duran Pachon, M. B. Thathagar, F. Hartl and G. Rothenberg, *Phys. Chem. Chem. Phys.*, 2006, **8**, 151.
- [364] A. Renouprez, J. Faudon, J. Massardier, J. Rousset, P. Delichère and G. Bergeret, *J. Catal.*, 1997, **170**, 181.
- [365] U. A. Paulus, A. Wokaun, G. G. Scherer, T. J. Schmidt, V. Stamenkovic, V. Radmilovic, N. M. Markovic and P. N. Ross, *J. Phys. Chem. B*, 2002, **106**, 4181.
- [366] J. Montejano-Carrizales and J. Morán-López, *Surf. Sci.*, 1990, **239**, 178.

Bibliography

- [367] J. Montejano-Carrizales and J. Morán-López, *Surf. Sci.*, 1990, **239**, 169.
- [368] Z.-Y. Jiang, K.-H. Lee, S.-T. Li and S.-Y. Chu, *Phys. Rev. B*, 2006, **73**, 235423.
- [369] E. Janssens, S. Neukermans, X. Wang, N. Veldeman, R. E. Silverans and P. Lievens, *Eur. Phys. J. D*, 2005, **34**, 23.
- [370] W. Bouwen, F. Vanhoutte, F. Despa, S. Bouckaert, S. Neukermans, L. T. Kuhn, H. Weidele, P. Lievens and R. E. Silverans, *Chem. Phys. Lett.*, 1999, **314**, 227.
- [371] J. Ascencio, H. Liu, U. Pal, A. Medina and Z. Wang, *Microsc. Res. Tech.*, 2006, **69**, 522.
- [372] G. De and C. N. R. Rao, *J. Phys. Chem. B*, 2003, **107**, 13597.
- [373] M. J. López, P. A. Marcos and J. A. Alonso, *J. Chem. Phys.*, 1996, **104**, 1056.
- [374] D. T. Tran, I. P. Jones, R. L. Johnston, J. A. Preece and C. R. van den Brom, *J. Phys: Conf. Ser.*, 2010, **241**, 012086.
- [375] P. J. Hsu and S. K. Lai, *J. Chem. Phys.*, 2006, **124**, 044711.
- [376] D. T. Tran and R. L. Johnston, *Phys. Chem. Chem. Phys.*, 2009, **11**, 10340.
- [377] F. Cleri and V. Rosato, *Phys. Rev. B*, 1993, **48**, 22.
- [378] S. Darby, T. V. Mortimer-Jones, R. L. Johnston and C. Roberts, *J. Chem. Phys.*, 2002, **116**, 1536.
- [379] I. L. Garzón, K. Michaelian, M. R. Beltrán, A. Posada-Amarillas, P. Ordejón, E. Artacho, D. Sánchez-Portal and J. M. Soler, *Phys. Rev. Lett.*, 1998, **81**, 1600.
- [380] F. Chen, L. Yuan and R. L. Johnston, *J. Magn. Magn. Mater.*, 2012, **324**, 2625.
- [381] Z. Y. Li, J. P. Wilcoxon, F. Yin, Y. Chen, R. E. Palmer and R. L. Johnston, *Faraday Discuss.*, 2008, **138**, 363.
- [382] Y. Cao, R. Jin and C. A. Mirkin, *J. Am. Chem. Soc.*, 2001, **123**, 7961.
- [383] N. Toreis, X. E. Verykios, S. M. Khalid and G. B. Bunker, *Surf. Sci.*, 1988, **197**, 415.
- [384] D. I. Kondarides and X. E. Verykios, *J. Catal.*, 1996, **158**, 363.
- [385] F. Chen and R. L. Johnston, *ACS Nano*, 2008, **2**, 165.
- [386] F. Chen, B. C. Curley, G. Rossi and R. L. Johnston, *J. Phys. Chem. C*, 2007, **111**, 9157.
- [387] F. Chen and R. L. Johnston, *Appl. Phys. Lett.*, 2008, **92**, 023112.
- [388] F. Chen and R. L. Johnston, *Acta Mater.*, 2008, **56**, 2374.
- [389] S. Heiles, A. J. Logsdail, R. Schafer and R. L. Johnston, *Nanoscale*, 2012, **4**, 1109.
- [390] T. Mallát, S. Szabó and J. Petró, *Appl. Surf. Sci.*, 1990, **40**, 309.
- [391] G. Singh, I. Kapoor and S. Dubey, *J. Alloys Compd.*, 2009, **480**, 270.
- [392] K. I. Choi and M. Vannice, *J. Catal.*, 1991, **131**, 36.
- [393] J. Phillips, A. Auroux, G. Bergeret, J. Massardier and A. Renouprez, *J. Phys. Chem.*, 1993, **97**, 3565.
- [394] M. M. Maye, Y. Lou and C.-J. Zhong, *Langmuir*, 2000, **16**, 7520.
- [395] N. Toshima and T. Yonezawa, *New J. Chem.*, 1998, **22**, 1179.
- [396] Y. Lou, M. M. Maye, L. Han, J. Luo and C.-J. Zhong, *Chem. Commun.*, 2001, 473.
- [397] J. Zhang, H. Ma, D. Zhang, P. Liu, F. Tian and Y. Ding, *Phys. Chem. Chem.*

Bibliography

- Phys.*, 2008, **10**, 3250.
- [398] Z. Peng and H. Yang, *Nano Res.*, 2009, **2**, 406.
- [399] P. Hernández-Fernández, S. Rojas, P. Ocón, J. L. Gómez de la Fuente, J. San Fabián, J. Sanza, M. A. Peña, F. J. García-García, P. Terreros and J. L. G. Fierro, *J. Phys. Chem. C*, 2007, **111**, 2913.
- [400] A. Logsdail, L. O. Paz-Borbón and R. L. Johnston, *J. Comput. Theor. Nanosci.*, 2009, **6**, 857.
- [401] L. Xiong and A. Manthiram, *J. Mater. Chem.*, 2004, **14**, 1454.
- [402] H. Liu, W. Li and A. Manthiram, *Appl. Catal., A*, 2009, **90**, 184.
- [403] M. Oezaslan, F. Hasché and P. Strasser, *J. Electrochem. Soc.*, 2012, **159**, B394.
- [404] T. Guo, P. Nikolaev, A. Thess, D. Colbert and R. Smalley, *Chem. Phys. Lett.*, 1995, **243**, 49.
- [405] W.-Q. Deng, X. Xu and W. A. Goddard, *Nano Lett.*, 2004, **4**, 2331.
- [406] M.-H. Lin, B. Zhao and Y.-W. Chen, *Ind. Eng. Chem. Res.*, 2009, **48**, 7037.
- [407] R. Brayner, T. Coradin, F. Fievet-Vincent, J. Livage and F. Fievet, *New J. Chem.*, 2005, **29**, 681.
- [408] D. A. Eastham, Y. Qiang, T. H. Maddock, J. Kraft, J.-P. Schille, G. S. Thompson and H. Haberland, *J. Phys.: Condens. Matter*, 1997, **9**, L497.
- [409] B. Wang, X. Chen, G. Chen, G. Wang and J. Zhao, *Surf. Rev. Lett.*, 2004, **11**, 15–20.
- [410] P. Paulus, H. Bönnemann, A. van der Kraan, F. Luis, J. Sinzig and L. de Jongh, *Eur. Phys. J. D*, 1999, **9**, 501.
- [411] Q. Lu, L. Zhu, L. Ma and G. Wang, *Chem. Phys. Lett.*, 2005, **407**, 176.
- [412] Q. Lu, L. Zhu, L. Ma and G. Wang, *Phys. Lett. A*, 2006, **350**, 258.
- [413] J.-I. Park and J. Cheon, *J. Am. Chem. Soc.*, 2001, **123**, 5743.
- [414] A. F. Carlsson, M. Bäumer, T. Risse and H.-J. Freund, *J. Chem. Phys.*, 2003, **119**, 10885.
- [415] Z. A. Kaszkur and B. Mierzwa, *Philos. Mag. A*, 1998, **77**, 781.
- [416] W. Juszczyk, Z. Karpinski, D. Lomot, J. Pielaszek, Z. Paal and A. Stakheev, *J. Catal.*, 1993, **142**, 617.
- [417] J.-I. Park, M. G. Kim, Y.-w. Jun, J. S. Lee, W.-r. Lee and J. Cheon, *J. Am. Chem. Soc.*, 2004, **126**, 9072.
- [418] D. Bochicchio and R. Ferrando, *Nano Lett.*, 2010, **10**, 4211.
- [419] E. Janssens, T. V. Hoof, N. Veldeman, S. Neukermans, M. Hou and P. Lievens, *Int. J. Mass spectrom.*, 2006, **252**, 38.
- [420] T. van Hoof and M. Hou, *Phys. Rev. B*, 2005, **72**, 115434.
- [421] E. E. Zhurkin, T. Van Hoof and M. Hou, *Phys. Rev. B*, 2007, **75**, 224102.
- [422] J. Wang, G. Wang and J. Zhao, *Phys. Rev. B*, 2002, **66**, 035418.
- [423] V. Tzitzios, D. Niarchos, M. Gjoka, N. Boukos and D. Petridis, *J. Am. Chem. Soc.*, 2005, **127**, 13756.
- [424] H. L. Nguyen, L. E. M. Howard, S. R. Giblin, B. K. Tanner, I. Terry, A. K. Hughes, I. M. Ross, A. Serres, H. Burckstummer and J. S. O. Evans, *J. Mater. Chem.*, 2005, **15**, 5136.
- [425] L. E. M. Howard, H. L. Nguyen, S. R. Giblin, B. K. Tanner, I. Terry, A. K.

Bibliography

- Hughes and J. S. O. Evans, *J. Am. Chem. Soc.*, 2005, **127**, 10140.
- [426] W. Zhou, E. Carpenter, J. Lin, A. Kumbhar, J. Sims and C. O'Connor, *Eur. Phys. J. D*, 2001, **16**, 289.
- [427] D. Saha, K. Koga and H. Takeo, *Eur. Phys. J. D*, 1999, **9**, 539.
- [428] S. Sahoo, G. Rollmann and P. Entel, *Phase Transitions*, 2006, **79**, 693.
- [429] D. M. P. Mingos and D. J. Wales, *Introduction to Cluster Chemistry*, Prentice Hall, Englewood Cliffs, NJ, 1990.
- [430] G. Longoni, M. Manassero and M. Sansoni, *J. Am. Chem. Soc.*, 1980, **102**, 3242.
- [431] C. Tan, J. Chen, B. Liu and G. Chow, *J. Cryst. Growth*, 2006, **293**, 175.
- [432] M. Müller and K. Albe, *Phys. Rev. B*, 2005, **72**, 094203.
- [433] B. Yang, M. Asta, O. Mryasov, T. Klemmer and R. Chantrell, *Acta Mater.*, 2006, **54**, 4201.
- [434] J. M. Thomas, B. F. G. Johnson, R. Raja, G. Sankar and P. A. Midgley, *Acc. Chem. Res.*, 2003, **36**, 20.
- [435] R. Raja, S. Hermans, D. S. Shephard, B. F. G. Johnson, R. Raja, G. Sankar, S. Bromley and J. Meurig Thomas, *Chem. Commun.*, 1999, 1571.
- [436] P. A. Midgley, M. Weyland, J. M. Thomas and B. F. G. Johnson, *Chem. Commun.*, 2001, 907.
- [437] S. Wasmus and A. Küver, *J. Electroanal. Chem.*, 1999, **461**, 14.
- [438] Z. Liu, X. Y. Ling, X. Su and J. Y. Lee, *J. Phys. Chem. B*, 2004, **108**, 8234.
- [439] Y. Tong, H. S. Kim, P. K. Babu, P. Waszczuk, A. Wieckowski and E. Oldfield, *J. Am. Chem. Soc.*, 2002, **124**, 468.
- [440] P. K. Babu, H. S. Kim, E. Oldfield and A. Wieckowski, *J. Phys. Chem. B*, 2003, **107**, 7595.
- [441] G. Trégliã and B. Legrand, *Phys. Rev. B*, 1987, **35**, 4338.
- [442] D. Aberdam, R. Durand, R. Faure, F. Gloaguen, J. Hazemann, E. Herrero, A. Kabbabi and O. Ulrich, *J. Electroanal. Chem.*, 1995, **398**, 43.
- [443] R. J. Wiltshire, C. R. King, A. Rose, P. P. Wells, M. P. Hogarth, D. Thompsett and A. E. Russell, *Electrochim. Acta*, 2005, **50**, 5208.
- [444] E. M. Crabb, M. K. Ravikumar, D. Thompsett, M. Hurford, A. Rose and A. E. Russell, *Phys. Chem. Chem. Phys.*, 2004, **6**, 1792.
- [445] A. E. Russell and A. Rose, *Chem. Rev.*, 2004, **104**, 4613.
- [446] M. S. Nashner, A. I. Frenkel, D. Somerville, C. W. Hills, J. R. Shapley and R. G. Nuzzo, *J. Am. Chem. Soc.*, 1998, **120**, 8093.
- [447] F. Maillard, F. Gloaguen and J.-M. Leger, *J. Appl. Electrochem.*, 2003, **33**, 1.
- [448] L.-L. Wang, S. V. Khare, V. Chirita, D. D. Johnson, A. A. Rockett, A. I. Frenkel, N. H. Mack and R. G. Nuzzo, *J. Am. Chem. Soc.*, 2006, **128**, 131.
- [449] S. Bromley, G. Sankar, C. Catlow, T. Maschmeyer, B. Johnson and J. Thomas, *Chem. Phys. Lett.*, 2001, **340**, 524.
- [450] H. Bönemann and R. Richards, *Eur. J. Inorg. Chem.*, 2001, **2001**, 2455.
- [451] C. Lyman, R. Lakis and H. Stenger, *Ultramicroscopy*, 1995, **58**, 25.
- [452] Z. Jiang, J. Zhang, G. Wen, A. Liang, Q. Liu, C. Kang and X. He, *Chin. J. Chem.*, 2010, **28**, 1159.
- [453] G. Wang, M. A. Van Hove, P. N. Ross and M. I. Baskes, *J. Phys. Chem. B*, 2005,

Bibliography

- 109**, 11683.
- [454] V. Engels, F. Benaskar, N. Patil, E. V. Rebrov, V. Hessel, L. A. Hulshof, D. A. Jefferson, J. A. J. M. Vekemans, S. Karwal, J. C. Schouten and A. E. H. Wheatley, *Org. Process Res. Dev.*, 2010, **14**, 644.
- [455] R. M.A.Tehrani and S. A. Ghani, *Sens. Actuators, B*, 2010, **145**, 20.
- [456] T. Sondón and J. Guevara, *Physica B*, 2004, **354**, 303.
- [457] J. Hambroek, M. K. Schröter, A. Birkner, C. Wöll and R. A. Fischer, *Chem. Mater.*, 2003, **15**, 4217.
- [458] M. Cokoja, H. Parala, M. K. Schroter, A. Birkner, M. W. E. van den Berg, K. V. Klementiev, W. Grunert and R. A. Fischer, *J. Mater. Chem.*, 2006, **16**, 2420.
- [459] E. E. Zhurkin and M. Hou, *J. Phys.: Condens. Matter*, 2000, **12**, 6735.
- [460] N. Weiher, E. Bus, L. Delannoy, C. Louis, D. Ramaker, J. Miller and J. van Bokhoven, *J. Catal.*, 2006, **240**, 100.
- [461] A. Hinz, P.-O. Larsson, B. Skårman and A. Andersson, *Appl. Catal., B*, 2001, **34**, 161.
- [462] M. Chandra and Q. Xu, *J. Power Sources*, 2007, **168**, 135.
- [463] L. Piccolo, A. Valcarcel, M. Bausach, C. Thomazeau, D. Uzio and G. Berhault, *Phys. Chem. Chem. Phys.*, 2008, **10**, 5504.
- [464] M. C. Valero, P. Raybaud and P. Sautet, *Phys. Rev. B*, 2007, **75**, 045427.
- [465] P. D. Nellist and S. J. Pennycook, *Science*, 1996, **274**, 413.
- [466] B. Gates, *J. Mol. Catal. A: Chem.*, 2000, **163**, 55.
- [467] J. Batista, A. Pintar, D. Mandrino, M. Jenko and V. Martin, *Appl. Catal., A*, 2001, **206**, 113.
- [468] A. Pintar, J. Batista, I. Arčon and A. Kodre, in *Characterization of Al₂O₃ supported Pd-Cu bimetallic catalysts by EXAFS, AES and kinetic measurements*, ed. B. Delmon, P. Jacobs, R. Maggi, J. Martens, P. Grange and G. Poncelet, Elsevier, Amsterdam, 1998, p. 127.
- [469] A. S. Fung, M. J. Kelley, D. C. Koningsberger and B. C. Gates, *J. Am. Chem. Soc.*, 1997, **119**, 5877.
- [470] S.-P. Huang, D. S. Mainardi and P. B. Balbuena, *Surf. Sci.*, 2003, **545**, 163.
- [471] S. K. R. S. Sankaranarayanan, V. R. Bhethanabotla and B. Joseph, *Phys. Rev. B*, 2005, **72**, 195405.
- [472] L. J. Lewis, P. Jensen, N. Combe and J.-L. Barrat, *Phys. Rev. B*, 2000, **61**, 16084.
- [473] N. T. Cuong, A. Fujiwara, T. Mitani and D. H. Chi, *Comput. Mater. Sci.*, 2008, **44**, 163.
- [474] A. Siani, O. S. Alexeev, B. Captain, G. Lafaye, P. Marécot, R. D. Adams and M. D. Amiridis, *J. Catal.*, 2008, **255**, 162.
- [475] R. Wojcieszak, S. Monteverdi, J. Ghanbaja and M. Bettahar, *J. Colloid Interface Sci.*, 2008, **317**, 166.
- [476] G. Barcaro and A. Fortunelli, *Chem. Phys. Lett.*, 2008, **457**, 143.
- [477] G. Barcaro and A. Fortunelli, *New J. Phys.*, 2007, **9**, 22.
- [478] W. Vervisch, C. Mottet and J. Goniakowski, *Phys. Rev. B*, 2002, **65**, 245411.
- [479] R. Ferrando, G. Rossi, F. Nita, G. Barcaro and A. Fortunelli, *ACS Nano*, 2008, **2**, 1849.

Bibliography

- [480] Y. Long and N. Chen, *Surf. Sci.*, 2008, **602**, 46.
- [481] S. Giorgio and C. Henry, *Microsc. Microanal. Microstruct.*, 1997, **8**, 379.
- [482] L. Favre, V. Dupuis, E. Bernstein, P. Mélinon, A. Pérez, S. Stanescu, T. Epicier, J.-P. Simon, D. Babonneau, J.-M. Tonnerre and J.-L. Hodeau, *Phys. Rev. B*, 2006, **74**, 014439.
- [483] V. Dupuis, L. Favre, S. Stanescu, J. Tuailon-Combes, E. Bernstein and A. Perez, *J. Phys.: Condens. Matter*, 2004, **16**, S2231.
- [484] G. Barcaro, A. Fortunelli, F. Nita and R. Ferrando, *Phys. Rev. Lett.*, 2005, **95**, 246103.
- [485] G. Barcaro, A. Fortunelli, G. Rossi, F. Nita and R. Ferrando, *Phys. Rev. Lett.*, 2007, **98**, 156101.
- [486] J. Carrasco, N. Lopez, F. Illas and H.-J. Freund, *J. Chem. Phys.*, 2006, **125**, 074711.
- [487] G. Barcaro and A. Fortunelli, *J. Chem. Theory Comput.*, 2005, **1**, 972.
- [488] G. Barcaro and A. Fortunelli, *Faraday Discuss.*, 2008, **138**, 37.
- [489] G. H. Jóhannesson, T. Bligaard, A. V. Ruban, H. L. Skriver, K. W. Jacobsen and J. K. Nørskov, *Phys. Rev. Lett.*, 2002, **88**, 255506.
- [490] J. B. Foresman and A. Frisch, *Exploring Chemistry with Electronic Structure Methods*, Gaussian, 1996.
- [491] D. Schooss, M. N. Blom, J. H. Parks, B. v. Issendorff, H. Haberland and M. M. Kappes, *Nano Lett.*, 2005, **5**, 1972.
- [492] C. L. Cleveland, U. Landman, M. N. Shafiqullin, P. W. Stephens and R. L. Whetten, *Z. Phys. D: At., Mol. Clusters*, 1997, **40**, 503.
- [493] O. Kostko, B. Huber, M. Moseler and B. von Issendorff, *Phys. Rev. Lett.*, 2007, **98**, 043401.
- [494] A. A. Shvartsburg, R. R. Hudgins, P. Dugourd and M. F. Jarrold, *Chem. Soc. Rev.*, 2001, **30**, 26.
- [495] D. J. Wales and H. A. Scheraga, *Science*, 1999, **285**, 1368.
- [496] B. Hartke, *J. Comput. Chem.*, 1999, **20**, 1752.
- [497] F. Baletto, C. Mottet and R. Ferrando, *Phys. Rev. B*, 2001, **63**, 155408.
- [498] K. Bao, S. Goedecker, K. Koga, F. Lançon and A. Neelov, *Phys. Rev. B*, 2009, **79**, 041405.
- [499] H. Arslan, *Int. J. Mod. Phys. C*, 2007, **18**, 1351–1359.
- [500] J. P. K. Doye and D. J. Wales, *Phys. Rev. B*, 1999, **59**, 2292.
- [501] C. Barrón, S. Gómez and D. Romero, *Appl. Math. Lett.*, 1997, **10**, 25.
- [502] C. Barrón, S. Gómez, D. Romero and A. Saavedra, *Appl. Math. Lett.*, 1999, **12**, 85.
- [503] V. E. Bazterra, O. Oña, M. C. Caputo, M. B. Ferraro, P. Fuentealba and J. C. Facelli, *Phys. Rev. A*, 2004, **69**, 053202.
- [504] W. Cai, H. Jiang and X. Shao, *J. Chem. Inf. Comput. Sci.*, 2002, **42**, 1099.
- [505] C. J. H. Jacobsen, S. Dahl, B. S. Clausen, S. Bahn, A. Logadottir and J. K. Nørskov, *J. Am. Chem. Soc.*, 2001, **123**, 8404.
- [506] S. Hannongbua, S. Saen-oon, P. Pungpo and P. Wolschann, *Monatsh. Chem.*, 2001, **132**, 1157.

Bibliography

- [507] F. Bernardi, A. Bottoni, M. D. Vivo, M. Garavelli, G. Keserü and G. Náray-Szabó, *Chem. Phys. Lett.*, 2002, **362**, 1.
- [508] D. R. Hartree, *Math. Proc. Cambridge Philos. Soc.*, 1928, **24**, 89.
- [509] V. Fock, *Z. Phys. A: Hadrons Nucl.*, 1930, **62**, 795.
- [510] V. Fock, *Z. Phys. A: Hadrons Nucl.*, 1933, **81**, 195.
- [511] F. Jensen, *Introduction to Computational Chemistry*, Wiley, 2nd edn., 2006.
- [512] J. Cioslowski, *Many-Electron Densities and Reduced Density Matrices*, Kluwer Academic/Plenum Publishers, 2000.
- [513] Y. Akutsu, S.-Y. Tahara, M. Tamura and T. Yoshida, *J. Energetic Mat.*, 1991, **9**, 161.
- [514] D. B. Cook, *Handbook of Computational Quantum Chemistry (Dover Books on Chemistry)*, Dover Publications, 2005.
- [515] D. Daven, N. Tit, J. Morris and K. Ho, *Chem. Phys. Lett.*, 1996, **256**, 195.
- [516] Y. Xiang, H. Jiang, W. Cai and X. Shao, *J. Phys. Chem. A*, 2004, **108**, 3586.
- [517] B. C. Curley, R. L. Johnston, N. P. Young, Z. Y. Li, M. Di Vece, R. E. Palmer and A. L. Bleloch, *J. Phys. Chem. C*, 2007, **111**, 17846.
- [518] D. J. Wales and J. P. K. Doye, *J. Phys. Chem. A*, 1997, **101**, 5111.
- [519] R. H. Leary and J. P. K. Doye, *Phys. Rev. E*, 1999, **60**, R6320.
- [520] M. Born and R. Oppenheimer, *Ann. Phys.*, 1927, **389**, 457.
- [521] J. J. Sakurai and S. F. Tuan, *Modern Quantum Mechanics*, Benjamin/Cummings Pub. and Addison-Wesley Pub, Menlo Park, Calif. and Redwood City, Calif, 1985.
- [522] P. Hohenberg and W. Kohn, *Phys. Rev.*, 1964, **136**, B864.
- [523] M. Levy, *Proc. Natl. Acad. Sci. U.S.A.*, 1979, **76**, 6062.
- [524] L. H. Thomas, *Math. Proc. Cambridge Philos. Soc.*, 1927, **23**, 542.
- [525] E. Fermi, *Z. Phys. A: Hadrons Nucl.*, 1928, **48**, 73.
- [526] W. Kohn and L. J. Sham, *Phys. Rev.*, 1965, **140**, A1133.
- [527] T. L. Gilbert, *Phys. Rev. B*, 1975, **12**, 2111.
- [528] J. E. Harriman, *Phys. Rev. A*, 1981, **24**, 680.
- [529] U. von Barth, in *NATO ASI Series*, ed. Phariseau and Temmerman, Plenum Press, 1984.
- [530] A. D. Becke, *J. Chem. Phys.*, 1993, **98**, 1372.
- [531] M. Ernzerhof, *Chem. Phys. Lett.*, 1996, **263**, 499.
- [532] E. Schrödinger, *Ann. Phys.*, 1926, **384**, 361.
- [533] P. A. M. Dirac, *Proc. R. Soc. London, Ser. A*, 1928, **117**, 610.
- [534] D. R. Hartree, *Math. Proc. Cambridge Philos. Soc.*, 1928, **24**, 111.
- [535] D. R. Hartree, *Math. Proc. Cambridge Philos. Soc.*, 1928, **24**, 426.
- [536] J. C. Slater, *Phys. Rev.*, 1930, **36**, 57.
- [537] V. Fock, *Z. Phys. A: Hadrons Nucl.*, 1930, **61**, 126.
- [538] E. Wigner and F. Seitz, *Phys. Rev.*, 1933, **43**, 804.
- [539] E. Wigner, *Phys. Rev.*, 1934, **46**, 1002.
- [540] C. F. v. Weizsäcker, *Z. Phys. A: Hadrons Nucl.*, 1935, **96**, 431.

Bibliography

- [541] J. C. Slater, *Phys. Rev.*, 1937, **51**, 846.
- [542] J. C. Slater, *Phys. Rev.*, 1951, **81**, 385.
- [543] J. C. Phillips and L. Kleinman, *Phys. Rev.*, 1959, **116**, 287.
- [544] D. Pines, in *Solid State Physics, Vol. I*, ed. F. Seitz and D. Turnbull, Academic Press, Inc., New York, 1955.
- [545] M. Gell-Mann and K. A. Brueckner, *Phys. Rev.*, 1957, **106**, 364.
- [546] U. von Barth and L. Hedin, *J. Phys.: Condens. Matter C*, 1972, **5**, 1629.
- [547] O. K. Andersen, *Phys. Rev. B*, 1975, **12**, 3060.
- [548] M. Levy, *Phys. Rev. A*, 1982, **26**, 1200.
- [549] E. Runge and E. K. U. Gross, *Phys. Rev. Lett.*, 1984, **52**, 997.
- [550] E. Gross, J. Dobson and M. Petersilka, in *Density Functional Theory II*, ed. R. Nalewajski, Springer Berlin / Heidelberg, 1996, vol. 181, p. 81.
- [551] M. Parrinello and W. Andreoni, *computer code CPMD V3.9*, <http://www.cpmid.org/>.
- [552] A. D. Becke, *Phys. Rev. A*, 1988, **38**, 3098.
- [553] C. Lee, W. Yang and R. G. Parr, *Phys. Rev. B*, 1988, **37**, 785.
- [554] M. Frisch, G. Trucks, M. Head-Gordon, P. Gill, M. Wong, J. Foresman, B. Johnson, H. Schlegel, M. Robb, E. Replogle, R. Gomperts, J. Andres, K. Raghavachari, J. Binkley, C. Gonzales, R. Martin, D. Fox, D. DeFrees, J. Baker, J. Stewart and J. Pople, *Gaussian 92/DFT*, 1992.
- [555] http://www.nobelprize.org/nobel_prizes/chemistry/laureates/1998/.
- [556] O. J. Wacker, R. Kümmel and E. K. U. Gross, *Phys. Rev. Lett.*, 1994, **73**, 2915.
- [557] F. Illas and R. L. Martin, *J. Chem. Phys.*, 1998, **108**, 2519.
- [558] B. Gyorffy, J. Staunton and G. Stocks, in *Fluctuations in Density Functional Theory: Random Metallic Alloys and Itinerant Paramagnets*, ed. E. Gross and R. Dreizler, Plenum, NY, 1995, p. 461.
- [559] S. Kümmel and M. Brack, *Phys. Rev. A*, 2001, **64**, 022506.
- [560] R. Car and M. Parrinello, *Phys. Rev. Lett.*, 1985, **55**, 2471.
- [561] M. Koskinen, P. Lipas and M. Manninen, *Nucl. Phys. A*, 1995, **591**, 421.
- [562] R. N. Schmid, E. Engel and R. M. Dreizler, *Phys. Rev. C*, 1995, **52**, 164.
- [563] W. Kohn, Y. Meir and D. E. Makarov, *Phys. Rev. Lett.*, 1998, **80**, 4153.
- [564] R. O. Jones and O. Gunnarsson, *Rev. Mod. Phys.*, 1989, **61**, 689.
- [565] A. Zupan, P. Blaha, K. Schwarz and J. P. Perdew, *Phys. Rev. B*, 1998, **58**, 11266.
- [566] J. Theilhaber, *Phys. Fluids B*, 1992, **4**, 2044.
- [567] R. Stadler and M. J. Gillan, *J. Phys.: Condens. Matter*, 2000, **12**, 6053.
- [568] N. Argaman and G. Makov, *Am. J. Phys.: Condens. Matter*, 2000, **68**, 69.
- [569] J. P. Perdew and W. Yue, *Phys. Rev. B*, 1986, **33**, 8800.
- [570] J. P. Perdew, *Phys. Rev. B*, 1986, **33**, 8822.
- [571] J. P. Perdew, J. A. Chevary, S. H. Vosko, K. A. Jackson, M. R. Pederson, D. J. Singh and C. Fiolhais, *Phys. Rev. B*, 1992, **46**, 6671.
- [572] J. P. Perdew, K. Burke and M. Ernzerhof, *Phys. Rev. Lett.*, 1996, **77**, 3865.
- [573] W. Koch and M. C. Holthausen, *A Chemist's Guide to Density Functional Theory*, Wiley-VCH, New York, 2000.

Bibliography

- [574] S. Kurth, J. P. Perdew and P. Blaha, *Int. J. Quantum Chem.*, 1999, **75**, 889.
- [575] L. A. Curtiss, K. Raghavachari, P. C. Redfern and J. A. Pople, *J. Chem. Phys.*, 1997, **106**, 1063.
- [576] J. Paier, M. Marsman and G. Kresse, *J. Chem. Phys.*, 2007, **127**, 024103.
- [577] J. Wang, G. Wang and J. Zhao, *Chem. Phys. Lett.*, 2003, **380**, 716.
- [578] M. D. Morse, *Chem. Rev.*, 1986, **86**, 1049.
- [579] A. Khein, D. J. Singh and C. J. Umrigar, *Phys. Rev. B*, 1995, **51**, 4105.
- [580] P. H. T. Philipsen and E. J. Baerends, *Phys. Rev. B*, 1996, **54**, 5326.
- [581] N. E. Schultz, Y. Zhao and D. G. Truhlar, *J. Phys. Chem. A*, 2005, **109**, 4388.
- [582] N. E. Schultz, Y. Zhao and D. G. Truhlar, *J. Phys. Chem. A*, 2005, **109**, 11127.
- [583] X. Gonze, J.-M. Beuken, R. Caracas, F. Detraux, M. Fuchs, G.-M. Rignanese, L. Sindic, M. Verstraete, G. Zerah, F. Jollet, M. Torrent, A. Roy, M. Mikami, P. Ghosez, J.-Y. Raty and D. Allan, *Comput. Mater. Sci.*, 2002, **25**, 478.
- [584] M. A. L. Marques, A. Castro, A. Rubio, K. Yabana and G. W. Bertsch, *Octopus*, 2002, <http://www.tddft.org/programs/octopus/>.
- [585] M. Valiev, E. Bylaska, N. Govind, K. Kowalski, T. Straatsma, H. V. Dam, D. Wang, J. Nieplocha, E. Apra, T. Windus and W. de Jong, *Comput. Phys. Commun.*, 2010, **181**, 1477.
- [586] P. Giannozzi, S. Baroni, N. Bonini, M. Calandra, R. Car, C. Cavazzoni, D. Ceresoli, G. L. Chiarotti, M. Cococcioni, I. Dabo, A. D. Corso, S. de Gironcoli, S. Fabris, G. Fratesi, R. Gebauer, U. Gerstmann, C. Gougoussis, A. Kokalj, M. Lazzeri, L. Martin-Samos, N. Marzari, F. Mauri, R. Mazzarello, S. Paolini, A. Pasquarello, L. Paulatto, C. Sbraccia, S. Scandolo, G. Sclauzero, A. P. Seitsonen, A. Smogunov, P. Umari and R. M. Wentzcovitch, *J. Phys.: Condens. Matter*, 2009, **21**, 395502.
- [587] D. Sundholm, *Chem. Phys. Lett.*, 1999, **302**, 480.
- [588] P. Carloni, *Quant. Struct.-Act. Relat.*, 2002, **21**, 166.
- [589] T. Frauenheim, G. Seifert, M. Elsterner, Z. Hajnal, G. Jungnickel, D. Porezag, S. Suhai and R. Scholz, *Phys. Status Solidi B*, 2000, **217**, 41.
- [590] I. Daizadeh, E. S. Medvedev and A. A. Stuchebrukhov, *Proc. Natl. Acad. Sci. U.S.A.*, 1997, **94**, 3703.
- [591] Z. He, V. Sundström and T. Pullerits, *FEBS Lett.*, 2001, **496**, 36.
- [592] Y. Xiao and D. E. Williams, *Chem. Phys. Lett.*, 1993, **215**, 17.
- [593] Y. Zeiri, *Phys. Rev. E*, 1995, **51**, R2769.
- [594] D. M. Deaven and K. M. Ho, *Phys. Rev. Lett.*, 1995, **75**, 288.
- [595] C. Roberts, R. L. Johnston and N. T. Wilson, *Theor. Chem. Acc.*, 2000, **104**, 123.
- [596] C. Roberts and R. L. Johnston, *Phys. Chem. Chem. Phys.*, 2001, **3**, 5024.
- [597] F. F. Guimarães, J. C. Belchior, R. L. Johnston and C. Roberts, *J. Chem. Phys.*, 2002, **116**, 8327.
- [598] R. A. Lordeiro, F. F. Guimarães, J. C. Belchior and R. L. Johnston, *Int. J. Quantum Chem.*, 2003, **95**, 112.
- [599] M. Bailey, N. Wilson, C. Roberts and R. Johnston, *Eur. Phys. J. D*, 2003, **25**, 41.

Bibliography

- [600] R. L. Johnston, in *Metal Nanoparticles and Nanoalloys*, ed. J. W. Roy Johnston, Elsevier, UK, 2012.
- [601] R. H. Byrd, P. Lu, J. Nocedal and C. Zhu, *SIAM J. Sci. Comput.*, 1994, **16**, 1190.
- [602] Z. Li and H. A. Scheraga, *Proc. Natl. Acad. Sci. U.S.A.*, 1987, **84**, 6611.
- [603] F. H. Stillinger and T. A. Weber, *J. Stat. Phys.*, 1988, **52**, 1429.
- [604] J. P. K. Doye and D. J. Wales, *J. Chem. Phys.*, 1996, **105**, 8428.
- [605] J. P. K. Doye and D. J. Wales, *Phys. Rev. Lett.*, 1998, **80**, 1357.
- [606] J. A. Niesse and H. R. Mayne, *J. Chem. Phys.*, 1996, **105**, 4700.
- [607] C. Baysal and H. Meirovitch, *J. Chem. Phys.*, 1996, **105**, 7868.
- [608] P. Derreumaux, *J. Chem. Phys.*, 1997, **106**, 5260.
- [609] P. Derreumaux, *J. Chem. Phys.*, 1997, **107**, 1941.
- [610] J. P. K. Doye and D. J. Wales, *J. Chem. Soc., Faraday Trans.*, 1997, **93**, 4233.
- [611] J. P. K. Doye, D. J. Wales and R. S. Berry, *J. Chem. Phys.*, 1995, **103**, 4234.
- [612] G. Rossi and R. Ferrando, *Chem. Phys. Lett.*, 2006, **423**, 17.
- [613] R. Ferrando, G. Rossi, A. C. Levi, Z. Kuntová, F. Nita, A. Jelea, C. Mottet, G. Barcaro, A. Fortunelli and J. Goniakowski, *J. Chem. Phys.*, 2009, **130**, 174702.
- [614] R. Ferrando, *personal communication*.
- [615] L. Zhan, B. Piwowar, W.-K. Liu, P. J. Hsu, S. K. Lai and J. Z. Y. Chen, *J. Chem. Phys.*, 2004, **120**, 5536.
- [616] R. P. Gupta, *Phys. Rev. B*, 1981, **23**, 6265.
- [617] D. Bazin, D. Guillaume, C. Pichon, D. Uzio and S. Lopez, *Oil Gas Sci. Technol.*, 2005, **60**, 801.
- [618] A. Fortunelli and G. Barcaro, *personal communication*.
- [619] N. T. Wilson, M. S. Bailey and R. L. Johnston, *Inorg. Chim. Acta*, 2006, **359**, 3649.
- [620] R. Ismail and R. L. Johnston, *Phys. Chem. Chem. Phys.*, 2010, **12**, 8607.
- [621] E. J. Bylaska, W. A. de Jong, K. Kowalski, T. P. Straatsma, M. V. D. Wang, E. Aprà, T. L. W. S. Hirata, M. T. Hackler, Y. Zhao, P.-D. Fan, R. J. Harrison, M. Dupuis, D. M. A. Smith, J. Nieplocha, V. Tipparaju, M. Krishnan, A. A. Auer, M. Nooijen, E. Brown, G. Cisnerosand, G. I. Fann, H. Früchtl, J. Garza, K. Hirao, R. Kendall, J. A. Nichols, K. Tsemekhman, K. Wolinski, J. Anchell, D. Bernholdt, P. Borowski, T. Clark, D. Clerc, H. Dachsel, M. Deegan, K. Dyll, D. Elwood, E. Glendening, M. Gutowski, A. Hess, J. Jaffe, B. Johnson, J. Ju, R. Kobayashi, R. Kutteh, Z. Lin, R. Littlefield, X. L. B. Meng, T. Nakajima, S. Ni, L. Pollack, M. Rosing, G. Sandrone, M. Stave, H. T. G. Thomas, J. van Lenthe, A. Wong and Z. Zhang, *NWChem, A Computational Chemistry Package for Parallel Computers, Version 5.0, Pacific Northwest National Laboratory, Richland, Washington 99352-0999, USA*, 2006.
- [622] L. O. Paz-Borbón, *Ph.D. thesis*, University of Birmingham, United Kingdom, 2009.
- [623] A. Schäfer, C. Huber and R. Ahlrichs, *J. Chem. Phys.*, 1994, **100**, 5829.
- [624] <ftp://ftp.chemie.uni-karlsruhe.de/pub/basen/>.
- [625] D. Andrae, U. Haeussermann, M. Dolg, H. Stoll and H. Preuss, *Theor. Chem.*

Bibliography

- Acc.*, 1990, **77**, 123.
- [626] F. Weigend, M. Häser, H. Patzelt and R. Ahlrichs, *Chem. Phys. Lett.*, 1998, **294**, 143.
- [627] L. O. Paz-Borbón, R. L. Johnston, G. Barcaro and A. Fortunelli, *Eur. Phys. J. D*, 2009, **52**, 131.
- [628] J. P. Perdew and A. Zunger, *Phys. Rev. B*, 1981, **23**, 5048.
- [629] R. Ismail and R. L. Johnston, *unpublished results*.
- [630] R. Ferrando, G. Barcaro and A. Fortunelli, *Phys. Rev. B*, 2011, **83**, 045418.
- [631] S. de Gironcoli, *Phys. Rev. B*, 1995, **51**, 6773.
- [632] M. M. Mariscal, N. A. Oldani, S. A. Dassie and E. P. M. Leiva, *Faraday Discuss.*, 2008, **138**, 89.
- [633] L. B. Hansen, P. Stoltze, J. K. Nørskov, B. S. Clausen and W. Niemann, *Phys. Rev. Lett.*, 1990, **64**, 3155.
- [634] S. Ö. Kart, A. Erbay, H. K. T. Cagin and M. Tomak, *JAMME*, 2008, **31**, 11–13.
- [635] M. Itoh, V. Kumar, T. Adschiri and Y. Kawazoe, *J. Chem. Phys.*, 2009, **131**, 174510.
- [636] F. Aguilera-Granja, A. Vega, J. Rogan, X. Andrade and G. García, *Phys. Rev. B*, 2006, **74**, 224405.
- [637] D. S. Goodsell and A. J. Olson, *Annu. Rev. Biophys. Biomol. Struct.*, 2000, **29**, 105.
- [638] M. Istvan Hargittai and M. Hargittai, *Symmetry: A Unifying Concept*, Pgw, 1994.
- [639] *The concise Oxford dictionary*, ed. J. Pearsall, Oxford Univ. Press, Oxford, 10th edn., 1999.
- [640] H. Weyl, *Symmetry*, Princeton University Press, New York, 1989.
- [641] J. P. Elliott and P. G. Dawber, *Symmetry in Physics*, Macmilan, London, 1979.
- [642] F. H. C. Crick and J. D. Watson, *Nature*, 1956, **177**, 473.
- [643] J. C. Kendrew, G. Bodo, H. M. Dintzis, R. G. Parrish and H. Wyckoff, *Nature*, 1958, **181**, 662.
- [644] T. L. Blundell and N. Srinivasan, *Proc. Natl. Acad. Sci. U.S.A.*, 1996, **93**, 14243.
- [645] H. W. Kroto, J. R. Heath, S. C. O'Brien, R. F. Curl and R. E. Smalley, *Nature*, 1985, **318**, 162.
- [646] J. Li, X. Li, H.-J. Zhai and L.-S. Wang, *Science*, 2003, **299**, 864.
- [647] I. A. Solov'yov, A. V. Solov'yov and W. Greiner, *Phys. Rev. A*, 2002, **65**, 053203.
- [648] S.-K. Lin, *J. Chem. Inf. Comput. Sci.*, 1996, **36**, 367.
- [649] I. Prigogine, *Order Out of Chaos: Man's New Dialogue with Nature*, Random House, 1984.
- [650] W. F. A. Magie, *Source Book in Physics*, McGraw-Hill, New York, 1935.
- [651] E. Schrödinger, *Statistical Mechanics*, University Press, London, 1952.
- [652] E. Schrödinger, *What is life? The Physical Aspect of the Living Cell*, Cambridge University Press, London, 1944.
- [653] D. J. Depew, B. H. Weber and J. D. Smith, *Entropy, information, and evolution : new perspectives on physical and biological evolution*, MIT Press, Cambridge, Mass., 1988.

Bibliography

- [654] L. Onsager, *Phys. Rev.*, 1931, **37**, 405.
- [655] D. Halliday, R. Resnick and J. Walker, *Fundamentals of Physics - 4th Ed.*, J. Wiley & Sons, Ltd., New York, 1993.
- [656] J. Rosen, *Entropy*, 2005, **7**, 308.
- [657] A. M. Lesk, *J. Phys.: Condens. Matter A*, 1980, **13**, L111.
- [658] J. von Neumann, *Mathematical Foundations of Quantum Mechanics*; Princeton University Press, Princeton, 1955.
- [659] S.-K. Lin, *Entropy*, 2008, **10**, 55.
- [660] S.-K. Lin, *ArXiv Phys. e-prints*, 2001, 1.
- [661] M. Petitjean, *Entropy*, 2003, **5**, 271.
- [662] X. Yang, W. Cai and X. Shao, *J. Phys. Chem. A*, 2007, **111**, 5048.
- [663] D. Reinhard, B. D. Hall, D. Ugarte and R. Monot, *Phys. Rev. B*, 1997, **55**, 7868.
- [664] C. Li, N. Lu, Q. Xu, J. Mei, W. Dong, J. Fu and Z. Cao, *J. Cryst. Growth*, 2011, **319**, 88.
- [665] J. P. K. Doye, M. A. Miller and D. J. Wales, *J. Chem. Phys.*, 1999, **111**, 8417.
- [666] M. N. Blom, D. Schooss, J. Stairs and M. M. Kappes, *J. Chem. Phys.*, 2006, **124**, 244308.
- [667] A. L. Mackay, *Acta Cryst.*, 1962, **15**, 916.
- [668] M. R. Hoare, in *Structure and Dynamics of Simple Microclusters*, John Wiley and Sons, Inc., Hoboken, NJ, USA, 2007.
- [669] O. Echt, O. Kandler, T. Leisner, W. Miehle and E. Recknagel, *J. Chem. Soc., Faraday Trans.*, 1990, **86**,
- [670] I. A. Harris, R. S. Kidwell and J. A. Northby, *Phys. Rev. Lett.*, 1984, **53**, 2390.
- [671] E. M. Fernández, J. M. Soler and L. C. Balbás, *Phys. Rev. B*, 2006, **73**, 235433.
- [672] K. Jug, B. Zimmermann, P. Calaminici and A. M. Köster, *J. Chem. Phys.*, 2002, **116**, 4497.
- [673] H. Häkkinen and U. Landman, *Phys. Rev. B*, 2000, **62**, R2287.
- [674] J. Zhao, J. Yang and J. G. Hou, *Phys. Rev. B*, 2003, **67**, 085404.
- [675] G. Bravo-Pérez, I. Garzón and O. Novaro, *Chem. Phys. Lett.*, 1999, **313**, 655.
- [676] V. Bonačić-Koutecký, L. Češpiva, P. Fantucci and J. Koutecký, *J. Chem. Phys.*, 1993, **98**, 7981.
- [677] R. Fournier, *J. Chem. Phys.*, 2001, **115**, 2165.
- [678] L. Xiao and L. Wang, *J. Phys. Chem. A*, 2004, **108**, 8605.
- [679] J. Pillardy and L. Piela, *J. Phys. Chem.*, 1995, **99**, 11805.
- [680] J. P. Doye and D. J. Wales, *Chem. Phys. Lett.*, 1995, **247**, 339.
- [681] J. L. Rodríguez-López, J. M. Montejano-Carrizales, J. P. Palomares-Báez, H. Barrón-Escobar, J. J. Velázquez-Salazar, J. M. Cabrera-Trujillo and M. José-Yacamán, *Key Eng. Mater.*, 2010, **444**, 47–68.
- [682] L. D. Marks, *Rep. Prog. Phys.*, 1994, **57**, 603.
- [683] M. Alvarez, J. Khoury, T. Schaaff, M. Shafiqullin, I. Vezmar and R. Whetten, *Chem. Phys. Lett.*, 1997, **266**, 91.
- [684] R. Esparza, G. Rosas, E. Valenzuela, S. Gamboa, U. Pal and R. Pérez, *Matéria (Rio J.)*, 2008, **13**, 579.

Bibliography

- [685] Z. Y. Li, N. P. Young, M. Di Vece, S. Palomba, R. E. Palmer, A. L. Bleloch, B. C. Curley, R. L. Johnston, J. Jiang and J. Yuan, *Nature*, 2008, **451**, 06470.
- [686] A. S. Barnard and L. A. Curtiss, *ChemPhysChem*, 2006, **7**, 1544.
- [687] R. L. Whetten, J. T. Khoury, M. M. Alvarez, S. Murthy, I. Vezmar, Z. L. Wang, P. W. Stephens, C. L. Cleveland, W. D. Luedtke and U. Landman, *Adv. Mater.*, 1996, **8**, 428.
- [688] A. Pinto, A. R. Pennisi, G. Faraci, G. D'Agostino, S. Mobilio and F. Boscherini, *Phys. Rev. B*, 1995, **51**, 5315.
- [689] J. Uppenbrink and D. J. Wales, *J. Chem. Phys.*, 1992, **96**, 8520.
- [690] B. Wang, M. Liu, Y. Wang and X. Chen, *J. Phys. Chem. C*, 2011, **115**, 11374.
- [691] S. H. Baker, M. Roy, S. C. Thornton, M. Qureshi and C. Binns, *J. Phys.: Condens. Matter*, 2010, **22**, 385301.
- [692] J. A. Ascencio, M. Pérez and M. José-Yacamán, *Surf. Sci.*, 2000, **447**, 73.
- [693] S. Tehuacanero, R. Herrera, M. Avalos and M. J. Yacamán, *Acta Metall. Mater.*, 1992, **40**, 1663.
- [694] L. O. Paz-Borbón, T. V. Mortimer-Jones, R. L. Johnston, A. Posada-Amarillas, G. Barcaro and A. Fortunelli, *Phys. Chem. Chem. Phys.*, 2007, **9**, 5202.
- [695] E. Groppo, W. Liu, O. Zavorotynska, G. Agostini, G. Spoto, S. Bordiga, C. Lamberti and A. Zecchina, *Chem. Mater.*, 2010, **22**, 2297.
- [696] J. He, I. Ichinose, T. Kunitake, A. Nakao, Y. Shiraishi and N. Toshima, *J. Am. Chem. Soc.*, 2003, **125**, 11034.
- [697] P. V. Kamat, R. Huehn and R. Nicolaescu, *J. Phys. Chem. B*, 2002, **106**, 788.
- [698] S. Sun, C. B. Murray, D. Weller, L. Folks and A. Moser, *Science*, 2000, **287**, 1989.
- [699] R. P. Andres, J. D. Bielefeld, J. I. Henderson, D. B. Janes, V. R. Kolagunta, C. P. Kubiak, W. J. Mahoney and R. G. Osifchin, *Science*, 1996, **273**, 1690.
- [700] H.-X. Xie, C.-Y. Wang and T. Yu, *Modell. Simul. Mater. Sci. Eng.*, 2009, **17**, 055007.
- [701] J.-B. Zhu, S. Wang, M.-H. Qiao, W.-N. Wang and K.-N. Fan, *J. Non-Cryst. Solids*, 2007, **353**, 2638.
- [702] R. W. Cahn and P. Haasen, *Physical Metallurgy*, Elsevier, Amsterdam, 1996.
- [703] E. E. Zhurkin, G. Hautier and M. Hou, *Phys. Rev. B*, 2006, **73**, 094108.
- [704] D. Shi, B. Wen, R. Melnik, S. Yao and T. Li, *J. Solid State Chem.*, 2009, **182**, 2664.
- [705] H. Okamoto and T. Massalski, *J. Phase Equilib.*, 1985, **6**, 229.
- [706] F. R. De Boer, R. Boom, W. C. M. Mattens, A. R. Miedama and A. K. Niessen, *Cohesion in Metals: Transition Metal Alloys*, Elsevier, Amsterdam, 1988.
- [707] S. Pabi and B. Murty, *Mater. Sci. Eng., A*, 1996, **214**, 146.
- [708] A. J. Bradley and A. Taylor, *Philos. Mag. Ser. 7*, 1937, **23**, 1049.
- [709] A. J. Bradley and A. Taylor, *Proc. R. Soc. A*, 1937, **159**, 56.
- [710] K. Michaelian, N. Rendón and I. L. Garzón, *Phys. Rev. B*, 1999, **60**, 2000.
- [711] L. D. Marks, *Philos. Mag. A*, 1984, **49**, 81.
- [712] J. P. K. Doye and L. Meyer, *Phys. Rev. Lett.*, 2005, **95**, 063401.
- [713] L. Pauling, *The Nature of the Chemical Bond: An Introduction to Modern Struc-*

Bibliography

- tural Chemistry*, Cornell University Press, Ithaca, NY, 1960.
- [714] D. Cheng, W. Wang and S. Huang, *J. Phys. Chem. C*, 2007, **111**, 8037.
- [715] H. Cox, *Surf. Sci.*, 1998, **397**, 374.
- [716] J. L. Rousset, A. M. Cadrot, F. J. C. S. Aires, A. Renouprez, P. Mélinon, A. Perez, M. Pellarin, J. L. Vialle and M. Broyer, *J. Chem. Phys.*, 1995, **102**, 8574.
- [717] R. Ferrando, A. Fortunelli and R. L. Johnston, *Phys. Chem. Chem. Phys.*, 2008, **10**, 640.
- [718] J. P. K. Doye, D. J. Wales, W. Branz and F. Calvo, *Phys. Rev. B*, 2001, **64**, 235409.
- [719] K. Luo, T. Wei, C.-W. Yi, S. Axnanda and D. W. Goodman, *J. Phys. Chem. B*, 2005, **109**, 23517.
- [720] L. D. Lloyd and R. L. Johnston, *J. Chem. Soc., Dalton Trans.*, 2000, **3**, 307.
- [721] D. Belić, R. L. Chantry, Z. Y. Li and S. A. Brown, *Appl. Phys. Lett.*, 2011, **99**, 171914.
- [722] D. Watson and G. Attard, *Surf. Sci.*, 2002, **515**, 87.
- [723] D. Cheng, W. Wang and S. Huang, *J. Phys. Chem. B*, 2006, **110**, 16193.
- [724] D. G. Lee and U. A. Spitzer, *J. Org. Chem.*, 1970, **35**, 3589.
- [725] P. Prabhakaran, S. Venkatachalam and K. Ninan, *Eur. Polym. J.*, 1999, **35**, 1743.
- [726] K. Roy and S. Lahiri, *Anal. Chem.*, 2008, **80**, 7504.
- [727] W. S. Jung, J. Han, S. P. Yoon, S. W. Nam, T.-H. Lim and S.-A. Hong, *J. Power Sources*, 2011, **196**, 4573.
- [728] X. Yu and P. G. Pickup, *J. Power Sources*, 2009, **187**, 493.
- [729] X. Yu and P. G. Pickup, *Electrochem. Commun.*, 2009, **11**, 2012.
- [730] Y. Zhou, J. Liu, J. Ye, Z. Zou, J. Ye, J. Gu, T. Yu and A. Yang, *Electrochim. Acta*, 2010, **55**, 5024.
- [731] D. I. Enache, J. K. Edwards, P. Landon, B. Solsona-Espriu, A. F. Carley, A. A. Herzing, M. Watanabe, C. J. Kiely, D. W. Knight and G. J. Hutchings, *Science*, 2006, **311**, 362.
- [732] R. W. J. Scott, C. Sivadinarayana, O. M. Wilson, Z. Yan, D. W. Goodman and R. M. Crooks, *J. Am. Chem. Soc.*, 2005, **127**, 1380.
- [733] W. Zhou and J. Y. Lee, *Electrochem. Commun.*, 2007, **9**, 1725.
- [734] Y. Suo and I.-M. Hsing, *Electrochim. Acta*, 2011, **56**, 2174.
- [735] N. Dimitratos, J. A. Lopez-Sanchez, J. M. Anthonykutty, G. Brett, A. F. Carley, R. C. Tiruvalam, A. A. Herzing, C. J. Kiely, D. W. Knight and G. J. Hutchings, *Phys. Chem. Chem. Phys.*, 2009, **11**, 4952.
- [736] D. Wang, A. Villa, F. Porta, L. Prati and D. Su, *J. Phys. Chem. C*, 2008, **112**, 8617.
- [737] E. Gross, I. Popov and M. Asscher, *J. Phys. Chem. C*, 2009, **113**, 18341.
- [738] V. I. Pârvulescu, V. Pârvulescu, U. Endruschat, G. Filoti, F. E. Wagner, C. Kübel and R. Richards, *Chem. Eur. J.*, 2006, **12**, 2343.
- [739] H. Bönemann, U. Endruschat, B. Tesche, A. Rufínska, C. W. Lehmann, F. E. Wagner, G. Filoti, V. Pârvulescu and V. I. Pârvulescu, *Eur. J. Inorg. Chem.*,

Bibliography

- 2000, **2000**, 819.
- [740] M. O. Nutt, J. B. Hughes and M. S. Wong, *Environ. Sci. Technol.*, 2005, **39**, 1346.
- [741] J. K. Edwards, B. E. Solsona, P. Landon, A. F. Carley, A. Herzing, C. J. Kiely and G. J. Hutchings, *J. Catal.*, 2005, **236**, 69.
- [742] B. E. Solsona, J. K. Edwards, P. Landon, A. F. Carley, A. Herzing, C. J. Kiely and G. J. Hutchings, *Chem. Mater.*, 2006, **18**, 2689.
- [743] Y.-F. Han, J.-H. Wang, D. Kumar, Z. Yan and D. Goodman, *J. Catal.*, 2005, **232**, 467.
- [744] F. Menegazzo, P. Burti, M. Signoretto, M. Manzoli, S. Vankova, F. Boccuzzi, F. Pinna and G. Strukul, *J. Catal.*, 2008, **257**, 369.
- [745] T. Balcha, J. R. Strobl, C. Fowler, P. Dash and R. W. J. Scott, *ACS Catal.*, 2011, **1**, 425.
- [746] S. Marx and A. Baiker, *J. Phys. Chem. C*, 2009, **113**, 6191.
- [747] F. Liu, D. Wechsler and P. Zhang, *Chem. Phys. Lett.*, 2008, **461**, 254.
- [748] P. Dash, T. Bond, C. Fowler, W. Hou, N. Coombs and R. W. J. Scott, *J. Phys. Chem. C*, 2009, **113**, 12719.
- [749] J. Xu, T. Zhao, S. Shen and Y. Li, *Int. J. Hydrogen Energy*, 2010, **35**, 6490.
- [750] D. Wang, A. Villa, P. Spontoni, D. S. Su and L. Prati, *Chem. Eur. J.*, 2010, **16**, 10007.
- [751] Y.-L. Fang, K. N. Heck, P. J. J. Alvarez and M. S. Wong, *ACS Catalysis*, 2011, **1**, 128.
- [752] A. Staykov, T. Kamachi, T. Ishihara and K. Yoshizawa, *J. Phys. Chem. C*, 2008, **112**, 19501.
- [753] H. C. Ham, G. S. Hwang, J. Han, S. W. Nam and T. H. Lim, *J. Phys. Chem. C*, 2009, **113**, 12943.
- [754] C. J. Baddeley, M. Tikhov, C. Hardacre, J. R. Lomas and R. M. Lambert, *J. Phys. Chem.*, 1996, **100**, 2189.
- [755] S. Bertarione, D. Scarano, A. Zecchina, V. Johánek, J. Hoffmann, S. Schauer-
mann, J. Libuda, G. Rupprechter and H.-J. Freund, *J. Catal.*, 2004, **223**, 64.
- [756] T. Lear, R. Marshall, J. A. Lopez-Sanchez, S. D. Jackson, T. M. Klapötke,
M. Bäumer, G. Rupprechter, H.-J. Freund and D. Lennon, *J. Chem. Phys.*, 2005,
123, 174706.
- [757] T. Lear, R. Marshall, E. K. Gibson, T. Schutt, T. M. Klapötke, G. Rupprechter,
H.-J. Freund, J. M. Winfield and D. Lennon, *Phys. Chem. Chem. Phys.*, 2005,
7, 565.
- [758] S. Bertarione, D. Scarano, A. Zecchina, V. Johánek, J. Hoffmann, S. Schauer-
mann, M. M. Frank, J. Libuda, G. Rupprechter and H.-J. Freund, *J. Phys. Chem.
B*, 2004, **108**, 3603.
- [759] H. Borchert, B. Jürgens, V. Zielasek, G. Rupprechter, S. Giorgio, C. Henry and
M. Bäumer, *J. Catal.*, 2007, **247**, 145.
- [760] I. Garzón, K. Michaelian, M. Beltrán, A. Posada-Amarillas, P. Ordejón, E. Ar-
tacho, D. Sánchez-Portal and J. Soler, *Eur. Phys. J. D*, 1999, **9**, 211.
- [761] M. Mandal, S. Kundu, S. K. Ghosh and T. Pal, *J. Photochem. Photobiol., A*,
2004, **167**, 17.

Bibliography

- [762] A. Henglein, *J. Phys. Chem. B*, 2000, **104**, 6683.
- [763] H. B. Liu, U. Pal, R. Perez and J. A. Ascencio, *J. Phys. Chem. B*, 2006, **110**, 5191.
- [764] S. Loiha, K. Föttinger, K. Zorn, W. Klysubun, G. Rupprechter and J. Wittayakun, *J. Ind. Eng. Chem.*, 2009, **15**, 819.
- [765] T. Fujikawa, K. Idei, T. Ebihara, H. Mizuguchi and K. Usui, *Appl. Catal., A*, 2000, **192**, 253.
- [766] J. Barbier, E. Lamy-Pitara, P. Marecot, J. Boitiaux, J. Cosyns and F. Verna, *Adv. Catal.*, 1990, **37**, 279.
- [767] B. H. Cooper and B. B. Donnis, *Appl. Catal., A*, 1996, **137**, 203.
- [768] A. Stanislaus and B. H. Cooper, *Catal. Rev.*, 1994, **36**, 75.
- [769] C.-A. Jan, T.-B. Lin and J.-R. Chang, *Ind. Eng. Chem. Res.*, 1996, **35**, 3893.
- [770] E. Guillon, J. Lynch, D. Uzio and B. Didillon, *Catal. Today*, 2001, **65**, 201.
- [771] T. Kabe, W. Qian, Y. Hirai, L. Li and A. Ishihara, *J. Catal.*, 2000, **190**, 191.
- [772] M. Jacquín, D. J. Jones, J. Rozière, A. J. López, E. Rodríguez-Castellón, J. M. T. Menayo, M. Lenarda, L. Storaro, A. Vaccari and S. Albertazzi, *J. Catal.*, 2004, **228**, 447.
- [773] R. Navarro, B. Pawelec, J. Trejo, R. Mariscal and J. Fierro, *J. Catal.*, 2000, **189**, 184.
- [774] T.-B. Lin, C.-A. Jan and J.-R. Chang, *Ind. Eng. Chem. Res.*, 1995, **34**, 4284.
- [775] W. Qian, H. Shirai, M. Ifuku, A. Ishihara and T. Kabe, *Energy Fuels*, 2000, **14**, 1205.
- [776] K. Thomas, C. Binet, T. Chevreau, D. Cornet and J.-P. Gilson, *J. Catal.*, 2002, **212**, 63.
- [777] J.-K. Lee and H.-K. Rhee, *J. Catal.*, 1998, **177**, 208.
- [778] S. Jongpatiwut, Z. Li, D. E. Resasco, W. E. Alvarez, E. L. Sughrue and G. W. Dodwell, *Appl. Catal., A*, 2004, **262**, 241.
- [779] F. Alcaide, G. Álvarez, P. L. Cabot, H.-J. Grande, O. Miguel and A. Querejeta, *Int. J. Hydrogen Energy*, 2011, **36**, 4432.
- [780] T. Matsui, M. Harada, K. K. Bando, M. Toba and Y. Yoshimura, *Appl. Catal., A*, 2005, **290**, 73.
- [781] N. Toshima, H. Yan and Y. Shiraiishi, in *Metal Nanoclusters in Catalysis and Materials Science*, ed. B. Corain, G. Schmid and N. Toshima, Elsevier, Amsterdam, 2008, p. 49.
- [782] Y. Shao-Horn, W. Sheng, S. Chen, P. Ferreira, E. Holby and D. Morgan, *Top. Catal.*, 2007, **46**, 285.
- [783] A. Chen and P. Holt-Hindle, *Chem. Rev.*, 2010, **110**, 3767.
- [784] C. Bianchini and P. K. Shen, *Chem. Rev.*, 2009, **109**, 4183.
- [785] F. Alcaide, G. Álvarez, P. L. Cabot, O. Miguel and A. Querejeta, *Int. J. Hydrogen Energy*, 2010, **35**, 11634.
- [786] R. Inada, K. Shimazu and H. Kita, *J. Electroanal. Chem. Interfacial Electrochem.*, 1990, **277**, 315.
- [787] T. Iwasita, *Electrochim. Acta*, 2002, **47**, 3663.
- [788] A. Niquille-Röthlisberger and R. Prins, *Ind. Eng. Chem. Res.*, 2007, **46**, 4124.

Bibliography

- [789] M. Ruiz-Vizcaya, O. Novaro, J. Ferreira and R. Gómez, *J. Catal.*, 1978, **51**, 108.
- [790] H. Yasuda, T. Kameoka, T. Sato, N. Kijima and Y. Yoshimura, *Appl. Catal., A*, 1999, **185**, L199.
- [791] B. Pawelec, R. Mariscal, R. Navarro, S. van Bokhorst, S. Rojas and J. Fierro, *Appl. Catal., A*, 2002, **225**, 223.
- [792] K. K. Bando, T. Kawai, K. Asakura, T. Matsui, L. L. Bihan, H. Yasuda, Y. Yoshimura and S. T. Oyama, *Catal. Today*, 2006, **111**, 199.
- [793] G. Carturan, G. Cocco, G. Facchin and G. Navazio, *J. Mol. Catal.*, 1984, **26**, 375.
- [794] R. W. J. Scott, A. K. Datye and R. M. Crooks, *J. Am. Chem. Soc.*, 2003, **125**, 3708.
- [795] G. Bernardotto, F. Menegazzo, F. Pinna, M. Signoretto, G. Cruciani and G. Strukul, *Appl. Catal., A*, 2009, **358**, 129.
- [796] A. Niquille-Röthlisberger and R. Prins, *J. Catal.*, 2006, **242**, 207–216.
- [797] S. Elangovan, C. Bischof and M. Hartmann, *Catal. Lett.*, 2002, **80**, 35.
- [798] M. Bonarowska and Z. Karpiński, *Catal. Today*, 2008, **137**, 498.
- [799] E. Blomsma, J. Martens and P. Jacobs, *J. Catal.*, 1997, **165**, 241.
- [800] R. Strobel, J.-D. Grunwaldt, A. Camenzind, S. Pratsinis and A. Baiker, *Catal. Lett.*, 2005, **104**, 9.
- [801] T. Fujikawa, K. Idei, K. Ohki, H. Mizuguchi and K. Usui, *Appl. Catal., A*, 2001, **205**, 71.
- [802] Y. Yoshimura, M. Toba, T. Matsui, M. Harada, Y. Ichihashi, K. Bando, H. Yasuda, H. Ishihara, Y. Morita and T. Kameoka, *Appl. Catal., A*, 2007, **322**, 152.
- [803] M. Harada, K. Asakura, Y. Ueki and N. Toshima, *J. Phys. Chem.*, 1992, **96**, 9730.
- [804] G. Guisbiers, G. Abudukelimu and D. Hourlier, *Nanoscale Res. Lett.*, 2011, **6**, 1–5.
- [805] Y. Liu, M. Chi, V. Mazumder, K. L. More, S. Soled, J. D. Henao and S. Sun, *Chem. Mater.*, 2011, **23**, 4199.
- [806] S.-M. Hwang, C. H. Lee, J. J. Kim and T. P. Moffat, *Electrochim. Acta*, 2010, **55**, 8938.
- [807] N. Castillo, R. Pérez, M. Martínez-Ortiz, L. Díaz-Barriga, L. García and A. Conde-Gallardo, *J. Alloys Compd.*, 2010, **495**, 453.
- [808] K. Persson, A. Ersson, K. Jansson, J. Fierro and S. Järås, *J. Catal.*, 2006, **243**, 14.
- [809] A. Lebon, A. García-Fuente, A. Vega and F. Aguilera-Granja, *J. Phys. Chem. C*, 2012, **116**, 126.
- [810] F. Calvo, *Faraday Discuss.*, 2008, **138**, 75.
- [811] P. L. Hansen, A. M. Molenbroek and A. V. Ruban, *J. Phys. Chem. B*, 1997, **101**, 1861.
- [812] J. Rousset, A. Cadrot, L. Lianos and A. Renouprez, *Eur. Phys. J. D*, 1999, **9**, 425.
- [813] F. Bernardi, G. H. Fecher, M. C. M. Alves and J. Morais, *J. Phys. Chem. Lett.*, 2010, **1**, 912.

Bibliography

- [814] L. D. Lloyd, R. L. Johnston and S. Salhi, *J. Comput. Chem.*, 2005, **26**, 1069.
- [815] F. Bernardi, A. Traverse, L. Olivi, M. C. M. Alves and J. Morais, *J. Phys. Chem. C*, 2011, **115**, 12243.
- [816] I. Moysan, V. Paul-Boncour, S. Thiébaud, E. Sciora, J. Fournier, R. Cortes, S. Bourgeois and A. Percheron-Guégan, *J. Alloys Compd.*, 2001, **322**, 14.
- [817] J. Seweryn and A. Lewera, *J. Power Sources*, 2012, **205**, 264.
- [818] H. Jiang, H. Yang, R. Hawkins and Z. Ring, *Catal. Today*, 2007, **125**, 282.
- [819] J. Xu, L. Ouyang, G.-J. Da, Q.-Q. Song, X.-J. Yang and Y.-F. Han, *J. Catal.*, 2012, **285**, 74.
- [820] M. P. Humbert, L. E. Murillo and J. G. Chen, *ChemPhysChem*, 2008, **9**, 1262.
- [821] M. Lukaszewski, K. Hubkowska and A. Czerwinski, *Phys. Chem. Chem. Phys.*, 2010, **12**, 14567.
- [822] M. Kaneeda, H. Iizuka, T. Hiratsuka, N. Shinotsuka and M. Arai, *Appl. Catal., A*, 2009, **90**, 564.
- [823] A. Niquille-Röthlisberger and R. Prins, *Catal. Today*, 2007, **123**, 198.
- [824] T. Fujikawa, K. Tsuji, H. Mizuguchi, H. Godo, K. Idei and K. Usui, *Catal. Lett.*, 1999, **63**, 27–33.
- [825] S. Thiebaut, A. Bigot, J. Achard, B. Limacher, D. Leroy and A. Percheron-Guegan, *J. Alloys Compd.*, 1995, **231**, 440.
- [826] J. D. Clewley, J. F. Lynch and T. B. Flanagan, *J. Chem. Soc., Faraday Trans.*, 1977, **73**, 494.
- [827] M. Calleja, C. Rey, M. M. G. Alemany, L. J. Gallego, P. Ordejón, D. Sánchez-Portal, E. Artacho and J. M. Soler, *Phys. Rev. B*, 1999, **60**, 2020.
- [828] V. Shah and D. G. Kanhere, *Phys. Rev. B*, 2009, **80**, 125419.
- [829] D. Yuan, X. Gong and R. Wu, *Phys. Rev. B*, 2007, **75**, 085428.
- [830] D. Yuan, X. Gong and R. Wu, *Phys. Rev. B*, 2008, **78**, 035441.
- [831] F. R. Negreiros, G. Barcaro, Z. Kuntová, G. Rossi, R. Ferrando and A. Fortunelli, *Surf. Sci.*, 2011, **605**, 483.
- [832] J. Goniakowski, *Phys. Rev. B*, 1998, **58**, 1189.
- [833] B. Pauwels, G. Van Tendeloo, W. Bouwen, L. Theil Kuhn, P. Lievens, H. Lei and M. Hou, *Phys. Rev. B*, 2000, **62**, 10383.
- [834] C. Duriez, C. Henry and C. Chapon, *Surf. Sci.*, 1991, **253**, 190.
- [835] X. Wang, N. S. Venkataramanan, H. Kawanami and Y. Ikushima, *Green Chem.*, 2007, **9**, 1352.
- [836] L. Kesavan, R. Tiruvalam, M. H. A. Rahim, M. I. bin Saiman, D. I. Enache, R. L. Jenkins, N. Dimitratos, J. A. Lopez-Sanchez, S. H. Taylor, D. W. Knight, C. J. Kiely and G. J. Hutchings, *Science*, 2011, **331**, 195.
- [837] J. K. Edwards, A. Thomas, A. F. Carley, A. A. Herzing, C. J. Kiely and G. J. Hutchings, *Green Chem.*, 2008, **10**, 388.
- [838] A. Sandoval, A. Gómez-Cortés, R. Zanella, G. Díaz and J. M. Saniger, *J. Mol. Catal. A: Chem.*, 2007, **278**, 200.
- [839] V. E. Henrich, *The Surface Science of Metal Oxides*, Cambridge University Press, Cambridge, 1994.
- [840] C. Duriez, C. Chapon, C. Henry and J. Rickard, *Surf. Sci.*, 1990, **230**, 123.

Bibliography

- [841] L. M. Molina and B. Hammer, *Phys. Rev. B*, 2004, **69**, 155424.
- [842] J. Goniakowski, *Phys. Rev. B*, 1998, **57**, 1935.
- [843] K. Judai, S. Abbet, A. S. Wörz, U. Heiz, L. Giordano and G. Pacchioni, *J. Phys. Chem. B*, 2003, **107**, 9377.
- [844] L. Giordano, A. D. Vitto, G. Pacchioni and A. M. Ferrari, *Surf. Sci.*, 2003, **540**, 63.
- [845] I. Yudanov, G. Pacchioni, K. Neyman and N. Rösch, *J. Phys. Chem. B*, 1997, **101**, 2786.
- [846] G. Renaud, A. Barbier and O. Robach, *Phys. Rev. B*, 1999, **60**, 5872.
- [847] S. Giorgio, C. Henry, C. Chapon and J. Penisson, *J. Cryst. Growth*, 1990, **100**, 254.
- [848] C. Li, R. Wu, A. J. Freeman and C. L. Fu, *Phys. Rev. B*, 1993, **48**, 8317.
- [849] A. Sanchez, S. Abbet, U. Heiz, W.-D. Schneider, H. Häkkinen, R. N. Barnett and U. Landman, *J. Phys. Chem. A*, 1999, **103**, 9573.
- [850] C. Goyhenex and C. Henry, *J. Electron. Spectrosc. Relat. Phenom.*, 1992, **61**, 65.
- [851] K. Yamamoto, Y. Kasukabe, R. Takeishi and T. Osaka, *J. Vac. Sci. Technol. A*, 1996, **14**, 327.
- [852] L. Xu, G. Henkelman, C. T. Campbell and H. Jónsson, *Phys. Rev. Lett.*, 2005, **95**, 146103.
- [853] J. Goniakowski and C. Mottet, *J. Cryst. Growth*, 2005, **275**, 29.
- [854] C. R. Henry, *Surf. Sci. Rep.*, 1998, **31**, 231.
- [855] C. T. Campbell, *Surf. Sci. Rep.*, 1997, **27**, 1.
- [856] E. Aprà, R. Ferrando and A. Fortunelli, *Phys. Rev. B*, 2006, **73**, 205414.
- [857] S. Olivier, R. Conte and A. Fortunelli, *Phys. Rev. B*, 2008, **77**, 054104.
- [858] T. Kizuka and N. Tanaka, *Phys. Rev. B*, 1997, **56**, R10079.
- [859] C. Chapon, C. Henry and A. Chemam, *Surf. Sci.*, 1985, **162**, 747.
- [860] N. W. Ashcroft and N. D. Mermin, *Solid State Physics*, Harcourt College Publishers, New York, 1976.
- [861] L. B. Garmon and D. L. Doering, *Thin Solid Films*, 1983, **102**, 141.
- [862] K. Heinemann, T. Osaka, H. Poppa and M. Avalos-Borja, *J. Catal.*, 1983, **83**, 61.
- [863] G. Haas, A. Menck, H. Brune, J. V. Barth, J. A. Venable and K. Kern, *Phys. Rev. B*, 2000, **61**, 11105.
- [864] R. Ferrando, G. Barcaro and A. Fortunelli, *Phys. Rev. Lett.*, 2009, **102**, 216102.
- [865] W. C. Conner and J. L. Falconer, *Chem. Rev.*, 1995, **95**, 759.
- [866] C. Becker and C. Henry, *Surf. Sci.*, 1996, **352-354**, 457.
- [867] H. Fornander, L.-G. Ekedahl and H. Dannelun, *Surf. Sci.*, 1999, **441**, 479.
- [868] C. R. Henry, C. Chapon and C. Duriez, *J. Chem. Phys.*, 1991, **95**, 700.
- [869] L. Piccolo, C. Becker and C. R. Henry, *Appl. Surf. Sci.*, 2000, **164**, 156.
- [870] P. Nolte, A. Stierle, O. Balmes, V. Srot, P. van Aken, L. Jeurgens and H. Dosch, *Catal. Today*, 2009, **145**, 243.
- [871] L. Piccolo and C. R. Henry, *Surf. Sci.*, 2000, **452**, 198.
- [872] L. Piccolo and C. R. Henry, *Appl. Surf. Sci.*, 2000, **162D163**, 670.

Bibliography

- [873] L. Piccolo and C. R. Henry, *J. Mol. Catal. A: Chem.*, 2001, **167**, 181.
- [874] H. Fornander, J. Birch, P. Sandström and J.-E. Sundgren, *Thin Solid Films*, 1999, **349**, 4.
- [875] I. Deliy, N. Maksimchuk, R. Psaro, N. Ravasio, V. D. Santo, S. Recchia, E. Paukshtis, A. Golovin and V. Semikolenov, *Appl. Catal., A*, 2005, **279**, 99.
- [876] C. Henry, C. Chapon, C. Goyhenex and R. Monot, *Surf. Sci.*, 1992, **272**, 283.
- [877] J. Goniakowski, A. Jelea, C. Mottet, G. Barcaro, A. Fortunelli, Z. Kuntová, F. Nita, A. C. Levi, G. Rossi and R. Ferrando, *J. Chem. Phys.*, 2009, **130**, 174703.
- [878] R. Ferrando and A. Fortunelli, *J. Phys.: Condens. Matter*, 2009, **21**, 264001.
- [879] G. Rossi, C. Mottet, F. Nita and R. Ferrando, *J. Phys. Chem. B*, 2006, **110**, 7436.
- [880] L. Giordano, J. Goniakowski and G. Pacchioni, *Phys. Rev. B*, 2001, **64**, 075417.
- [881] F. R. Negreiros, Z. Kuntová, G. Barcaro, G. Rossi, R. Ferrando and A. Fortunelli, *J. Chem. Phys.*, 2010, **132**, 234703.
- [882] J. Goniakowski, C. Mottet and C. Noguera, *Phys. Status Solidi B*, 2006, **243**, 2516.
- [883] <http://www.cinam.univ-mrs.fr/mottet/param/metalMgO.pdf>.
- [884] <http://www.bear.bham.ac.uk>.
- [885] W. Fa, J. Zhou, X. Li and J. Dong, *J. Phys. Chem. C*, 2010, **114**, 13035.

Appendix A

Gupta Potential Parameters

A.1 Gupta potential parameterisations of Pd-Au

parameter	0.0	0.1	0.2	0.3	0.4	0.5	0.6	0.7	0.8	0.9	1.0
	parameter set I										
<i>A</i>	0.2061	0.2030	0.1998	0.1966	0.1935	0.1904	0.1872	0.1840	0.1809	0.1778	0.1746
ξ	1.7900	1.7828	1.7756	1.7684	1.7612	1.7540	1.7468	1.7396	1.7324	1.7252	1.7180
<i>p</i>	10.2290	10.2928	10.3566	10.4204	10.4842	10.5480	10.6118	10.6756	10.7394	10.8032	10.8670
<i>q</i>	4.0360	4.0066	3.9772	3.9478	3.9184	3.8890	3.8596	3.8302	3.8008	3.7714	3.7420
<i>r</i> ₀	2.8840	2.8704	2.8569	2.8433	2.8298	2.8163	2.8027	2.7891	2.7756	2.7621	2.7485
	parameter set II										
<i>A</i>	0.2061	0.2030	0.1998	0.1966	0.1935	0.1904	0.1872	0.1840	0.1809	0.1778	0.1746
ξ	1.7900	1.7828	1.7756	1.7684	1.7612	1.7540	1.7468	1.7396	1.7324	1.7252	1.7180
<i>p</i>						10.5480					
<i>q</i>						3.8890					
<i>r</i> ₀						2.8163					
	parameter set III										
<i>A</i>	0.2061	0.2030	0.1998	0.1966	0.1935	0.1904	0.1872	0.1840	0.1809	0.1778	0.1746
ξ	1.7180	1.7252	1.7324	1.7396	1.7468	1.7540	1.7612	1.7684	1.7756	1.7828	1.7900
<i>p</i>						10.5480					
<i>q</i>						3.8890					
<i>r</i> ₀						2.8163					

A.2 Gupta potential parameterisations of Pd-Pt

parameter	0.0	0.1	0.2	0.3	0.4	0.5	0.6	0.7	0.8	0.9	1.0
parameter set I											
<i>A</i>	0.2975	0.2852	0.2729	0.2606	0.2483	0.2361	0.2238	0.2115	0.1992	0.1869	0.1746
ξ	2.6950	2.5973	2.4996	2.4019	2.3042	2.2065	2.1088	2.0111	1.9134	1.8157	1.7180
<i>p</i>	10.6120	10.6375	10.6630	10.6885	10.7140	10.7395	10.7650	10.7905	10.8160	10.8415	10.8670
<i>q</i>	4.0040	3.9778	3.9516	3.9254	3.8992	3.8730	3.8468	3.8206	3.7944	3.7682	3.7420
<i>r</i> ₀	2.7747	2.7721	2.7695	2.7668	2.7642	2.7616	2.7590	2.7564	2.7537	2.7511	2.7485
parameter set II											
<i>A</i>	0.2975	0.2852	0.2729	0.2606	0.2483	0.2361	0.2238	0.2115	0.1992	0.1869	0.1746
ξ	2.6950	2.5973	2.4996	2.4019	2.3042	2.2065	2.1088	2.0111	1.9134	1.8157	1.7180
<i>p</i>						10.7395					
<i>q</i>						3.8730					
<i>r</i> ₀						2.7616					
parameter set III											
<i>A</i>	0.2975	0.2852	0.2729	0.2606	0.2483	0.2360	0.2238	0.2115	0.1992	0.1869	0.1746
ξ	1.7180	1.8157	1.9134	2.0111	2.1088	2.2065	2.3042	2.4019	2.4996	2.5973	2.6950
<i>p</i>						10.7395					
<i>q</i>						3.8730					
<i>r</i> ₀						2.7616					

A.3 Gupta potential parameterisations of Ni-Al

parameter	0.0	0.1	0.2	0.3	0.4	0.5	0.6	0.7	0.8	0.9	1.0
parameter set I											
A	0.1221	0.1137	0.1052	0.0967	0.0883	0.0799	0.0714	0.0629	0.0545	0.0461	0.0376
ξ	1.3160	1.2914	1.2668	1.2422	1.2176	1.1930	1.1684	1.1438	1.1192	1.0946	1.0700
p	8.6120	9.4507	10.2894	11.1281	11.9668	12.8055	13.6442	14.4829	15.3216	16.1603	16.9990
q	2.5160	2.3833	2.2506	2.1179	1.9852	1.8525	1.7198	1.5871	1.4544	1.3217	1.1890
r_0	2.8637	2.8264	2.7892	2.7519	2.7147	2.6774	2.6401	2.6029	2.5656	2.5284	2.4911
parameter set II											
A	0.1221	0.1137	0.1052	0.0967	0.0883	0.0799	0.0714	0.0629	0.0545	0.0461	0.0376
ξ	1.3160	1.2914	1.2668	1.2422	1.2176	1.1930	1.1684	1.1438	1.1192	1.0946	1.0700
p						12.8050					
q						1.7198					
r_0						2.6774					
parameter set III											
A	0.1221	0.1137	0.1052	0.0967	0.0883	0.0799	0.0714	0.0629	0.0545	0.0461	0.0376
ξ	1.0700	1.0946	1.1192	1.1438	1.1684	1.1930	1.2176	1.2422	1.2668	1.2914	1.3160
p						12.8050					
q						1.7198					
r_0						2.6774					

Appendix B

Publications

Ramli Ismail and Roy L. Johnston. Investigation of the Structures and Chemical Ordering of Small Pd-Au Clusters as a Function of Composition and Potential Parameterisation. *Phys. Chem. Chem. Phys.* 2010, **12**, 8607-8619. DOI:10.1039/C004044D

Alina Bruma, **Ramli Ismail**, L. Oliver Paz-Borbón, Haydar Arslan, Giovanni Barcaro, Alessandro Fortunelli, Z. Y. Li and Roy L. Johnston. DFT study of the structures and energetics of 98-atom AuPd clusters. *Nanoscale* 2013, **5**, 646-652. DOI:10.1039/c2nr32517a.

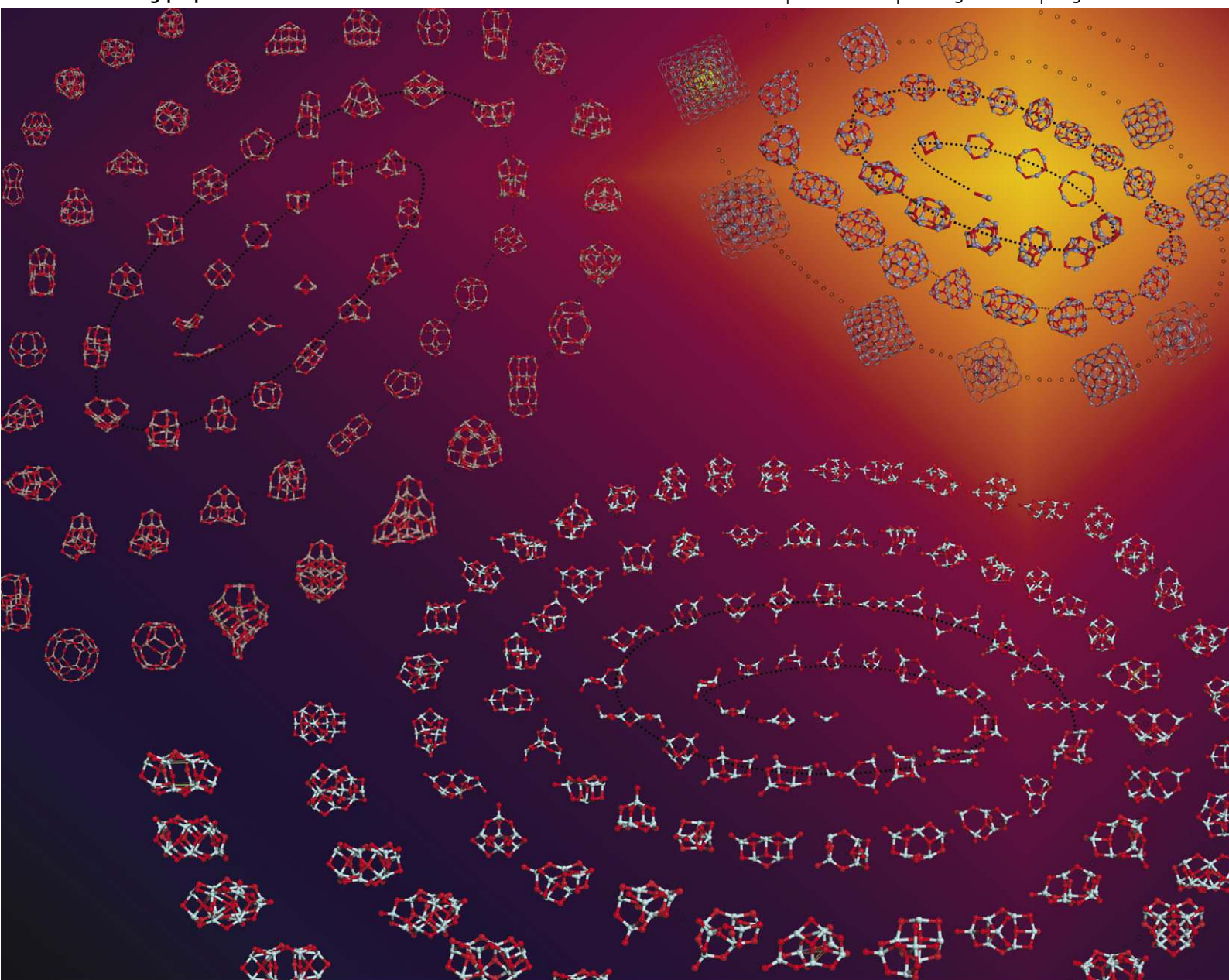
Ramli Ismail, Riccardo Ferrando and Roy L. Johnston. Theoretical Study of the Structures and Chemical Ordering of Palladium-Gold Nanoalloys Supported on MgO(100). *J. Phys. Chem. C* 2013, **117**, 293-301. DOI:10.1021/jp3093435.

PCCP

Physical Chemistry Chemical Physics

www.rsc.org/pccp

Volume 12 | Number 30 | 14 August 2010 | Pages 8421–8648



Themed issue: Solid state and cluster structure prediction

ISSN 1463-9076

COVER ARTICLE

Woodley *et al.*
Evolutionary structure prediction and
electronic properties of indium oxide
nanoclusters

COMMUNICATION

Sokol *et al.*
On the problem of cluster structure
diversity and the value of data mining



1463-9076(2010)12:30;1-0

Investigation of the structures and chemical ordering of small Pd–Au clusters as a function of composition and potential parameterisation

Ramli Ismail and Roy L. Johnston*

Received 9th March 2010, Accepted 30th June 2010

First published as an Advance Article on the web 12th July 2010

DOI: 10.1039/c004044d

The energetics, structures and segregation of Pd–Au nanoalloys (all compositions for 34- and 38-atoms) have been studied using a genetic algorithm global optimization technique with the Gupta empirical potential. Three modifications of the Pd–Au parameters have been studied: parameter set *I* in which all parameters (A , ζ , p , q and r_0) in the Gupta potential are weighted in a symmetrical fashion; parameter set *II* (symmetric weighting of only the pair and many-body energy scaling parameters A and ζ); and parameter set *III* (antisymmetric weighting of A and ζ). Structural analysis reveals competition between a range of structural families; decahedra, polyicosahedra and truncated octahedra (for 34 atoms) and incomplete-icosahedra-Mackay, decahedra, polyicosahedra (low-symmetry), six-fold-polyicosahedra and a mixed octahedron–icosahedron (Oh–Ih) structure (for 38 atoms). It is shown that, by finely tuning the Gupta potential, it is possible to qualitatively reproduce the results observed at higher levels of theory (e.g. Density Functional Theory). There are four main types of chemical ordering which are observed: core–shell; spherical cap; ball-and-cup; and mixed. It is shown that the chemical ordering and the proportion of Pd–Au heteronuclear bonds in these clusters are strongly dependent on the potential parameters. Comparison of the results from parameter set *III* and two previously fitted potentials shows that the **DFT-fit** potential gives rise to similar results for energies, and lowest energy structures and homotops to those for parameter set *III* with $w_a = 0.8$, but the **exp-fit** potential gives rise to qualitatively different results.

1. Introduction

There is considerable interest in the chemical and physical properties and potential applications of metal nanoparticles.^{1,2} Much of the interest has focused on mono- and bimetallic nanoparticles formed from elements in the nickel and copper groups of the periodic table: Ni, Pd, Pt; Cu, Ag, Au.^{3,4} For example, palladium, which has fcc symmetry in the bulk,⁵ shows a variety of structures, ranging from fcc cuboctahedra, icosahedra and truncated decahedra to twinned fcc structures for nanoparticles with 1–5 nm diameter. These structures have been produced using either colloidal methods or vapour deposition and have been characterised with the aid of high-resolution electron microscopy (HREM). All structural motifs appear to have very similar energies, so that transitions between different states are possible. Icosahedra are only expected for very small clusters with a high surface to volume ratio, while decahedra and fcc cuboctahedral or truncated octahedral particles are more stable than icosahedra for larger sizes.⁶

Gold clusters have been studied intensively in recent years. The structural size evolution in gold may be described as a sequence of transitions from specific “molecular” structures, at the extremely small size range, with effective cluster diameter ≤ 1 nm (40 atoms), to ordered “non-crystallographic”

(decahedral) structures at larger sizes, culminating for sizes > 2 nm (> 250 atoms) in crystallites of the bulk lattice structure (fcc) with specific faceted morphologies (i.e., variants of truncated octahedra and their twins).⁷

Gold clusters have been grown from metal ions reduced at the oil–water interface in the presence of a surface passivating agent. Observation by HREM shows a variety of structures (decahedron, truncated octahedron, icosahedron, and amorphous) for passivated particles of a few nanometres diameter, with a prevalence, however, of Marks and Ino-decahedra. The smallest fcc clusters observed correspond to the truncated octahedron, whilst at sizes ~ 15 Å, the Marks decahedron is the most stable motif.⁸ Marks-decahedral motifs have also been found as stable structures for 1–2 nm gold clusters by X-ray powder diffraction. Based on atomistic modelling, these were assigned as 75-, 101- and 146-atom clusters.⁹

Among bimetallic nanoclusters (“nanoalloys”) the Pd–Au system has been widely studied.⁴ In a study by Liu *et al.*, for example, bimetallic Pd–Au nanoclusters have been synthesized by the reduction of metal ions in the presence of a polymer stabilizer. HREM results confirmed three stable configurations: Pd_{core}Au_{shell}, random solid solutions and eutectic-like configurations. Coexistence of fcc-like and multiple twinned (octahedral and decahedral) structures was found because of the close separation of energies between these structures. Although Pd_{core}Au_{shell} structures are stable at low temperature, inversion to the Au_{core}Pd_{shell} structure was observed upon heating to approximately 500 K.¹⁰

School of Chemistry, University of Birmingham, Edgbaston, Birmingham, B15 2TT, United Kingdom.
E-mail: r.l.johnston@bham.ac.uk; Tel: +44(0)121 414 7477

Pd–Au clusters are of great interest to theoretical and experimental researchers because of their interesting properties that are not found for the respective pure metals. The electronic structures of Pd–Au clusters are quite distinct from Pd or Au, due to their differing atomic electron configurations and electronegativities.⁴ Nanoclusters of Pd–Au supported on a variety of surfaces (*e.g.* magnesia, titania, silica, alumina) show great potential for a wide range of catalytic reactions, such as: acetylene cyclotrimerization (to yield benzene) and related reactions;¹³ selective hydrogenation;^{14–16} hydrodechlorination of trichloroethene in water at room temperature;¹⁷ low-temperature synthesis of hydrogen peroxide from oxygen and hydrogen,^{18,19} CO and alcohol reduction;²⁰ the Sonagashira cross-coupling reaction;²¹ and synthesis of vinyl acetate by acetoxylation of ethylene.^{22,23}

In this paper, the energetics, structures and segregation (chemical ordering) of Pd–Au nanoalloys are investigated as a function of composition for 34- and 38-atom clusters, using a genetic algorithm for global geometry optimisation (*i.e.* global energy minimisation) of the clusters and with the interatomic interactions described by the Gupta many-body potential. We also present a detailed study of how the structures and chemical ordering displayed by these nanoalloys change when the heteronuclear potential parameters are varied systematically. The analysis is aided by the calculation of excess (mixing) energies, average nearest-neighbour distances and a chemical ordering parameter.

The reason for concentrating here on 34- and 38-atom clusters, is that our previous work on Pd–Au (and other nanoalloy systems)^{11,24–26} have shown that 34-atom clusters typically exhibit a wide range of structural motifs as a function of composition, while 38-atom clusters (for which truncated octahedral structures typically dominate) are of interest for testing how different chemical orderings are stabilised by different heteroatomic interaction strengths.

2. Theoretical methods

2.1 The Gupta potential

The Gupta potential, used to model inter-atomic interactions in metal systems,^{12,27} is a semi-empirical potential derived within the tight-binding second-moment approximation. The configurational energy of a cluster is written as the sum over all the atoms of attractive and repulsive energy components:

$$V_{\text{clus}} = \sum_i^N \{V^r(i) - V^m(i)\} \quad (1)$$

where the Born–Mayer pair repulsive term $V^r(i)$ is expressed as:

$$V^r(i) = \sum_{j \neq i}^N A(\alpha, \beta) \exp \left\{ -p(\alpha, \beta) \left(\frac{r_{ij}}{r_0(\alpha, \beta)} - 1 \right) \right\} \quad (2)$$

and the many-body attractive term $V^m(i)$ is expressed as:

$$V^m(i) = \sqrt{\sum_{j \neq i}^N \xi^2(\alpha, \beta) \exp \left\{ -2q(\alpha, \beta) \left(\frac{r_{ij}}{r_0(\alpha, \beta)} - 1 \right) \right\}} \quad (3)$$

In eqn (2) and (3), α and β represent the atomic species of atoms i and j , respectively. A , ξ , p and q are the potential parameters that are usually fitted to experimental properties of bulk metals and alloys, such as the cohesive energy, lattice parameters, and independent elastic constants for the reference crystal structure at 0 K. r_0 denotes the nearest-neighbour distance of the pure bulk elements, often taken as the average of the pure distances, but it can also be taken as the experimental nearest-neighbour distance in some specific ordered bulk alloy. r_{ij} is the distance between atoms i and j .

Values of the Gupta potential parameters describing Pd–Pd and Au–Au interactions, taken from the work of Cleri and Rosato,¹² are listed in Table 1, along with three alternative sets of Pd–Au parameters considered in a previous study by Pittaway *et al.*¹¹

2.2 Parameterisations of the Gupta potential

A study of Pd–Pt clusters by Massen *et al.*²⁸ concluded that parameters obtained by averaging the parameters of elemental Pd and Pt, gave a good qualitative fit to previous experimental and theoretical studies of Pd–Pt bimetallic clusters.^{29–31} A more detailed investigation of the effect on structure and chemical ordering of varying the heteronuclear (Pd–Pt) parameters for 34-atom Pd–Pt clusters gave more decahedral motifs for Pd–Pt parameters which are slightly biased towards the weaker Pd–Pd interaction,²⁴ which is consistent with DFT results.²⁶ These parameters still favour core–shell ordering, as for the average potential. Recent GA calculations for 34- and 38-atom Pd–Pt clusters have shown that the heteronuclear parameters for a new Gupta potential (fitted to DFT calculations on pure metals and alloy solids)³² lie slightly to the weaker bonding (*i.e.* closer to the Pd–Pd parameters) side of the average.³³ The calculated excess energies and structural motifs are consistent with this.

DFT calculations of small Pd, Au and Pd–Au (1 : 1 composition) clusters (2–20 atoms), have shown that the mixed clusters have binding energies which are intermediate between those of Pd and Au, but are biased towards Pd, indicating that the Pd–Au bonding is greater than the average of Pd–Pd and Au–Au.³³

In this study, the heteronuclear Pd–Au Gupta potential parameters $\{P\}$ are derived as the weighted average of the corresponding pure metal Pd–Pd and Au–Au parameters:²⁴

$$P(\text{Pd–Au}) = w_1 P(\text{Pd–Pd}) + w_2 P(\text{Au–Au}) \quad (4)$$

where $w_1 + w_2 = 1$. Weighting parameters have been investigated in the range $0 \leq w \leq 1$, in steps $\Delta w = 0.1$. The following parametrisations have been studied.

Parameter set I. All the Pd–Au Gupta potential parameters $\{P\} = \{A, \xi, p, q$ and $r_0\}$ are obtained as:

$$P(\text{Pd–Au}) = w P(\text{Pd–Pd}) + (1 - w) P(\text{Au–Au}) \quad (5)$$

This is symmetrical weighting of all parameters, since all of the parameters vary in the same sense—*i.e.* from the value for Au–Au (for $w = 0$) to the value for Pd–Pd (for $w = 1$).

Table 1 Comparison of the **average**, **DFT-fit** and **exp-fit** Gupta potential parameters.¹¹ For the **average** potential, the homonuclear parameters are taken from Cleri and Rosato,¹² while in the other potentials they are fitted along with the heteronuclear parameters

Parameter	Pd–Pd			Au–Au			Pd–Au		
	average	DFT-fit	exp-fit	average	DFT-fit	exp-fit	average	DFT-fit	exp-fit
A/eV	0.1746	0.1653	0.171493044	0.2061	0.2091	0.209570656	0.19	0.1843	0.2764
ξ/eV	1.718	1.6805	1.701873210	1.79	1.8097	1.815276400	1.75	1.7867	2.082
p	10.867	10.8535	11.000	10.229	10.2437	10.139	10.54	10.5420	10.569
q	3.742	3.7516	3.794	4.036	4.0445	4.033	3.89	3.8826	3.913
$r_0/\text{\AA}$	2.7485	2.7485	2.7485	2.884	2.8840	2.884	2.816	2.8160	2.816

In parameter sets **II** and **III**, instead of weighting all the parameters in the Gupta potential only the A (pair repulsion) and ξ (many-body) parameters were varied with parameters p , q and r_0 being fixed at their arithmetic mean values ($w = 0.5$).

Parameter set II. As for parameter set **I**, parameters A and ξ are varied in the same sense (“symmetric”), with the weighting factor being denoted w_s :

$$A(\text{Pd–Au}) = w_s A(\text{Pd–Pd}) + (1 - w_s) A(\text{Au–Au}) \quad (6)$$

$$\xi(\text{Pd–Au}) = w_s \xi(\text{Pd–Pd}) + (1 - w_s) \xi(\text{Au–Au}) \quad (7)$$

Comparison of the results for parameter sets **I** and **II** will enable us to judge the importance of the energy scaling parameter (A and ξ) compared to the range exponents (p and q).

Parameter set III. In contrast to parameter set **II**, parameters A and ξ are varied in the opposite sense (“antisymmetric”—*i.e.* as A varies between the limits of the values for Pd–Pd and Au–Au, ξ varies in the opposite direction), with the weighting factor being denoted w_a :

$$A(\text{Pd–Au}) = w_a A(\text{Pd–Pd}) + (1 - w_a) A(\text{Au–Au}) \quad (8)$$

$$\xi(\text{Pd–Au}) = (1 - w_a) \xi(\text{Pd–Pd}) + w_a \xi(\text{Au–Au}) \quad (9)$$

The reason for investigating parameter set **III** is that it allows regions of Pd–Au parameter space to be explored which have: (i) low A and high ξ values, corresponding to strong Pd–Au

bonding; and (ii) high A and low ξ , corresponding to weak Pd–Au bonding.

The parameter values for parameter sets **I**, **II** and **III** are all listed in Table 2.

In this study, the results obtained for parameter sets **I–III** have also been compared with those reported by Pittaway *et al.*¹¹ using the Pd–Au heteronuclear parameters that were fitted to the results of first-principles Density Functional Theory (DFT) calculations¹¹ (“**DFT-fit**”) and those fitted to experimental properties of bulk Pd, Au and Pd–Au alloys³⁴ (“**exp-fit**”), as listed in Table 1. It should be noted that the “**average**” (arithmetic mean) potential previously reported,^{11,25,26} corresponds to $w = 0.5$ (set **I**), $w_s = 0.5$ (**II**) and $w_a = 0.5$ (**III**).

2.3 The Birmingham cluster genetic algorithm (BCGA)

The Birmingham Cluster Genetic Algorithm (BCGA) program, which has been described elsewhere,³⁵ was used to find the putative global minima (GM) and other low-lying energy minima of 34- and 38-atom Pd–Au clusters, for all compositions. The BCGA parameters used in this work were: population size = 40 clusters; crossover rate = 80% (*i.e.*, 32 offspring are produced per generation); crossover type = 1-point weighted cut-and-splice (the cut position is calculated based on the fitness values of the parents); selection = roulette wheel; mutation rate = 0.1; mutation type = mutate_move; maximum number of generations = 400. 100 GA runs were performed for each composition. The GA was terminated when the population was found to have converged for 10 consecutive generations.

Table 2 The potential parameters for parameter set: **I** [symmetric weighting (w) of all parameters]; **II** [symmetric weighting (w_s) of A and ξ]; and **III** [antisymmetric weighting (w_a) of A and ξ]

Set	w	0.0	0.1	0.2	0.3	0.4	0.5	0.6	0.7	0.8	0.9	1.0
I	A	0.2061	0.2030	0.1998	0.1967	0.1935	0.1904	0.1872	0.1841	0.1809	0.1778	0.1746
	ξ	1.7900	1.7828	1.7756	1.7684	1.7612	1.7540	1.7468	1.7396	1.7324	1.7252	1.7180
	p	10.2290	10.2928	10.3566	10.4204	10.4842	10.5480	10.6118	10.6756	10.7394	10.8032	10.8670
	q	4.0360	4.0066	3.9772	3.9478	3.9184	3.8890	3.8596	3.8302	3.8008	3.7714	3.7420
	r_0	2.8840	2.8705	2.8569	2.8434	2.8298	2.8163	2.8027	2.7892	2.7756	2.7621	2.7485
	w_s	0.0	0.1	0.2	0.3	0.4	0.5	0.6	0.7	0.8	0.9	1.0
II	A	0.2061	0.2030	0.1998	0.1967	0.1935	0.1904	0.1872	0.1841	0.1809	0.1778	0.1746
	ξ	1.7900	1.7828	1.7756	1.7684	1.7612	1.7540	1.7468	1.7396	1.7324	1.7252	1.7180
	p	10.5480 (fixed at average)										
	q	3.8890 (fixed at average)										
	r_0	2.8163 (fixed at average)										
	w_a	0.0	0.1	0.2	0.3	0.4	0.5	0.6	0.7	0.8	0.9	1.0
III	A	0.2061	0.2030	0.1998	0.1967	0.1935	0.1904	0.1872	0.1841	0.1809	0.1778	0.1746
	ξ	1.7180	1.7252	1.7324	1.7396	1.7468	1.7540	1.7612	1.7684	1.7756	1.7828	1.7900
	p	10.5480 (fixed at average)										
	q	3.8890 (fixed at average)										
	r_0	2.8163 (fixed at average)										

2.4 Energetic analysis

When studying fixed-size bimetallic clusters, the excess (or mixing) energy as a function of composition, Δ_N^{Gupta} , is a useful quantity. For binary nanoalloys with fixed size ($N = 34$ or 38 atoms) but different compositions, Δ_N^{Gupta} is defined as

$$\Delta_N^{\text{Gupta}} = E_N^{\text{Gupta}}(A_M B_{N-M}) - M \frac{E_N^{\text{Gupta}}(A_N)}{N} - (N-M) \frac{E_N^{\text{Gupta}}(B_N)}{N} \quad (10)$$

where $E_N^{\text{Gupta}}(A_M B_{N-M})$ is the total energy of a given cluster calculated at the Gupta level and $E_N^{\text{Gupta}}(A_N)$ and $E_N^{\text{Gupta}}(B_N)$ are the total energies of the GM of the pure metal clusters (*i.e.* Pd_N and Au_N). This excess energy is an unbiased quantity, defined as zero for the global minima of the pure clusters. Negative values of Δ_N^{Gupta} indicate that mixing is favourable.

2.5 Pair distribution function (PDF) and average nearest-neighbour distance (ANND)

For quantitative purposes, it is appropriate to calculate the pair distribution function (PDF), $g_p(r)$ as follows:

$$g_p(r) = \frac{V}{N^2} \left\langle \sum_i^N \sum_{j \neq i}^N \delta[r - r_{ij}] \right\rangle \quad (11)$$

where N is the total number of atoms, V is the volume, r_{ij} denotes the distance between atoms i and j , and the brackets represent a time average. The $g_p(r)$ function gives the probability of finding an atom of any type at a distance r , and it allows characterization of the lattice structure during the generation of the nanoalloy.³⁶

From $g_p(r)$, the average nearest-neighbour distance (ANND) can be defined as:

$$\text{ANND} = \frac{\int_0^{r_c} r g(r) 4\pi r^2 dr}{\int_0^{r_c} g(r) 4\pi r^2 dr} \quad (12)$$

where the cut-off r_c is chosen to be half way between the average nearest- and second-nearest-neighbour distances in the cluster.³⁷ This term can be simplified as the sum of the nearest neighbour atomic distances divided by the number of bonds in the cluster.³⁸

2.6 Chemical ordering

Binary nanoalloys generally present more complex structures than monometallic clusters and global optimisation is more difficult due to the existence of homotops,³⁹ which are isomers with the same geometry and composition but with a different arrangement of the two types of atoms.

For an A–B alloy system, the chemical order parameter, σ is defined as;

$$\sigma = \frac{N_{A-A} + N_{B-B} - N_{A-B}}{N_{A-A} + N_{B-B} + N_{A-B}} \quad (13)$$

where N_{A-B} is the number of nearest-neighbour A–B bonds and N_{A-A} and N_{B-B} denote the numbers of homonuclear

bonds in the binary cluster. The σ value is positive when phase separation (segregation) takes place, close to zero when disordered mixing occurs, and negative when there is more ordered mixing (including layering and onion-like configurations).⁴⁰

3. Results and discussion

3.1 34-Atom palladium–gold clusters

This study produced results which corroborate those obtained previously, using the **average, exp-fit** and **DFT-fit** Gupta parameters,¹¹ that incomplete decahedral (Dh) structures dominate as the putative GM for 34-atom Pd–Au clusters. In this study, for parameter sets **I–III**, in addition to the Dh motif, polyicosahedral (pIh)⁴¹ and truncated octahedral (TO) structures (Fig. 1) were also found to be stable structures in GA searches. However, none of the parameterisations gave rise to the decahedron with a close-packed double tetrahedral core [Dh-cp (DT)] motif that is found as the GM for 34-atom Pd–Pt clusters across a wide composition range according to Density Functional Theory (DFT) studies,²⁶ even after exhaustive searching (500 GA runs).

Energetics and structural motifs. Fig. 2 shows the variation of the Gupta excess energy $\Delta_{34}^{\text{Gupta}}$ as a function of composition and weighting parameter, for parameter sets **I–III**. Fig. 2(a) shows that for set **I** all weighting factors (w) give rise to negative excess energies, for all compositions, indicating that mixing is favourable. The GM structures of the clusters are dominated by Dh, with several Au-rich pIh ($N_{\text{Au}} = 31–33$) and TO ($N_{\text{Au}} = 24–26$) found for Pd-biased parameters ($w = 0.8–1.0$). On the other hand, changing just A and ζ symmetrically (parameter set **II**) gives a distinctly different pattern of excess energies, as shown in Fig. 2(b), where some Pd-rich compositions do not favour mixing (excess energies are positive) at $w_s = 0.0$ ($N_{\text{Au}} = 1–3$) and $w_s = 0.1$ ($N_{\text{Au}} = 1$). The minima in the excess energy curves deepen to a more negative value at $w_s = 1.0$, but the structural motifs are consistent with those from set **I**.

Fig. 2(c) shows that endothermic (positive) excess energies ($w_a = 0.0–0.3$ and partially for $w_a = 0.4$) are calculated for weighting set **III**, which may be explained by the fact that $\zeta_{\text{PdAu}} \rightarrow \zeta_{\text{Pd}}$ and $A_{\text{PdAu}} \rightarrow A_{\text{Pd}}$. Another important finding is that the lowest excess energy (at $w_a = 1.0$) for this set is -7.1647 eV, which is considerably larger than the values of

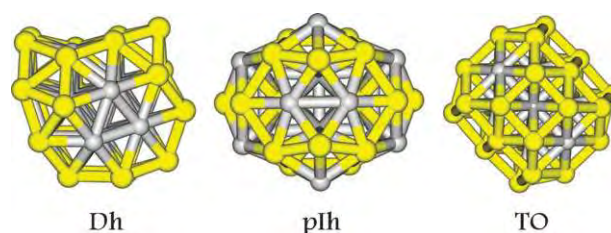


Fig. 1 GM Structural motifs found for PdAu-34. Au and Pd atoms are denoted by yellow and grey colours, respectively, here and in subsequent figures.

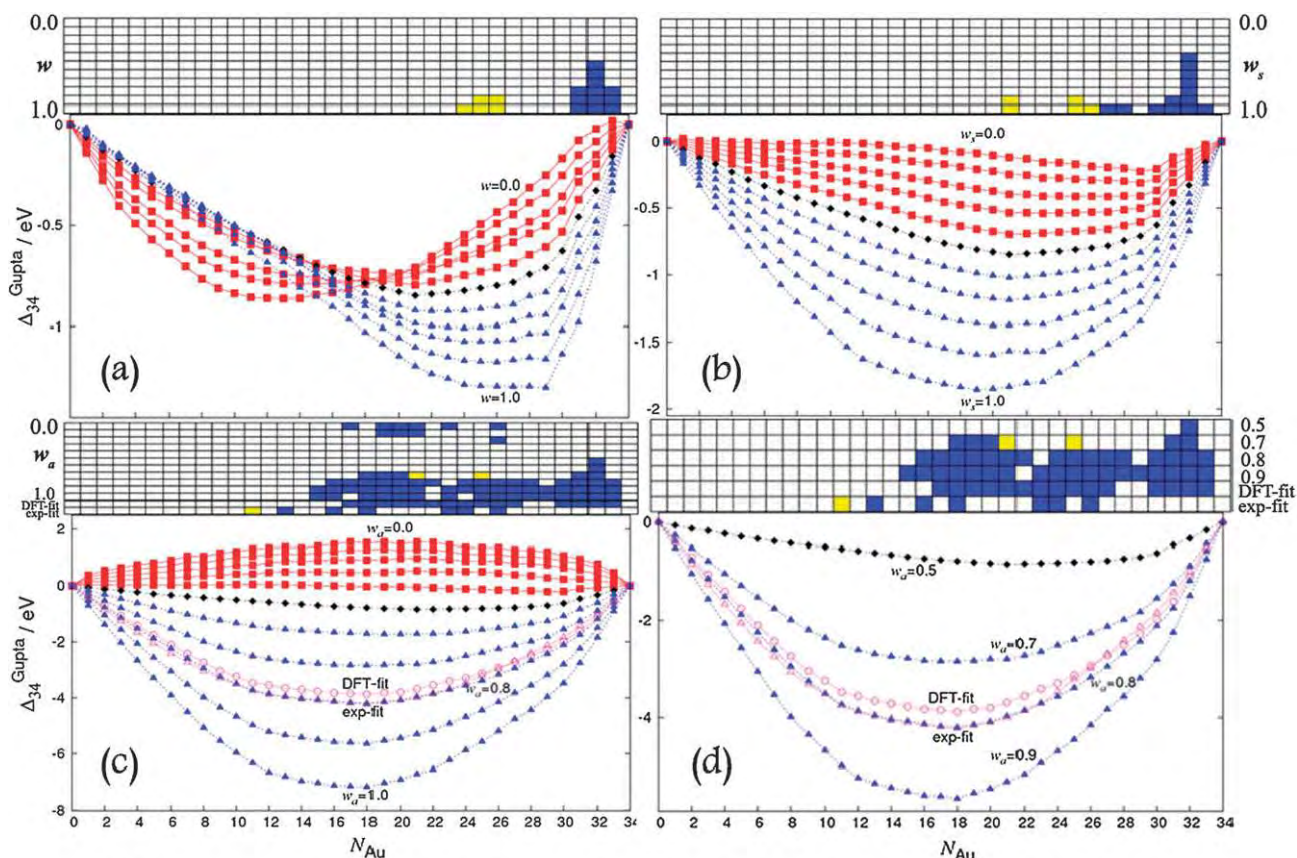


Fig. 2 (Bottom) Excess energy variation ($\Delta_{34}^{\text{Gupta}}$) for 34-atom Pd–Au clusters using parameter sets *I* (a), *II* (b), and *III* (c). (d) is a comparison between set *III* ($w_a = 0.5, 0.7-0.9$) and the **DFT-fit** and **exp-fit** potentials. (Top) GM Structural motifs found, as a function of composition (number of Au atoms) and weighting factor (w , w_s or w_a): Dh (white); pIh (blue); TO (yellow).

–1.3026 eV (set *I*) and –1.85515 eV (set *II*). Generally, we can see that for Pd-rich compositions, Dh structures are the lowest in energy, while for the Au-rich compositions Dh and pIh structures compete, with pIh prevailing as $w_a \rightarrow 1.0$ and TO are only the GM at $w_a = 0.7$, for compositions (13,21) and (9,25).

Observation of pIh structures as the GM for Au-rich compositions in the range $w = 0.5-0.8$ in Fig. 2(a) (parameter set *I*) and $w_s = 0.4-0.8$ in Fig. 2(b) (parameter set *II*) shows that the variation of structures for these parameter sets is dominated by composition dependence. However, extremely biased weighting shows no more pIh (for low w and w_s) and the occurrence of TO as GM (for high w and w_s), indicating that there is some dependence on parameterisation for these weighting schemes. In contrast, parameterisation effects clearly dominate composition effects in Fig. 2(c) (parameter set *III*), in which pIh structures are predicted as putative GM for a wider range of compositions at both low and high w_a .

The differences between parameter set *III* (for $w_a = 0.5$ and $0.7-0.9$) and the parameters of the fitted (**DFT-fit** and **exp-fit**) potentials are shown in Fig. 2(d). As noted above, $w_a = 0.5$ is the **average** potential that has previously been used in generating cluster structures for Pd–Au clusters.^{11,24–26} The range of $w_a = 0.7-0.9$ is chosen due to the interesting results at this weighting, having excess energies and structural motifs close to the fitted potentials. From Table 1, the parameters of the

DFT-fit potential have the following characteristics which are similar to those in set *III* (Table 2): $A_{\text{DFT-fit}} (0.1843) \sim A_{w_a=0.7} (0.1841)$; and $\zeta_{\text{DFT-fit}} (1.7867) \sim \zeta_{w_a=0.9} (1.7828)$. Parameter set *III* with $w_a > 0.5$ gives stronger Pd–Au bonding, as shown by the more negative excess energies. These parameters correspond to less repulsion ($A_{\text{PdAu}} \rightarrow A_{\text{Pd}}$) and more attraction ($\zeta_{\text{PdAu}} \rightarrow \zeta_{\text{Au}}$). This is because $A_{\text{Pd}} (0.1746) < A_{\text{Au}} (0.2061)$ and $\zeta_{\text{Pd}} (1.7180) < \zeta_{\text{Au}} (1.7900)$; and $w_a \rightarrow 1.0$ will reduce A (repulsion) and increase ζ (attraction). On the other hand, the **exp-fit** potential has A (0.2764) and ζ (2.082) parameters which are out of the range of Pd and Au parameters, both being greater than the corresponding Au parameters ($A = 0.2096$, $\zeta = 1.8153$).¹¹

Comparing the excess energy plots in Fig. 2(d), it can be seen that the **DFT-fit** potential curve lies between those of parameter set *III* with $w_a = 0.7$ and 0.8 . For the **exp-fit** potential, the plot overlaps with that for $w_a = 0.8$, especially for mid-range compositions. The excess energies of the GM obtained for the **exp-fit** parameters are more negative than those obtained for the **average** parameters but only slightly more negative than for the **DFT-fit** potential, indicating that Pd–Au mixing is preferred (at the empirical potential level) in this size regime. This highly exothermic mixing is similar to the energy curves obtained for 34-atom Pd–Pt clusters with parameters weighted toward the strongest (Pt–Pt) homonuclear interactions.^{11,24}

GM cluster structures for the **DFT-fit** potential are similar to those for parameter set **III** for $w_a = 0.8$ and 0.9 , with competition between Dh and pIh motifs. However, for the **exp-fit** potential, the GM structures do not match with any weighting (w_a) for set **III**. As for $w_a = 0.7$, a TO GM was found, but at a completely different composition (23,11).

GM structural variation and segregation profiles. Fig. 3 shows the structures of the lowest energy PdAu-34 clusters found for parameter sets **I**, **II** and **III**. The lowest energy structure for set **I** (Fig. 3(a)) changes from Dh ($w = 0.0$ – 0.8) to TO ($w = 0.9$) and pIh ($w = 1.0$). For set **II** (Fig. 3(b)), the GM structures for all weighting factors are Dh, changing from Marks-Dh ($w_s = 0.0$ – 0.7) to mixed Dh-Ih ($w_s = 0.8$ – 1.0). For set **III** (Fig. 3(c)), all compositions show positive excess energies for $w_a = 0.0$ – 0.3 , so the structures selected are the compositions with the most positive excess energies. These structures change from low-symmetry pIh [pIh(LS)] ($w_a = 0.0$ – 0.1), to Dh ($w_a = 0.2$ – 0.5), mixed Dh-Ih ($w_a = 0.6$) and pIh ($w_a = 0.7$ – 1.0).

Fig. 3(d) shows that the lowest energy structures for both the **DFT-fit** and **exp-fit** potentials occur at composition Pd₁₆Au₁₈, which is a similar composition to those found for all minima for set **III** ($w_a = 0.7$ – 1.0) with $A_{\text{PdAu}} \rightarrow A_{\text{Pd-Pd}}$ and $\xi_{\text{PdAu}} \rightarrow \xi_{\text{Au-Au}}$. These structures are pIh with excess energies of -3.8828 and -4.2045 eV, for the **DFT-fit** and **exp-fit** potentials, respectively. Meanwhile, the minima for set **III** potentials are -2.8464 ($w_a = 0.7$), -4.2170 ($w_a = 0.8$) and -5.6482 eV ($w_a = 0.9$), all with the same structure. Even though all the minima belong to the same structural family, there are slight differences, particularly for the **exp-fit** potential, where two square faces (for set **III** with $w_a = 0.8$ and for **DFT-fit**) expand to become a hexagonal plane and where only

12 (rather than 13) Au atoms lie on the surface. As reported earlier, the structures derived from both fitted potentials tend to maximize the number of Pd–Au bonds; hence, they tend to form incomplete icosahedra or pIh.¹¹

There are a number of experimental results^{10,42–44} and theoretical calculations^{11,25,42,45,46} which indicate the prevalence of Pd_{core}Au_{shell} ordering and are consistent with the lower heat of formation, compared to inverse Au_{core}Pd_{shell} and other configurations.¹⁰ Core–shell segregation is also favoured by: the lower surface energy of Au (Au = $96.8 \text{ meV } \text{Å}^{-2}$ vs. Pd = $131 \text{ meV } \text{Å}^{-2}$ —forming a surface shell of atoms with the lower surface energy lowers the overall cluster surface energy^{47,48}); the higher cohesive energy of Pd (Au = 3.81 eV/atom vs. Pd = 3.89 eV/atom ⁴⁹—maximizing the number of stronger Pd–Pd bonds) and the smaller atomic radius of Pd (Pd = 1.375 Å vs. Au = 1.44 Å ⁴⁹—a Pd core minimizes bulk elastic strain).

In this work, calculations on 34-atom Pd–Au clusters corroborated the prevalence of core–shell phase segregation behaviour (Fig. 4). When there are a limited number of Au atoms on the surface, three types of incomplete core–shell configurations are observed: *incomplete core–shell type-A* (i-CS(A)—having Au atoms occupying low-coordinate surface sites); *incomplete core–shell type-B* (i-CS(B)—having a uniform partial monolayer coverage of the surface); and *incomplete core–shell type-C* (i-CS(C)—having an intermixed surface). The Au atoms in the i-CS(A) and i-CS(C) configurations occupy the surface sites with the lowest coordination (edge and corner sites) of the Dh, leaving isolated Pd atoms on the higher-coordination surface sites. This segregation is also adopted in AgCu-34 clusters, where Ag atoms occupy the low coordination surface sites.⁴⁹

In addition to core–shell configurations, varying the potential parameters can result in low (spherical cap (layered)

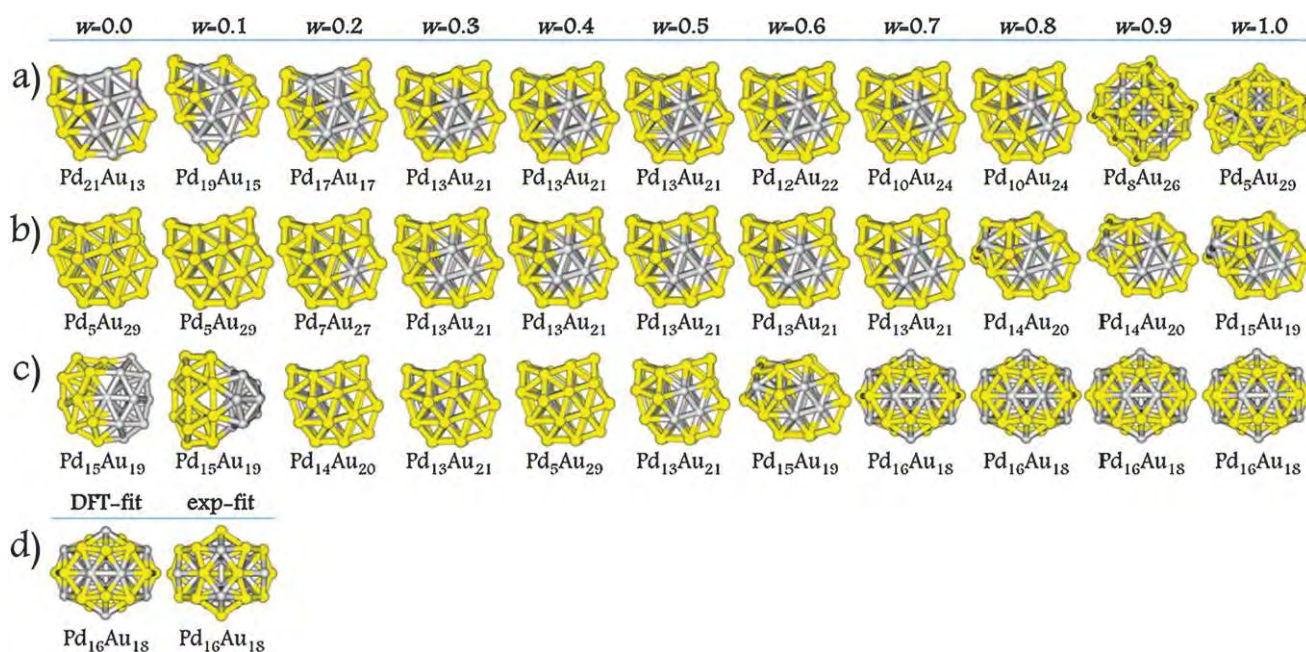


Fig. 3 Structural variation of the lowest excess energy PdAu-34 isomers found for parameter sets **I** (a), **II** (b), **III** (c), and the **DFT-fit** and **exp-fit** potentials (d).

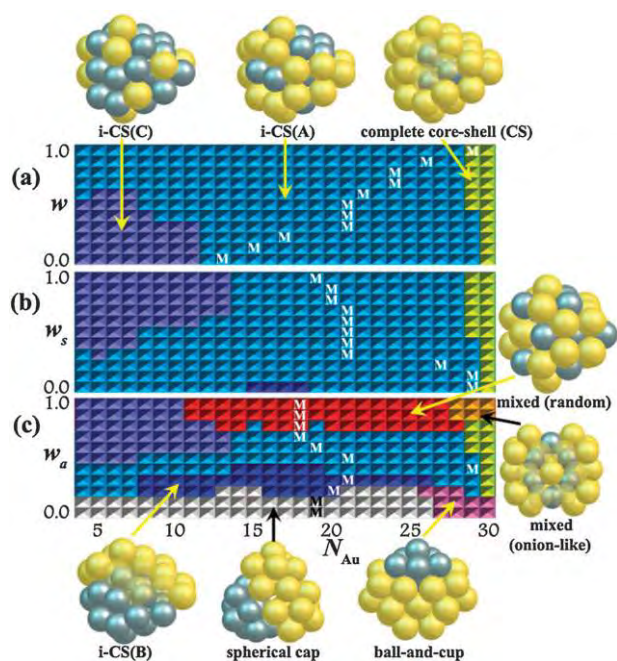


Fig. 4 Segregation profiles of PdAu-34 using parameter sets *I* (a), *II* (b), and *III* (c).

configurations) to high (mixed configurations) degrees of intermixing, especially for parameter set *III*. Au-rich compositions with parameter sets *I*, *II* and *III* (mid to high w_a) possess complete core-shell configurations at $N_{Au} = 29/30$ (for Dh), but at low w_a (0.0–0.2) the GM with the same compositions adopt “ball-and-cup” segregation. Compared to core-shell, the ball-and-cup configurations have several exposed Pd atoms and a preponderance of surface Au atoms on one side, making the “core” of Pd atoms off-centre, corresponding to an intermediate segregation between core-shell and spherical cap. This configuration was previously reported for PdPt-34 by Paz-Borbón *et al.*²⁴

In contrast to Pd–Pt systems,²⁴ no evidence of complex crossover between chemical ordering types was detected especially in the medium composition range for parameter set *I* (Fig. 4(a)). A possible explanation for this might be the small difference between the A and ζ values of Pd–Pd and Au–Au (Table 1), leading to dominant i-CS(A) and i-CS(C) segregation over the entire weighting and composition range. It is possible to hypothesise that the Pd–Pt situation is more likely to occur for the systems Ag–Au, Ag–Pt and Au–Cu, which all have more widely differing elemental potential parameters.^{12,50} While parameter set *II* (Fig. 4(b)) also showed a prevalence of i-CS(A) and i-CS(C) configurations, at $w_s = 0.0$ the GM structures have i-CS(B) configurations for mid-range compositions. Consistent with the variation of structures, the variation in segregation type for parameter sets *I* and *II* is dominated by the composition dependence, while potential parameter effects are dominant for parameter set *III* (Fig. 4(c)), which exhibits a wider range of segregation types, with the most stable configuration (M) changing from spherical cap ($w_a = 0.0$ –0.1), to i-CS(A) ($w_a = 0.2$ –0.7) and mixed ($w_a = 0.8$ –1.0).

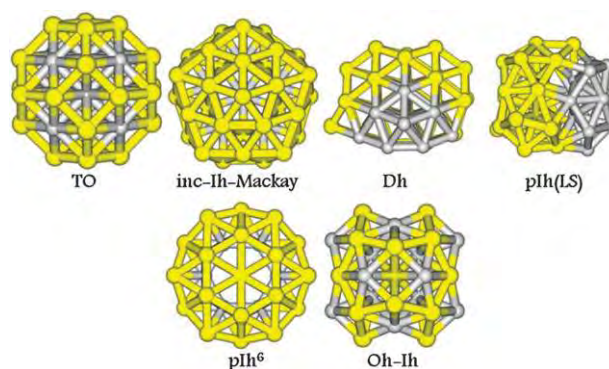


Fig. 5 GM structural motifs found for PdAu-38.

3.2 38-Atom palladium–gold clusters

GA calculations for 38-atom clusters very often present truncated octahedra (TO) as the preferred structure.²⁵ In a previous study of 38-atom Pd–Au clusters, TO structures were found to be the GM for all compositions when using the **average** potential, and to predominate for the **DFT-fit** and **exp-fit** potentials.¹¹ TO structures of Pd–Au typically have Au atoms segregated to the surface and Pd atoms occupying core positions, though the **DFT-fit** and **exp-fit** potentials give rise to more surface Pd–Au mixing than the **average** potential.

In this study, the TO structure is again found to predominate for parameter sets *I–III*. However, by varying the parameters of the Gupta potential, other structures are found to be competitive; incomplete Mackay-icosahedra (inc-Ih-Mackay), decahedra (Dh), low symmetry-polyicosahedra (pIh(LS)), six-fold symmetric polyicosahedra (pIh⁶)⁴¹ and mixed octahedra-icosahedra (Oh-Ih)²⁵ (see Fig. 5).

Energetics and structural motifs. Fig. 6 shows the variation of the Gupta excess energy $\Delta_{38}^{\text{Gupta}}$ as a function of composition and weighting factor for parameter sets *I–III*. Fig. 6(a) shows that, except for $w = 0.0$ at compositions (2,36) and (1,37), all the other GM for parameter set *I* exhibit Pd–Au mixing. A similarity between the excess energy profiles of 34- and 38-atom clusters for parameter set *I* is the occurrence of crossings of the excess energy curves (for different weighting factors) from mid-range to Pd-rich compositions. All GM in the range $w = 0.0$ to 0.8 are TO, with inc-Ih-Mackay only competitive for Pd-biased weighted parameters in the composition range (10,28) to (5,33).

Several straight line regions are evident from the plotted excess energies that were not found for the 34-atom clusters. The first straight line region is from the pure-Pd composition (38,0) to composition (26,12), after which more gradual changes of excess energy correspond to the formation of new Au–Au bonds on the surface of the cluster, as shown in Fig. 7(a) (substitution of 1–12 Au atoms into Pd₃₈ for $w_a = 0.0$ –0.2 only introduces heteronuclear Pd–Au interactions). The next straight line region commences at composition (14,24) (Fig. 7(b)), after which point Au atoms start to occupy the centroids of the (111) facets on the cluster surfaces. The transition from 12 to 13 Au atoms and from 24 to 25 Au atoms specifically shows how Au prefers (100) sites, leaving Pd on (111) facets, consistent with the findings of DFT

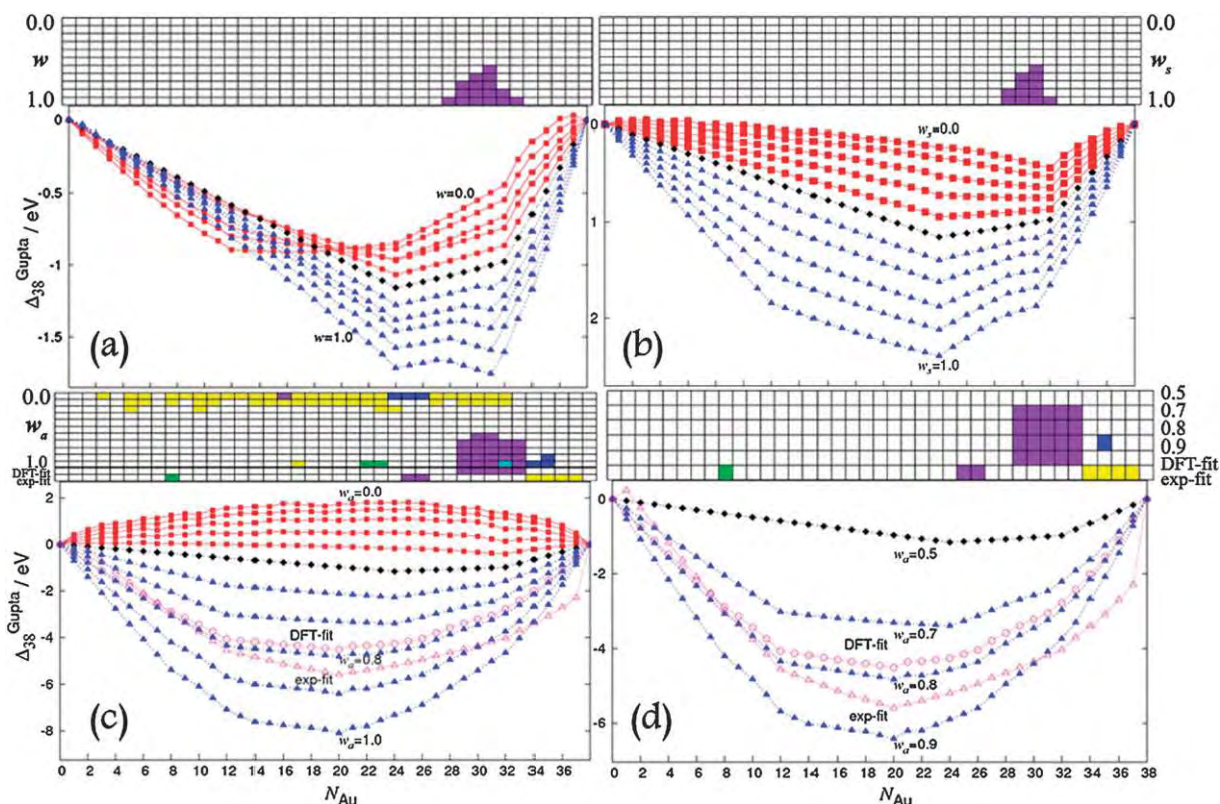


Fig. 6 (Bottom) Excess energy variation ($\Delta_{38}^{\text{Gupta}}$) for 38-atom Pd–Au clusters using parameter sets **I** (a), **II** (b), and **III** (c). (d) is a comparison between set **III** ($w_a = 0.5, 0.7–0.9$) and the **DFT-fit** and **exp-fit** potentials. (Top) GM Structural motifs found, as a function of composition (number of Au atoms) and weighting factor (w , w_s or w_a): TO (white); inc-Ih-Mackay (purple); Dh (yellow); pIh[LS] (blue); Oh-Ih (green); pIh⁶ (cyan).

calculations.⁵¹ This behaviour, also observed for Au₅₅, Au₉₈, Au₇₉, and Au₉₂, is promoted because of the stronger Pd–Au bond compared to either Au–Au or Pd–Pd bonds.⁵² Subsequent transitions with large jumps of energy for compositions (6–32) to (5,33), correspond to Au atoms starting to occupy the inner cluster core, as shown in Fig. 7(c). For $w = 0.6–1.0$, an almost identical transition occurs as a result of the structure changing from a pIh with 7 interior Pd atoms into a TO with 6 interior Pd atoms (Fig. 7(d)).

Using parameter set **II** (Fig. 6(b)), the excess energy plot shows no crossings for different weighting factors but the

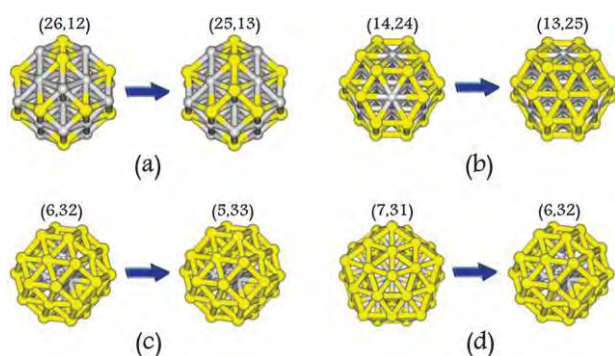


Fig. 7 Configurational changes in PdAu-38 using parameter set **I**: (a) 12Au to 13Au; (b) 24Au to 25Au; (c) 32Au to 33Au; and (d) structural change from 31Au to 32Au.

structural motifs are almost the same as for set **I**. The same straight lines and transition-points are also observed.

For parameter set **III** (Fig. 6(c)), Pd–Au mixing is not favourable (the excess energy is positive) for $w_a = 0.0–0.3$ and also for Pd-rich ($N_{\text{Au}} = 1–12$) clusters at $w_a = 0.4$. Straight line regions can again be seen, with transitions at compositions (26,12) (for $w_a = 0.6–0.8$) and (14,24) (for $w_a = 0.6–0.7$), which are correlated with the introduction of new Au–Au bonds on the surface and the establishment of complete 7 Au-atom hexagonal (111) faces of the clusters, respectively, and are also observed for parameter sets **I** and **II**. The most stable cluster for parameter set **III** at $w_a = 1.0$ (Pd₁₈Au₂₀) has an excess energy of -8.1008 eV, which is much lower than for set **I** (-1.7552 eV for Pd₇Au₃₁) and set **II** (-2.3922 eV for Pd₁₄Au₂₄). The more negative excess energies for 38-atom Pd–Au clusters, using parameter set **III**, are consistent with the results for the 34-atom clusters, and indicates an increase in the proportion of heteronuclear Pd–Au bonds in the cluster, which is favoured by the asymmetric weighting.

Overall, TO were found to be the most stable structures for set **III**, except for low w_a (0.0–0.1), where Dh structures dominate. For larger w_a (0.6–1.0), inc-Ih-Mackay is a competitive structure, especially in the Au-rich range from (9,29) to (5,33). Other structures that might be competitive for Pd–Au clusters are pIh⁶ ($w_a = 1.0, (6,32)$), pIh[LS] and the new structures of Oh-Ih ($w_a = 1.0, (16,22)$ and $(15,23)$) that were

not found previously for the **average** Gupta potential.^{11,25} For $w_a = 0.8$ – 1.0 , the minima in excess energy occur at (18,20), after which there is a sudden increase of energy that can be explained by adding a single Au atom to the unfavourable core of the TO cluster.

Similar to the results for the 34-atom clusters, the variation of structures in the 38-atom Pd–Au clusters for parameter set **I** (Fig. 6(a)) and parameter set **II** (Fig. 6(b)) is mainly affected by the composition effect, in which the inc-Ih-Mackay structure is found as the putative GM for Au-rich compositions for weightings biased towards Pd (high w and w_s). Moving to parameter set **III** (Fig. 6(c)), the composition effect still plays a role in intermediate parameterisation (close to the average), but the emergence of Dh and pIh[LS] structures (at low w_a) and Oh–Ih and pIh⁶ structures (at high w_a) clearly shows the large effect of varying the parameter weighting for set **III**.

For the **DFT-fit** potential, the excess energy plot for 38-atom Pd–Au clusters is consistent with that for 34 atoms; it is located between $w_a = 0.7$ and 0.8 of parameter set **III** (Fig. 6(d)). The structural motifs are also in line with this trend, showing the same GM for all compositions. On the other hand, the **exp-fit** excess energy plot dips down below $w_a = 0.8$ and at some points (for very rich Au compositions) the GM of this potential are more stable than the extreme parameters of set **III** ($w_a = 0.9$ – 1.0). In terms of structural motifs, as for the 34-atom clusters, the **exp-fit** potential gives a totally different composition variation compared to the GM of set **III**. Along with the dominant TO, other structures from the **exp-fit** potential calculations are Dh [(4,34) to (1,37)], inc-Ih-Mackay [(13,25) and (12,26)] and Oh–Ih [(30,8)]; with the latter structure also found at $w_a = 1.0$ for set **III**.

GM structural variation and segregation profiles. Fig. 8(a) shows TO ($w = 0.0$ – 0.8) and inc-pIh-Mackay ($w = 0.9$ – 1.0) structures have the most negative excess energies for parameter set **I**. However, if just A and ξ are varied in a symmetrical manner (set **II**) (Fig. 8(b)) then the lowest excess energies only correspond to TO, either with composition (6,32) ($w_s = 0.0$ – 0.3) or (14,24) ($w_s = 0.4$ – 1.0). Parameter set **III** (Fig. 8(c)) has a pIh(LS) structure as the lowest excess energy for $w_a = 0.0$, followed by a range of TO structures with different compositions for $w_a = 0.1$ – 0.7 , and the most negative excess energies of all are distorted-TO (towards Oh–Ih) for $w_a = 0.8$ – 1.0 .

Similar to parameter set **III** ($w_a = 0.8$ and 0.9), the lowest excess energy structures for the **DFT-fit** and **exp-fit** potentials have composition (18,20) with structures which are TO distorted towards Oh–Ih, as shown in Fig. 8(d). It should be noted that mixed Oh–Ih motifs can only be found at very Pd-rich compositions, *i.e.* (30,8) for the **exp-fit** potential, and also for set **III** (with $w_a = 1.0$) at compositions (16,22) and (15,23). For medium compositions, it shows a similar type of structure (TO distorted towards Oh–Ih) with core–shell chemical ordering. Compared to 34-atom clusters,²⁶ 38-atom Pd–Au clusters do not exhibit a rich diversity of structures and segregation, but this size produces stable TO structures—which is a fragment of fcc packing—as in the bulk phases of pure palladium and gold.^{5,7}

The segregation profiles in Fig. 9 agree with our earlier observations, showing a tendency towards TO structures

having Au atoms segregated to the surface and Pd atoms occupying core positions.²⁵ All the minimum excess energy isomers (M) (for all weighting factors) for parameter sets **I** (Fig. 9(a)) and **II** (Fig. 9(b)) display i-CS(C) chemical ordering, with all Au atoms on the surface. This is in agreement with experimental^{11,42} and other theoretical studies.⁴⁵ In addition to a wide range (in composition and weighting) of stability of the i-CS(A) configuration, i-CS(C) emerges as a favourable configuration for Pd-rich clusters for parameter sets **I** (low w) and **II** (high w_s). Compared to the 34-atom clusters, 38-atom PdAu clusters with TO geometries show stronger evidence of the tendency of Au atoms to occupy the sites with the lowest coordination—*i.e.* the square (100) facet sites—leaving Pd atoms at the centres of the hexagonal (111) facets. The ionic contribution to the Pd–Au bonding plays a role in promoting a large number of Pd–Au bonds on the surface compared to Pd–Pd and Au–Au bonds,^{25,51,52} resulting in a strong dominance of i-CS(A) configurations for parameter set **I** and **II**. The strength of the slightly ionic Pd–Au bond is increased by electron transfer from the Pd atom to the region between Au and Pd, which is due to the slightly larger Pauling electronegativity of Au (2.54) than that of Pd (2.20).⁵³ The i-CS(A) and i-CS(C) configurations were observed previously with the **average** parameter set for 38-atom Pd_{core}Au_{shell} clusters,²⁵ as well as for Ni_{core}Ag_{shell},⁴⁹ Au_{core}Ag_{shell} and Pt_{core}Pd_{shell}⁵⁴ clusters, and agrees with the observation of isolated Pd surface sites surrounded by Au atoms in several experimental studies.^{55–58}

As for the 34-atom Pd–Au clusters, $w_s = 0.0$ is found to generate GM with i-CS(B) configurations. Interestingly, 38-atom Pd–Au clusters exhibit this type of segregation over a wider composition range, and also for $w_s = 0.1$, with a **type-B**–**type-A** transition at $w_s = 0.1$.

In contrast to parameter sets **I** and **II**, chemical ordering of minimum excess energy structures (M) for parameter set **III** (Fig. 9(c)) varies from spherical cap ($w_a = 0.0$) to ball-and-cup ($w_a = 0.1$), i-CS(B) ($w_a = 0.2$ – 0.3), complete core–shell ($w_a = 0.4$) and i-CS(A) ($w_a = 0.5$ – 1.0). Mixed clusters (with 1–4 Au atoms in the core), which are favoured over a wide range of compositions for $w_a = 0.8$ – 1.0 , do not have the lowest excess energies. Again, the crossover of chemical ordering for parameter set **III** indicates the dominance of parameterisation over composition effects (with composition dominating for parameter sets **I** and **II**).

Comparison of GM and metastable structured motifs. In this paper, we mainly focus on the putative GM, as it would involve a very long discussion to include (even some of the) local minimum structures for all compositions of two cluster sizes (34 and 38 atoms) and for three parameterisation schemes (parameter sets **I**, **II** and **III**). However, a brief consideration of metastable structures is presented here.

A detailed study for all compositions of 38-atom Pd–Au clusters, using the average potential ($w = w_a = w_s = 0.5$) (Fig. 10), shows that there is close competition between Dh, inc-Ih-Mackay and TO structures across the entire composition range, with pIh⁶ being relatively unstable. TO are the putative GM found by the GA for all compositions.

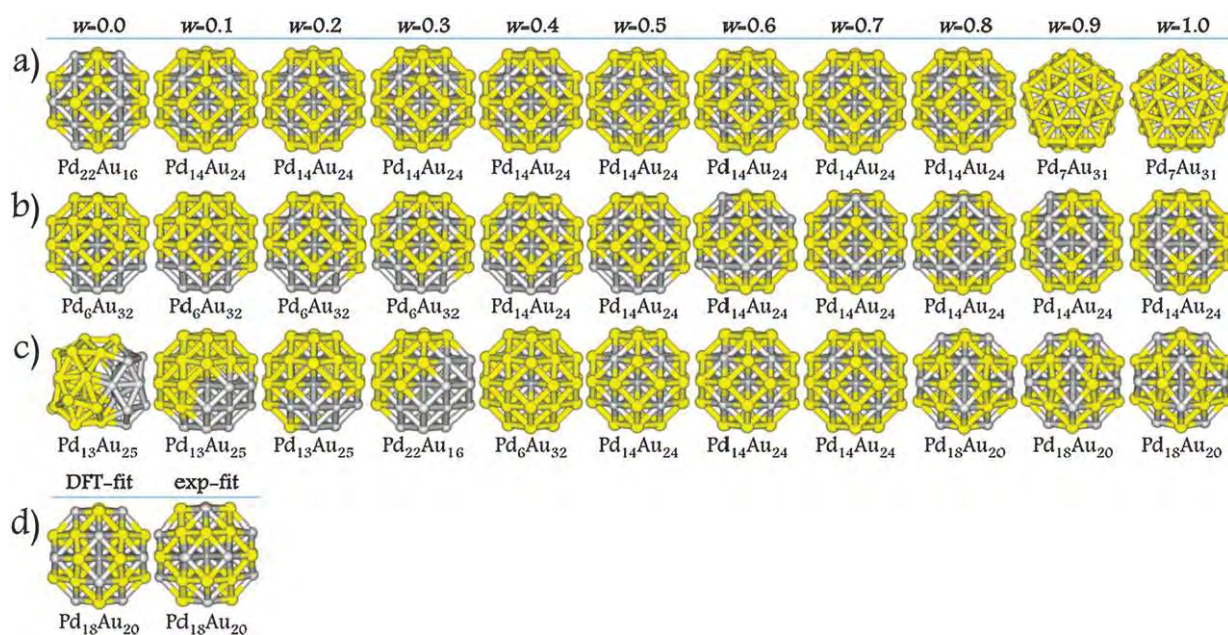


Fig. 8 Structural variation of the lowest excess energy PdAu-38 isomers found for parameter sets *I* (a), *II* (b), *III* (c), and the DFT-fit and exp-fit potentials (d).

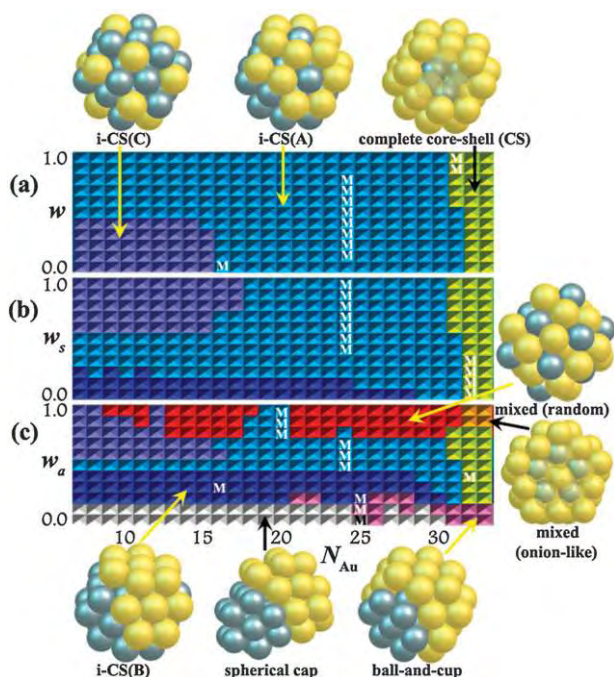


Fig. 9 Segregation profiles of PdAu-38 using parameter sets *I* (a), *II* (b), and *III* (c).

GA calculations for the fixed composition $\text{Pd}_6\text{Au}_{32}$, as a function of the weightings w , for parameter set *I* (Fig. 11(a)) give the TO as the GM for all weightings except $w = 0.9$ and 1.0, for which the inc-Ih-Mackay structure is more stable. Parameter set *II* (Fig. 11(b)) gives inc-Ih-Mackay as the GM only for $w_s = 1.0$. However, for parameter set *III* (Fig. 11(c)), the GM predicted varies significantly with weighting: Dh (with ball-and-cup segregation) ($w_a = 0.0-0.1$); TO ($w_a = 0.2-0.6$); inc-Ih-Mackay ($w_a = 0.7-0.9$); and pIh⁶ ($w_a = 1.0$). This shows

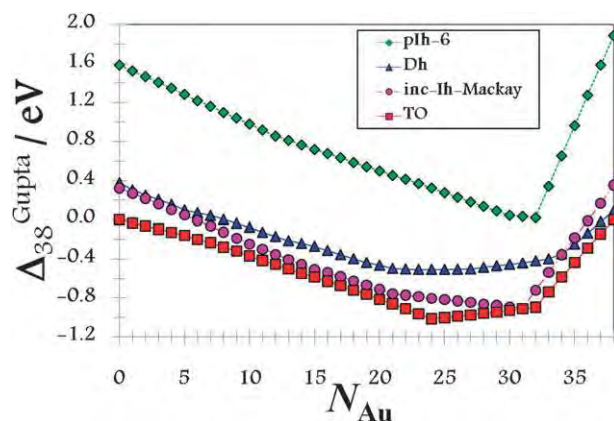


Fig. 10 Composition-dependent variation of the excess energies of four structural motifs of 38-atom Pd-Au clusters using the average potential ($w = 0.5$).

the sensitivity of the Gupta potential to varying the potential parameters, especially for parameter set *III*.

3.3 Analysis of segregation in Pd-Au clusters

Pair distribution function (PDF). Based on the bulk fcc lattice, the nearest- and second-nearest neighbour distances are 2.7485 and 3.8479 Å for Pd and 2.8840 and 4.037 Å for Au, respectively. By examining each of the PDF plots, it was decided to select the values of 3.3 Å (Pd-Pd), 3.5 Å (Au-Au) and 3.4 Å (Pd-Au), as the cut-off for defining each respective type of bond. This is consistent with the bulk data ($r_{\text{Pd-Pd}} < r_{\text{Pd-Au}} < r_{\text{Au-Au}}$) and the bulk distances mentioned above. PDFs for 34-atom clusters are more complex than for the 38-atom clusters for all parameter sets, due to the greater bond length distribution variation of the structural families.

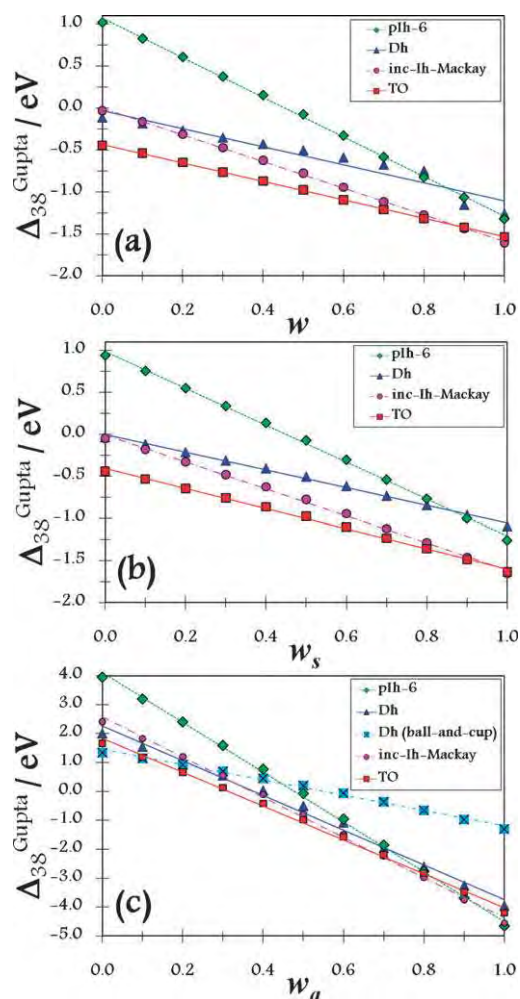


Fig. 11 Parameter weighting-dependent variation of the excess energies of four structural motifs of Pd₆Au₃₂ using parameter sets **I** (a), **II** (b) and **III** (c).

Average nearest neighbour distance (ANND). Calculations on the GM derived from the GA search give ANNDs of pure Pd clusters of 2.6760 Å (34-atoms) and 2.6696 Å (38-atoms), while pure Au clusters display smaller values of 2.7932 Å (34-atoms) and 2.7886 Å (38-atoms). Consistent with previous research on Pd–Au clusters using the **average** potential ($w = 0.5$ in this work), there is a steady increase in ANND with increasing Au content, due to the larger atomic radius of Au, in accordance with Vegard’s law. Sudden changes in ANND are consistent with a change of structural motif.¹¹

Due to the relatively small difference in the Gupta potential parameters between Pd and Au,¹² it is expected that ANND data for bimetallic clusters combining the two, would result in a straightforward pattern. However, moving from Au-biased parameters ($w = w_a = 0.0$) to Pd-biased parameters ($w = w_a = 1.0$) (Fig. 12(a), (b), (d) and (e)), there is a slight deviation of the curve, with a large plateau at Pd-rich compositions. This slow movement means that the ANND remains low (close to bulk Pd), in line with shifting towards Pd-biased Gupta parameters. The antisymmetric weighting potential for PdAu-34 (Fig. 12(c)) shows more fluctuation, in agreement with the heterogeneous plh structures, compared to continual

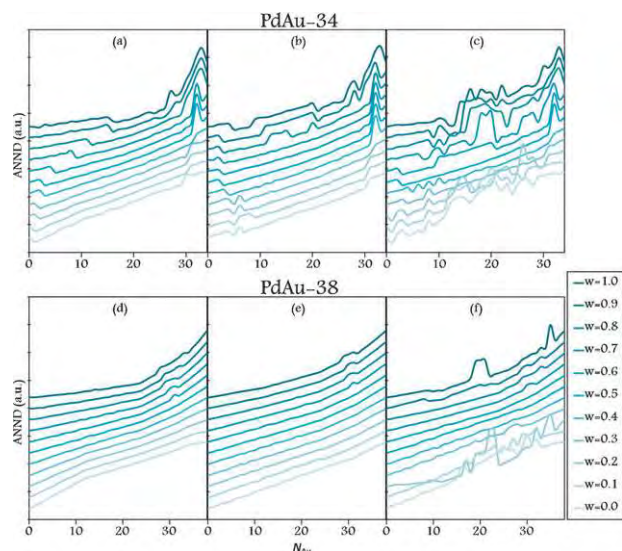


Fig. 12 ANND variation for PdAu-34 using parameter sets **I** (a), **II** (b), and **III** (c) and for PdAu-38 using sets **I** (d), **II** (e), and **III** (f).

TO structures of PdAu-38 (Fig. 12(f)). The ANNDs for parameter set **III**, with high values of w_a , exhibit a high degree of Pd–Au mixing, similar to the **DFT-fit** and **exp-fit** potentials reported earlier with jagged behaviour of ANNDs.¹¹

Chemical order. An earlier study of 38-atom Pd–Au clusters using the **average** Gupta parameters ($w = 0.5$) showed that the chemical order parameter, σ , has positive values for all compositions, with minima ($\sigma = 0$) at Pd₁₅Au₂₃ and Pd₁₄Au₂₄.¹¹ These positive σ values correspond to core–shell segregation. For PdAu-34 clusters, the lowest σ value occurs at Pd₁₄Au₂₀, and is more positive than for PdAu-38, with all compositions again having positive σ values, corresponding to core–shell segregation.

Using parameter set **I**, PdAu-34 (Fig. 13(a)) does not show significant differences compared to the **average** potential ($w = 0.5$). In contrast, 38-atom Pd–Au clusters (Fig. 13(d)) exhibit better mixing at $w = 0.6$ – 1.0 , specifically for medium compositions. Parameter set **II** shows some increase in mixing for PdAu-34 (Fig. 13(b)), but is consistent with set **I** for PdAu-38 (Fig. 13(e)). Interestingly, parameter set **III** reveals considerable deviations from the **average** potential results. PdAu-34 clusters (Fig. 13(c)) possess σ values close to zero ($w_a = 0.6$) and negative values ($w_a = 0.7$ – 1.0), indicating a higher degree of mixing. For PdAu-38 clusters (Fig. 13(f)) negative σ values are only found over a wide composition range for $w_a = 0.8$ – 1.0 . This is consistent with previous calculations on 38-atom Pd–Au clusters using the **DFT-fit** and **exp-fit** potentials. Consistent with other analyses, parameter set **III** displays the largest variation from the **average** potential curve ($w = w_s = w_a = 0.5$). Biasing the parameters towards higher w_a (> 0.5) leads to increased Pd–Au mixing, as shown by the increased number of Pd–Au bonds relative to homonuclear bonds, and hence the more negative values of σ . At $w_a = 1.0$, the tendency to form mixed bonds distorts the clusters towards an ordered mixing arrangement. For PdAu-34 a distorted bcc/Dh structure is adopted at composition

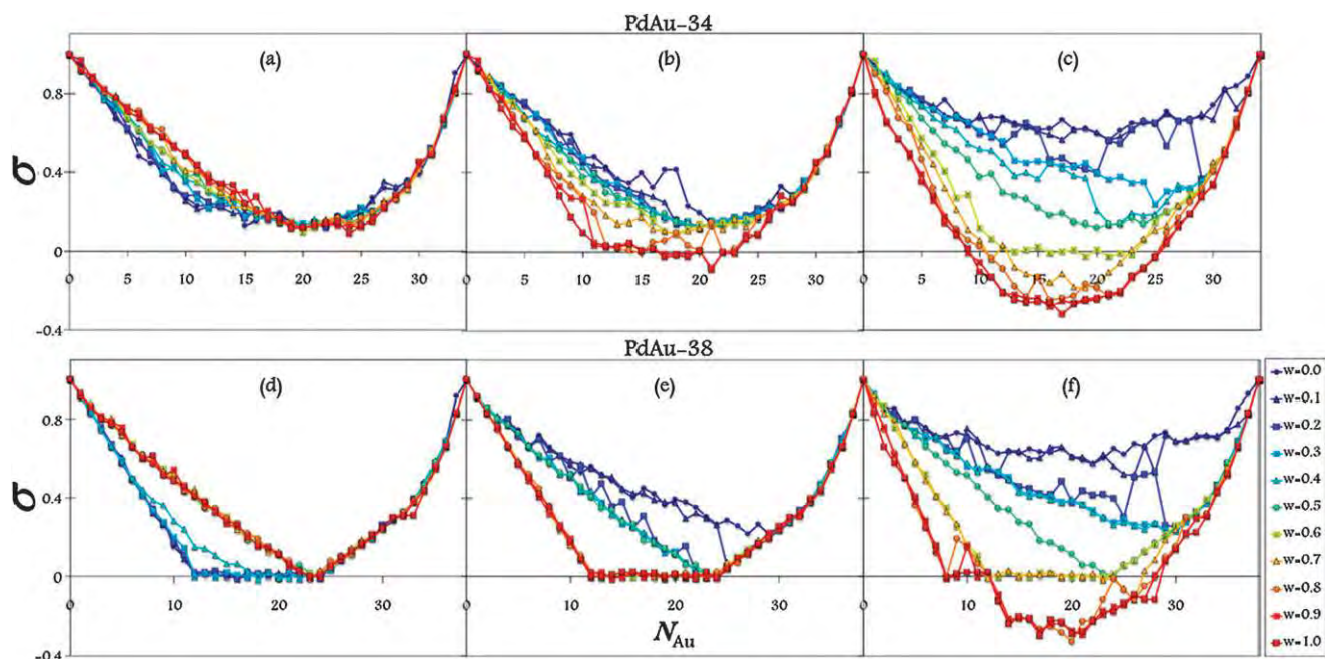


Fig. 13 Chemical order parameter (σ) for PdAu-34 using parameter sets *I* (a), *II* (b), and *III* (c) and for PdAu-38 using sets *I* (d), *II* (e), and *III* (f).

(17,17), while for PdAu-38 the Oh–Ih motif is found as the GM at (16,22) and (15,23), rather than the TO structure.

4. Conclusions

A detailed discussion of the energetics, structures and segregation of Pd–Au nanoalloy clusters has been presented, for 34- and 38-atom Pd–Au clusters, using three types of heteronuclear potential parameterisation. Parameter set *I* (in which all parameters in the Gupta potential are weighted symmetrically) and parameter set *II* (where only the energy-scaling parameters A and ζ are varied, with the remaining parameters kept at their average values) give very slight variation in structures, with the ordering being dominated by changes in elemental composition. However a clear dependence of structure on parameter weighting is observed for parameter set *III* (antisymmetric variation of A and ζ).

The in-depth structural analysis of 34-atom clusters showed Dh, pIh and TO structural motifs as the putative global minima, while the TO structure faces competition from inc-Ih-Mackay, Dh, pIh(LS), pIh⁶ and Oh–Ih for 38-atom clusters. Generally, the new Oh–Ih configuration ($w_a = 1.0$, (16,22) and (15,23)) was not found as a GM for the **average** Gupta potential, but it has been found as the lowest-energy isomer for Ag–Pt clusters at the DFT level.²⁵ These results show that, by finely tuning the Gupta potential, it is possible to qualitatively reproduce the results observed at higher levels of theory.

The significant crossover of chemical ordering type (core–shell, spherical cap, ball-and-cup and mixed) observed for parameter set *III* also indicates that parameter weighting dominates composition effects for this parameter set. Chemical ordering of the GM are consistent with the ANND and sigma (σ) profiles, in which parameter set *III* displays an evolution of structural families towards an ordered mixing arrangement

(the distorted bcc/Dh structure for PdAu-34 and Oh–Ih for PdAu-38) for higher w_a values (> 0.5).

Comparing the results from parameter set *III* and the fitted (**DFT-fit** and **exp-fit**) potentials generated some interesting conclusions. Parameter set *III* with $w_a > 0.5$ gave stronger Pd–Au bonding, as shown by the more negative excess or mixing energies for both cluster systems. This weighting scheme results in less Pd–Au repulsion ($A_{\text{PdAu}} \rightarrow A_{\text{Pd}}$) and more Pd–Au attraction ($\zeta_{\text{PdAu}} \rightarrow \zeta_{\text{Au}}$) in the clusters. This is because $A_{\text{Pd}} (0.1746) < A_{\text{Au}} (0.2061)$ and $\zeta_{\text{Pd}} (1.7180) < \zeta_{\text{Au}} (1.7900)$; so that as $w_a \rightarrow 1.0$ the A parameter (repulsion) is reduced and the ζ parameter (attraction) increases. The **DFT-fit** potential gives more comparable results to those of parameter set *III*. The **DFT-fit** potential has the following characteristics which are similar to those in the antisymmetric (set *III*) weighted Gupta potential: $A_{\text{DFT-fit}} (0.1843) \sim A_{w_a = 0.7} (0.1841)$ and $\zeta_{\text{DFT-fit}} (1.7867) \sim \zeta_{w_a = 0.9} (1.7828)$. These correlations are consistent with the overall results for 34- and 38-atom PdAu clusters, that show the **DFT-fit** potential giving similar results of excess energies and lowest energy structures and homotops to those for $w_a = 0.8$. The **exp-fit** potential also gives similar excess energies to the results for $w_a = 0.8$, though the shape of the curve is a little different—but the structures and homotops are often quite different to the results from parameter set *III*. This is not surprising, since, as noted previously,¹¹ the **exp-fit** parameters are qualitatively very different. In particular we note that for the **exp-fit** potential: $A_{\text{PdAu}} > A_{\text{PdPd}}$ and $A_{\text{AuAu}}; \zeta_{\text{PdAu}} > \zeta_{\text{PdPd}}$ and ζ_{AuAu} .

We have shown, therefore, that a simple asymmetrical weighting (parameter set *III*) of the Pd–Au pair (A) and many-body (ζ) energy scaling parameters in the Gupta potential can qualitatively reproduce the energetic, structures and chemical ordering of the **DFT-fit** potential. As the next step in this research, we will select new, low-energy structures and homotops arising from set *III* that were not found in previous

work¹¹ and we will carry out DFT re-minimisations in order to evaluate how they compare with those obtained previously. Finally, since it is known that the Gupta potential typically underestimates bulk surface energies,³ in future work, we will also address the effect of modifying the potential, so as to reproduce Pd, Au and Pd–Au surface energies accurately, on the structures and chemical ordering of Pd–Au clusters.

Acknowledgements

RI is grateful to Universiti Pendidikan Sultan Idris and the Ministry of Higher Education (Malaysia) for the award of a PhD scholarship. Calculations were performed on the University of Birmingham's BueBEAR high-performance computer.⁵⁹ The authors acknowledge Profs Riccardo Ferrando and Alessandro Fortunelli for helpful discussions and RI is grateful to Dr Oliver Paz-Borbón for his initial help in running the BCGA program.

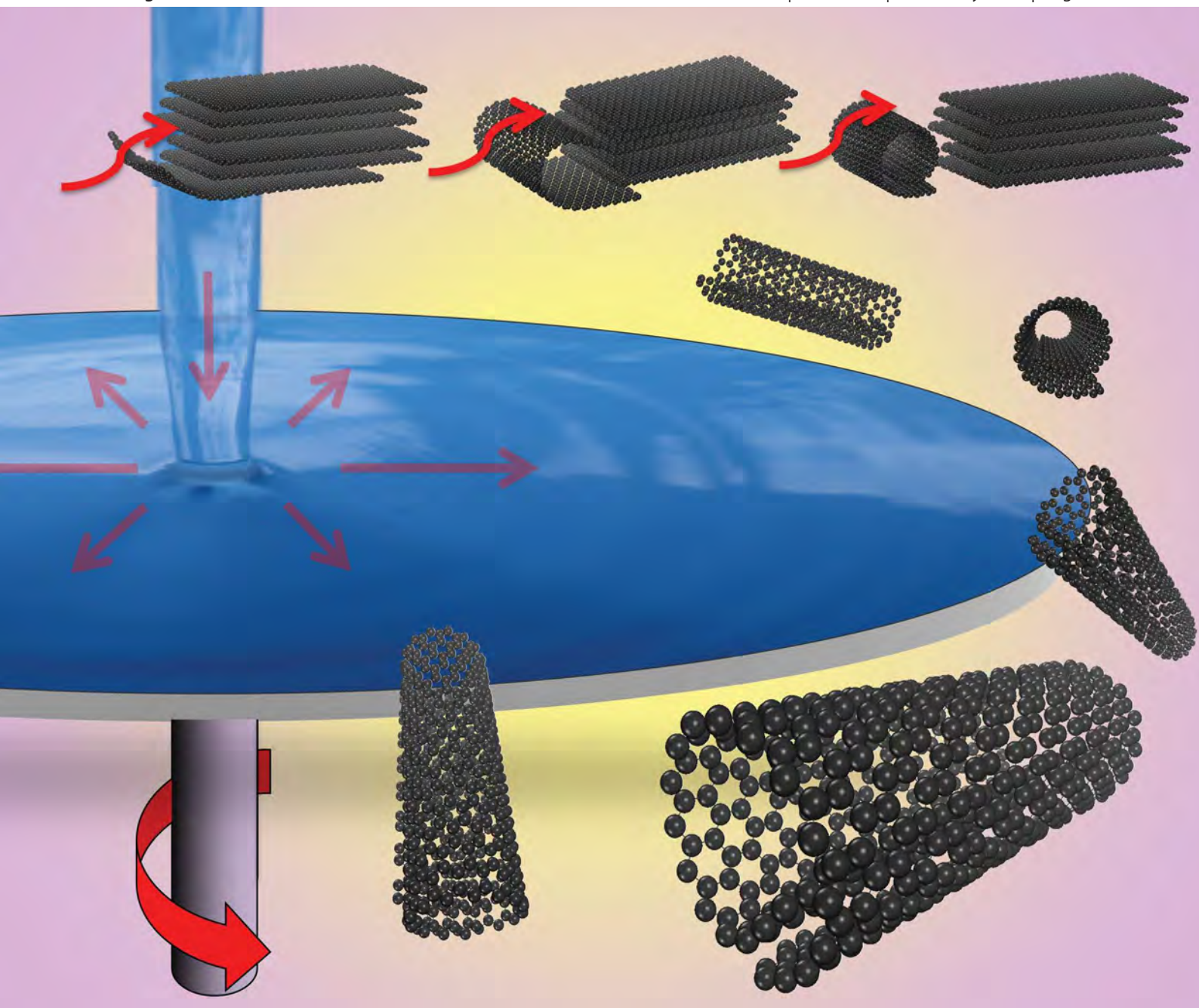
References

- 1 R. L. Johnston, *Atomic and Molecular Clusters*, Taylor & Francis, London, 2002.
- 2 T. P. Martin, *Phys. Rep.*, 1996, **273**, 199.
- 3 F. Baletto and R. Ferrando, *Rev. Mod. Phys.*, 2005, **77**, 371.
- 4 R. Ferrando, J. Jellinek and R. L. Johnston, *Chem. Rev.*, 2008, **108**, 845.
- 5 D. Schebarchov and S. Hendy, *Phys. Rev. B: Condens. Matter Mater. Phys.*, 2006, **73**, 121402.
- 6 M. José-Yacamán, M. Marín-Almazoc and J. A. Ascencio, *J. Mol. Catal. A: Chem.*, 2001, **173**, 61.
- 7 D. M. P. Mingos, *J. Chem. Soc., Dalton Trans.*, 1996, 561.
- 8 J. A. Ascencio, C. Gutiérrez-Wing, M. E. Espinosa, M. Marín, S. Tehuacanero, C. Zorrilla and M. José-Yacamán, *Surf. Sci.*, 1998, **396**, 349.
- 9 C. L. Cleveland, U. Landman, T. G. Schaaff, M. N. Shafiqullin, P. W. Stephens and R. L. Whetten, *Phys. Rev. Lett.*, 1997, **79**, 1873.
- 10 H. B. Liu, U. Pal, A. Medina, C. Maldonado and J. A. Ascencio, *Phys. Rev. B: Condens. Matter Mater. Phys.*, 2005, **71**, 075403.
- 11 F. Pittaway, L. O. Paz-Borbón, R. L. Johnston, H. Arslan, R. Ferrando, C. Mottet, G. Barcaro and A. Fortunelli, *J. Phys. Chem. C*, 2009, **113**, 9141.
- 12 F. Cleri and V. Rosato, *Phys. Rev. B: Condens. Matter*, 1993, **48**, 22.
- 13 A. F. Lee, C. J. Baddeley, C. Hardacre, R. M. Ormerod, R. M. Lambert, G. Schmid and H. West, *J. Phys. Chem.*, 1995, **99**, 6096.
- 14 H. Bönemann, U. Endruschat, B. Tesche, A. Rufinska, C. W. Lehmann, F. E. Wagner, G. Filoti, V. Pärulescu and V. I. Pärulescu, *Eur. J. Inorg. Chem.*, 2000, 819.
- 15 V. I. Pärulescu, V. Pärulescu, U. Endruschat, G. Filoti, F. E. Wagner, C. Kübel and R. Richards, *Chem.–Eur. J.*, 2006, **12**, 2343.
- 16 E. Gross, I. Popov and M. Asscher, *J. Phys. Chem. C*, 2009, **113**, 18341.
- 17 M. O. Nutt, J. B. Hughes and M. S. Wong, *Environ. Sci. Technol.*, 2005, **39**, 1346.
- 18 N. Toshima, T. Yonezawa and K. Kushiashi, *J. Chem. Soc., Faraday Trans.*, 1993, **89**, 2537.
- 19 J. K. Edwards, B. E. Solsona, P. Landon, A. F. Carley, A. Herzing, C. J. Kiely and G. J. Hutchings, *J. Catal.*, 2005, **236**, 69.
- 20 D. I. Enache, J. K. Edwards, P. Landon, B. Solsona-Espriu, A. F. Carley, A. A. Herzing, M. Watanabe, C. J. Kiely, D. W. Knight and G. Hutchings, *Science*, 2006, **311**, 362.
- 21 D. H. Turkenburg, A. A. Antipov, M. B. Thathagar, G. Rothenberg, G. B. Sukhorukov and E. Eiser, *Phys. Chem. Chem. Phys.*, 2005, **7**, 2237.
- 22 Y. F. Han, J. H. Wang, D. Kumar, Z. Yan and D. W. Goodman, *J. Catal.*, 2005, **232**, 467.
- 23 M. Chen, D. Kumar, C. W. Yi and D. W. Goodman, *Science*, 2005, **310**, 291.
- 24 L. O. Paz-Borbón, A. Gupta and R. L. Johnston, *J. Mater. Chem.*, 2008, **18**, 4154.
- 25 L. O. Paz-Borbón, R. L. Johnston, G. Barcaro and A. Fortunelli, *J. Chem. Phys.*, 2008, **128**, 134517.
- 26 L. O. Paz-Borbón, R. L. Johnston, G. Barcaro and A. Fortunelli, *J. Phys. Chem. C*, 2007, **111**, 2936.
- 27 R. P. Gupta, *Phys. Rev. B: Condens. Matter*, 1981, **23**, 6265.
- 28 C. Massen, T. V. Mortimer-Jones and R. L. Johnston, *J. Chem. Soc., Dalton Trans.*, 2002, 4375.
- 29 A. J. Renouprez, J. L. Rousset, A. M. Cadrot, Y. Soldo and L. Stievano, *J. Alloys Compd.*, 2001, **328**, 50.
- 30 J. L. Rousset, L. Stievano, F. J. Cadete Santos Aires, C. Geantet, A. J. Renouprez and M. Pellarin, *J. Catal.*, 2001, **202**, 163.
- 31 D. Bazin, D. Guillaume, C. Pichon, D. Uzio and S. Lopez, *Oil Gas Sci. Technol.*, 2005, **60**, 801.
- 32 A. Fortunelli and G. Barcaro, personal communication.
- 33 R. Ismail and R. L. Johnston, unpublished work.
- 34 R. Hultgren, P. D. Desai, D. T. Hawkins, M. Gleiser and K. K. Kelley, *Values of the Thermodynamic Properties of Binary Alloys*, American Society for Metals, Metals Park, Ohio, 1973.
- 35 R. L. Johnston, *Dalton Trans.*, 2003, 4193.
- 36 M. M. Mariscal, N. A. Oldani, S. A. Dassie and E. P. M. Leiva, *Faraday Discuss.*, 2008, **138**, 89.
- 37 L. B. Hansen, P. Stoltze, J. K. Norskov, B. S. Clausen and W. Niemann, *Phys. Rev. Lett.*, 1990, **64**, 3155.
- 38 M. Itoh, V. Kumar, T. Adschiri and Y. Kawazoe, 2009, ar Xiv:0902.0080.
- 39 J. Jellinek and E. B. Krissinel, *Theory of Atomic and Molecular Clusters*, Springer-Verlag, Berlin, 1999.
- 40 F. Aguilera-Granja, A. Vega, J. Rogan, X. Andrade and G. Garcia, *Phys. Rev. B: Condens. Matter Mater. Phys.*, 2006, **74**, 224405.
- 41 G. Rossi, A. Rapallo, C. Mottet, A. Fortunelli, F. Baletto and R. Ferrando, *Phys. Rev. Lett.*, 2004, **93**, 105503.
- 42 J. L. Rousset, J. C. Bertolini and P. Miegge, *Phys. Rev. B: Condens. Matter*, 1996, **53**, 4947.
- 43 M. Mandal, S. Kundu, S. K. Ghosh and T. J. Pal, *J. Photochem. Photobiol., A*, 2004, **167**, 17.
- 44 A. Henglein, *J. Phys. Chem. B*, 2000, **104**, 6683.
- 45 H. B. Liu, U. Pal, A. Medina, C. Maldonado and J. A. Ascencio, *Phys. Rev. B: Condens. Matter Mater. Phys.*, 2005, **71**, 075403.
- 46 H. B. Liu, U. Pal, R. Perez and J. A. Ascencio, *J. Phys. Chem. B*, 2006, **110**, 5191.
- 47 W. R. Tyson and W. A. Miller, *Surf. Sci.*, 1977, **62**, 267.
- 48 A. R. Miedema, *Z. Metallkd.*, 1978, **69**, 287.
- 49 A. Rapallo, G. Rossi, R. Ferrando, A. Fortunelli, B. C. Curley, L. D. Lloyd, G. M. Tarbuck and R. L. Johnston, *J. Chem. Phys.*, 2005, **122**, 194308.
- 50 D. T. Tran and R. L. Johnston, *Phys. Chem. Chem. Phys.*, 2009, **11**, 10340.
- 51 D. Yuan, X. Gong and R. Wu, *Phys. Rev. B: Condens. Matter Mater. Phys.*, 2007, **75**, 085428.
- 52 D. Yuan, X. Gong and R. Wu, *Phys. Rev. B: Condens. Matter Mater. Phys.*, 2008, **78**, 035441.
- 53 J. E. Huheey, *Inorganic Chemistry: Principles of Structure and Reactivity*, Harper & Row, New York, 1983.
- 54 G. Rossi, R. Ferrando, A. Rapallo, A. Fortunelli, B. C. Curley, L. D. Lloyd and R. L. Johnston, *J. Chem. Phys.*, 2005, **122**, 194309.
- 55 K. Luo, T. Wei, C. W. Yi, S. Axnanda and D. W. Goodman, *J. Phys. Chem. B*, 2005, **109**, 23517.
- 56 S. J. Mejía-Rosales, C. Fernandez-Navarro, E. Prez-Tijerina, D. A. Blom, L. F. Allard and M. Jose-Yacamán, *J. Phys. Chem. C*, 2007, **111**, 1256.
- 57 M. José-Yacamán, E. Pérez-Tijerina and S. J. Mejía-Rosales, *J. Mater. Chem.*, 2007, **17**, 1035.
- 58 C. W. Yi, K. Luo, T. Wei and D. W. Goodman, *J. Phys. Chem. B*, 2005, **109**, 18535.
- 59 <http://www.bear.bham.ac.uk>.

Nanoscale

www.rsc.org/nanoscale

Volume 5 | Number 2 | 21 January 2013 | Pages 445–824



ISSN 2040-3364

RSC Publishing

COMMUNICATION

Raston *et al.*

Shear induced formation of carbon and boron nitride nano-scrolls



NCNST



2040-3364(2013)5:2;1-M

DFT study of the structures and energetics of 98-atom AuPd clusters†

Cite this: *Nanoscale*, 2013, 5, 646

Alina Bruma,^a Ramli Ismail,^{bc} L. Oliver Paz-Borbón,^{bd} Haydar Arslan,^e Giovanni Barcaro,^f Alessandro Fortunelli,^f Z. Y. Li^a and Roy L. Johnston^{*b}

The energetics, structures and segregation of 98-atom AuPd nanoclusters are investigated using a genetic algorithm global optimization technique with the Gupta empirical potential (comparing three different potential parameterisations) followed by local minimizations using Density Functional Theory (DFT) calculations. A shell optimization program algorithm is employed in order to study the energetics of the highly symmetric Leary Tetrahedron (LT) structure and optimization of the chemical ordering of a number of structural motifs is carried out using the Basin Hopping Monte Carlo approach. Although one of the empirical potentials is found to favour the LT structure, it is shown that Marks Decahedral and mixed FCC-HCP motifs are lowest in energy at the DFT level.

Received 30th August 2012

Accepted 20th November 2012

DOI: 10.1039/c2nr32517a

www.rsc.org/nanoscale

Introduction

Bimetallic nanoparticles (“nanoalloys”)¹ have received considerable attention for their unique properties, which are different from those of pure clusters^{2,3} especially in the domain of nanocatalysis.^{4–9} Gold–palladium (AuPd) nanoparticles are one of the most attractive systems because of their promising activity in catalysis.¹⁰ This superior performance has been widely attributed to electronic and/or geometric effects.^{11,12} Previous experimental studies have emphasized that it is possible to design various configurations of the same catalyst (*i.e.* alloy structure,¹³ Pd_{core}Au_{shell},¹⁴ Au_{core}Pd_{shell}¹⁵ or even 3 layer onion-like AuPd nanoparticles¹⁶) whereas theoretical studies¹⁷ have emphasized that a Pd_{core}Au_{shell} structure is favoured. From a theoretical point of view, empirical potentials (EP) have been widely employed for the determination of the structural and energetic configurations of nanoclusters in order to overcome the computational limitations imposed by more computationally expensive first principles approaches. The EP are suitable and versatile for modelling noble and quasi-noble

metals. However, as it is known that important modifications can be introduced by electronic effects,¹⁸ it is important to verify the predictions of the EP using first principles calculations. Density Functional Theory (DFT) is one of the most accurate methods for describing such effects. We have previously reported¹⁹ that a systematic search of the global minimum (GM) for 50-atom PdAu clusters is highly demanding for high level calculations because of the computational limitations in exploring vast areas of the configurational space. In the case of bimetallic clusters, it is generally accepted^{20,21} that the search is even more difficult due to the existence of homotops (isomers related by swapping the positions of one or more heterometallic pairs). In the present study, a hybrid approach has been adopted, based on a genetic algorithm (GA) for structural searching and Basin-Hopping Monte Carlo homotop searching²² at the EP level, followed by DFT local relaxation, to perform a thorough search of the configurational space for 98 atom AuPd nanoclusters. Three different parameterisations of the Gupta many-body empirical potential have been investigated and DFT local relaxations are performed for the putative global minimum (GM) structures identified for all parameter sets.

Fig. 1 shows a series of typical experimental images of AuPd nanoparticles obtained with a 200 kV Aberration-Corrected JEOL JEM2100F Scanning Transmission Electron Microscope (STEM) equipped with a High Angle Annular Dark Field (HAADF) detector. The images show AuPd nanoparticles deposited *via* physical vapour deposition onto amorphous carbon substrate and subsequently annealed *in situ* for 2 hours at 473 K. It can be seen that, for the same sample, a variety of sizes (from 1 to ~3 nm) and morphologies can be encountered, with chemical ordering ranging from alloy to Janus nanoparticles. However, although DFT calculations are limited to smaller sizes, these studies can be considered important

^aNanoscale Physics Research Laboratory, School of Physics and Astronomy, University of Birmingham, Edgbaston, Birmingham, B152TT, UK

^bSchool of Chemistry, University of Birmingham, Edgbaston, Birmingham, B152TT, UK. E-mail: r.l.johnston@bham.ac.uk

^cMax Planck Institute for Solid State Research, Heisenbergstrasse 1, D-70569 Stuttgart, Germany

^dCompetence Centre for Catalysis, Chalmers University of Technology, Gothenburg, SE-41296, Sweden

^eDepartment of Physics, Bulent Ecevit University, Zonguldak, 67100, Turkey

^fCNR-IPCF, Istituto per i Processi Chimico-Fisici del Consiglio Nazionale delle Ricerche, Via G. Moruzzi 1, 56124, Pisa, Italy

† Electronic supplementary information (ESI) available. See DOI: 10.1039/c2nr32517a

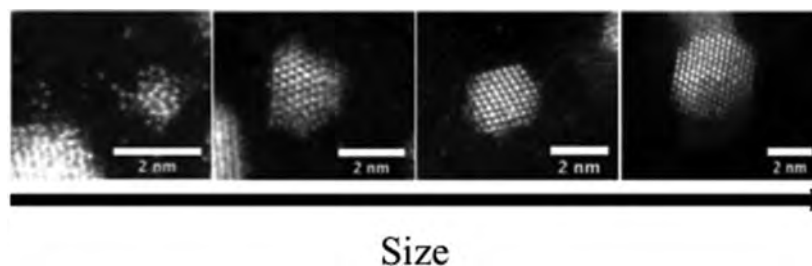


Fig. 1 Structural evolution with size of AuPd nanoparticles deposited *via* physical vapor deposition on amorphous carbon substrate and annealed at 473 K for 2 hours. Various morphologies of AuPd nanoparticles can be observed as size increases, from alloy to Janus structures.

starting points in understanding the metal–metal interactions in larger nanoparticles.

Computational details

The first step of this study involves the use of an empirical atomistic potential to allow a rapid search for the lowest energy isomers in configurational space. The Gupta potential has been used in order to model the interatomic interactions, with parameters chosen as described by Cleri and Rosato²³ and Ismail and Johnston.²⁴ The Gupta potential is based on the second moment approximation to tight-binding theory. The configurational energy of a cluster is written as the sum over all atoms of the many body attractive (V^m) and pair repulsive (V^r) energy components:

$$V_{\text{clus}} = \sum_{i=1}^N \left\{ V^r(i) - V^m(i) \right\} \quad (1)$$

where $V^r(i)$ and $V^m(i)$ are defined as:

$$V^r(i) = \sum_{j \neq i}^N A(\alpha, \beta) \exp \left\{ -p(\alpha, \beta) \left(\frac{r_{ij}}{r_0(\alpha, \beta)} - 1 \right) \right\} \quad (2)$$

$$V^m(i) = \left[\sum_{j \neq i}^N \xi^2(\alpha, \beta) \exp \left\{ -2q(\alpha, \beta) \left(\frac{r_{ij}}{r_0(\alpha, \beta)} - 1 \right) \right\} \right]^{1/2} \quad (3)$$

In eqn (1)–(3), the parameters α and β represent the atomic species of atoms i and j . Parameters A , r_0 , ξ , p and q are usually fitted to the experimental values of the cohesive energy, lattice parameters and independent elastic constants for the reference crystal structure of pure metals and bulk alloys at 0 K. The values of the Gupta potential parameters describing the Pd–Pd, Pd–Au and Au–Au interactions are described in Table 1 and are taken from ref. 23 and 24. Here, the three sets of parameters are described as: (a) ‘Average’: the heteronuclear Pd–Au parameters are obtained by averaging the pure Pd–Pd and Au–Au parameters; (b) ‘Exp-fit’: the Pd–Pd, Au–Au and Pd–Au parameters are fitted to the experimental properties of bulk Pd, Au and features of the bulk Pd–Au phase diagrams; (c) ‘DFT-fit’: the homo- and heteronuclear parameters were fitted to DFT calculations of solid phases.¹⁹

Global structural optimization has been performed using a GA, as encoded in the Birmingham Cluster Genetic Algorithm

(BCGA) program.²⁶ The GA parameters are: population size = 40; crossover rate = 0.8 (*i.e.* 32 offspring are produced per generation); crossover type = 1-point weighted (the splice position is calculated based on the fitness values of the parents); selection = roulette wheel; mutation rate = 0.1; mutation type = mutate_move; number of generations = 400; the number of GA runs for each composition is 100. This high number of GA runs is necessary due to the relatively large size of clusters and the presence of homotops.

For selected compositions, homotop optimization has been performed using the Basin Hopping Monte Carlo algorithm^{30,31} allowing only Pd–Au atom exchange moves,^{31–33} for a fixed structural configuration and composition. Typically, for each size and composition, a search of 50 000 steps at $k_B T = 0.05$ eV has been performed, followed by a final refinement of 20 000 steps at $k_B T = 0.01$ eV.

The 98-atom Leary Tetrahedron (LT) cluster is of interest as it has been discovered by Leary and Doye as the GM for the 98-atom Lennard-Jones cluster (LJ₉₈).³⁵ Furthermore, this structure has also been proposed as the lowest in energy for 98-atom silver clusters, described by the Sutton-Chen (SC) potential and for an aggregate of C₆₀ molecules.³⁶ Paz-Borbon *et al.* have established that the LT is the preferred structure over a wide compositional range for 98-atom Pd–Pt clusters at the Gupta potential level.²² A shell optimization program has been used to generate all possible high symmetry Leary Tetrahedron (LT) isomers, in order to assess how stable this structure is for 98-atom AuPd clusters. A substantial reduction in the search space is obtained if all sets of symmetry-equivalent atoms (*i.e.* ‘atomic shells’ or orbits of the T_d point group) in the LT structure are constrained to be of the same chemical species.³⁴ This reduces the number of inequivalent compositional and permutational isomers (homotops) to 2^S where S is the total number of atomic shells. The 98-atom LT has $S = 9$ shells (in order of increasing distance from the centre of the clusters these shells contain 4 : 12 : 12 : 12 : 4 : 6 : 12 : 12 : 24 atoms) resulting in a total of $2^9 = 512$ LT isomers.²²

DFT calculations were carried out using the Plane Wave Self Consistent Field (PWscf) code in Quantum Espresso (QE).²⁷ Calculations were made using the Perdew–Burke–Ernzerhof (PBE)²⁸ exchange-correlation functional and ultrasoft pseudo-potentials. Following convergence and accuracy tests, the following parameters have been selected: values of 40 and 160 Ry (1Ry = 13.606 eV) were used as the energy cut-off for the

Table 1 Comparison of the Average, DFT-fit and Exp-fit Gupta potential parameters

Parameter	Pd-Pd			Pd-Au			Au-Au		
	Average	DFT-fit	Exp-fit	Average	DFT-fit	Exp-fit	Average	DFT-fit	Exp-fit
A (eV)	0.1746	0.1653	0.171493044	0.19	0.1843	0.2764	0.2016	0.2019	0.209570656
ξ (eV)	1.718	1.6805	1.701873210	1.75	1.7867	2.082	1.79	1.8097	1.815276400
p	10.867	10.8535	11.000	10.54	10.5420	10.569	10.229	10.2437	10.139
q	3.742	3.7516	3.794	3.89	3.8826	3.913	4.036	4.0445	4.033
r_0	2.7485	2.7485	2.7485	2.816	2.8160	2.816	2.884	2.8840	2.884

selection of the plane-wave basis set for the description of the wave function and the electron density respectively. Eigenvalues and eigenstates of the Kohn–Sham Hamiltonian have been calculated at the Gamma point only of a cubic cell of side of approximately 20 Å, applying a Gaussian smearing technique with a broadening of the one-particle levels of 0.03 eV. The DFT local relaxations were performed by fully relaxing the coordinates of the metal atoms until the forces were smaller than 0.1 eV Å⁻¹.

Energetic analysis

The potential energy of a cluster calculated at the Gupta level, V_{clus} , can be written as:

$$V_{\text{clus}} = -NE_{\text{b}}^{\text{Gupta}} \quad (4)$$

where N is the total number of atoms in the cluster and $E_{\text{b}}^{\text{Gupta}}$ is the binding energy per atom of the cluster. For a fixed size of bimetallic clusters, the excess energy (mixing energy), Δ_N^{Gupta} calculated at the empirical level is a useful quantity, described as in eqn (5).²⁵

$$\Delta_N^{\text{Gupta}} = E_N^{\text{Gupta}}(\text{Pd}_m\text{Au}_n) - m \frac{E_N^{\text{Gupta}}(\text{Pd}_m)}{N} - n \frac{E_N^{\text{Gupta}}(\text{Au}_n)}{N} \quad (5)$$

here, $E_N^{\text{Gupta}}(\text{Pd}_m\text{Au}_n)$ represents the total energy of a given cluster calculated at the Gupta level and $E_N^{\text{Gupta}}(\text{Pd}_m)$ and $E_N^{\text{Gupta}}(\text{Au}_n)$ represent the total energies of the GM of the pure metal clusters.

The excess energy quantifies the energy of mixing (the energy associated with alloying) between two different metals. The most negative values of the excess energy indicate the presence of compositions for which mixing between the two metals is most favourable^{18,29} and thus more stable clusters. At the DFT level, the calculated total potential energy of a cluster is E_{clus} and the total energy of a single atom is E_{atom} (corresponding to the atom type present in the cluster, Pd or Au). The average binding energy of a pure N -atom cluster is:

$$E_{\text{b}} = E_{\text{atom}} - \frac{E_{\text{clus}}}{N} \quad (6)$$

The average binding energy of a bimetallic cluster is then given by:

$$E_{\text{b}}^{\text{DFT}} = -\frac{1}{N} [E_{\text{clus}} - mE_{\text{atom}}^{\text{Pd}} - nE_{\text{atom}}^{\text{Au}}] \quad (7)$$

where m , n , $E_{\text{atom}}^{\text{Pd}}$ and $E_{\text{atom}}^{\text{Au}}$ are the numbers of Pd and Au atoms in the cluster and the energies of a single atom of Pd and Au

respectively. $N = m + n$ represents the total number of atoms in a given cluster.

Results and discussions

The energetics of the 98-atom AuPd clusters have been investigated using a combination of BCGA and Basin Hopping Monte Carlo (BHMC) approaches for all the three Gupta potentials. First, the potential energy surface (PES) has been investigated using a GA search for all compositions, $\text{Pd}_m\text{Au}_{98-m}$; then the BHMC approach has been employed in order to optimize the chemical ordering corresponding to the structures located around the minima of the excess energy curves.

Gupta potential with DFT-fit parameters

In Fig. 2, the DFT-fit potential excess energy curve is shown in blue. The lowest values of the excess energy have been found in the compositional range $\text{Pd}_{39}\text{Au}_{59}$ – $\text{Pd}_{59}\text{Au}_{39}$, indicating that these are relatively stable structures. The vast majority of compositions in the range $\text{Pd}_{34}\text{Au}_{54}$ – $\text{Pd}_{74}\text{Au}_{42}$ are Marks Decahedron (M-Dh) structures (see Fig. 3 at Pd_{98}). Several other structural families such as Ino Decahedron (Ino-Dh) (e.g. $\text{Pd}_2\text{Au}_{96}$, $\text{Pd}_{14}\text{Au}_{84}$), incomplete icosahedron (In-Ico) (e.g. $\text{Pd}_{21}\text{Au}_{77}$), FCC (e.g. $\text{Pd}_1\text{Au}_{97}$) and FCC-HCP (e.g. $\text{Pd}_{93}\text{Au}_5$ and Au_{98}) with geometries exemplified in Fig. 3 can also be identified. The Ino-Dh clusters have been also reported for 98-atom Ni clusters modelled by the Sutton-Chen potential.³⁵ Other structures identified as a function of composition are described in detail in ESI S1.†

Gupta potential with Exp-fit parameters

The Exp-fit excess energy curve is shown in red in Fig. 2. For this choice of potential, in terms of structural variety, a structural

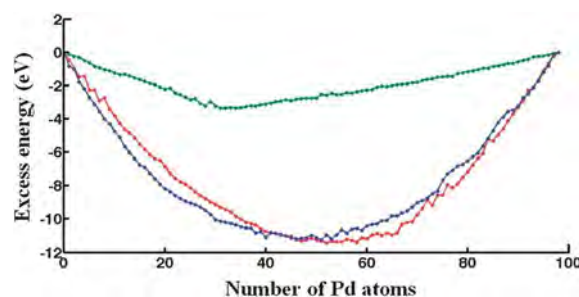


Fig. 2 Excess energy for 98-atom $\text{Pd}_m\text{Au}_{98-m}$ clusters determined for the: DFT fit (blue curve), Exp-fit (red curve) and Average (green curve) Gupta potentials.

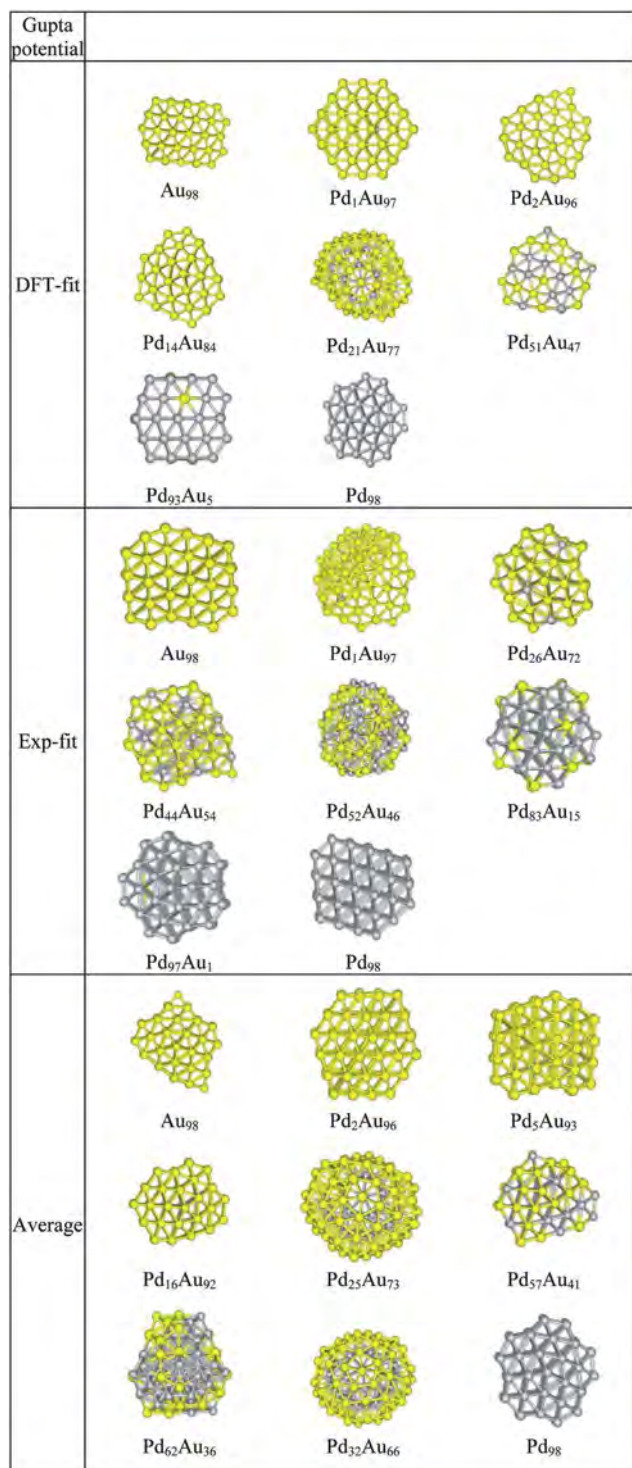


Fig. 3 Structural motifs found for selected Pd_mAu_{98-m} clusters using the three Gupta potentials.

transition from In-Ico to Ino-Dh or M-Dh appears on the left side of the minimum excess energy (*i.e.* biased towards pure Au), from $Pd_{47}Au_{51}$ to $Pd_{24}Au_{64}$ with exceptions including $Pd_{32}Au_{66}$ and $Pd_{45}Au_{53}$ (In-Ico) and $Pd_{37}Au_{61}$ with an FCC-HCP structure (see ESI S2†). The Au_{98} cluster has an FCC-HCP structure, whereas Pd_{98} is FCC-like. These structures are shown in Fig. 3 along with other interesting motifs.

Gupta potential with Average parameters

The excess energy for the Average potential is plotted in Fig. 2 (green curve). Compared with the other two potentials, the values of the excess energies are noticeably less negative and the shape of the curve is quite different. The minimum excess energy is found for $Pd_{32}Au_{66}$. This is an interesting structure, as the 32 Pd atoms sit in the centre of an In-Ico configuration, surrounded by a shell of Au atoms (Fig. 3). Also (see ESI S3†), we notice that Dh structures are predominantly encountered for Pd-rich compositions and there is a general trend of a transition to In-Ico and Dh clusters for Au-rich compositions. From a structural point of view, the pure Au_{98} cluster has a low symmetry Dh structure, whereas Pd_{98} has a M-Dh structure. As we increase the concentration of Au, the Au atoms tend to occupy surface sites forming patches distributed over the cluster surface. Another interesting cluster is $Pd_{62}Au_{36}$ which has a structure based on a fragment of the Leary Tetrahedron (Fig. 3).

It is interesting to note that both DFT-fit and Exp-fit Gupta potentials offered a larger degree of mixing between Pd and Au, than for the Average Gupta potential. This is confirmed by the quantification of the homonuclear and heteronuclear bonds, as shown in ESI S4.† As shown in Table 1, the Exp-fit potential has a pair (repulsive) energy scaling parameter (A) that is larger for Pd–Au than for either Pd–Pd or Au–Au. This has been shown to favour layer segregation in PdPt structures, in the paper of Massen *et al.*³⁷ However, this potential also has a larger value of the many-body energy scaling parameter, ξ , which is greatest for Pd–Au, favouring heteronuclear mixing.¹⁹ The value of the ξ parameter will eventually dominate overall, so the fitted potentials should favour more Pd–Au mixing.

Leary Tetrahedron (LT) clusters

Based on previous studies, the LT structure is difficult to find using the GA program – in the case of PdPt clusters, it is typically found about 1% of the time.²⁵ This is probably due to the existence of a narrower but deeper potential energy basin for the LT structures. The shell program constraints the structure to be LT (and in particular the high symmetry isomers and homotops) such that if the shell program finds (for a given composition) a LT isomer lower in energy than the structure found by

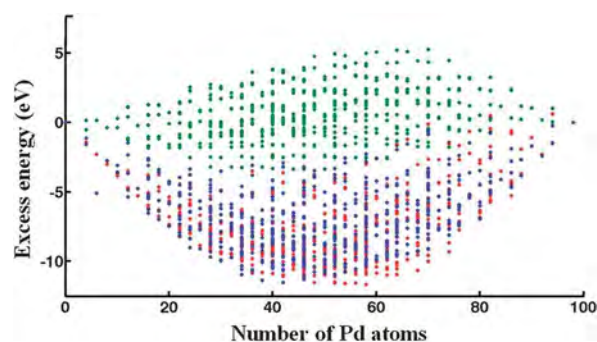


Fig. 4 Plot of the LT excess energy as a function of Pd content for high-symmetry 98-atom clusters modeled by the DFT-fit (blue dots), Exp-fit (red dots), Average (green dots) Gupta potentials.

the GA it shows that the GA obviously has not found the true GM. Possibly there could be a lower structure still – or even a lower symmetry LT – by exchanging positions of unlike atoms. This possibility has been tested using the BHMC technique, with exchange-only moves, as carried out for 98-atom Pd–Pt clusters.²⁵

The excess energy of LT clusters with respect to LT Au₉₈ and Pd₉₈ clusters are plotted in Fig. 4 as a function of Pd content for all three Gupta potentials. After optimization of the chemical ordering, the energies of the LT clusters are in close competition with those of other structural motifs; for example, when using the Average potential, the LT is found to be the lowest energy motif over a broad range, around the 50%/50% composition. Analysis of the LT structures with the lowest excess energies reveal that they possess segregated Pd_{core}Au_{shell} chemical ordering. Segregation of Au atoms to the surface can be rationalized in terms of the lower surface energy and cohesive energy of Au. The smaller atomic radius of Pd also favours Pd occupation of core sites.^{25,38}

DFT relaxation calculations and study of competition between different structural families

GM structures found at the EP level for compositions Pd₄₆Au₅₂–Pd₅₂Au₄₆ (*i.e.* in the region of the minima in the excess energy curves) were relaxed at the DFT level *before* the optimization of the chemical ordering with the BHMC code. The variation of excess energies as a function of number of Pd atoms, calculated at the DFT level (Δ_{98}^{DFT}), is shown in Fig. 5.

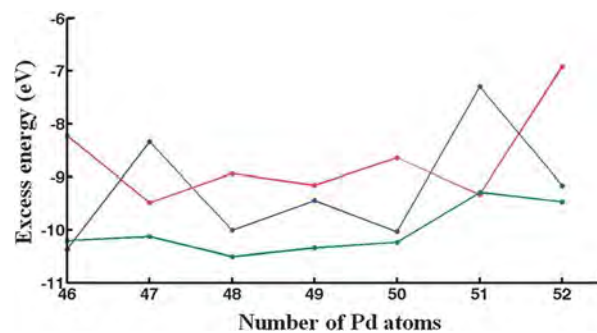


Fig. 5 DFT excess energies of the 'putative' GM for the DFT-fit (blue curve), Exp-fit (red curve) and Average (green curve) Gupta potentials, in the range Pd₄₆Au₅₂–Pd₅₂Au₄₆.

In contrast to the plots of $\Delta_{98}^{\text{Gupta}}$ shown in Fig. 2, which are quite smooth, the Δ_{98}^{DFT} plots are rather jagged, especially for the isomers produced by the DFT-fit and Exp-fit potentials. Fig. 5, shows that the Average potential leads to more negative excess energies at the DFT level for nearly all compositions compared to the DFT-fit and Exp-fit isomers (the exceptions are Pd₄₆Au₅₂, for which the DFT-fit isomer is lower, and Pd₅₁Au₄₇, for which the Exp-fit isomer is lower). As mentioned above, the Average potential stabilises Pd_{core}Au_{shell} homotops in contrast to the DFT-fit and Exp-fit, which prefer more mixed configurations. This is supported by the quantification of the homonuclear and heteronuclear bonds, as shown in ESI S4,[†] as well as the isomers shown in ESI S5.[†] It seem therefore that the Exp-fit and DFT-fit

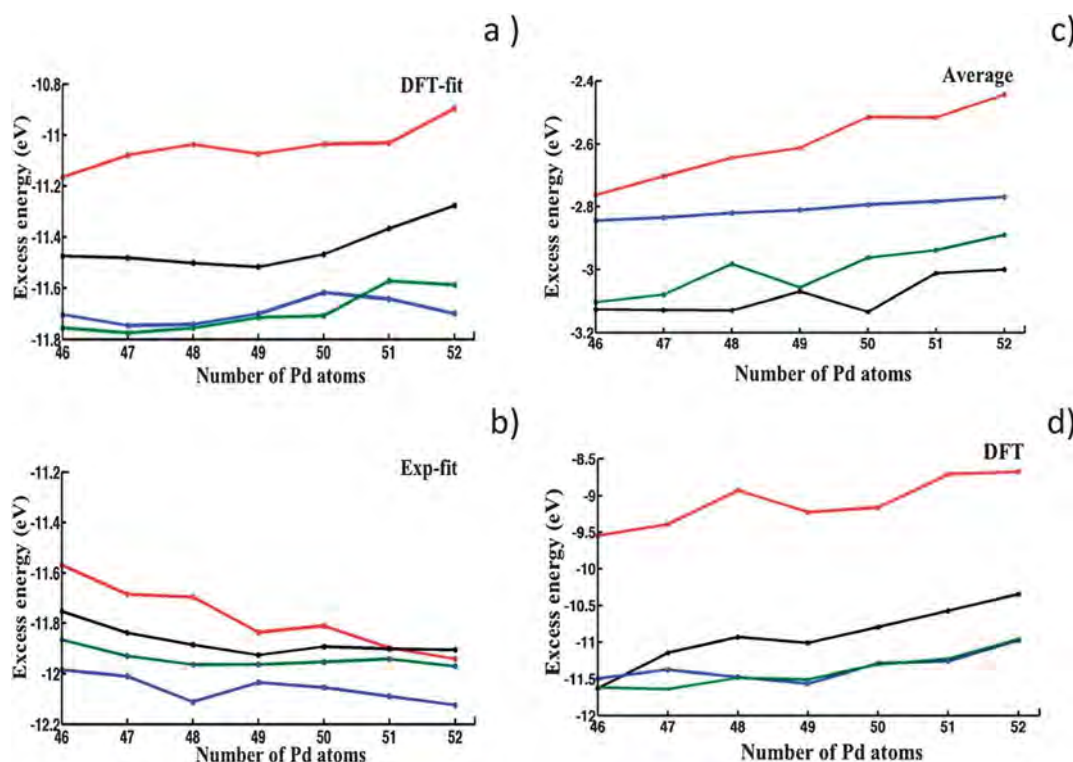


Fig. 6 Excess energy plots comparing LT (black), FCC-HCP (blue), M-Dh (green) and In-Ico (red) structural motifs in the range Pd₄₆Au₅₂–Pd₅₂Au₄₆. (a–c) Results of BHMC optimization of chemical ordering for: (a) DFT-fit; (b) Exp-fit; and (c) Average Gupta potentials. (d) Results of relaxation of Average potential isomers at the DFT level.

potentials overestimate the stability of mixed isomers relative to DFT calculations.

Fig. 6a–c shows the excess energies *after* optimization of chemical ordering for each of the three Gupta potentials, starting from the lowest-energy homotops of each structural motif found in the GA runs (FCC-HCP, M-Dh, In-Ico and LT). For compositions for which these structural motifs have not been found by GA and BH, these have been constructed, and subsequently subjected to BH atom-exchange in order to optimize the chemical ordering.

We have then performed DFT local relaxations on the optimized homotops obtained with the Average potential, with the DFT excess energies shown in Fig. 6d. This is justified because the Average potential was earlier shown to yield homotops with the lowest excess energy values after relaxation at the DFT level (Fig. 5).

In Fig. 6a and b it is interesting to note that, at the EP level, for the DFT-fit and Exp-fit potentials there is a close competition between the FCC-HCP and M-Dh motifs, which are significantly lower in energy than the LT motif by approximately 0.3 eV. The order is reversed for the Average potential (Fig. 6c), for which the LT isomers are competitive with M-Dh but are much lower in energy by 0.3 eV or more than FCC-HCP. All three potentials agree in predicting the In-Ico to lie higher in energy than the other three motifs (apart from the Exp-fit potential which finds In-Ico < LT for the composition Pd₅₂Au₄₆).

As shown in Fig. 6d, DFT relaxation of the structural motifs optimized for the Average potential (see also ESI S5[†]) leads to a change in the stability order, with the lowest excess energies now belonging (as for the DFT-fit and Exp-fit potentials) to the FCC-HCP and M-Dh motifs. It is clear that the LT is destabilised at the DFT level compared to the FCC-HCP and M-Dh structures, though it still lies considerably lower in energy than the In-Ico structures and is almost degenerate with the M-Dh (and lower than FCC-HCP) for Pd₄₆Au₅₂. This theoretical prediction can be directly linked to our experimental study of evaporated AuPd nanoparticles (Fig. 1), where structural motifs such as FCC are often encountered, whereas LT structures have not yet been observed for AuPd nanoparticles.

Conclusions

Three parameter sets (DFT-fit, Exp-fit and Average) have been compared for the Gupta potential in order to study the structures and energetics of 98-atom PdAu nanoclusters. An extensive search of the configurational space has been performed using a genetic algorithm in order to identify the global minimum for all three potentials, at the empirical potential level. It was found that the DFT-fit and Exp-fit potentials favour a higher degree of Pd–Au mixing compared to the Average potential, which favours core–shell configurations – which are in better agreement with DFT calculations. A shell optimization program has been employed to generate Leary Tetrahedron structures, which were found to be the most stable motif for the Average potential. However, Basin Hopping Monte Carlo optimization of the homotops of a number of low-energy structures, followed by DFT relaxation, reveal that the FCC-HCP and Marks Decahedron structural motifs are lower in energy than Leary

Tetrahedron and Icosahedron structures. These observations seem to be consistent with our experimental study of evaporated AuPd nanoparticles.

Acknowledgements

We acknowledge support from the Engineering and Physical Science Research Council (EPSRC), COST Action MP0903: “Nanoalloys as Advanced Materials—from Structure to Properties and Applications”, including COST STSM MP0903-240712-021238. The STEM used in this research was obtained through the Birmingham Science City project “Creating and Characterizing Next Generation Advanced Materials” supported by Advantage West Midlands (AWM) and partly funded by the European Regional Development Fund. Calculations have been performed on the University of Birmingham’s BlueBEAR high performance computer.³⁹ AB thanks Paul West for helpful discussions and valuable advice.

References

- 1 R. Ferrando, J. Jellinek and R. L. Johnston, *Chem. Rev.*, 2008, **168**, 845–910.
- 2 V. Ortalan, A. Uzun, B. C. Gates and N. Browning, *Nat. Nanotechnol.*, 2010, **5**, 843–847.
- 3 T. Shibata, B. A. Bunker, Z. Zhang, D. Meisel, C. F. Vardeman and J. D. Gezelter, *J. Am. Chem. Soc.*, 2002, **124**, 11989–11996.
- 4 J. Huang, T. Akita, J. Faye, T. Fujitani, T. Takei and M. Haruta, *Angew. Chem., Int. Ed.*, 2009, **48**, 7862–7866.
- 5 J. K. Edwards, *Science*, 2009, **323**, 1037–1041.
- 6 H. Zhang, T. Watanabe, M. Okumura, M. Haruta and N. Toshima, *Nat. Mater.*, 2012, **11**, 49–52.
- 7 A. Naitabi and B. R. Cuenya, *Appl. Phys. Lett.*, 2007, **91**, 113110.
- 8 J. Zhang, F. H. B. Lima, M. H. Shao, K. Sasaki, J. X. Wang, J. Hanson and R. R. Adzic, *J. Phys. Chem. B*, 2005, **109**, 22701–22704.
- 9 M. P. Humbert, L. E. Murillo and J. G. Chen, *ChemPhysChem*, 2008, **9**, 1262–1264.
- 10 M. S. Chen, D. Kumar, C. W. Yi and D. W. Goodman, *Science*, 2005, **310**, 291–293.
- 11 J. H. Sinfelt and G. D. Meitzner, *Acc. Chem. Res.*, 1993, **26**, 1–6.
- 12 B. R. Cuenya, *Thin Solid Films*, 2010, **518**, 3127–3150.
- 13 N. T. Tran, D. R. Powell and L. F. Dahl, *Dalton Trans.*, 2004, 217–223.
- 14 R. C. Tiruvalam, J. C. Pritchard, N. Dimitratos, J. A. Lopez-Sanchez, J. K. Edwards, A. F. Carley, G. J. Hutchins and C. J. Kiely, *Faraday Discuss.*, 2011, **152**, 63–86.
- 15 T. Akita, T. Hiroki, S. Tanaka, T. Kojima, M. Kohyama, A. Iwase and F. Hori, *Catal. Today*, 2008, **131**, 90–97.
- 16 D. Ferrer, D. A. Blom, L. F. Allard, S. Mejia, E. P. Tijerina and M. J. Yacaman, *J. Mater. Chem.*, 2008, **18**, 2242–2446.
- 17 L. O. Paz-Borbon, R. L. Johnston, G. Barcaro and A. Fortunelli, *J. Chem. Phys.*, 2008, **128**, 134517.
- 18 R. Ferrando, A. Fortunelli and G. Rossi, *Phys. Rev. B: Condens. Matter Mater. Phys.*, 2005, **72**, 085449.

- 19 F. Pittaway, L. O. Paz-Borbon, R. L. Johnston, H. Arslan, R. Ferrando, C. Mottet, G. Barcaro and A. Fortunelli, *J. Phys. Chem. C*, 2009, **113**, 9141–9152.
- 20 J. Jellinek and E. B. Krisinel, *Theory of Atomic and Molecular Clusters*, Springer, Berlin, 1999.
- 21 R. L. Johnston, *Atomic and Molecular Clusters*, Taylor and Francis, London, 2002.
- 22 L. O. Paz-Borbon, T. V. Mortimer-Jones, R. L. Johnston, A. Posada-Amarillas, G. Barcaro and A. Fortunelli, *Phys. Chem. Chem. Phys.*, 2007, **9**, 5202–5208.
- 23 F. Cleri and V. Rosato, *Phys. Rev. B: Condens. Matter Mater. Phys.*, 1993, **48**, 22–32.
- 24 R. Ismail and R. L. Johnston, *Phys. Chem. Chem. Phys.*, 2010, **12**, 8607–8619.
- 25 L. O. Paz-Borbon, R. L. Johnston, G. Barcaro and A. Fortunelli, *J. Phys. Chem. C*, 2007, **111**, 2936–2941.
- 26 R. L. Johnston, *Dalton Trans.*, 2003, 4193–4207.
- 27 P. Giannozzi, S. Baroni, N. Bonini, M. Calandra, R. Car, C. Cavazzoni, D. Ceresoli, G. L. Chiarotti, M. Cococcioni, I. Dabo, A. D. Corso, D. De Gironcoli, S. Fabris, G. Fratesi, R. Gebauer, U. Gerstmann, C. Gougoussis, A. Kokalj, M. Lazzeri, L. Martin-Samos, N. Marzari, F. Mauri, R. Mazzarello, S. Paolini, A. Pasquarello, L. Paulatto, C. Sbraccia, S. Scandolo, G. Sclauzero, A. P. Seitsonen, A. Smogunov, P. Umari and R. M. Wentzcovich, *J. Phys.: Condens. Matter*, 2009, **21**, 395502.
- 28 J. P. Perdew, K. Burke and M. Erzenhorf, *Phys. Rev. Lett.*, 1996, **77**, 3865.
- 29 A. Rapallo, G. Rossi, R. Ferrando, A. Fortunelli, B. C. Curley, L. D. Lloyd, G. M. Tarbuck and R. L. Johnston, *J. Chem. Phys.*, 2005, **122**, 194308.
- 30 J. Doye and D. Wales, *J. Phys. Chem. A*, 1997, **101**, 5111–5116.
- 31 G. Rossi and R. Ferrando, in *Nanomaterials: Design and Simulation*, ed. P. B. Balbuena and J. M. Seminario, Elsevier, Amsterdam, 2006.
- 32 G. Schmid, A. Lehnert, J. O. Malm and J. O. Bovin, *Angew. Chem., Int. Ed. Engl.*, 1991, **30**, 874–876.
- 33 A. F. Lee, C. J. Baddley, C. Hardacre, R. M. Orneord, R. M. Lambert, G. Schmid and H. West, *J. Phys. Chem.*, 1995, **99**, 6096.
- 34 G. Barcaro, A. Fortunelli, M. Polak and L. Rubinovich, *Nano Lett.*, 2011, **11**, 1766–1769.
- 35 R. H. Leary and J. P. K. Doye, *Phys. Rev. E: Stat. Phys., Plasmas, Fluids, Relat. Interdiscip. Top.*, 1999, **60**, R6320.
- 36 J. P. K. Doye, D. J. Wales, W. Branz and F. Calvo, *Phys. Rev. B: Condens. Matter Mater. Phys.*, 2001, **64**, 235409.
- 37 C. Massen, T. V. Mortimer-Jones and R. L. Johnston, *J. Chem. Soc., Dalton Trans.*, 2002, **23**, 4375–4388.
- 38 G. Rossi, R. Ferrando, A. Rapallo, A. Fortunelli, B. C. Curley, L. D. Lloyd and R. L. Johnston, *J. Phys. Chem.*, 2005, **122**, 194309.
- 39 <http://www.bluebear.bham.ac.uk>.

